



HAL
open science

Design and reactivity of homogeneous and surface-supported heterobimetallic aluminum/iridium complexes for cooperative catalysis

Léon Escomel

► **To cite this version:**

Léon Escomel. Design and reactivity of homogeneous and surface-supported heterobimetallic aluminum/iridium complexes for cooperative catalysis. Catalysis. Université Claude Bernard - Lyon I, 2022. English. NNT: 2022LYO10061 . tel-04745589

HAL Id: tel-04745589

<https://theses.hal.science/tel-04745589v1>

Submitted on 21 Oct 2024

HAL is a multi-disciplinary open access archive for the deposit and dissemination of scientific research documents, whether they are published or not. The documents may come from teaching and research institutions in France or abroad, or from public or private research centers.

L'archive ouverte pluridisciplinaire **HAL**, est destinée au dépôt et à la diffusion de documents scientifiques de niveau recherche, publiés ou non, émanant des établissements d'enseignement et de recherche français ou étrangers, des laboratoires publics ou privés.



THESE de DOCTORAT DE L'UNIVERSITE CLAUDE BERNARD LYON 1

Ecole Doctorale ED 206
Ecole doctorale de Chimie de Lyon

Discipline : Chimie organométallique de surface et catalyse

Soutenue publiquement le 18/10/2022, par :
Léon ESCOMEL

Design and reactivity of homogeneous and surface-supported heterobimetallic aluminum/iridium complexes for cooperative catalysis

Devant le jury composé de :

Pr. Abderrahmane AMGOUNE
Pr. Marine DESAGE-EL MURR
Pr. Stephan HOHLOCH
Dr. Narcis AVARVARI
Dr. Chloé THIEULEUX
Dr. Clément CAMP

Université Claude Bernard Lyon 1
Université de Strasbourg
University of Innsbruck
CNRS-UMR 6200-Angers
CNRS-UMR 5128-Villeurbanne
CNRS-UMR 5128-Villeurbanne

Président
Rapportrice
Rapporteur
Examineur
Directrice
Co-directeur

Abstract

The association of two distinct metals in a given complex, exhibiting intermetallic interactions, and immobilized on a solid support is an open door to new perspectives. These so called heterobimetallic architectures take advantages of metal-metal and metal-support cooperation effects that can enhance a given chemical transformation or promote new and original modes of reactivity. This PhD work is included in this context and aims to increase our fundamental understanding of heterobimetallic entities and especially homogeneous and surface-supported aluminum-iridium edifices for cooperative reactivity and catalysis. In order to selectively assemble the two metal centers, two synthetic approaches have been used in this project: the first is based on a bifunctional alkoxy-NHC (N-Heterocyclic carbene) ligand. This strategy successfully led to a series of monometallic alkyl-Al(NHC) species where a competitive reactivity between NHC and alkyl protonolysis is noticed. This metal-ligand cooperation is interesting but limits the access to heterobimetallic species. That is why we paid a particular attention to another approach: the alkane elimination. The reaction between an acidic iridium-hydride precursor (IrCp^*H_4) and basic isobutyl aluminum (III) derivatives led to the liberation of isobutane gas and to the formation of a series of heterobimetallic Al-Ir species with various nuclearities and topologies. Reactivity studies were undertaken to get insights into the nature of the Ir-Al interactions. These investigations especially revealed strongly polarized $\text{Ir}^{\delta-}\text{Al}^{\delta+}$ pairs that are capable to promote unconventional bimetallic reductive cleavage of heteroallenes such as CO_2 or R-NCO . Armed with a robust understanding about the behaviors of these molecular complexes, we transposed this knowledge to the surface organometallic chemistry (SOMC) area. Notably, the direct grafting of a tetranuclear $[\text{Ir}_3\text{Al}]$ cluster $-\{\text{Ir}(\text{Cp}^*)(\text{H})(\mu\text{-H}_2)\}_3\text{Al}$ – onto the surface of a mesostructured silica (SBA-15) support produced a new well-defined $\text{Ir}_2\text{-Al}$ site. The post-treatment (heating, H_2) of this surface species led to the formation of small Ir(o) nanoparticles (NPs) homogeneously distributed on the silica surface and surrounded with interfacial Al(III) sites. This heterobimetallic material exhibited enhanced catalytic performances for the hydrogen/deuterium exchange of methane compared to its monometallic iridium analogue, showing a promoting effect of the Al(III) site on the Ir(o) NPs.

Keywords

Heterobimetallic complexes, aluminum, NHCs, iridium, hydrides, cooperative reactivity, surface organometallic chemistry, nanoparticles, H/D exchange of methane.

Laboratory

Catalysis, Polymerization, Processes and Materials (CP2M)
UMR 5128
43 Bd du 11 Nov. 1918 (B. P. 82007)
69616 Villeurbanne CEDEX FRANCE.

Résumé

L'association de deux métaux distincts dans un complexe donné, présentant des interactions intermétalliques, et immobilisés sur un support solide est une porte ouverte à de nouvelles perspectives. Ces architectures dites hétérobiméalliques tirent profit d'effets de coopération métal-métal et métal-support pouvant améliorer une transformation chimique donnée ou promouvoir des modes de réactivité nouveaux et originaux. Cette thèse s'inscrit dans ce contexte et vise à accroître notre compréhension fondamentale des entités hétérobiméalliques et en particulier des édifices aluminium-iridium homogènes et supportés pour de la réactivité et de la catalyse coopérative. Afin d'assembler sélectivement les deux métaux, deux approches synthétiques ont été utilisées : la première est basée sur un ligand bifonctionnel alkoxy-NHC (*N-Heterocyclic carbene*). Cette stratégie a permis le développement d'espèces alkyl-Al(NHC) où une réactivité compétitive entre la protonolyse du NHC et de l'alkyle est montrée. Cette coopération métal-ligand est intéressante mais limite l'accès aux espèces hétérobiméalliques. Pour cette raison, nous avons opté pour une autre approche : l'élimination d'alcane. La réaction entre un précurseur acide d'hydrures d'iridium (IrCp^*H_4) avec des dérivés basiques d'isobutylaluminium (III) a conduit au dégagement d'isobutane et à la formation d'une série d'espèces hétérobiméalliques Al-Ir de nucléarités et de topologies variables. Des études de réactivité ont été menées afin de mieux comprendre la nature des interactions Ir-Al. Ces investigations ont notamment révélé des paires $\text{Ir}^{\delta-}\text{Al}^{\delta+}$ fortement polarisées capables de promouvoir un clivage réducteur biméallique non conventionnel d'hétéroallènes tels que le CO_2 ou le R-NCO. Forts d'une compréhension du comportement de ces complexes moléculaires, nous avons transposé ces connaissances au domaine de la chimie organométallique de surface (COMS). Notamment, le greffage direct d'un cluster tétranucléaire $[\text{Ir}_3\text{Al}] - [\{\text{Ir}(\text{Cp}^*)(\text{H})(\mu\text{-H}_2)\}_3\text{Al}]$ - sur la surface d'une silice mésostructurée (SBA-15) a produit à un nouveau site $[\text{Ir}_2\text{-Al}]$ de surface bien défini. Le post-traitement (chauffage, H_2) de cette espèce de surface a conduit à la formation de petites nanoparticules (NPs) de Ir(o) distribuées de manière homogène sur le support et entourées de sites interfaciaux Al(III). Ce solide à sites de surface hétérobiméalliques présente de meilleures performances catalytiques pour l'échange H/D du méthane que son analogue monométallique d'iridium, montrant un effet promoteur du site Al(III) sur les NPs d'Ir(o).

Mots-clés

Complexes hétérobiméalliques, aluminium, NHCs, iridium, hydrures, réactivité coopérative, chimie organométallique de surface, nanoparticules, échange H/D du méthane.

Laboratoire

Catalyze, Polymérisation, Procédés et Matériaux (CP2M)
UMR 5128
43 Bd du 11 Nov. 1918 (B. P. 82007)
69616 Villeurbanne CEDEX FRANCE.

Résumé Substantiel

La ligne directrice de ce projet de thèse est d'accroître notre compréhension fondamentale de la chimie des architectures hétérobimétalliques homogènes et supportées sur la surface d'une silice mésostructurée. Ce projet s'est particulièrement concentré sur la construction et l'étude d'édifices aluminium/iridium (Figure R1).

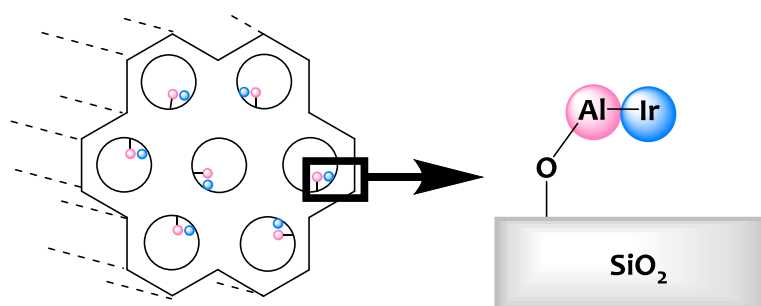


Figure R1. Structure générale représentant les édifices aluminium/iridium visés.

L'une des frontières actuelles de la chimie organométallique est l'étude de l'action combinée de deux centres métalliques afin de promouvoir de nouveaux modes de réactivité dans lesquels les deux partenaires métalliques agissent en synergie, en vue d'accéder à une chimie impossible avec des espèces monométalliques.^[1-6] De tels phénomènes de coopérativité métal-métal ont été proposés depuis longtemps pour expliquer les propriétés et les modes d'action de certains sites actifs d'enzymes, de catalyseurs hétérogènes et de complexes hétérobimétalliques. Cependant, la nature exacte des espèces impliquées est souvent mal connue ou mal définie et les mécanismes à l'origine des effets synergiques peuvent être d'origines très diverses et restent mal compris. Compte tenu de la diversité des combinaisons offertes par le tableau périodique et de la richesse des structures possibles, le champ des possibilités est immense. Il s'agit donc d'un champ d'étude extrêmement ouvert et prometteur, qui ne fait qu'émerger.

Ce projet de thèse s'inscrit dans ce contexte et vise à développer et étudier des espèces hétérobimétalliques associant un métal oxophile à un métal de transition tardif. Compte tenu du tout nouveau regain d'intérêt pour les complexes associant l'aluminium à des métaux du bloc d et présentant une chimie originale et peu commune,^[7,8] ce projet s'est concentré sur l'aluminium comme premier partenaire métallique dur et oxophile. D'autre part, en vue de leur éminence dans les domaines de la recherche universitaire et industrielle, en particulier dans le domaine de la catalyse organométallique, nous avons porté notre attention sur l'iridium comme deuxième partenaire métallique mou.^[9]

Sur un autre plan, ce projet s'intéresse au greffage de ces espèces hétérobimétalliques moléculaires sur la surface d'une silice mésostructurée (SBA-15) en utilisant une stratégie de chimie organométallique de surface (COMS). En plus des avantages inhérents à la catalyse hétérogène, l'avantage de l'approche COMS est de tirer parti du support solide pour accéder à des espèces faiblement coordonnées conduisant à des réactivités nouvelles.^[10-13] Ces espèces de surface hautement réactives n'ont pas d'équivalents moléculaires et ne pourraient pas être stabilisées en solution. A ce jour, les études de COMS se sont principalement concentrées sur des composés monométalliques. Un des axes de ce projet de thèse est donc de développer de nouvelles approches méthodologiques combinant les connaissances et les compétences de la chimie organométallique moléculaire afin de préparer des espèces hétérobimétalliques originales de manière propre et sélective, puis de transposer ces concepts à la COMS afin de diriger sélectivement l'assemblage des deux centres métalliques. Deux stratégies complémentaires ont été employées dans ce projet.

Stratégie 1. L'utilisation de ligands bifonctionnels possédant deux types de fonctions de coordination différents, l'un, de type dur, capable de former une liaison forte avec un métal dur (tel qu'un métal à transition précoce ou oxophile) et l'autre, de type mou, capable de former une liaison forte avec un métal à transition tardive, a grandement contribué au développement de complexes hétérobimétalliques originaux.^[14-17] Ceci est particulièrement vrai pour les systèmes hétérobimétalliques associant l'aluminium à un métal du bloc d comme explicité dans l'introduction de ce manuscrit (voir chapitre 1, partie 1.2.1.1 - page 23).

Bien que différents types de donneurs aient été utilisés pour coordiner le centre métallique dur, la littérature montre une omniprésence des ligands phosphines pour le métal tardif. Les carbènes N-hétérocycliques (NHCs), capables de former des liaisons fortes avec de nombreux métaux, et dont l'intérêt en tant que ligand en catalyse homogène n'est plus à démontrer, constituent une alternative intéressante. Récemment au laboratoire, nous avons développé un ligand de type alcoxy-carbène (NHC-OH) et des premiers résultats encourageants ont démontré l'intérêt de cette plateforme pour coordiner à la fois des métaux précoces (Ta) et tardifs (Rh) aboutissant à une série de composés monométalliques et hétérobimétalliques.^[18-20]

Dans la continuité de ces travaux préliminaires, nous avons exploré dans un premier temps la réactivité de ce ligand bifonctionnel avec des précurseurs aluminium-alkyles et des métaux de transition tardifs afin d'accéder à des complexes hétérobimétalliques. Dans un premier temps, lors que ce ligand est mis en contact avec des dérivés aluminium-alkyles, réactivité compétitive entre les unités NHC et alcool - O-H - est observée (Schéma R1). Cette compétition s'avère être régulée par le profil stérique du dérivé d'aluminium utilisé. Ainsi, cette première étude a permis de

mettre en évidence le caractère non-innocent de la liaison aluminium-carbène dans ces systèmes et montre une coopérativité métal-ligand originale.^[21] Ces résultats fournissent des indications précieuses sur la chimie des Al-NHC. Cependant, cette réactivité montre aussi certaines limitations concernant la réactivité de ces espèces telle que la difficulté d'accès à des espèces hétérobimétalliques car un seul complexe hétérobimétallique Al/Cu a pu être mis en évidence dans cette étude. C'est pourquoi, nous nous sommes ensuite intéressés à une autre approche pour accéder à des complexes hétérobimétalliques : l'élimination d'alcane.

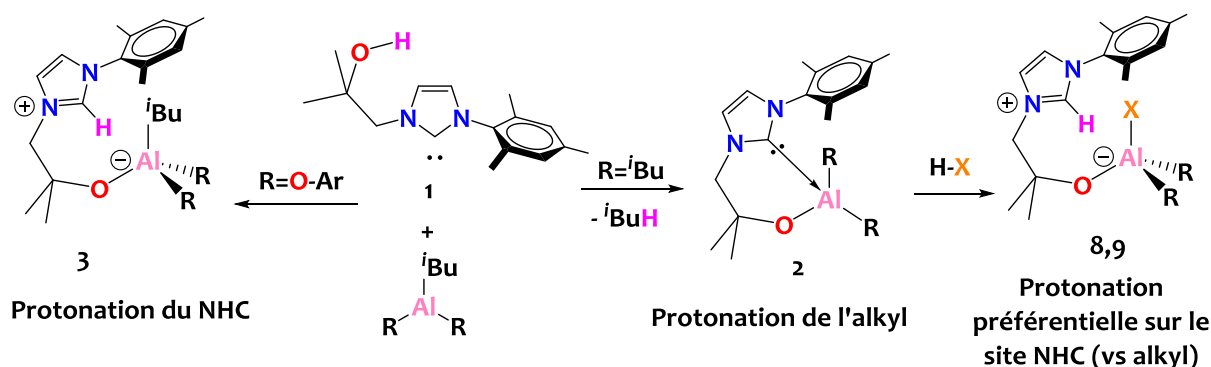


Schéma R1. Réactivité du ligand bifonctionnel NHC-OH (composé 1) avec aluminium-alkyles.^[21]

Stratégie 2. L'utilisation d'une voie d'élimination (réductrice) d'alcane entre un hydrure métallique acide et un métal-alkyle basique (au sens de Brønsted) pour accéder à des composés hétérobimétalliques avec une liaison métal-métal s'avère être une méthodologie de synthèse très efficace. Cette approche présente l'avantage supplémentaire de ne générer comme sous-produits que des alcanes volatiles, inertes et facilement éliminables. Enfin, cette voie de synthèse permet d'obtenir des espèces faiblement coordinées et très réactives. Il est important de mentionner que ce n'est pas le cas de la **stratégie 1**, qui est basée sur l'utilisation de ligands encombrants et chélatants pour ponter les deux métaux et stabiliser ce type d'édifice hétérobimétallique, empêchant ainsi l'approche et la coordination concertées de substrats sur les deux centres métalliques et réduisant fortement la réactivité de ces dérivés. De manière assez inattendue, la **stratégie 2** n'est qu'au stade de l'enfance.^[22,23] En effet, elle s'avère quasiment inexplorée pour les couples métalliques associant l'aluminium à un métal du bloc d.^[24-26] Par exemple, cette stratégie de synthèse a été récemment utilisée avec succès en laboratoire pour isoler sélectivement une première génération de complexes hétérobimétalliques tantale-iridium avec de bons rendements en faisant réagir des précurseurs tantale-alkyles/alkylidène - $\text{Ta}(\text{CH}^t\text{Bu})(\text{CH}_2^t\text{Bu})_3$ - avec un réactif polyhydrure d'iridium IrCp^*H_4 .^[27-29]

Inspiré par ces travaux prometteurs, nous avons étendu avec succès cette stratégie pour la préparation d'une nouvelle famille d'espèces hétérobimétalliques iridium-aluminium à partir de

dérivés aluminium-isobutyles et du précurseur IrCp^*H_4 (Schéma R2).^[30,31] Ici, les hydrures d'iridium sont suffisamment acides pour induire un clivage de la liaison isobutyl-aluminium (base de Brønsted) conduisant à des espèces Al-Ir présentant des interactions intermétalliques directes et au dégagement gazeux d'isobutane. En outre, les complexes hétérobimétalliques obtenus ont été caractérisés à l'état solide par diffraction aux rayons X (DRX) et analyse élémentaire ainsi qu'en solution par spectroscopie RMN multi-noyaux et IR. Des calculs computationnels de type DFT ont également été réalisés pour confirmer ces structures. Les résultats de ces analyses montrent que ces espèces hétérobimétalliques présentent des interactions $\text{Ir}^{\delta-}\text{-Al}^{\delta+}$ fortement polarisées qui sont décrites par : Des liaisons à 3 centres et 2 électrons - 3c-2e (Ir-H-Al) - avec une donation électronique du centre Ir vers le centre Al.

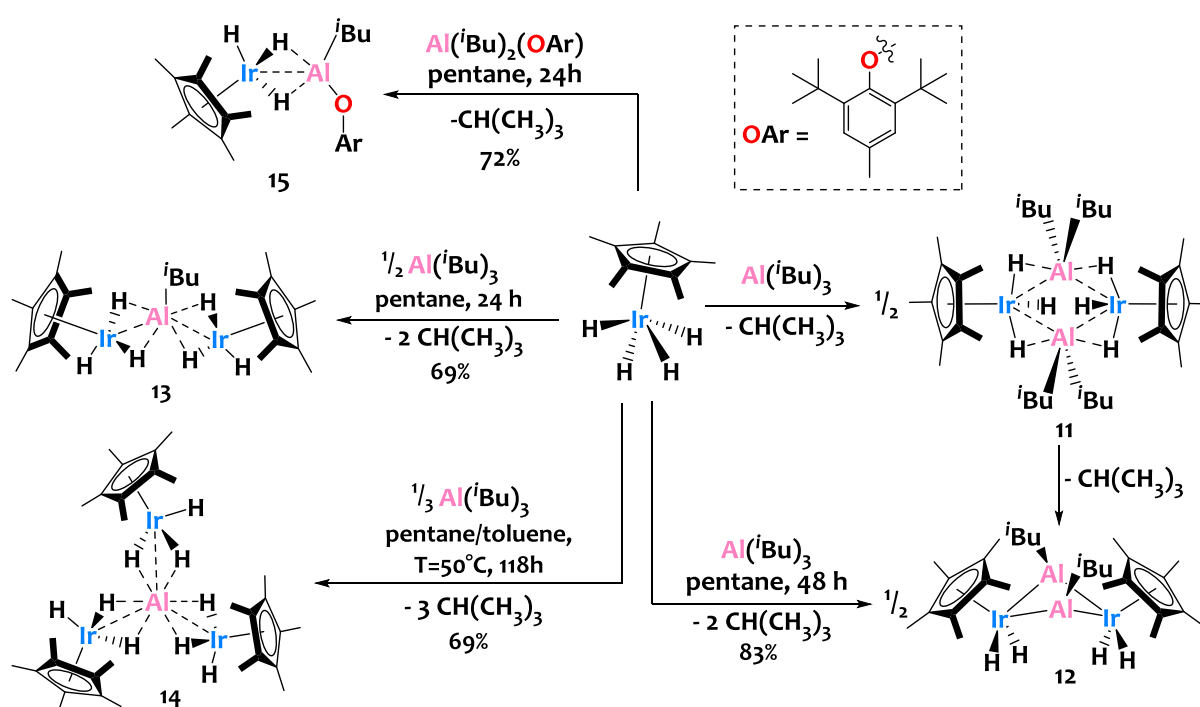


Schéma R2. Réactivité de IrCp^*H_4 avec des dérivés aluminium-isobutyles produisant des complexes hétérobimétalliques Ir-Al ayant une topologie variée.^[30,31]

Afin de mieux comprendre la nature des interactions bimétalliques Ir-Al, nous avons étudié leur réactivité vis-à-vis de divers réactifs dans un troisième temps. Une première série d'expériences a révélé que le centre Al de ces systèmes est hautement électrophile et peut réagir avec des bases de Lewis comme la pyridine ou des nucléophiles tel que l'anion benzylate (voir Schéma R3).

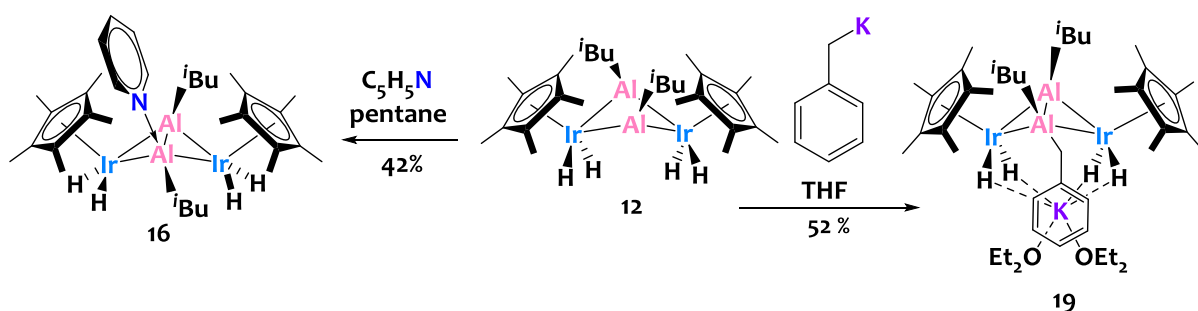


Schéma R3. Réactivité du cluster 12 avec la pyridine et le benzylate de potassium montrant le caractère électrophile du centre aluminium.

De plus, les hydrures de ces espèces ne sont plus acides (pas de déprotonation avec des bases fortes de Brønsted). Au contraire, les unités Ir-Al sont réactives et peuvent être soumises à des réactions de transmétallation avec l'argent ou le potassium par exemple. Il est important de noter qu'aucun comportement redox n'a été observé pour ces complexes lors de leur réaction avec des agents redox communs tel que le triflate d'argent(I) (voir Schéma R4).

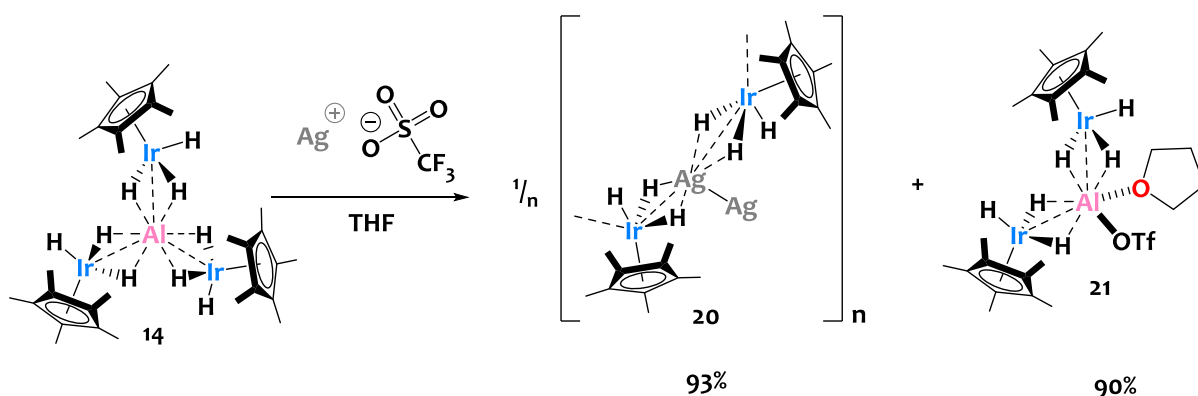


Schéma R4. Réactivité du cluster 14 avec le triflate d'argent (I).

Finalement, une activation coopérative bimétallique originale d'hétéroallènes (CO_2 , R-NCO , R-NCN-R) a été mise en évidence. Par exemple, le complexe $\text{Cp}^*\text{IrH}_3\text{-Al}(\text{iBu})(\text{OAr})(\text{Py})$ est capable de promouvoir le clivage réducteur coopératif du dioxyde de carbone en CO (piégé en tant que dihydrures d'iridium carbonyle) et O_2^- (piégé en tant qu'une espèce oxo d'aluminium dimérique) par des voies réactionnelles hétérobimétalliques peu communes (Schéma R5).

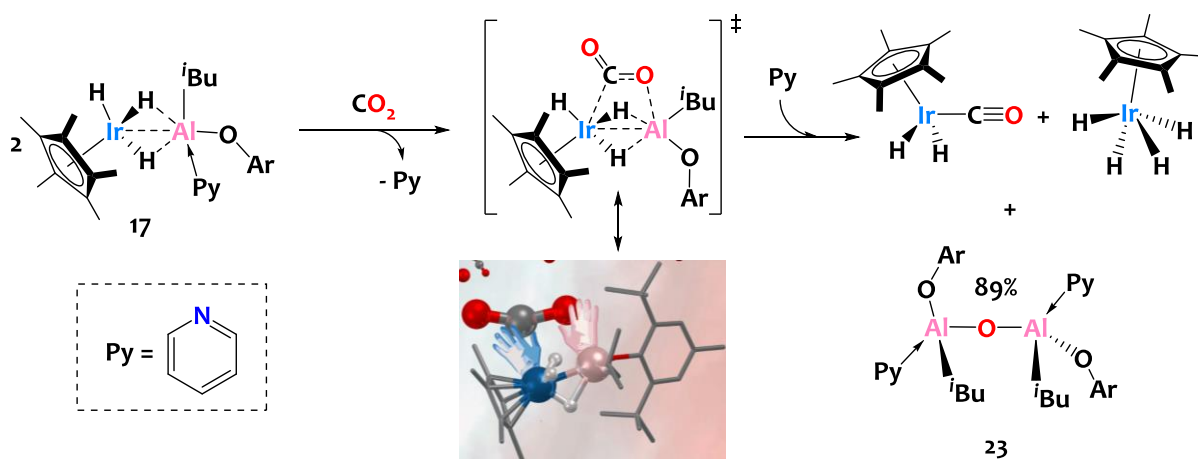


Schéma R5. Réactivité du complexe hétérobimétallique 17 avec le CO₂.

Forts d'une compréhension approfondie du comportement de ces espèces Ir-Al, nous avons envisagé dans un quatrième temps de transposer ces connaissances dans le domaine de la chimie organométallique de surface.

Ce raisonnement avait également été utilisé dans notre laboratoire sur les composés Ta/Ir mentionnés ci-dessus. En effet, le greffage de ces espèces sur une silice de type SBA-15 déshydroxylée à T=700°C- SBA-15₇₀₀ - avait permis d'obtenir de nouvelles espèces Ta/Ir de surface, qui ne pouvaient être obtenues en solution. Ces espèces supportées sont plus de 100 fois plus actives en catalyse d'échange H/D d'arènes (TON et TOF) que leurs analogues moléculaires en solution et démontrent ainsi l'intérêt de combiner les coopérativités métal-métal et métal-support. [27-29]

Parallèlement, la préparation de petites nanoparticules (NPs) contenant des métaux tardifs (Rh, Ir ou Pt) distribuées de manière homogène sur la surface d'un support (silice ou alumine) par une approche SOMC a été décrite. [32-34]. Certaines de ces études reportent des systèmes hétérobimétalliques comprenant des nanoparticules supportés (sous forme monométallique ou d'alliages) entourés de sites monométalliques interfaciaux. De tels systèmes s'avèrent très intéressants car ils combinent les avantages de l'utilisation de nanoparticules métalliques, d'espèces hétérobimétalliques et de sites supportés en surface bien définis permettant de catalyser des transformations très difficiles (comme par exemple la réduction du CO₂ ou la déhydrogénation du propane). [32,35-38]

Ainsi, dans la continuité de ce qui a été réalisé précédemment dans notre laboratoire concernant l'approche SOMC pour les systèmes hétérobimétalliques, et en s'inspirant des études susmentionnées sur les NPs, nous avons étudié le greffage par voie COMS des complexes Ir-Al susmentionnés et leur possible transformation en NPs sous traitement réducteur. Pour ce faire, nous nous sommes intéressés dans un premier temps à la réactivité des espèces Ir-Al avec des

modèles moléculaires mimant la surface d'une silice. Ces études ont révélé que seule l'espèce $[\{\text{Ir}(\text{Cp}^*)(\text{H})(\mu\text{-H}_2)\}_3\text{Al}]$ (composé **14**) est approprié pour réaliser un greffage propre et quantitatif sur un support silicique de type SBA-15. En conséquence, nous avons conçu une nouvelle espèce supportée hétérobimétallique bien définie - $[\equiv\text{SiOAl}\{(\mu\text{-H})_2\text{Ir}(\text{H})\text{Cp}^*\}_2]$, matériau **27** (voir Schéma R6) - dont la structure a été confirmée par spectroscopie IR et RMN à l'état solide, analyse élémentaire, et par la conception de son analogue moléculaire - $[\{(\text{Ir}(\text{Cp}^*)(\text{H})(\mu\text{-H}_2))_2\text{Al}(\text{OAr}')\}]$ (voir en haut du Schéma R6).^[39] La stabilité thermique du site $[\equiv\text{SiOAl}\{(\mu\text{-H})_2\text{Ir}(\text{H})\text{Cp}^*\}_2]$ sous H_2 a également été étudiée et a révélé la possibilité de former un nouveau matériau - noté Ir-Al/SiO₂, matériau **28** (voir Schéma R6, à droite) - caractérisé par de petites nanoparticules de Ir(o) bien dispersées sur la surface de la silice et entourées de sites interfaciaux d'Al(III). Afin de fournir un matériau analogue contenant des NPs monométallique d'iridium, nous avons également conçu un nouveau matériau, noté Ir/SiO₂, matériau **30** - à partir du précurseur IrCp*H₄ en utilisant une approche d'imprégnation à humidité naissante (IWI) suivi d'un post-traitement thermique sous H_2 (voir Schéma R6, en bas). L'analyse des matériaux Ir-Al/SiO₂ et Ir/SiO₂ par des techniques avancées (STEM, chimisorption, XPS) ont révélé que les nanoparticules d'iridium avaient des caractéristiques similaires (taille, dispersion et nature de la surface).^[39]

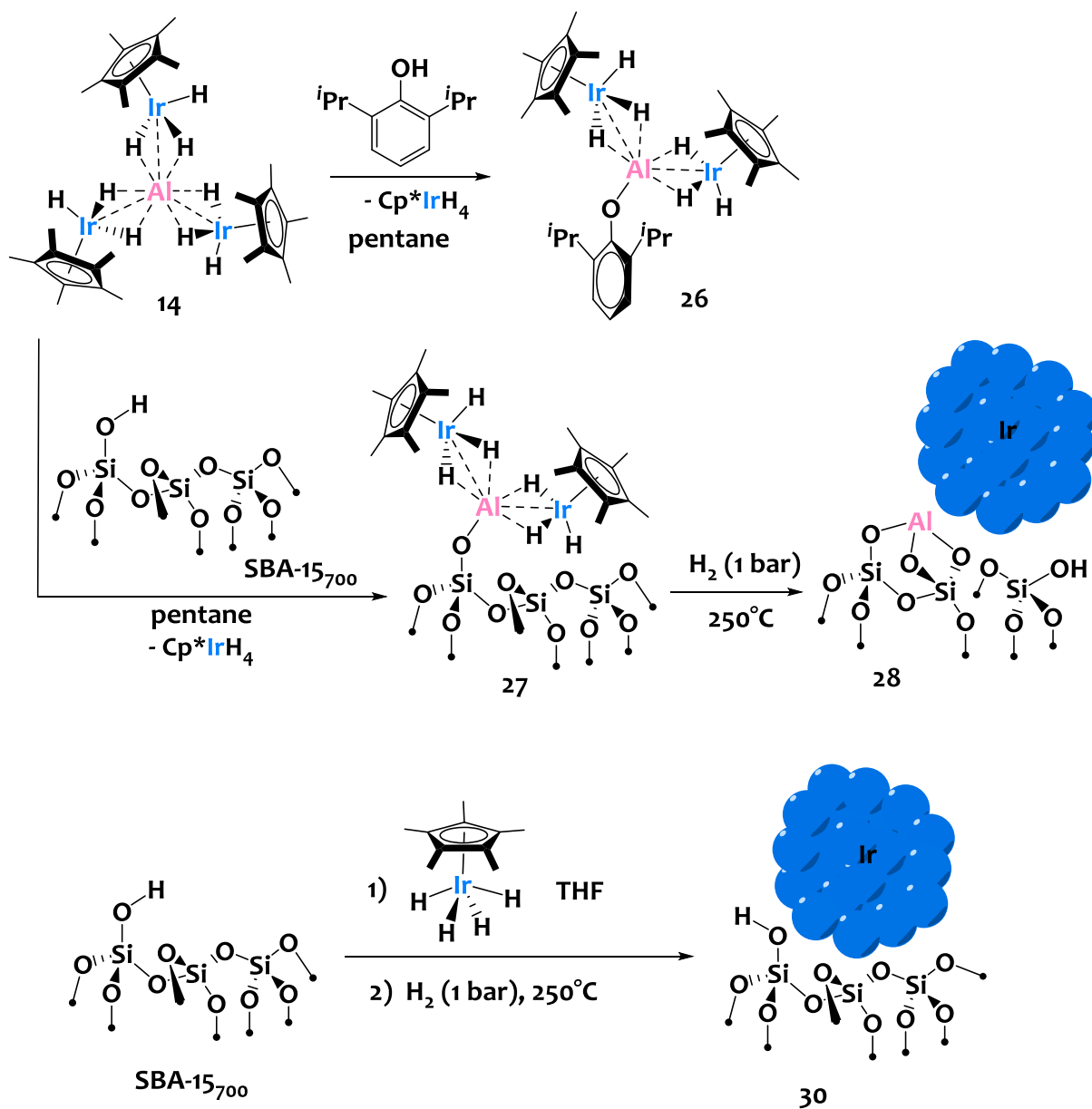


Schéma R6. Préparation de sites Ir-Al et Ir de surface et formation de nanoparticules.^[39]

Nous avons ensuite étudié les performances catalytiques des matériaux Ir-Al/SiO₂ et Ir/SiO₂ en réaction d'échange isotopique hydrogène/deutérium du méthane (Schéma R7). Ces travaux ont montré des performances catalytiques accrues du matériau Ir-Al/SiO₂ par rapport à son analogue monométallique Ir/SiO₂ (Figure R2). Ainsi, cette observation a mis en évidence l'effet promoteur des sites Al(III) et démontre l'intérêt d'ajouter un acide de Lewis à proximité des nanoparticules métalliques.^[39] De plus, les matériaux Ir-Al/SiO₂ et Ir/SiO₂ sont stables à l'air et robustes dans ces conditions expérimentales. Ainsi, cela représente une plus-value importante par rapport aux hydrures métalliques supportés sur silice qui sont connus pour être hautement sensibles à l'air et désactiver facilement.^[40,41]

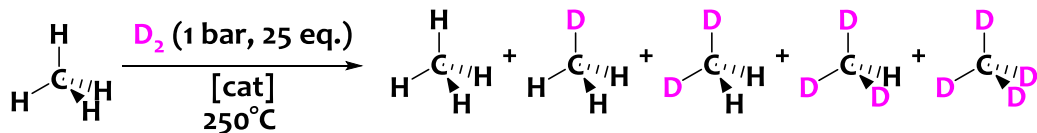


Schéma R7. Deutération du méthane (≈ 40 mbars) en isotopomères $\text{CH}_{4-x}\text{D}_x$ à $T=250^\circ\text{C}$ en utilisant le gaz D_2 (≈ 1020 mbars) comme source de deutérium.

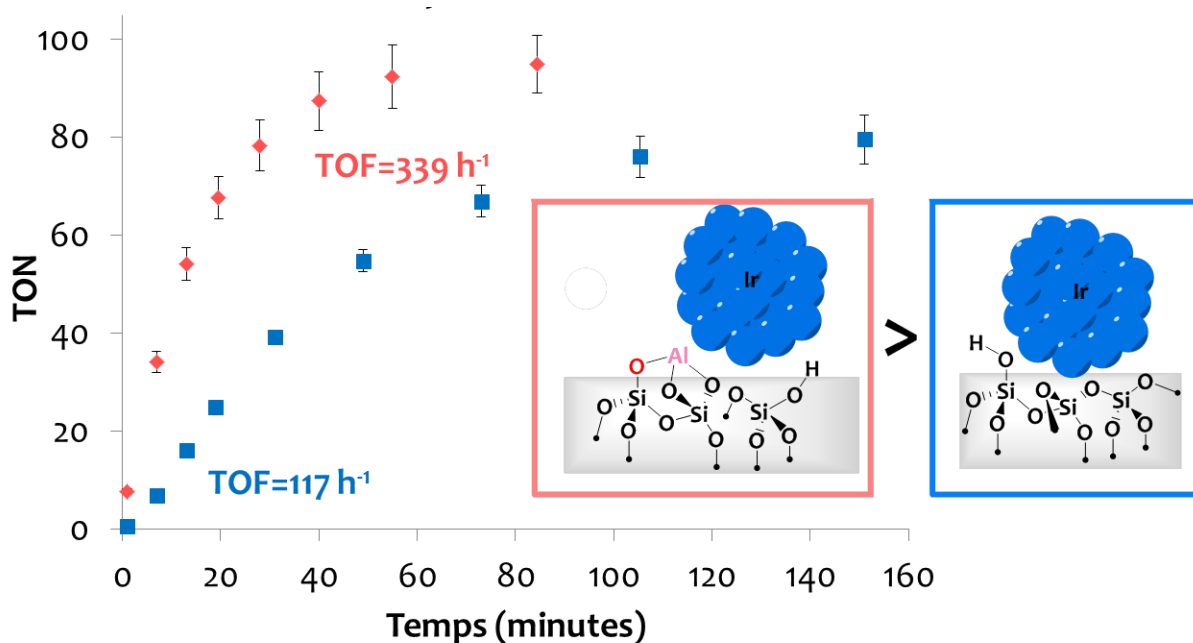


Figure R2. Suivi de l'échange H/D catalytique du méthane. TON en fonction du temps de réaction pour les catalyseurs Ir-Al/SiO₂ (diamants bleus) et Ir/SiO₂ (carrés rouges) à 250°C et 0,67 mol% de sites de surface Ir. Toutes les données ont été extraites en faisant la moyenne des calculs de Dibeler-Mohler^[42] et Schoofs.^[43] Les barres d'erreur tiennent compte de l'incertitude sur la charge du catalyseur et sur l'écart type entre les calculs de Dibeler-Mohler et de Schoofs.

En conclusion, ce projet de thèse nous a permis de poser de nouvelles pierres angulaires dans l'édifice de la chimie hétérobimétallique moléculaire et de surface et en particulier la chimie associant l'aluminium et l'iridium. Plus précisément, ce travail a mis en évidence des coopérativités aluminium-iridium originales, capables de favoriser des réactivités stœchiométriques inédites et pouvant être utilisées pour améliorer des transformations catalytiques.

Aussi, dans la continuité de deux récents travaux de doctorat menés dans notre laboratoire sur ce type de chimie, ce projet de thèse incarne un véritable tremplin vers un nouveau champ d'investigations. Parmi les pistes à explorer dans le futur afin d'approfondir et d'étendre ce travail, nous pouvons citer :

- (i) L'extension de la **stratégie 1** - ligand bifonctionnel - à la génération d'autres types de ponts bifonctionnels et à la préparation d'autres couples acides de Lewis/métaux du bloc d.

(ii) l'extension de la **stratégie 2** - l'élimination des alcanes - pour la synthèse d'autres couples métal-hydrures tardif/métal-alkyles dur.

(iii) Le développement de la chimie hétérobimétallique de surface à d'autres (pré)assemblages hétérobimétalliques appropriés.

(iv) l'extension de l'approche SOMC/post-traitement à d'autres sites hétérobimétalliques de surface pour former des nanoparticules de métal(o) supportées par de la silice et entourées de sites interfaciaux monométalliques.

(v) l'extension des réactivités stœchiométriques et catalytiques de ces espèces hétérobimétalliques à un plus large éventail de substrats et de réactions afin de démontrer l'applicabilité plus large de ces constructions et d'établir des relations structure-activité robustes pour mieux comprendre leur comportement synergique.

Références

- [1] P. Buchwalter, J. Rosé, P. Braunstein, *Chem. Rev.* **2014**, *115*, 28–126.
- [2] N. P. Mankad, *Chem. Commun.* **2018**, *54*, 1291–1302.
- [3] I. G. Powers, C. Uyeda, *ACS Catal.* **2016**, *7*, 936–958.
- [4] B. G. Cooper, J. W. Napoline, C. M. Thomas, *Catal. Rev.* **2012**, *54*, 1–40.
- [5] E. Bodio, M. Picquet, P. Le Gendre, *Top. Organomet. Chem.* **2015**, *59*, 139–186.
- [6] L. H. Gade, *Angew. Chem. Int. Ed* **2000**, *39*, 2658–2678.
- [7] F. Rekhroukh, W. Chen, R. K. Brown, A. J. P. White, M. R. Crimmin, *Chem. Sci.* **2020**, *11*, 7842–7849.
- [8] M. J. Butler, M. R. Crimmin, *Chem. Commun.* **2017**, *53*, 1348–1365.
- [9] P. G. Andersson, in *Top. Organomet. Chem.*, **2011**, p. 234.
- [10] C. Copéret, D. P. Estes, K. Larmier, K. Searles, *Chem. Rev.* **2016**, *116*, 8463–8505.
- [11] V. Vidal, A. Théolier, J. Thivolle-Cazat, J. M. Basset, *Science (80-)*. **1997**, *276*, 99–102.
- [12] P. Avenier, M. Taoufik, A. Lesage, X. Solans-Monfort, A. Baudouin, A. De Mallmann, L. Veyre, J. M. Basset, O. Eisenstein, L. Emsley, E. A. Quadrelli, *Science (80-)*. **2007**, *317*, 1056–1060.
- [13] C. Copéret, A. Comas-Vives, M. P. Conley, D. P. Estes, A. Fedorov, V. Mougél, H. Nagae, F. Núñez-Zarur, P. A. Zhizhko, *Chem. Rev.* **2016**, *116*, 323–421.
- [14] L. M. Slaughter, P. T. Wolczanski, *Chem. Commun.* **1997**, 2109–2110.
- [15] B. P. Greenwood, G. T. Rowe, C. H. Chen, B. M. Foxman, C. M. Thomas, *J. Am. Chem. Soc.* **2010**, *132*, 44–45.
- [16] T. Miyazaki, Y. Tanabe, M. Yuki, Y. Miyake, Y. Nishibayashi, *Organometallics* **2011**, *30*, 2394–2404.
- [17] L. J. Clouston, R. B. Siedschlag, P. A. Rudd, N. Planas, S. Hu, A. D. Miller, L. Gagliardi, C. C. Lu, *J. Am. Chem. Soc.* **2013**, *135*, 13142–13148.
- [18] R. Srivastava, M. Jakoobi, C. Thieuleux, E. A. Quadrelli, C. Camp, *Dalt. Trans.* **2021**, *50*, 869–879.
- [19] R. Srivastava, E. A. Quadrelli, C. Camp, *Dalt. Trans.* **2020**, *49*, 3120–3128.
- [20] R. Srivastava, R. Moneuse, J. Petit, P. A. Pavard, V. Dardun, M. Rivat, P. Schiltz, M. Solari, E. Jeanneau, L. Veyre, C. Thieuleux, E. A. Quadrelli, C. Camp, *Chem. - A Eur. J.* **2018**, *24*, 4361–4370.
- [21] V. Dardun, L. Escomel, E. Jeanneau, C. Camp, *Dalt. Trans.* **2018**, *47*, 10429–10433.
- [22] M. V. Butovskii, C. Döring, V. Bezugly, F. R. Wagner, Y. Grin, R. Kempe, *Nat. Chem.* **2010**, *2*, 741–744.
- [23] J. A. Marsella, J. C. Huffman, K. G. Caulton, B. Longato, J. R. Norton, *J. Am. Chem. Soc.* **1982**, *104*, 6360–6368.
- [24] M. Oishi, M. Oshima, H. Suzuki, *Inorg. Chem.* **2014**, *53*, 6634–6654.

- [25] J. T. Golden, T. H. Peterson, P. L. Holland, R. G. Bergman, R. A. Andersen, *J. Am. Chem. Soc.* **1998**, *120*, 223–224.
- [26] M. Ohashi, K. Matsubara, T. Iizuka, H. Suzuki, *Angew. Chemie - Int. Ed.* **2003**, *42*, 937–940.
- [27] S. Lassalle, R. Jabbour, P. Schiltz, P. Berruyer, T. K. Todorova, L. Veyre, D. Gajan, A. Lesage, C. Thieuleux, C. Camp, *J. Am. Chem. Soc.* **2019**, *141*, 19321–19335.
- [28] S. Lassalle, R. Jabbour, I. Del Rosal, L. Maron, E. Fonda, L. Veyre, D. Gajan, A. Lesage, C. Thieuleux, C. Camp, *J. Catal.* **2020**, *392*, 287–301.
- [29] I. Del Rosal, S. Lassalle, C. Dinoi, C. Thieuleux, L. Maron, C. Camp, *Dalt. Trans.* **2021**, *50*, 504–510.
- [30] L. Escomel, I. Del Rosal, L. Maron, E. Jeanneau, L. Veyre, C. Thieuleux, C. Camp, *J. Am. Chem. Soc.* **2021**, *143*, 4844–4856.
- [31] L. Escomel, N. Soulé, E. Robin, I. Del Rosal, L. Maron, E. Jeanneau, C. Thieuleux, C. Camp, *Inorg. Chem.* **2022**, *61*, 5715–5730.
- [32] J. Llop Castelbou, K. C. Szeto, W. Barakat, N. Merle, C. Godard, M. Taoufik, C. Claver, *Chem. Commun.* **2017**, *53*, 3261–3264.
- [33] F. Héroguel, G. Siddiqi, M. D. Detwiler, D. Y. Zemlyanov, O. V. Safonova, C. Copéret, *J. Catal.* **2015**, *321*, 81–89.
- [34] F. Héroguel, D. Gebert, M. D. Detwiler, D. Y. Zemlyanov, D. Baudouin, C. Copéret, *J. Catal.* **2014**, *316*, 260–269.
- [35] L. Rochlitz, K. Searles, J. Alfke, D. Zemlyanov, O. V. Safonova, C. Copéret, *Chem. Sci.* **2020**, *11*, 1549–1555.
- [36] E. Lam, G. Noh, K. W. Chan, K. Larmier, D. Lebedev, K. Searles, P. Wolf, O. V. Safonova, C. Copéret, *Chem. Sci.* **2020**, *11*, 7593–7598.
- [37] S. R. Docherty, N. Phongprueksathat, E. Lam, G. Noh, O. V. Safonova, A. Urakawa, C. Copéret, *JACS Au* **2021**, *1*, 450–458.
- [38] K. Searles, K. W. Chan, J. A. Mendes Burak, D. Zemlyanov, O. Safonova, C. Copéret, *J. Am. Chem. Soc.* **2018**, *140*, 11674–11679.
- [39] L. Escomel, D. F. Abbott, V. Mougel, L. Veyre, C. Thieuleux, C. Camp, *Chem. Commun.* **2022**, 8214–8217.
- [40] G. L. Casty, M. G. Matturro, G. R. Myers, R. P. Reynolds, R. B. Hall, *Organometallics* **2001**, *20*, 2246–2249.
- [41] L. Lefort, C. Copéret, M. Taoufik, J. Thivolle-Cazat, J. M. Basset, *Chem. Commun.* **2000**, *12*, 663–664.
- [42] F. L. Mohler, V. H. Dibeler, E. Quinn, *J. Res. Natl. Bur. Stand. (1934)*. **1958**, *61*, 171.
- [43] B. Schoofs, J. A. Martens, P. A. Jacobs, R. A. Schoonheydt, *J. Catal.* **1999**, *183*, 355–367.

Acknowledgements/Remerciements

Firstly, I would like to thank all the jury members for accepting to review this thesis work.

I would also like to thank the University Claude Bernard Lyon 1 and the Ecole Normale Supérieure de Lyon for having granted me this doctoral scholarship within the framework of the *Contrats Doctoraux Spécifiques Normaliens (CDSN)*.

I thank the laboratory CP2M and its director, Timothy McKenna, for hosting me. I also thank the Ecole Doctorale de Chimie de Lyon (ED 206) and its director Stéphane Daniele.

Through these few lines, I wish to express my gratitude to my supervisors Dr. Clément Camp and Dr. Chloé Thieuleux.

Dr. Clément Camp is a dynamic, enthusiastic and passionate supervisor, dedicated to his work. During all these years, Clément has been my supervisor in the field. Clément, it has been a real pleasure to be trained and taught by you over the years. In fact, I realize that it has been a real privilege to discover and learn the profession of academic research with you. You are both professional and caring. Thank you for your multiple advices, tips, and encouragements but also for your hindsight on various daily professional situations. Thank you for your listening, your patience, your transparency, and your ability to adapt. I am also grateful to you because you trusted me throughout the project, giving me the flexibility and room to express my creativity and ideas. These aspects gave me the joy and the motivation to lead this beautiful project.

I am also grateful to Dr. Chloé Thieuleux. First of all, thank you for having directed and overseen my thesis project. Then, thank you for the precious scientific advice you gave me during our weekly meetings. Thank you for sharing your expertise and knowledge in catalysis, materials science and surface organometallic chemistry. I also thank you for your professionalism and integrity. It was formative to work under your direction.

Je souhaite également exprimer ma reconnaissance envers Laurent Veyre, notre précieux ingénieur de la plateforme nanochimie. Merci pour les nombreux problèmes techniques et pratiques que tu as pu résoudre tout au long de ces années. D'une certaine façon, je te vois un peu comme un « Mac Gyver » de la recherche. Merci de m'avoir transmis une partie de ton savoir-faire, mais aussi d'avoir partagé tes connaissances techniques et pratiques. Merci pour ta

disponibilité et ta polyvalence en toutes circonstances. Merci pour avoir mené nos analyses en microscopie TEM, merci aussi d'avoir conduit nos études en chimisorption. Je réalise que ton expertise en TEM, BET, GC, UV, IR, COMS (etc.) est un minerais de pépites, et je suis reconnaissant d'avoir pu en recevoir quelques unes au cours de ces années. Merci d'avoir soufflé le verre et d'avoir scellé ces nombreuses ampoules pour les analyses élémentaires. Laurent est un « couteau suisse » qui sait résoudre un nombre important de situations ; c'est assez incroyable d'avoir pu côtoyer une telle personne, alors encore Merci !

During this thesis project, we have made some collaborations and I want to thank all these people:

I would like to express my gratitude to Pr. Laurent Maron and Dr. Iker Del Rosal (from LCPNO Toulouse) for performing all the DFT calculations of our compounds.

I would also like to thank Pr. Victor Mougél and Dr. Daniel F. Abbott (from ETH Zurich) for performing the XPS studies of this PhD project.

A big thanks to Dr. Erwann Jeanneau (from ISA Lyon 1) for performing all the XRD collections (single crystal setup, data acquisition, and processing). Thank you Erwann because you have done a valuable and important work for our laboratory.

I thank Anne Badouin and Emmanuel Chefdeville for performing the advanced NMR analysis on the AV500 and AV400 spectrometers.

I would like to thank the Mikroanalytisches Labor Pascher (Germany) for performing the elemental analysis of our samples.

Je souhaite dédier également ces quelques mots à notre très chère gestionnaire, Emmanuelle Fouilhe. Un très grand merci pour l'ensemble des tâches administratives et logistiques que tu as effectué tout au long de ma thèse. Tu es vraiment une personne très appliquée et professionnelle.

Durant ces années, j'ai cotoyé de nombreux autre permanents, post-doctorants et étudiants (stagiaires et doctorants). Je dédie quelques lignes pour les remercier :

Un grand merci à Vincent Dardun, mon ami de promotion de l'ENS et puis mon ami au cours de ce doctorat. Vincent, depuis 2015 on se suit et je suis joyeux de t'avoir cotoyé durant toutes ces années. Vincent est un jeune homme sensible, dévoué, toujours prêt à rendre service et passionné par la transmission de connaissances scientifiques. Je suis reconnaissant pour ces belles qualités qui t'habitent mon ami. Aujourd'hui, je suis joyeux que tu te diriges vers l'enseignement car je crois que c'est ta place. Nos chemins professionnels se séparent mais je continuerai à penser à toi.

Je suis reconnaissant envers Sébastien Lassalle que j'ai cotoyé de 2018 à 2021 durant sa thèse. Sébastien a travaillé sur un projet très proche du mien et je suis reconnaissant pour tous ces nombreux conseils techniques et pratiques qu'il m'a donnés. Il m'a notamment formé sur le terrain concernant la chimie organométallique de surface et sur tout ce qui touche à la chimie sur les lignes de haut-vide COMS. Merci donc à toi mon cher Sébastien.

Un merci à Naïme Soulé et Emmanuel Robin, deux beaux stagiaires micro-projet CPE que j'ai eu la joie de superviser durant l'été 2021.

Finanlement un grand merci à vous autres pour votre présence et qui vous êtes : Clément, Ravi, Isis, Martin, Alessandra, Walid, Nghia, Rosalyn, Cynthia, Medet, Chloé, Anthony, Abdelhak, Zija, Alexandre, Pauline, Lisa-Lou, Nesrine (merci pour la RMN du solide), Christine, Kai (merci pour les bouteilles de gaz), Virginie, Anna, Iurii, Julien, Alexis, Walid, Henry, Eva, Tania, Loïc, Valentin, Jessy, Marie, Vincent, Marc, Rémy, Alexis et Georges.

Finalement, je crois qu'il est très difficile de mener une thèse à son aboutissement sans un équilibre dans sa vie. Je crois que cet équilibre est donné par de l'Amour et de la Joie. Ces derniers sont principalement véhiculés par des personnes qui nous sont chères, nos bien-aimés et bien-aimées, nos proches, nos amis, nos voisins, notre prochain etc. Je souhaite donc dédier ces dernières lignes pour eux :

Je souhaite exprimer ma reconnaissance à mon berger, mon guide, mon conseiller, mon enseignant, mon consolateur, mon défenseur et mon libérateur. Sans toi, tout serait différent et ma vie n'aurait pas de sens. Merci pour ta paix, ta joie et ta faveur que tu me donnes et que tu m'as donné tout au long de ce doctorat. Merci pour les portes que tu as ouvertes et les situations que tu as débloquées durant cette tranche de vie de doctorant. C'est merveilleux de vivre avec toi et pour toi !

Un grand merci à ma famille de sang, mes parents (Roger et Odile), ma fraterie (Mickaël, Kyria, Mathilde, Florian) et mes neveux/nièces (Baptiste, Léah, Lucas, Eden). Merci pour votre soutien et pour qui vous êtes, je vous aime. Merci également à mes oncles et tantes/cousins/cousines (en particulier Monique et Yves, Benjamin et Victoire, Emmanuelle et Matthieu, Clairette et vous autres) qui ont été des sources d'encouragement. Il me tient aussi à cœur de dresser une liste (non-exhaustive je crois) de tous mes amis et amies qui me sont chers et qui ont participé de près ou de loin au bien-être de cette saison de ma vie : Gratien (mon colocataire mais surtout mon frère), Benjamin (mon ancien colocataire), Thibaut, Sedera, Aude, Yannick, Noëlline, Gaëtan, Annabelle, Claude, Salomé, Brian, Sofia, Vincent, Georgia, George, Gill, Rémi, Sylvain, Jérémy, Manou, Matthieu, Cyrille, Mélody, Johannes, Sylvain, Thomas, Caroline, Nicolas, Marine, Julie, Cyprian, Adele, Léo, Antoine, Guillaume, Bastien, Daniel, Josh, Joshua, Rémy, Jean Baptiste, Elie,

Acsa, Romain, Claudine, Hanna-Maria, Marc, Louis, Amandine, Ezechiel, Simon, Cédric, Béatriz, Mokhtar, Khenny, Noémie, Pauline, Flore, Lina, Andrea, Rida, Dorian, Samy, Melaine, Célia, Pierre-Henry, Nathan, Ophélie, Joris, Hugo, Ando, JB, Chloé, Jean-Jacques, Laurence, Chirstine, Jean-Michel, Stéphanie, Geneviève, Noaa, Mélodie, René, Jean-Paul, Nadine, Marie-Pierre et encore bien d'autres.

Table Of Contents

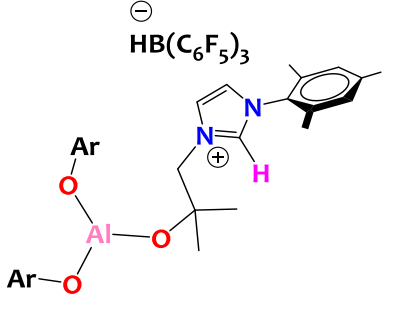
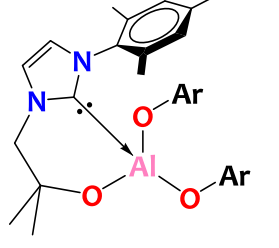
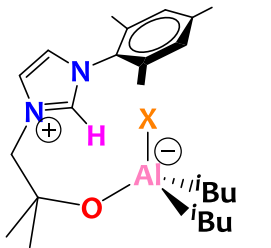
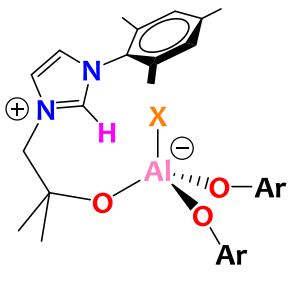
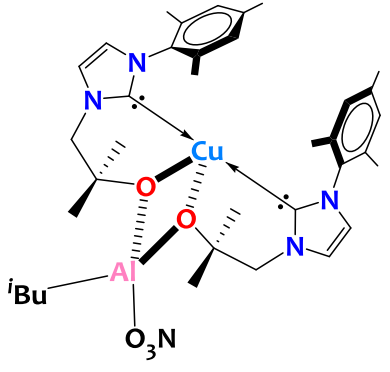
List Of Compounds	29
List Of Abbreviations And Acronyms	37
List Of Publications Related To This PhD Manuscript	41
CHAPTER 1. Introduction	43
1.1 Preamble	45
1.2 Overview of Al/M heterobimetallic complexes: construction and reactivity	48
1.2.1 Design strategies	48
1.2.2 Stoichiometric and catalytic reactivity	65
1.3 Surface organometallic chemistry (SOMC):	73
1.3.1 General concepts	73
1.3.2 Immobilization of aluminum species on SiO ₂ : conception and reactivity	78
1.3.3 Immobilization of iridium derivatives on solid supports: conception and reactivity	85
1.3.4 Development of supported heterobimetallic catalysts onto silica	89
1.4 Purposes and aims of the project	99
CHAPTER 2. Towards Heterobimetallic Aluminum/M Complexes Bridged By Bifunctional NHC Ligands	103
2.1 Introduction	105
2.1.1 Development of bifunctional NHCs to access heterobimetallic species	105
2.1.2 Interests of alkyl aluminum species	108
2.2 Development of new Al-NHC species	109
2.2.1 Design of an alkoxy bis-alkyl Al(III)-NHC complex	109
2.2.2 Formation of aluminate-imidazolium zwitterions	112
2.2.3 Discussion	116
2.2.4 Restoration of the Al(III)-NHC motifs	118
2.2.5 Reactivity of Al-NHCs with protic substrates	124
2.3 Towards heterobimetallic Al/M (<i>d</i> -block metal) species	127
2.4 Conclusions	131
CHAPTER 3. Development Of Molecular Aluminum/Iridium Heterobimetallic Species Using An Alkane Elimination Approach	135

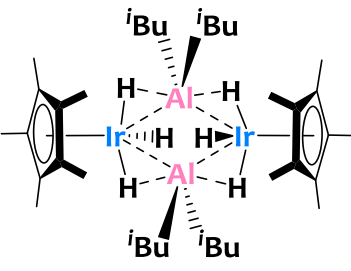
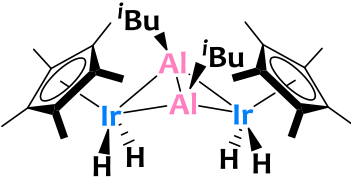
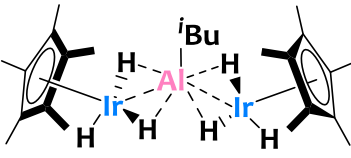
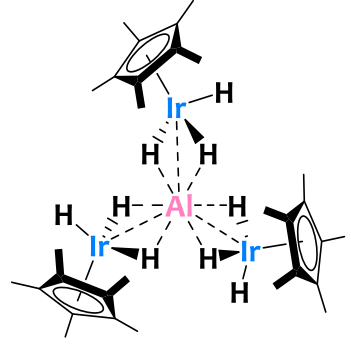
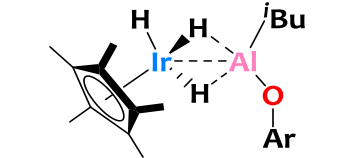
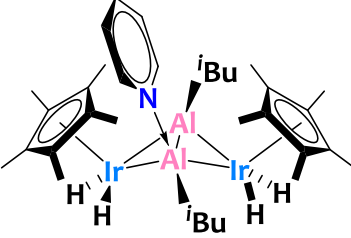
3.1	Context	137
3.2	Rational preparation of well-defined multinuclear Al/Ir clusters	138
3.2.1	Synthesis and characterization of tetranuclear heterobimetallic [Al ₂ Ir ₂] clusters	138
3.2.2	Synthesis and characterization of a trinuclear heterobimetallic [AlIr ₂] cluster	146
3.2.3	Synthesis and characterization of a tetranuclear heterobimetallic [AlIr ₃] cluster	151
3.3	Synthesis of a binuclear [Ir-Al] heterobimetallic complex	157
3.3.1	Context	157
3.3.2	Synthesis and characterization	157
3.3.3	Structural investigation by DFT	160
3.4	Conclusion	161
CHAPTER 4. Reactivity Studies Of Al/Ir Heterobimetallic Complexes		165
4.1	Introduction	167
4.2	Reactivity towards Lewis bases and nucleophiles	168
4.2.1	Reactivity with pyridine derivatives	168
4.2.2	Reactivity with benzyl-potassium and silver triflate	178
4.3	Reactivity towards Lewis acids	186
4.3.1	Pyridine abstraction of adduct 17 leading back to the formation of complex 15	186
4.3.2	Synthesis of a borate salt [Ir ₂ (Cp*) ₂ (H ₂) ₂ Al ₂ (THF) ₃ (ⁱ Bu)][HB(C ₆ F ₅) ₃], 22	188
4.4	Reactivity with heteroallenes	192
4.4.1	Reactivity with carbon dioxide	192
4.4.2	Reactivity with adamantyl isocyanate	198
4.4.3	Reactivity with dicyclohexylcarbodiimine	204
4.5	Conclusions	208
CHAPTER 5. Development Of Al/Ir Heterobimetallic Sites Supported On A Mesostructured SBA-15₇₀₀ Silica		211
5.1	Introduction	213
5.1.1	Description and interests of the SBA-15 support	213
5.1.2	Molecular models of silica surface	215
5.2	Reactivity with molecular models of the silica surface	217
5.3	Preparation of silica-supported iridium-aluminum catalysts	225
5.3.1	Grafting of complex 14 onto dehydroxylated silica: preparation of the surface species [≡SiOAl{(μ-H) ₂ Ir(H)Cp* ₂ }], 27	225
5.3.2	Stability studies	227
5.4	Formation of a new heterobimetallic material – Ir-Al/SiO ₂	229

5.4.1	Synthesis and preliminary characterizations	229
5.4.2	Advanced characterizations	230
5.5	Synthesis of a monometallic analogue - Ir/SiO ₂	235
5.5.1	Preparation and preliminary characterizations	235
5.5.2	Advanced characterizations	237
5.6	Conclusions	242
CHAPTER 6. Towards Bimetallic Cooperative Catalysis: Example On The Hydrogen/Deuterium Exchange Reaction Of Methane		245
6.1	Introduction	247
6.1.1	Interests of using methane	247
6.1.2	HDE catalysis of methane	247
6.2	Description of the catalytic system	250
6.2.1	Experimental conditions and preliminary studies	250
6.2.2	Data processing	252
6.3	Catalytic performances	253
6.3.1	Comparative activities between Ir-Al/SiO ₂ and Ir/SiO ₂ .	253
6.3.2	Selectivity	258
6.4	Conclusions	260
CHAPTER 7. General Conclusions And Prospects		263
CHAPTER 8. Experimental Section		269
8.1	General considerations	271
8.2	Characterizations	271
8.3	Synthesis	274
8.3.1	CHAPTER 2 Towards Heterobimetallic Aluminum/M Complexes Bridged By Bifunctionnal NHC Ligands	274
8.3.2	CHAPTER 3 Development Of Molecular Aluminum/Iridium Heterobimetallic Species Using An Alkane Elimination Approach	279
8.3.3	CHAPTER 4 Reactivity studies of Al/Ir Heterobimetallic Complexes	282
8.3.4	CHAPTER 5 Development Of Al/Ir Heterobimetallic Sites Supported On A Mesoporous SBA-15 ₇₀₀ Silica	288
CHAPTER 9. References		293
Appendix		315

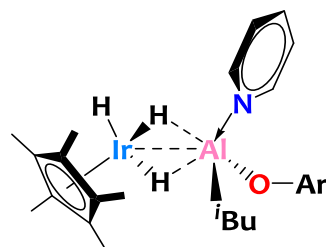
List Of Compounds

Number	Name	Structure	Description
1	NHC-OH ligand (LH)		Scheme 45 (page 107)
2	$[\text{Al}(\text{L})(i\text{Bu})_2]$		Scheme 47 (page 110)
3	$[\text{HL}][\text{Al}(i\text{Bu})(\text{OAr})_2]$		Scheme 48 (page 112)
4	$[\text{HL}][\text{Al}(\text{Me})(\text{OAr})_2]$		Scheme 48 (page 112)
5	$[\text{K}(\text{THF})_2\text{L}][\text{Al}(i\text{Bu})(\text{OAr})_2]$		Scheme 52 (page 119)

6	$[(HL)Al(OAr)_2][HB(C_6F_5)_3]$		Scheme 52 (page 119)
7	$Al(L)(OAr)_2$		Scheme 52 (page 119)
8	$[HL][Al(iBu)_2(OPh)]$		Scheme 53 (page 126)
9	$[HL][Al(OAr)_2(OPh)]$		Scheme 53 (page 126)
10	$[Cu(L)_2Al(O_3N)(iBu)]$		Scheme 55 (page 129)

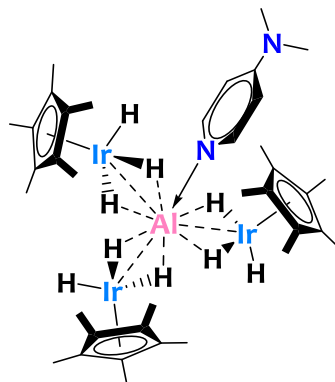
11	$[\text{Ir}(\text{Cp}^*)\text{H}_3\text{Al}(\text{iBu})_2]_2$		Scheme 58 (page 139)
12	$[\text{Ir}(\text{Cp}^*)\text{H}_2\text{Al}(\text{iBu})_2]_2$		Scheme 58 (page 139)
13	$[\{(\text{Ir}(\text{Cp}^*)(\text{H})(\mu\text{-H}_2))_2\text{Al}(\text{iBu})\}]$		Scheme 59 (page 147)
14	$[\{(\text{Ir}(\text{Cp}^*)(\text{H})(\mu\text{-H}_2))_3\text{Al}\}]$		Scheme 60 (page 151)
15	$[\text{Ir}(\text{Cp}^*)(\text{H})(\mu\text{-H}_2)\text{Al}(\text{OAr})(\text{iBu})]$		Scheme 61 (page 157)
16	$[\text{Ir}_2(\text{Cp}^*)_2(\text{H}_2)_2\text{Al}_2(\text{Py})(\text{iBu})_2]$		Scheme 63 (page 169)

17 $[\text{Ir}(\text{Cp}^*)(\text{H})(\mu\text{-H}_2)\text{Al}(\text{Py})(\text{OAr})(i\text{Bu})]$



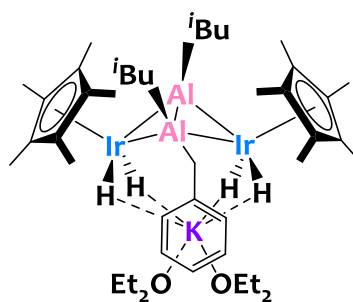
Scheme 63
(page 169)

18 $[\{\text{Ir}(\text{Cp}^*)(\text{H})(\mu\text{-H}_2)\}_3\text{Al}(\text{DMAP})]$



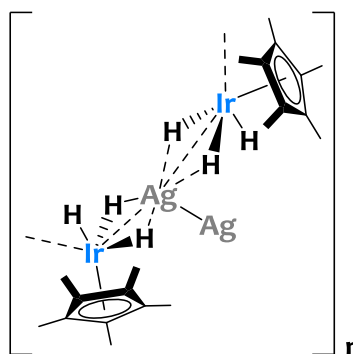
Scheme 63
(page 169)

19 $[\text{Ir}_2(\text{Cp}^*)_2(\text{H}_2)_2\text{Al}_2(\text{KBn})(i\text{Bu})_2]$

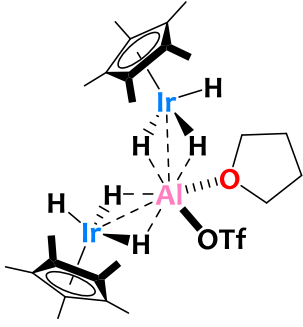
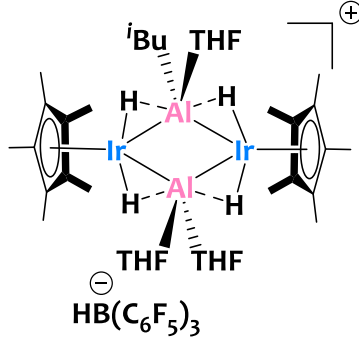
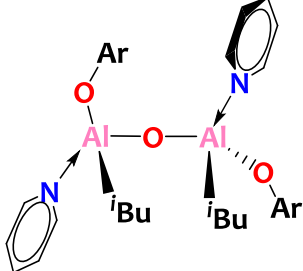
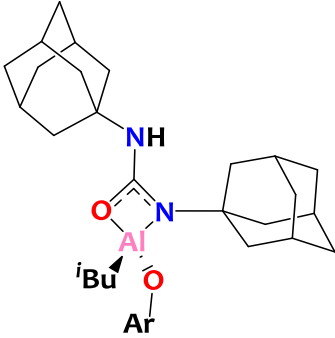
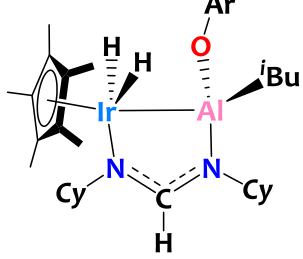


Scheme 64
(page 178)

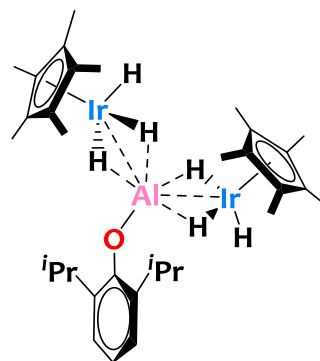
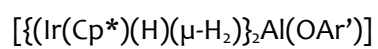
20 $[\text{IrCp}^*\text{H}_3\text{Ag}]_n$



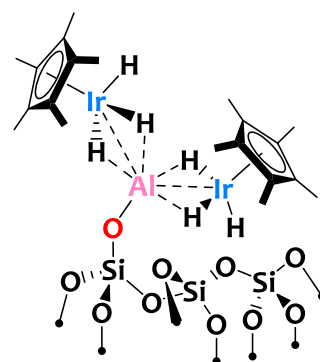
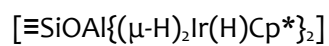
Scheme 65
(page 182)

21	$[((\text{Ir}(\text{Cp}^*)(\text{H})(\mu\text{-H}_2))_2\text{Al}(\text{OTf})(\text{THF}))]$		Scheme 65 (page 182)
22	$[\text{Ir}_2(\text{Cp}^*)_2(\text{H}_2)_2\text{Al}_2(\text{THF})_3(\text{iBu})]$ $[\text{HB}(\text{C}_6\text{F}_5)_3]$		Scheme 66 (page 186)
23	$[\text{Al}(\text{iBu})(\text{OAr})(\text{Py})]_2(\mu\text{-O})$		Scheme 67 (page 192)
24	$\{\text{Al}(\text{OAr})(\text{iBu})$ $[\kappa^2\text{-}(\text{N},\text{O})\text{AdNC}(\text{O})\text{NHAd}]\}$		Scheme 68 (page 199)
25	$[\text{Ir}(\text{Cp})^*\text{H}_2(\mu\text{-CyNC}(\text{H})\text{NCy})$ $\text{Al}(\text{iBu})(\text{OAr})]$		Scheme 69 (page 204)

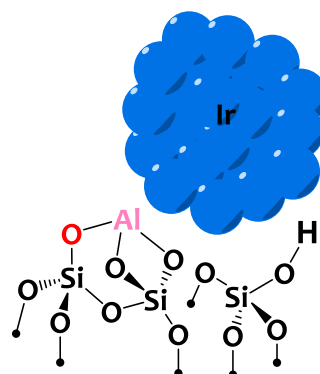
26

Scheme 74
(page 222)

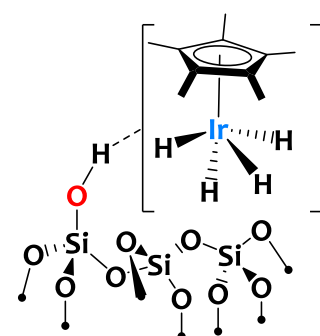
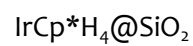
27

Scheme 75
(page 225)

28

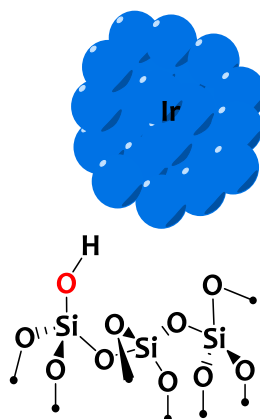
Scheme 76
(page 229)

29

Scheme 77
(page 236)

30

Ir/SiO₂



Scheme 77

(page 236)

List Of Abbreviations And Acronyms

$\%V_{\text{Bur}}$ =M-NHC buried volume

3c-2e=3 centers-2 electrons bond

Ad=Adamantyl

Al/M or Al-M=heterobimetallic aluminum/d-block metal (complexes)

Ar=Aromatic

Ar'=1,3-diisopropylbenzene

BCF= $\text{B}(\text{C}_6\text{F}_5)_3$

BDE=Bond Dissociation Energy

B.E.=Binding Energy

BHT=Butylated hydroxytoluene

$\text{CH}_{4-x}\text{D}_x$ =Deuteromethanes

Cp=Cyclopentadienyl

CP=alkynylphosphine

Cp*=1,2,3,4,5-pentamethylcyclopentadienyl

Cp'=Me₃SiC₅H₄

CP-MAS-NMR= Cross-Polarization-Magic Angle Spinning-NMR

Cy=Cyclohexyl

Dbz= Dibenzylideneacetone

DCC=N,N'-Dicyclohexylcarbodiimide

DEAC=Diethylaluminum chloride

DFT=Density Functional Theory

DIBALH=Diisobutylaluminum hydride

Dipp=2,6-ⁱPr₂C₆H₃

DMAP=4-dimethylaminopyridine

DRIFTS=Diffuse Reflectance Infrared Fourier Transform Spectroscopy

EDS or EDX= Energy-dispersive X-ray Spectroscopy

Et₂O=Diethyl ether

FG=Functional Group

FLP=Frustrated Lewis Pair

FSR=formal shortness ratio

FT-IR=Fourier Transform Infrared spectroscopy

GC=Gas Chromatography

GC-MS= Gas Chromatography-Mass Spectrometry
HAADF=High Angle Annular Dark Field
HDE=Hydrogen/Deuterium Exchange
HMDS=Hexamethyldisilazane
HSQC=Heteronuclear Single Quantum Coherence
IR=Infrared
IWI=Incipient Wetness Impregnation
KHMDs=Potassium bis(trimethylsilyl)amide
M=Metal
M1=Hard metal
M2=Soft metal
MCM-41=Mobil Composition of Matter No. 41
ME=Multiple Exchange
Mes=Mesityl
MOLP=Metal-Only Lewis Pair
nbd= Norbornadiene ligand
NBO=Natural Bonding Orbital
NH-PR₂=Amino-phosphine ligand
NHC=N-Heterocyclic Carbene
NMR=Nuclear Magnetic Resonance
NON=4,5-bis(2,6-diisopropylanilido)-2,7-di-tert-butyl-9,9-dimethylxanthene
Np=Neopentyl
NP=Nanoparticle
NPA=Natural Population Analysis
OH-Py=Hydroxyl-pyridine ligand
PAIP=Aluminum species bearing nitrogenous-phosphine chelating ligands
PE=Polyethylene
pmdeta=N,N,N',N'',N'''-Pentamethyldiethylenetriamine
Por=Porphyrin
Poxlms=N-phosphine-oxide-substituted imidazolylidene
SBA-15=Santa Barbara Amorphous No. 15
SBA-15₇₀₀=SBA-15 dehydroxylated at T=700°C
SDA=Structure-Directing Agent
SE=Single Exchange
SOMC=Surface Organometallic Chemistry or Surface Organometallic Catalysis

SS-NMR= Solid-State NMR
STEM=Scanning Transmission Electron Microscopy
TEA=Triethylaluminum(III)
TEM=Transmission Electron Microscopy
TEOS=Tetraethyl orthosilicate
THF=Tetrahydrofuran
TIBA=Triisobutylaluminum(III)
TOF=Turnover Frequency
TON=Turnover Number
TM=Transition Metal
TMA=Trimethylaluminum(III)
TMP=Thermolytic Molecular Precursor
 τ =Deuteration rate
VT-NMR=Variable Temperature-NMR
WBI=Wiberg Bond Index
XPS=X-ray Photoelectron Spectrometry
XRD=X-Ray Diffraction

List Of Publications Related To This PhD Manuscript

4. L. Escomel, D. F. Abbott, V. Mougel, L. Veyre, C. Thieuleux and C. Camp “Highly dispersed silica-supported iridium and iridium–aluminium catalysts for methane activation prepared *via* surface organometallic chemistry” *Chem. Commun.* **2022**, 58, 8214–8217.
3. L. Escomel, N. Soulé, E. Robin, I. D. Rosal, L. Maron, E. Jeanneau, C. Thieuleux, and C. Camp “Rational Preparation of Well-Defined Multinuclear Iridium–Aluminum Polyhydride Clusters and Comparative Reactivity” *Inorg. Chem.* **2022**, 61, 15, 5715–5730. **Cover Article.**
2. L. Escomel, I. D. Rosal, L. Maron, E. Jeanneau, L. Veyre, C. Thieuleux, and C. Camp “Strongly Polarized Iridium^{δ-}-Aluminum^{δ+} Pairs: Unconventional Reactivity Patterns Including CO₂ Cooperative Reductive Cleavage” *J. Am. Chem. Soc.* **2021**, 143 (12), 4844-4856.
1. V. Dardun, L. Escomel, E. Jeanneau and C. Camp « On the Alcoholysis of Alkyl-Aluminum(III) Alkoxy-NHC Derivatives: Reactivity of the Al-Carbene Lewis Pair versus Al-Alkyl” *Dalton Trans.* **2018**, 47, 10429–10433.

CHAPTER 1. Introduction

1.1 Preamble

Organometallic chemistry embodies the central area of study that cements the different parts of this PhD project. Consequently, we will briefly introduce this chemistry and then, we will present some definitions and interests of a sub-part of this field: heterobimetallic chemistry.

Organometallic chemistry is defined as the study of compounds containing at least one bond between a carbon atom of an organic ligand to a metal center. Another definition is that organometallic chemistry lies at the interface between organic chemistry and inorganic chemistry fields.^[44,45] The metallic element can be part of the *s*-block (such as potassium or magnesium), *p*-block (such as aluminum), *d*-block (e.g. Ir or Cu) or *f*-block (lanthanides and actinides) of the periodic table. On the other side, there is a wide range of possibilities regarding the organic moieties bound to the metal atom, the most representative and classical examples being carbonyls, carbenes, cyclopentadienyls, alkyls and arenes ligands.

Until now, organometallic chemistry has been studied mainly through the prism of monometallic molecular species (see Figure 1) and the wide possibilities they offer in catalysis are no longer in question. However, the addition of a second metal center within these structures is a real bridge to new reaction pathways and novel reactivity not possible with monometallic analogues.

The study of heterobimetallic assemblies thus embodies an open door towards innovation and to a greater diversity of possibilities. In this vein, Ekkehardt Hahn claimed at a roundtable for the journal *Organometallics* in 2011: *"If you look at the diverse chemistry of mononuclear complexes, imagine what the future would hold in polymetallic systems for cooperative reactivity in catalysis or related fields. I think we are just seeing the beginning of that, the toolbox is not even half full."*^[46]

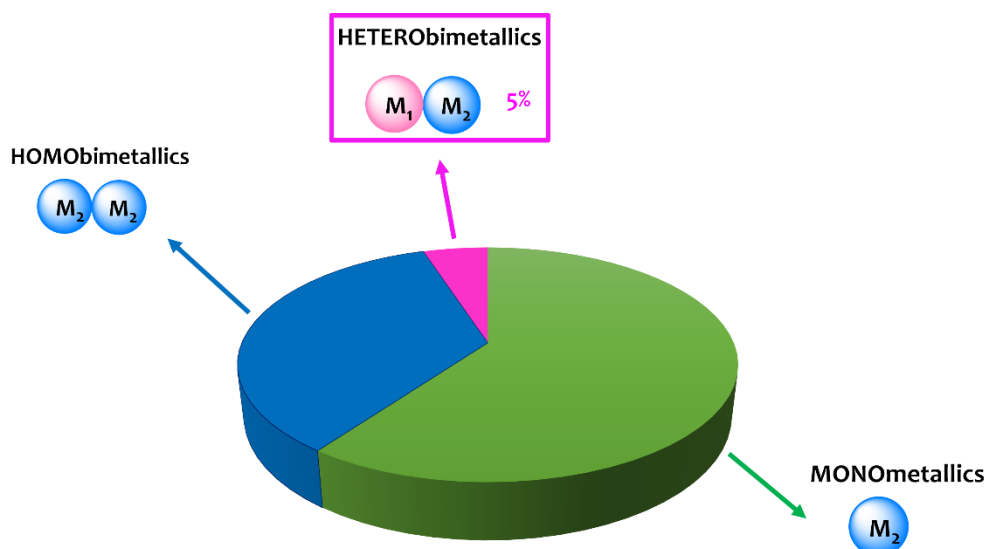
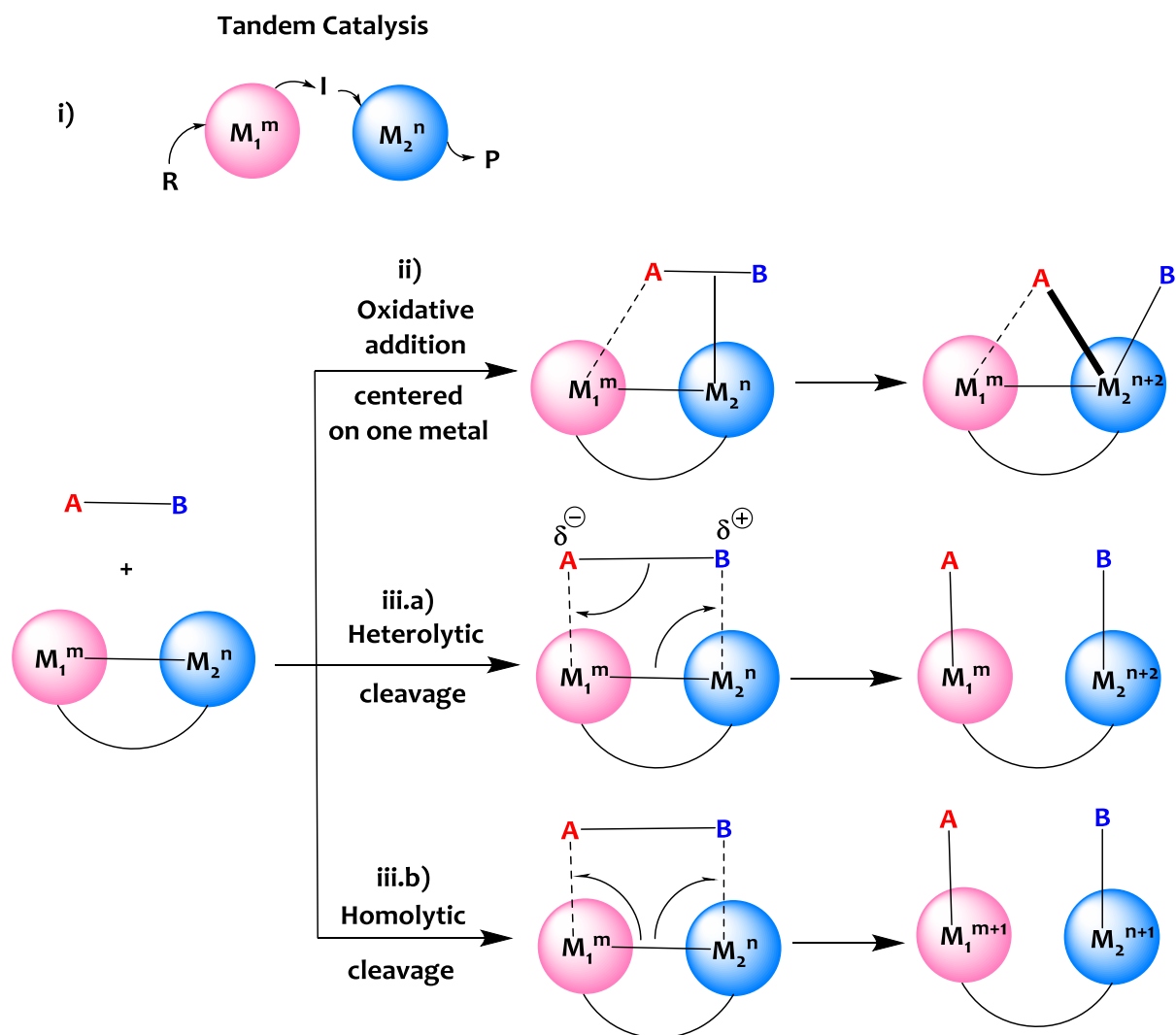


Figure 1. Pie chart representing the proportion of heterobimetallic complexes (c.a. 5%) among crystallographically characterized organometallic compounds (from the CCDC database).

Several modes of action are possible for these types of bimetallic architectures, and a few examples are listed below.

- i) The two metal centers are not (necessarily) in interaction and can act independently in distinct elementary transformations: for example, the hard metal (M_1) as a Lewis acid and the late transition metal (M_2) in redox processes, to finally promote new reactivities. This is typically the case in tandem catalysis for example (Scheme 1, top left).
- ii) One metal – M_2 – can be involved in the activation process of a specific substrate, for example through an oxidative addition route and the other metal – M_1 – at close proximity, can tune the properties of M_2 and possibly promote a particular activity or selectivity. Such systems thus exhibit synergistic effects.
- iii) Eventually, the most characteristic mode of action of heterobimetallic species is the concerted activation of a substrate by both metals simultaneously. This can proceed through the heterolytic cleavage of a substrate bond, resulting in a formal two electron oxidation of one metal center only, with no oxidation state change at the second metal (Scheme 1 bottom, case iii.a). Alternatively, homolytic bond cleavage resulting in a formal one electron oxidation of each metal sites (Scheme 1 bottom, case iii.b)) is another possibility.^[4-6]



Scheme 1. Representation of the different modes of actions of heterobimetallic species. (Top) catalytic routes from a reactant R to a product P, possibly passing through intermediates I. (Bottom) activation of a polarized substrate.

Unlike homobimetallic metal-metal pairs, which generally have low polarity, metal-metal bonds between a late transition metal and a hard metal (typically early *d*-block metals or group 13 elements such as Al) are generally strongly polarized due to the difference in the metallic elements electronegativity and oxidation state, the hard metal being electrophilic while the late metal is more soft and electron-rich.

Accessing sophisticated heterobimetallic species in a controlled and rational fashion remains a big challenge. Dedicated synthetic methodologies are thus required to avoid the formation of statistical mixtures, clusters or nanoparticles, and to prevent ligand redistribution or unwanted redox processes. This is particularly true when the two metal centers exhibit quite different chemical properties which are often incompatible.

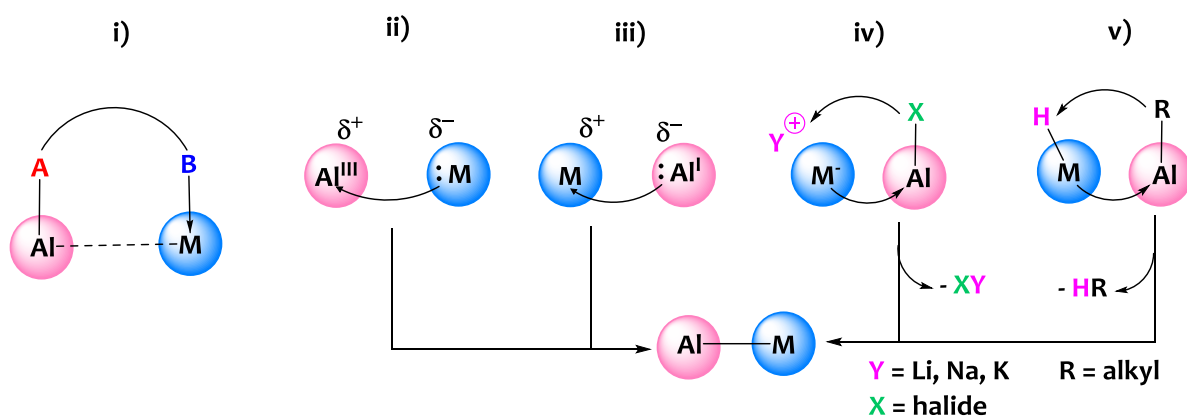
All the above-mentioned assertions are specifically true regarding the case of Al/M (M = late *d*-block metal) heterobimetallic species, which are the focus of this thesis work. In the next part, we will therefore restrict our discussion around Al/M complexes, which are well-representative of the various synthetic challenges and reactivity interests of heterobimetallic species in general.

1.2 Overview of Al/M heterobimetallic complexes: construction and reactivity

1.2.1 Design strategies

We identified five synthetic strategies to construct heterobimetallic aluminum/*d*-block metal assemblies - noted Al/M thereafter - that are represented on Scheme 2:

- i) The first one is to take advantage of original hetero-bifunctional ligands associating a soft with a hard donor to coordinate and bridge the two metals.
- ii) The second approach entails to coordinate a nucleophilic metallic precursor – Lewis base - with an electrophilic aluminum(III) derivative – Lewis acid - in order to form an Al/M Lewis adduct.
- iii) An original methodology which only emerged in the last years involves the preparation of a nucleophilic aluminum(I) derivative, which is then coordinated to an electrophilic metallic precursor leading to Al/M species.
- iv) A more classical strategy consists in performing a salt metathesis reaction between a halide aluminum precursor with an alkali cation metallate salt, to yield the desired Al/M species along with an alkali halide salt which generally precipitates and can drive the reaction.
- v) The last approach, which is almost unexplored yet, entails to carry out alkane elimination between an aluminum-alkyl precursor – acting as a Brønsted base -and a metallic hydride derivative which features Brønsted acidity, releasing a volatile alkane and triggering the formation of an Al/M edifice.



Scheme 2. Five reported approaches to design Al/M complexes.

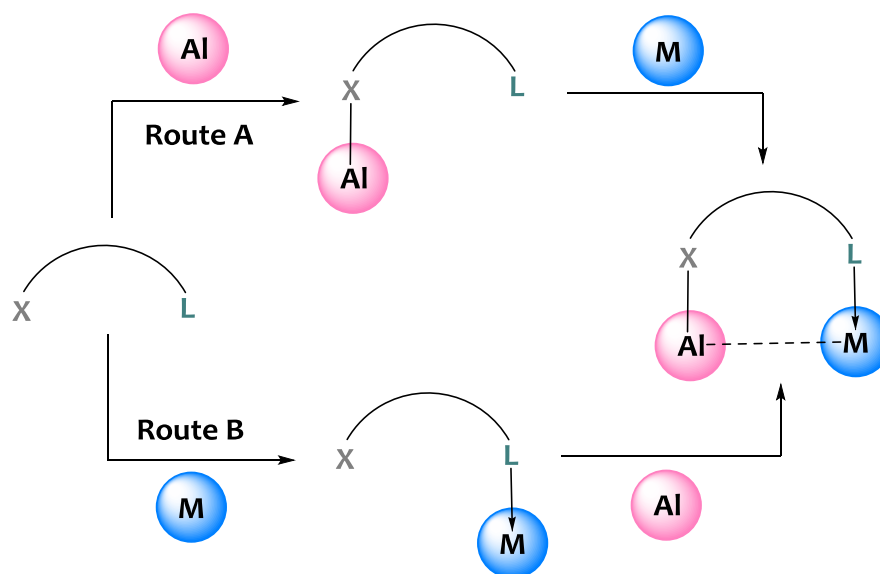
In the next sections, we will explain these five strategies in details, supplemented by relevant examples found in the literature.

1.2.1.1 Use of bifunctional ligands

Different sorts of bifunctional ligands are used to bridge an aluminum center with a *d*-block metal one. But, in most reported structures, the bifunctional platforms used to assemble the two metal centers share common features. Indeed, most of the time, the aluminum center is bound to a X-type hard O or N donor such as alkoxide, amido, guanidinate, amidinate or diketiminate groups. On the other side, the late TM is coordinated by a soft donor and more specifically by a L-type neutral ligand with a strong σ -donation such as phosphine, N-heterocyclic carbene (NHC) or pyridine moieties.

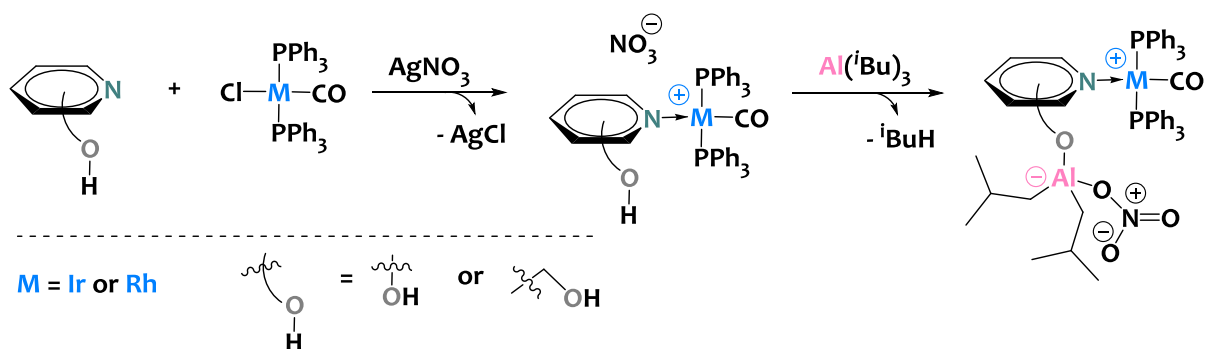
In order to get the ultimate heterobimetallic architecture, two synthetic routes are envisioned in the literature. In the first one, an aluminum precursor is first attached to the bifunctional ligand through its X-type hard donor. The resulting aluminum monometallic species is then treated with a late metallic derivative, which promotes coordination of the L-type soft donor onto the M center leading ultimately to the targeted heterobimetallic edifice (Scheme 3, route A). The second route is the reverse of the first one (Scheme 3, route B).

We will see through well-chosen examples in the literature that the order of addition (Al or M first) is important as the two synthetic routes are generally not equivalent, and in some cases only one of the two routes is possible.



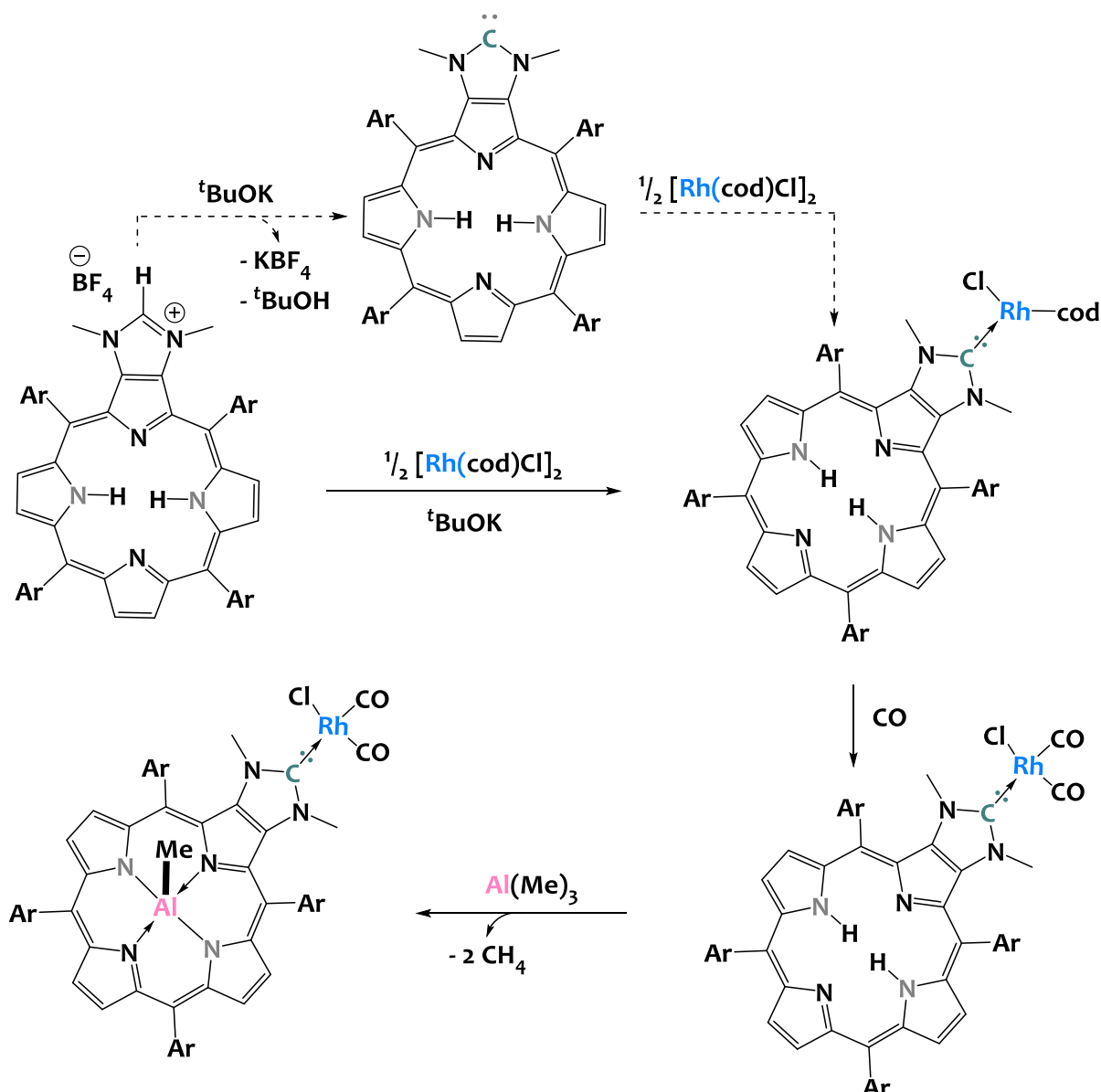
Scheme 3. Synthetic routes to access Al/M heterobimetallic complexes assembled by bifunctional ligands.

From 2018 to 2020, N.J. DeYonker and his coworkers reported a series of Al/M heterobimetallic molecules assembled by original hydroxyl-pyridine platforms (OH-Py).^[47-50] Their studies focused on synthetic route B (see Scheme 3). They first showed the possibility to prepare a series of cationic hydroxyl-pyridine iridium and rhodium complexes featuring nitrate counter anions. In this case, the pyridine moiety is N-coordinated to the metal center and the hydroxyl pendant arm does not interact with the *d*-metal centers (Scheme 4, middle). These Ir and Rh monometallic species are then treated with triisobutylaluminum (TIBA) triggering a protonolysis reaction between the alcohol side-arm and TIBA, which ultimately results to the elimination of isobutane and the formation of Al-(O-Py)-Ir and Al-(O-Py)-Rh zwitterions. Note that a η^1 -coordination of the nitrate anion onto the Al center is observed (Scheme 4, right side).



Scheme 4. Reported synthesis of heterobimetallic Al/Ir and Al/Rh species through route B (Scheme 3). The two metal centers are assembled using hydroxyl pyridine bifunctional ligands.^[47-50]

In the same vein, S. Richeter and his coworkers reported in 2013 the synthesis of an original Al/Rh heterobimetallic entity using route B (Scheme 5).^[51]

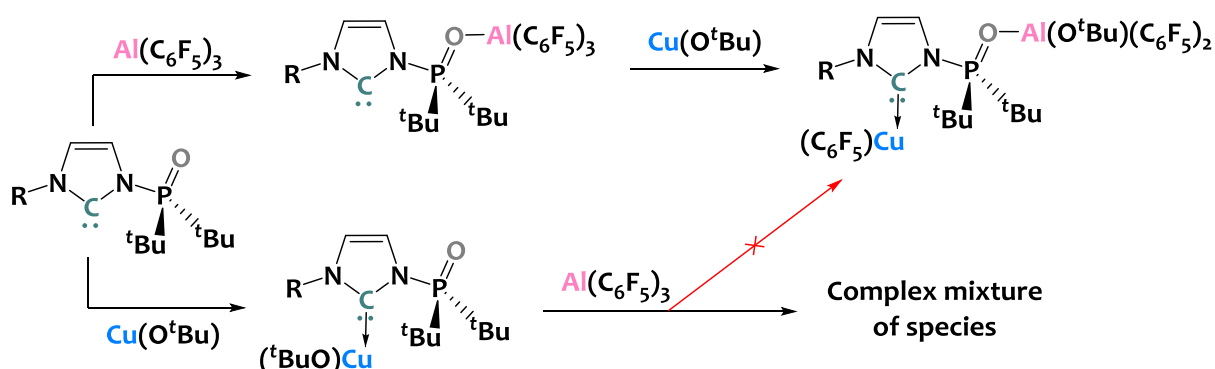


Scheme 5. Synthesis of an Al/Rh heterobimetallic architecture using a bifunctional NHC-functionalized porphyrin ligand along route B (see Scheme 3).^[51]

Here, the Al and Rh metallic ions are assembled by an original bifunctional porphyrin fused to an N-heterocyclic carbene unit – abbreviated NHC-Por thereafter. The first step of this approach involves the *in situ* deprotonation of an imidazolium moiety by KO^tBu to form an L-type N-heterocyclic carbene donor (Scheme 5, top) followed by coordination of the carbene moiety onto Rh resulting in the monometallic Rh(NHC-Por)(COD)Cl complex (Scheme 5, right). In order to evaluate the electron-donating properties of the NHC ligand, the authors synthesized a Rh(NHC-Por)(CO)₂Cl complex (by substitution of cyclooctadiene by two carbonyl ligands through bubbling of CO) to characterize the CO stretching vibrations by IR spectroscopy. Eventually, Rh(NHC-Por)(CO)₂Cl is subjected to a protonolysis reaction with trimethylaluminum (TMA), which releases two equivalents of methane and the targeted MeAl(Por-NHC)Rh(CO)₂Cl heterobimetallic edifice

where the Al center is located in the porphyrin pocket (Scheme 5, bottom left).

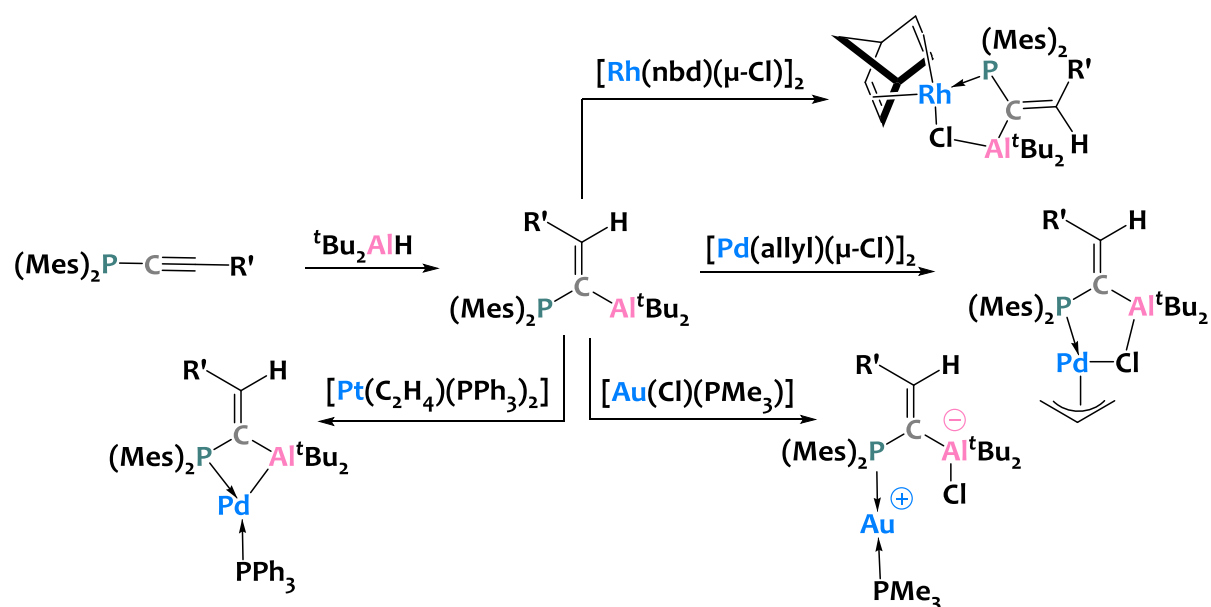
Note that in the two above-discussed cases, the authors do not mention attempts to design the same molecular objects using route A (Scheme 3). However, literature analysis reveals a few studies where routes A and B are compared with one another. One very interesting article reported in 2020 the sophisticated conception of bifunctional N-phosphine oxide substituted imidazolylidenes (Poxlms) for bridging an Al center with a Cu derivative.^[52] This work assessed the viability of both synthetic routes (Scheme 6) and demonstrated that only route A is a workable synthetic path to get the targeted Al(Poxlms)Cu species. Specifically, when the bifunctional Poxlms is contacted with tris(pentafluorophenyl)aluminum, a monometallic Al(Poxlms) is isolated in which the Al atom is bound to O-atom of the hard phosphine oxide donor (Scheme 6, top left). Subsequent reaction of Al(Poxlms) with copper(I) (*tert*-butoxide) leads selectively (yield >98%) to the heterobimetallic architecture where the Cu center forms a dative bond with the soft NHC moiety (Scheme 6, top right). Reversely, when the same Poxlms platform is reacted with Cu(O^{*t*}Bu), the monometallic (Poxlms)Cu complex is isolated (Scheme 6, bottom left). However, the second step involving to treat (Poxlms)Cu with Al(C₆F₅)₃ does not cleanly form the targeted product but leads instead to a complex mixture of numerous species where the heterobimetallic entity is detected in low quantities (33% NMR yield) along with HC₆F₅ (9 % NMR yield) and isobutene (10% NMR yield) (Scheme 6, bottom right). This investigation therefore testifies to the non-equivalence of the two synthetic routes.



Scheme 6. Comparative syntetic routes (route A and route B) towards the design of an Al/Cu heterobimetallic complex. The two metal centers were assembled by bifunctional N-phosphine-oxide-substituted imidazolylidenes (Poxlms) platforms.^[52]

Success of route A (Scheme 3) is also demonstrated by D. Bourissou and coworkers who reported the conception of a series of Al/M heterobimetallic complexes based on bifunctional

alkynylphosphine bridges – abbreviated CP thereafter (Scheme 7).^[53-55] The authors took inspiration from an earlier study reporting the design of geminal phosphorus/aluminum-based Frustrated Lewis Pairs (FLPs) by performing hydroalumination of alkynylphosphine ligands (first step of Scheme 7).^[56] Here, the Al center is covalently bonded to the X-type alkenic carbon. The resulting monometallic Al(CP) species is then contacted with late transition metallic derivatives, such as $[\text{Rh}(\text{nbd})(\mu\text{-Cl})_2]$ (nbd=norbornadiene), $[\text{Pd}(\text{allyl})(\mu\text{-Cl})_2]$, $[\text{Au}(\text{Cl})(\text{PMe}_3)]$, or $[\text{Pt}(\text{C}_2\text{H}_4)(\text{PPh}_3)_2]$, yielding the ultimate Al/M heterobimetallic entities where the L-type phosphine donor is coordinated on the M centers (second step of Scheme 7). In comparison with the systems described earlier in this chapter, the originality of these compounds is the close distance between the Al and M sites, allowing good M→Al dative interactions. This unusual bonding situation is promising for reactivity purposes.



Scheme 7. Synthesis of heterobimetallic Al/M species starting with bifunctional alkynylphosphine ligands.^[53-56]

In recent years, Route A is also employed to generate a range of original Al/M heterobimetallic species assembled by bifunctional nitrogenous-phosphine type chelating ligands, commonly named PAIP pincer-ligands. Structures of the reported (PAIP)M complexes are represented in Figure 2.^[57-66]

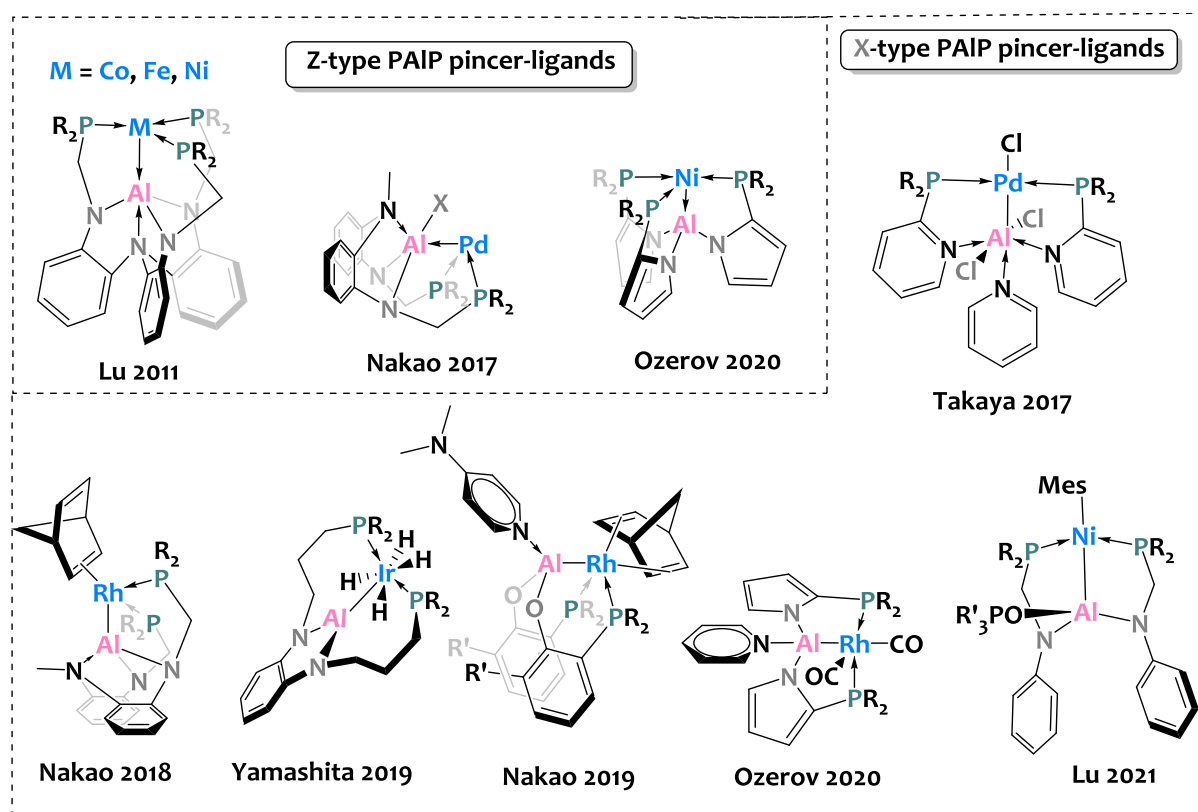
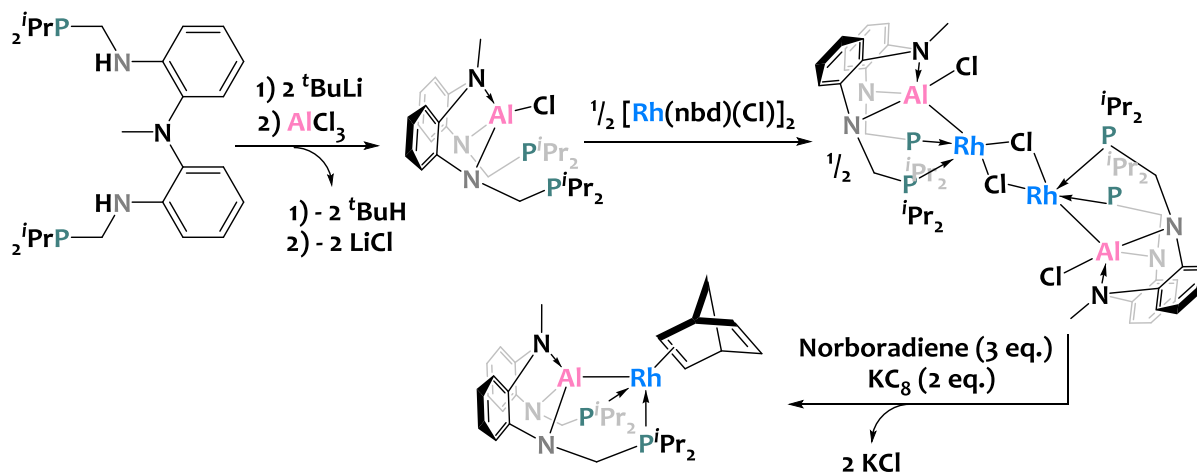


Figure 2. Structures of M complexes bearing PAIP ligands. (Top left) Z-type PAIP pincer-ligands.^[57–59] (Top right and bottom) X-type PAIP pincer-ligands.^[60–67] The colors notation follows Green formalism in agreement with the drawing of Scheme 3.

The different reported M(PAIP) heterobimetallic entities can be divided into two categories. The first one corresponds to late transition metal complexes linked to Z-type alane PAIP ambiphilic scaffolds through dative $M \rightarrow Al$ bonds (Figure 2, top left). In this case, the Al center has a formal charge of +III and is covalently bound to 3 exogenous X-type amido or halide ligands. The second category relates to X-type aluminyl PAIP pincers in which the Al center is covalently bound to only 2 exogenous X-type N or O donors, and eventually to additional N or O Lewis bases. One electron from the Al site is thus engaged in the covalent bond with the *d*-bloc M center (Figure 2, right and bottom).

An illustrative example, developed by Y. Nakao and his team, is represented on Scheme 8.^[66]



Scheme 8. Synthesis steps to form a PAIP(Rh) complex starting from a di(amino-phosphine) ligand.^[66]

After designing a sophisticated $(\text{NH-PR}_2)_2$ platform,^[68] the di(amino-phosphine) ligand is deprotonated with two equivalents of *tert*-butyl lithium. The resulting $(\text{N}^-\text{PR}_2)_2$ intermediate is contacted with aluminum trichloride yielding an alane PAIP species (first step on Scheme 8). This monometallic Al(III) complex is then reacted with norbornadiene rhodium(I) chloride dimer to form a first Al(III)/Rh(I) dimer (second step on Scheme 8). Reduction of this complex by two equivalents of KC_8 affords the targeted PAIP-Rh product (third step on Scheme 8).

In summary, the chemistry of Al/M complexes assembled by bifunctional ligands is quite diversified, whether in terms of structures or ways of accessing such molecular objects. This subsection highlights the richness of the bifunctional platforms containing different sorts of hard X-type and soft L-type donors. These are very effective to drive the selective assembly of Al and *d*-bloc metal centers. However, the stabilization of the heterobimetallic architectures by chelating ligands can sometimes drastically diminish their reactivity. Furthermore, the smart design of sophisticated pro-ligands, as well as original but sometimes challenging metallation strategies are required to enter this chemistry. This implies extra synthetic efforts and costs. We will see in the next subsections that there are more straightforward synthetic approaches to construct heterobimetallic Al/M architectures.

1.2.1.2 Formation of Lewis adducts

Lewis acidic aluminum(III) centers may be directly coordinated by Lewis basic transition metal precursors to form $\text{M} \rightarrow \text{Al}$ adducts, in the absence of bridging ligands.^[69,70] The term Metal-Only Lewis Pairs (noted MOLPs thereafter) emerged recently to refer to such compounds. Until 2007, only one XRD structural evidence of a metal-only Lewis pair featuring an unsupported $\text{M} \rightarrow \text{Al}$

dative bond was known (Figure 3, left).^[71] Then, from 2007 to 2012, K. Radacki, J. Bauer and coworkers reported a series of neutral platinum(0)-alane adducts featuring dative Pt→Al bonds (Figure 3, middle).^[72-74] In 2020, J. Campos and coworkers reported a metal-only Lewis pair of rhodium(I) with trimethylaluminum(III) (Figure 3, right).^[69]

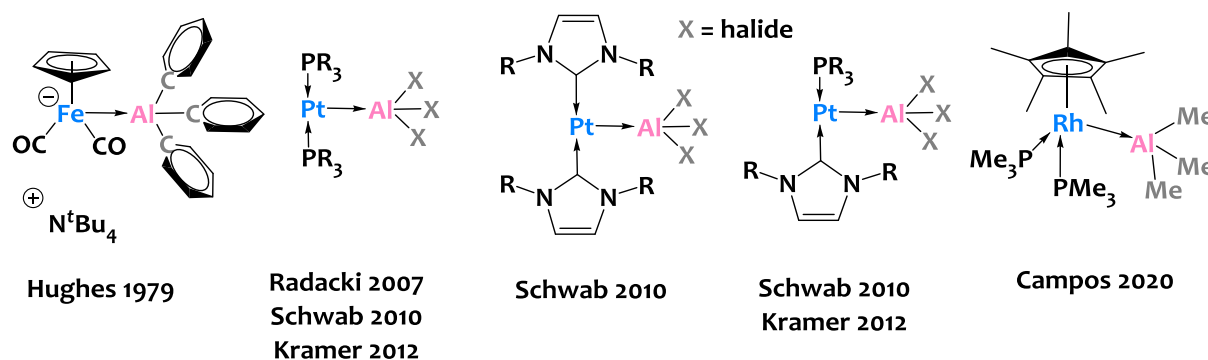
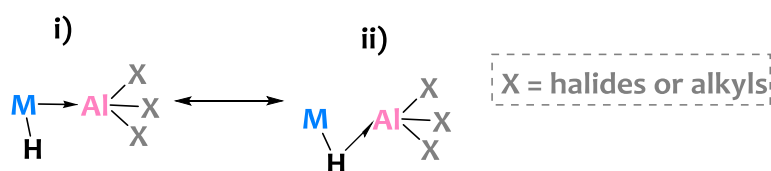


Figure 3. Reported XRD structures of MOLPs of d-block metals with aluminum.^[69-74]

When the M precursor has potentially bridging ligands in its coordination sphere, typically hydrides, different modes of ligation between the Al and M centers are possible.^[8] Scheme 9 represents two limiting resonance forms of hydride Lewis adducts.

i) The first describes a dative bond between a nucleophilic L-type metal-hydride derivative to an electrophilic Z-type Al(III) precursor through a donation of d electrons of the TM center to the Al atom (Scheme 9, case i)). In other terms, the metallic donor gives its lone pair to an empty p orbital of an aluminum acceptor resulting in an unsupported M→Al motif. Here, the hydride is not participating in the intermetallic interactions meaning they are in terminal positions.

ii) Also, the Al and M centers can be bridged by one or several hydrides featuring 3 centers-2 electrons (3c-2e) bond. In this case, the electronic donation is centered from the hydride to the Al.



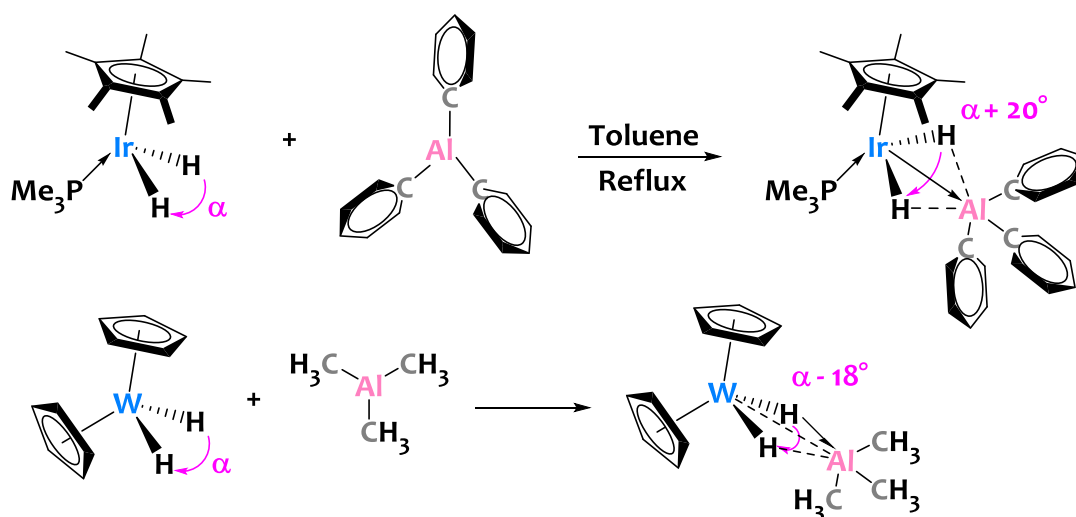
Scheme 9. Mesomeric forms of Lewis adducts describing interactions between a TM hydride and an AlX₃ derivative.

However, nature of the bonding between M-H and Al centers in hydride Lewis adducts is most of the time very complex to categorize in cases i) or ii) because each can contribute to the intermetallic interactions. This discussion is further complicated when several hydrides are bonded to the transition metal atom. Common ways to rationalize mesomeric forms i) and ii) for

one given Al/M adduct is to use metrical parameters of its XRD solid-state structure or to perform DFT calculations to get insights into the nature of the $M(H)_n\text{-Al}$ interactions.

Recently, M. R. Crimmin and M. J. Butler published an interesting review regarding transition metals hydrides Lewis adducts.^[8] They especially reviewed metal hydrides ligated to aluminum Lewis acids in a subsection of their publication. Here, we will not survey all the transition metal aluminum adducts but we will instead depict two relevant examples of strong interest for this PhD project.

An interesting and rare case of a $M(H)_n\text{-Al}$ adduct was reported by R. G. Bergman and his team in 1998 (Scheme 10, top).^[25] In this paper, an iridium dihydride precursor is reacted with triphenylaluminum(III) in refluxing toluene to yield an original $\text{Cp}^*(\text{PMe}_3)\text{H}_2\text{Ir} \rightarrow \text{Al}(\text{Ph})_3$ Lewis adduct.



Scheme 10. Reported synthesis of $(\text{Cp}^*)(\text{PMe}_3)\text{H}_2\text{IrAl}(\text{Ph})_3$ (top)^[25], and $(\text{Cp})_2\text{W}(\text{H})(\mu\text{-H})\text{Al}(\text{Me})_3$ adducts.^[75-77]

To get insights into the nature of the bonding in this Ir/Al species, the authors emphasized two XRD metrical parameters. The first one is the formal shortness ratio (FSR) which is the ratio between the apparent metal-metal distance and the sum of the metal radii of the two metals: $\text{FSR} = d_{\text{MM}}/(r_{\text{M}_1} + r_{\text{M}_2})$. The FSR thus translates here into the measured Ir-Al distance divided by the sum of Al and Ir covalent radii.^[78] J. F. Berry and his team have established a scale of covalency according to the FSR.^[79] According to their work, two metals can form a covalent bond if the FSR is lower than 1.22. Generally, a single metal-metal bond corresponds to a FSR ~ 1.01 ; a double bond to a FSR ~ 0.92 and a higher order bond to a FSR < 0.92 . However, while the use of this parameter is relevant for the description of σ and π bonds, it remains limited for delta bonds. Indeed, the

small overlap of d orbitals in δ symmetry does not significantly impact the intermetallic distance. In this case, theoretical calculations are generally necessary and more informative than the simple analysis of metrical parameters. In the case of this Ir/Al derivative, the FSR is close to unity and might suggest fairly strong interactions between Al and Ir centers.

The second parameter is the H-Ir-H angle (noted α on Scheme 10), which opens by 20° upon coordination of the iridium center to the aluminum and indicates that the two H atoms move away from each other to make room for the $\text{Al}(\text{Ph})_3$ fragment.

Such observations are quite similar to the mesomeric form i) depicted on Scheme 9 and discussed above. However, we cannot exclude the presence of weak interactions between the hydrides and the Al center and resonance form ii) (Scheme 9) is also likely at place in this hydride Al/Ir adduct.

This first example is kind of opposite to the one presented at the bottom of Scheme 10. In fact, A. Storr, G. Caulton and coworkers reported the reaction of a dihydride tungsten motif with TMA to give a bimetallic $\text{W}(\text{H}_2)\text{Al}$ species.^[75,77] In this case, XRD studies show a long separation of $3.110(3)$ Å between W and Al, which translates into a FSR quite far from 1.00.^[75] Furthermore, H-W-H angle (α parameter on Scheme 10) closes by 18° when the $\text{W}(\text{Cp})_2(\text{H})_2$ fragment binds the $\text{Al}(\text{Me})_3$ portion, suggesting therefore an approach of the two hydrogen atoms that prevents the proper proximity between the W and Al atoms.^[75] Eventually, an asymmetrization between the two hydrides is observed since H1-W and H2-W distances are not equals (1.71 Å vs 1.22 Å) as well as H1-Al and H2-Al (1.97 Å vs 2.08 Å). These aspects trend to describe the dihydride Al/W species close to the mesomeric form ii) represented on Scheme 9, *i.e.* the Al and W atoms are bridged by a single hydride to give a $3c-2e$ bond-type. However DFT calculations performed on this species show more contrasted conclusions as a donation of d-electrons from W to Al is also to be considered and therefore mesomeric form i) is also participating in the intermetallic interactions.^[76]

In conclusion, $\text{M} \rightarrow \text{Al}$ and $(\text{H})_n\text{M} \rightarrow \text{Al}$ adducts are very interesting compounds because their synthesis is very simple (just mix the two Lewis partners, no side products, etc). Moreover, the resulting heterobimetallic species, exhibiting either a dative $\text{M} \rightarrow \text{Al}$ bond or a $3c-2e$ $\text{M}(\text{H}) \rightarrow \text{Al}$ bond or both types of bonds, embody preferred architectures for gaining a fundamental understanding of bimetallic bonding. However, there is a synthetic limitation: in fact, a great challenge lies in the selection and synthesis of a suitable metallic Lewis base that should combine many properties such as a low oxidation state, a nucleophilic character, and an unsaturated coordination sphere to accommodate an Al(III) Lewis acceptor.

We will see in the following sections that other synthetic strategies exist to circumvent this type of limitation.

1.2.1.3 Design of alumylene, or alumanyl metallo-ligands

An original strategy to construct heterobimetallic Al/M species, which can be seen as the reverse of the approach discussed just above, consists in using uncommon nucleophilic aluminum donors (generally in the +I oxidation state), which can be coordinated to electrophilic late transition metal centers (Scheme 2, approach **iii**). Two families of aluminum ligands have been developed (see Figure 4).

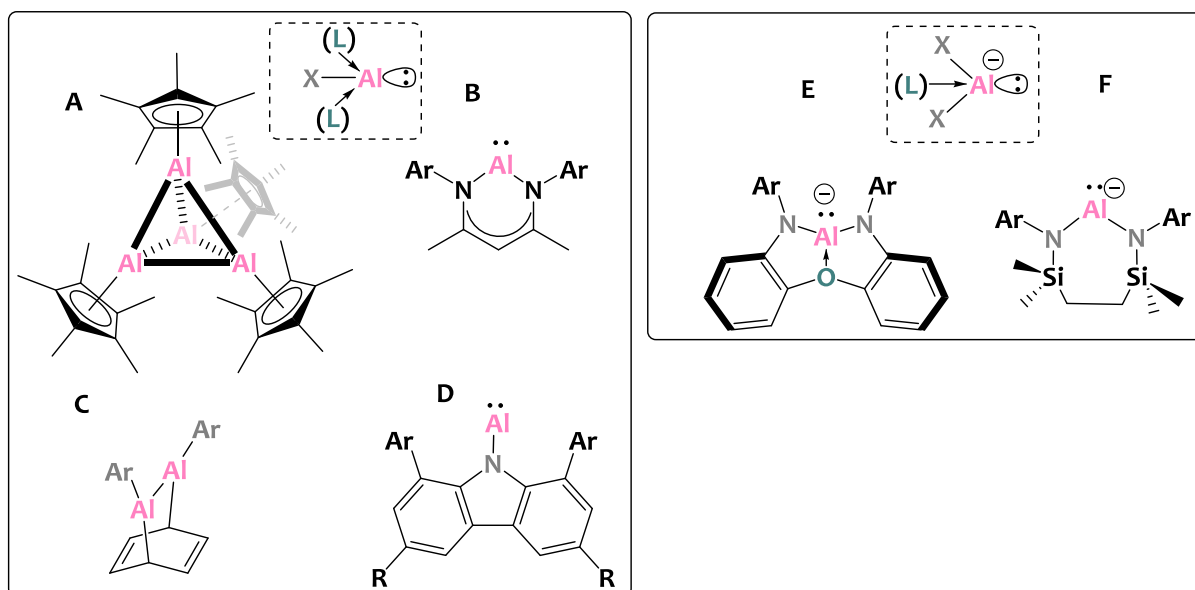
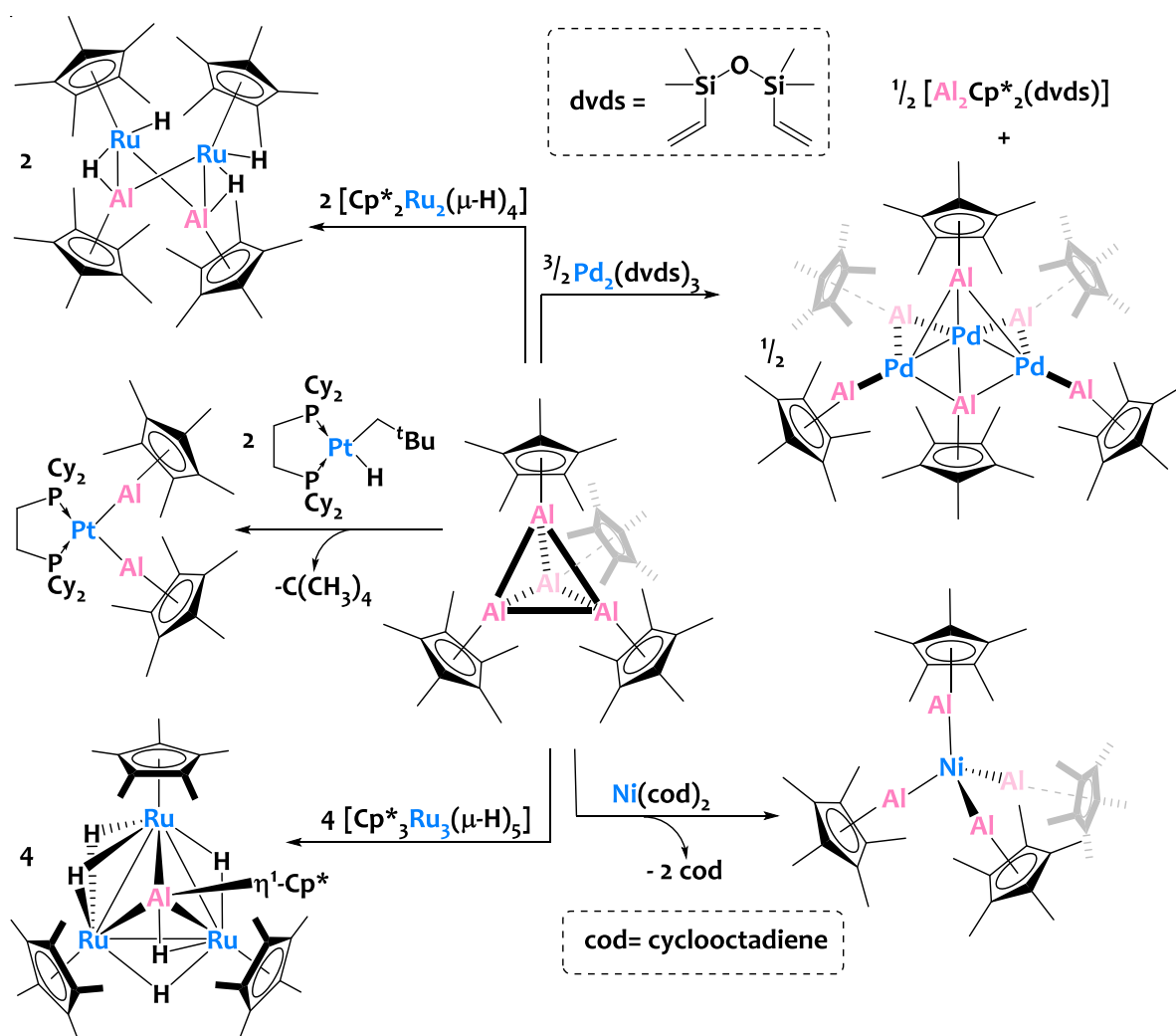


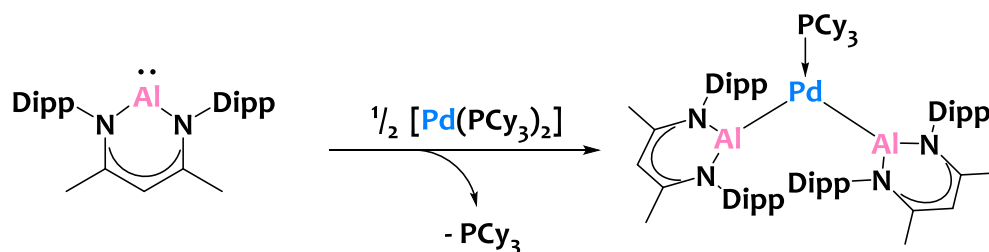
Figure 4. Known neutral L-type alumylene (Family 1 - left)^[80–83] and anionic X-type alumanyl ligands (Family 2 - right)^[84–89] used to form heterobimetallic Al-M complexes.

Family 1 denotes neutral L-type alumylene donors (Figure 4, left). Within this first class of compounds, four reported neutral Al species are used to coordinate late transition metallic precursors. The first one is the tetrahedral $[Al_4Cp^*_4]$ cluster (Figure 4A), discovered in 1991 by H. Schnöckel and coworkers.^[90] and featuring Al-Al bonds. A few years later, this precursor is especially used to coordinate Pt,^[91] Pd,^[92] Ru,^[93,94] Fe,^[94] or Ni^[95] complexes leading to original heterobimetallic Al-M clusters (Scheme 11). The second alumylene ligand, reported in 2000 by F. Cimpoesu and colleagues, is a monomeric aluminum (I) analogue of carbene, which is based on a crowded β -diketoiminato ligand (Figure 4B).^[81] Such molecule features a low-coordinate Al(I) center with a lone pair. This Al(I) donor is successfully ligated to a series of Pd,^[96–98] Pt,^[96] Cu,^[99,100] Co,^[100] Mn,^[100] Cr,^[100] or Fe^[100] metallic derivatives to yield heterobimetallic Al-M species. For instance, M. R. Crimmin and coworkers reported the synthesis of a trinuclear Al_2Pd species from the monomeric Al(BDIDipp) precursor (BDIDipp = $[HC(CMeNDipp)_2]^-$ Dipp = 2,6-*i*-Pr₂C₆H₃) and $[Pd(PCy_3)_2]$ (see Scheme 12).^[98] The third Al ligand was reported by N. Tokitoh and his team in

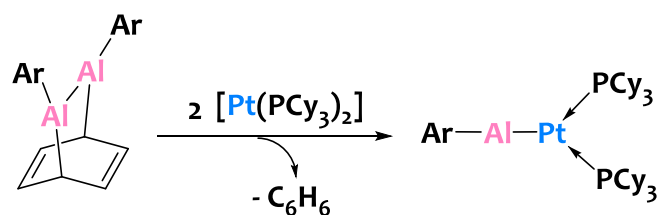
2013 and relates to a dialumene-benzene adduct (Figure 4C).^[83,101] The latter is contacted with $[\text{Pt}(\text{PCy}_3)_2]$ to yield a remarkable low-valent terminal arylaluminum-platinum complex (Scheme 13).^[101] Very recently, at the end of the year 2021, L. L. Liu and his team reported the design of a new monocoordinated L-type carbazoylaluminum (Figure 4D).^[80] The latter is treated with tungsten, chromium, and copper derivatives to form original heterobimetallic Al-M complexes (Scheme 14).



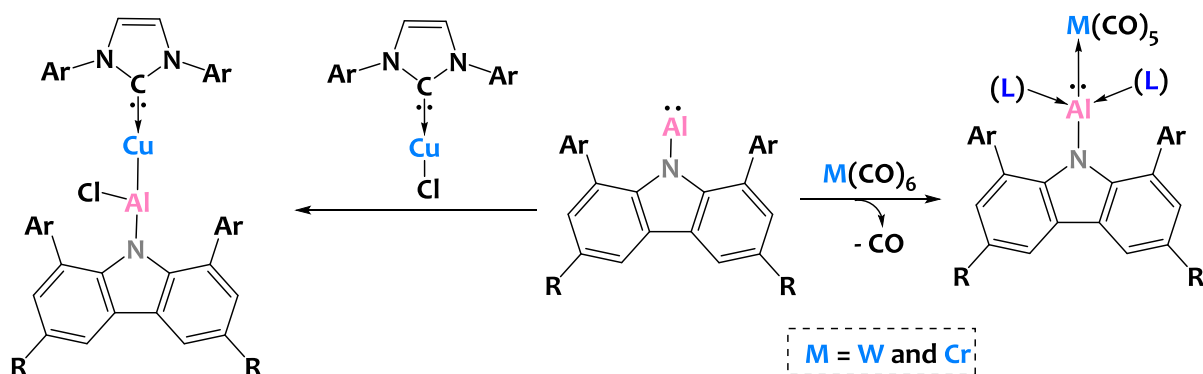
Scheme 11. Examples of reported synthesis of heterobimetallic Al-M clusters from $[\text{Al}_4\text{Cp}^*_4]$ precursor.^[91-93,95]



Scheme 12. Reported synthesis of a $\text{Al}_2\text{-Pd}$ complex from Al(BDIDipp) aluminylene precursor.^[98]

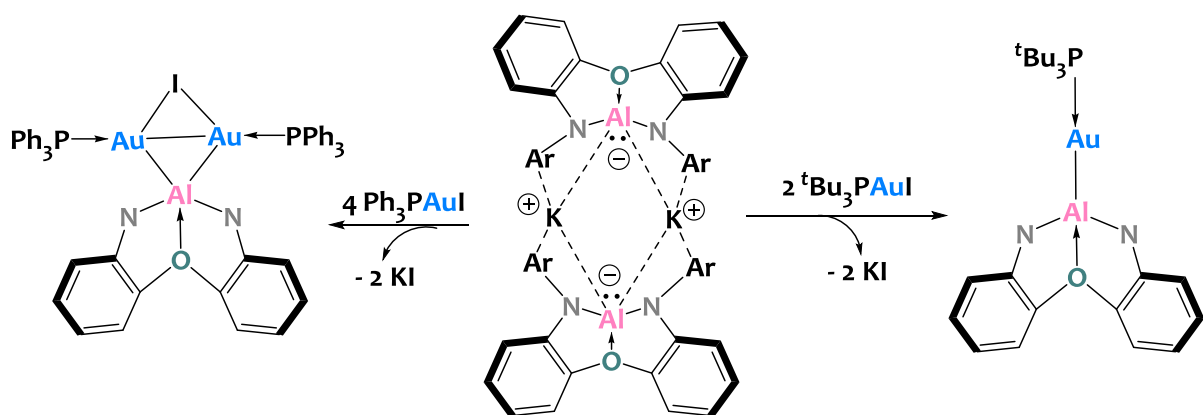


Scheme 13. Reported synthesis of a Al-Pt complex from a dialumene-benzene adduct.^[101]



Scheme 14. Reported synthesis of Al-M species from a carbazolyaluminumylene precursor.^[80]

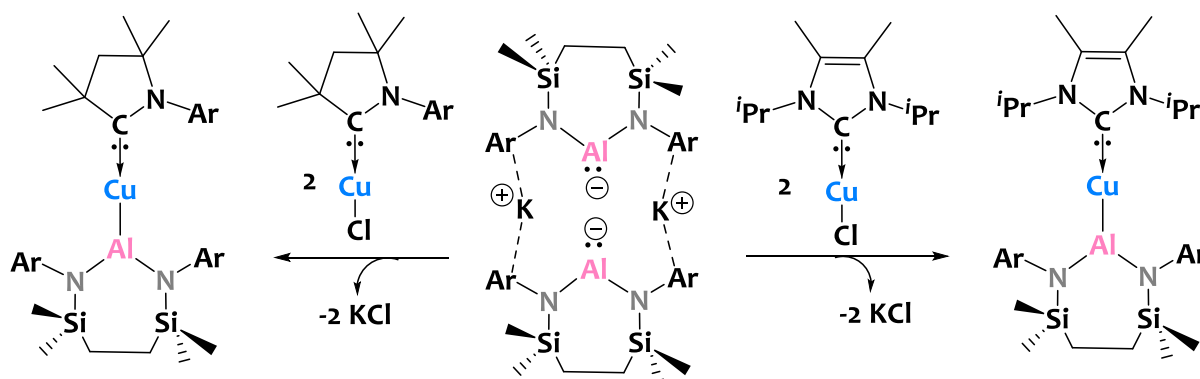
In 2018, the discovery of a new series of anionic Al(I) compounds by S. Aldridge and colleagues - family 2 (Figure 4, right) - named aluminyl anions, reignited important interests in the area of Al chemistry. The originally reported species consisted of a three-coordinate Al center supported by a dianionic, di(amido)dimethylxanthene-based scaffold (Figure 4E), with the charge balanced by potassium cations (full structure drawn on Scheme 12 - middle).^[84] This remarkable nucleophilic aluminyl species - $[\text{K}\{\text{Al}(\text{NON})\}]_2$ (NON = 4,5-bis(2,6-diisopropylanilido)-2,7-di-tert-butyl-9,9-dimethylxanthene) - is contacted with electrophilic phosphine-ligated gold iodide precursors, to give heterobimetallic Al-Au₂ and Al-Au complexes featuring strongly polarized $\text{Al}^{\delta+}\text{-Au}^{\delta-}$ bonds.^[87]



Scheme 15. Reported synthesis of aluminum-gold complexes starting from $[\text{K}\{\text{Al}(\text{NON})\}]_2$ aluminyl species.^[87]

According to the same line of reasoning, C. L. Mc Mullin, N. A. Rajabi and coworkers reported in

2020 the sophisticated design of a seven-membered heterocyclic diamidoaluminum species (Figure 4F) stabilized by potassium cations, named $[K\{Al(SiNDipp)\}]_2$ ($SiNDipp = \{CH_2SiMe_2NDipp\}$, full structure drawn on the middle of Scheme 16).^[85] The next year, same authors reported the reaction of this nucleophilic $[K\{Al(SiNDipp)\}]_2$ with copper(I) chloride carbene adducts to form unprecedented Al-Cu complexes (Scheme 16).^[89]

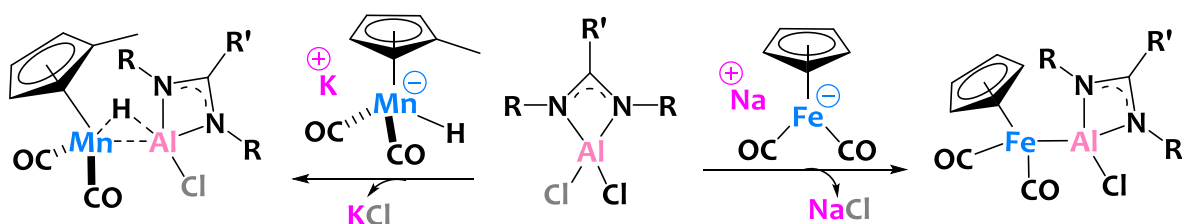


Scheme 16. Reported synthesis of unsupported aluminum-copper starting from $[K\{Al(SiNDipp)\}]_2$ precursor.^[89]

In conclusion, the use of L-type alumylene $AIX(L)_n$ and X-type alumanyl $AIX_2(L)_n$ metallo-ligands is an elegant approach to design original heterobimetallic Al-M complexes through, most of the time, σ -donation from the Al lone pair to the d-block metal center. This strategy attracted increased attention in the last three years. However, the conception of Al metallo-ligands is very challenging, especially for the alumanyl anions, which require multi-step syntheses and harsh reduction conditions (KC_8 typically). Furthermore, intelligent design of robust and sophisticated bulky side arms (aromatics most of the time) around the aluminum center is required to stabilize the Al species. All these aspects may therefore represent synthetic limitations.

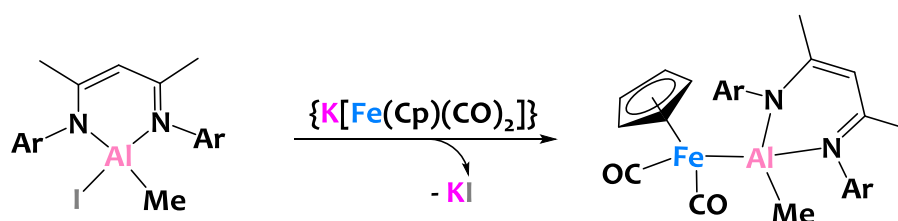
1.2.1.4 Salt metathesis

A classical method to form Al-M bonds entails to contact an aluminum(III) halide derivative with a sodium or potassium metallate salt (Scheme 2 – approach **iv**). This strategy – named salt metathesis – leads to the elimination of an insoluble alkali halide salt (in apolar solvent), which, by precipitation, shifts the equilibrium of the reaction toward the formation of the desired product. For instance, S. Aldridge and coworkers reported in 2013 the use of salt metathesis for the design of Al-Fe, Al-Ru, and Al-Mn species by reacting guanidinato or amidinato aluminum dichlorides reactants with iron, ruthenium, or manganese-based organometallic anions (Scheme 17).^[102]



Scheme 17. Illustrative example of the salt metathesis between an aluminum halide reactant and sodium or potassium metal carbonylate anions leading to Al-Fe and Al-H-Mn complexes.^[102]

Another example was reported in 2022 by N.P. Mankad and coworkers. In this study, a β -diketoiminate-methyl-aluminum(III) iodide is treated with $\{K[Fe(Cp)(CO)_2]\}$, yielding an Al-Fe heterobimetallic complex along with potassium iodide salt (Scheme 18).^[103]



Scheme 18. Another illustrative example of the salt metathesis between a β -diketoiminate-Al reactant and a potassium iron carbonylate derivative leading to an heterobimetallic Al-Fe complex.^[103]

Salt metathesis is employed for a diversity of aluminum(III) halide precursors.^[102–109] However, this strategy is only limited to anionic metallocarbonylate species of iron^[102–109], ruthenium^[102], manganese^[102], chromium^[105,109], molybdenum^[109], and tungsten^[105,109] derivatives. This assertion therefore demonstrates the challenge in choosing a potassium or sodium metallate species with suitable properties (good nucleophile, well-adjusted redox potential etc.). Moreover, depending on the experimental conditions, the separation of the alkali halide salt from the Al-M product is sometimes difficult, which represents practical limitations.

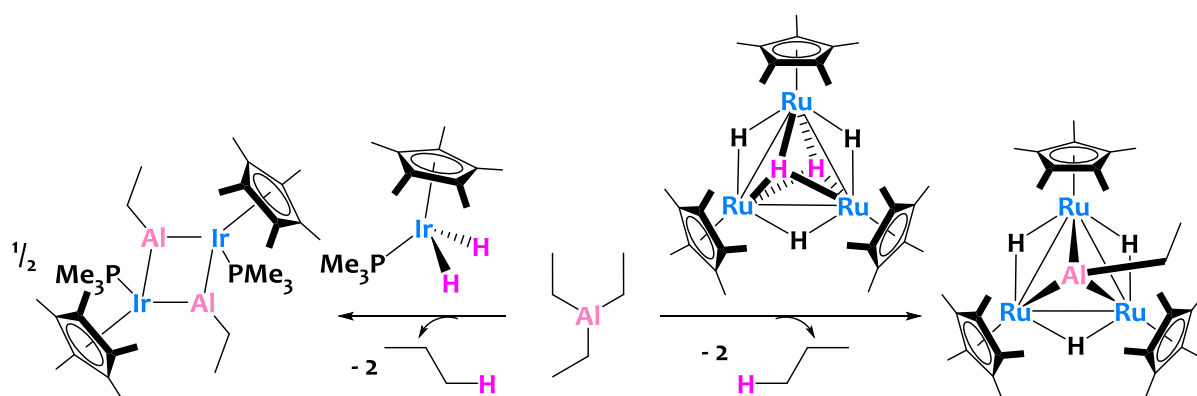
To sum up, salt metathesis is - on paper - straightforward to implement and embodies a choice of interest to selectively form Al-M bonds. However, as discussed above, there are some experimental limitations, which probably explain why this approach is not so much extended to a wider variety of Al/M couples.

1.2.1.5 Alkane elimination

Another simple and powerful approach to design Al-M heterobimetallic complexes or clusters involves an acid-base reaction of a late transition metal hydride precursor, featuring Brønsted acidic properties, with an alkyl-aluminum reagent acting as Brønsted base. This protonolysis

reaction leads to the targeted Al-M edifice along with volatile alkanes (Scheme 2, case **v**)). This synthetic strategy is most of the time straightforward, selective and clean as the generated alkane can be easily separated from the reactional medium and no further purification of the product is generally required.

To our surprise, only five occurrences in literature refer to this strategy for forming Al-M species (M=Ir, Ru, Pt, and Mo).^[24–26,110,111] Among these, only two research works clearly highlight this mechanism.^[25,26] The first was reported by R.G. Bergman and his team in 1998.^[25] In this study, they carried out a double deprotonation of a bis-hydride iridium(III) derivative by triethylaluminum(III) (TEA) to yield an original centrosymmetric [Ir-Al]₂ dimer with evolution of two equivalents of ethane (Scheme 19, left). In the same vein, H. Suzuki and colleagues reported in 2003 the double deprotonation of a pentahydride trinuclear ruthenium precursor by TEA leading to the formation of an original trishydride Al-Ru₃ cluster (Scheme 19, right).^[26]



Scheme 19. Alkane elimination of triethylaluminum with $[\text{IrCp}^*\text{H}_2\text{P}(\text{Me})_3]$ yielding an Al-Ir cluster (left side) and with $[\text{Ru}_3\text{Cp}^*(\mu\text{-H})_3]$ yielding an Al-Ru₃ cluster (right side).^[25,26]

Alkane elimination is therefore not well established for Al/M species. One limitation to extend this chemistry is linked to the challenge of associating metal-hydrides (MH_n) and alkyl-aluminum (AlR_3) species with well-adjusted pKas to trigger alkane elimination. In other terms, the pKa of the MH_n partner should be low (acidic) enough while the pKa of the alkyl aluminum partner should be high (basic) enough to trigger this reaction. Another practical limitation could be connected to the high pyrophoric property and air and moisture sensitivity of these precursors. However, we strongly believe these drawbacks do not offset the benefits discussed above. Indeed, alkane elimination made its proofs in our research team for preparing Ta-Ir species.^[27–29] This approach is also well-adapted for surface chemistry on supports since alkanes are easily eliminated and there are no side-products. That is why a big part of this project will focus on extending alkane elimination strategy for Al-M species.

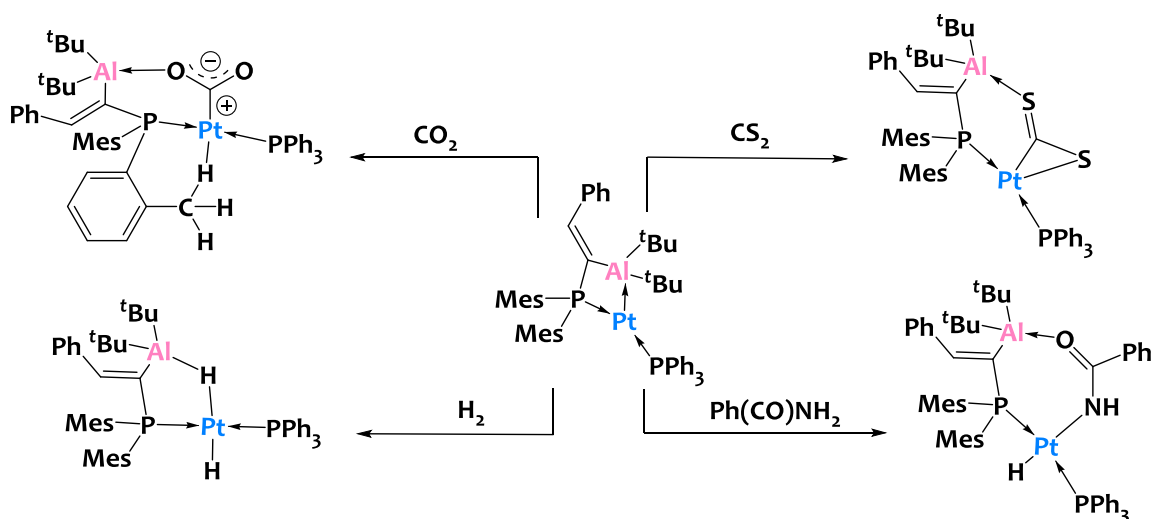
1.2.2 Stoichiometric and catalytic reactivity

In the previous section (1.2.1), we depicted an overview of the different synthetic approaches to design Al/M heterobimetallic edifices. This bibliographical screening highlighted not only a plethora of reported Al/M structures but also a strong diversity of synthetic strategies to construct such molecular entities. However, and quite surprisingly, very few research works paid attention to study the stoichiometric or catalytic reactivity of these heterobimetallic species. In the following section, we will describe some of these few reported reactivities of Al/M complexes that are relevant to this PhD project.

1.2.2.1 Cooperative stoichiometric activation of substrates

From 2016 to today, a few research teams were interested in the study of the reactivity of Al/M heterobimetallic species towards small molecules. They particularly focused on the behaviors of CX₂-type heteroallenes substrates (such as CO₂, CS₂, R-N=C=N-R, etc).

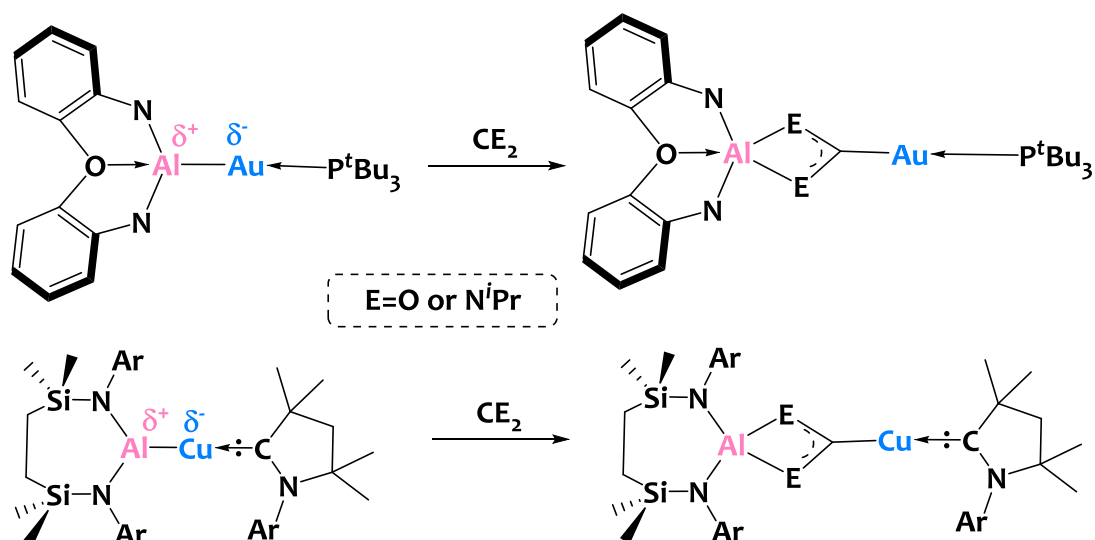
For example, D. Bourissou and coworkers demonstrated in 2016 the rich reactivity of a Pt→Al complex towards CO₂, CS₂, H₂, and Ph(CO)NH₂ (Scheme 20).^[55] Notably, a CO₂ molecule is inserted into the Pt→Al bond where the electrophilic carbon is coordinated to the nucleophilic Pt center while the Al center stabilizes one of the two nucleophilic oxygen atoms (Scheme 20, top left). Similarly, this study shows the reductive insertion of carbon disulfide into the Pt→Al bond resulting in the formation a new Pt-CS₂-Al species where the electrophilic carbon and the thiolate moiety are bond to the Pt atom while the nucleophilic S interacts with the Al center (Scheme 20, top right). Next, treatment of the bimetallic precursor with dihydrogen leads to the oxidative addition of H₂ across the Pt→Al bond that forms a dihydride-platinum/aluminum species where one H is at terminal position while the other is bridging the two metal atoms (Scheme 20, bottom left). The authors also reported oxidative addition of benzamide onto this Pt/Al species (Scheme 20, bottom right). In these reactions, the platinum center is formally oxidized by 2 electrons while the aluminum center acts as an assisting Lewis acid to stabilize the inserted fragment via O,S→Al or Pt-H→Al interactions. In conclusion, this work testifies to a remarkable Al/TM cooperativity reminiscent of the case **ii**) described in Scheme 1 (see page 47).



Scheme 20. Reported reactivity of a Pt,Al-complex with small molecules.^[55]

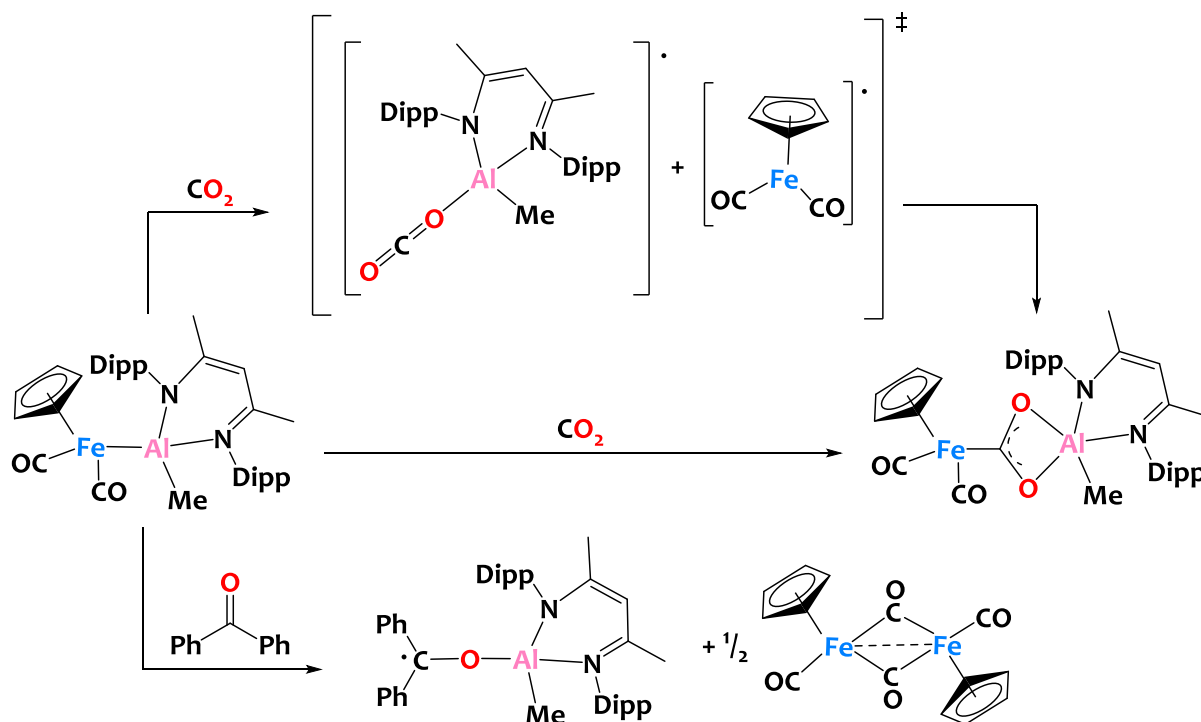
Bimetallic Al-M cooperative insertion of heteroallenes (CO_2 , $\text{C}(\text{N}^i\text{Pr})_2$) was reported by S. Aldridge, N. A. Rajabi and coworkers in 2019 and 2020 (Scheme 21).^[87,89] In this work, the authors reported the design of bimetallic Al-Au and Al-Cu species featuring polarized $\text{Al}^{\delta+}\text{-M}^{\delta-}$ bonds. Reductive insertion of carbon dioxide or N,N'-diisopropylcarbodiimide (noted CE_2 thereafter) into the Al-M bond produce copper or gold metallacarboxylate $\text{M-CE}_2\text{-Al}$ complexes. In these compounds, the electrophilic carbon is coordinated to the nucleophilic copper or gold atom while the nucleophilic oxygen or nitrogen atoms are bond to the electrophilic Al center. Note that this coordination mode of CE_2 is quite uncommon, but was already encountered for a homobimetallic amido-digermyne intermediate – $[\text{Ge-CE}_2\text{-Ge}]$.^[112] The authors initially assumed that carbon dioxide activation operates by considering the $[(\text{NON})\text{Al-Au}(\text{tBu}_3)]$ molecule as a combination of a $[(\text{NON})\text{Al}]^+$ fragment with a nucleophilic $[\text{Au}(\text{tBu}_3)]^-$ fragment. However, DFT calculations performed in 2021 by P. Belanzoni and her team demonstrate that the Au-Al interactions turns out to be dominated by an electron-sharing nature, *i.e.* the two metal fragments are better described as $[(\text{NON})\text{Al}]^\bullet$ and $[\text{Au}(\text{tBu}_3)]^\bullet$ radicals, which display a diradical-like reactivity with CO_2 .^[113] Same authors showed similar conclusions for the Al-Cu complex.

In conclusion, the reported reactivities of Al/M complexes with heteroallenes are very interesting and testify to an Al/M cooperativity reminiscent of the general case **iii**) presented in Scheme 1 (see page 47), although the exact mechanism in place in these systems is still matter to debate.



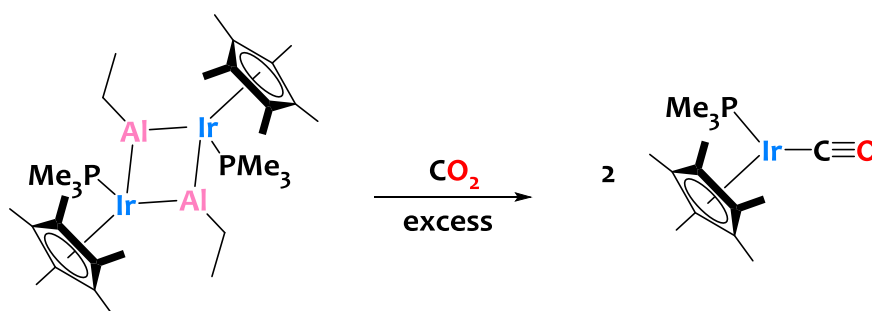
Scheme 21. Reported cooperative insertion of carbon dioxide or N,N'-Diisopropylcarbodiimide into an Al-Au^[87] and Al-Cu^[89] complexes.

Along the same line, N. P. Mankad and coworkers reported in 2022 the cooperative activation of carbon dioxide by an heterobimetallic Al-Fe complex operating through a radical pair mechanism (Scheme 22, middle).^[103] The most favourable calculated reaction pathway shows first a homolytic dissociation of the Al-Fe complex into Al(II) and Fe(I) metalloradicals. Then, carbon dioxide is fixed by the metalloradicals in pairwise fashion through a kinetically accessible $\text{CO}_2\text{-Al}^\bullet$ transition state (represented at the top of Scheme 22), which ultimately yields an iron metalcarboxylate product, quoted here $[\text{Fe}(\text{CO}_2)\text{Al}]$ (Scheme 22, right). To experimentally confirm a radical pathway, the authors conducted a study where they react benzophenone with the bimetallic complex. This leads to the formation of a stable Al(II) metalloradical along with $[\text{Fe}(\text{Cp})(\text{CO})_2]_2$ presumably originating from the dimerization of the $[\text{Fe}(\text{Cp})(\text{CO})_2]^\bullet$ radical (Scheme 22, bottom). Compared to the other above-studies, this work is quite remarkable since there is experimental evidence to support the proposed mechanism.



Scheme 22. Reaction of an Al-Fe complex with CO₂ and benzophenone.^[103]

One last example that deserves special attention was reported by R. Bergman and coworkers in 1998.^[25] Indeed, reaction of an [Ir₂Al₂] dimer with excess carbon dioxide leads to the breaking of Al-Ir bonds and to the reductive cleavage of CO₂ into CO – trapped as an iridium carbonyl species (see Scheme 23). Surprisingly, the authors do not mention any comments on the evolution of the aluminum-alkyl moiety or whether or not an oxo species was formed. Therefore, this preliminary work is interesting and quite remarkable because it suggests that CO₂ can be reductively cleaved into CO and O²⁻ by an heterobimetallic species, which, to the best of our knowledge, has never been observed for Al-M species.



Scheme 23. Reported reaction of [Cp*(PMe₃)IrAl(Et)]₂ with CO₂.^[25]

1.2.2.2 Activities in homogeneous catalysis

Applications in homogeneous catalysis of Al-M heterobimetallic complexes are still very limited. Furthermore, very few works demonstrate their superiority in terms of performances and selectivities compared to their monometallic analogues. Yet, these studies testify to the powerfulness and high potential of Al-M catalysts for promoting original transformations not accessible with usual monometallic catalysts.

These works can be classified into two categories: class i): Al/M catalysts where the two metal centers do not interact with each other and/or are not in direct proximity (separated by an organic bridge). Class ii): Al/M catalysts where the two metal centers interact directly with each other and act as a bimetallic entity that promotes the simultaneous activation of an external substrate.

A notable work regarding class i) was reported by M. Yamashita and colleagues in 2017.^[114] They developed an aluminumbenzene-Ir catalyst (Figure 5 - left) that promotes the α -selective C-H borylation of triethylamine (catalyst loading= 5 mol% at T=110°C). The authors showed that this selective catalysis is not possible when using a monometallic iridium analogue - IrOMe(cod)₂ - or a mixture of IrOMe(cod)₂ with an external Lewis acid (methylaluminum bis(2,6-di-*tert*-butyl-5-methylphenoxide)).

Another interesting study of class i) was reported by J-Q Yu and coworkers in 2021.^[115] Their study describe a bifunctional alkoxy-NHC-ligated Ni/Al catalyst that promotes the selective C₃-H alkenylation of functionalized pyridine derivatives thereby overriding the more common C₂ or C₄ selectivity. The proposed Ni/Al active species (represented in Figure 5, right) is formed by mixing Ni(cod)₂ (10 mol%), Al(*i*Bu)₃ (10 mol%) and the alkoxy-NHC (10 mol%, prepared from deprotonation of the corresponding imidazolium proligand by ^tBuONa).

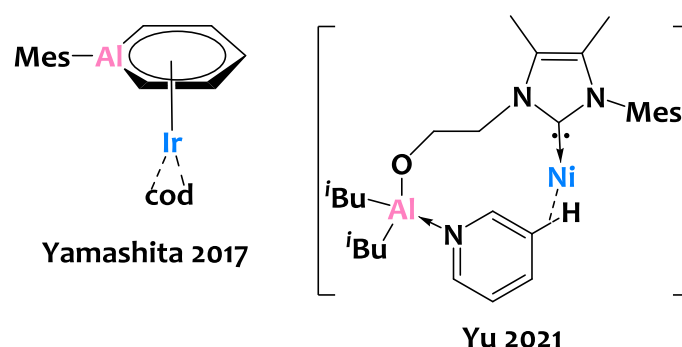
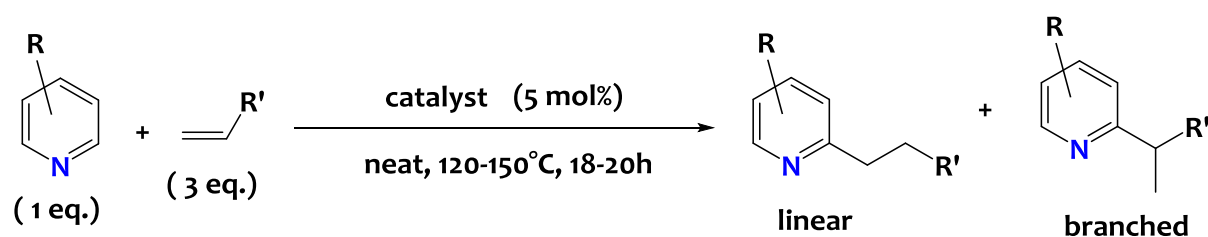


Figure 5. (Left) Reported Al/Ir catalyst promoting the selective alpha borylation of triethylamine.^[114] (Right) Proposed Al/Ni active species promoting the C₃-H alkenylation of pyridine derivatives.^[115]

From 2018 to 2022, Y. Nakao and his research team described very interesting catalytic systems using Al-Rh heterobimetallic complexes of class ii).^[66] For instance, they developed an original C2-selective alkylation of pyridines catalyzed by an Al-Rh species.^[66,116] Description of the catalytic system is presented in Scheme 24. Experimental conditions, performances and selectivity are gathered in Table 1.

The authors found optimal performances when using pyridine with three equivalents of styrene in the presence of 5 mol% of the heterobimetallic Al-Rh catalyst at T=110°C.^[66] After 20 hours of reaction, a 96% NMR yield of C2-alkyl pyridines (linear and branched in a ratio 1/3.4 respectively) is obtained (entry 1 of Table 1). By comparison, no conversion is observed when using a mixture of norbornadiene rhodium(I) chloride dimer (5 mol%/Rh), different types of phosphine ligands (10 mol%/P), and diethylaluminum chloride (5 mol%/Al) under the same experimental conditions (entry 4 of Table 1). Similarly, when using the monometallic alane PAIP precursor as catalyst, no conversion is achieved (entry 5 of Table 1). Note that an excellent selectivity towards the linear product is obtained when changing the alkene source from styrene to 1-octene (entry 2 of Table 1) or trimethylvinylsilane (entry 3 of Table 1) at a temperature of 150°C. The same research team expanded the use of this catalytic system towards 4-methoxypyridine (1 equivalent) and 1,1,1,3,5,5,5-heptamethyl-3-vinyltrisiloxane (3 equivalents) at T=120°C.^[116] Here, the linear product is selectively obtained in excellent yields (entry 6 of Table 1). By comparison, almost no products are quantified by GC when using a mixture of the monometallic Al and Rh analogues in combination with phosphine ligands (entry 7 of Table 1), or with the alane PAIP precursor (entry 8).



Scheme 24. Reported catalysis of a C2-selective alkylation of pyridines.^[66,116]

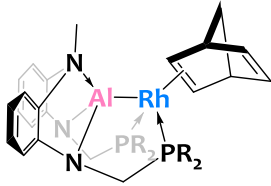
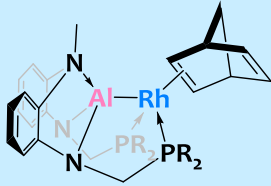
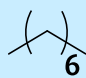
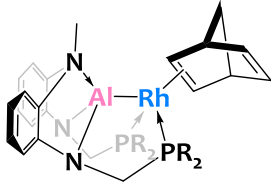
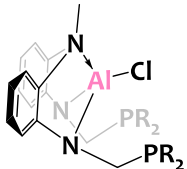
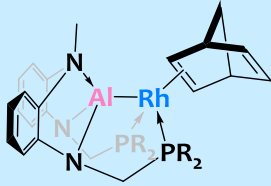
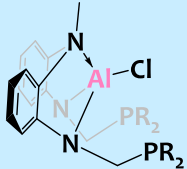
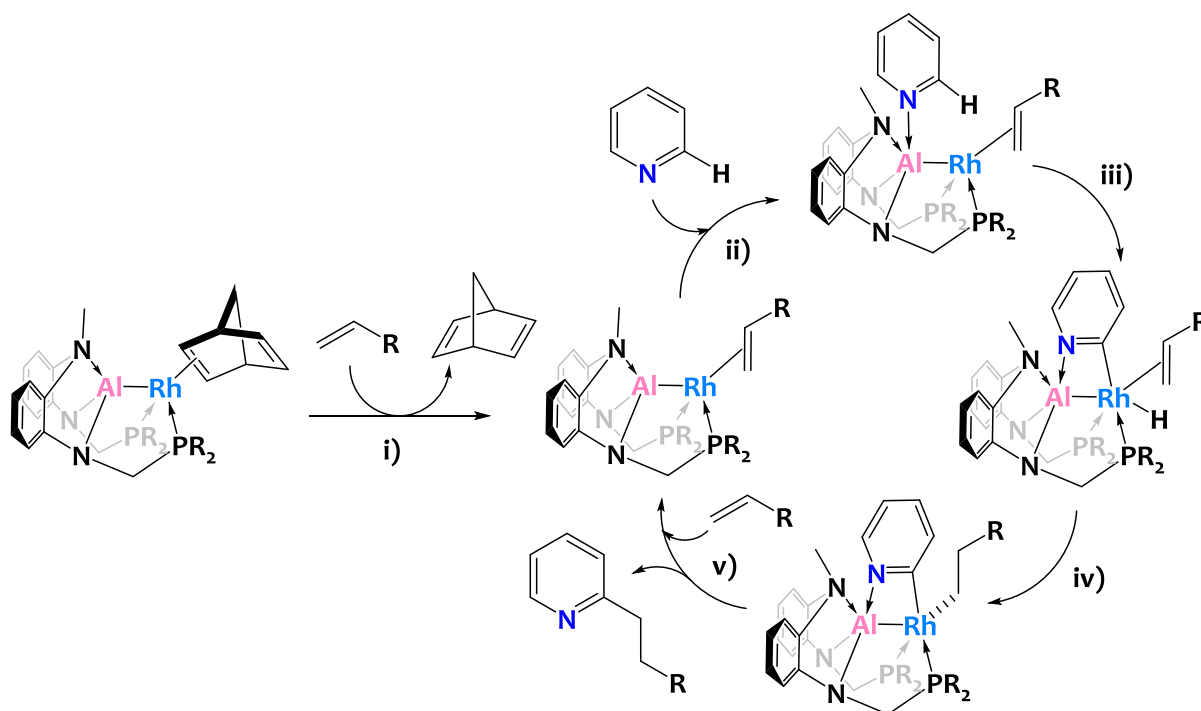
Entry	Temperature & time	Catalyst	R and R'	Yield	Selectivity ^a
1	110°C, 20h		R=H R'=Ph	96%	1/3.4
2	150°C, 20h		R=H R' = 	26%	>99/1
3	150°C, 20h		R=H R'=SiMe ₃	67%	>99/1
4	110°C, 20h	[RhCl(nbd)] ₂ Ligand PR ₃ AlEt ₂ Cl	R=H R'=Ph	0%	/
5	110°C, 20h		R=H R'=Ph	0%	/
6	120°C, 18h		R=p-OMe R'=SiMe(OSiMe ₃)	94%	90/7
7	120°C, 18h	[RhCl(nbd)] ₂ Ligand PR ₃ AlEt ₂ Cl	R=p-OMe R'=SiMe(OSiMe ₃)	trace	/
8	120°C, 18h		R=p-OMe R'=SiMe(OSiMe ₃)	<5%	/

Table 1. Presentation of the different experimental conditions. ^aLinear/branched ratio.^[66,116]

This study shows that this Rh-Al heterobimetallic catalyst far outperforms its monometallic counterparts in terms of selectivity and yields. To explain the reasons of such differences, the authors depicted a plausible catalytic cycle supported by experimental evidences and DFT computations of the proposed intermediates (Scheme 25).^[60] The mechanism can be divided into five steps.



Scheme 25. Proposed catalytic cycle for the C2-alkylation of pyridine.^[60]

i) First, an exchange between the norbornene ligand and the alkene substrate occurs. ii) Next, pyridine is N-coordinated onto the Al center. iii) The ortho-C-H bond of pyridine adds oxidatively onto the Rh center to give a (2-pyridyl)rhodium-hydride species. iv) The Rh-H bond is subjected to a migratory insertion on the alkene to form an alkyl rhodium complex. v) Finally, the C₂-pyridine-C_{alkyl} bond is formed upon reductive elimination to regenerate the complex of step i).

In conclusion, these reported results highlight an original cooperativity between the Rh and Al centers where the key parameter explaining the success of this catalytic transformation is the C2-H activation of pyridine by the Rh center oriented by prior N-coordination of pyridine on the nearby Lewis acidic Al center. More importantly, this process is not favored or even not possible if a Rh complex and an external Al Lewis acid are mixed together.

In the same vein, Y. Nakao and coworkers reported in 2021 a C2-selective silylation of pyridine using the same Rh-Al catalyst.^[117]

The same research team reported in 2020 a Rh-Al cooperative catalysis for the magnesiation of aryl-fluoride. In this case, the key step is the C1 activation of the fluorophenyl substrate by the Rh center, which is mediated and orientated by the fluoride coordination on the Al center.^[118]

As a general conclusion of this section, these few discussed cases shine a spotlight on original and interesting modes of action conferred by Al-M heterobimetallic complexes, which are promising for future developments in stoichiometric reactivity and homogeneous catalysis. However, these complexes often present several limitations. The first is the saturation of the metal coordination sphere in most of the species (related to the use of multidentate ligands to stabilize and isolate the polymetallic complexes) which strongly prevents the access of a substrate to both metals simultaneously. The second is the difficulty of accessing the active species without decomposition or rearrangement of these edifices. The third is to maintain the integrity of the bimetallic assembly in the course of the catalytic process.

To circumvent these issues and access unsaturated species that would be impossible to develop and stabilize in solution, the use of a solid support to immobilize these derivatives is a promising alternative. To this aim, a Surface Organometallic Chemistry (SOMC) approach is targeted in this PhD project, and will be discussed in the next section.

1.3 Surface organometallic chemistry (SOMC):

1.3.1 General concepts

This introductory subsection draws primarily on a comprehensive, exhaustive, and thorough review about SOMC.^[13]

1.3.1.1 Context

Today, metal catalysis is an indispensable tool widely employed in the industry. Indeed, up to 90% of everyday consumer products have "seen" a catalyst at some point in their design and a reasonable portion of these catalysts are based on organometallic complexes.^[119] Synthetic catalysts traditionally fall into two separate groups: heterogeneous or homogeneous catalysts.

Heterogeneous catalysis is defined by a catalytic process in which at least two phases characterize the system. In most catalytic processes, the catalyst is part of the solid phase while

the reactant and products are part of a liquid and/or gaseous phase. Nowadays, the chemical industry mainly uses heterogeneous catalytic processes because heterogeneous catalysis offers several advantages of a practical and effectiveness nature. Indeed, heterogeneous catalysis allows to easily separate the catalyst from the reaction products (by simple filtration techniques most of the time). It also provides the possibility of recycling or re-injecting the catalyst into the process. Heterogeneous catalysis is also well adapted for continuous flow processes. Most importantly, heterogeneous catalysts are often efficient and robust (withstanding high temperatures and pressures) for a wide range of chemical reactions, including the chemical transformation of raw materials and fuels or fine chemicals. Heterogeneous catalysts include a diversity of materials such as metal oxides, metal films, supported metal nanoparticles, zeolites or sulfide materials. Therefore, heterogeneous catalysis requires skills and expertise in surface science, materials and solid-state chemistry, process and materials engineering and related fields. Furthermore, despite the current sophisticated analytical tools that the fields of materials and surface science can offer to study the nature of active sites of heterogeneous catalysts, our level of understanding at the molecular level of such surface sites is still limited and often precludes the reliable establishment of elementary steps and mechanisms involved in the catalytic reaction. This is mainly due to the intrinsic complexity of these catalysts characterized by a wide range of active sites. Therefore, most heterogeneous catalysts can also be described as "ill-defined materials".

In contrast, homogeneous catalysis describes a catalytic system in which the reactants, products and catalyst are part of a single phase (most often the compounds are dissolved in a given solvent). The disadvantages and advantages of homogeneous catalysis are completely opposite to those of heterogeneous catalysis listed above. Indeed, separation and recyclability considerations are difficult to resolve when using homogeneous catalysis. In addition, homogeneous catalysts rely on molecular organometallic complexes that are often not robust or stable under aggressive experimental conditions (e.g. high pressure or high temperature). Nevertheless, the step-by-step rationalization of the structure-activity relationship of homogeneous catalysts is more easily achievable at the molecular level using standard molecular chemistry analytical tools such as liquid-state multi-nuclear NMR and IR spectroscopies, single-crystal X-ray diffraction or mass spectrometry. Therefore, most homogeneous catalysts can be described as uniform and well-defined species.

In the early 1970s, part of the scientific community became interested in developing chemical approaches at the interface between heterogeneous and homogeneous catalysis with the aim of combining the advantages of these two types of catalysis. This desire to bridge the gap between

these two fields of study gave rise to a new field called surface organometallic chemistry (SOMC). The latter has been considerably developed over the last twenty years.^[13,120–122] SOMC consists in grafting a molecular complex on the surface of a solid support (most of time an oxide - MO_x), which is considered as an extended ligand. The objective of SOMC is to have well-defined and isolated active sites, characterized by a known coordination sphere on the surface of the support, which can be described at the molecular level in the same way as organometallic complexes in solution. In other words, SOMC aims to rationalize the design of heterogeneous single-site catalysts to establish structure-activity relationships. SOMC is also a powerful approach because most of the analytical tools used in molecular organometallic chemistry (e.g. IR and Raman spectroscopy, solid-state NMR spectroscopy, UV spectroscopy, or elemental analysis) can be transposed to this field. Another effective tool used in SOMC is the design and analysis of homogeneous molecular models of the surface species in order to obtain precise structural information about the active site (provided mainly by single-crystal XRD technique).

1.3.1.2 Silica as a preferred solid support

Many types of oxides have been reported in the literature for anchoring organometallic complexes using a SOMC approach (e.g. silica (SiO_2), alumina (Al_2O_3), titania (TiO_2), ceria (CeO_2) or sulfated metal oxides).^[13] However, most of the occurrences in the SOMC refer to the use of SiO_2 , and in particular mesostructured silicas such as MCM-41 or SBA-15, since these materials have a high specific surface area - up to $1000 \text{ m}^2/\text{g}$ - enabling for significant incorporation of grafted organometallic species and thus facilitating materials characterizations (by NMR or IR spectroscopies for example) upon enhancing signal over noise ratios. In addition, the surface of silica is less complex than that of other oxides, such as alumina characterized by numerous types of Lewis acidic sites, or titania and ceria exhibiting redox sites. Because of these considerations, we will limit our discussion to SiO_2 supports for the remainder of this section.

Silica is an amorphous material, and the bulk material is composed of SiO_4 tetrahedral units bridged by siloxanes rings - $(\equiv\text{Si-O-Si}\equiv)_n$ - of various sizes ranging from 4 to 12-members ring. The surface of silica is composed of siloxane bridges and different types of terminal silanols, which are shown in the upper left of Figure 6. Indeed, silica surface exhibits three types of surface silanols: i) Isolated silanols refer to SiOH groups without neighboring silanols. ii) Geminal silanols describe two OH groups bonded to a single Si atom. iii) Vicinal silanols describe two nearby SiOH moieties interacting though H-bonding. Without specific treatment, silica surface is characterized by a mixture of isolated, geminal, vicinal silanols, and physisorbed water molecules. Thermal treatment of silica between 150°C and 200°C *in vacuo* (typically 10^{-5} mbars) triggers desorption of

the water molecules. Above this temperature range, vicinal and geminal SiOHs undergo a condensation reaction, also known as dehydroxylation, which results in the formation isolated silanols and siloxane bridges with the release of water molecules. Finally, at high temperatures (<400°C), isolated SiOHs predominate on the silica surface (Figure 5, bottom left). In this context, L.T. Zhuravlev modeled in 2000 the evolution of different SiOHs (per unit area – nm²) as a function of temperature for amorphous silica (Figure 5, right).^[123] As the temperature increases, the surface density of total silanol sites decreases drastically from T=200°C to T=400°C and then decreases more gradually until they disappear at T=1200°C. In addition, this model testifies to the dehydroxylation reaction during heating since the density of vicinal and geminal silanols decreases rapidly until they disappear (from T=400°C for vicinal SiOH and T=800°C for geminal SiOH).

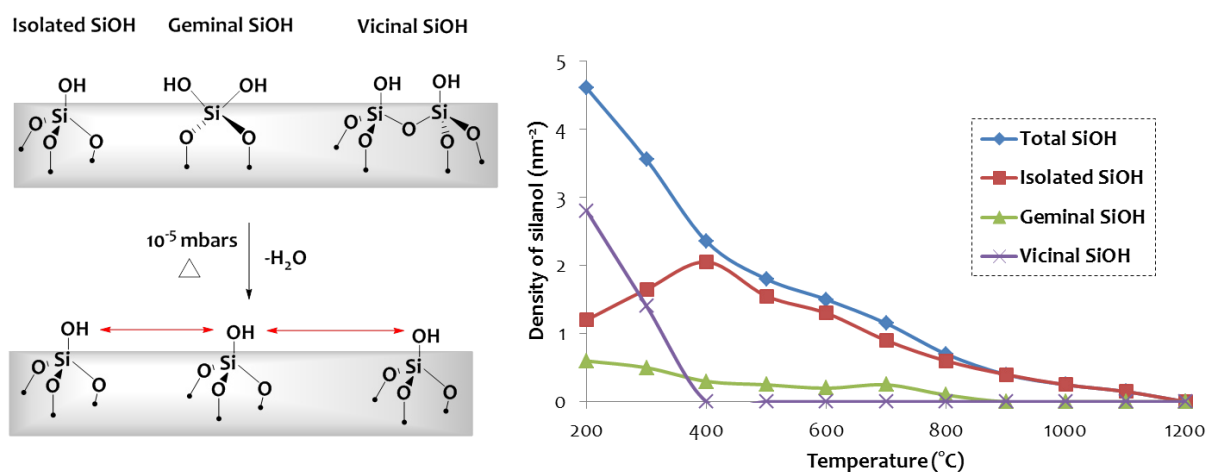


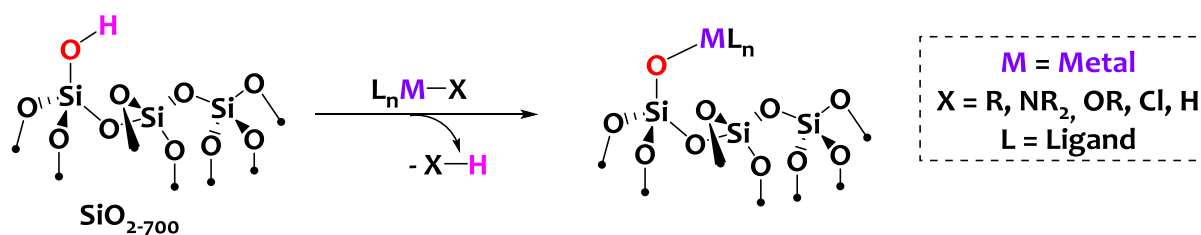
Figure 6. (Left) Schematic representation regarding evolution of geminal and vicinal surface silanols after a pretreatment at high temperature under vacuum. (Right) Distribution of the surface silanol groups of silica as a function of the pretreatment temperature (performed *in vacuo*).^[123]

Consequently, this study highlights the significant impact of the pretreatment temperature on the composition and concentration of the different sites at a silica surface. In fact, the control of the density and nature of the surface silanols is a key parameter to consider for subsequent grafting of the organometallic complexes. Notably, careful adjustment of the density and nature of the surface SiOHs allows precise control of the podality and surface density of grafted organometallic sites.

1.3.1.3 Concepts of the grafting reaction

The most common strategy for anchoring organometallic complexes to the surface of silica involves two steps: i) SiO₂ is dehydroxylated at T=700°C under high vacuum (10⁻⁵ mbars). This

pretreatment represents a good compromise between obtaining an acceptable concentration of surface sites without a significant loss of surface area while ensuring a good isolation of SiOHs (≈ 0.8 accessible and isolated SiOHs/nm²).^[13,123,124] ii) Then, the isolated surface SiO-H bond is subjected to a protonolysis reaction with an alkyl, amino, alkoxy, chloro, or hydride molecular organometallic X-M(L)_n species leading to a monopodal organometallic grafted species ≡Si-O-M(L)_n with evolution of alkane, amine, alcohol, hydrochloric acid or dihydrogen or as a coproduct (Scheme 26).



Scheme 26. Protonolysis reaction between an isolated surface silanol of a silica dehydroxylated at T=700°C and an organometallic complex resulting in the formation of a metallic grafted species.

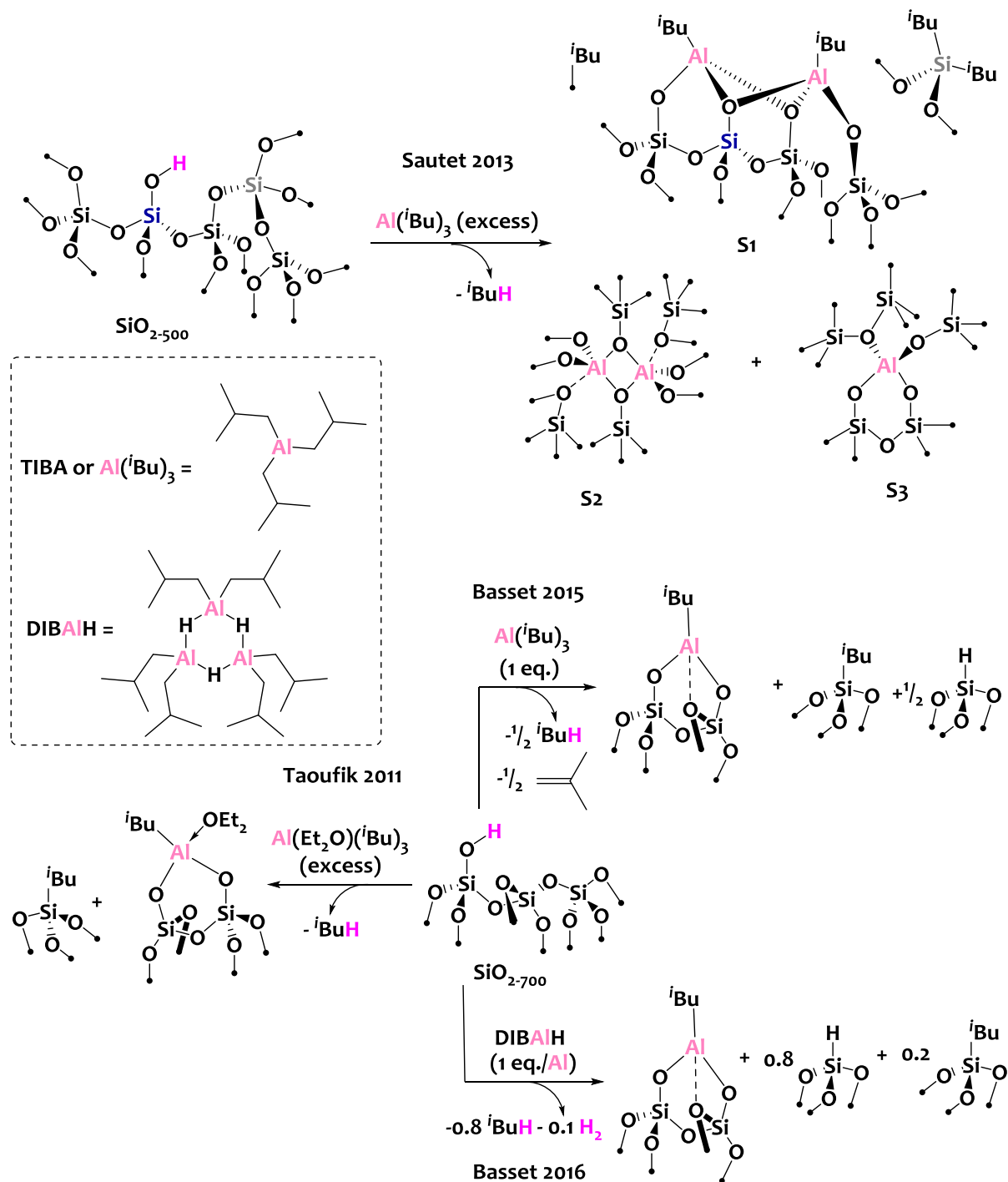
The choice of ligand X is important because the released coproduct (HX) may physisorbed on the materials or causes undesirable reactions with the surface sites. As a result, a significant portion of the SOMC community prefers to adopt homoleptic alkyl-metal precursors - MR_n - for the grafting onto SiO₂₋₇₀₀ as the generated alkane coproduct is volatile (easily removed) and inert. In terms of practical aspects, anchoring a metal complex onto silica supports implies strict anhydrous and anaerobic conditions (working under an inert atmosphere of argon). Indeed, many alkyl-organometallic species are pyrophoric and very sensitive to air and moisture. Moreover, high surface dehydroxylated silicas are highly hygroscopic, and the resulting metal surface species are also very sensitive to water and oxygen. As a consequence, two suitable methods for working under inert atmosphere are used to perform the grafting: i) break-seal technique, it entails to graft a volatile metallic precursor onto silica by cold sublimation in static vacuum. ii) Grafting in a Schlenck or double-Schlenck flask. This approach consists in impregnating the silica support with a solution of the metallic precursor. Both methods (i) and (ii) have advantages and disadvantages, but method (ii) is preferred for large-scale synthesis and is more suitable for the recovery of the unreacted metal precursor (if an excess is used, for example). In the next subsections, we will develop and discuss detailed examples that are relevant to this thesis work. In particular, since our studies focus primarily on aluminum, iridium, and heterobimetallic species, we will pay special attention to the grafting of these three types of compounds on silica.

1.3.2 Immobilization of aluminum species on SiO₂: conception and reactivity

1.3.2.1 Grafting of aluminum precursors onto silica

Immobilization of aluminum species on the surface of silica materials using the protonolysis strategy (see Scheme 26) is an attractive choice. Indeed, Al is strongly oxophilic and the resulting surface species are expected to exhibit robust Al-O bond(s). As a consequence, it is expected that there will be no leaching of surface Al species in the course of catalysis, and limited redistribution of sites, aggregation or reduction phenomena upon chemical or thermal post-treatment. On another note, the ²⁷Al isotope is NMR active with a nuclear spin of 5/2, which offers the possibility to study surface Al species by advanced solid-state NMR spectroscopy.^[125] However, despite these advantages, the literature reports several cases where the chemistry of aluminum on silica surfaces is very complex. Notably, some research works have investigated the grafting of trimethylaluminum (TMA), triethylaluminum (TEA), and diethylaluminum chloride (DEAC) onto silica materials dehydroxylated at T=500°C and T=700°C (SiO₂₋₅₀₀ and SiO₂₋₇₀₀ respectively).^[13,126-129] Throughout these studies, numerous surface species are obtained due to a complex surface reactivity of these alkylaluminum derivatives. In fact, the grafting reaction of AlR₃ is not only limited to protonolysis with silanols but also to mono or multiple alkyl transfers on adjacent siloxane bridges. Furthermore, TMA, TEA, and DEAC exist predominantly as dimers – (AlR₃)₂ – in solution and in the solid state where two alkyls (in the cases of TMA and TEA) or two chloro ligands (in the case of DEAC) bridge the two Al centers^[130]. Therefore, mixtures of mononuclear and multinuclear surface species are obtained, which leads to an inhomogeneity of sites, making this chemistry even more complex.

To circumvent these limitations, some studies proposed the use of more sterically hindered alkylaluminum precursors, such as triisobutylaluminum (TIBA) or diisobutylaluminum hydride (DIBALH). For instance, P. Sautet and coworkers reported in 2013 the grafting of TIBA on a silica dehydroxylated at T=500°C (Scheme 27 top).^[131]



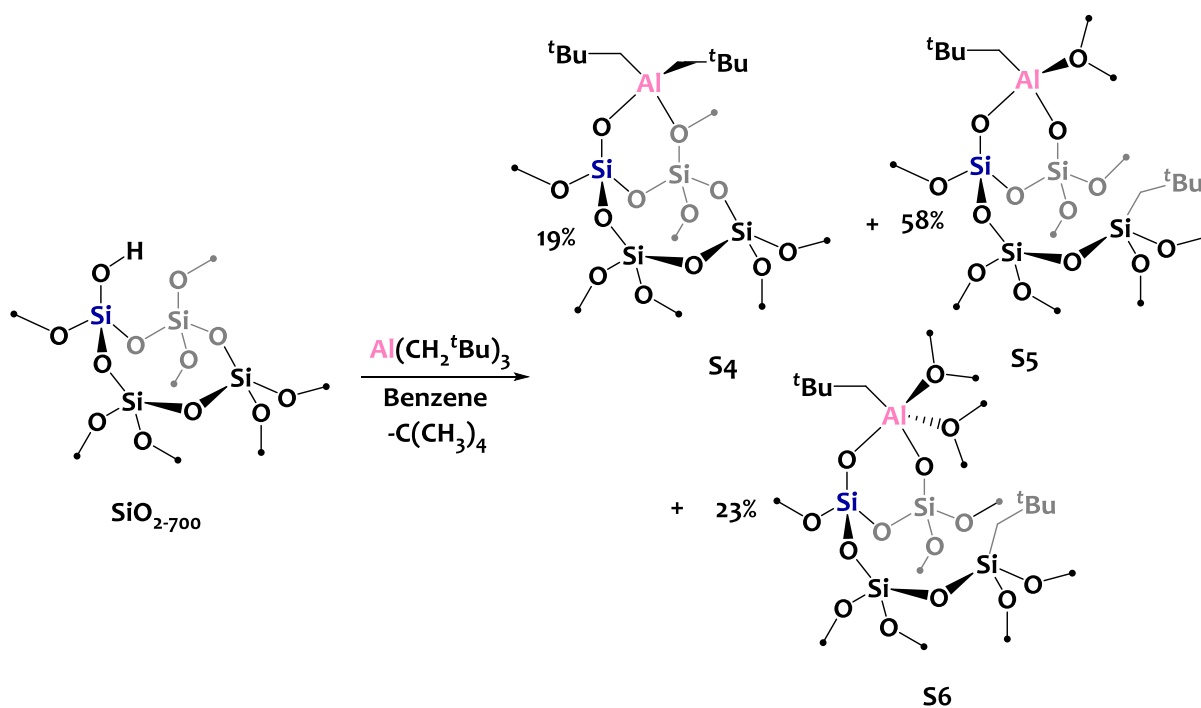
Scheme 27. Grafting of triisobutylaluminum (TIBA) and diisobutylaluminum hydride (DIBAlH) on dehydroxylated silicas SiO_{2-500} ^[131] and SiO_{2-700} ^[132-134]

This work demonstrates the high and complex reactivity of TIBA towards the silica surface since, at least, three aluminum surface sites (S1, S2, and S3 in Scheme 27) are identified using a combination of spectroscopic techniques and DFT calculations. In addition, the authors observed a significant incorporation of Al into the silica matrix due to the unstability of μ^2 -alkyl species that induce easier reaction with the silica surface. An excess of TIBA (3 equivalents per isolated silanol)

and a mesostructured silica dehydroxylated at a moderate temperature of 500°C (SBA-15₅₀₀, leading to a rather high surface silanol density, see Figure 6) are used. These aspects are therefore not in favor of simplifying the surface aluminum chemistry, or in other words, are not optimal for the rationalization and development of single surface Al sites. In this context, J. M. Basset, M. Taoufik, and coworkers reported modified experimental conditions to improve the SOMC of TIBA.^[132,133] In these studies, silica supports dehydroxylated at higher temperature (700°C), only featuring isolated surface silanols, are used. The grafting of TIBA is either performed in diethyl ether to saturate the Al coordination sphere and decreases its reactivity,^[133] or using stoichiometric amounts of TIBA with respect to surface SiOH groups to avoid over-reactivity phenomena.^[132] As a result, Al-isobutyl tetrahedral single sites, $(\equiv\text{SiO})_3\text{Al}(\text{iBu})$, are identified as well as silicon isobutyl and/or silicon hydride coming from an isobutyl transfer from Al to an adjacent siloxane bridge and/or β -H elimination of Al-C_{isobutyl} bond to form isobutene and eventually a $\equiv\text{Si-H}$ site respectively (see middle and bottom left of Scheme 27). However, a nuanced analysis of the data by ²⁷Al-NMR spectroscopy indicates the presence of at least three different geometries (tetrahedral, pentahedral and octahedral) around the Al center still revealing a complex surface chemistry.

Note that J.M. Basset and colleagues reported in 2016 the same surface species starting with DIBAlH (see bottom of Scheme 27).^[134] But in this case, the ratio of the $\equiv\text{Si-H}$ and $\equiv\text{Si-iBu}$ sites is different.

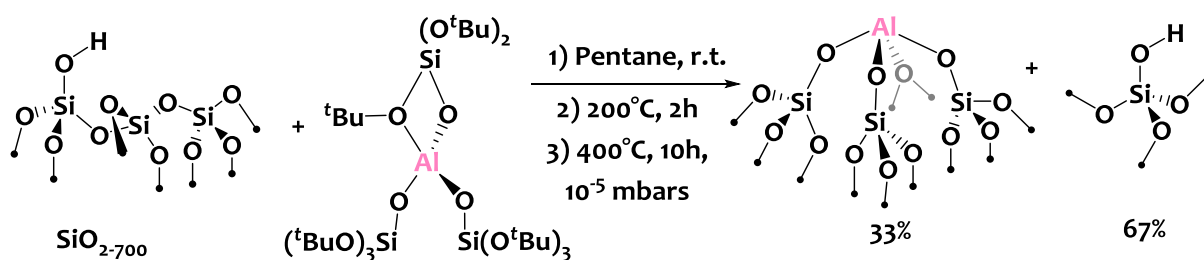
In the same vein, C. Copéret and his team reported in 2020 the grafting of tris(neopentyl)aluminum(III) onto a SiO₂₋₇₀₀ support. In this study, the authors still observed a complex chemistry, where a tetra-coordinated di(neopentyl)aluminum mono-grafted site (S4 in Scheme 28), a tetrahedral mono(neopentyl)Al bis-grafted site (S5 in Scheme 28), and a penta-coordinated Al surface species (S6 in Scheme 28) are identified in the following percentage: 19%, 58%, and 23%, respectively. These different sites are discriminated by a combination of advanced ²⁷Al-solid state NMR spectroscopy and DFT calculations.^[135]



Scheme 28. Reported grafting of tris(neopentyl)aluminum(III) onto SiO₂₋₇₀₀.^[135]

Based on these observations, we can state that increasing the bulkiness of the alkyl moiety in the AlR₃ precursors does not seem to significantly improve the obtention of Al single sites on dehydroxylated silica materials.

Another known methodology to perform a clean impregnation of metal sites at the surface of dehydroxylated silica supports is based on a combination of SOMC and thermolytic molecular precursor (TMP) approaches.^[136] This strategy has been successfully used with tris(tert-butoxy)silanolate metal precursors of chromium,^[137,138] tantalum,^[139,140] titanium,^[141,142] molybdenum,^[143,144] or tungsten.^[144,145] Specifically, this methodology involves two steps: i) SOMC impregnation of the silanolate metal precursor onto silica at room temperature. ii) Thermal treatment of the materials *in vacuo* at high temperature (between 300 and 500°C) to remove the alkoxy/siloxy ligands, which results to the formation of single and well-defined metal silicate sites. In this context and inspired by a preliminary work on aluminosilicate,^[146] C. Copéret and colleagues reported in 2016 the design of a single tetrahedral Al silicate site onto the surface of a dehydroxylated SiO₂₋₇₀₀ following a SOMC and TMP methodology (Scheme 29).^[147] Note that in this case, the authors demonstrated a partial impregnation of aluminum on silica since 0.75 Al/nm² and 1.6 OH/nm² are obtained showing one surface Al site for two remaining silanol functionalities.

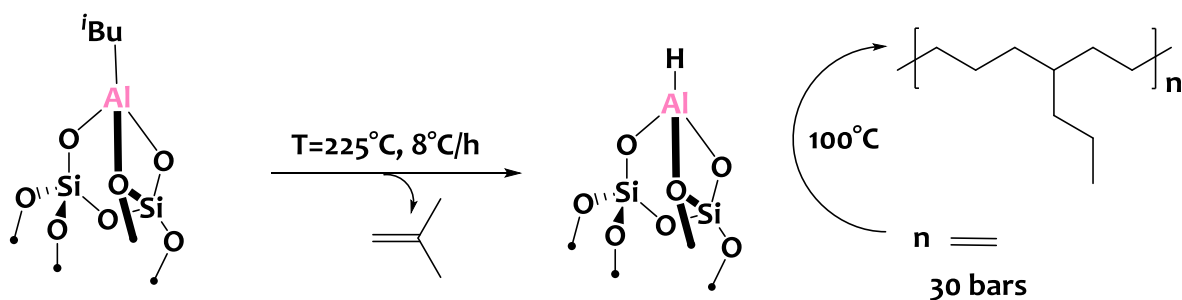


Scheme 29. Impregnation of $\text{Al}(\text{OSi}(\text{O}^t\text{Bu})_3)_3$ onto SiO_{2-700} followed by a thermolysis.^[147]

1.3.2.2 Reactivity and interests in catalysis

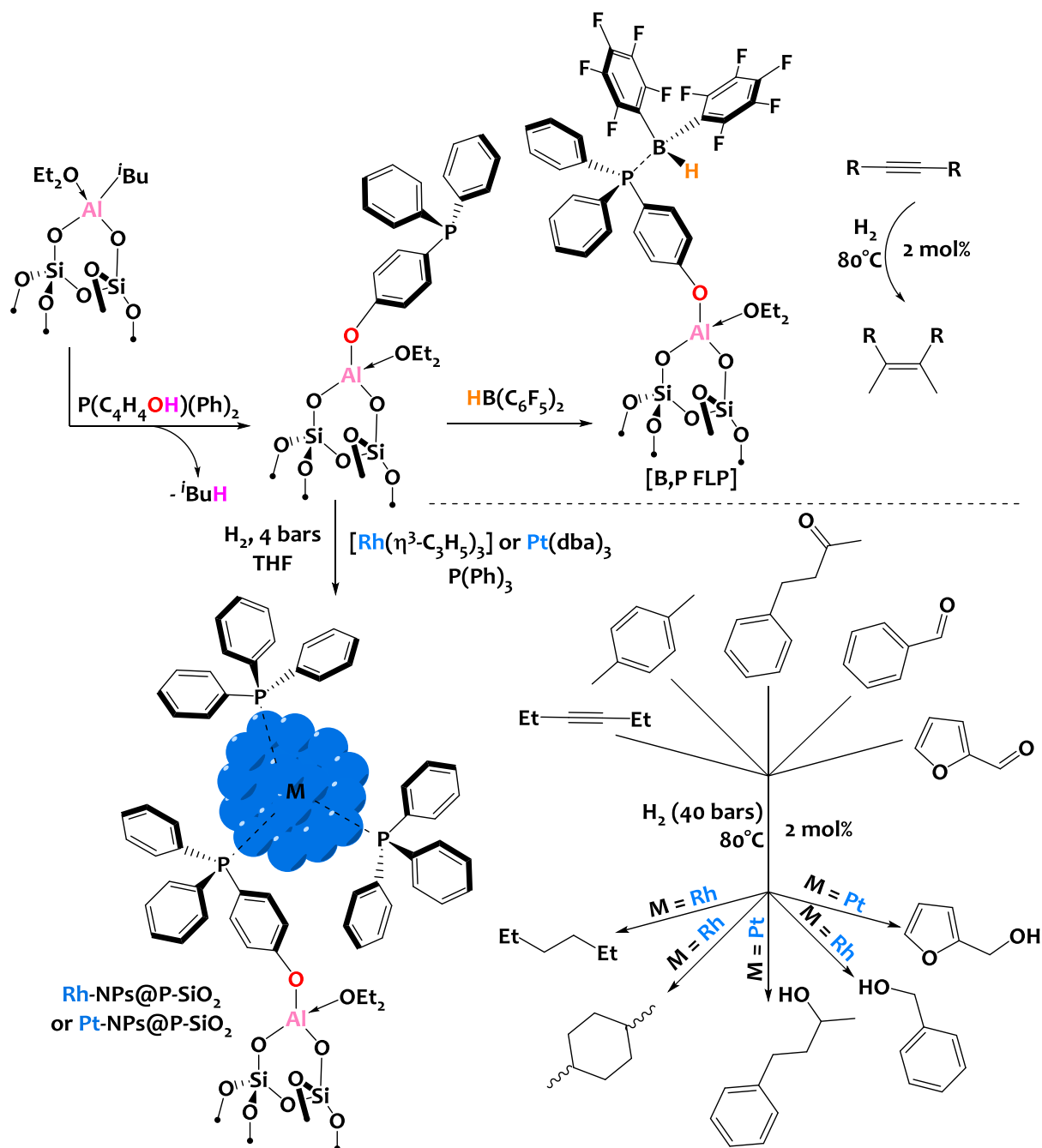
As mentioned above, one of the benefits of supported aluminum(III) species on silica lies on the robustness of the $\text{Al}-\text{OSi}\equiv$ bond. As a consequence, once grafted on a silica surface, the Al sites will not be detached from the material surface (no leaching or formation of nanoparticles for example) even upon chemical and/or thermal treatments of the material. However, the reactivity of the Al sites can be tuned by changing their coordination spheres.

For example, J.M. Basset and colleagues reported the formation of reactive tetra-coordinated aluminum hydride surface sites, $(\equiv\text{SiO})_3\text{Al}-\text{H}$, upon heating gradually to a temperature of 225°C a material containing tetrahedral Al-isobutyl sites, $(\equiv\text{SiO})_3\text{Al}-i\text{Bu}$ (Scheme 30).^[134] The thermal treatment triggers β -H elimination at the isobutyl moiety to generate gaseous isobutene and the hydride surface species. Interestingly, these unique aluminum hydride sites are found to be active for the production of high molecular mass branched polyethylene (PE) from ethylene (30 bars) at 100°C (Scheme 30, right). This study contrasts with a similar reported aluminum hydride supported on dehydrated alumina. Indeed, under the same experimental conditions (30 bars of ethylene, 100°C) linear PE is obtained.^[148]



Scheme 30. Formation of a tetrahedral aluminum hydride site used for the polymerization of ethylene.^[134]

In another interesting example, M. Taoufik and coworkers took profit of the protonolysis reactivity of $(\equiv\text{SiO})_2\text{Al}(\text{iBu})(\text{OEt}_2)$ surface sites with (4-hydroxyphenyl)diphenylphosphine to attach a phosphine moiety onto the solid support and then prepare supported boron-phosphine frustrated Lewis pairs – [B,P FLP] (Scheme 31 top).^[149] This [B,P FLP] material is found active for the selective reduction of 3-hexyne into Z-3-hexene.



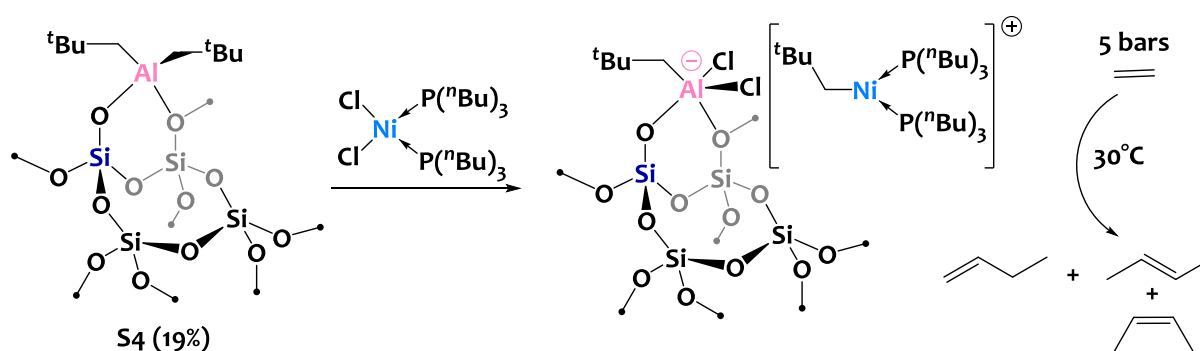
Scheme 31. (Top) reported synthesis of a boron, phosphine frustrated Lewis pair catalyst supported on a grafted Al-site – [B,P FLP] – active for a Z-selective hydrogenation of alkynes.^[149] (Bottom) Reported synthesis of Rh and Pt nanoparticles stabilized by phosphine moieties and supported on the same grafted Al-site – Rh-NPs@P-SiO₂ and Pt-NPs@P-SiO₂ active in the hydrogenation of aromatics and ketones.^[32]

The same phosphine derivative, $[(\equiv\text{SiO})_2\text{Al}(\text{OC}_4\text{H}_4\text{-PPh}_2)(\text{Et}_2\text{O})]$, (top of Scheme 31, structure after the first step) is employed to form small Rh and Pt nanoparticles of 1.2 nm and 1.5 nm respectively, quoted Rh-NPs@P-SiO₂ and Pt-NPs@P-SiO₂. These NPs are stabilized by triphenylphosphine ligands to avoid formation of aggregates or bigger NPs. In this study, the authors showed that these supported NPs are active and selective for hydrogenation reactions of aromatics and ketones (see Scheme 31, bottom).^[32]

In the two above studies, the Al site is spectator in these catalytic systems and serves as an anchor point to immobilize a reactive FLP or metal NPs.

The same group also reported the well-defined $[(\equiv\text{SiO})_2\text{Al}(\text{tBu})(\text{Et}_2\text{O})]$ species to prepare a supported ammonium bis(pentafluorophenoxy)aluminate activator - $[(\equiv\text{RSiO})_2\text{Al}(\text{OC}_6\text{F}_5)_2][\text{HNEt}_2\text{Ph}]^+$ - which, in combination with zirconium metallocene precursors, is able to promote the polymerization of ethylene.^[150]

In a similar perspective, C. Copéret and colleagues used in 2020 a silica-supported monomeric neopentylaluminum sites (synthesis discussed in the previous subsection) as a co-catalyst for the dimerization of ethylene.^[135] Notably, treatment of the silica-supported neopentylaluminum species with a solution of $({}^n\text{Bu}_3\text{P})_2\text{NiCl}_2$ under an ethylene pressure of 5 bars at 30°C converts 9400 moles of C₂H₄ per mol of Ni into isomers of butenes (93% of selectivity) after 1 hour of reaction. This catalyst outperforms the silica-supported AlEt₂Cl (TON of ca. 2800). The authors proposed that only the monografted bis-neopentylaluminum site (S4, see Scheme 32, left) is capable to generate the active ionic pair (see Scheme 32, right).

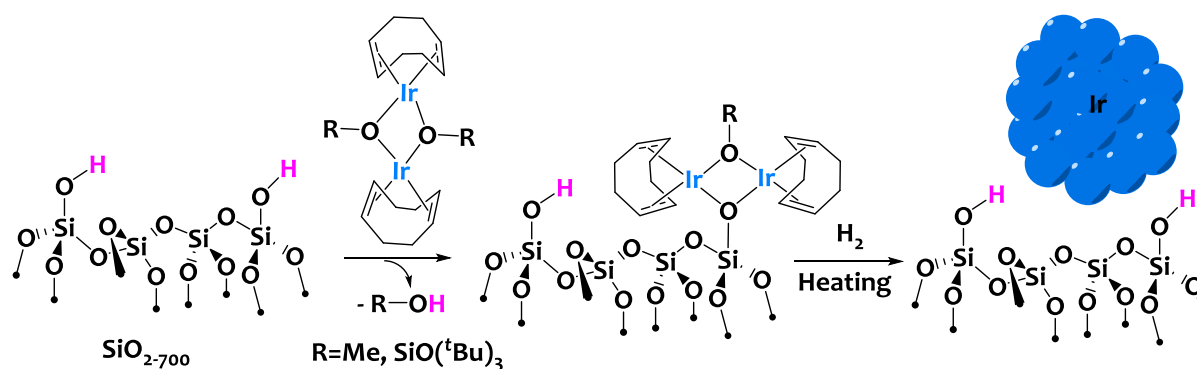


Scheme 32. Proposed active species when treating the Al site S4 with $({}^n\text{Bu}_3\text{P})_2\text{NiCl}_2$ for the oligomerization of ethylene.^[135]

1.3.3 Immobilization of iridium derivatives on solid supports: conception and reactivity

The grafting of late transition metal complexes on silica supports *via* a protonolysis reaction (Scheme 26), and especially iridium species, is less easy than for oxophilic metal centers. In fact, the resulting M-O bonding with the solid support is more fragile and may be still reactive. Typically, the bond dissociation energy (BDE) of Al-O is $501.9 \pm 10.6 \text{ kJ.mol}^{-1}$ while $\text{BDE}(\text{Ir-O}) = 414 \pm 42 \text{ kJ.mol}^{-1}$, which translates in a weaker Ir-O bond.^[151] These behaviors become more significant in a reducing medium known to cause a decrease in the M-O bond strength thus favoring the leaching of metals and/or the formation of nanoparticles and metal aggregates. Furthermore, late metal hydrides supported on silica can react with nearby siloxy functionalities to reform surface silanols by reductive elimination (thermodynamically favored, $\text{BDE SiO-H} = 499.5 \text{ kJ.mol}^{-1}$)^[152] and result in degrafted metal species. To illustrate these different points, we will present detailed examples regarding the grafting and reactivity of iridium species on silica surfaces.

In 2014, C. Copéret and coworkers carried out the grafting of (1,5-cyclooctadiene)(methoxy)iridium(I) and (1,5-cyclooctadiene)(siloxy)iridium(I) dimers onto a dehydroxylated silica (Scheme 33, first step).^[34] Here, the grafting is rather clean as the authors observe only one type of iridium surface species. Nevertheless, despite using an excess of the iridium complex for the impregnation of the material, the authors observed the persistence of a significant portion of unreacted isolated silanols, indicating partial anchoring. Typically, only 50% to 70% of surface $\equiv\text{Si-OH}$ moieties are metallated, as shown by elemental analysis (Ir loading of 4.4% wt when $\text{R} = \text{SiO}(\text{tBu})_3$ and 5.6% wt when $\text{R} = \text{Me}$). This moderate grafting emphasizes the aspects discussed in the previous paragraph.

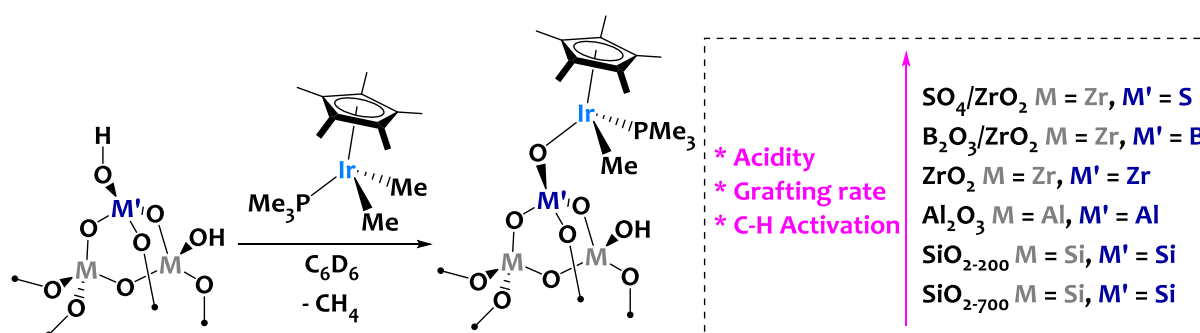


Scheme 33. Grafting of $[\text{Ir}(\text{cod})(\text{OR})]_2$ onto SiO_{2-700} and thermal treatment of the resulting material over H_2 .^[34]

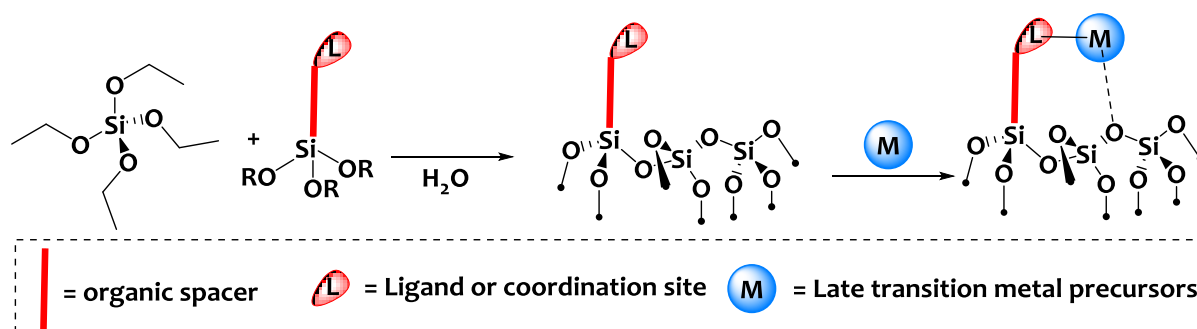
Then, treatment of the Ir-functionalized silica under a H₂ atmosphere, either under static conditions at 300°C or under flow conditions at 500°C, triggers the formation of small Ir(0) nanoparticles (Ir-NPs, second step of Scheme 33) with a narrow size distribution (1.2±0.3 nm) and a homogeneous spatial distribution. This study thus illustrates the fragility of the grafted molecular iridium species featuring Ir-O interactions, which are not robust enough under these conditions. But more importantly, this study also demonstrates how SOMC can be an interesting approach to develop small and narrowly distributed supported metal nanoparticles characterized by a high density of NPs that are homogeneously distributed on the surface of the support. The same group developed a similar approach to support Ir NPs on alumina supports, which are active for the catalytic hydrogenolysis/hydroisomerization of ethylcyclohexane.^[33] The development of supported nanoparticles with interesting and relevant properties (for catalysis in particular) such as those mentioned above remains a major challenge nowadays. Indeed, most supported iridium nanoparticles are prepared by impregnation approaches,^[153-155] which are simple and efficient to implement. However, a common limitation resulting from impregnation techniques is the uncontrolled formation of particle aggregates and a wide particle size distribution. This is especially related to the fact that iridium precursors are only physisorbed on the surface of the support. Therefore, the SOMC approach - where the Ir species are chemically grafted on the surface of the support - is an attractive alternative to develop well-defined supported metal NPs.

One proposed strategy to improve the robustness of grafted metal species consists in using bulky pincer ligands to stabilize the metallic center. In this sense, A. Mezzetti and colleagues reported in 2013 the immobilization of a dihydride iridium species^[156] onto a partially dehydroxylated (at T=400°C) SBA-15 silica (Scheme 34, left).^[157] The authors proposed that the grafting occurs upon reaction of iridium hydride moieties with surface silanols, releasing H₂ and forming a Ir-O bond. The resulting grafted species is stabilized by a bulky tridentate POCOP ligand - 2,6-bis(di-tert-butylphosphinito)-phenyl. In order to show the evolution of dihydrogen gas, authors conducted the grafting in a NMR tube with a minimum head-space. ¹H and ³¹P-NMR spectra of the liquid supernatant exhibit signals of unreacted dihydride iridium - IrH₂(POCOP) - along with a new tetrahydride species - IrH₄(POCOP) - formed by scavenging of dihydrogen by IrH₂(POCOP). Note that IR and elemental analysis data of the solid show a partial grafting (up to ca. 50% of surface ≡Si-OH moieties are metalated, resulting in remaining isolated Si-OH stretches in the IR spectrum and a maximum achievable Ir loading of 6.9% wt).

organotrialkoxysilanes ($L-Si(OR)_3$), ultimately leading to organically functionalized mesoporous silica frameworks (Scheme 36, first step). As a consequence, the late transition metallic precursor could be selectively coordinated to the organic ligands (eg. NHCs, thiolates, etc.) already present at the surface of the silica matrix (Scheme 36, second step). Some research works, including those from our research group, have discussed the advantages and interests of such an approach^[124,159–162], however, we will not elaborate further on this chemistry since this thesis work focused only on the direct grafting of metal precursors by a protonolysis route (see Scheme 26).



Scheme 35. Reported grafting of $IrCp^*(PMe_3)(Me)_2$ on various metal oxides. The resulting surface species was tested for the C-H activation of aromatics and alkyls.^[158]



Scheme 36. General strategy to synthesize organically functionalized mesoporous silica used for the coordination of late transition metal derivatives.

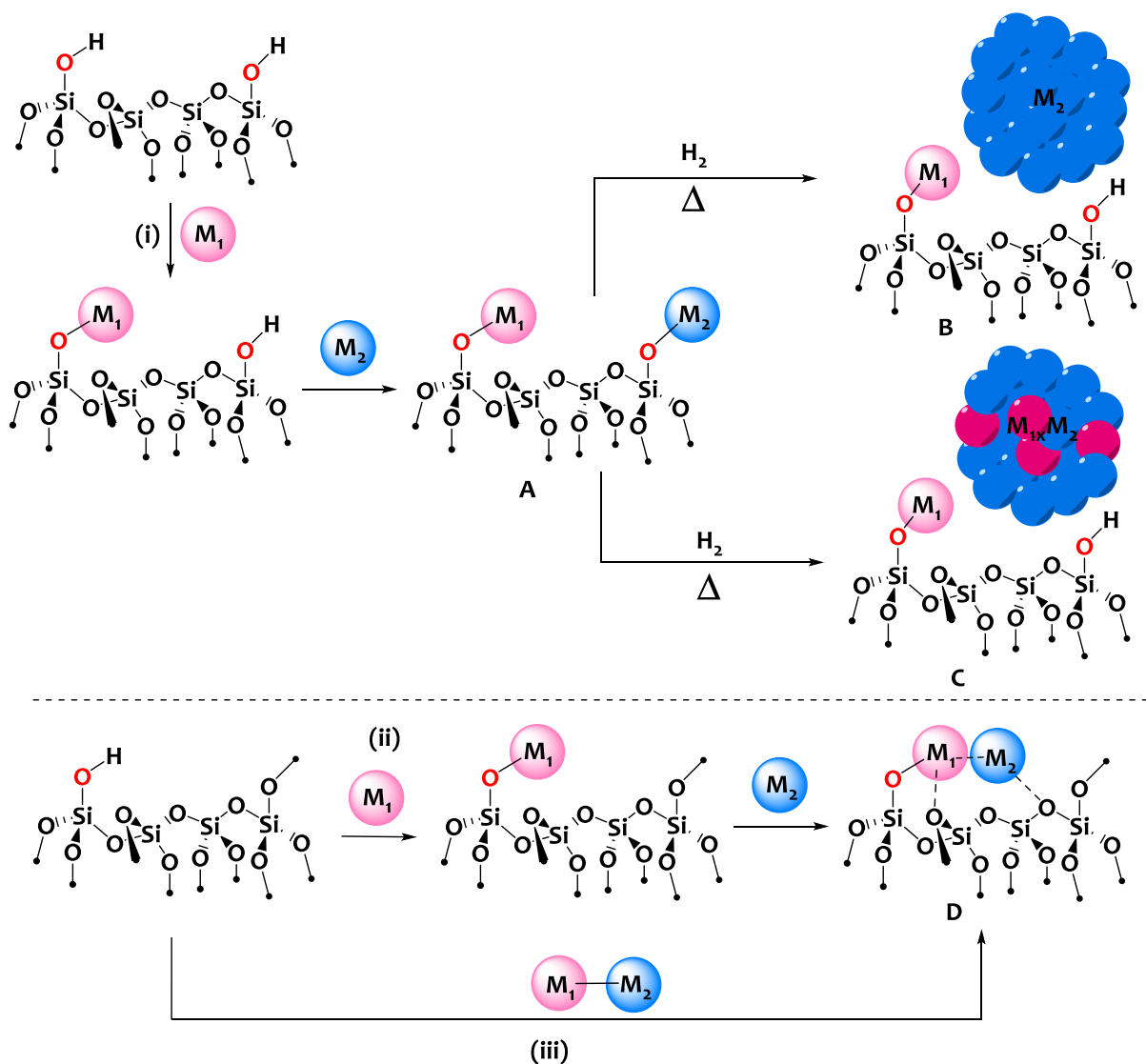
1.3.4 Development of supported heterobimetallic catalysts onto silica

1.3.4.1 Introduction

Most SOMC catalysts developed to date are monometallic. Materials containing two different metal components and prepared by the SOMC methodology are thus quite rare and include a diversity of systems that can be categorized into four main families according to the nature of the surface sites (Scheme 37).

Material A: this type of materials is prepared in two steps. A first organometallic precursor – noted M1 on Scheme 37 – is grafted on a silica surface using a stoichiometry of about 0.5 M1/SiOH. Most of the time, M1 is a metallic complex with oxophilic properties (e.g. Al, Ga, Zr, Ti etc.) in order to obtain a robust grafting. Next, a second organometallic precursor – noted M2 on Scheme 37 – is anchored onto the remaining surface silanols so as to achieve a stoichiometry M1/M2 of 1.0. M2 could be an early or a late transition metal complex which has a relatively good affinity with the silica surface, *i.e.* it could be immobilized onto the support by a protonolysis reaction (Scheme 26). As a result, a statistical distribution of M1 and M2 onto the silica surface is obtained. Note that this strategy – noted route (i) on Scheme 37 – requires specific conditions. Indeed, the two metallic precursors must efficiently react on surface SiOH groups. Furthermore, they must be orthogonal, *i.e.* they must react independently onto the support without interacting with each other.

Then, treatment of material **A** at high temperature (typically $T=500^{\circ}\text{C}$) under reducing conditions (H_2 atmosphere) can form two types of materials. When M1 is not easily reduced and forms strong M1-O bonds, only M2 is subjected to reduction and aggregation forming supported metal NPs, while the M1 component remains as isolated sites during the process. Such treatment thus yields material **B** (top right of Scheme 37) that can be described as supported monometallic M2 NPs decorated with M1 isolated surface sites. On the contrary, when M1 is reducible under these experimental conditions, this treatment can yield material **C** (middle right of Scheme 37) featuring supported $\text{M}_{1,x}\text{M}_2$ (where x is comprised between 0 and 1) alloyed nanoparticles. Intermediate situations are of course possible (and are actually the most frequent cases), in which a fraction of M1 atoms is incorporated into alloyed NPs while another fraction of M1 atoms remains as isolated sites.



Scheme 37. Schematic representation of the synthesis methodologies available for the preparation of heterobimetallic species supported on silica: (i) statistical juxtaposition of two distinct metal sites on SiO₂ (material A). Thermal treatment of material A under H₂ forming either late transition metal nanoparticles and isolated metal sites (material B) or alloyed NPs with a fraction of isolated metal sites (material C). Sequential approach (ii) or direct grafting of a pre-assembled bimetallic pre-cursor (iii) for the design of well-defined heterobimetallic sites (material D).

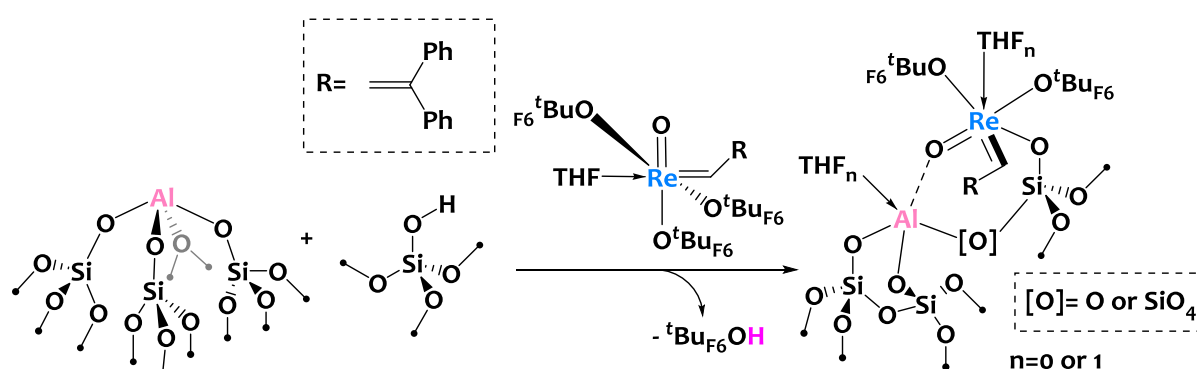
The last category (Material D, bottom right in Scheme 37) represents well-defined surface heterobimetallic sites in which the two metal atoms are at close proximity, forming metal pairs. The terms Dual-Atom Catalysts (DACs) or Pair-Site Catalysts (PSCs) have been coined very recently to refer to these catalytic objects, which is a hot emerging and rapidly growing area of research. These catalytic objects are at the interface of materials A and C and they combine the possibility to activate substrates in a concerted fashion across the two metals with the advantages of maximizing metal atom exposure. The main challenge of the field is the difficulty to prepare these classes of materials, featuring uniform structures on the support with a precise control of metal nuclearities, coordination spheres and precise positioning of metals at close proximity. Two synthetic routes can

be envisioned. The first route (quoted route (ii) in Scheme 37) involves the quantitative grafting of an oxophilic metal precursor, M₁, (all surface silanols are metallated with M₁) onto the surface of silica. The resulting M₁ sites are then used as reactive centers to incorporate the second metal center M₂. Another possibility (route (iii) in Scheme 37) is to prepare a M₁-M₂ heterobimetallic complex in solution, which is then grafted onto silica.

In the next subsection, we will describe the synthesis and catalytic interests of a series of silica supported heterobimetallic systems belonging to all of these classes of materials (**A**, **B**, **C**, and **D**) through detailed examples from the literature relevant to this thesis work.

1.3.4.2 Juxtaposition of two supported single-sites: construction and reactivity

Route (i) leading to type **A** materials (Scheme 37, top) was successfully reported in 2016 by C. Copéret and colleagues for the conception of an Al/Re supported material (Scheme 38).^[147] The first step consists in immobilizing an Al silicate site onto SiO₂, as previously depicted on Scheme 29 (see page 82). The second step involves the grafting of a rhenium oxo-alkylidene complex onto the remaining surface silanols leading to a bimetallic material (Re/Al ≈ 1.0). In this study, the Re and Al centers are found statistically distributed at the surface of the material, and are probably separated from one another by one, two or more siloxane bridges. Yet, on the basis of ²⁷Al-SS NMR spectroscopy, the authors proposed a close proximity between some of the two metallic centers to allow interactions between a rhenium oxo moiety with the Lewis acidic Al sites.



Scheme 38. Grafting of a Re oxo alkylidene species onto an Al@SiO₂ material (synthesis described on Scheme 29) yielding a bimetallic Al/Re supported catalyst.^[147]

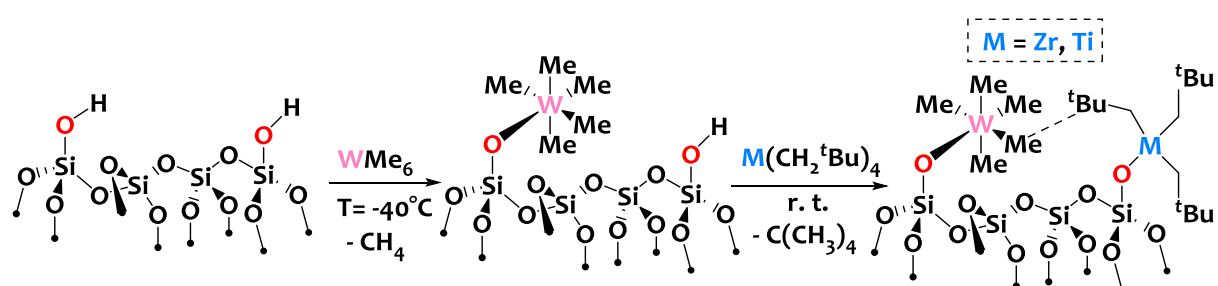
Afterwards, the authors tested the Al/Re catalyst for a cross-metathesis reaction between C₉ olefins (*cis*-4-nonene and 1-nonene) and ethyloleate. They demonstrated that the bimetallic

supported catalyst is active for this transformation while both supported and homogeneous Re monometallic analogues^[147,163] are not active under the same experimental conditions. Furthermore, this catalyst, which can be described as Re single sites juxtaposed with adjacent Lewis acidic sites, is also more active than the supported Re monometallic counterpart combined with an external Lewis acid ($B(C_6F_5)_3$). This shows the interest of these bimetallic materials in which adjacent Al sites play a promotor role.

J. M. Basset and coworkers reported in 2016 and 2017 the co-grafting of tungsten and zirconium^[164] or titanium^[165] onto dehydroxylated silica. These systems are constructed through a SOMC sequential approach: $W(Me)_6$ is first grafted onto some of the available silanols at $T = -40^\circ C$ followed by grafting of $TiNp_4$ (or $ZrNp_4$) at room temperature (Scheme 39).

The proximity of the two metal centers (for at least part of the sites) on silica is determined by two-dimensional double-quantification (DQ) solid-state 1H NMR spectroscopy allowing to observe a strong correlation signal between the protons of the methyl groups on the tungsten centers with those of the neopentyl ligands on the group 4 metals.

Next, these bimetallic catalysts were tested for the alkane metathesis reactions. In the case of the W-Zr couple, the TON increases from 650 (W alone) to 1436 (W/Zr) for the *n*-decane metathesis reaction at $150^\circ C$. In the case of the W-Ti couple, this increase is even more significant with a TON of 10000 in propane metathesis at $150^\circ C$. To explain these enhanced performances in alkane metathesis, the authors proposed a tandem catalysis resulting from the association of the Ti or Zr centers that are more efficient in the dehydrogenation/hydrogenation steps, with tungsten (W) centers that are more active in olefin metathesis. This spectacular improvement of the activity is linked to a tandem catalysis but also to the strong proximity of the two metals. Indeed, the physical mixing of the two corresponding monometallic solid catalysts shows an increase in catalytic activity compared to the monometallic systems, suggesting a tandem catalysis, but the resulting TON is much lower than that of the bimetallic system containing the two metals in close proximity.

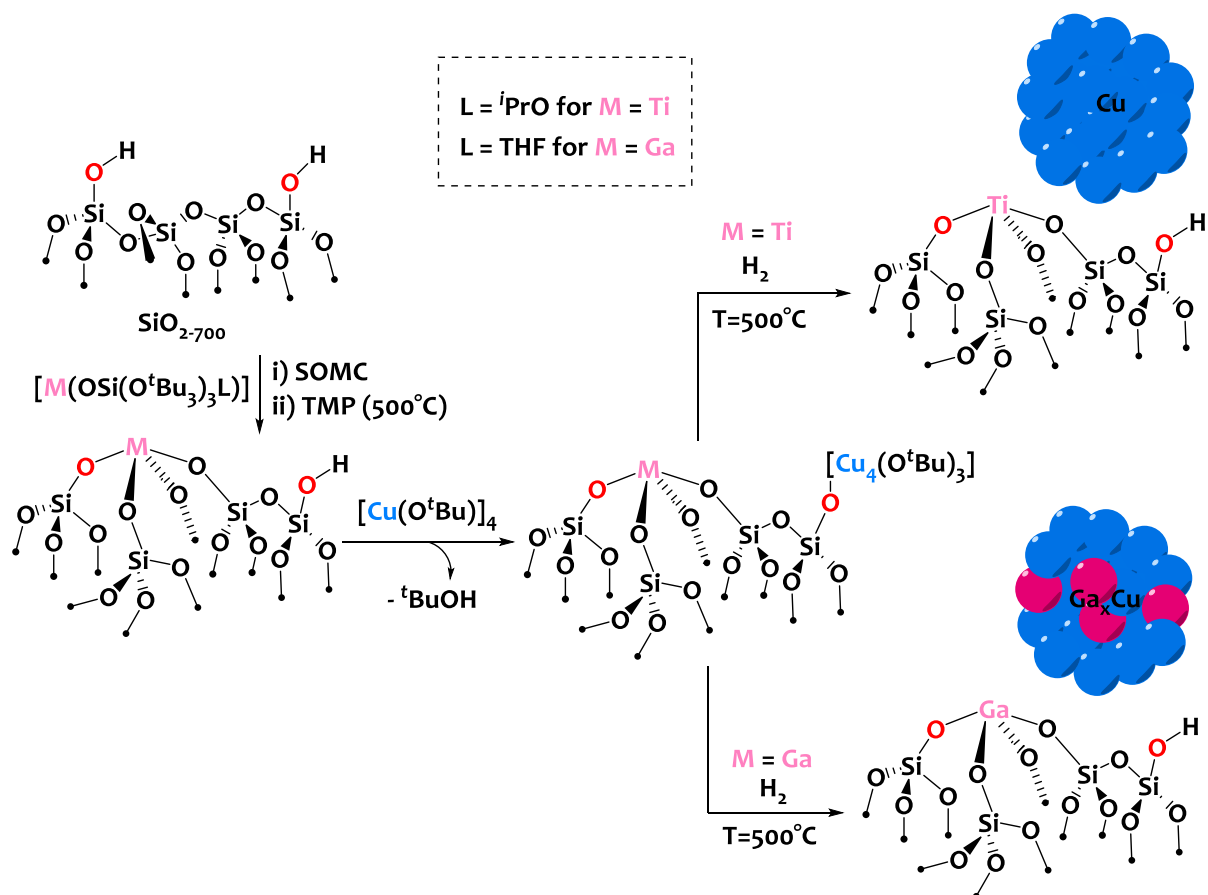


Scheme 39. Reported juxtaposition of $W(Me)_6$ with $Zr(Np)_4$ or $Ti(Np)_4$ yielding a silica-supported bimetallic

catalyst.^[164,165]

As presented above, the reductive thermal treatment (under H₂ atmosphere at T=500°C) of type **A** materials (Scheme 37) is particularly interesting as it opens a new door towards the controlled formation of small, narrowly distributed metal(o) nanoparticles (with a size ranging from 1 nm to 10 nm) supported onto dehydroxylated silica in combination with low-coordinated single sites (materials **B** and **C** on Scheme 37). As mentioned in paragraph 1.3.4.1 (page 89), the chemical composition of the NPs (monometallic or bimetallic) depends on the chemical properties of the two metal components, and impacts the resulting reactivity. This methodology is particularly developed by the group of C. Copéret who recently reported a series of bimetallic Zr-Cu, Ti-Cu materials **B**^[166,167] and Ga-Cu, Ga-Pd, and Zn-Cu materials **C**^[35-38,168] highly active for CO₂ hydrogenation^[36,37,166-168] and propane dehydrogenation.^[35,38]

To illustrate this point, the comparative design of a bimetallic Ti-Cu/SiO₂ catalyst of type **B** and a bimetallic Ga-Cu/SiO₂ of type **C** are presented on Scheme 40.^[36,167] The synthesis of M-Cu/SiO₂ materials takes place in three stages. First, well-defined Ti(IV) or Ga(III) isolated sites are prepared by grafting titanium(IV)^[169] or gallium(III)^[170,171] siloxy precursors which are then thermolyzed to remove the organic component from the ligands *via* a classical SOMC/TMP approach (first arrow on Scheme 40).^[136] Then, a copper(I) *tert*-butoxide tetramer precursor is grafted onto residual surface silanols leading to the formation of Cu(I) sites and the release *tert*-butanol in stoichiometric amounts (second arrow on Scheme 40). Eventually, the thermal treatment (T=500°C) under H₂ of the resulting anchored species leads to two types of materials. In the case of Ti-Cu/SiO₂, monometallic Cu NPs of 2.8 ± 0.7 nm surrounded by isolated interfacial Ti(IV) sites are obtained (right side on Scheme 40). In contrast, in the case of Ga-Cu/SiO₂, some gallium atoms are incorporated in the NPs to produce statistical alloyed Ga_xCu NPs of 4.6 ± 1.4 nm surrounded by Ga(III) single-sites.



Scheme 40. (Left side) Juxtaposition of a titanium(IV)^[167] or a gallium(III)^[36] silicate site with a copper(I) tert-butoxide fragment onto silica dehydroxylated at $T=700^\circ\text{C}$ (the two first steps, left side). Thermal treatment under hydrogen of the bimetallic materials yielding either supported Cu NPs with single monometallic Ti(IV) sites (top right) or supported Cu-Ga alloyed NPs surrounded by isolated Ga(III) sites (bottom right).

Then, the authors assessed the catalytic performances of these bimetallic catalysts versus those of their monometallic counterparts for carbon dioxide hydrogenation. The reaction is performed in a fixed-bed reactor under continuous flow conditions using a temperature of 230°C and a total gas pressure of 25 bars containing a mixture of H_2/CO_2 in 3/1 ratio. The obtained results for the gallium-copper system are presented in Figure 7.^[36]

In this catalytic study, the intrinsic rate of formation of methanol (arising from CO_2 reduction)^[172] for the bimetallic Ga-Cu/ SiO_2 is four times higher than that for the monometallic copper analogue^[172] ($1.30 \text{ g}\cdot\text{h}^{-1} \text{ g}_{\text{Cu}}^{-1}$ vs $0.32 \text{ g}\cdot\text{h}^{-1} \text{ g}_{\text{Cu}}^{-1}$ respectively). No formation of methanol is detected with the gallium monometallic catalyst. More importantly, a high selectivity in favor of methanol with respect to carbon monoxide is obtained for the Ga-Cu/ SiO_2 catalyst compared to Cu/ SiO_2 (93% vs 48% respectively). Note that during the process, the authors observed that the Ga-Cu/ SiO_2 material de-alloyed to quantitatively form back Ga(III) sites (oxidation of Ga(o) in the NPs into Ga(III) by CO_2). On the basis of this information, authors proposed that this increase in activity and

selectivity is likely due to the increased interfacial area between the Cu(o) NPs and the Ga(III) sites that would promote the formation of methanol. This study therefore shows enhanced catalytic performances of the Ga-Cu bimetallic catalyst compared to the monometallic analogues, highlighting a significant promoting effect of the Ga(III) single-site on the reactive Cu(o) NPs and this not only in term of CO₂ conversion rate but also in term of CH₃OH selectivity. Note that related catalytic studies with similar trends and conclusions have been established for Zr-Cu/SiO₂^[166], Ga-Pd/SiO₂^[37], and Zn-Cu/SiO₂^[168] catalysts with respect to their monometallic counterparts.

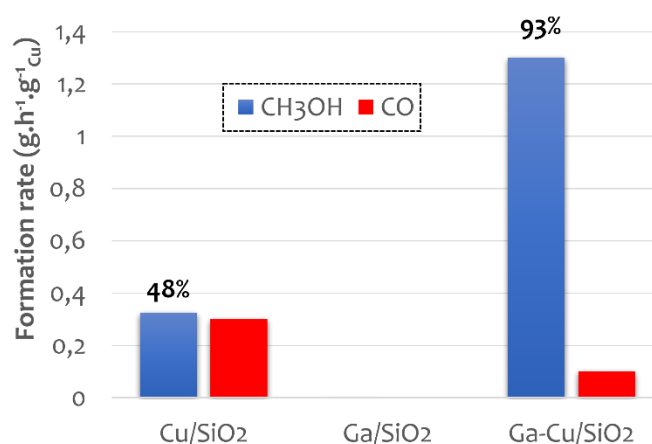
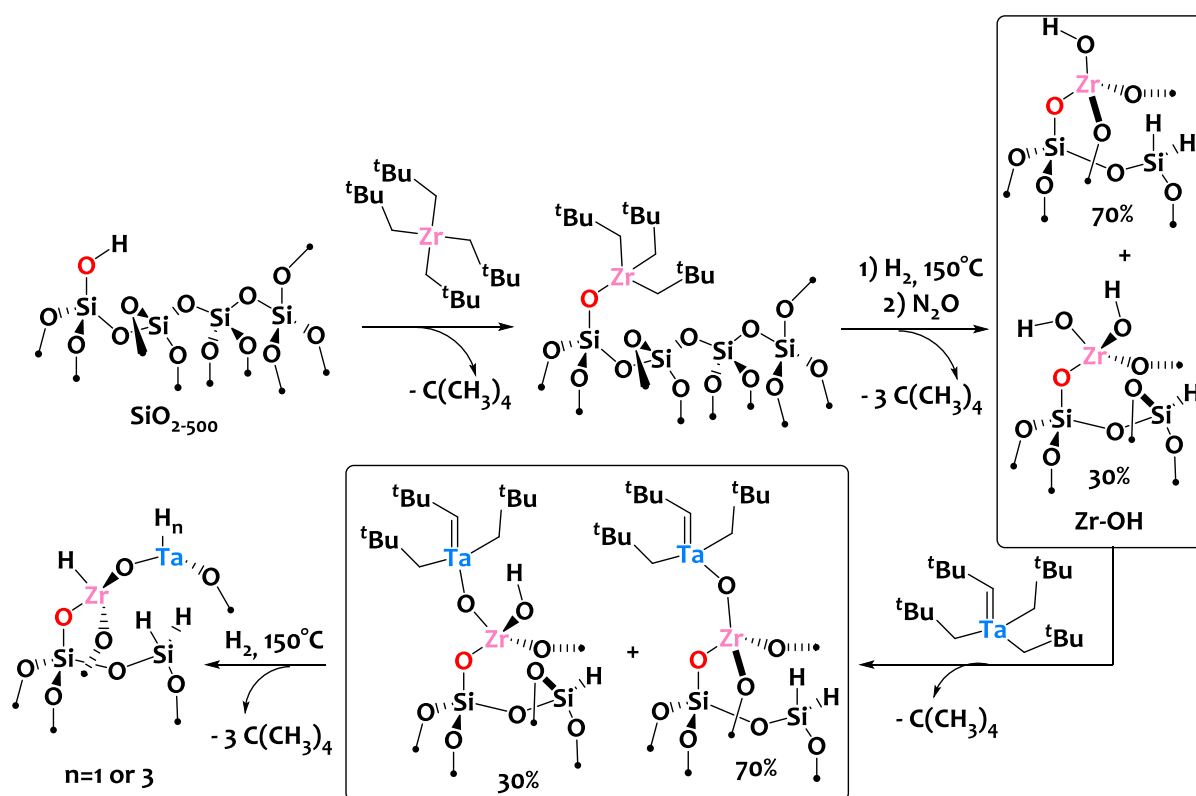


Figure 7. Bar chart histogram representing the intrinsic formation rates of CO and CH₃OH for Cu/SiO₂, Ga/SiO₂, and Ga-Cu/SiO₂ catalysts. Selectivity (%) in methanol versus carbon monoxide appears above the blue bars.^[36]

1.3.4.3 Formation of surface heterobimetallic single-sites: construction and reactivity

The development of D-type materials through routes (ii) and (iii) (Scheme 37 bottom) is still in its infancy. Indeed, only a dozen of research works report the design of heterobimetallic single sites supported onto silica. Furthermore, the vast majority of these studies focus on route (ii) using metals of similar nature, specifically two early transition metals (groups 4-6).^[173-177] Among them, one specific study describing the design of an original zirconium-tantalum site supported onto a silica dehydroxylated at T=500°C (SiO₂₋₅₀₀) (synthesis presented in Scheme 41).^[177,178] and reported by J.M. Basset and coworkers in 2007, has attracted our attention. The design of such a material involves many steps. First, tetraneopentylzirconium(IV) - Zr(Np)₄ - is grafted onto surface silanols yielding a ≡Si-O-Zr(Np)₃ site. Second, hydrogenation of these surface sites, followed by oxidation with N₂O, leads to the formation of zirconium hydroxide surface sites (≡Si-O)_nZr(OH)_{4-n} (n = 3, 70%; n = 2, 30% see Scheme 41 right). Third, treatment of this material with the tris-neopentyl(neopentylidene)tantalum(V) complex^[179] results in a protonolysis reaction with the Zr-

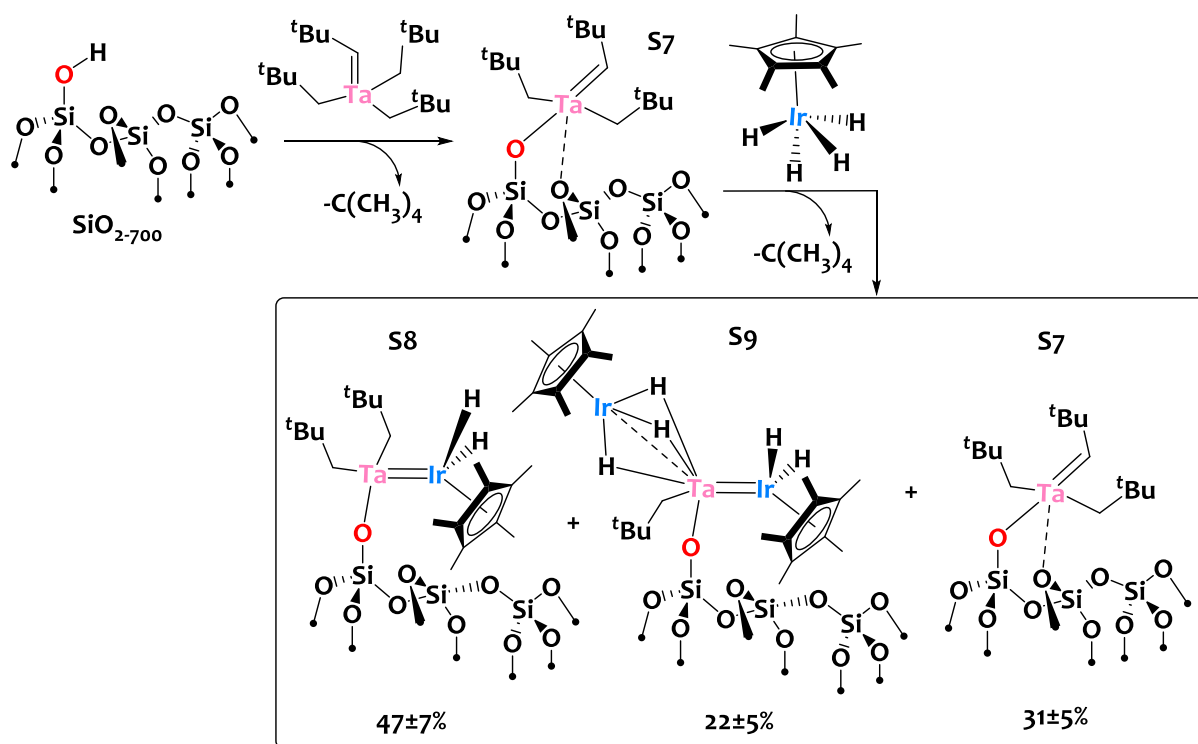
OH sites and incorporation of Ta atoms at close proximity of the Zr sites through bridging oxo bonds (Scheme 41 bottom). Finally, hydrogenation of the resulting sites leads to well-defined supported zirconium-tantalum hydrides. Next, the authors investigated the catalytic activity and selectivity of this bimetallic material for propane metathesis. The resulting bimetallic Zr-Ta(H)_n catalyst exhibits higher TON and lifetime compared to its monometallic analogue (≡SiO)₂-Ta(H)_n. In addition, the bimetallic catalyst is more selective towards the C_{n-1} and C_{n+1} products. More importantly, the Zr-Ta(H)_n catalyst exhibits improved catalytic performances compared to tantalum hydride species supported on zirconium-based mixed oxide supports - Ta(H)/(SiO₂)_n-ZrO₂ (n=2, 4, and 10) – proving that it is not only the presence of adjacent Zr centers that confers higher activity, but also the peculiar tetrahedral geometry around the Zr atom. Presumably, the latter observation is in favor of the formation of weakly coordinated Ta species that cannot be obtained with mixed oxide supports. As a consequence, this research work is a good example showing the promoting effect of zirconium on the Ta-H reactive center.



Scheme 41. Stepwise development of an heterobimetallic Zr-Ta site supported on a dehydroxylated silica via a SOMC approach.^[177,178]

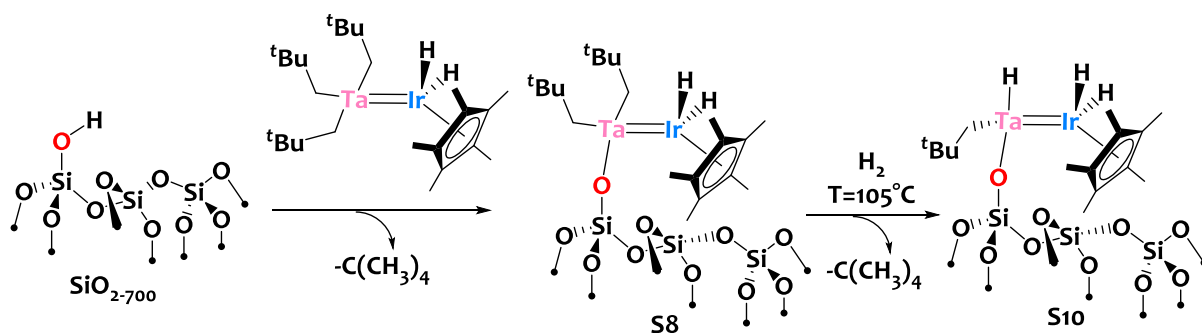
From another point of view, it is important to note that route (ii) (Scheme 37 bottom) has some conceptual limitations such as the inherent difficulty in controlling the precise M1/M2 stoichiometry or the complex surface chemistry that may be the result of a local excess of the second metal precursor onto the first metallic site when performing the second grafting step.

Therefore, obtaining a single well-defined site is very challenging. In the above example, several surface species are obtained. Another representative example of these limitations has been recently reported by our group (Scheme 42).^[28] In this work, a silica-supported tantalum species $[\equiv\text{SiO-Ta}(\text{CH}^t\text{Bu})(\text{CH}_2^t\text{Bu})_2]^{[180]}$ – noted S7 thereafter (see the upper right part of Scheme 42) – is used as a reactive center to coordinate an iridium hydride complex (IrCp^*H_4)^[181] by elimination protonolysis reaction resulting in the elimination of neopentane. Advanced characterizations of this material, notably via EXAFS and multiple-quantum solid-state NMR, reveal that the resulting Ta-Ir material (Scheme 42, bottom) features a mixture of three surface species: the unreacted Ta monometallic site (S7), a dinuclear Ta-Ir sites (S8), and a trinuclear TaIr_2 sites (S9). The formation of these surface species is explained by a competition between the reaction of IrCp^*H_4 with S7 and S8 (forming S8 and S9 respectively).



Scheme 42. Stepwise construction of silica-supported Ta-Ir edifices using a sequential SOMC approach.^[28]

To overcome these limitations, one approach, only explored and developed in our laboratory, consists in directly grafting a heterobimetallic complex which synthesis is previously performed in solution. Following this strategy, our team reported in 2019 the design of a well-defined tantalum-iridium single site supported onto a silica SBA-15 dehydroxylated at $T=700^\circ\text{C}$ (Scheme 43).^[27]



Scheme 43. (i) Direct grafting of a Ta-Ir species onto SiO₂₋₇₀₀ leading to a single well-defined silica-supported Ta-Ir site (3-s). (ii) Hydrogenation of the resulting supported species yielding a reactive heterobimetallic Ta-Ir site.^[27]

Notably, reaction of the heterobimetallic [Ta(CH₂^tBu)₃{IrH₂(Cp*)}] species with isolated surface silanols leads to the clean and quantitative formation of the well-defined monopodal [≡SiOTa(CH₂^tBu)₂{IrH₂(Cp*)}] site (Scheme 43, first step) – noted S8 thereafter – along with the release of neopentane gas (note that S8 is also partly obtained when using route (ii) (Scheme 42 bottom)). Here, the oxophilic early metal (Ta) is used to efficiently attach the bimetallic assembly onto silica. Next, thermal treatment of S8 under a H₂ atmosphere results to the evolution of one equivalent of neopentane and to the formation of a reactive Ta-Ir tris-hydride site – S10 (Scheme 43, second step). Importantly, it is shown that catalyst S10 drastically outperforms its supported and homogeneous monometallic counterparts as well as its molecular heterobimetallic analogue in the catalytic hydrogen/deuterium exchange reaction of arenes by a factor of about 100 in terms of TON and TOF. In particular, S10 promotes the H/D exchange of fluorobenzene using C₆D₆ or D₂ as deuterium sources with excellent catalytic performances (TON up to 1422; TOF up to 23.3 h⁻¹) under mild conditions (25 °C, sub-atmospheric D₂ pressure) without any additives. This study thus shows the value of having a well-defined heterobimetallic site supported on silica.

It is important to stress that hydrogenation of this bimetallic Ta/Ir species is carried out at moderate temperature (105°C) and, to date, no study regarding the stability of **D**-type materials (Scheme 37) at high temperature (up to 500°C) and under reducing conditions (H₂ atmosphere) has been reported. Yet, it would be very interesting to study the possibility of obtaining **B**-type or **C**-type materials from **D**-type materials (Scheme 37) and, if so, what are the similarities and differences with respect to route (i)? In other terms, can these silica-supported heterobimetallic sites featuring M₁-M₂ pairs decompose under aggressive conditions to form small, narrowly distributed monometallic and/or bimetallic nanoparticles as well as interfacial monometallic sites, and what is their interest for catalysis? Part of this thesis work aims at answering these questions and providing new milestones in this field.

1.4 Purposes and aims of the project

The guide line of this PhD project is to increase our fundamental understanding of the chemistry of homogeneous and surface-supported heterobimetallic architectures, and more particularly aluminum/iridium edifices. One of the current frontiers in organometallic chemistry is to study the combined action of two metal centers to promote new modes of reactivity, where the two metallic partners act synergistically, in view of accessing a chemistry not possible with monometallic species.^[1-6] Such metal-metal cooperation phenomena have long been proposed to explain the properties and modes of action of specific active sites of enzymes, heterogeneous catalysts and heterobimetallic complexes. However, the exact nature of the species involved is often unknown or poorly defined and the mechanisms of action behind the synergistic effects can be of very diverse origins and remain poorly understood. Given the diversity of combinations offered by the periodic table and the wealth of possible structures, the field of possibilities is huge. It is therefore an extremely open and promising field of study, which is only just beginning to emerge.

Essence of this thesis project is part of this context and aims to develop and study molecular and surface-supported heterobimetallic complexes associating an oxophilic metal (such as Al, Ga, Hf or Ta) with a late transition metal - TM (such as Ir, Rh or Cu). Given the very new surge of interest for complexes associating aluminum with d-block metals featuring original and uncommon chemistry (as shown in section 1.2),^[7,8] we particularly focused on aluminum as the first metallic partner. On the other side, in view of their eminence in academic and industrial research areas, especially in the field of organometallic catalysis, we turned our attention to iridium as the second metallic partner.^[9] Given the interest of the SOMC approach (as mentioned in section 1.2.2.2), we envisioned the grafting of these molecular heterobimetallic species upon the surface of a mesoporous SBA-15 silica using such strategy. Indeed, in addition to the inherent advantages of heterogeneous catalysis, the benefit of employing a SOMC approach is to take advantage of the solid support in order to access low-coordinated species with original electronic counts leading to novel reactivities.^[10-13] These highly reactive surface species have no direct molecular counterparts and could not be stabilized in solution. To date, SOMC studies have focused mainly on monometallic or, in very rare cases, on homobimetallic compounds. One axis of this thesis project is therefore to develop new methodological approaches combining the knowledge and skills of molecular organometallic chemistry to isolate original heterobimetallic species in a clean and selective manner, and then to transpose these concepts to surface chemistry. In order to

selectively direct the assembly of the two metal centers, two complementary strategies were employed in this project.

Strategy 1. The use of bifunctional ligands that have two different types of coordinating functions, one hard donor capable of forming a strong bond with a hard metal center (typically Al^{3+}) and one soft donor featuring a strong affinity for late transition metals (herein Ir), have greatly contributed to the development of original heterobimetallic complexes.^[14-17] This is particularly true for heterobimetallic systems associating aluminum with a *d*-block metal (see part 1.2.1.1 - page 49).

While various types of donors have been used to coordinate the hard metal center, the literature shows an omnipresence of phosphine ligands for the late metal. N-heterocyclic carbenes (NHCs), capable of forming strong bonds with many metals, and whose interest as a ligand in homogeneous catalysis is no longer in question, constitute an interesting alternative. Recently, in the laboratory, we have developed an alkoxy-carbene (NHC-OH) type ligand and initial encouraging results have demonstrated the interest of this platform to coordinate both early (Ta) and late (Rh) metals to give a series of monometallic and heterobimetallic compounds.^[18-20] In continuity of this preliminary work, we will present in this thesis an extension of this strategy towards aluminum-alkyl precursors. This led to a range of original and new monometallic aluminum species which reactivity towards common reagents will be depicted. In accordance with this PhD project, we will then show that these complexes embody a gateway towards the formation of heterobimetallic assemblies. All these aspects will be discussed in CHAPTER 2 (page 103).

Strategy 2. The use of an alkane elimination route to access heterobimetallic compounds turns out to be a very elegant and efficient synthetic methodology. As discussed in part 1.2.1.5 (from page 63), this approach has the additional advantage of generating only volatile, inert and easily eliminated alkanes as by-products. Finally, this synthetic route makes possible to obtain highly reactive low-coordinated species. Note that this is less true in the case of **strategy 1**, which is based on the use of chelating ligands to bridge the two metals and stabilize this heterobimetallic edifices, but can restrict the concerted approach and coordination of substrates on the two metal centers and can thus reduce the reactivity of these derivatives. Quite unexpectedly, **strategy 2**^[22,23] is almost unexplored for metallic couples associating aluminum with a *d*-block metal (as depicted in part 1.2.1.5).^[24-26] There is therefore a huge potential in developing, extending, and studying this methodology to form new and original heterobimetallic architectures.

For instance, this synthesis strategy has been successfully used recently in the laboratory to prepare a first generation of heterobimetallic tantalum-iridium complexes in good yields by reacting metal-alkyl/alkylidene precursors of tantalum with an iridium polyhydride reagent.^[27-29] Inspired by these promising results, we will present an important extension of **strategy 2** using mainly metal-alkyl derivatives of aluminum and the same iridium polyhydride precursor. This led to the rational preparation of a series of polyhydrides heterobimetallic Al/Ir species of different nuclearity and topologies. Synthesis, experimental characterizations, and theoretical investigations of these complexes will be described in CHAPTER 3 (page 135). Then, reactivity studies of these edifices towards Lewis bases and acids, Brønsted bases, nucleophiles, oxidants, and heteroallenes will be presented and discussed in CHAPTER 4 (page 165).

Armed with a deep understanding of the behaviors of heterobimetallic Al/Ir complexes formed along **strategy 2**, we aimed to transpose this molecular knowledge to SOMC in order to uncover a cooperativity between the surface of the support and the metallic centers, and therefore accessing novel well-defined heterobimetallic active sites grafted on the support.

This approach was also used in our laboratory for the above-mentioned Ta/Ir compounds, as discussed at the end of part 0 (from page 91).

In parallel, as discussed in parts 1.3.2.2 (page 82) and 1.3.4.2 (page 91), some studies show the possibility to form small, dense, and narrowly distributed silica-supported rhodium, iridium, or platinum nanoparticles prepared in a controlled manner by a SOMC approach followed by a thermal/chemical post-treatment.^[32-34] These supported nanoparticles are original and feature various interests for catalytic purposes. In this vein, some of these studies focus on the use of a second metallic partner to form mixed systems of isolated monometallic sites and surface supported alloys nanoparticles. Such systems turn out to be very interesting as they combine the benefits of using metallic nanoparticles, heterobimetallic species and well-defined surface supported sites.^[32,35-38] Inspired by the above-mentioned studies, we will describe the preparation of new, well-defined, heterobimetallic Ir/Al surface species supported on SBA-15₇₀₀ using SOMC. We will then show that this heterobimetallic active site can be used as precursors to access materials featuring aluminum isolated sites with small and narrowly distributed iridium NPs. These aspects will be discussed in CHAPTER 5 (page 211).

Finally, we will describe a comparative catalytic study of these materials for the catalytic hydrogen/deuterium exchange reaction on methane. This study especially revealed a promoting effect of the Al sites on the Ir NPs and thus demonstrated the bimetallic cooperativity phenomena. This comparative catalytic investigation will be presented in CHAPTER 6 (page 245).

CHAPTER 2. Towards Heterobimetallic Aluminum/M Complexes Bridged By Bifunctional NHC Ligands

2.1 Introduction

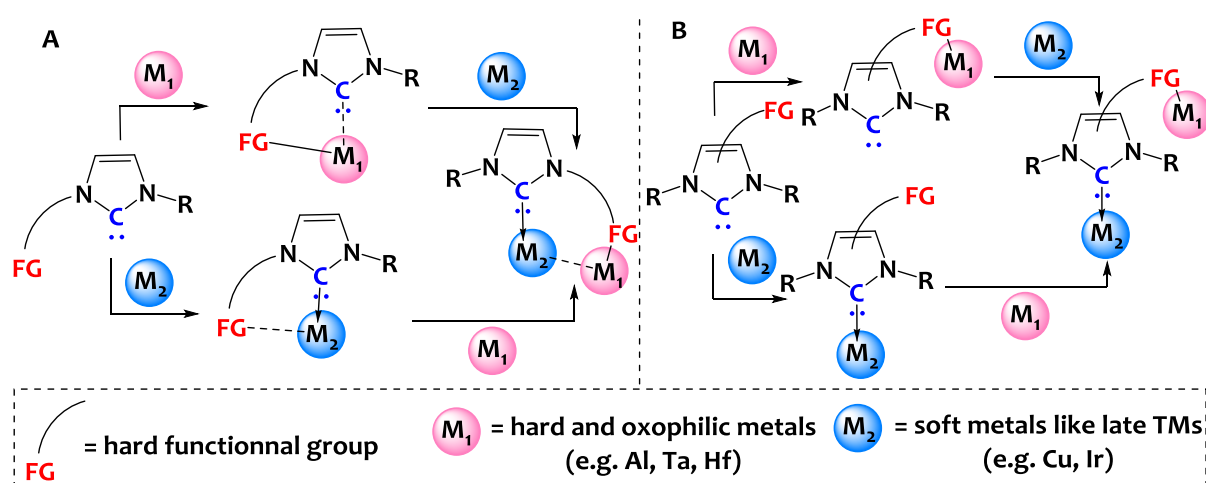
As mentioned in section 1.2.1 for Al/M species, access to heterobimetallic complexes associating two metals of different nature (such as the combination of aluminum with a late transition metal center) is not easy. Smart and dedicated methodologies are needed to avoid the occurrence of undesirable ligand redistribution phenomena, or the formation of oligomers or nanoparticles. One identified strategy to assemble and stabilize the two metal centers relies on the use of ancillary bifunctional ligands. Indeed, bifunctional scaffolds with two distinct coordination sites are particularly relevant to stabilize the two metals simultaneously. In this case, Lewis acids such as aluminum derivatives would be covalently bound to the hard donors (e.g. phosphine-oxide, amino, azanide (R-NH-), guanidinate, amidinate or diketiminate groups) of the ligand, while the late transition metal precursors are typically coordinated by soft donors. In section 1.2.1.1 (from page 49), we presented an overview of these bifunctional platforms used to assemble late transition metal and aluminum centers. This literature survey shows a diversity of hard σ and π donors. However, the majority of the soft donors used to accommodate late transition metal derivatives are based on phosphine groups (PR_3 type). In this project, we target NHCs as an interesting and relevant alternative to phosphine donors for the following reasons: i) NHCs are known to have remarkable stereoelectronic properties when coordinating to a metal center.^[182-184] In particular, an NHC is a strong σ -donor and a moderate π -acceptor. ii) The synthesis of NHCs is quite straightforward and now very well mastered.^[185] iii) NHCs are excellent auxiliary ligands involved in many catalytic processes.^[186]

In the next introductory section, we will directly discuss the functionalization of NHC rings.

2.1.1 Development of bifunctional NHCs to access heterobimetallic species

NHC ligands can be easily functionalized to install a hard functional group (FG) onto the heterocycle in order to either i) access stable bifunctional NHC-based monometallic complexes with possibly a chelate effect or ii) assemble two distinct metal centers. A large range of complexes can be obtained depending on which position the hard FG is attached on the NHC skeleton, as illustrated in Scheme 44. Indeed, the substitution of the imidazol-2-ylidene scaffold can be performed either at one of the nitrogen atoms (Scheme 44.A) or at the carbon positions (Scheme 44.B) resulting in different types of structures. Although a large number of functionalized NHCs are available in the literature, there are only a few literature reports

describing soft-hard heterobimetallic complexes – *i.e.* compounds associating a soft and a hard metal center - supported by bifunctional NHC scaffolds.^[187] Relevant examples of such species are shown in Figure 8. The first derivative is a rhodium(I)-NHC complex functionalized with hard phosphine-oxide moieties on the carbon positions of the NHC ring. As a consequence, one P=O site is able to bind a titanium chloride precursor resulting in an original Ti-(OP-NHC)-Rh edifice (Figure 8, left).^[188] In a somewhat similar manner, T.D. Tilley and coworkers reported in 2016 an Ir(I)-NHC species with hard oxalamine donors on both carbons that can bind titanium or zirconium metallocenes leading to Ti/Ir and Zr/Ir heterobimetallic entities, which are more active than the monometallic Ir analogues for the catalytic hydrosilylation of aldehydes (Figure 8, middle).^[189] In these two examples, the metal centers are far from one another and metal-metal interactions are unlikely to happen. More recently, as discussed in part 1.2.1.1, S. Ogoshi and his team reported in 2020 a relevant N-phosphine-oxide-substituted-NHC platform capable of assembling a Al(III) Lewis acid site with a Cu(I) center (Figure 8, right).^[52] In this case, it is interesting to notice that the Al and Cu centers can be brought closer to each other by the rotation of the N-phosphinoyl side arm, leading to an exchange reaction by transmetallation.



Scheme 44. Different conceptual synthetic paths to access monometallic and heterobimetallic NHC complexes depending on the position of the hard functional group onto the NHC ring (on N atom = case A, on C atom(s) = case B).

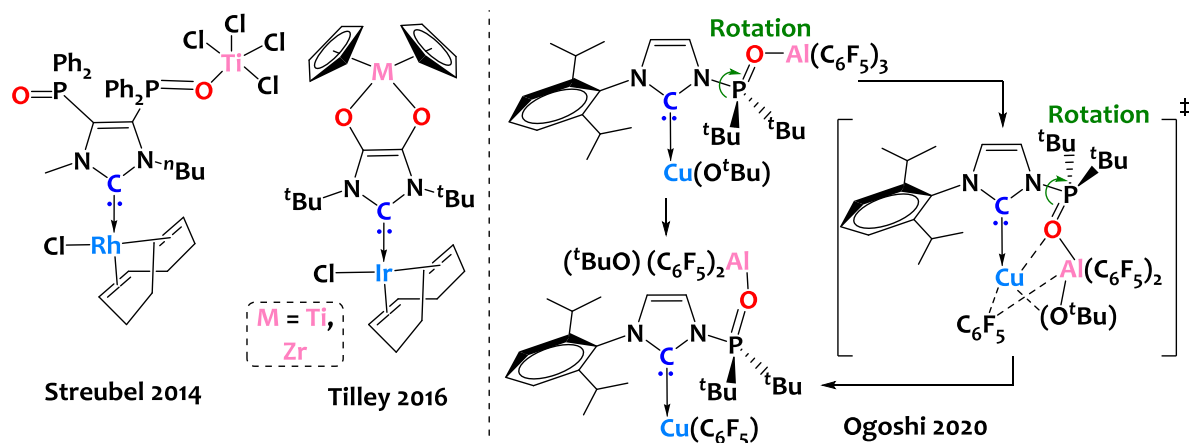
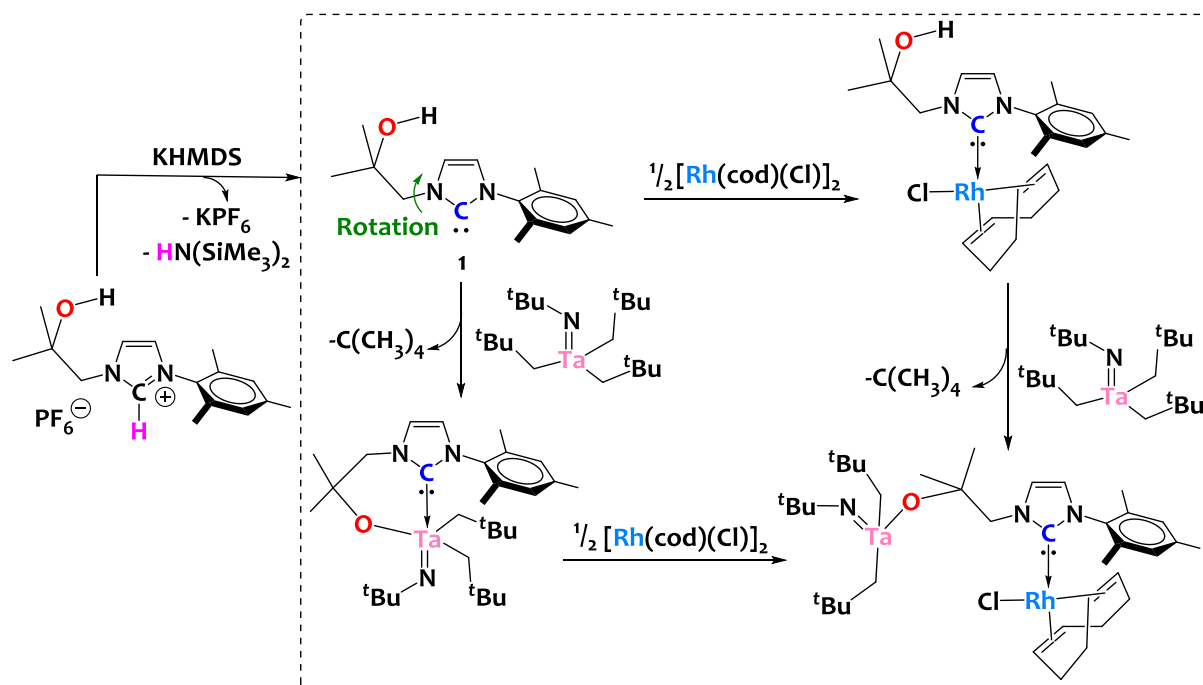


Figure 8. Selected reported soft-hard heterobimetallic complexes assembled through bifunctional NHC ligands.^[52,187-189]

In this train of thought, a bifunctional hydroxyl tethered NHC ligand – compound **1** – was designed in 2018 in our research team by performing deprotonation (with KHMDS) of its respective imidazolium hexafluorophosphate pro-ligand (Scheme 45, left).^[20] Next, this bifunctional ligand platform, **1**, is used to assemble a neopentyl-tantalum *tert*-butylamido moiety with a cyclooctadiene rhodium chloride fragment yielding an original heterobimetallic Ta-(O-NHC)-Rh edifice (Scheme 45, square with dotted lines). Interestingly, both synthetic routes (addition of Ta first followed by Rh and *vice versa*) lead to the same heterobimetallic complex in high yields.



Scheme 45. Synthesis of a NHC-OH ligand **1** used as a bifunctional platform to assemble Ta and Rh species.^[20]

It is also important to mention that the Ta and Rh centers are distant from each other, most likely due to geometry constraints. However, it can be assumed that the hydroxyl side arm of ligand **1** can rotate along the C-N_{NHC} bond resulting potentially in a geometric approach of the two metals, as suggested by the formation of the bidentate alkoxy-NHC tantalum species shown in the lower left of Scheme 45.

Inspired by these promising preliminary works, we aimed to extend the chemistry of ligand **1** to other metals. In this respect, we first developed this specific chemistry with alkyl-aluminum derivatives. In the next sub-section, we will describe the reasons of such a choice.

2.1.2 Interests of alkyl aluminum species

The initial motivation to use alkyl aluminum precursors is rooted in the project itself. Indeed, since one of our ultimate goals is to develop heterobimetallic complexes that can be used for grafting reactions on silica, it is important to have a robust anchor point on the bimetallic species to chemically immobilize it on the solid support. Most of the time, this is achieved by using a hard, oxophilic metal center through protonolysis. Therefore, as discussed in section 1.3.2.1 (page 78) describing SOMC of Al derivatives, alkyl-Al species are candidates of choice to achieve this goal (Figure 9).

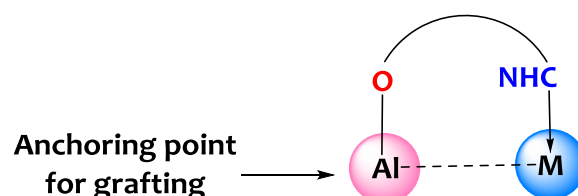


Figure 9. General structure of the heterobimetallic target of this project.

In terms of practical considerations, it also makes sense to use alkyl-aluminum sources because these commercial precursors are rather cheap and accessible facilitating our work in the laboratory. It should be mentioned, however, that alkyl aluminum reagents are highly pyrophoric and must be handled with great care (in an atmosphere completely free of moisture and air).

Furthermore, the rich, diverse, and sometimes complex reactivity of alkyl Al species, which translates into their widespread use in catalysis^[130] (for instance as a co-catalyst in the polymerization of alkenes or as a Lewis acid promoters^[190]) have attracted our attention.

In the rest of this chapter, we will depict the chemistry of platform **1** towards different Al sources.

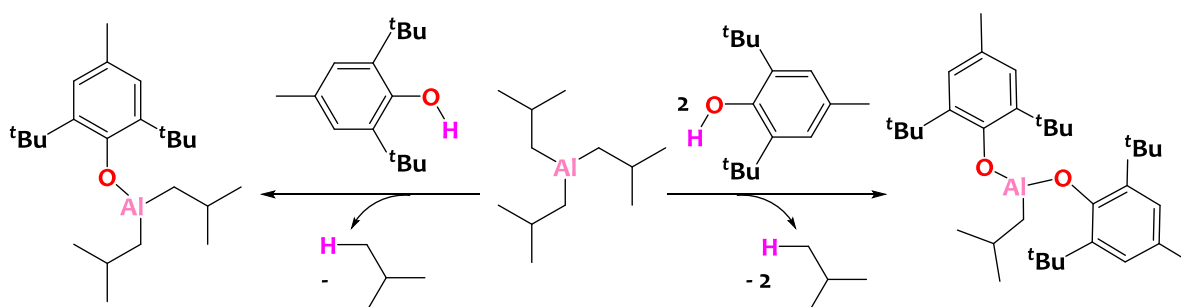
Next, we will present the reactivity and the interest of the obtained monometallic Al complexes. Finally, we will conclude about the relevance of these systems in view to access soft-hard heterobimetallic architectures.

2.2 Development of new Al-NHC species

2.2.1 Design of an alkoxy bis-alkyl Al(III)-NHC complex

In a first approach, we chose to use triisobutylaluminum(III) as a source of Al because TIBA is mostly in a monomeric form in solution.^[130]

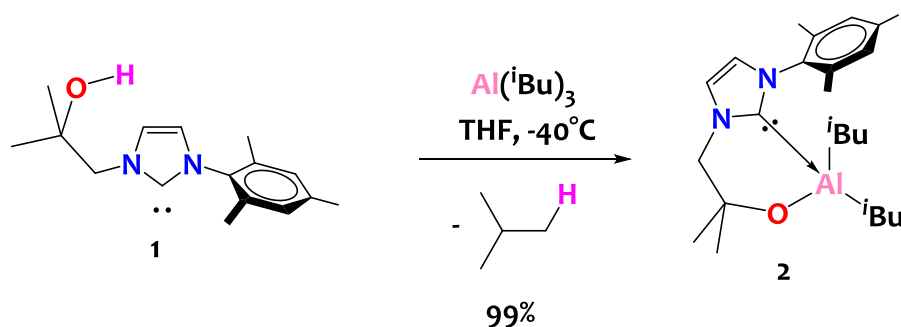
We projected that the Al center should be easily attached to the hydroxyl side arm of ligand **1** by a protonolysis reaction. Indeed, treatment of alkyl aluminum reagents with alcohols or phenols usually leads to the formation of aluminum alkoxides or phenoxides together with the liberation of volatile alkanes. For instance, the reaction of butylated hydroxytoluene (BHT) with TIBA (one equivalent or half an equivalent) gives the corresponding mono-phenoxy(diisobutyl)aluminum(III) or bis-phenoxy(isobutyl)aluminum(III) products with the evolution of one or two equivalents of isobutane gas (Scheme 46).^[191] Note that monometallic species are obtained in this particular case due to the large steric hindrance of the ligands, preventing the formation of dimeric/oligomeric structures.



Scheme 46. Reported synthesis of $\text{Al}(\text{tBu})(\text{OAr})_2$ and $\text{Al}(\text{tBu})_2(\text{OAr})$ ($\text{Ar} = 2,6\text{-}(\text{tBu})\text{-3-MeC}_6\text{H}_2$) starting from TIBA and one (left side) or two equivalents (right side) of butylated hydroxytoluene (BHT).^[191]

In a somewhat similar manner, an alkoxy bis-alkyl Al(III)-NHC species, **2**, is prepared from the protonolysis between triisobutyl aluminum(III) (TIBA) and the bifunctional alcohol-NHC ligand **1** (Scheme 47). Suitable experimental conditions to successfully isolate a pure complex are essential. It appears that temperature of the reactional medium as well as ways of adding the

reactants are particularly important. Indeed, with the aim of preventing a local excess of hydroxyl functional group in the reactional medium (from ligand **1**), which would lead to an irreversible tri-*ortho*-alcoholysis of the TIBA (because of its very strong oxophilic properties), a dropwise addition of a diluted THF solution of **1** onto a diluted THF solution of TIBA at low temperature (-40°C) is adopted. This procedure affords the target complex **2** through mono-substitution of TIBA and the release of isobutane gas as side product. Recrystallization in a minimal amount of pentane is required to isolate and purify **2** as block shaped yellow crystals with an excellent yield of 99%.



Scheme 47. Reaction of triisobutyl aluminum(III) (TIBA) with the bifunctional NHC-OH ligand **1**.

Structural elucidation of species **2** is determined *via* a combination of characterization techniques. Its empirical formula (C₂₄H₃₉N₂OAl) is confirmed by elemental analysis. The proposed structure is also supported by multi-nuclei solution NMR spectroscopy. The ¹H-NMR spectrum of **2** (Figure 10) displays shifted imidazole (δ= 7.38 and 7.20 ppm), aromatic (δ= 7.00 ppm) and aliphatic resonances (δ= 4.00 and 1.12 ppm) with respect to the free NHC-OH ligand.^[20] It also shows two isobutyl fragments *per* Al-NHC since CH_{iBu} (1.56 ppm), CH_{3iBu} (0.77 ppm), and CH_{2iBu} (-0.51 ppm) signals are integrating for 2H, 12H, and 4H respectively.

¹³C-NMR studies of the ¹³C-enriched analogue of **2** - **2**-¹³C – used for enhancing the carbene (N-¹³C-N) signal, showcase a typical resonance at 173.5 ppm in THF-d₈ and at 174.0 ppm in C₆D₆ in agreement with the expected range of chemical shifts for a typical carbene-aluminum bond (NCN-Al).^[192,193]

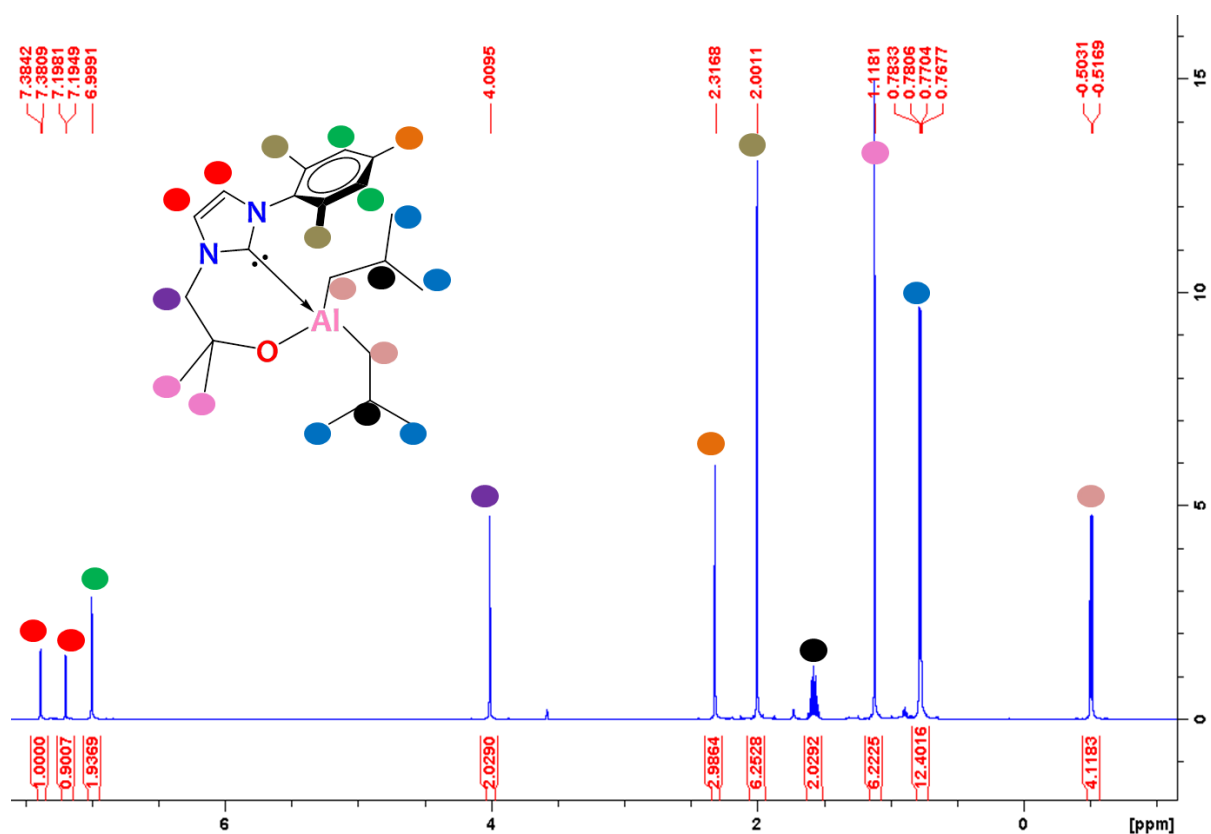


Figure 10. $^1\text{H-NMR}$ spectrum (500 MHz, THF-d_8 , 293 K) of complex **2**.

The 3D molecular structure of **2** is established through X-Ray Diffraction (XRD) on single crystals. Its solid-state structure (Figure 11) validates a bidentate coordination of the alkoxy-NHC ligand to the Al(III) metallic center. Indeed, there is on one side, an Al–alkoxy bond exhibiting a distance of $1.770(4) \text{ \AA}$, and, on the other side, an Al–carbene bond averaged at a length of $2.069(5) \text{ \AA}$, which matches with the expected range of Al–NHC distances.^[192–194] Regarding the other metrical parameters, an expected slight relaxation of the internal NCN ring angle is noticed compared to that of the free carbene in ligand **2** ($104.5(4)^\circ$ vs $102.5(1)^\circ$).^[20,194]

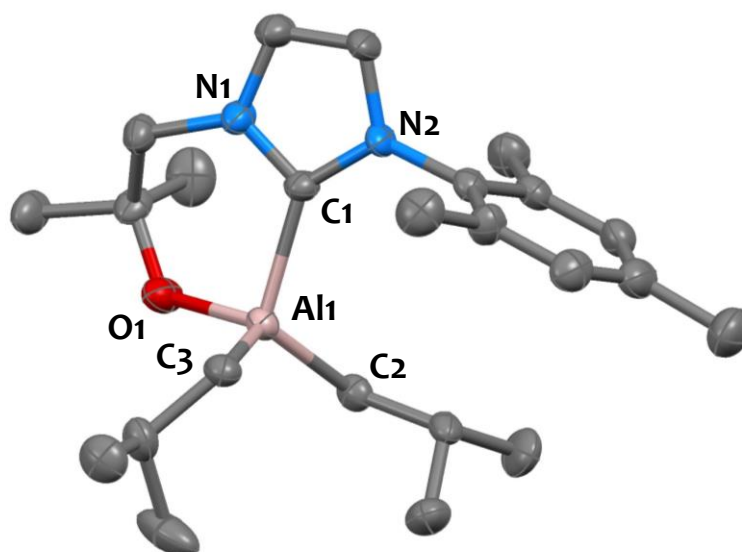
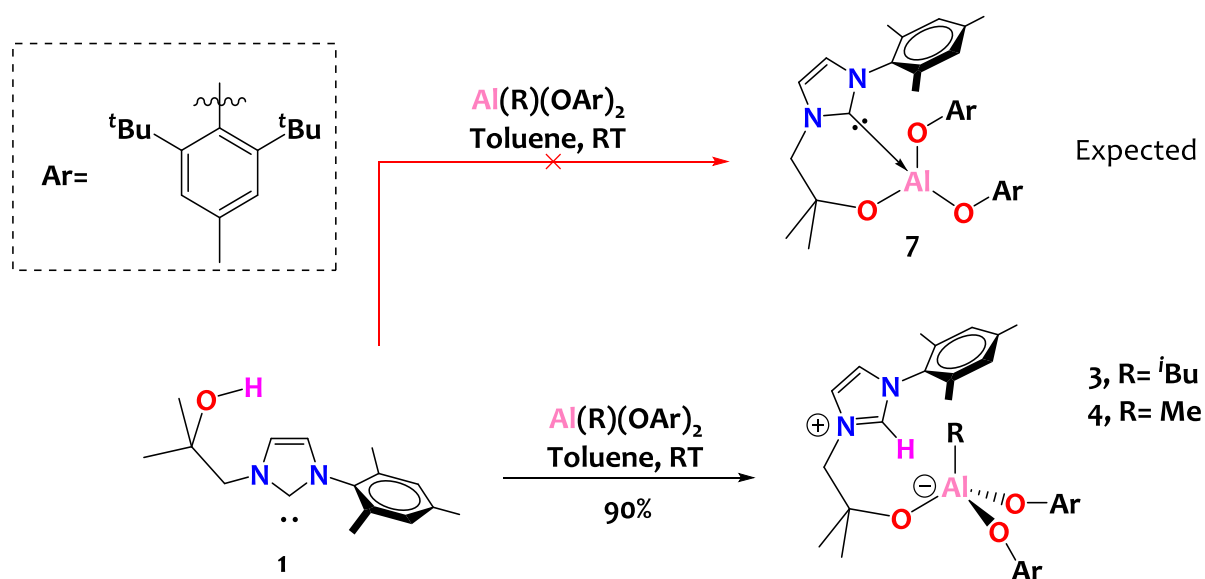


Figure 11. Solid-state molecular structure of **2** (50% probability ellipsoids). Hydrogen atoms have been omitted for clarity. Selected bond distances [Å] and angles [°] (averaged parameters found in the asymmetric unit): Al1-C1 2.069(5); Al1-C_iBu 1.978(17); Al1-O1 1.770(4); C1-N_{imid} 1.354(8); N1-C1-N2 104.5(4); C1-Al1-O1 95.2(6); Al1-C1-N1 118.8(4); Al1-C1-N2 136.7(1).

2.2.2 Formation of aluminate-imidazolium zwitterions

We then tried to prepare the bis-phenolate alkoxy-NHC aluminum species **7** by treating **1** with $\text{Al}(\text{R})(\text{OAr})_2$ (R = Me or ⁱBu). Such procedure leads instead to the formation of imidazolium-aluminate zwitterions [**HL**][$\text{Al}(\text{R})(\text{OAr})_2$], **3** (R = ⁱBu) and **4** (R = Me) as shown on Scheme 48.



Scheme 48. Synthesis of zwitterions **3** and **4**.

Compound **3** is stable in toluene at 110°C for at least several hours and no proof of Al-R protonolysis was noticed.

The identity of **3** in solution is underpinned by multi-nuclei NMR spectroscopy. Particularly, the ¹H-NMR spectrum of **3** (recorded in C₆D₆) displays three ¹H-imidazolium signals at 7.70, 6.14 and 5.34 ppm indicating a protonated NHC ring (Figure 12). The ¹³C-NMR spectrum of the ¹³C-labelled analogue [HL][Al(¹³Bu)(OAr)₂], **3**-¹³C, confirms the imidazolium structure with a characteristic resonance found at 135.6 ppm.

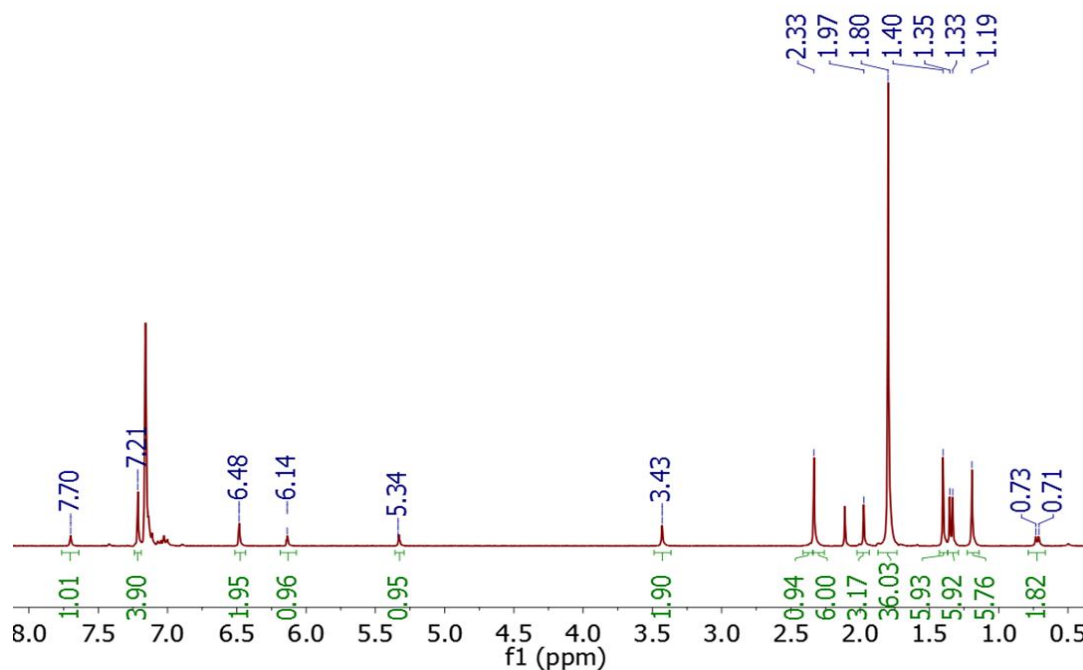


Figure 12. ¹H-NMR (300 MHz, C₆D₆, 293K) spectrum of zwitterion **3**.

Analysis of single crystals of **3** by X-Ray Diffraction confirms all these aforementioned aspects. The solid-state structure (Figure 13) shows a tetra-coordinated aluminate center with a pendant imidazolium group. Metrical parameters are clearly in agreement with a protonated NHC ring since there is (i) a shortening of the C-N_{imid} bonds compared to Al-NHC motifs such as in compound **2** (Al(L)(^tBu)₂) or to free-NHCs such as in ligand **1** (respectively 1.328 Å vs 1.354 Å in compound **2** or 1.328 Å vs 1.361 Å in ligand **1**) and (ii) a relaxation of the internal NCN cycle angle compare to those in Al-NHCs or free NHCs motifs (108.6° vs 104.5° in compound **2** or 102.5° in ligand **1**).^[20,194]

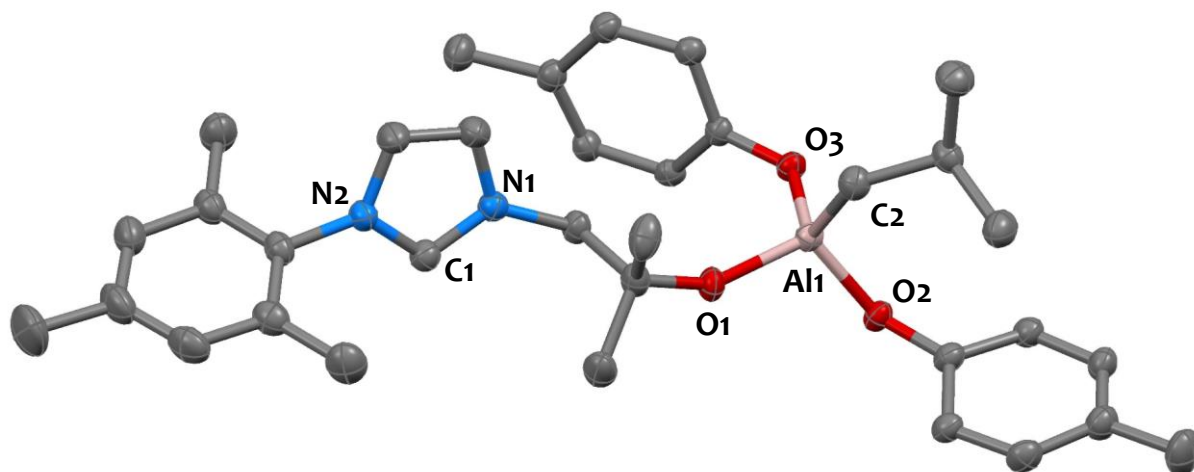


Figure 13. Solid-state molecular structure of **3** (50% probability ellipsoids). Hydrogen atoms and ^tBu aryl substituents have been omitted for clarity. Selected bond distances [Å] and angles [°] (averaged parameters found in the asymmetric unit) Al1-O1 1.731(6); Al1-O_{Ar} 1.787(6); Al1-C2 1.986(8); C1-N_{imid} 1.328(11); N1-C1-N2 108.6(1).

Changing the nature of the alkyl group in $[Al(R)(OAr)_2]$, from an isobutyl fragment to a less hindered methyl group, does not influence the outcome of the reaction which leads to a similar zwitterion, compound **4** (Scheme 48). The zwitterionic form of **4** is validated in solution using similar characterization techniques than those for compound **3**. Indeed, the ¹H-NMR spectrum of the ¹³C-labelled analogue, **4**-¹³C, shows a typical doublet δ (¹³C-H_{imid.}) averaged at 8.28 ppm with a coupling constant of 227 Hz in deuterated toluene (Figure 14). The ¹³C-NMR spectrum of **4**-¹³C confirms the imidazolium pattern with a typical enhanced signal at 136.6 ppm in C₆D₆ (Figure 15).

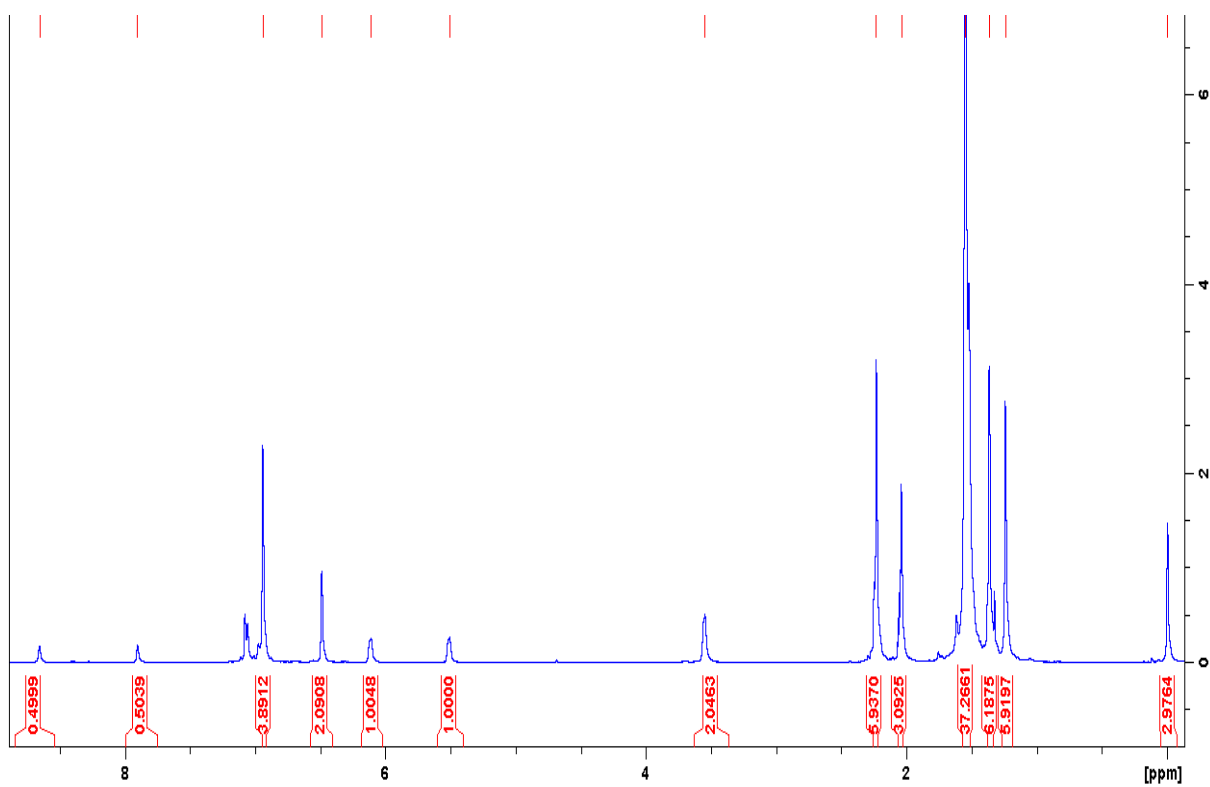


Figure 14. $^1\text{H-NMR}$ spectrum (300 MHz, tol-d_8 , 293 K) of the ^{13}C -labelled analogue zwitterion $[\text{HL}][\text{Al}(\text{Me})(\text{OAr})_2]$, $4\text{-}^{13}\text{C}$.

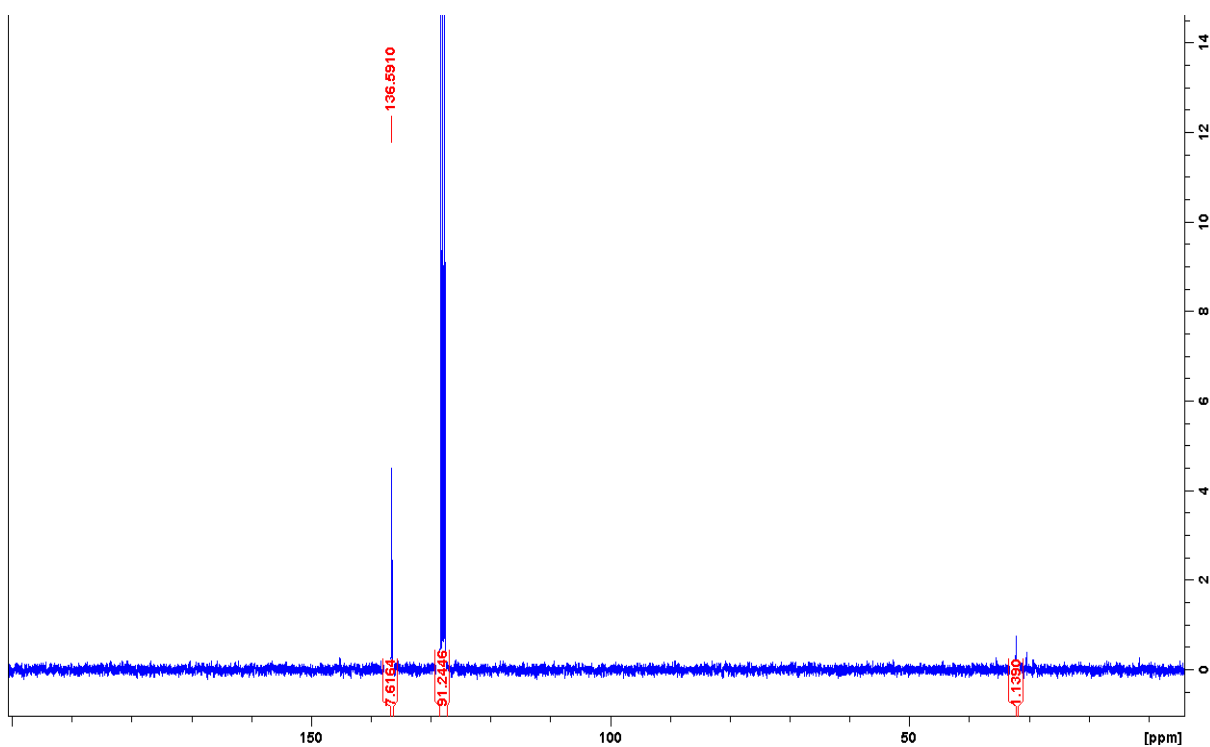
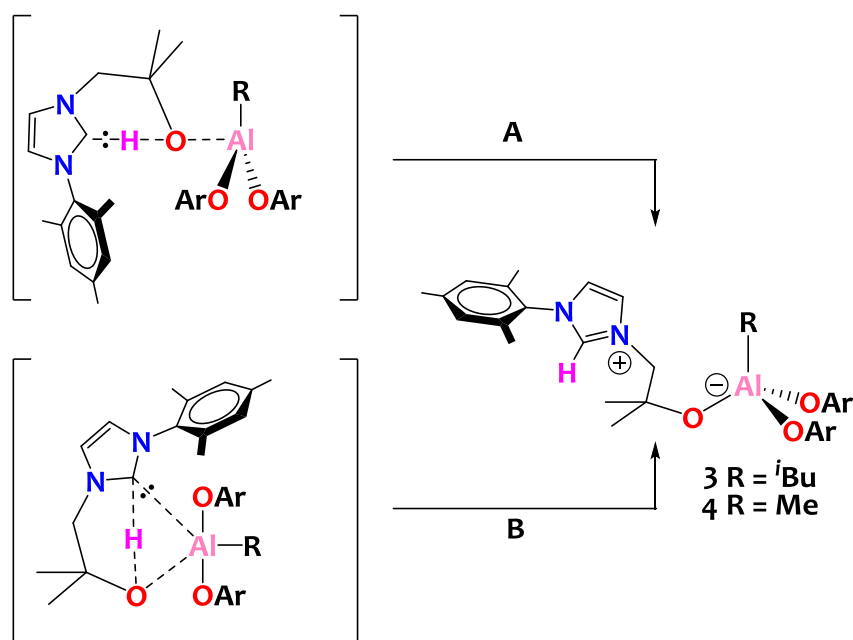


Figure 15. $^{13}\text{C-NMR}$ spectrum (75 MHz, C_6D_6 , 293 K) of the ^{13}C -labelled analogue zwitterion $[\text{HL}][\text{Al}(\text{Me})(\text{OAr})_2]$, $4\text{-}^{13}\text{C}$.

2.2.3 Discussion

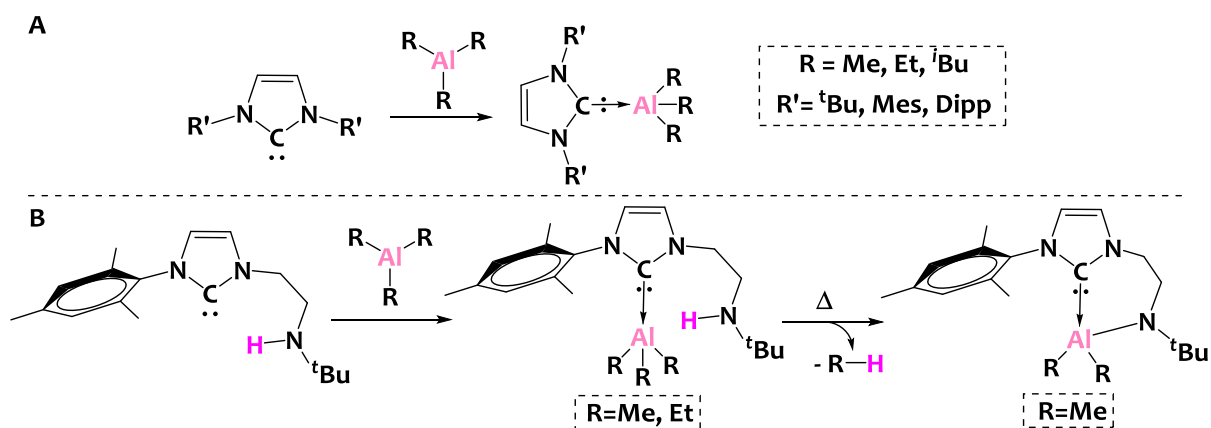
Results of these reactions highlight the strong impact of the aluminum functional groups on the reactivity of the Al-R motif. In fact, treatment of ligand **1** with $\text{Al}(i\text{Bu})_3$ leads to the anticipated metallated product **2** with evolution of isobutane gas, which is characteristic of a classical protonolysis reaction. Notwithstanding, reaction of **1** with $\text{Al}(i\text{Bu})(\text{OAr})_2$ or $\text{AlMe}(\text{OAr})_2$ generates imidazolium-aluminate zwitterions proving a reactivity on the NHC site. This difference in reactivity might be driven by steric factors around the Al center when considering the high bulkiness of phenoxy substituents in $\text{Al}(\text{R})(\text{OAr})_2$ compared to isobutyl ones in $\text{Al}(i\text{Bu})_3$. Sterically-driven reactivity is evocative of the heterolytic cleavage of polar O-H bonds by FLPs (Scheme 49A).^[195-197] Another possibility is a concerted proton transfer mechanism evocative of a sigma-bond metathesis (Scheme 49B) involving ligation of the aluminum center to the carbene site and migration of a proton from the hydroxyl group to the carbene.



Scheme 49. Proposed FLP (A) or bond metathesis (B) mechanisms for the formation of **3** and **4**

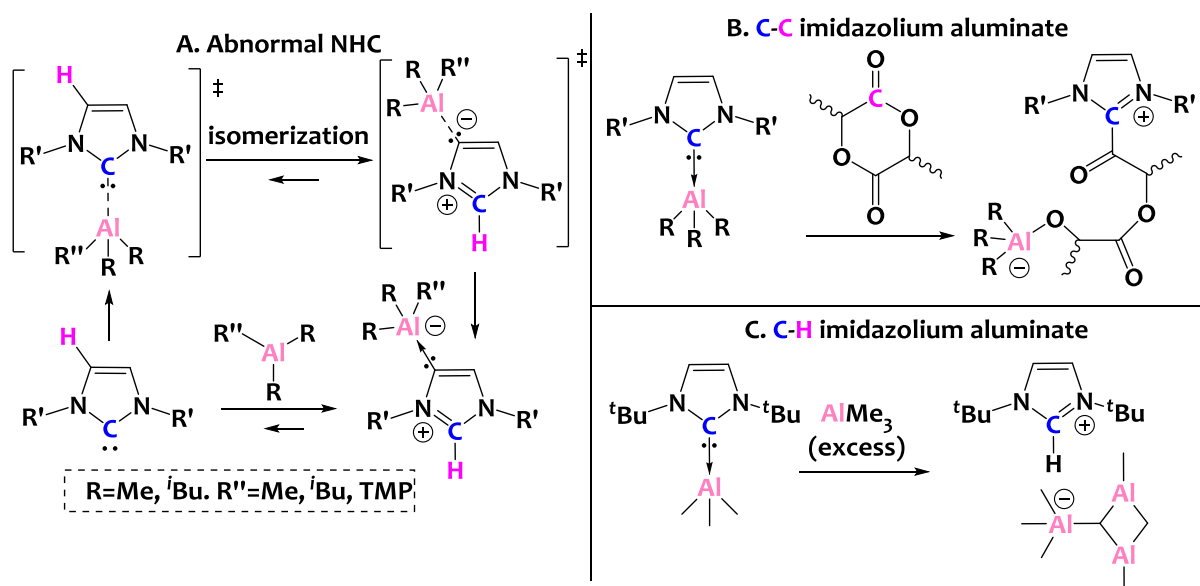
Most of the time, NHC coordination to Al(III) centers results in the formation of stable aluminum derivatives featuring robust NHC-Al bonds. Indeed, alkyl aluminum species are known to form Lewis adducts with NHCs, as described by S. Dagorne, F. Garcia and their collaborators who reported a series of trialkyl-aluminum-NHC adducts – noted $\text{NHC} \rightarrow \text{AlR}_3$ (R = methyl, ethyl or isobutyl groups) hereafter – where the carbene site and the AlR_3 fragment play the role of a Lewis base and a Lewis acid respectively (Scheme 50-A).^[192,198-202] Interestingly, T.-G. Ong and coworkers reported the design of a bifunctional amino-tethered NHC ligand (Scheme 50-B, left) which is

found to react preferentially with AlR_3 (TMA and TEA) through the C_{NHC} site over N-H, leading to the formation of $\text{NHC} \rightarrow \text{AlR}_3$ adducts (Scheme 50-B, middle).^[203,204] Here, the protonolysis reaction between the secondary amine group (NH) and one Al-R moiety (forming an Al-N bond and releasing an alkane R-H) is only observed when R is a methyl group and heating is applied (Scheme 50-B, right).



Scheme 50. A. Reported symmetrical $\text{NHC} \rightarrow \text{AlR}_3$ adducts.^[192,198–202] B. Reported dissymmetrical $\text{NHC} \rightarrow \text{AlR}_3$ adducts and their stability.^[203,204]

However, in a few cases, the $\text{C}_{\text{NHC}}\text{-Al}$ motif is found to be reactive and non-innocent. As a consequence, original activation processes across the carbene-aluminum bond can occur. For instance, S. Dagorne and coworkers reported the formation of imidazolium aluminate salts through a rearrangement of the imidazolidene ring from normal NHCs into abnormal NHCs (Scheme 51-A).^[198,202,205] S. Dagorne and colleagues also reported the catalytic lactide ring-opening polymerization using $\text{NHC} \rightarrow \text{AlR}_3$ adducts as pre-catalysts. In this work, the authors postulated that $\text{NHC} \rightarrow \text{AlR}_3$ species can promote insertion of a lactide substrate by breaking C-O bonds across the $\text{C}_{\text{NHC}}\text{-Al}$ motif leading to C-C imidazolium aluminate products (Scheme 51-B).^[200] The same group also reported the formation of an unusual imidazolium aluminate zwitterion by reacting a bulky $\text{NHC} \rightarrow \text{AlMe}_3$ with an excess of TMA. Here, TMA (which is dimeric in solution)^[130] is suspected to be deprotonated by the Al-C_{NHC} motif (Scheme 51-C, left).^[198,201]



Scheme 51. Reactivity of Al-NHCs adducts: **A.** Rearrangement into abnormal NHCs.^[198,202,206] **B.** Insertion of a lactide substrate in the $\text{C}_{\text{NHC}}\text{-Al}$ motif yielding a C-C imidazolium aluminate salt.^[200] **C.** Formation of C-H imidazolium aluminate zwitterions through deprotonation of excess TMA by bulky NHCs (bottom left)^[198,201]

Consequently, these reported studies highlight not only the simple coordination of NHCs towards Lewis acidic alkyl-Al precursors, but also a large variety of metal-ligand reactivity of the resulting Lewis adducts. Herein, the steric congestion around the Al(III) center seems to be key and could be employed as a supplementary tool to tune the reactivity of Al-NHC fragments.

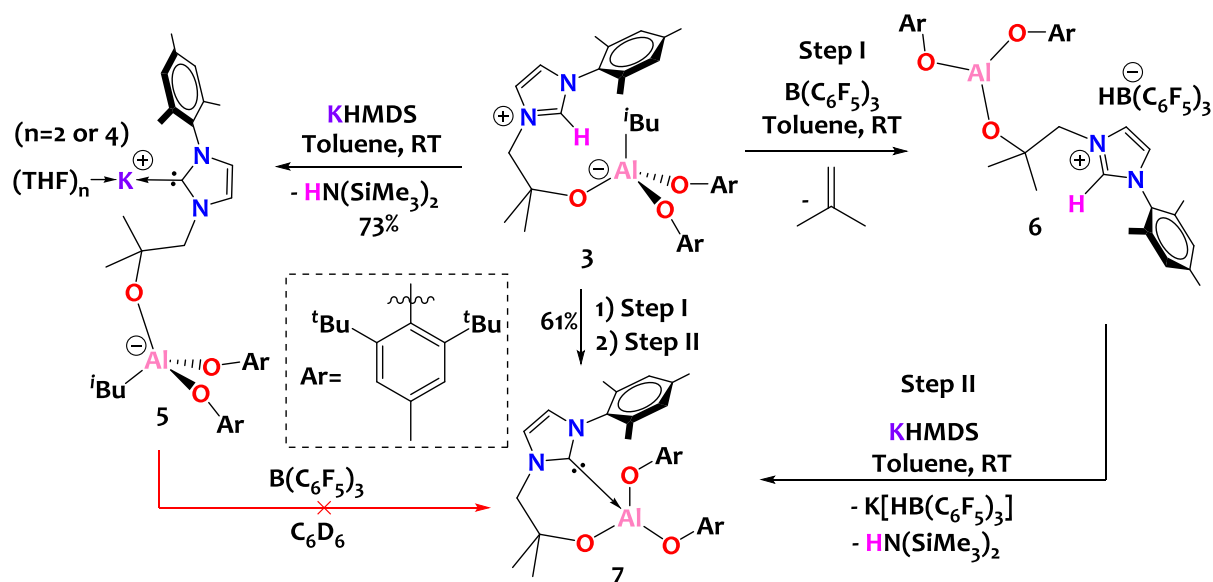
In summary, the reaction path entailing to perform metalation of $\text{Al}(\text{R})(\text{OAr})_2$ with ligand **1** in view of getting complex **7** is a deadlock (Scheme 48). Consequently, an alternative synthetic route is implemented to synthesize complex **7**.

2.2.4 Restoration of the Al(III)-NHC motifs

Two approaches can be used to prepare compound **7** from zwitterion **3**: i) deprotonation of the imidazolium site and further alkyl abstraction of the aluminate moiety or ii) the reverse of strategy i).

The carbene site is regenerated by reacting **3** with a strong base such as KHMDS (HMDS = hexamethyldisilylamide) in toluene, affording after crystallization in THF complex $[\text{K}(\text{THF})_n\text{L}][\text{Al}(\text{tBu})(\text{OAr})_2]$ ($n = 4$), **5** (Scheme 52- left). Upon drying in vacuum, two THF molecules are removed from complex **5** which is isolated in good yields (73%) as a bis-THF derivative ($n = 2$). The ^{13}C NMR C_{NHC} signal for **5** ($\delta = 211.1$ ppm in $\text{THF-}d_8$; $\delta = 204.8$ ppm in C_6D_6) is strongly shifted towards downfield values when comparing to the related resonance in the imidazolium salt **3**

($\delta = 135.6$ ppm) or to $\delta_{\text{NHC-Al}}$ in **2** ($\delta = 173.5$ ppm), as expected for a K-NHC ligation.^[207] The solid-state structure for **5**, shown on Figure 13 is as expected, with a N1-C1-N2 ring angle of $101.8(2)^\circ$, average N-C_{carbene} bond length of $1.372(7)$ Å and a K1-C1 distance of $2.921(3)$ Å, which fall in the expected typical range.^[20,207–209]



Scheme 52. Deprotonation of **3** leading to species **5**. Two steps procedure – step I = alkyl abstraction and step II = deprotonation - leading to product **7**.

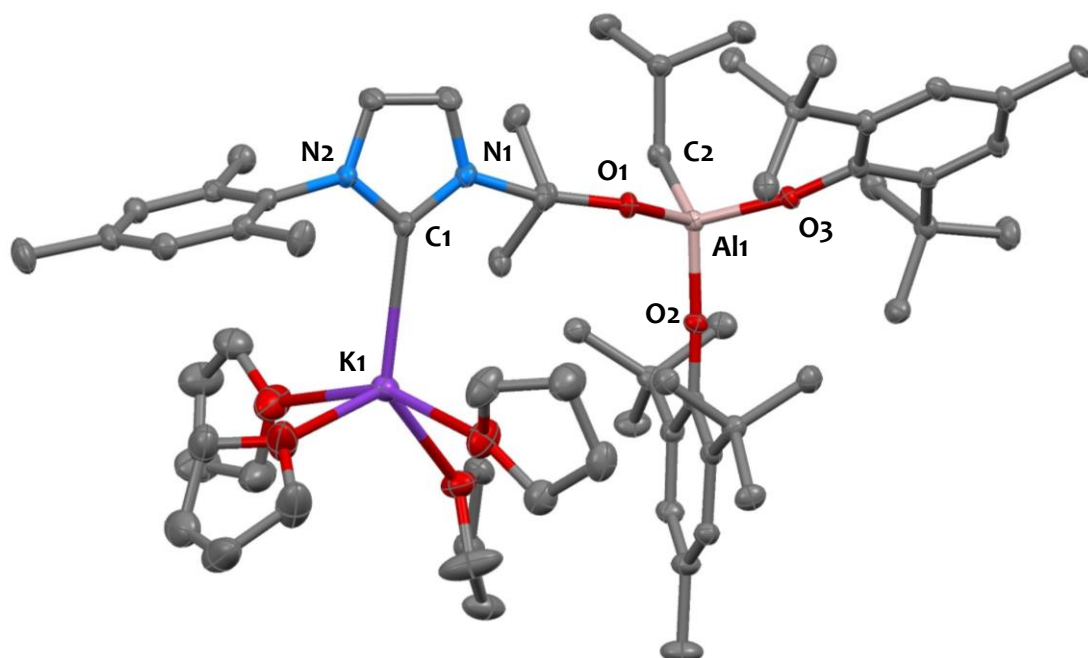


Figure 16. Solid-state molecular structure of **5** (50% probability ellipsoids). Hydrogen atoms have been omitted for clarity. Selected bond distances [Å] and angles [°]: Al1-O1 1.7447(18); Al1-O2 1.7647(18); Al1-O3 1.7711(18); Al1-C2 2.003(2); N1-C1 1.365(3); N2-C1 1.379(3); C1-K1 2.921(3); N1-C1-N2 101.8(2).

Unfortunately, abstraction of the alkyl moiety with $B(C_6F_5)_3$ from compound **5** to yield **7** are unsuccessful (Scheme 52, bottom left).

We thus investigated the abstraction of the isobutyl moiety from the aluminum center from zwitterion **3** upon reaction with $B(C_6F_5)_3$. $B(C_6F_5)_3$ is reported to perform alkyl abstractions from a variety of metal derivatives, including aluminum, and releasing typically alkylborate anions $[RB(C_6F_5)_3]^-$.^[210-218] Here, 1H , ^{11}B , ^{19}F , and ^{13}C -NMR reaction monitoring (in C_6D_6) indicates the exclusive formation of a bis-(aryloxy)(alkoxy)Al(III) imidazolium borohydride adduct $[(HL)Al(OAr)_2][HB(C_6F_5)_3]$, **6** (Scheme 52- top right).

The ^{11}B NMR spectrum of **6** displays a signal at $\delta = -24.5$ ppm (Figure 17, top right) consistent with the formation of a 4-coordinate borate center, but this resonance is shifted with respect to that of alkylborates $[RB(C_6F_5)_3]^-$ (typical range: -10 to -14 ppm)^[219] and appears as a doublet ($^1J_{B-H} = 79$ Hz). Consequently, it is instead assigned to the borohydride anion signature $[HB(C_6F_5)_3]^-$.^[213,219-222] The ^{19}F NMR spectrum of **6** confirms the presence of a borohydride anion with three typical resonances at $\delta = -134.7, -161.0$ and -165.1 ppm (vs $\delta = -128.7, -141.6$ and -159.9 ppm for the $B(C_6F_5)_3$ reagent, see Figure 17, top left) consistent with literature data for $[HB(C_6F_5)_3]^-$.^[213,219-221,223] The 1H NMR spectrum of **6** (Figure 17, bottom) shows a septet at $\delta = 4.75$ ppm and a triplet at $\delta = 1.60$ ppm typical of isobutene.^[224] Such observations suggest that $[HB(C_6F_5)_3]^-$ is formed, most probably *via* β -hydride elimination at the isobutyl group, to form isobutene. A similar phenomenon has been reported before in some occurrences.^[213,217-219,225,226]

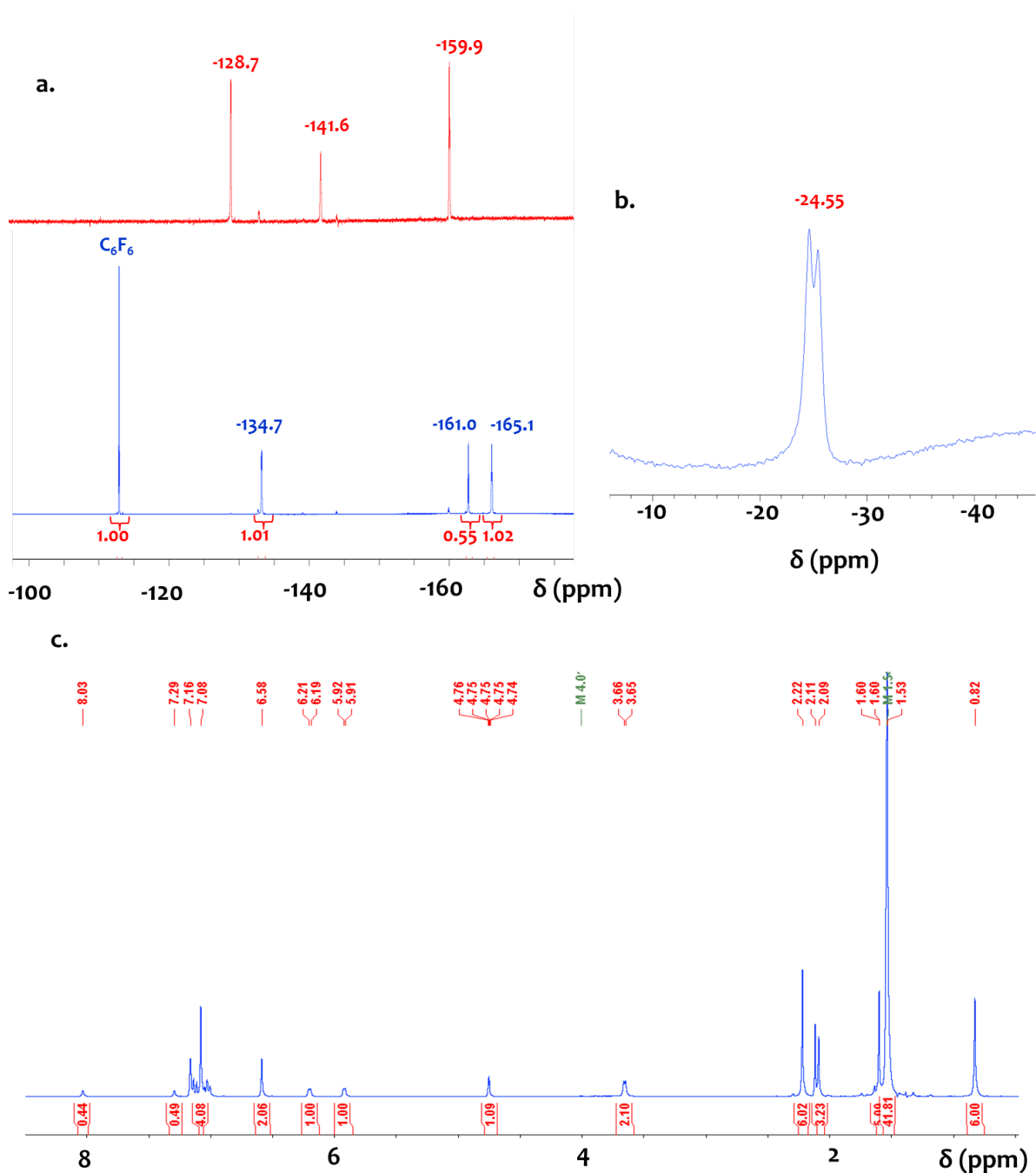


Figure 17. a.(red line): ^{19}F NMR spectrum of $\text{B}(\text{C}_6\text{F}_5)_3$ (282 MHz, C_6D_6 , 293 K) a.(blue line): ^{19}F NMR spectrum after reaction between **3** and $\text{B}(\text{C}_6\text{F}_5)_3$ (282 MHz, C_6D_6 , 293 K), showing the quantitative conversion of $\text{B}(\text{C}_6\text{F}_5)_3$ into $[\text{HB}(\text{C}_6\text{F}_5)_3]$ (fluorobenzene (6 eq.) was used as a ^{19}F NMR internal standard). b. ^{11}B NMR spectrum after reaction of **3** with $\text{B}(\text{C}_6\text{F}_5)_3$ (96 MHz, C_6D_6 , 293 K), showing the formation of $[\text{HB}(\text{C}_6\text{F}_5)_3]$. c. ^1H NMR reaction monitoring between **3** (^{13}C -labelled) and $\text{B}(\text{C}_6\text{F}_5)_3$ (300 MHz, C_6D_6 , 293 K) showing the quantitative formation of $[(\text{HL})\text{Al}(\text{OAr})_2][\text{HB}(\text{C}_6\text{F}_5)_3]$ **6** together with release of isobutene at $\delta = 4.75$ ppm and $\delta = 1.60$ ppm.

Subsequent deprotonation of zwitterion **6** by KHMDS yields a new product $[\text{Al}(\text{L})(\text{OAr})_2]$, **7**, that is first scrutinized by a NMR-scale reaction in C_6D_6 (Figure 18, a.). Indeed, ^1H -NMR monitoring starting with the ^{13}C -labelled zwitterion, $\text{6-}^{13}\text{C}$, shows the deprotonation of the imidazolium ring since the H-imidazolium resonance at $\delta = 8.03$ ppm in the spectrum of species $\text{6-}^{13}\text{C}$ disappears in

the spectrum of complex **7**-¹³C (Figure 18, a.). ¹³C-NMR monitoring (Figure 18, b.) also supports deprotonation of **6**-¹³C since the spectra show a downfield shifting from 136.0 ppm (protonated NHC in species **6**-¹³C) to a broad signal at 167.7 ppm (NHC form in complex **7**-¹³C), which is typical to Al-NHCs signatures.^[192,193]

Armed with this understanding, we thus established a large-scale synthesis of **7** from salt **3**. Stoichiometric treatment of zwitterion **3** with B(C₆F₅)₃ in toluene and subsequent addition onto KHMDS in toluene affords complex **7** in 61% yield (Step I+II on Scheme 52).

Species **7** is characterized by XRD. Its solid-state structure (Figure 19) validates a bidentate coordination of the NHC-O platform onto the Al(III) center. This aspect is highlighted through two metrical parameters: i) an Al-C_{NHC} bond featuring a length of 2.055 Å corresponding to the expected Al-NHC distances.^[192-194] ii) The Al-alkoxy bond exhibiting a distance of 1.732 Å. These two distances are slightly shorter than those found for complex **2** (respectively 2.055 Å vs 2.069 Å and 1.732 Å vs 1.770 Å) showing a closer proximity of the Al(III) center onto the NHC-O scaffold. Quite surprisingly, no relaxation of the N1-C1-N2 internal ring angle is noticed compare to the free-NHC analogue (102.7(4)° vs 102.5(1)°).^[20] These observations are likely connected to the distorted tetrahedral geometry around the Al(III) center since the C1-Al1-O1 metrical parameter displays a shorter angle compare to the theoretical one in a perfect tetrahedral configuration (94.2(16)° vs 109.5°). Furthermore, the NHC moiety is not coordinated in a linear manner to the Al(III) center since the Al1-C1-N1 and Al1-C1-N2 angles are distinct and relatively far from 120° (respectively 113.7(3) vs 120° and 143.1(3) vs 120°).

In conclusion, solid-state structure of species **7** is unambiguous regarding the Al-NHC ligation and validates the observed phenomena in solution. Also, such molecular structure clearly shows a noticeable rigidity of the alkoxy-NHC platform and a distortion around the Al(III) center. These geometric considerations are probably due to the constrained topology of the whole complex especially imparted by the overcrowded and bulky phenoxy fragments attached to the Al(III) site.

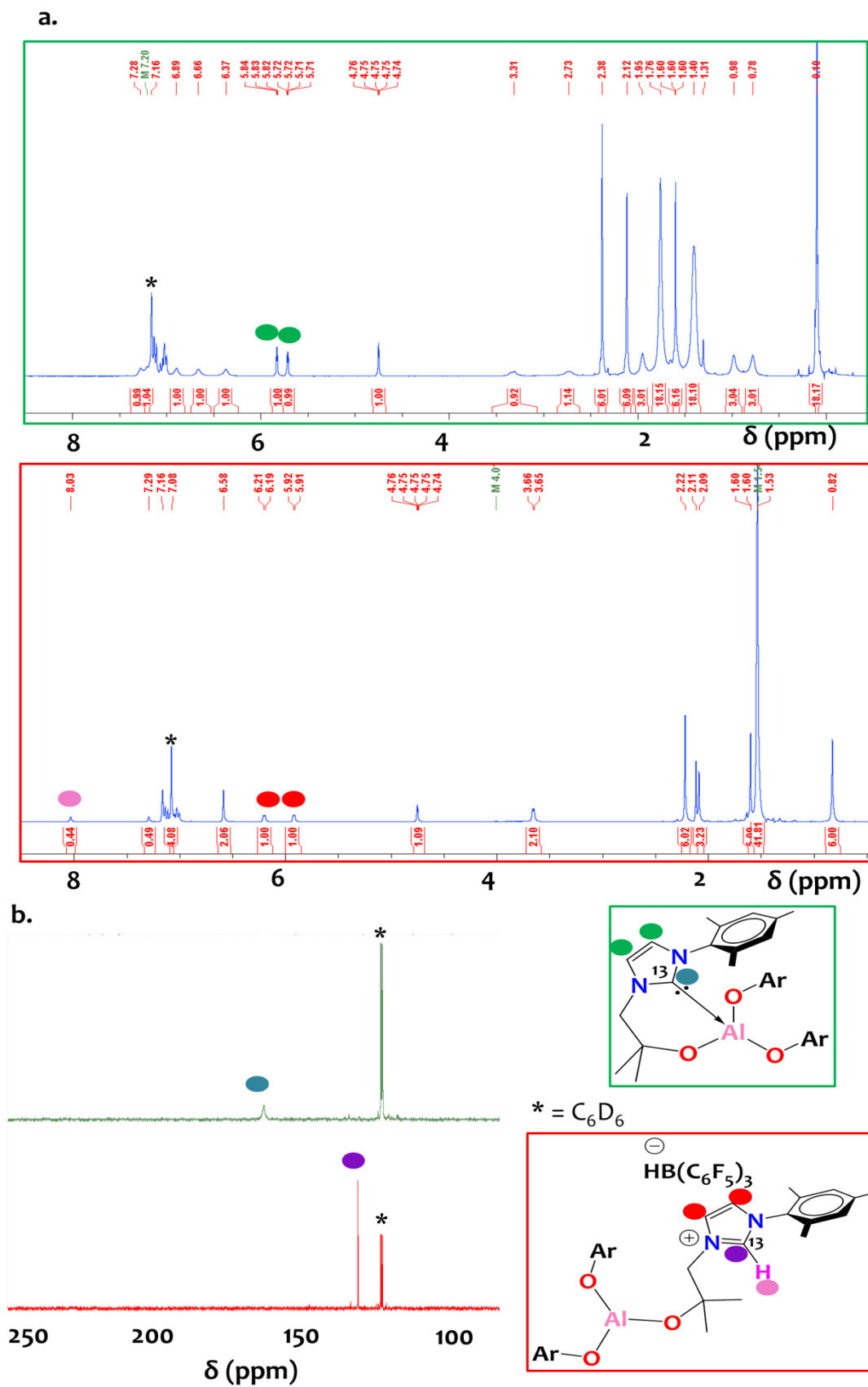


Figure 18. 1H NMR (300 MHz, C_6D_6 , 293 K) (a.) and ^{13}C -NMR (75 MHz, C_6D_6 , 293 K) (b.) reaction monitoring between the ^{13}C -labelled complex $[(HL)Al(OAr)_2][HB(C_6F_5)_3]$, $6-^{13}C$, and KHMDS showing the quantitative formation of the ^{13}C -labelled complex $Al(L)(OAr)_2$, $7-^{13}C$.

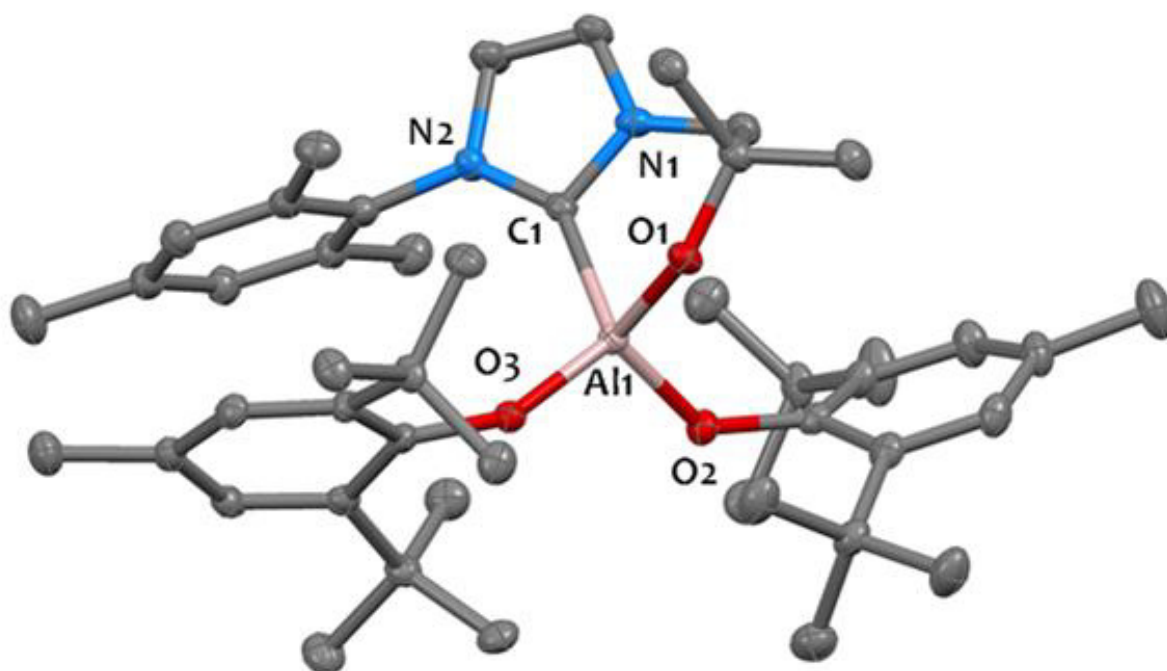


Figure 19. Solid-state molecular structure of **7** (30% probability ellipsoids). Hydrogen atoms have been omitted for clarity. Selected bond distances [Å] and angles [°]: Al₁-O₁ 1.732(3) Al₁-O₂ 1.766(3); Al₁-O₃ 1.728(3); Al₁-C₁ 2.055(2); N₁-C₁ 1.362(5); N₂-C₁ 1.374(5); N₁-C₁-N₂ 102.7(4); C₁-Al₁-O₁ 94.2(16); Al₁-C₁-N₁ 113.7(3); Al₁-C₁-N₂ 143.1(3).

2.2.5 Reactivity of Al-NHCs with protic substrates

In order to study the basic properties of complexes Al(L)(^{*i*}Bu)₂ and Al(L)(OAr)₂, we performed NMR-scale reactions (in THF-*d*₈ or C₆D₆) of the ¹³C-labelled species - **2**-¹³C and **7**-¹³C - with protic species such as phenol. ¹H-NMR and ¹³C-NMR spectra relating to the stoichiometric reaction of **2**-¹³C with phenol show the typical signature of the imidazolium moiety – δ(¹H) = 9.65 ppm (see Figure 20) and δ(¹³C) = 139.4 ppm (see Figure 21). The same behavior is observed when complex **7**-¹³C is treated with one equivalent of phenol.

Similar reactivities are noticed when using 2-naphthalenethiol or *tris*(*tert*-butoxy)silanol. However, when employing sterically hindered phenoxy substrates such as dibutylhydroxytoluene (BHT), no reaction is observed even after heating.

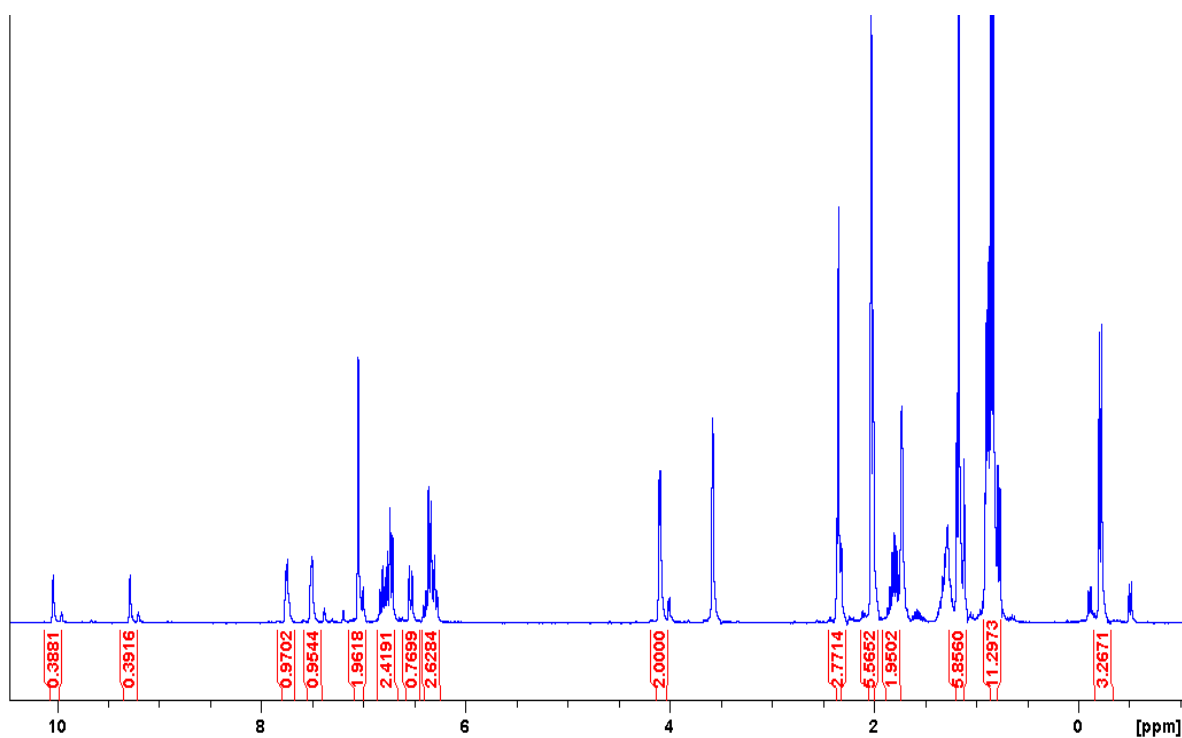


Figure 20. ^1H -NMR spectrum (300 MHz, $\text{THF-}d_8$, 293 K) of the ^{13}C -labelled $\text{Al(L)(}^t\text{Bu)}_2$ 2- ^{13}C + 1 eq. of phenol leading to species 8- ^{13}C

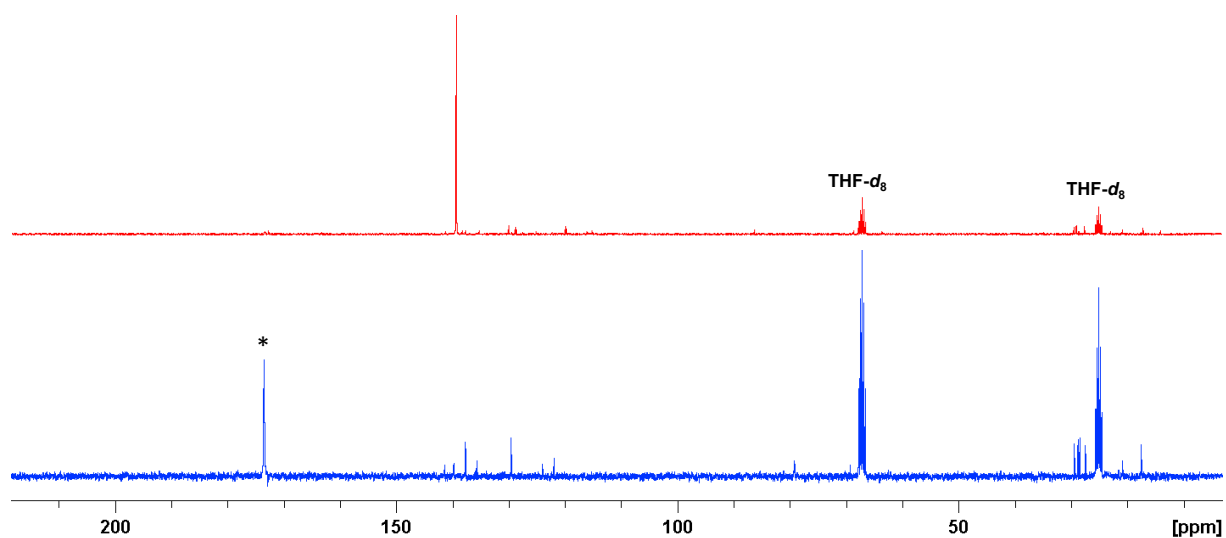
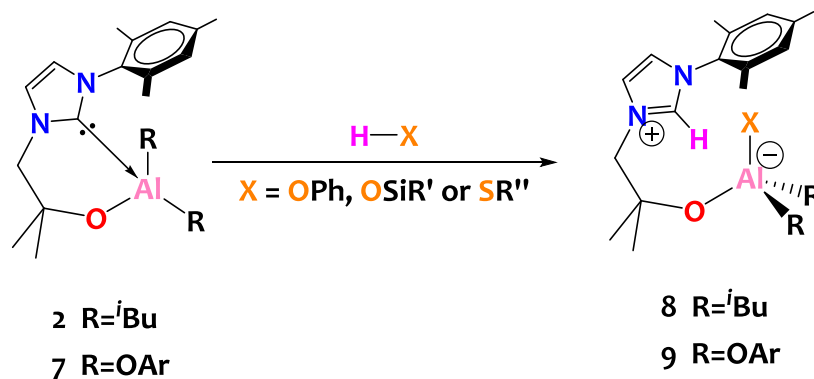


Figure 21. ^{13}C NMR reaction monitoring in $\text{THF-}d_8$ solution (75 MHz, 293 K) of the reaction between 2 and 1 eq. PhOH yielding an alcoxy-imidazolium zwitterion species 8 as shown with the disappearance of the aluminum-bound carbene resonance at $\delta = 173.5$ ppm from 2 (bottom spectrum – blue line) and the appearance of a characteristic imidazolium resonance at $\delta = 139.4$ ppm for 8 (top spectrum – red line) corresponding to the ^{13}C -labelled carbon from the C_3N_2 heterocycle.

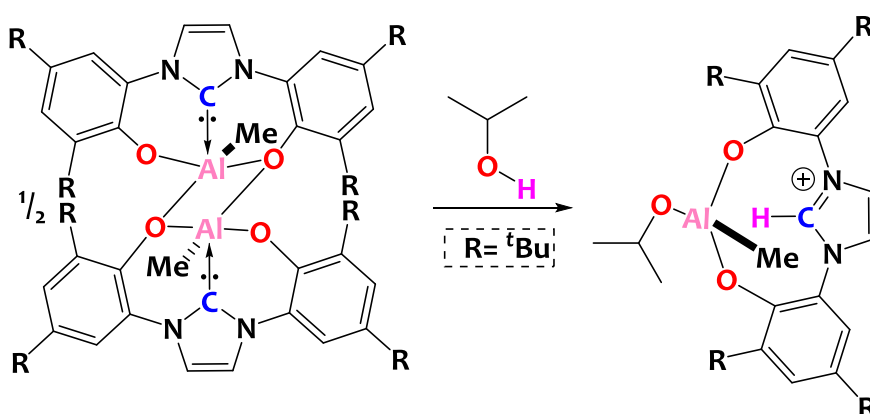
These studies testify that compounds 2 and 7 promote selective activation of the X-H bond of protic substrates (Scheme 53) to form aluminate imidazolium zwitterions species 8 and 9.



Scheme 53. Reactivity of complexes **2** and **7** with protic substrates.

In light of these investigations, some affirmations can be drawn: The aluminum-NHC motif is not inert and promotes the heterolytic cleavage of polar acidic H-X bonds ($\text{X} = \text{O}, \text{S}$). This is an uncommon example of the non-innocence of the metal-NHC motif since, to date, only rare occurrences in the literature of such reactivity are reported.^[227–230] Notably, C. Romain *et al.* reported in 2014 the formation of a somewhat similar imidazolium aluminate-alkoxide zwitterion by reacting a tridentate Al(NHC) dimer with isopropanol (Scheme 54).^[193] In this case, the isopropanol O-H cleavage occurs preferentially across the Al-C_{NHC} and not on the Al-C_{Me}, which is quite uncommon.

Therefore, these systems show a preferential 1,2 X-H addition across the Al-C_{NHC} bond versus Al-C_{iBu} bonds in **2** and **7**, leading to imidazolium formation rather than alkane elimination. Such aluminum-NHC cooperative reactivity is quite striking and unexpected as Al-isobutyl groups are known to be particularly basic. Importantly, although the NHC Lewis base interacts directly with the Al center in these compounds, this Lewis-pair reactivity parallels that of FLPs since it is hemilabile and can react with small molecules.



Scheme 54. Reported formation of a C-H imidazolium aluminate zwitterion through the alcoholysis of an Al-C_{carbene} bond.^[193]

2.3 Towards heterobimetallic Al/M (d-block metal) species

In view of getting heterobimetallic architectures, viability of transmetallation reactions from $\text{Al(L)}(\text{iBu})_2$ to late TM precursors has been assessed. Quite surprisingly, complex **2** does not react (even upon heating) with common late transition metal precursors such as bis-cyclooctadiene nickel(0), dichloro-bis(triphenylphosphine)nickel(II), or mesitylcopper(I). Also, treatment of complex **2** with cyclooctadiene rhodium chloride and cyclooctadiene iridium chloride dimers leads to a complex mixture of species and we decided not to pursue this chemistry further. Interestingly, we obtained more success when using a bis(triphenylphosphine)copper(I) nitrate as Cu(I) starting material, which is a commercially available compound. This phosphine derivative is chosen with the expectation of substituting a labile phosphine ligand with the NHC moiety from **2**.

NMR monitoring of the reaction between $[\text{Cu}(\text{PPh}_3)_2(\text{NO}_3)]$ and **2** (1 equiv.) in C_6D_6 shows relevant characteristics.

- 1) A prolonged heating makes possible a quantitative reaction. This is showcased by the spectrum recorded after 36h at 90°C featuring a new and different pattern compared to the one before reaction (Figure 22-d. vs a.).
- 2) A typical resonance of isobutene at 4.7 ppm is observed, suggesting a β -H elimination of an isobutyl fragment (Figure 22).^[224]
- 3) Interestingly, the N-CH_2 doublet at 3.50 ppm (from compound **2**) becomes two doublets at 3.35 ppm meaning these two protons are no longer equivalent (Figure 22-d.). This phenomenon suggests a constrained geometry around the pendant arm of the bifunctional NHC-O scaffold, which can no longer flip, as observed in some cases before.^[19,20]
- 4) A ^{13}C -NMR monitoring experiment starting with the ^{13}C -labelled Al(III) precursor, **2**- ^{13}C , is implemented as well. The initial Al-NHC carbene resonance at 173.9 ppm disappeared and is replaced by a new downfield resonance at 183.4 ppm after reaction (Figure 23-c.). This suggests first that a single carbene species is formed selectively, and the new chemical shift is in the expected range for Cu(I)-NHC resonances, lying in the range [175–200 ppm].^[231,232] This observation thus indicates a transmetallation from Al(III)-NHC to Cu(I)-NHC species.

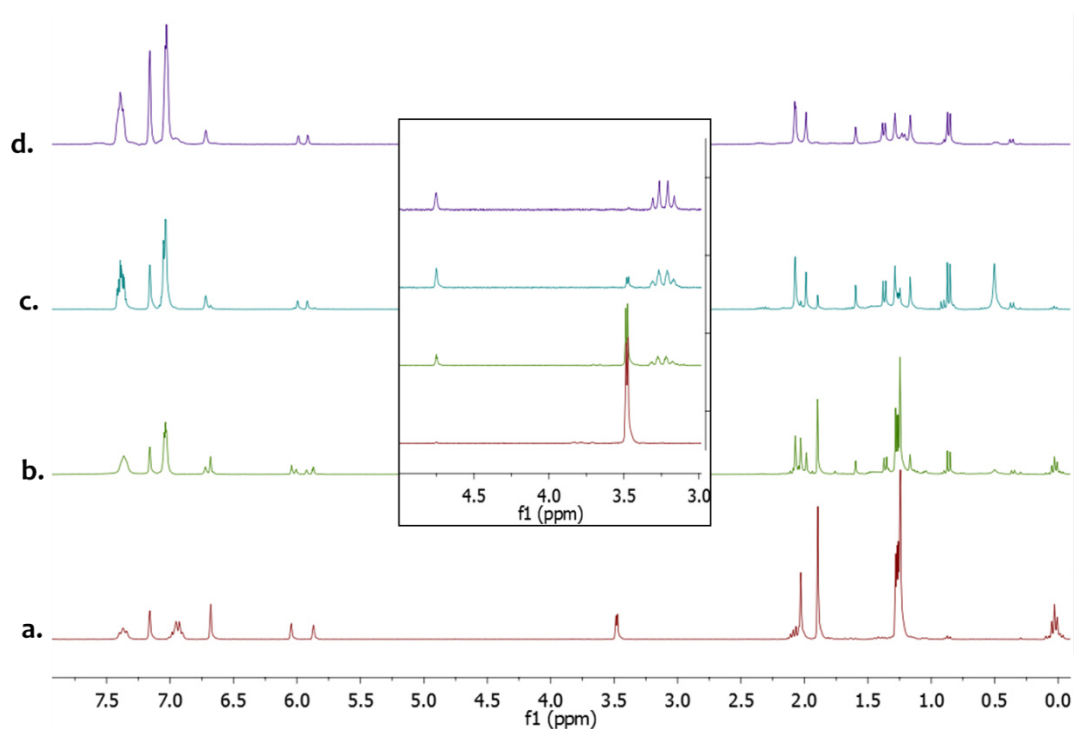


Figure 22. $^1\text{H-NMR}$ (300 MHz, C_6D_6) monitoring of the reaction between compound **2** and one equivalent of $[\text{Cu}(\text{PPh}_3)_2(\text{NO}_3)]$. Blue spectrum (a.): $T=25^\circ\text{C}$, $t=2\text{h}$. Red spectrum (b.): $T=60^\circ\text{C}$, $t=14\text{h}$. Green spectrum (c.): $T=80^\circ\text{C}$, $t=24\text{h}$. Purple spectrum (d.): $T=90^\circ\text{C}$, $t=36\text{h}$.

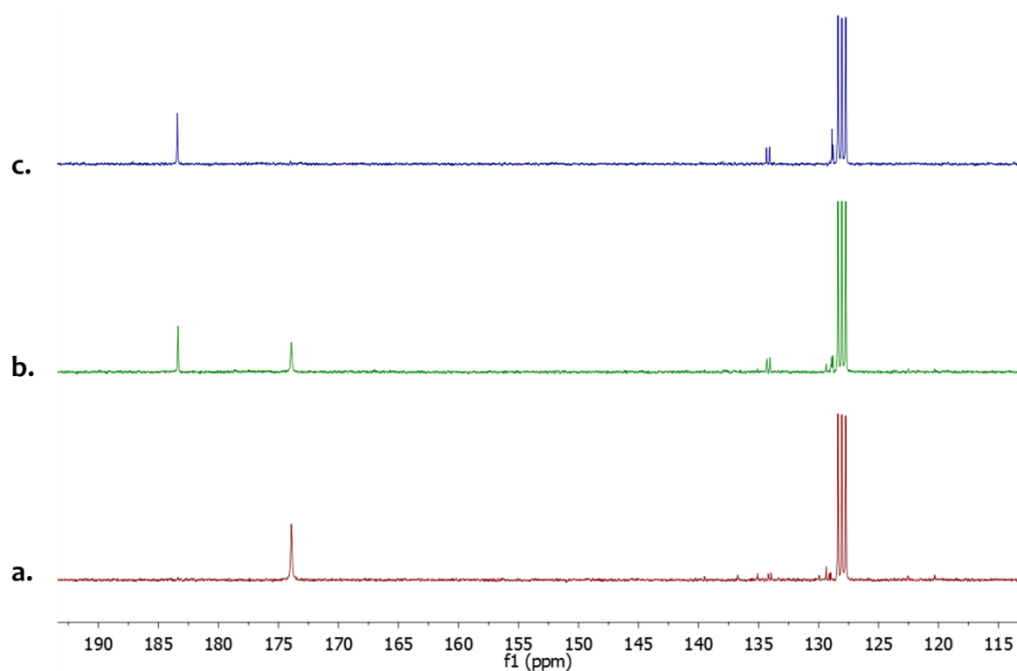
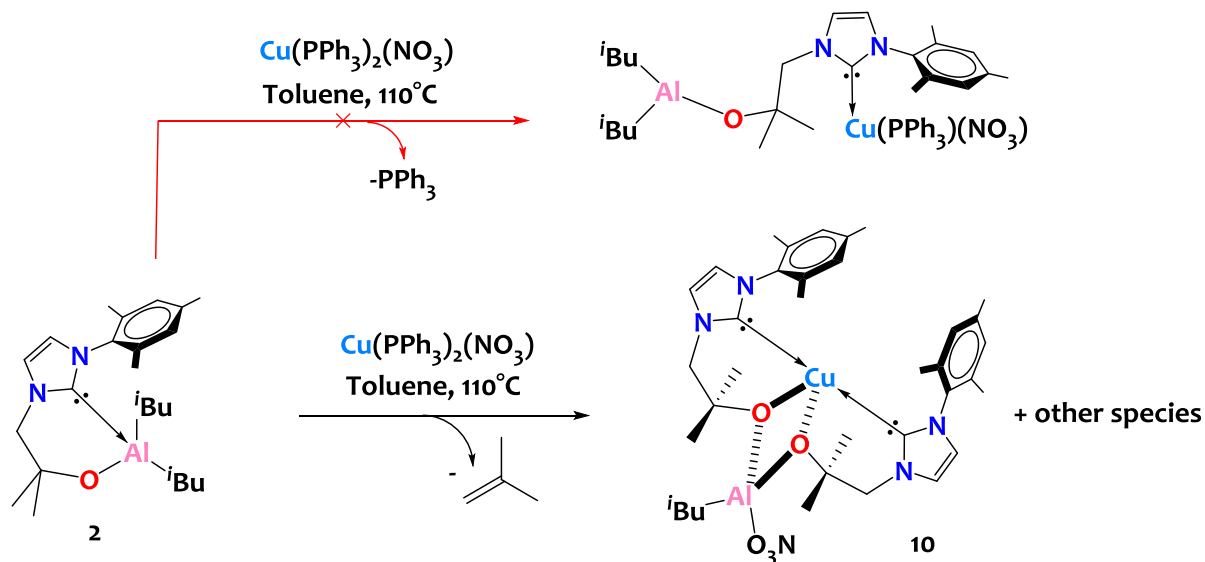


Figure 23. $^{13}\text{C-NMR}$ (75 MHz, C_6D_6) monitoring of the reaction between compound **2- ^{13}C** and one equivalent of $[\text{Cu}(\text{PPh}_3)_2(\text{NO}_3)]$. Blue spectrum: $T=25^\circ\text{C}$ (a.), $t=2\text{h}$. Red spectrum: $T=60^\circ\text{C}$, $t=14\text{h}$ (b.). Green spectrum: $T=80^\circ\text{C}$, $t=24\text{h}$ (c.).

Accordingly, we repeated the reaction on a larger scale, in hot toluene ($T=110^\circ\text{C}$) for 36 hours. This procedure leads to a brown solid in a yellow solution. The brown solid is filtered off and the

volatiles from the yellow filtrate were removed *in vacuo*.

Gratifyingly, crystals of complex **10** (Scheme 55) suitable for XRD analysis are obtained from this yellow filtrate upon recrystallization of a saturated pentane/toluene solution at -40°C . The solid-state structure of **10** is shown on Figure 24.



Scheme 55. Reaction of complex **2** with one equivalent of $[\text{Cu}(\text{PPh}_3)_2(\text{NO}_3)]$.

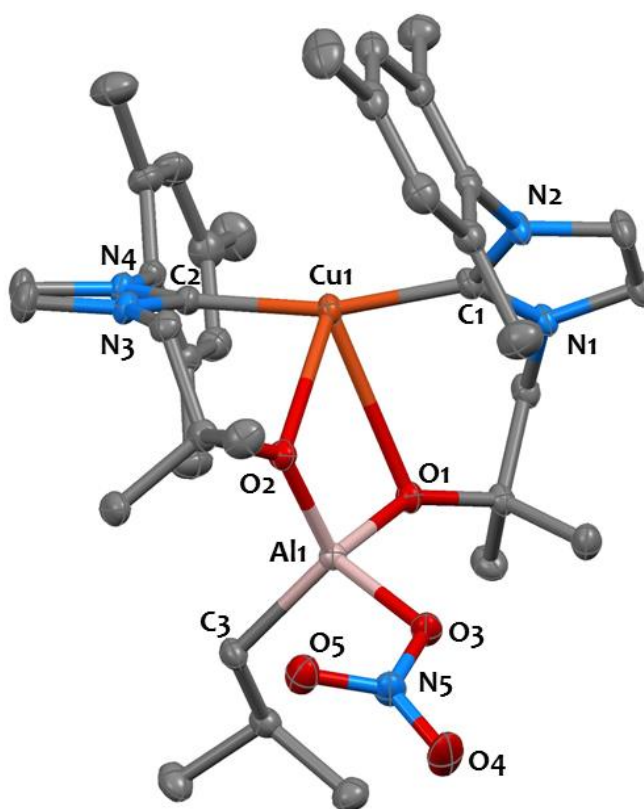


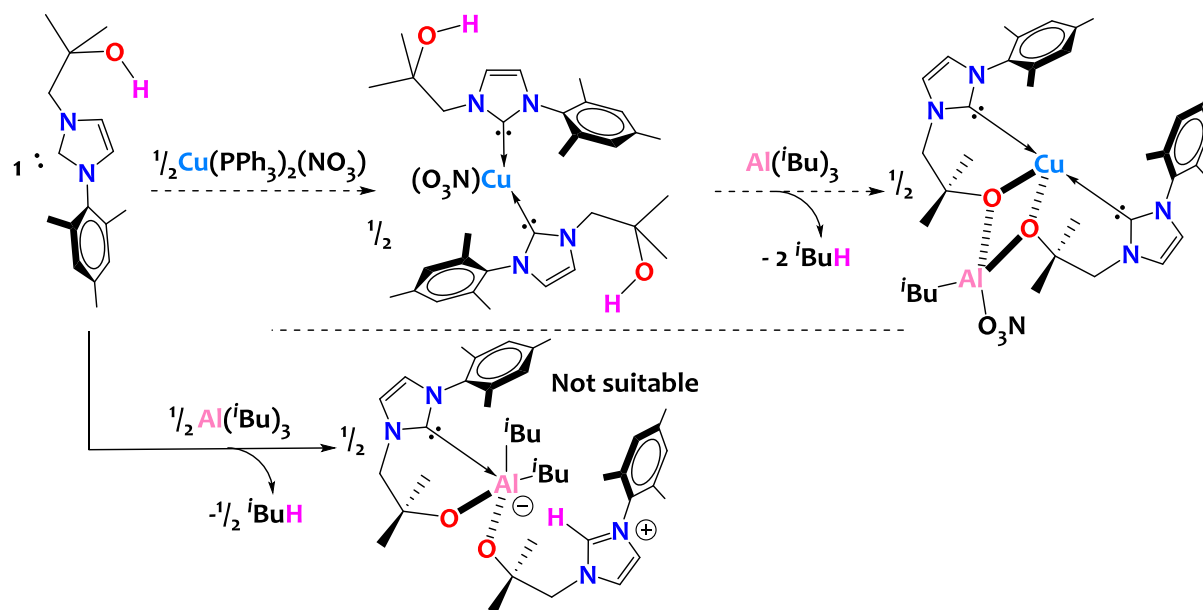
Figure 24. Solid-state molecular structure of **10** (50% probability ellipsoids). Hydrogen atoms are omitted for clarity. Selected bond distances [\AA] and angles [$^{\circ}$]: $\text{Cu}_1\text{-O}_1$ 2.731(2); $\text{Cu}_1\text{-O}_2$ 2.539(2); $\text{Cu}_1\text{-C}_1$ 1.884(2); $\text{Cu}_1\text{-C}_2$ 1.889(2); $\text{Cu}_1\cdots\text{Al}_1$ 3.3188(9); $\text{Al}_1\text{-O}_1$ 1.734(2); $\text{Al}_1\text{-O}_2$ 1.737(2); $\text{Al}_1\text{-O}_3$ 1.880(2); $\text{Al}_1\text{-C}_3$ 1.969(3).

The molecular structure of **10** shows unexpected features. First of all, an interesting constrained and tight coordination geometry around the Cu(I) metallic ion is observed. This 3D arrangement is a slightly distorted seesaw molecular geometry, away from the usual tetrahedral coordination often found for 4-coordinate Cu(I) species of d^{10} electronic configuration. In particular, this is imposed by: on one side, a pseudo-linear coordination of two NHC moieties onto the copper(I) center leading to a bis(NHC)-based copper(I) pattern; and, on the other side, two alkoxy bridging moieties allowing to connect the Cu(I) center with the Al(III) center. Furthermore, an unexpected nitrate migration from the Cu(I) center to the aluminum is noticed. Such phenomenon has been already observed using trialkyl-aluminum(III) starting materials onto late transition metal-based complexes with nitrate counter ions.^[47-50] Importantly, isobutene elimination (highlighted during the ¹H-NMR monitoring) is clearly confirmed since only one isobutyl functional group remains on the Al atom. Most impressively, an unanticipated ligand redistribution at the aluminum center occurred since two alkoxy-NHCs are bound to the Al center. Overall, the structure comprises a tetracoordinated aluminate Al(III) anion and a copper(I) site leading to a neutral complex. Regarding the metrical parameters, bond lengths of 1.88 and 1.89 Å are found for the copper(I)-carbene bonds matching with the expected Cu-bis(NHC) distances.^[232,233]

In summary, the expected Al(*i*Bu)₂-alkoxy-NHC-Cu(I) heterobimetallic complex (structure shown in Scheme 55) is not formed starting with compound **2** and [Cu(PPh₃)₂(NO₃)]. With that said, the expected transmetalation phenomenon of the NHC motif occurred, leading to an unprecedented heterobimetallic Cu(I)-bis(NHC-O)-Al(III) complex **10**. This original species features a bis(NHC)-Cu(I) cationic motif, which can be found in rare occurrences in the form of a [Cu(NHC)₂]⁺X⁻ salts (X = non-coordinating counter-ion such as BF₄⁻ or PF₆⁻) and these salts are relevant for catalysis purposes.^[232-234] Yet, complex **10** results from a β-hydride elimination of one isobutyl group from compound **2** as well as a nitrate migration from the Cu(I) precursor to the Al(III) center. Furthermore, the generation of complex **10** also brings to light stoichiometric issues as well as a complex reactivity. Indeed, compound **10** features two NHC-alkoxy ligands per aluminum and copper centers, which is antagonist with the expected stoichiometry NHC-O/Cu-Al of 1/1. Therefore, this result confirms the formation of a complex mixture of species where one of them is compound **10**, which could only be isolated in very low yields and prevents further reactivity studies.

In perspective of this work, we propose an alternative to optimize the synthesis of complex **10**. To adjust the stoichiometry of the reaction and to favor a quantitative formation of the bimetallic species **10**, two synthetic routes can be envisioned. The first would involve the preparation of a

bis-(alkoxy-NHC) aluminum species. However, preliminary studies revealed instead the formation of an unsuitable imidazolium-aluminate zwitterion (structure drawn on Scheme 56, bottom), therefore this approach is not investigated further. An alternative synthetic method would involve the reaction of two equivalents of the bifunctional ligand **1** with 1 eq. of $\text{Cu}(\text{NO}_3)(\text{PPh}_3)_2$ (Scheme 56, top left). Then, the putative bis(NHC)-Cu(I) species could be treated with a stoichiometric amount of TIBA to trigger its double protonolysis on the hydroxyl side-arms (Scheme 56, top right). This approach has not been investigated yet.



Scheme 56. Proposed synthetic paths to optimize the synthesis of compound 10.

2.4 Conclusions

The chemistry of the bifunctional alkoxy-NHC ligand **1** with alkyl aluminum precursors is interesting in terms of diversity and originality. Indeed, in this chapter, we have shown that different kinds of reactivities can be obtained depending on the steric profile of the Al reagent:

- i) When TIBA is used: classical protonolysis between the ligand hydroxyl group and the Al-C_{iBu} bond occurs, together with the formation of a carbene-aluminum interaction, leading to the formation of the chelated species, **2**.
- ii) When $\text{Al}(\text{R})(\text{OAr})_2$ precursors are employed: the unexpected formation of imidazolium aluminate zwitterions is observed (compounds **3** and **4**).
- iii) In the cases of compounds **3** and **4**: we have demonstrated the possibility to restore the carbene moiety and the Lewis acidity at the Al site, leading ultimately to the formation of the chelated complex **7**.

iv) Species **2** and **7**, exhibit similar reactivity and promote the activation of X-H bonds across the Al-C_{NHC} bond and not across the Al-C_{iBu}, showing the non-innocence of the carbene-aluminum interaction.

We also demonstrated the possibility to use complex **2** as a precursor to obtain heterobimetallic assemblies by transmetallation-like reactivity. Despite numerous attempts with many late transition metal derivatives, our proof of concept has been limited only to the formation of the Cu-Al heterobimetallic complex **10**, in low yields. This glimmer of hope is of course promising, but insufficient to extend this strategy further on large scale and to a family of compounds. We believe that these observations are related to some inertia of the Al-NHC motif (within complex **2**) for a transmetallation reaction, maybe related to the stabilizing chelate effect in **2**.

More generally, this study constitutes an important contribution to the scientific community concerned with the chemistry of Al-NHC species. Therefore, this work of rationalization and understanding is to be credited to this study.

However, this work also argues for some limitations of using bifunctional NHC-based ligands to bridge an Al center with a late d-block metal in terms of synthetic considerations. In addition, it can be assumed that the use of bifunctional ligands to construct reactive Al-M edifices may represent a "thorn in the side." In fact, NHC-based bifunctional bridges and other bifunctional platforms mostly rely on bulky, chelating motifs used to stabilize the two metal centers. In addition, clever and specialized methodologies are required to design a suitable spacer between the two sites of the ligand in order to obtain two metals close enough to each other to interact and be reactive as a bimetallic entity. As a result, simultaneous access and activation of an external substrate on both metals seems difficult to achieve. One strategy to circumvent these limitations is to use simple metal derivatives and to assemble them without bridging ligands. This is the purpose of the following chapters.

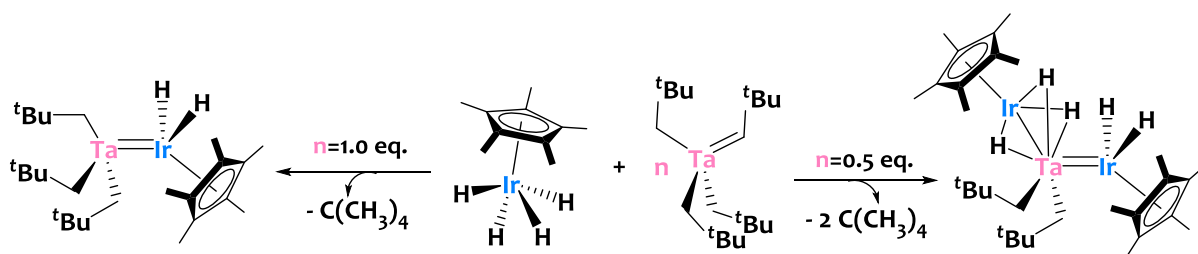
CHAPTER 3. Development Of Molecular Aluminum/Iridium Heterobimetallic Species Using An Alkane Elimination Approach

3.1 Context

As detailed in CHAPTER 1 for Al/M species (section 1.2.1.5-page 63), alkane elimination is a powerful and simple approach to design multinuclear Al-M heterobimetallic species exhibiting direct and reactive intermetallic interactions. As also discussed in this same section, this approach relies on a Brønsted acid/base reactivity between a basic alkyl metal and an acidic metal hydride.

On another level, we described in the introduction and in the corpus of CHAPTER 2 the interests of using alkylaluminum derivatives (and particularly isobutylaluminum) for protonolysis-type reactivity, that is to say a reaction between an acidic species X-H (eg. hydroxyl groups) and an Al-C_{alkyl} bond to give the corresponding volatile alkane (H-C_{alkyl}) and a X-Al product. Therefore, it is within this framework that we have chosen to use isobutyl aluminum precursors, as they appear particularly suitable for the targeted reactivity.

Regarding the acidic metal hydride partner, our research team recently reported the interests of a half sandwich tetrahydride complex of iridium – Ir(η^5 -C₅Me₅)(H)₄ (named IrCp*H₄ thereafter) – for promoting alkane elimination reactions (Scheme 57).^[27-29]



Scheme 57. Reported synthesis of heterobimetallic binuclear TaIr (left side) and trinuclear (right side) TaIr₂ species via an alkane elimination approach starting from IrCp*H₄ and Ta(CH^tBu)(CH₂-^tBu)₃.^[27-29]

Particularly, stoichiometric treatment of IrCp*H₄ with tris-neopentyl(neopentylidene)tantalum(V)^[179] promotes the elimination of one equivalent of neopentane gas and the formation of a binuclear Ta/Ir heterobimetallic complex (Scheme 57, left).^[27] The alkane elimination sequence can go further when using two equivalents of IrCp*H₄ precursor per tantalum complex, which yields a trinuclear Ta/Ir₂ cluster and the release of two equivalents of neopentane gas (Scheme 57, right).^[28] IrCp*H₄ is thus an ideal acidic metal hydride candidate because, according to the above study, up to two hydrogen atoms bound to Ir are acidic enough to react with alkyl/alkylidene tantalum moieties. Also, IrCp*H₄ has a rather

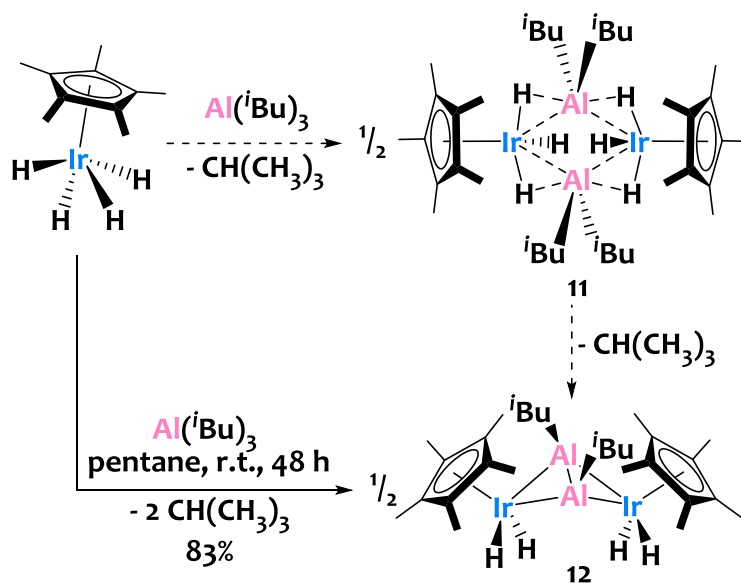
uncluttered coordination sphere, which makes the Ir center accessible and reactive.^[181,235-237]

Based on these inspiring preliminary studies from our laboratory regarding the alkane elimination strategy, and in continuation of CHAPTER 2, we present herein an extension of this approach using isobutylaluminum derivatives and IrCp*H₄.

3.2 Rational preparation of well-defined multinuclear Al/Ir clusters

3.2.1 Synthesis and characterization of tetranuclear heterobimetallic [Al₂Ir₂] clusters

In a first approach, we used TIBA as the isobutylaluminum precursor. Treatment of IrCp*H₄ with one equivalent of triisobutylaluminum in pentane at room temperature leads to the formation of the tetranuclear complex [Cp*H₃IrAl(ⁱBu)₂]₂, **11** with evolution of one equivalent of isobutane *per* aluminum site (Scheme 58). The identity of **11** is first scrutinized by ¹H-NMR in C₆D₆ solution (Figure 25). In the alkyl region, the spectrum displays one Cp* signal at δ = 1.94 ppm integrating for 15H *per* iridium center, in agreement with 1 Cp* ligand *per* Ir site. The resonances relating to the isobutyl groups showcase a stoichiometry of 2 isobutyl fragments *per* aluminum center and the hydride signal appears as a singlet at δ = -16.54 ppm integrating for 3H *per* Ir site. The latter result suggests a rapid exchange between the six hydrides on the NMR time scale at room temperature, which is expected on the basis of literature precedents for metal-polyhydride systems.^[28,29,238,239] Yellow block-shaped single crystals of **11** are isolated upon cold crystallization (-40°C) of the reactional medium after 2 hours of reaction. The solid-state molecular structure of **11**, determined by X-Ray diffraction, is shown in Figure 29-top. The first noticeable feature of this structure is the centrosymmetric {Ir₂Al₂} core. This tetranuclear diamond-shape core is perfectly planar, with Ir-Al-Ir angles of 101.18(6)° and Al-Ir-Al angles of 78.82(6)°. The geometry around the aluminum centers is pseudo-tetrahedral (C_{iBu}-Al-C_{iBu} angles = 119.0(3)°, C_{iBu}-Al-Ir angles in the range 103.90(19)°-114.93°). The Ir-Al distances (averaged at 2.72(1) Å) are longer than those reported in the rare examples of unsupported Ir-Al bonds (2.45-2.51 Å),^[24,25] and the average formal shortness ratio (FSR=1.085)^[78,240] is above unity. Therefore, the close proximity between the Al and Ir centers in **11** is most likely the result of the presence of bridging hydrides.



Scheme 58. Synthesis of Al/Ir heterotetrametallic species 11 and 12.

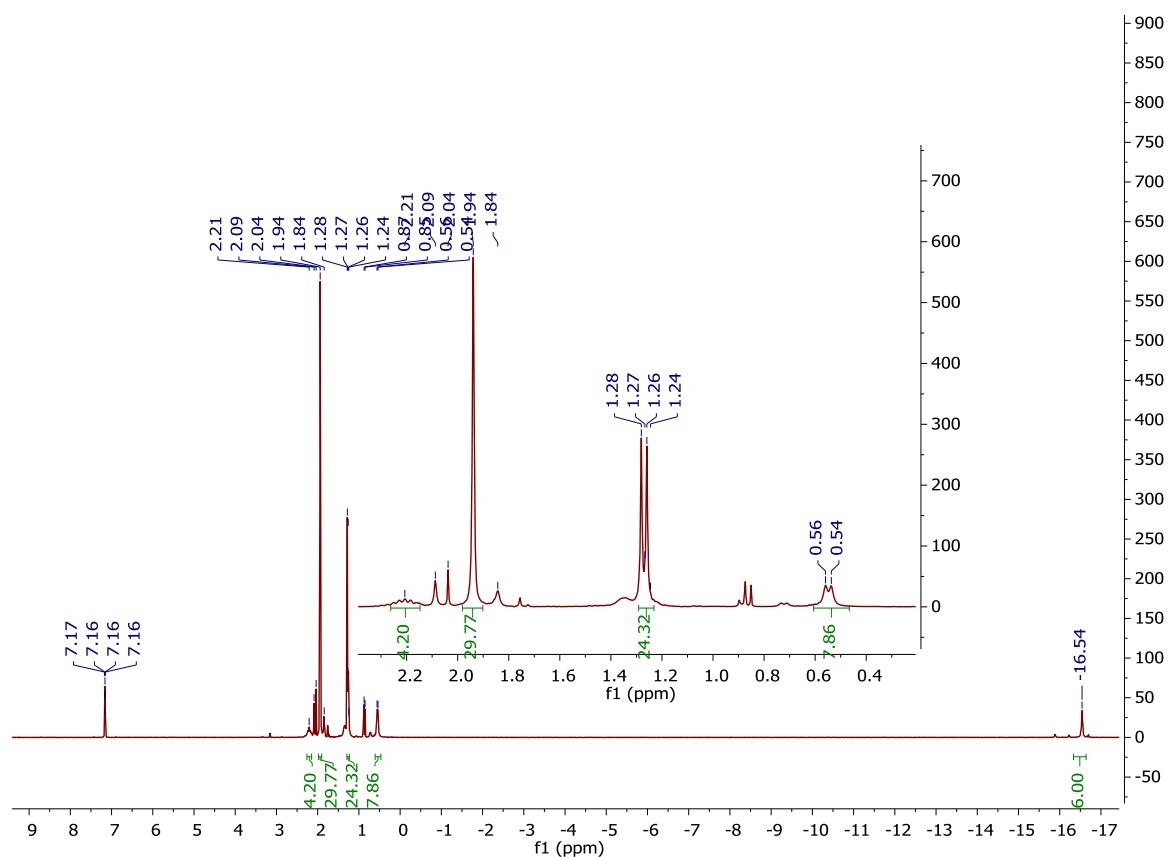


Figure 25. ¹H-NMR spectrum (300 MHz, C₆D₆, 293K) of compound 11.

Even if the hydrides could not be located in the XRD Fourier Map, hint of their presence and potential position can be given in these series of complexes by the tilting of the Cp* ligand. To evaluate this distortion, we propose a new descriptor, $\alpha = \frac{1}{2}(\theta + \theta')$ (see Figure 26), which

measures the difference in the two angles between the Cp*centroids, the iridium centers and the centroid of the Ir₂Al₂ core. In the case of **11**, $\alpha = 163.7(1)^\circ$, indicates a moderate twisting of the Cp* rings. This suggests that at least some of the hydrides are bridging the Ir and the Al sites. Note however that a related iridium-tantalum complex, [IrHCp*Ta(Np)₂]₂,^[27] featuring a similar α angle of 160.10° , has been recently reported by our group. In this complex, the hydride is located in terminal position on the Ir site, thus terminal hydride positions are also compatible with the structure of **11**. We thus conducted DFT calculations, and in the most stable computed structure, which reproduces very well all the geometrical parameters of the crystallographic structure (see details below), one terminal hydride is found *per* iridium center, along with four bridging Ir-H-Al hydrides (two per iridium center), as represented in Scheme 58.^[27] Note that these considerations and proposed hydride topology are only relevant in the solid state. Fluxional behavior with rapid exchange between the hydrides positions occurs in solution, as frequently found in metal-polyhydride compounds,^[28–30,239] since only one hydride signal integrating for 3H *per* Ir is found in the ¹H NMR spectrum of **11** (Figure 25).

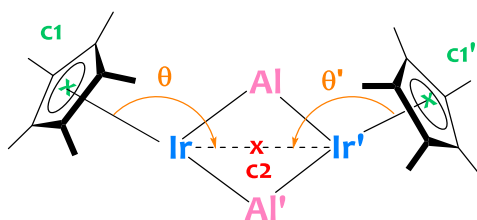


Figure 26. Definition of a new metrical parameter $\alpha = (\theta + \theta')/2$ characteristic of iridium-hydride locations (terminal or bridging).

Complex **11** is unstable in C₆D₆ solution at room temperature and evolves within a few hours to form the stable complex [Cp*H₂IrAl(^{*i*}Bu)]₂, **12** (Scheme 58), through the loss of one additional isobutyl fragment *per* Al, which is released as isobutane. After two days of reaction at room temperature, complex **12** is isolated in 83% yield. The molecular structure of **12** is confirmed by multi-nuclei (¹H, ¹³C) solution NMR and infrared (IR) spectroscopies, elemental analysis and X-ray diffraction studies. The ¹H-NMR spectrum of **12** (recorded in C₆D₆, Figure 27) shows a very high field hydride resonance emerging as a singlet at $\delta = -16.68$ ppm and integrating for 4H. The infrared spectrum of **12** exhibits a strong stretching vibration at $\sigma = 1989$ cm⁻¹ typical of a terminal Ir-H stretch (Figure 28).^[27]

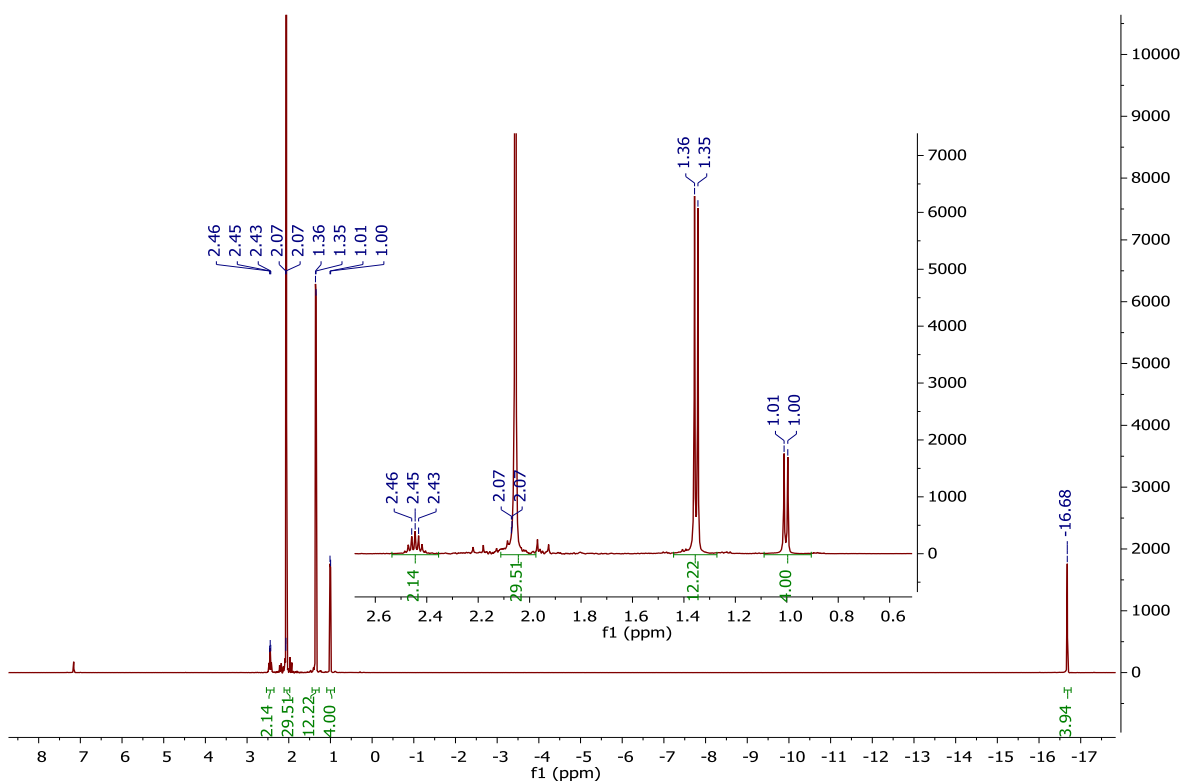


Figure 27. ¹H-NMR spectrum (500 MHz, C₆D₆, 293K) of compound 12.

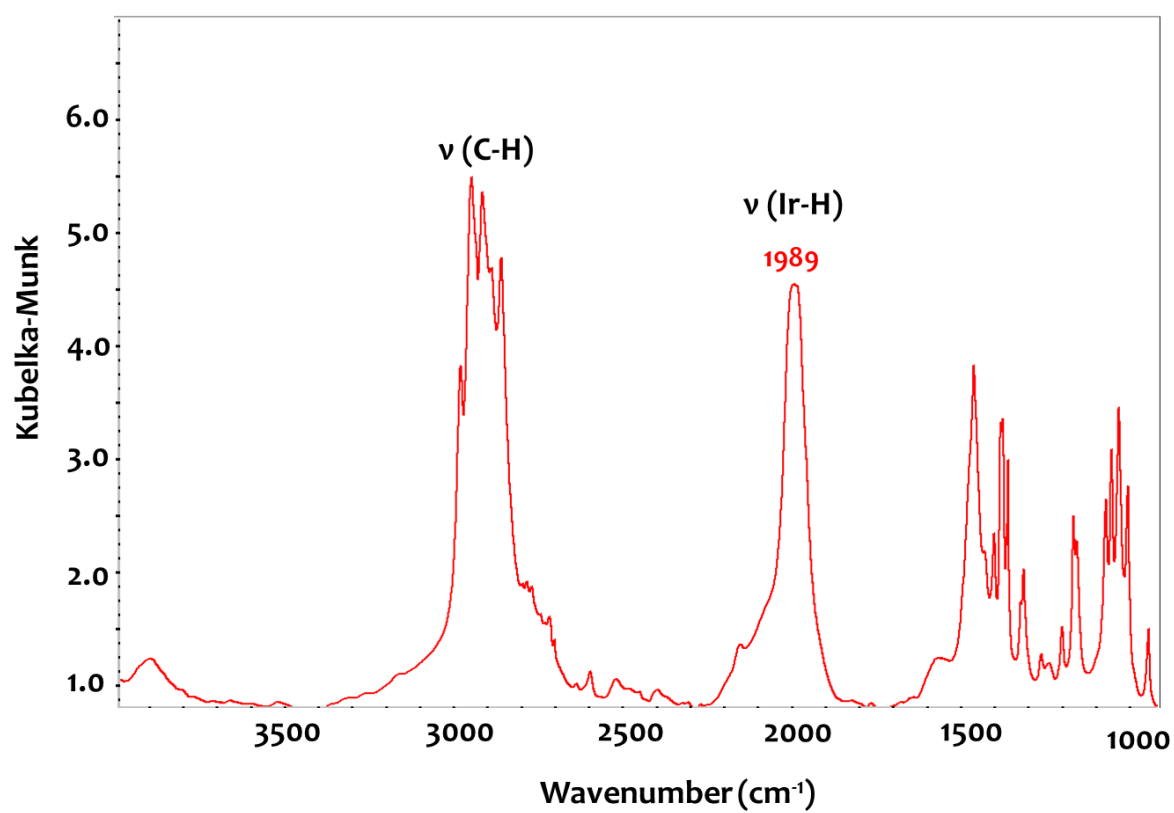
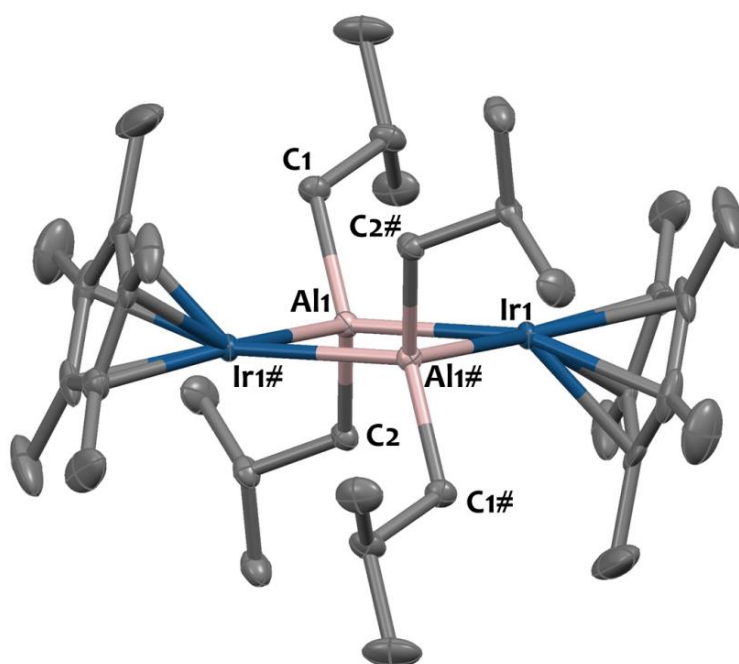


Figure 28. DRIFT spectrum (298K, diluted in KBr, under argon) of compound 12.

Yellow plate-shaped single-crystals of **12** suitable for X-ray diffraction analysis are grown in a cold ($T=-40^{\circ}\text{C}$) and saturated pentane solution of **12**. The solid-state molecular structure of **12** (Figure 25, bottom) displays unusual structural features. Contrary to **11** and to the related $[\text{Cp}^*\text{IrPMe}_3\text{AlEt}]_2$ complex reported by Bergman,^[25] the tetranuclear $\{\text{Ir}_2\text{Al}_2\}$ core in **12** is not centrosymmetric nor planar, but adopts a saddle topology with the two Al centers lying slightly above the two Ir centers (mean deviation from plane = $0.19(2)$ Å). The Ir-Al distances lie in the range $2.426(6)$ - $2.449(6)$ Å, which is considerably shorter than in **11** ($2.72(1)$ Å) and in the range of the rare unsupported Ir-Al bonds (2.45 - 2.51 Å).^[24,25] The formal shortness ratio (FSR= 0.972)^[78,240] is slightly below unity suggesting some degree of metal-metal interactions between the Ir and the Al sites. The Ir-Al-Ir angles in **12** ($112.5(2)^{\circ}$ and $113.4(2)^{\circ}$) are considerably more obtuse than in **11** ($101.18(6)^{\circ}$) to favor trigonal planar geometries at the Al sites, which are located only within $0.01(1)$ Å of the Ir1-Ir2-C1 or Ir1-Ir2-C2 planes. As a result, the Al-Ir-Al angles in **2** ($63.8(2)^{\circ}$ and $64.1(2)^{\circ}$) are much shorter than in **1** ($78.82(6)^{\circ}$). This peculiar geometric arrangement results in an unexpected very short Al-Al distance of $2.582(8)$ Å. This Al-Al separation is remarkably short when compared to reported Al-Al single bonds: the Al-Al distance in $[\text{Cp}^*\text{Al}]_4$ is 2.77 Å^[90] and Al-Al single bond distances in dinuclear Al-Al species lie in the range $[2.53$ - 2.70 Å].^[83,241-246] However, DFT calculations (see below) suggest that compound **12** is best described as containing two Al(III) cations with little to no Al-Al bonding despite their close proximity. The twisting of the Cp* rings with respect to the Ir_2Al_2 core is more pronounced in **12** ($\alpha = 151.5(1)^{\circ}$) than in **11** ($\alpha = 163.7(1)^{\circ}$), as a result of the presence of two hydrides in terminal positions on each Ir center, as supported by DFT calculations (see below).



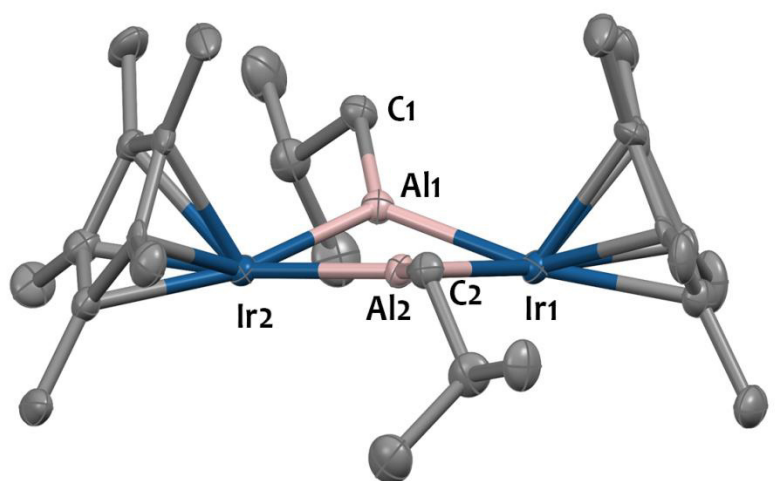


Figure 29. Solid-state molecular structures of **11** (top) and **12** (bottom). Displacement ellipsoids are plotted at a 30% probability level. Hydrogen atoms have been omitted for clarity. Selected bond distances (Å) and angles (°) for **11**: Ir1-Al1 2.7344(17), Ir1#-Al1# 2.7195(18), Al1-C2 1.998(6), Al1-C1 2.008(6), Ir1-Al1-Ir1# 101.18(6), Al1-Ir1-Al1# 78.82(6), (Ir1#-Al1#-Ir1-Al1)_{centroid}-Ir-Cp*_{centroid} 163.77. For **12**: Ir1-Al1 2.449(6), Ir1-Al2 2.438(6), Ir2-Al1 2.440(6), Ir2-Al2 2.426(6), Al1-Al2 2.582(8), Al1-C1 1.96(2), Al2-C2 1.987(19). Ir2-Al1-Ir1 112.5(2), Ir2-Al2-Ir1 113.4(2) Al2-Ir1-Al1 63.80(18), C1-Al1-Ir1 125.3(7), C1-Al1-Ir2 122.2(7), C5-Al2-Ir1 119.6(6), C5-Al2-Ir2 126.9(6), (Ir1-Al1-Ir2-Al2)_{centroid}-Ir1-Cp*_{centroid} 151.78, (Ir1-Al1-Ir2-Al2)_{centroid}-Ir2-Cp*_{centroid} 151.21.

In summary, the acidic hydrides from Cp*IrH₄ promote the protonolysis of Al-isobutyl groups, leading to [Cp*IrH₃] moieties which then act as proton sources to cleave another Al-isobutyl group, resulting in formally doubly deprotonated [Cp*IrH₂]²⁻ fragments, which are bridged by Al(^{*i*}Bu)²⁺ units in cluster **12**.

To get deeper insights into the structure and bonding in these systems, and help deciphering the metal-hydride and metal-metal interactions, DFT calculations (B3PW91) – conducted in the framework of a collaboration with Pr Laurent Maron and Iker Del Rosal of the LCPNO laboratory in Toulouse - are carried out for complexes **11** and **12**. DFT optimized structures are shown in Figure 30. Computed electronic and structural parameters are gathered in Table 2.

Regarding complex **11**, only one stable structure is obtained, despite a large exploration of possible conformers. The optimized tetranuclear diamond-shape geometry is in good agreement with the solid state molecular structure of **11** (e.g. Ir-Al-Ir angles of 100.5°, Al-Ir-Al angles of 79.5° and averaged Ir-Al distances of 2.75 Å, see Table 2). The moderate twisting ($\alpha = 163.8^\circ$) of the Cp* rings is also reproduced computationally. For the hydride positions, as aforementioned, one terminal hydride, labeled as H(η), is found per iridium center, along with four bridging hydrides, called H(μ), Ir-H-Al (two per iridium center). Natural bonding orbital (NBO) analyses of **11** clearly indicate six covalent Ir-H interactions (with 47–56% contribution from the Ir *spd* hybrid orbital). At the second-order donor-acceptor level, donations from the Ir-H(μ) bonds into the Al empty *sp*

orbital are observed, in line with the presence of three-center-two-electron (3c-2e) Ir-H(μ)-Al bonds. The presence of a covalent bond between Ir and H(μ) is also corroborated by the calculated Ir-H(μ) Wiberg bond indexes (WBIs, Table 2) of 0.66. Al - H(μ) WBIs of 0.13 are found, in line with electron delocalization from the Ir-H(μ) bonds onto acceptor orbitals on Al atoms. Interestingly, a similar donation is obtained from the Ir-H(η) bonds into the Al empty *sp* orbital of each Al atom as well as similar calculated WBIs of 0.08 between these H(η) atoms and each Al atom. These calculations suggest a pseudo-face capping character of these terminal hydrides in agreement with the experimentally observed fluxional behaviour leading to the exchange between the hydride positions. Natural charges in **11** are calculated as -0.958 on Ir and +1.776 on Al, with a calculated Ir-Al WBIs of 0.2 indicating the presence of a slightly bonding interaction between Ir and Al (donation from a Ir *d* lone pair into the Al empty *sp* orbital). These analyses also show the absence of any Al-Al bonding interaction in complex **11** (Al - Al WBI of 0.03).

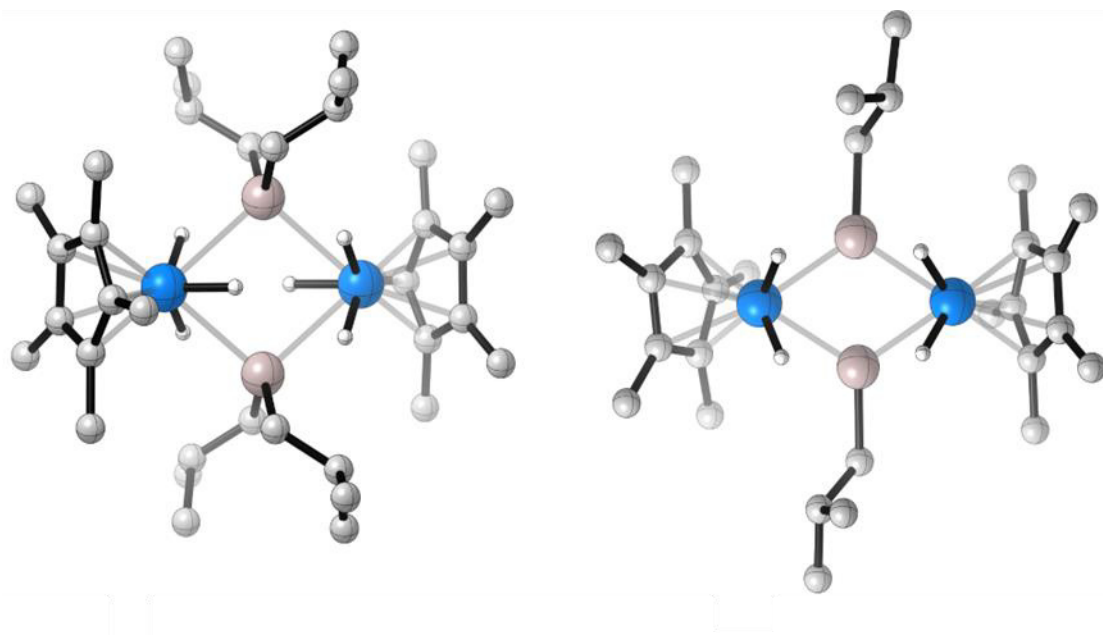


Figure 30. DFT computed structures for clusters **11** (left) and **12** (right).

	Complex 11	Complex 12
NPA charges	Al: 1.78 / Ir: -0.96	Al: 1.64 / Ir: -1.29
WBIs	Ir-H: 0.66 / Ir-Al: 0.21 / Al-H(μ): 0.13 / Al-H(η): 0.08 Al-Al: 0.03 / C-Al 0.44	Ir-H: 0.67 / Ir-Al: 0.45 Al-Al: 0.18 / C-Al: 0.49
Ir-H bands (cm⁻¹)	μ : 2220.7 / 2218.7 η : 2208.9 / 2207.1 μ : 2182.1 / 2181.1	η : 2011 / 2007 η : 1991 / 1977
Ir-H distances (Å)	1.602 / 1.603x3 / 1.604x2	1.618 / 1.624 / 1.623 / 1.619
Al-H distances (Å)	1.977 / 1.993 / 1.996 / 1.979 2.191 / 2.189 / 2.183 / 2.195	2.086 / 2.038 / 2.042 / 2.097
Ir-Al distances (Å)	2.776 / 2.739 / 2.774 / 2.743	2.451 / 2.465 / 2.449 / 2.463
XRD Ir-Al distances (Å)	2.734 / 2.720 / 2.734 / 2.720	2.450 / 2.441 / 2.439 / 2.427
Al-Al distances (Å)	3.528	2.643
XRD Al-Al distances (Å)	3.463	2.583
Ir-Al-Ir angles (°)	100.4 / 100.6	113.5
XRD Ir-Al-Ir angles (°)	101.2/101.2	113.0
Al-Ir-Al angles (°)	79.5	65.0
XRD Al-Ir-Al angles (°)	78.8	63.8
α angle (°)	163.8	154.3
XRD α angle (°)	163.8	151.5

Table 2. Computed NPA charges, Wiberg bond indexes (WBIs), and structural data of clusters 11 (left) and 12 (right).

For complex 12, a conformational analysis has revealed four possible conformers in an energy range of only 14.0 kcal.mol⁻¹ (see appendix section for more information). The most stable structure exhibits four hydrides in terminal position on Ir centers while the structure with two terminal and two bridging hydrides is less stable by 6.5 kcal.mol⁻¹. Finally, two other conformers with four bridging hydrides Ir-H-Al are also obtained but are the least stable (10.6 and 14.0 kcal.mol⁻¹ above the lowest energy structure). Interestingly, only the most stable structure

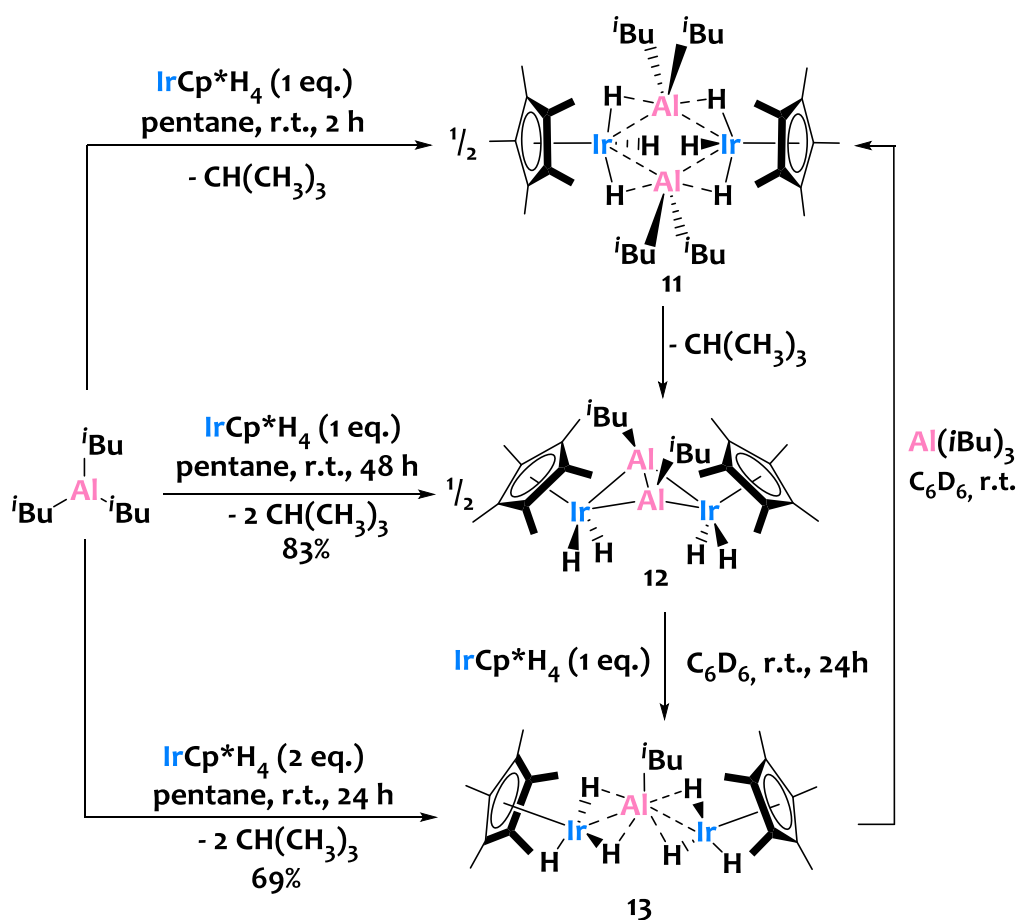
exhibits an Ir-H stretching vibrational mode in between 1977 and 2011 cm^{-1} in agreement with the IR data. Finally, there is a good correlation between the crystallographic and the calculated structure of the most stable conformer since:

- 1) As experimentally observed, this complex adopts a saddle topology.
- 2) Computed Ir-Al distances lie in the range 2.449 - 2.465 Å and the short Al-Al distance is equal to 2.643 Å.
- 3) Ir-Al-Ir, Al-Ir-Al and α angles are equal to, respectively, 113.5°, 65.0° and 154.3°.

Similarly to complex **11**, the NBO analyses and the calculated WBIs clearly indicate the presence of a covalent bond between Ir and H (0.67) as well as an electron delocalization from these bonds onto acceptor orbitals on Al atoms. Note that Ir-Al WBIs are averaged at a value of 0.45 (vs 0.21 in complex **11**) suggesting stronger interaction between Ir and Al (as supported experimentally by XRD data with smaller Ir-Al FSR for cluster **12** than **11**). However, as aforementioned, these calculations underpin the absence of Al-Al bond even though the Al-Al WBI in complex **12** is higher than that in complex **11** (0.18 vs. 0.03).

3.2.2 Synthesis and characterization of a trinuclear heterobimetallic [AlIr₂] cluster

To better understand the alkane elimination sequence in these systems and access clusters of various nuclearities and compositions, we studied the reaction of triisobutylaluminum with excess IrCp*H₄. Treatment of Al(ⁱBu)₃ with 2 equivalents of IrCp*H₄ in pentane leads, after one day at room temperature, to the formation of the trinuclear [Ir((Cp*)(H)(μ-H₂))₂Al(ⁱBu)] complex **13** in 69% yield as a light yellow powder (Scheme 59).



Scheme 59. Synthesis of the $[\text{AlIr}_2]$ trimetallic species **13**.

Single-crystals of **13** suitable for XRD analysis are grown in a cold ($T=-40^\circ\text{C}$) saturated solution of **13** in pentane. The solid-state structure of **13**, shown on Figure 31, settles the trinuclear nature of the complex where two $[\text{Cp}^*\text{IrH}_3]$ fragments are bridged by an $\text{Al}(\text{iBu})_2^{2+}$ motif. The aluminum center adopts a pseudo trigonal planar geometry with angles lying in the $115\text{-}126^\circ$ range. The averaged Al-Ir distances of $2.435(6) \text{ \AA}$ in **13** are in the same range than those in complex **12**.

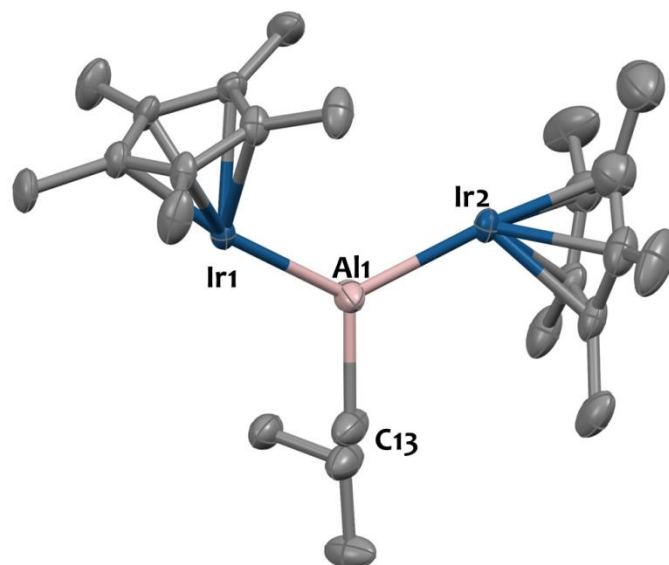


Figure 31. Solid-state molecular structure of compound **13**. Displacement ellipsoids are plotted at a 30% probability level. Hydrogen atoms have been omitted for clarity. Selected bond distances (Å) and angles (°): Ir1-Al1 2.437(6), Ir2-Al1 2.432(6), Al1-C13 2.04(3), Ir2-Al1-Ir1 125.4(3), C13-Al1-Ir1 116.4(10), C13-Al1-Ir2 115.7(10), Al1-Ir1-Cp*_{centroid} 140.20, Al1-Ir2-Cp*_{centroid} 141.24.

The $^1\text{H-NMR}$ spectrum of **13**, recorded in C_6D_6 solution (Figure 32), shows a hydride signal at $\delta = -16.64$ ppm integrating for 6H, two IrCp* fragments ($\delta = +2.03$ ppm integrating for 30H) and one Al^{*i*}Bu pattern ($\delta_{\text{CH}} = 2.49$ ppm, 1H; $\delta_{\text{CH}_3} = 1.29$ ppm, 6H; $\delta_{\text{CH}_2} = 0.56$ ppm, 2H) in agreement with the proposed molecular structure for **13**. The DRIFT spectrum of **13** (Figure 33) displays two intense M-H vibrators at $\sigma = 2151\text{ cm}^{-1}$ and 2014 cm^{-1} suggesting the presence of both terminal and bridging iridium hydrides. This assumption is further supported by the observed tilting of Cp* rings with respect of the Ir-Al axes in the solid-state structure of **13** (Figure 31), with Al-Ir-Cp*_{centroid} angles averaged at $140.7(2)^\circ$, probably imparted by the presence of a terminal hydride. Note that D. W. Stephan and co-workers reported in 1998 a zirconium-aluminum complex, $[(\text{Cp}')_2\text{ZrH}(\mu\text{-H})_2]_2\text{AlH}$ (Cp' = $\text{Me}_3\text{SiC}_5\text{H}_4$), related to the present species.^[247]

Quite interestingly, the reaction of complex **12** with 2 equivalents of IrCp*H₄ leads also to product **13** quantitatively. This reaction is quite informative regarding the processes at place in these systems. Here, Cp*IrH₄ acts as a Brønsted acid, but the proton transfers preferentially occur at the Ir sites from **12**, rather than at the isobutylaluminum groups, as confirmed by the absence of isobutane elimination. This testifies to the strong basicity of the $[\text{Cp}^*\text{IrH}_2]^{2-}$ fragment. This reaction also advocates for some degrees of lability in these systems, since the di-aluminum derivative **12** is converted into a mono-aluminum species, **13**, as a result of iridate ligands redistribution. This motivated us to investigate the reaction of **13** with 1.0 equivalent of Al(^{*i*}Bu)₃,

(Scheme 59). NMR reaction monitoring (see Figure 34) shows that, after two hours at room temperature, compound **13** is quantitatively converted into **11**, as a result of isobutyl/iridate ligands redistribution (Scheme 59). Complex **11** further slowly evolves into **12** through isobutane elimination, as expected. This confirms that these assemblies are labile, leading to metal/ligand redistribution phenomena, which are faster than the protonolysis reactivity in the present case. This paves the way towards the preparation of more diverse architectures through metal substitution.

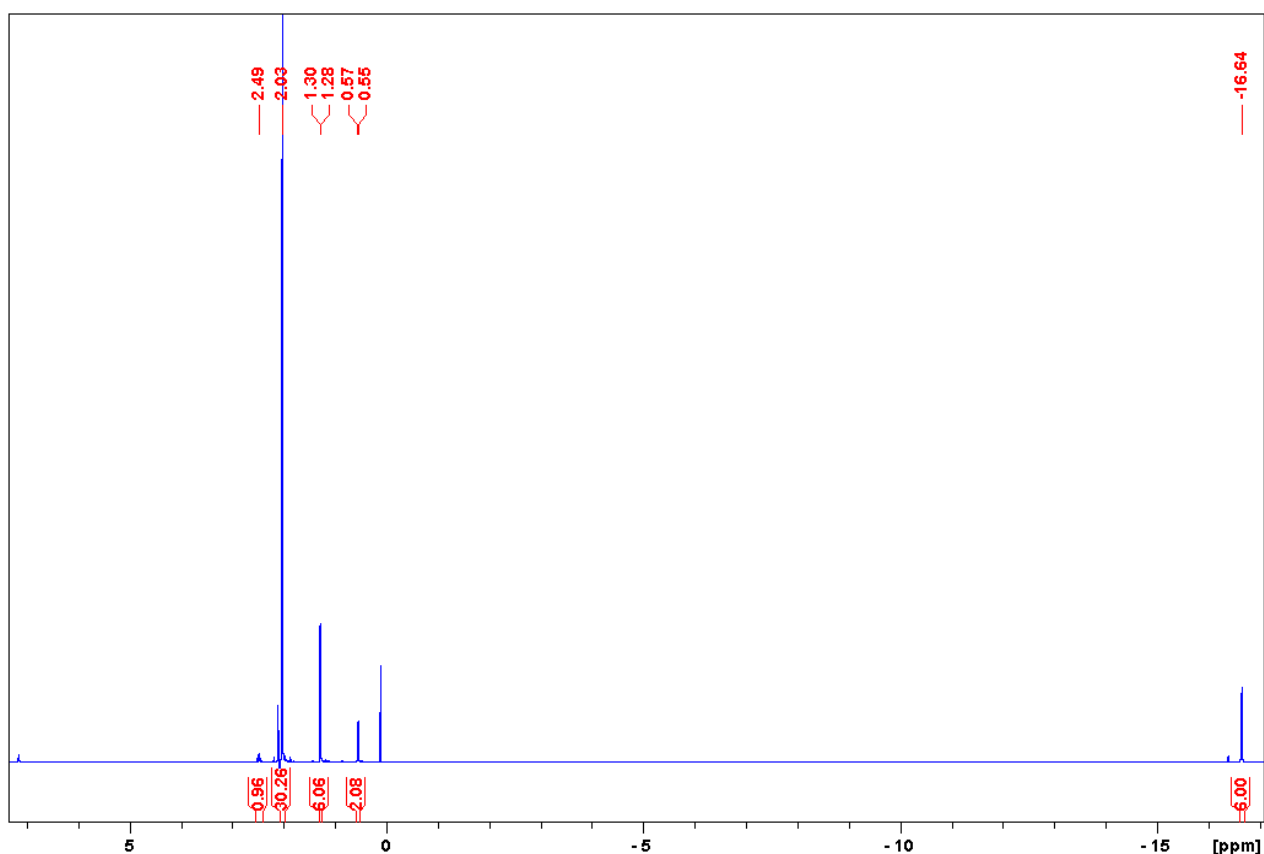


Figure 32. $^1\text{H-NMR}$ spectrum (400 MHz, C_6D_6 , 293K) of cluster **13**.

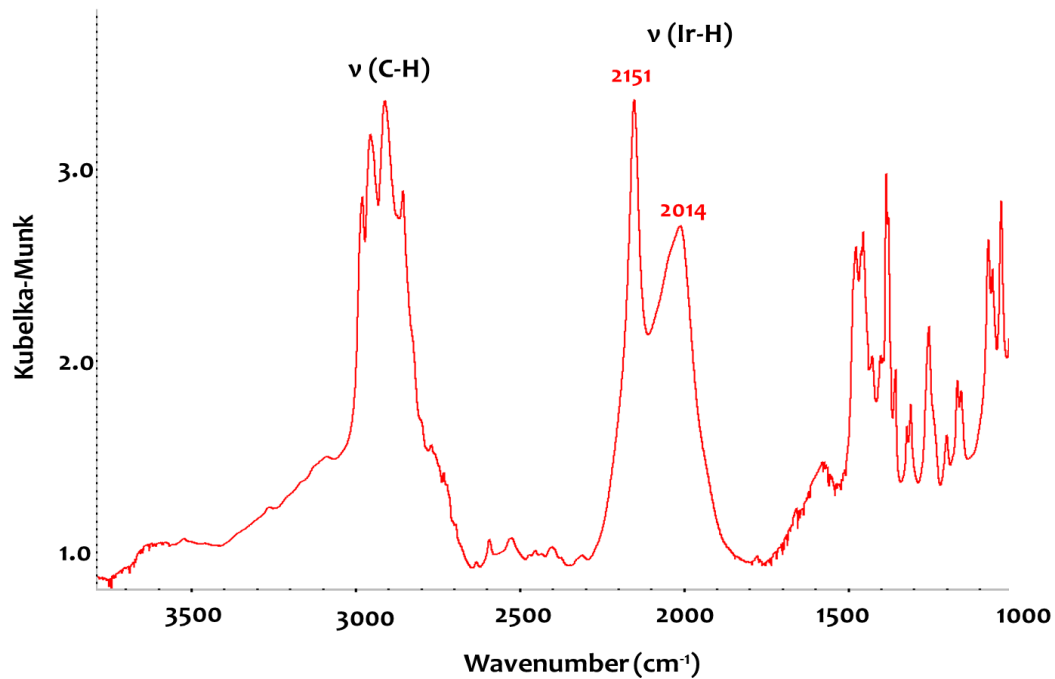


Figure 33. DRIFT spectrum (298K, diluted in KBr, under argon) of cluster 13.

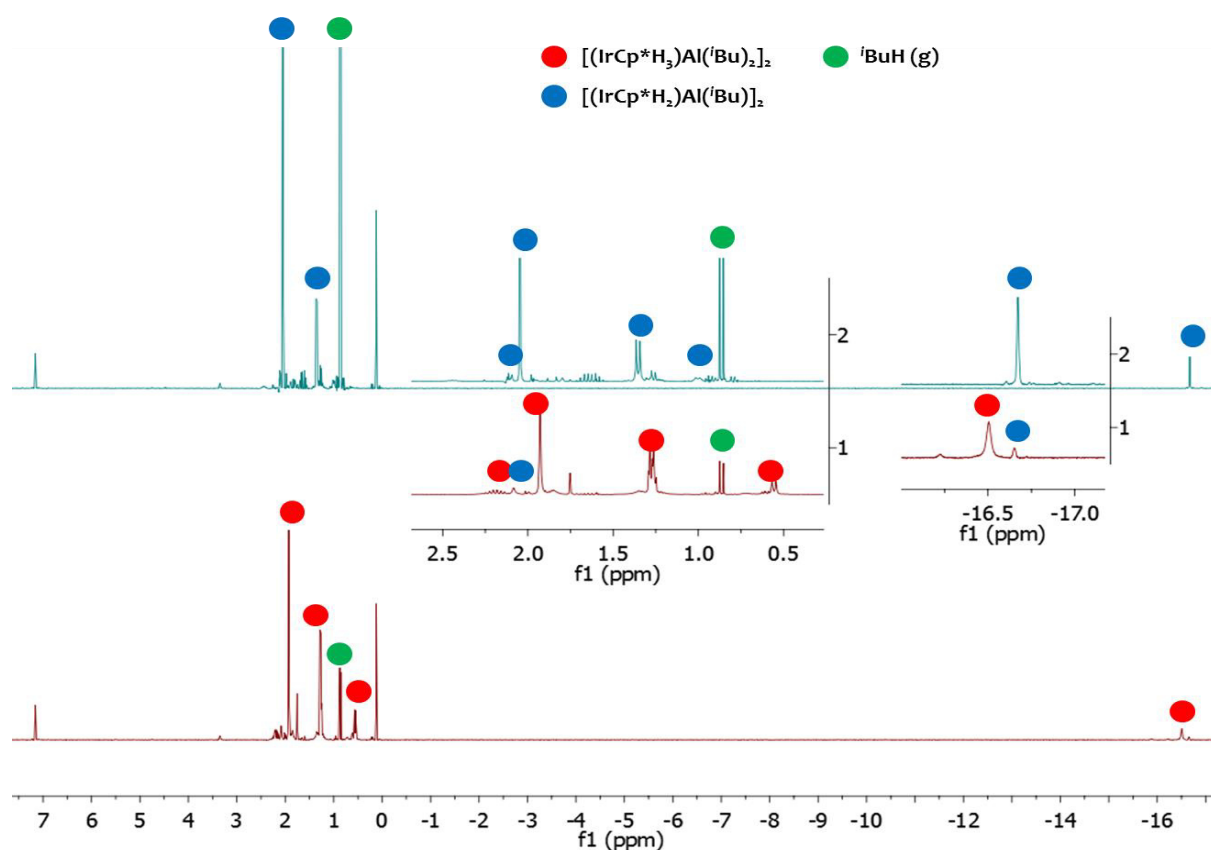
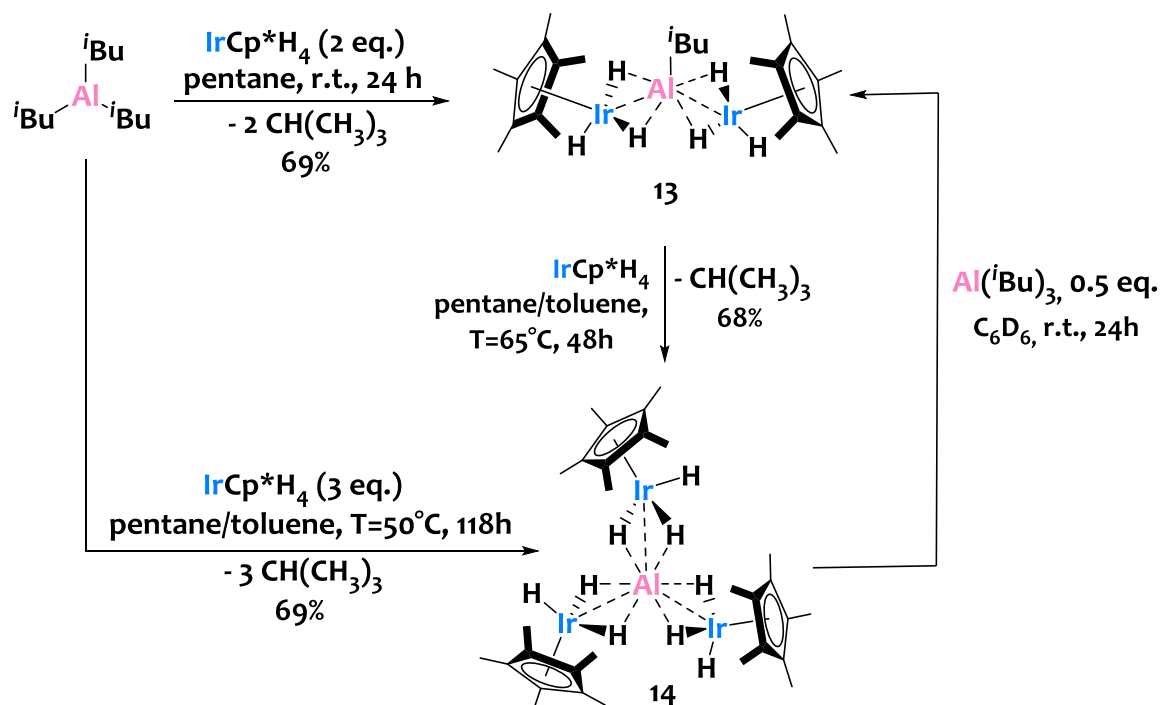


Figure 34. ¹H-NMR spectra (300 MHz, C₆D₆, 293K) relating to the reaction of complex 13 with triisobutylaluminum (1 eq.). Bottom (red lines): after 2 hours of reaction; complex 11 is the main product. Top (blue lines) after 2 days of reaction; complex 12 is the main product.

3.2.3 Synthesis and characterization of a tetranuclear heterobimetallic [AlIr₃] cluster

Since double isobutane elimination readily occurred from triisobutylaluminum and 2 equivalents of IrCp*H₄, we contemplated the total desalkylation - *i.e.* triple isobutane elimination - of triisobutylaluminum by IrCp*H₄. Gratifyingly, we proved this sequence by stirring TIBA with 3 equivalents of IrCp*H₄ in a hot toluene/pentane solution (T~50°C) for one week. This procedure leads to the formation of the tetranuclear [Ir((Cp*)(H)(μ-H₂))₃Al] cluster **14** (Scheme 60) isolated as single colorless block crystals after cold fractionated recrystallizations in a minimum of pentane (69 % yield). Interestingly, species **13** is formed during the reaction as an intermediate. We therefore established the feasibility of designing complex **14** by mixing stoichiometric amounts of cluster **13** and IrCp*H₄ in a hot toluene/pentane solution (T=65°C) for 2 days (Scheme 60).

The total de-alkylation sequence is proved by the absence of isobutyl signals in ¹H and ¹³C-NMR spectra of **14** since they only display Ir-Cp* (δ_{1H}=2.11 ppm ; δ_{13C}=93.62 & 11.26 ppm, see Figure 35) and Ir-H resonances (δ_{1H}=-16.38 ppm). Note that all the Ir-H are equivalent in solution even at low temperature (down to T=-50°C).



Scheme 60. Synthesis of the tetranuclear [AlIr₃] cluster **14**.

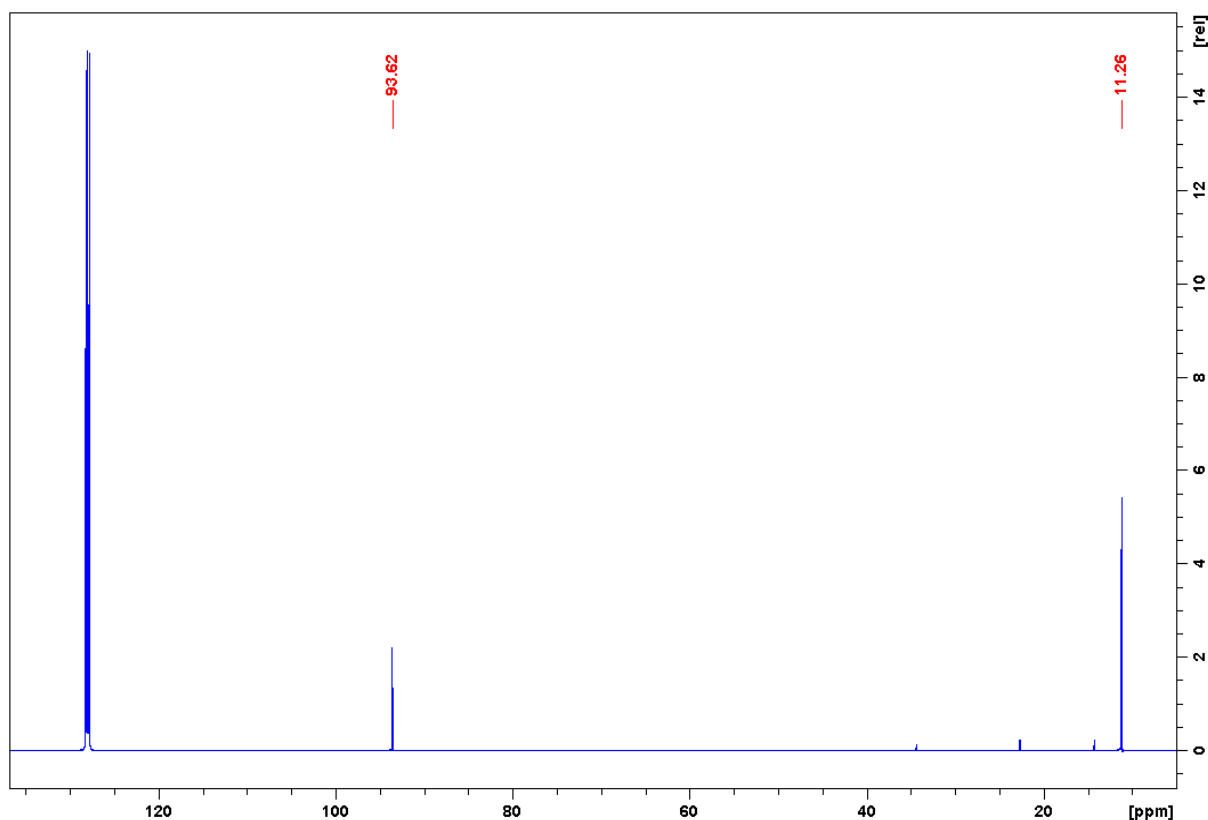


Figure 35. $^{13}\text{C}\{^1\text{H}\}$ -NMR spectrum (100 MHz, C_6D_6 , 293K) of cluster **14**

The solid-state structure of **14** (obtained by XRD analysis) is showed on Figure 38. It highlights some interesting features. The complex adopts a helicoidal structure where three IrCp* fragments are ligated to an Al center. The Al-Ir bonds are lying in the [247.5-248.5 pm] range resulting in an average FSR of 0.989^[78], slightly higher than those calculated for species **12-13**. The pronounced titling of the three Cp* rings, averaged at an angle $\beta=140.6^\circ$ (see Figure 37), suggests the presence of terminal hydrides onto the iridium metallic ions similarly to complex **13**. DRIFT spectroscopy of **14** displays a very close molecular print than species **13**, which also strongly supports both terminal and bridging Ir-H.

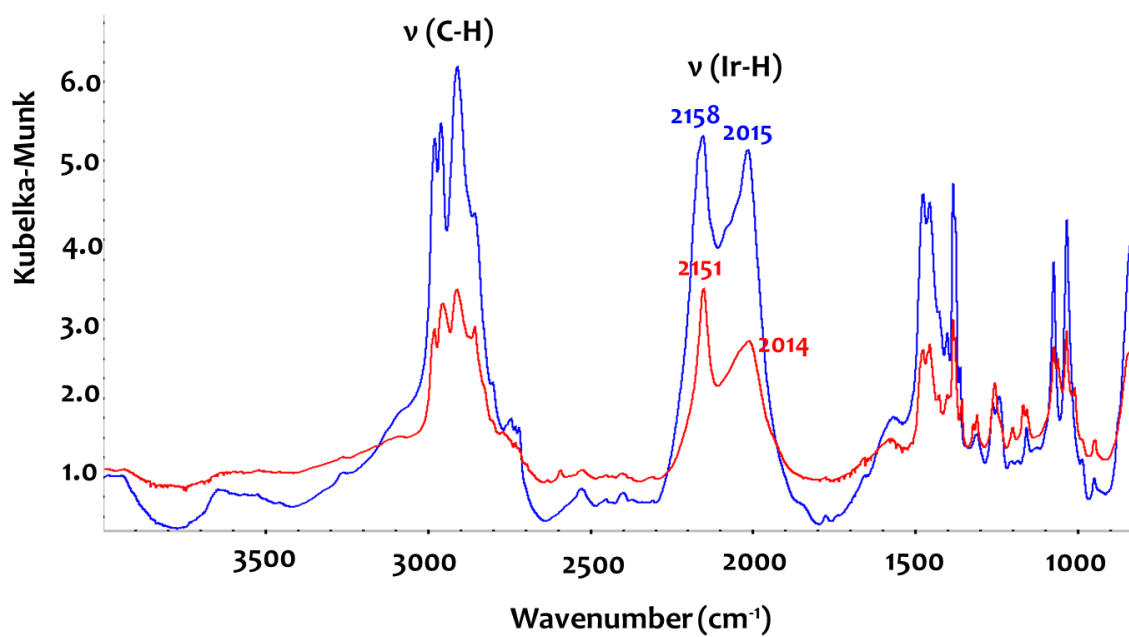


Figure 36. DRIFT spectra (298K, diluted in KBr, under argon) of cluster 13 (red) vs cluster 14 (blue).

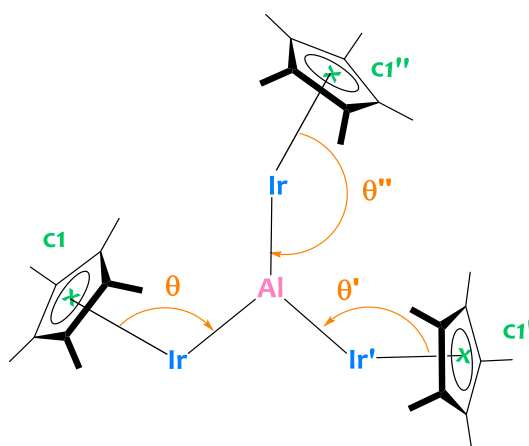


Figure 37. Definition of a new metrical parameter $\beta = (\theta + \theta' + \theta'')/3$ characteristic of iridium-hydride locations (terminal or bridging) regarding complex 14.

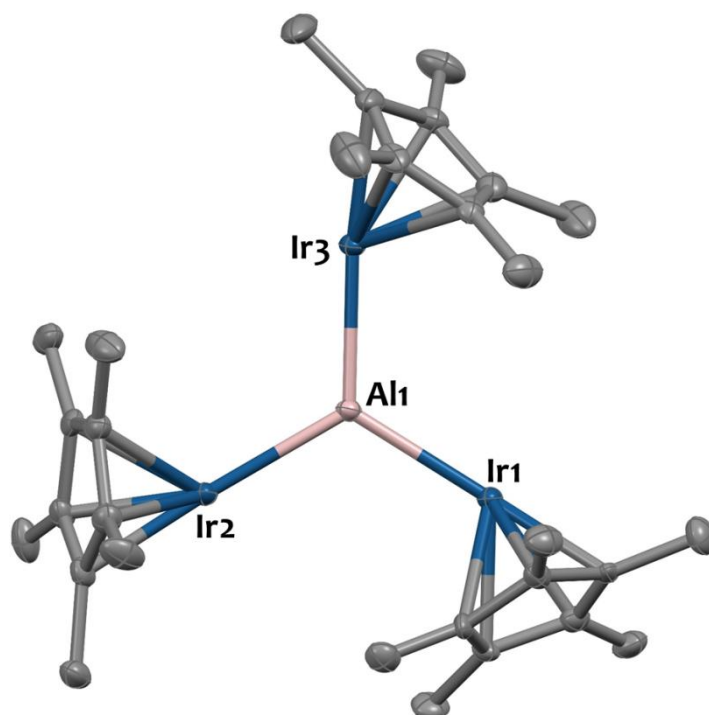


Figure 38. Solid-state molecular structure of compound **14**. Displacement ellipsoids are plotted at a 30% probability level. Hydrogen atoms have been omitted for clarity. Two independent molecules were found in the asymmetric unit ($Z'=2$) but one of them have been omitted for clarity. Selected bond distances (Å) and angles ($^{\circ}$) (averaged between both molecules): Ir1-Al1 2.477(8), Ir2-Al1 2.475(3), Ir3-Al1 2.484(8). Ir1-Al1-Ir2 118.57(62) Ir1-Al1-Ir3 120.14(62), Ir2-Al1-Ir3 121.13(62), Al1-Ir1-Cp*_{centroid} 139.26, Al1-Ir2-Cp*_{centroid} 140.25, Al1-Ir3-Cp*_{centroid} 142.22.

DFT calculations regarding the tetranuclear complex **14** are carried-out. In this case, the conformational analysis leads to only one stable structure (Figure 39). The optimized geometry indicates that six Ir-H-Al bridging hydrides are arranged around the central Al atom in a trigonal prismatic geometry as well as the presence of three terminal Ir-H hydride. Calculated parameters are gathered in Table 3. Here, the optimized structure is in excellent agreement with the experimental data since:

- 1) The calculated stretching vibrations for Ir-H(η) and Ir-H(μ) lie in the ranges of [2175-2183 cm^{-1}] and [2008-2049 cm^{-1}] respectively, which corroborates very well the experimental IR data.
- 2) The computed Al-Ir bonds are averaged at 2.486 Å (vs 2.479 Å for the crystallographic Ir-Al distances). The calculated β angle (140.8°) is also in excellent agreement with the experimental one (140.6°).
- 3) Al-Ir WBIs in complex **14** are slightly smaller (0.36) than in complex **12** (0.44) but higher than in complex **11** (0.20), in accordance with the observed variation of the intermetallic distances. Ir-H WBIs are averaged at 0.66 for bridging hydrides and 0.73 for terminal hydrides, in line with mainly covalent interaction. The Al-H WBIs are around 0.16 in line with electron delocalization from the Ir-H bond onto an acceptor orbital on Al. The Natural Population Analysis (NPA) charge on iridium

and aluminum are slightly smaller than in complexes **11** and **12**, taking values between -0.904 and -0.910 for iridium and +1.463 for aluminum.

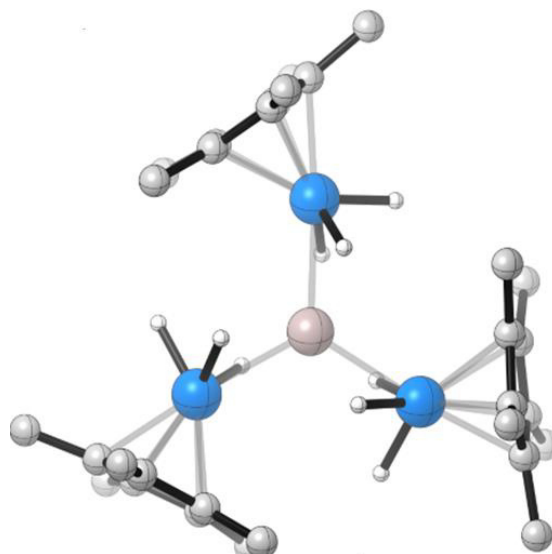


Figure 39. DFT computed structure for cluster 14.

Complex 14	
NPA charges	Al: 1.46 / Ir: -0.91
WBIs	Ir-H(μ): 0.66 / Ir-H(η): 0.73 / Al-H(μ): 0.16 / Ir-Al: 0.36
Ir-H bands (cm^{-1})	η : 2183 / 2177 / 2175. μ : 2049 / 2032 / 2022. μ : 2018 / 2009 / 2008
Ir-H distances (\AA)	1.581x3 / 1.1616x2 / 1.617 / 1.618 / 1.620x2
Al-H distances (\AA)	2.001 / 2.008 / 2.009 / 2.013 / 2.016 / 2.025 / 2.975 / 2.982 / 2.996
Ir-Al distances (\AA)	2.485 / 2.486 / 2.487
XRD Ir-Al distances (\AA)	2.475 / 2.478 / 2.485
Ir-Al-Ir angles ($^\circ$)	120.0x3
XRD Ir-Al-Ir angles ($^\circ$)	118.6 / 120.1 / 121.1
β angle ($^\circ$) ^a	140.8
XRD β angle ($^\circ$) ^a	140.6

Table 3. Computed NPA charges, Wiberg bond indexes (WBIs), and structural data for cluster 14. ^aGeometrical description of this angle is explained on Figure 37.

Compound **14** is an original cluster containing three iridium polyhydrides Cp* units. T. Takao, H. Suzuki, Z. Hou and coworkers reported similar $[(MCp^*(H)_n)_3]$ polyhydrides clusters based on ruthenium, iridium, osmium, tungsten and lanthanides metallic ions. ^[248-251] Secondly, cluster **14** features an Al center ligated to three IrCp*H₃ fragments through direct Ir-Al interactions as well as bridging hydrides. To the best of our knowledge, only four occurrences report such $[M_3Al]$ (M=Ru or Zr) edifice (Figure 40).^[26,93,247,252] This observation highlights the synthetic challenges to get stabilized molecular Al(III) center surrounded by only d-block transition metal hydride ions in a controlled fashion. This fact is likely explained by the relatively weak Al-(H_n(M))₃ interactions compare to Al-C or Al-O bonds for instance. At paramount, the synthesis of **14** embodies the first case of a total alkane elimination of a metal-alkyl precursor, *i.e.* a complete abstraction of the alkyl (R) to form the related alkanes (R-H), which supports the versatility and robustness of the alkane elimination route for our systems but also for a variety of other potential M-H/M'-R couples.

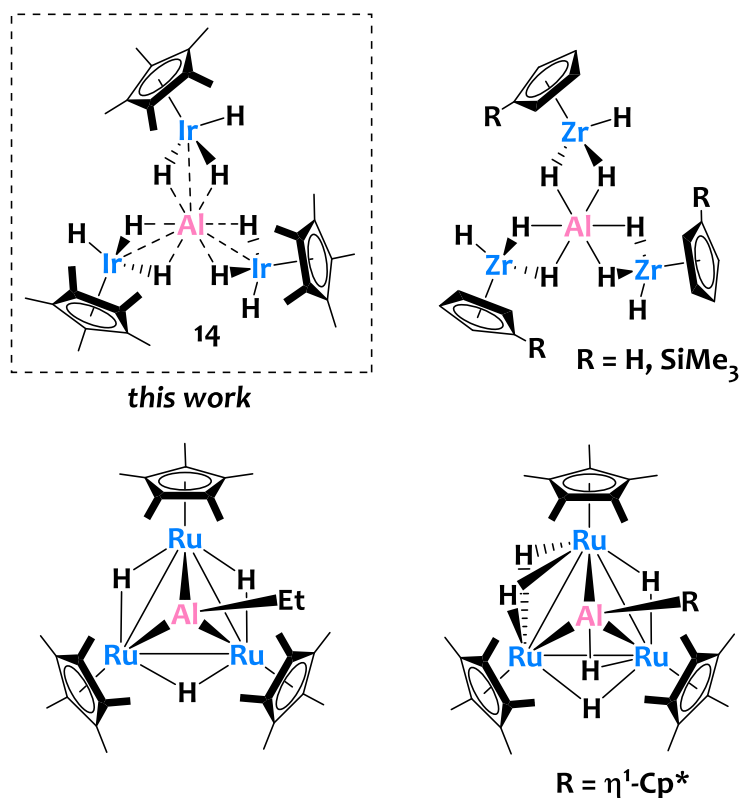


Figure 40. M_3Al tetranuclear polyhydrides (M = Zr,^[247,252] Ru,^[26,93] Ir) described to date.

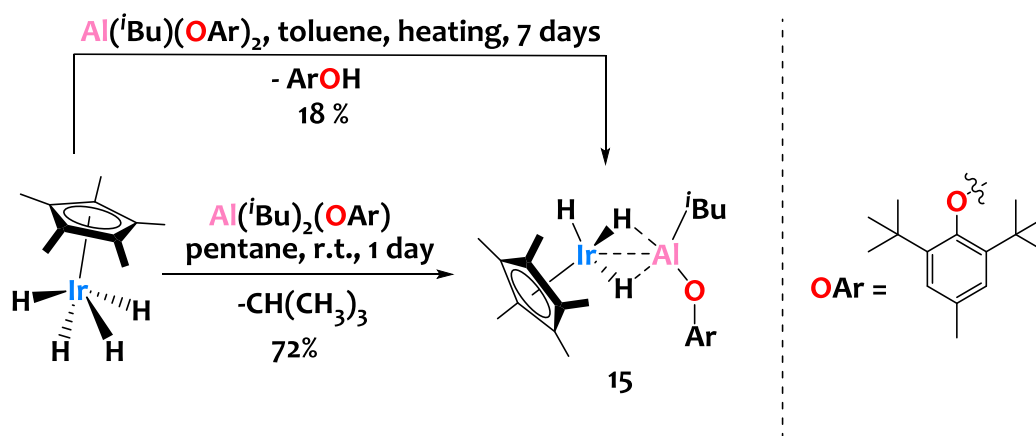
3.3 Synthesis of a binuclear [Ir-Al] heterobimetallic complex

3.3.1 Context

In view of preventing the formation of heterobimetallic polynuclear aggregates such as those observed in the previous section but also by R. G. Bergman and coworkers,^[25] we considered the use of sterically hindered Al-alkyl sources. For that purpose, we employed bulky isobutylaluminum aryloxy precursors and explored their reactivity towards Cp*IrH₄.

3.3.2 Synthesis and characterization

Treatment of aluminum(diisobutyl)(3,5-di-*tert*-butyl-4-hydroxytoluene), noted Al(*i*Bu)₂(OAr), with Cp*IrH₄ results in the formation of the heterobimetallic complex [Cp*IrH₃Al(*i*Bu)(OAr)], **15**, which is isolated in 72% yield after 24 hours of reaction at room temperature (Scheme 61). One equivalent of isobutane (quantified by ¹H NMR) is released during the reaction.



Scheme 61. Synthesis of the [Al-Ir] heterobimetallic complex **15**.

The ¹H-NMR spectrum of **15** (Figure 41), recorded in C₆D₆ solution, shows isobutyl signals at $\delta = 2.15, 1.08,$ and 0.31 ppm integrating respectively for 1H, 6H, and 2H and indicating the presence of one isobutyl group *per* Al center as expected. The hydride resonance is observed as a singlet at $\delta = -16.80$ ppm and integrating for 3H. Similarly to species **11-14**, this result suggests a rapid exchange between the three hydrides on the NMR time scale at room temperature.

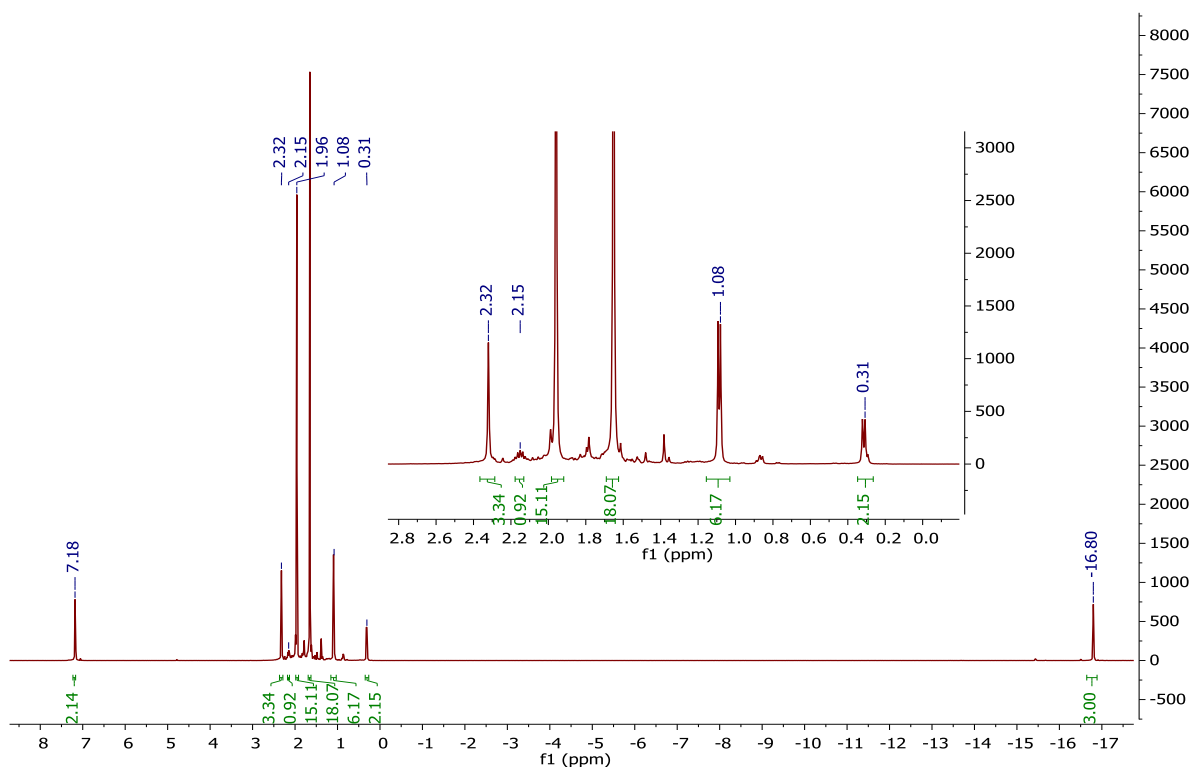


Figure 41. ¹H-NMR spectrum (500 MHz, C₆D₆, 293K) of complex 15

The IR spectrum of 15 exhibits two strong bands at $\sigma = 2144 \text{ cm}^{-1}$ and $\sigma = 1973 \text{ cm}^{-1}$ assigned to both terminal and bridging metal-hydride stretches (Figure 42).

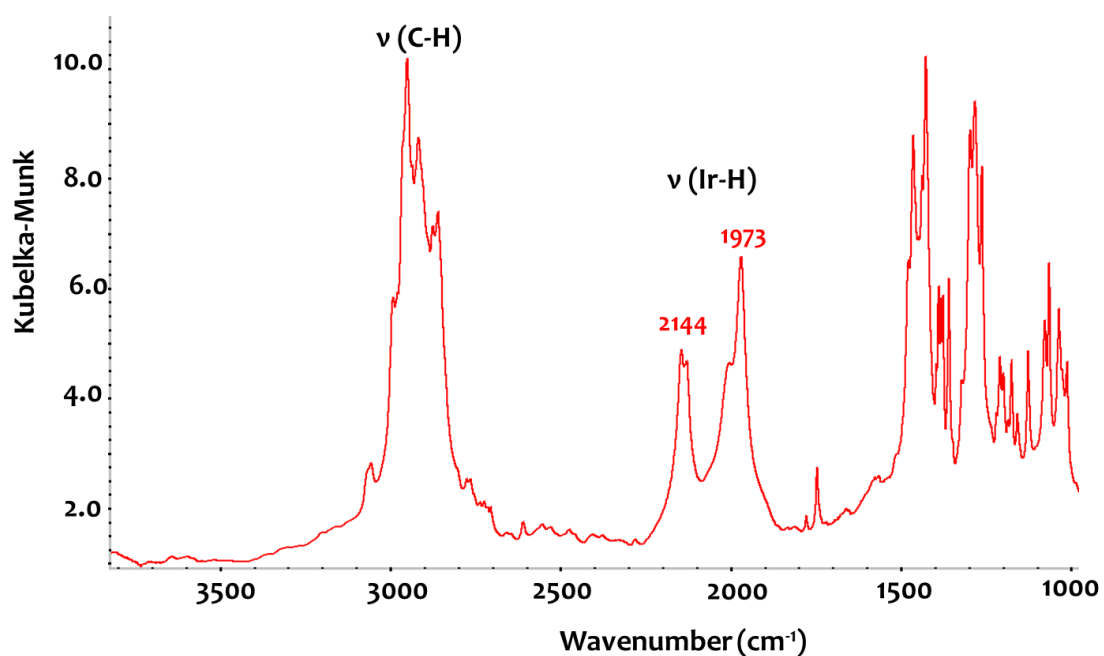


Figure 42. DRIFT spectrum (298K, diluted in KBr, under argon) of complex 15

Single colorless block-shaped crystals of **15** – suitable for XRD analysis – are grown from a cold saturated pentane solution of **15**. The solid-state structure of **15** is represented on Figure 43.

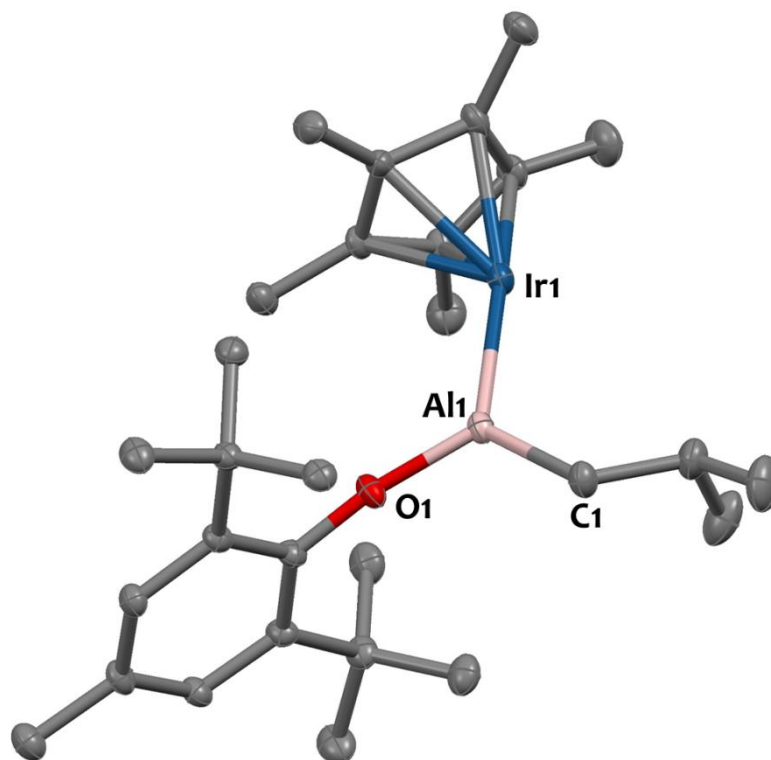


Figure 43. Solid-state molecular structure of **15**. Displacement ellipsoids are plotted at a 30% probability level. Hydrogen atoms have been omitted for clarity. Selected bond distances (Å) and angles (°): Ir1-Al1 2.406(2), Al1-O1 1.695(4), Al1-C1 1.961(6), O1-Al1-Ir1 120.60(18), O1-Al1-C1 115.4(3), C1-Al1-Ir1 124.0(2). Al1-Ir1-Cp*_{centroid} 143.8(2).

The most significant feature of the crystallographic structure of **15** is the Al-Ir distance of 2.406(2) Å, which is the second shortest reported distance for an Ir species bearing an Al atom in its coordination sphere.^[24,25,65,114] The only species featuring a shorter Al-Ir bond of 2.382(1) Å is the pincer complex [PAIP]Ir(H)₄ described by M. Yamashita and coworkers (see Figure 2 in CHAPTER 1).^[65] The metal-metal separation in **15** is 0.10 Å shorter than the sum of metallic radii of aluminum (1.248 Å) and iridium (1.260 Å),^[78] which translates into a formal shortness ratio below unity (FSR=0.959).^[240] Such metrical value is lower than that for species **11-14**, which suggests direct metal-metal interaction, at least to some extent. Nonetheless, this remarkable proximity between Al and Ir is also explained by the presence of bridging hydrides (as evidenced by IR spectroscopy and DFT calculations, see below). Overall, this result suggests a strong donation of the Cp*IrH₃ iridate fragment onto the cationic Al site. The high electrophilicity of the Al cation in **15** is also reflected in the short Al1-O₁ bond of 1.695(4) Å when compared to that observed for similar Al-O_{Ar} bonds found in the literature.^[21,191,253] Another characteristic of the structure of **15** is the marked tilting of the Cp* ring with respect to the Al-Ir axis (Al-Ir-Cp*_{centroid} angle of 143.8(1)°). We propose

that this geometrical arrangement is due to the presence of a terminal hydride on the Ir center, as confirmed by computational data (see below).

Contrary to $\text{Al}(\text{iBu})_2(\text{OAr})$, the more hindered aluminum(isobutyl)bis(3,5-di-tert-butyl-4-hydroxytoluene) species, noted $\text{Al}(\text{iBu})(\text{OAr})_2$, does not react with IrCp^*H_4 in toluene at room temperature. Upon heating at 110°C for one week, compound **15** is obtained from $\text{Al}(\text{iBu})(\text{OAr})_2$ and isolated in 18% yield from cold (-40°C) recrystallization in a saturated pentane solution (Scheme 5). ^1H NMR monitoring of this reaction indicates the release of 2,6-tertbutyl-4-methyl-phenol. We attribute the preferential elimination of HOAr versus isobutane to the particularly high steric hindrance of this phenoxy derivative.

3.3.3 Structural investigation by DFT

To get deeper insights into the nature of the Ir-hydrides, DFT calculations (B3PW91) are carried out for complex **15**. Two isoenergetic structures are found for **15** (see Figure 44 and Table 4 for the computed parameters) so that a rapid exchange of the hydrides in solution is expected, which is in line with the ^1H NMR data.

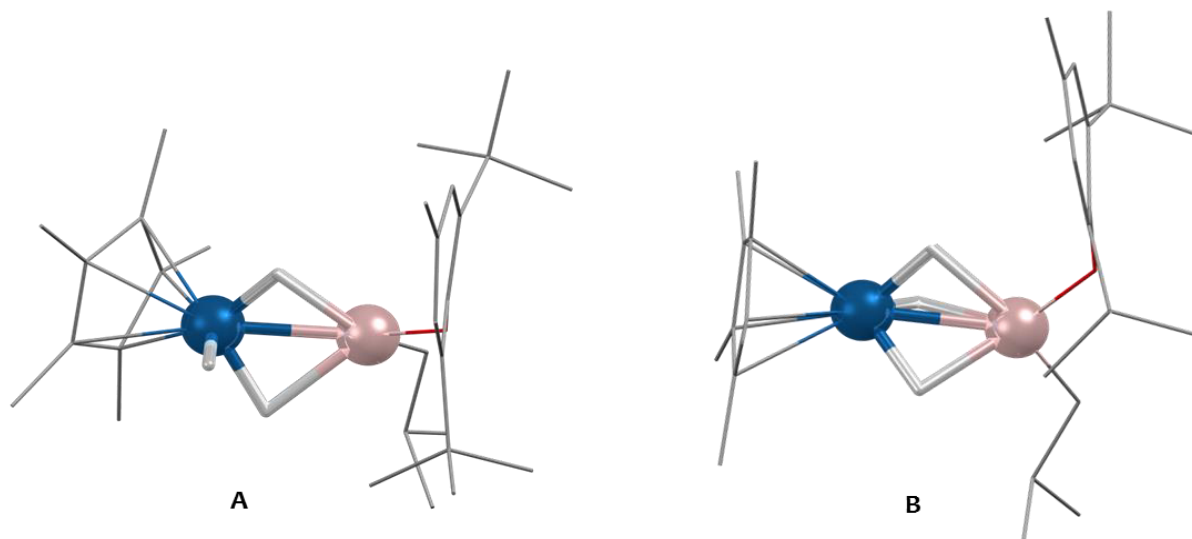


Figure 44. DFT optimized structures for the two conformers of complex **15**.

	Complex 15 (conformer A)	Complex 15 (conformer B)
Ir-H distances (Å)	1.579 / 1.603 / 1.621	1.607 / 1.632 / 1.634
Al-H distances (Å)	2.020 / 2.111	1.947 / 1.965 / 2.075
Ir-Al distances (Å)	2.423	2.422
Cp*_{centroid}-Ir-Al angle (°)	136.7	177.7

Table 4. Computed structural data regarding the two isoenergetic structures (A and B) of compound 15.

Conformer **15A** exhibits one terminal hydride on Ir and two bridging Ir- μ (H)-Al, while the three hydrogens have a μ -coordination in conformer **15B**. The calculated Ir-Al distances for both isomers (2.42 Å computed vs. 2.41 Å experimental), are in agreement with the X-ray crystallographic structure. Significantly, the presence of an iridium hydride in terminal position has a drastic impact on the distortion of the Cp* ring since the Al-Ir-Cp*_{centroid} angle for conformer **15A** is equal to 136.7° while this parameter is at 177.7° in conformer **15B**. Therefore, the experimental titling of the Cp* ring (143.8° in the crystallographic structure) is in line with the one calculated for conformer **15A** and strongly suggest that complex **15** adopts the conformation of **15A** in the solid state.

Note that NPA and WBI calculations are also conducted for conformer **15A** showing values (for Ir-H, Al-H, and Ir-Al) close to those of cluster **14**. As a consequence, the intermetallic bonding situation in conformer **15A** is similar to that of complex **14**.

3.4 Conclusion

In this chapter, we have described the stepwise alkane elimination strategy for the preparation of a series of well-defined iridium aluminum polyhydrides species of various nuclearities and compositions, starting from IrCp*H₄ and Al(ⁱBu)₃ or Al(OAr)(ⁱBu)₂. In the case of TIBA, tri- and tetranuclear Ir_nAl_m (n=2 or 3, m=1 or 2) clusters – compounds **11-14** – featuring original structures have been obtained. Exchange reactions from one species to another can be achieved by adjusting the correct Ir:Al stoichiometry, through the addition of either IrCp*H₄ or TIBA (e.g. **13** + 1 eq. of Al(ⁱBu)₃ gives **11** then **12**). Clusters **11-14** are therefore labile polymetallic assemblies, as testified by these metal/ligand redistribution reactions. Increasing the steric hindrance around the Al³⁺ center, through the implementation of a bulky aryloxy ligand, proved successful to prevent oligomerization and allowed to obtain a dinuclear Ir-Al heterobimetallic complex – compound **15**.

– DFT studies have been performed on these series of Ir-Al species to better understand the electronic structure of these molecules. The bonding situation can vary in these systems, from a direct *d*-electron donation of Ir to the Al atom (Z-type ligand, see case i) in Scheme 9), to 3-centre 2-electron hydride-bridged Lewis adducts Ir→HAl (see mesomeric form ii) in Scheme 9). Both types of interactions are at place to some extent in each of these species.^[8] Importantly, these interactions are polarized such as the negative charge is localized at the Ir site(s), while the positive charge is found at the Al site(s).

All these compounds are thus best described as a combination of iridate fragment(s) with cationic Al(III) moieties. For instance, complex **14** is a rare case of an Al³⁺ cationic center bound to 3 [IrCp*(μ-H)₂(H)] fragments *via* 6 bridging hydrides. This bonding situation appears opposite to that observed for most transition metal aluminohydride species where the polarity is reversed, and that are best depicted as [AlH_{x+3}]^{x-} and L_nM⁺ moieties. For instance, binary hydride materials, such as Li₃AlH₆, consist of [AlH₆]³⁻ octahedra surrounded by three Li⁺ cations. The bonding situation in Li₃AlH₆ consists in strong covalent bonding between Al and the hydrides and weaker ionic bonding between the aluminate [AlH₆]³⁻ units and the Li⁺ cations.^[254,255] Therefore, the bonding situation in these series of compounds appear unusual and could open attractive opportunities.^[8,256]

In order to consolidate these results and to gather information on the chemical behavior of compounds **11-15**, we considered studying their stoichiometric reactivity towards various reagents.

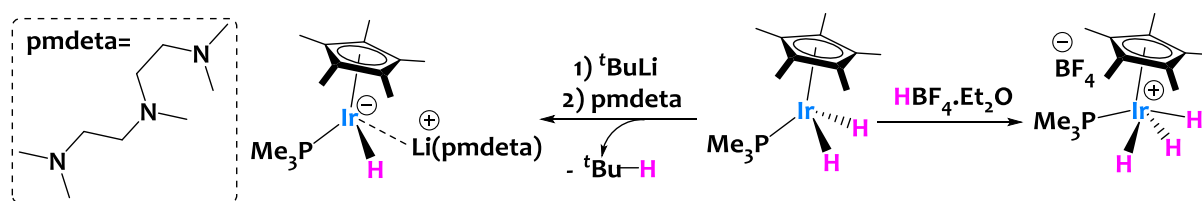
CHAPTER 4. Reactivity Studies Of Al/Ir Heterobimetallic Complexes

4.1 Introduction

In this chapter, we will present the main reactivity trends observed for the Ir-Al species described in CHAPTER 3 (mainly the archetypal compounds **12**, **14**, and **15**). The reactivity study of these complexes is relevant for many reasons:

i) As mentioned in CHAPTER 1, in a number of heterobimetallic Al/M assemblies the role of the Lewis acidic Al center is to provide an electrophilic assistance in cooperatives processes where the aluminum plays a promoting role. Therefore, it is important to experimentally evaluate the electrophilic character of the Al sites in these complexes for potential uses in reactivity or catalysis. Generally, the electrophilic character of Al(III) species is studied throughout their reaction with common Lewis bases (such as pyridine derivatives).

ii) Iridium hydrides can be acidic, basic, or amphoteric with respect to the Brønsted-Lowry acid-base definition. For instance, R.G. Bergman *et al* reported in 1985 the amphoteric behavior of a dihydride iridium species (Scheme 62).^[257] Indeed, $\text{IrCp}^*\text{H}_2(\text{PMe}_3)_3$ can be deprotonated by a strong base such as *tert*-butyl lithium in the presence of a chelating agent (pmdeta=*N,N,N',N'',N'''*-pentamethyldiethylenetriamin), to yield a monohydride iridate species with evolution of *tert*-butane (Scheme 62, left). Conversely, treatment of $\text{IrCp}^*\text{H}_2(\text{PMe}_3)_3$ with tetrafluoroboric acid yields a protonated cationic tris-hydride iridium species stabilized by a non-coordinating tetrafluoroborate counterion (Scheme 62, right). Note that R.H. Morris, L. Bonneviot, and their coworkers reported similar behaviour concerning a pentahydride iridium species – $\text{IrH}_5(\text{PR}_3)_2$.^[258,259] Consequently, it is interesting to get deeper insights into the iridium-hydride reactivity in these Ir-Al clusters in view of uses in SOMC and catalysis.



Scheme 62. Reported deprotonation (left) or protonation (right) of $\text{IrCp}^*\text{H}_2(\text{PMe})_3$.^[257]

iii) Alkyl aluminum moieties can also be reactive. As described in CHAPTER 2, section 2.2.4 (from page 116), the Al-C_{alkyl} bond can be cleaved upon reaction with strong Lewis acids such as $\text{B}(\text{C}_6\text{F}_5)_3$. Alkyl aluminum moieties can also be subjected to protonolysis reactions. Therefore, it is also relevant to gain insight into the reactivity of isobutyl aluminum groups in these clusters.

iv) It could also be interesting to study if these species are redox-active. Indeed, iridium can be

stable in different oxidation states varying from -III to +V. On the other hand, as mentioned in CHAPTER 1, aluminum is, most of the time, in a stable oxidation state of +III although research works beginning in the 1980s have shown the possibility of forming Al species with a formal oxidation state of +I or +II.^[130,260]

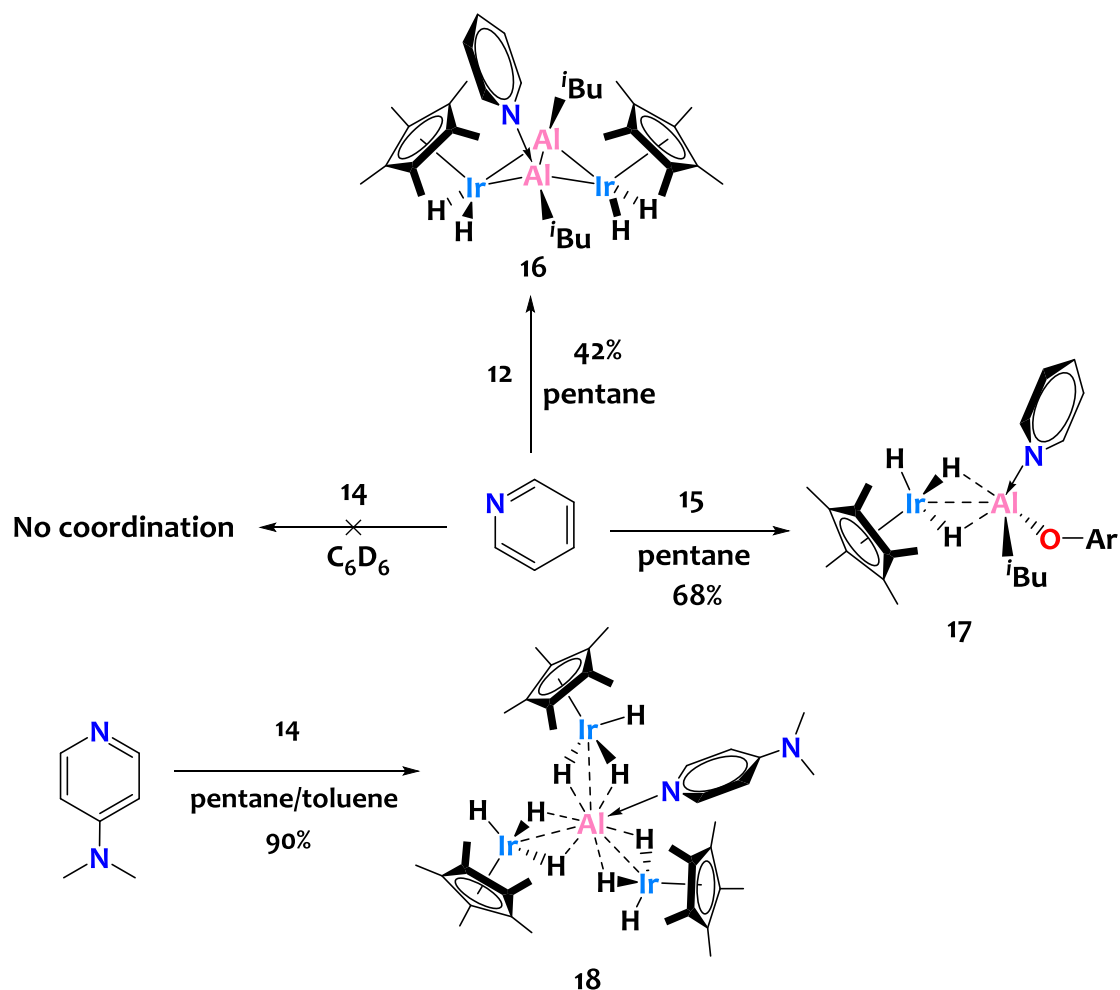
v) Last but not least, since one of the objectives of this project is to increase our fundamental understanding of bimetallic cooperative activation processes, we considered studying the activation of small molecules such as heteroallenes (CO_2 , R-N=C=O , R-N=C=N-R).

The next sections of this chapter will follow the essence of points i), ii), iii), iv) and v).

4.2 Reactivity towards Lewis bases and nucleophiles

4.2.1 Reactivity with pyridine derivatives

In view of understanding the behavior of Ir-Al complexes towards donor ligands, we first studied the reactivity of three archetypal species - compounds **12**, **14**, and **15** - towards typical L-donors like pyridine or 4-dimethylaminopyridine (DMAP). The obtained outcomes are summarized in Scheme 63.



Scheme 63. Stoichiometric treatment of Ir-Al species **12**, **14**, and **15** with pyridine derivatives.

4.2.1.1 Synthesis of a mono-adduct $[\text{Ir}_2(\text{Cp}^*)_2(\text{H}_2)_2\text{Al}_2(\text{Py})(i\text{Bu})_2]$, species **16**

Treatment of **12** with 1 equivalent of pyridine leads to the pyridine mono-adduct **16** (Scheme 63, top). When excess amounts of pyridine are added onto **12**, several species are observed by ^1H NMR spectroscopy monitoring in solution, most likely corresponding to poly-pyridine adducts, yet upon drying *in vacuo* the mono-adduct **16** is obtained quantitatively. Isolation of **16** as a pure dark orange crystalline material is performed by a cold recrystallization of the crude solid in the minimum amount of toluene. The ^1H -NMR spectrum of **16**, recorded in C_6D_6 solution, is quite similar to dimer **12** except it features shifted pyridine signals at $\delta = 8.72$, 6.81 and 6.55 ppm indicating its coordination to Al in solution (Figure 49).

The DRIFT spectral signature of **16** is also similar to that of **12** (Figure 46), with appearance of a new $\nu_{\text{Ir-H}}$ band at $\sigma=2112$ cm^{-1} assigned to an asymmetric stretching mode as a result of desymmetrization of the complex upon pyridine ligation.

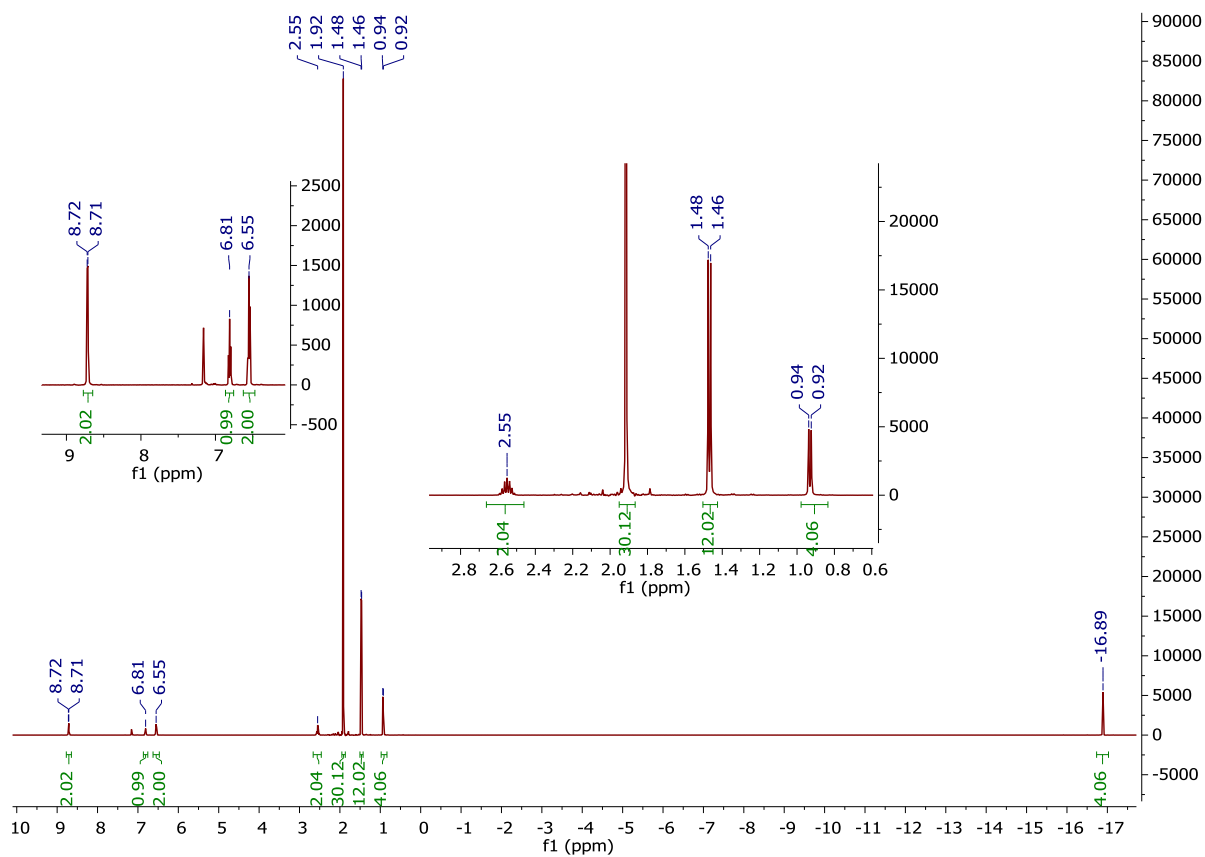


Figure 45. $^1\text{H-NMR}$ spectrum (500 MHz, C_6D_6 , 293K) of adduct 16

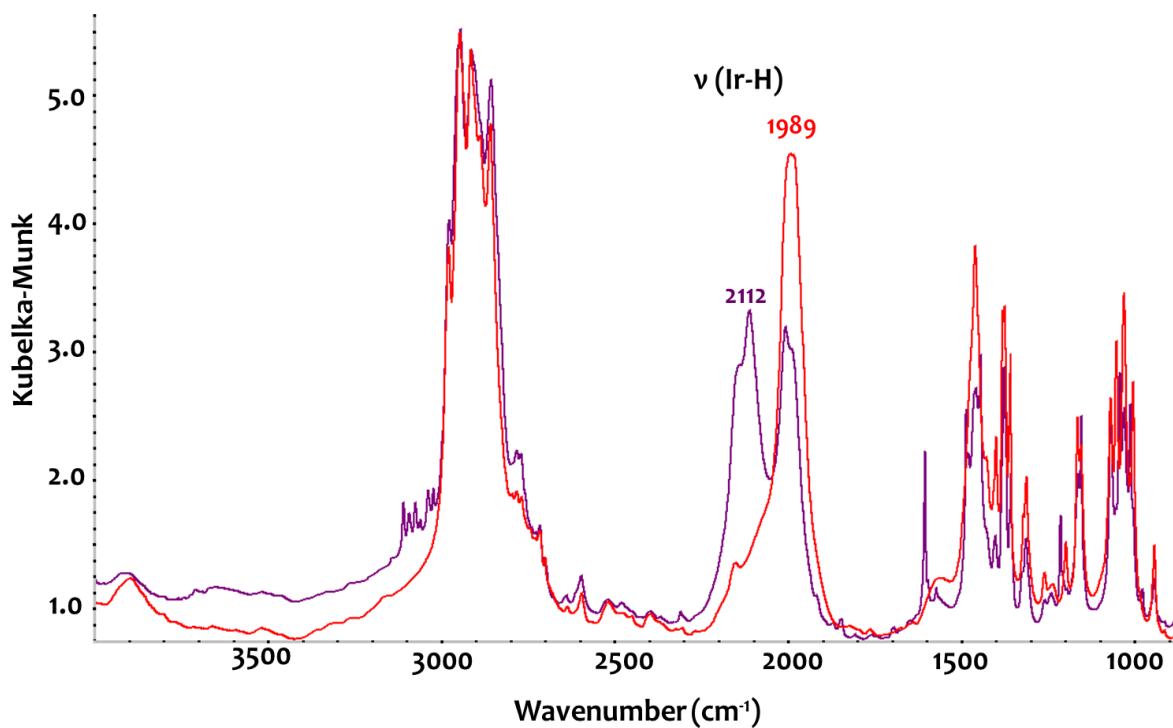


Figure 46. DRIFT spectra (298K, diluted in KBr, under argon) of the pyridine adduct 16 (purple) vs complex 12 (red).

The coordination of pyridine to one Al Lewis acidic center is confirmed by the crystallographic structure of **16** (see Figure 47). The Al2-N1 bond length (2.070(3) Å) is in the expected range.^[30] The pyridine ligation to Al2 imparts a substantial distortion of the tetranuclear Al₂Ir₂ core with respect to **12**. This notably results in an elongation of the Ir-Al2 distances (2.53(1) Å) and a shortening of the Ir-Al1 distances (2.42(1) Å). This rearrangement could explain why a subsequent pyridine ligation onto Al1 is less favorable. Parameter α is equal to 153.48° (Figure 26), suggesting the presence of some terminal iridium-hydrides as discussed in precedent cases in CHAPTER 3. The coordination of pyridine onto **12** to form adduct **16** is in line with the presence of an accessible empty p-orbital on the aluminum centers and confirm their Lewis acidity.

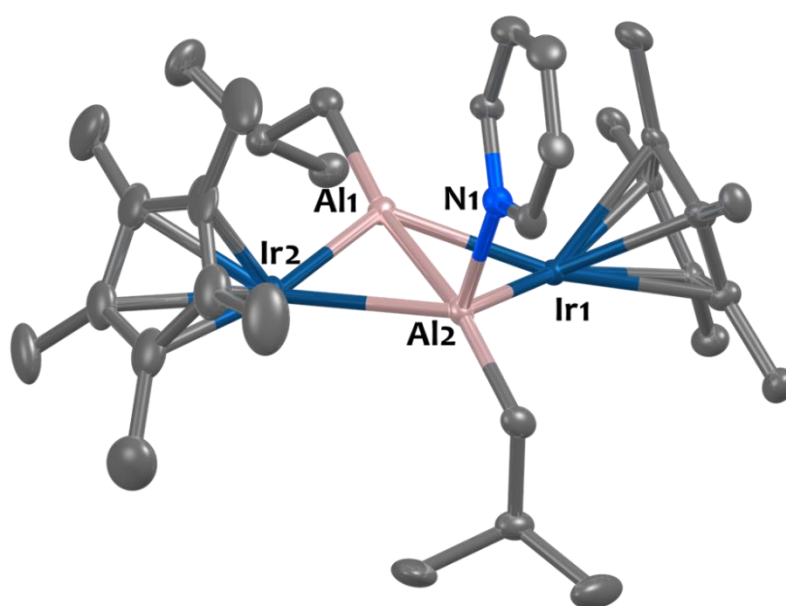


Figure 47. Solid-state molecular structure of **16**. Displacement ellipsoids are plotted at a 30% probability level. Hydrogen atoms have been omitted for clarity. Two independent molecules were found in the asymmetric unit ($Z' = 2$) but one of them have been omitted for clarity. Selected bond distances (Å) and angles (°) averaged between both molecules: Ir1-Al1 2.426(3), Ir1-Al2 2.535(8), Ir2-Al1 2.422(8), Ir2-Al2 2.522(3), Al1-Al2 2.651(4), Al2-N1 2.070(3). (Ir1-Al1-Ir2-Al2)_{centroid}-Ir1-Cp*_{centroid} 152.37, (Ir1-Al1-Ir2-Al2)_{centroid}-Ir2-Cp*_{centroid} 154.58.

4.2.1.2 Synthesis of an heterobimetallic mono-adduct [Ir(Cp*)(H)₃Al(Py)(OAr)(ⁱBu)], **17**

Similarly, the stoichiometric reaction of pyridine with the heterobimetallic complex **15** leads to a compound, [Ir(Cp*)(H)₃Al(Py)(OAr)(ⁱBu)], **17**, which is isolated in 68% yield by a cold recrystallization in pentane (Scheme 63, right).

The molecular structure of complex **17** is underpinned by multi-nuclei NMR and IR spectroscopies, elemental analysis, X-Ray diffraction analysis and DFT studies. The ¹H-NMR spectrum of **17** is for most part similar to that of **15** with a typically shielded hydride signal integrating for 3H at

$\delta = -17.26$ ppm. However, the DRIFT spectrum of **17** is quite different to that of **15** with appearance of new Ir-H stretches at $\sigma \sim 2100$ cm^{-1} and absence of ν Ir-H bands at wavenumbers ranging from 1900 to 2100 cm^{-1} (Figure 48).

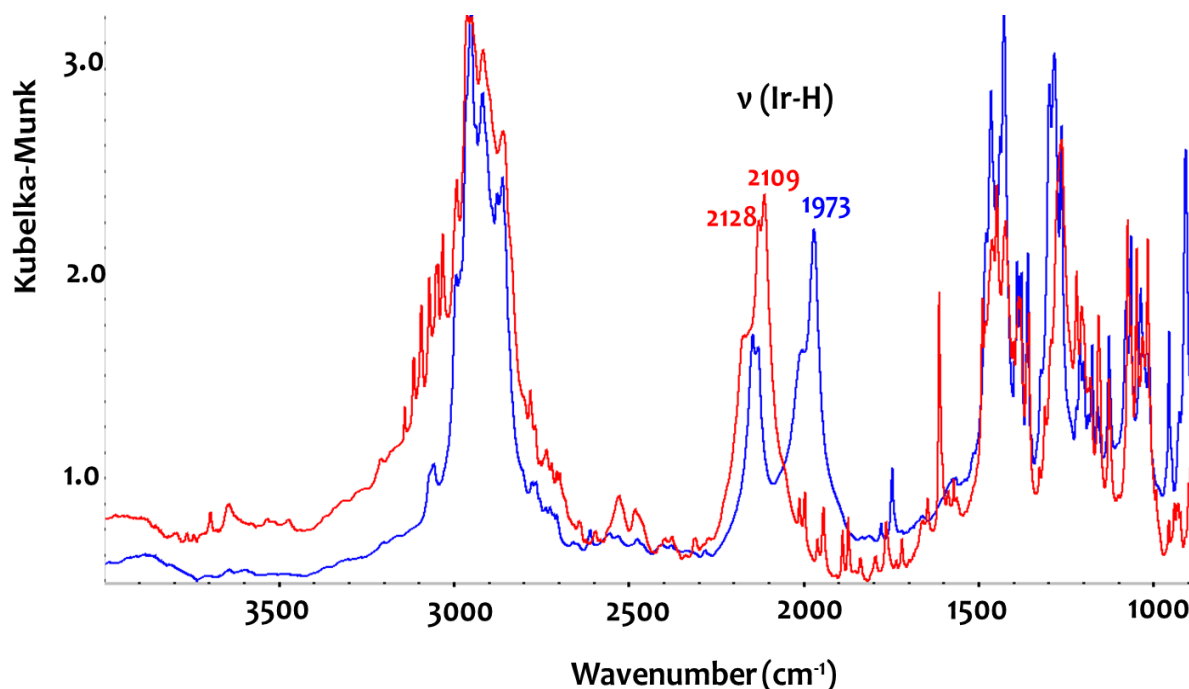


Figure 48. DRIFT spectra (298K, diluted in KBr, under argon) of adduct **17** (red) vs complex **15** (blue).

Colorless block single crystals of **17** suitable for XRD studies are grown by slow recrystallization of **17** in a cold octane/toluene (7/1) mixture. Its solid-state molecular structure (Figure 49) confirms the N-coordination of the pyridine onto aluminum, with an Al1-N1 bond length (2.032(7) Å) in the expected range.^[65,114] The Al cation adopts a pseudo-tetrahedral geometry with angles lying in the [92.6(3)°-119.9(2)°] range. The pyridine donation to Al results in an elongation of both the Al1-O1 bond (1.695(4) Å in **15** vs 1.776(6) Å in **17**) and the Al1...Ir1 distance from 2.406(2) Å in **15** to 2.502(2) Å in **17**. Note that the formal shortness ratio for the Ir-Al parameter (FSR=0.998)^[240] is at unity still indicating a strong interaction between the Cp*IrH₃ and Al(ⁱBu)(OAr)(Py) fragments. The acute bending of the Cp* ring with respect to the Ir-Al axis (Cp*_{centroid}-Ir-Al angle of 138.73° in **17** vs 143.79° in **15**) suggests a terminal coordination of at least one of the hydrides.

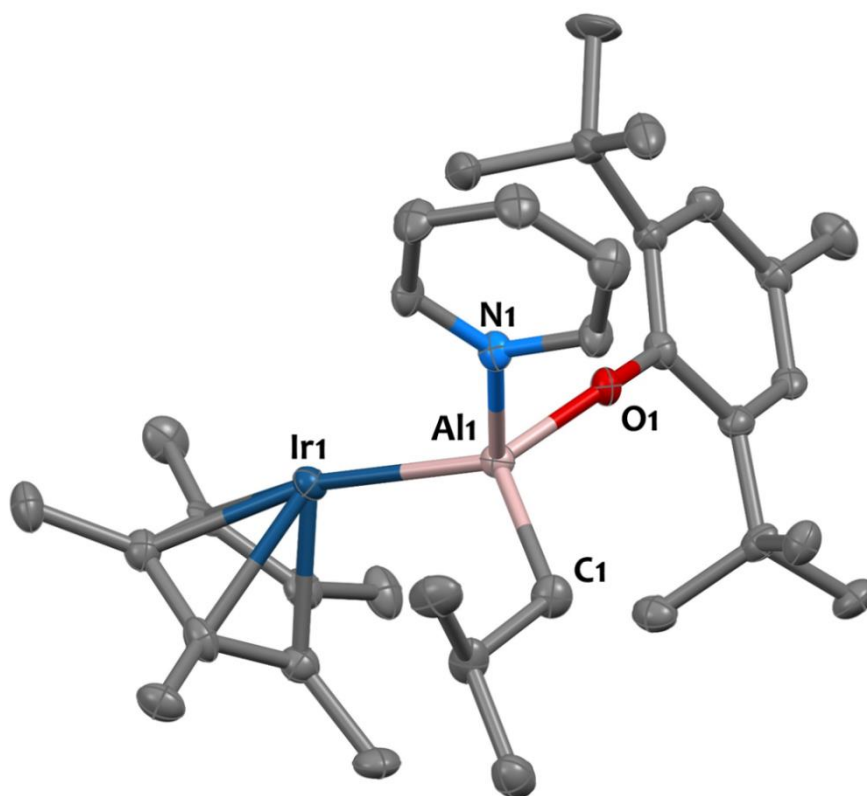


Figure 49. Solid-state molecular structure of **17**. Displacement ellipsoids are plotted at a 30% probability level. Hydrogen atoms have been omitted for clarity. Selected bond distances (Å) and angles (°): Ir1-Al1 2.502(2), Al1-O1 1.776(6), Al1-C1 1.986(9), Al1-N1 2.032(7), O1-Al1-Ir1 119.9(2), O1-Al1-N1 92.6(3), O1-Al1-C1 113.2(3), N1-Al1-Ir1 113.2(2), C1-Al1-Ir1 114.4(3), C1-Al1-N1 99.4(3), Al1-Ir1-Cp*_{centroid} 138.7(2).

In view of understanding nature of the Ir-Al interaction in complex **17**, DFT calculations (B3PW91) are undertaken. The bonding situation is very similar in **17** and **15**. Indeed, like compound **15** (see section 3.3.3, page 157), two similar isoenergetic structures are found for **17** (Figure 50). The most stable structure, **17A**, exhibits two bridging hydrides and one terminal Ir-H whereas the second isomer (+0.5 kcal/mol), **17B**, displays three μ -H. Similarly as complex **15**, the structural parameters (Table 5) of conformer **17A** are in accordance with the experimental crystallographic structure of **17** (Computed Cp*_{centroid}-Ir-Al = 142.6° vs 138.7° experimental; Computed Ir-Al distance = 2.515 Å vs 2.502 Å experimental). To go further, Natural Bonding Orbital (NBO) and Natural Population Analyses (NPA) as well as Wiberg Bond Indexes (WBIs) are computed. NBO analyses of the two isomers unambiguously indicate the presence of three covalent Ir-H interactions (with 50 to 58% contribution from Ir *spd* hybrid orbital). At the second order donor-acceptor level, donations from the Ir-H bonds as well from the Ir *d* lone pairs into the Al empty *sp* orbital are noticed in line with the presence of 3-center 2-electron (3c-2e) Ir-H-Al bonds as well as some Ir-Al interaction. The latter is corroborated by the analysis of the WBIs. The Ir-H WBIs are around 0.7, in agreement with mainly covalent interaction, whereas the Al-H one are close to 0.12-0.15 in line with electron

delocalization from the Ir-H bond onto an acceptor orbital on Al. Interestingly, the Ir-Al WBI is around 0.3, which is in accordance with some bonding interaction between Ir and Al. The NPA charge on iridium is significant in both cases (**17A** and **17B**), taking values of -1.033 and -0.882 respectively while the effective charges on the aluminum centers are +1.932 and +1.874 respectively.

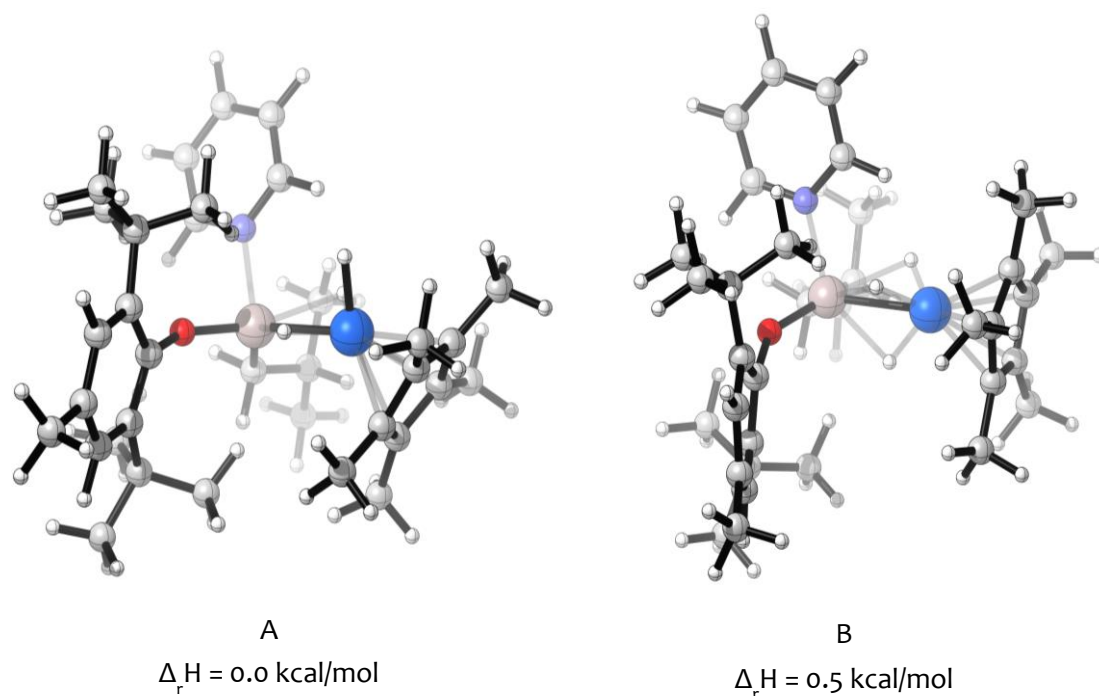


Figure 50. Calculated structures (A and B) for the two conformers of complex 17.

	Conformer 17A	Conformer 17B
NPA charges	Al: 1.93 / Ir: -1.033	Al: 1.87/ Ir: -0.88
WBIs	Ir-H: 0.70 / Ir-Al: 0.34 / Al-H(μ): 0.12	Ir-H: 0.70 / Ir-Al: 0.34 / Al-H(μ): 0.12
Ir-H distances (Å)	1.583 / 1.599 / 1.606	1.610 / 1.611 / 1.615
Al-H distances (Å)	2.051 / 2.072	1.983 / 2.010 / 2.125
Ir-Al distances (Å)	2.515	2.496
Cp*_{centroid}-Ir-Al angle (°)	142.6	175.3

Table 5. Computed NPA charges, Wiberg bond indexes (WBIs), and structural data of conformers 17A and 17B.

Consequently, this analysis is congruent with the DTF calculations regarding the other molecular Ir-Al edifices of this PhD work. This is also consistent with the works of M. R. Crimmin and S. Aldridge on related M-Al (M = Rh, Au) complexes. Indeed, a substantial negative charge on the transition metal is reported in these cases, as well as similar WBIs.^[87,261] These data support therefore the description of **15** and **17** as containing a strongly polarized iridate core, stabilized by Ir-H donation to the $[\text{Al}(\text{iBu})(\text{OAr})\text{Py}_x]^+$ ($x = 0,1$) fragment. This formalism is also consistent with the Pauling electronegativity gap between iridium and aluminum (2.20 vs 1.61, respectively). The strong polarity of these $\text{Ir}^{\delta-}\text{-Al}^{\delta+}$ pairs results in a substantial nucleophilic character of the Ir center, as confirmed by the reactivity studies described below.

4.2.1.3 Fromation of adduct $[\{\text{Cp}^*\text{Ir}(\text{H})(\mu\text{-H}_2)\}_3\text{Al}(\text{DMAP})]$, **18**

On the opposite, cluster **14** does not react with pyridine even after heating to 80°C in C_6D_6 (Scheme 63). We therefore contemplated the use of a stronger electron donor such as DMAP. Gratifyingly, stoichiometric treatment of **14** with DMAP leads to the adduct $[\{\text{Cp}^*\text{Ir}(\text{H})(\mu\text{-H}_2)\}_3\text{Al}(\text{DMAP})]$, **18**, isolated in 90% yield (Scheme 63).

Coordination of DMAP onto the Al center is first supported by NMR spectroscopy. Indeed, the ^1H -NMR spectrum of **18** displays new Cp* and Ir-H signals ($\delta=2.14$ ppm and -16.47 ppm respectively) in comparison to those of cluster **14** ($\delta=2.11$ ppm and -16.38 ppm respectively). DMAP resonances ($\delta=8.64$ ppm, 6.04 ppm, and 2.15 ppm; see left side of Figure 51) are also shifted with respect to those of free DMAP ($\delta=8.47$ ppm, 6.11 ppm, and 2.23 ppm; see right side of Figure 51). Similar trends are noticed by ^{13}C -NMR spectroscopy. These observations thus suggest ligation of DMAP onto the Al center in solution.

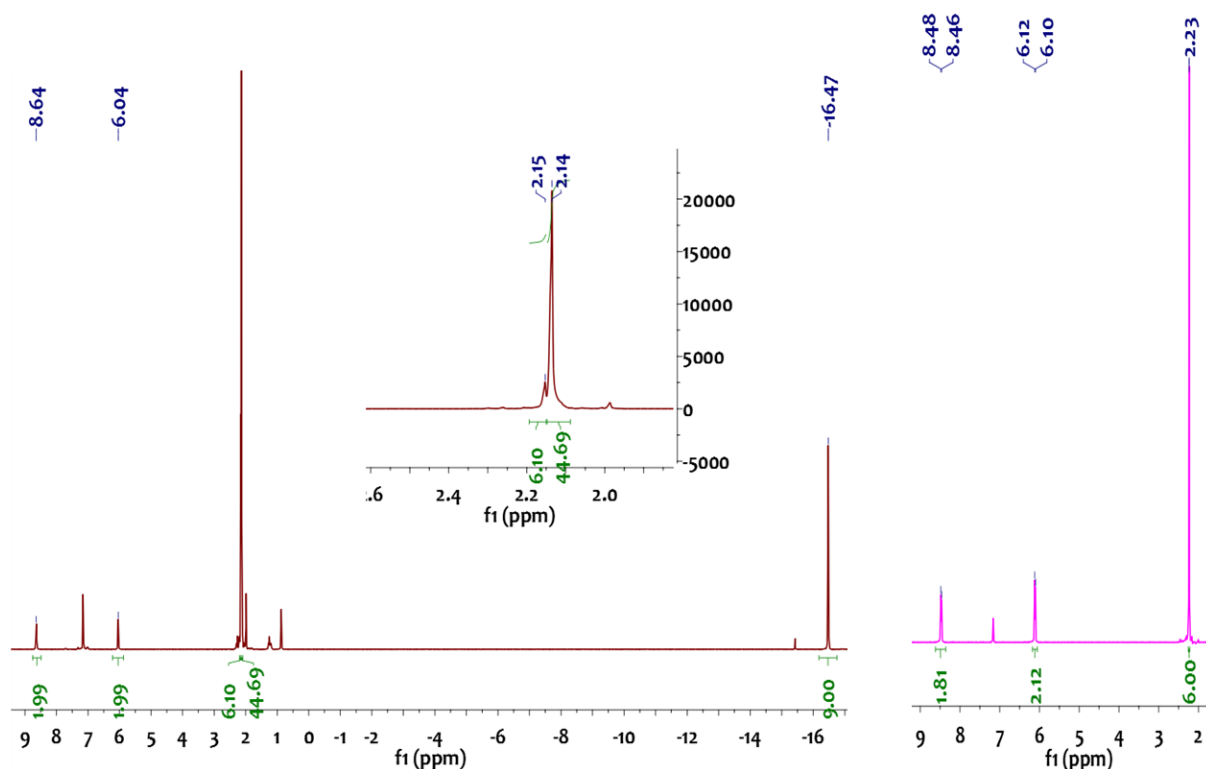


Figure 51. (Red line) $^1\text{H-NMR}$ spectrum (500 MHz, C_6D_6 , 293K) of adduct **18**. (Pink line) $^1\text{H-NMR}$ spectrum (300 MHz, C_6D_6 , 293K) of DMAP.

Other insights regarding the identity of **18** are provided by DRIFT spectroscopy. Indeed, the IR spectrum of **18** shows two Ir-H stretches at 2149 cm^{-1} and 2111 cm^{-1} , which are shifted compared to that in cluster **14** ($\sigma = 2158\text{ cm}^{-1}$ and 2015 cm^{-1}) suggesting a new chemical environment around the hydrides.

The solid-state molecular structure of **18** is established by X-ray diffraction (Figure 52). It first confirms the DMAP ligation to the Al site, which induces a pyramidalization of the Al center (average Ir-Al-Ir angle of $114(3)^\circ$) and an elongation of the Ir-Al distances ($2.56(2)\text{ \AA}$ in **18** vs $2.47(1)$ in **14**), as expected. Parameter β (Figure 37) is equal to 137.5° , which is quite close to that of species **14** (140.6°), suggesting one terminal and two bridging hydrides per iridium center.

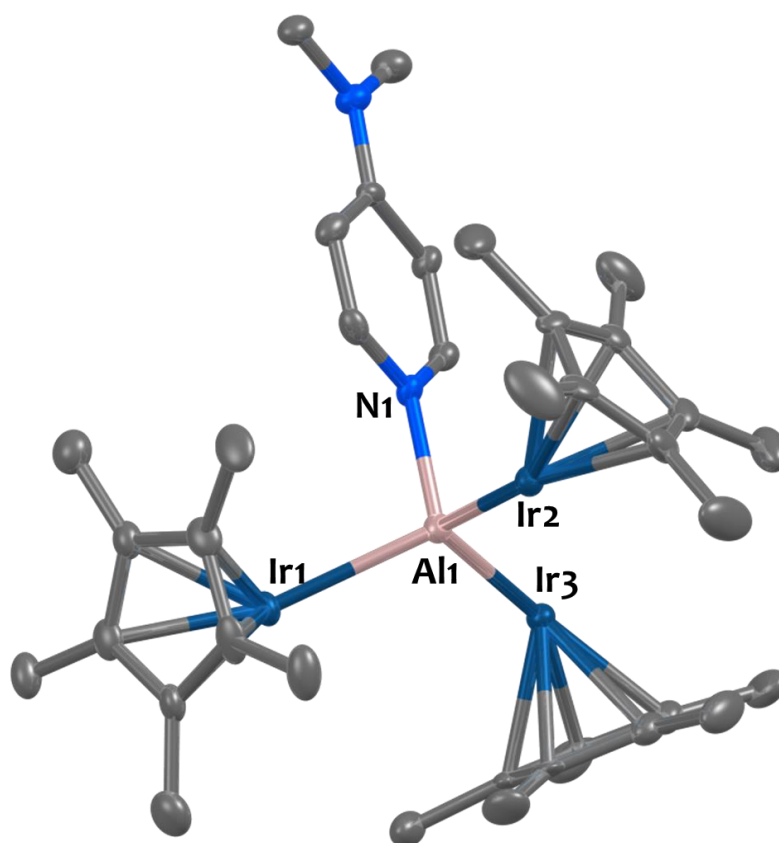


Figure 52. Solid-state molecular structure of compound 18. Ellipsoids are represented with 30% probability. Hydrogen atoms have been omitted for clarity. Two independent molecules were found in the asymmetric unit ($Z'=2$) but one of them has been omitted for clarity. Selected bond distances (Å) and angles ($^{\circ}$) have been averaged between both independent molecules: Ir1-Al1 2.567(3), Ir2-Al1 2.580(3), Ir3-Al1 2.550(3), Al1-N1 2.040(3), Ir1-Al1-Ir2 110.97(5), Ir1-Al1-Ir3 115.44(5), Ir3-Al1-Ir1 116.22(5), β parameter 137.5 (see Figure 37).

4.2.1.4 Conclusions

To sum up, the Al sites in complexes **12** and **15** are Lewis acidic, and are subjected to N-coordination of pyridine, which results to the clean formation of mono-adducts **16** and **17** respectively. These investigations highlight therefore a strong electrophilic character of aluminum centers in these systems. No coordination of pyridine (even after strong heating in presence of excess pyridine) was noticed onto cluster **14** (Scheme 63). In that case, only the use of a stronger neutral donor, namely DMAP, allowed to get such reactivity. This indicates that the environment around the Al(III) center in species **14** is still flexible enough to accommodate an extra Lewis base donor. Importantly, the coordination of pyridine or DMAP does not result in the dissociation of these clusters to form ion pairs.

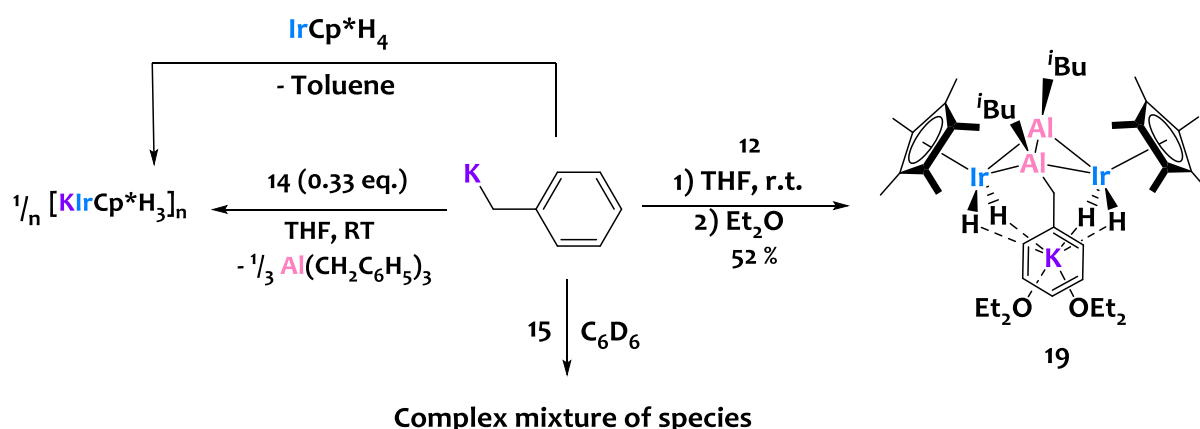
4.2.2 Reactivity with benzyl-potassium and silver triflate

Reactivity of the same archetypal complexes **12**, **14**, and **15** towards benzyl potassium and silver triflate (AgOTf) has also been studied. While benzyl-potassium is mainly known as a strong Brønsted base, it can also act as a nucleophile through the aliphatic carbanion lone pair. AgOTf is known as an oxidizing agent but can also act as a transmetallating agent or as a nucleophile through the sulfonate lone pair.

4.2.2.1 K-Benzyl

Reactivity of species **12**, **14**, and **15** towards benzyl potassium are sum up on Scheme 64.

R. G. Bergman and A. L. Rheingold have shown that in the presence of strong bases (typically organolithium reagents), Ir-H species could be deprotonated, to yield highly reactive iridate derivatives.^[257,262-264] Likewise, the reaction of Cp*IrH₄ with benzyl potassium (Scheme 64, top left) quantitatively yields the potassium iridate species {K[Cp*IrH₃]}_n, together with toluene. The structure of {K[Cp*IrH₃]}_n is inferred from spectroscopic data which are similar to that of the lithium analogue, and especially a strongly shifted ¹H NMR hydride signal at -19.29 ppm (see Figure 53), versus -19.27 ppm in (Cp*IrH₃Li(pmdeta));^[265] and a shielded ¹³C{¹H} NMR Cp* signal at 85.2 ppm, versus 87.4 ppm in (Cp*IrH₃Li(THF)_x).^[181] The DRIFT spectrum of {K[Cp*IrH₃]}_n displays a very intense and broad νIr-H band at σ=2018 cm⁻¹, alike that of (Cp*IrH₃Li(THF)_x) (σ=2019 cm⁻¹).^[181] Unfortunately, single crystals of {K[Cp*IrH₃]}_n could not be obtained despite several attempts.



Scheme 64. Reactivity of complexes IrCp*H₄, **12**, **14**, and **15** with K-benzyl.

In the cases of clusters **12** and **14**, we do not observe deprotonation of the hydrides.

Instead, treatment of cluster **14** with 3 equivalents of benzyl potassium also leads to the

transmetallated product $\{K[Cp^*IrH_3]\}_n$ obtained together with the putative $Al(CH_2C_6H_5)_3$ species (see 1H NMR spectrum in Figure 53). When **14** is treated with 1 or 2 equivalents of benzyl potassium, $K[Cp^*IrH_3]$ is also formed, together with a complex mixture of species, most likely due to benzyl transfer to aluminum and ligand redistribution phenomena. This reactivity is reminiscent of the $[Cp^*IrH_3]/$ alkyl exchange process described in the preparation of compound **13** from treatment of **14** with $Al(iBu)_3$ (see paragraph 3.2.2, page 146).

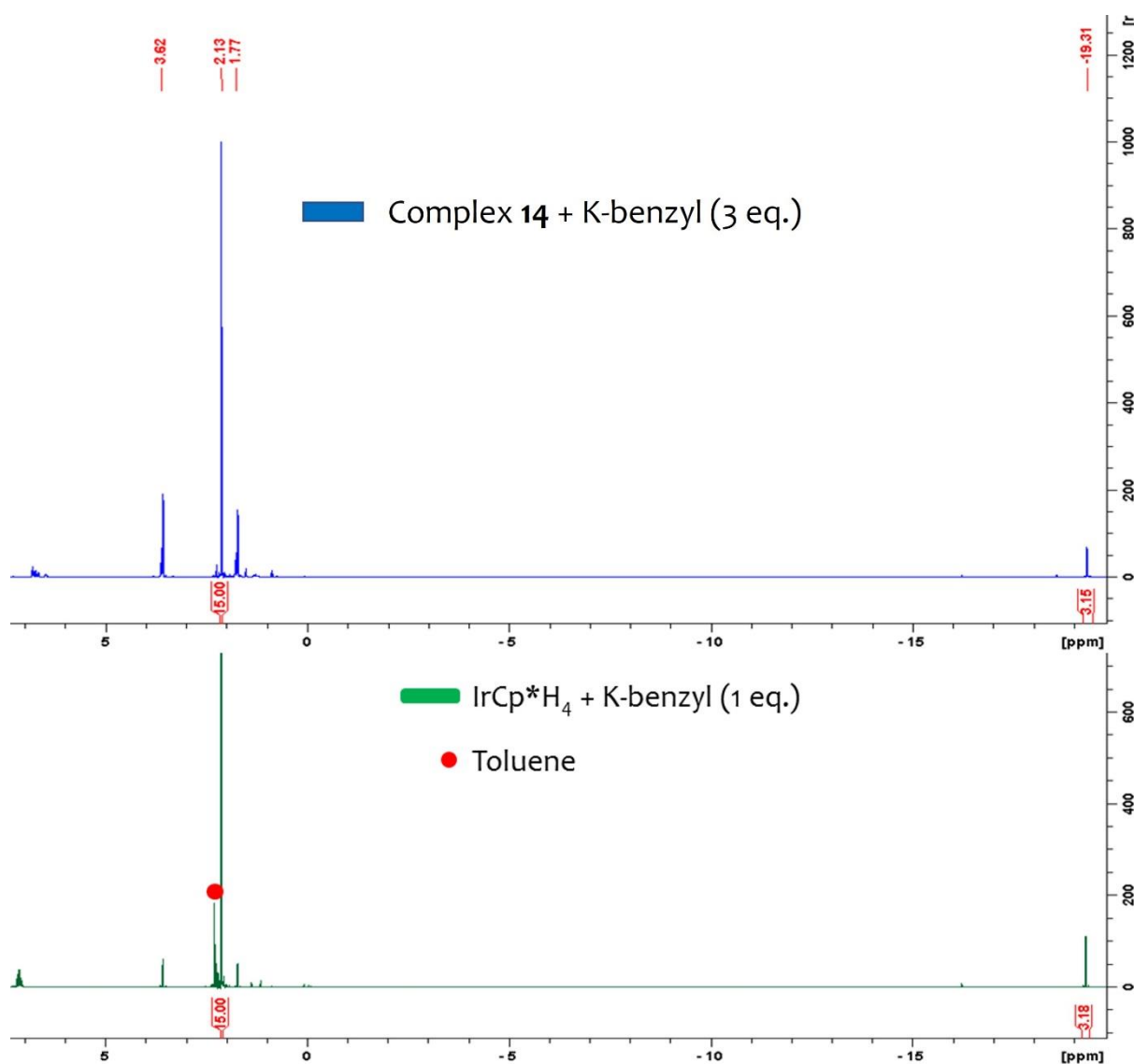


Figure 53. 1H -NMR spectra (300 MHz, THF- d_8 , 293K) of $[IrCp^*H_3K]_n$ compound. Blue line: originating from the reaction of complex **14** with 3 equivalents of benzyl potassium in THF (200 mg scale reaction). Green line: originating from the in-situ stoichiometric reaction of $IrCp^*H_4$ with K-benzyl in THF- d_8 (NMR-scale reaction), releasing toluene.

Next, stoichiometric treatment of **12** with K-benzyl in THF neither led to deprotonation nor to transmetallation reactions but rather to the nucleophilic addition of the benzyl anion onto the electrophilic aluminum center, to form the alkylated aluminate species **19** (Scheme 64, right).

Complex **19** is isolated as yellow block crystals after a cold ($-40^\circ C$) recrystallization in diethyl ether.

The $^1\text{H-NMR}$ spectrum of **19**, recorded in THF-d_8 (Figure 54), displays two new aromatic signals at $\delta = 7.00$ and 6.65 ppm, integrating for 4H and 1H respectively and supporting the coordination of the benzyl anion. The hydrides signal is noticeably shielded compared to that of **12** (-18.35 ppm for **19** vs -16.68 ppm for **12**) suggesting interactions of the potassium cation with hydrides. DRIFT spectrum of **19** displays new Ir-H stretches at $\sigma=2001$ and 2140 cm^{-1} compared to that of **12**. This phenomenon could be assigned to a desymmetrization of Ir_2Al_2 core upon ligation of the benzyl anion fragment. The solid-state molecular structure of **19** (Figure 55), determined by X-ray diffraction, confirms all the aforementioned aspects. Indeed, the ligation of the benzyl fragment onto the Al center is verified with an $\text{Al-C}_{\text{benzyl}}$ distance of $2.055(9)$ Å, falling in the expected range.^[266] The potassium cation is coordinated to the benzyl ring and stabilized by two diethyl ether molecules. This results in a noticeable distortion of the $[\text{Ir-Al}]_2$ core when compared to **12**, with an elongation of the Ir-Al₂ distances and a shortening of the Ir-Al₁ distances, alike that seen in the pyridine adduct **16**. The twisting of the Cp* rings ($\alpha = 154.0(1)^\circ$, Figure 26) is close to the that in complex **2** ($\alpha = 151.5(1)^\circ$), and accordingly we propose terminal Ir-H descriptions.

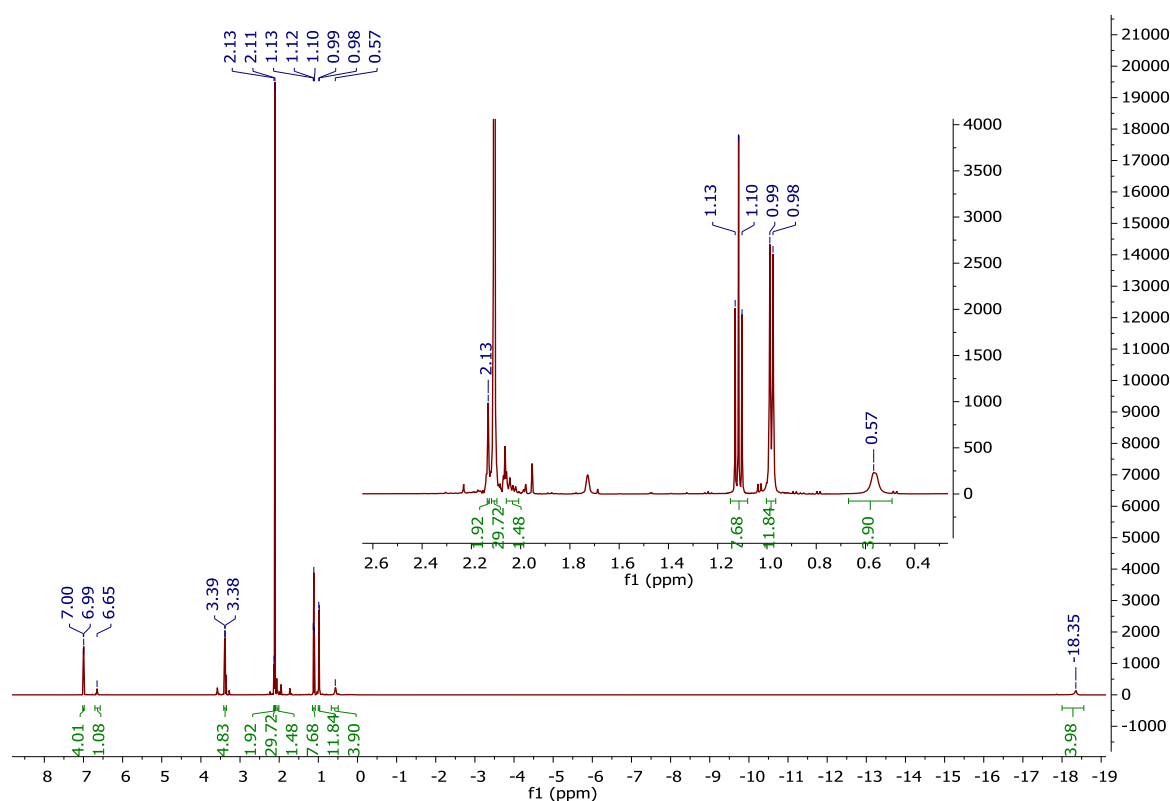


Figure 54. $^1\text{H-NMR}$ spectrum (500 MHz, THF-d_8 , 293K) of compound **19**

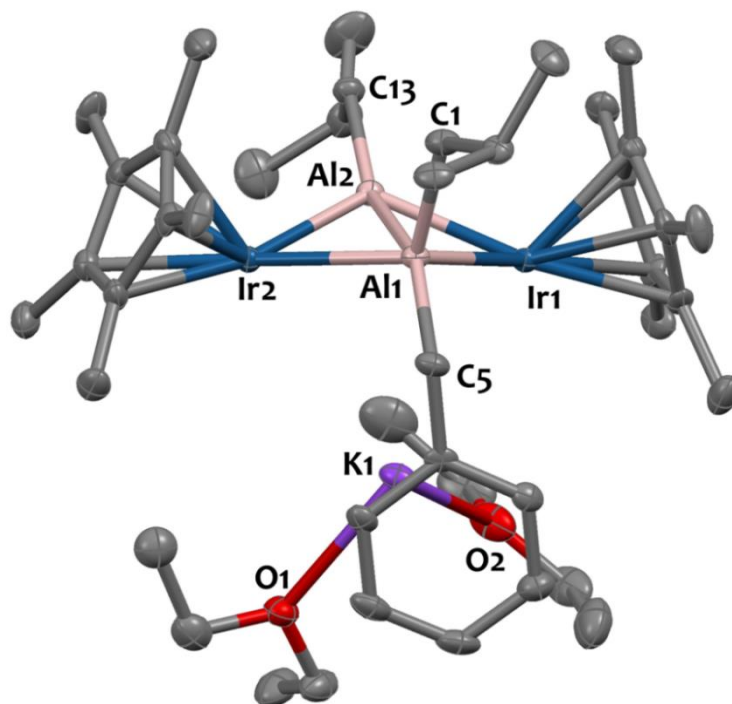


Figure 55. Solid-state molecular structure of 19. Displacement ellipsoids are plotted at a 30% probability level. Hydrogen atoms have been omitted for clarity. Selected bond distances (Å) and angles (°) Ir1-Al1 2.650(2), Ir1-Al2 2.424(2), Ir2-Al1 2.601(2), Ir2-Al2 2.410(2), K1-O1 2.750(7), K1-O2 2.759(8), Al1-Al2 2.657(3), Al1-C1 2.017(9), Al1-C5 2.055(9), Al2-C13 1.977(9), Al2-Ir1-Al1 62.98(8), Ir2-Al1-Ir1 102.60(8) Al2-Ir2-Al1 63.93(8), (Ir1-Al1-Ir2-Al2)_{centroid}-Ir1-Cp*_{centroid} 155.57, (Ir1-Al1-Ir2-Al2)_{centroid}-Ir2-Cp*_{centroid} 152.34.

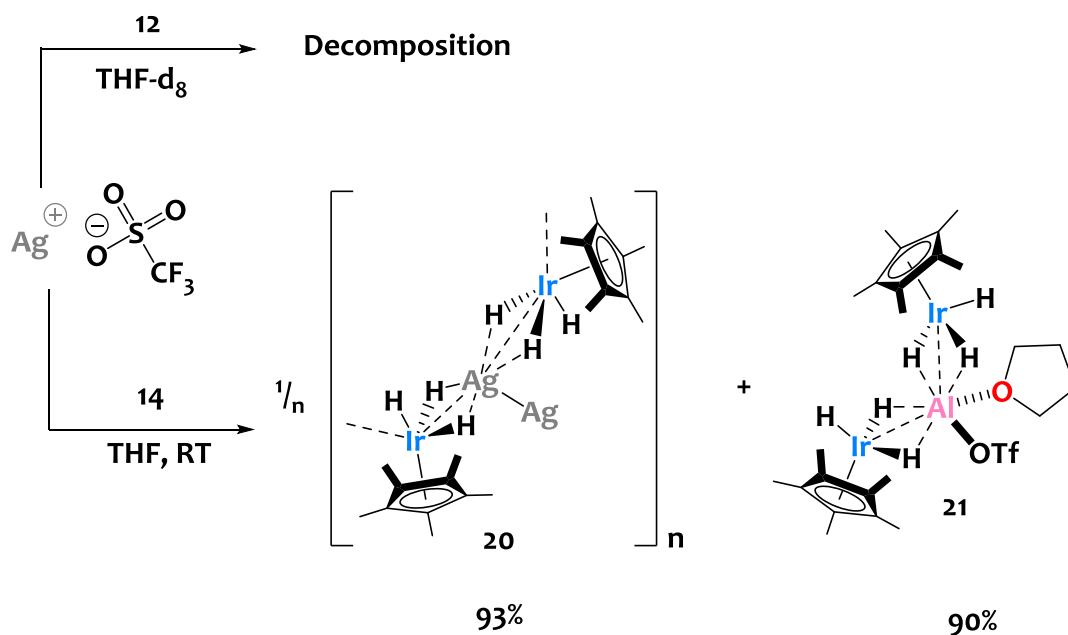
Reactivity of complex 15 with benzyl-potassium is also investigated. However, this leads to the formation of multiple products impossible to isolate (Scheme 64).

Overall, these reactions show that the Al sites in these compounds are electrophile and act as benzyl anion acceptors. [Cp*IrH₃] moieties are labile and can be displaced by benzyl ligands, resulting in the dissociation of the Ir/Al clusters. Furthermore, these experiments show that further deprotonation of the hydrides in these iridate derivatives is difficult.

4.2.2.2 Silver(I) triflate

Reactivity of clusters 12 and 14 towards silver(I) triflate is scrutinized.

The addition of 1 equivalent of AgOTf onto 14, in THF at room temperature, triggers the precipitation of cluster [AgCp*IrH₃]_n, noted 20, as a white solid and formation of product 21 that stays in solution (Scheme 65).



Scheme 65. Reactivity of complexes **12** and **14** with silver(I) triflate.

Solid **20** is isolated by filtration and characterized by different techniques. The DRIFT spectrum of **20** depicts an intense and broad metal-hydride stretching band shifted at lower wavenumbers when compared to that of compound **14** ($\sigma=1917 \text{ cm}^{-1}$ in **20** vs $\sigma=2015$ & 2158 cm^{-1} in **14**, see Figure 56). This suggests the presence of bridging Ir-(μ -H)-Ag vibrators, in accordance with literature data.^[267] ^1H NMR studies, conducted in dried deuterated pyridine (for solubility reasons), reveal a hydride signal at $\delta_{\text{H}}=-14.76$ ppm slightly shifted towards downfield values compared to that of complex **14** ($\delta_{\text{Ir-H}}=-16.39$ ppm in C_6D_6) and integrating for 3H (relative to Cp* signal).

The solid state structure of **20**, shown in Figure 58 (top), reveals an unprecedented infinite 2D-network which can be seen as two parallel zigzag chains, alternating $[\text{Ag}]^+$ and $[\text{Cp}^*\text{IrH}_3]^-$ motifs, facing each other in a head-to-tail fashion, and fused together through argentophilic interactions.^[268] Therein, the Ag1-Ag1\# distance of $2.973(3) \text{ \AA}$ falls in the range of metallophilic $4d^{10}\text{-}4d^{10}$ interactions,^[268] and thus compound **20** can be seen as $[\text{Ag}_2]^{2+}$ dications^[267] stabilized by iridate fragments. This leads to 6-membered Ag_4Ir_2 metallacycles which are fused together to give the 2D-network represented schematically in Figure 57. The Ir1-Ag1-Ir1\# angle is close to linearity ($161.72(6)^\circ$), in agreement with the strong preference for linear coordination of Ag(I), while the Ag1-Ir1-Ag1\# angle is of $102.24(2)^\circ$. The Ir1-Ag1 distance of $2.7200(4) \text{ \AA}$ is longer than the sum of the respective metallic radii (Ag: 1.339 \AA ; Ir: 1.260 \AA ; sum = 2.599 \AA).^[78] In other crystallographically characterized silver iridium complexes featuring bridging hydrides, distances between Ir and Ag vary between 2.71 \AA and 3.03 \AA .^[267,269-272] The Ir-Ag distance in **20** is in the low-end of this range,

suggesting a strong interaction which is compatible with the presence of bridging hydrides. Complexes featuring unsupported bonds between Ir centers and d^{10} Ag metal atoms are also known, and the Ir-Ag distances vary from 2.63 Å to 2.79 Å,^[273-279] thus a direct metal-metal interaction in **20** cannot be totally excluded.

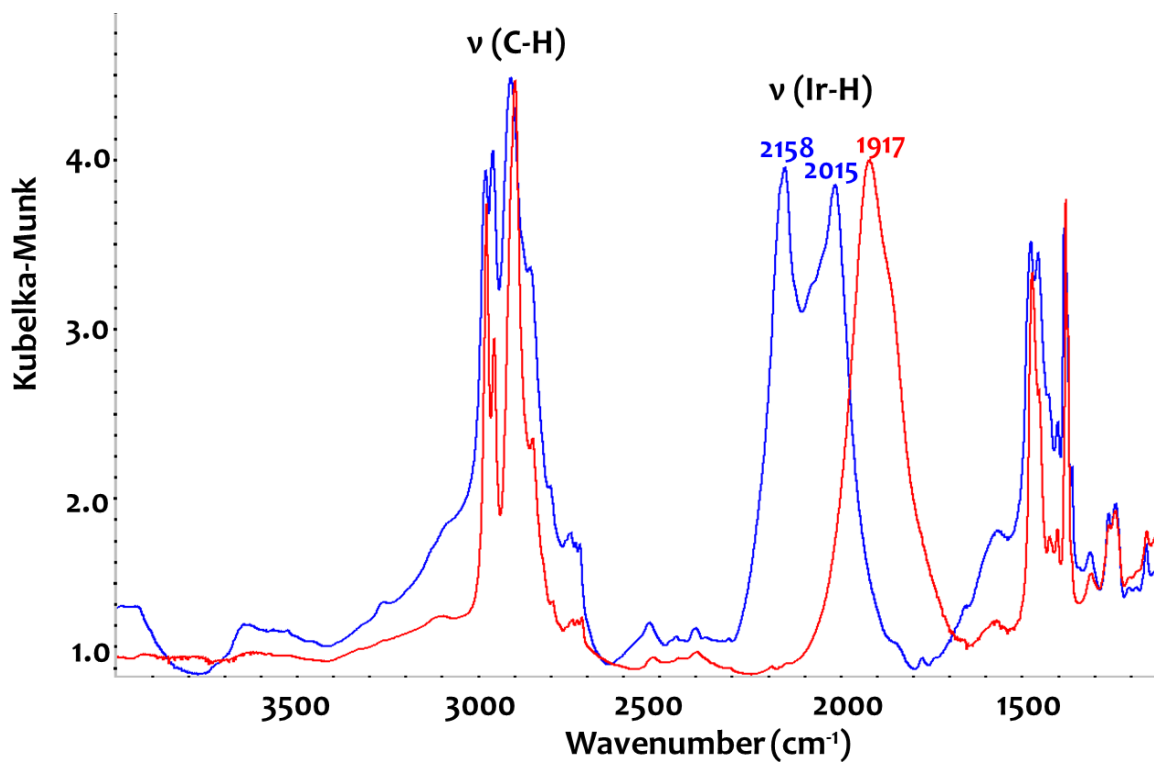


Figure 56. DRIFT spectra (298K, diluted in KBr, under argon) of cluster **20** (red) vs complex **14** (blue).

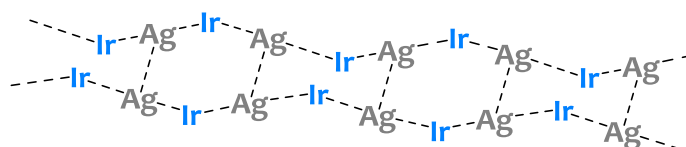


Figure 57. Schematic representation of the 2D fused metallacyclic network in **20**.

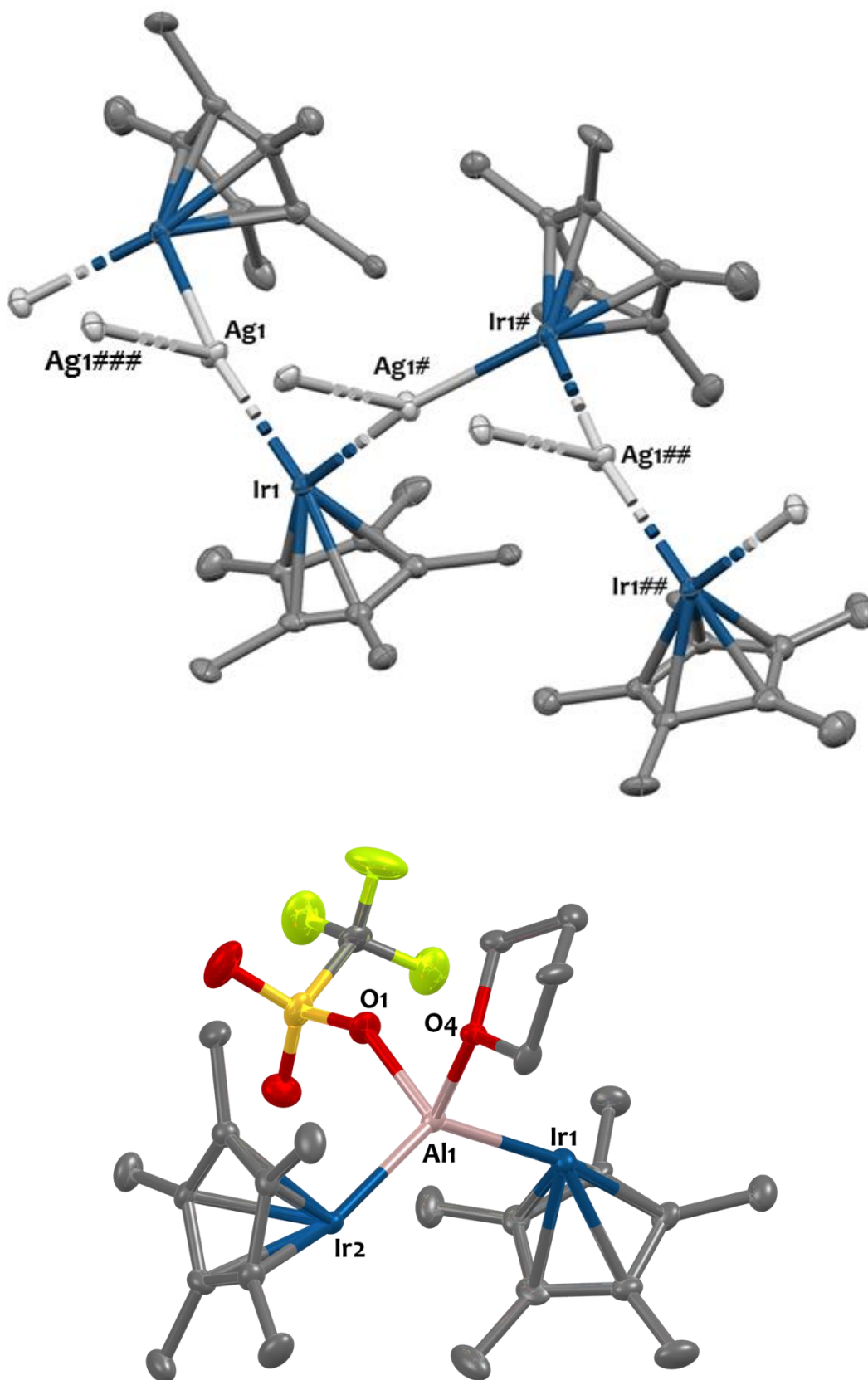


Figure 58. Solid-state molecular structures of 20 (top) and 21 (bottom). Displacement ellipsoids are plotted at a 30% probability level. Hydrogen atoms have been omitted for clarity. Selected bond distances (Å) and angles (°) for 20: Ir1-Ag1 2.7200(4), Ir1-Ag1# 2.7200(4), Ag1-Ag1### 2.973(3) Å, Ir1-Ag1#-Ir1# 161.72(6), Ir1-Ag1-Ag1### 99.14(3), Ag1-Ir1-Cp*Ir1-centroid 128.18. For 21: Ir1-Al1 2.449(3), Ir2-Al1 2.453(3), Al1-O1 1.895(6), Al1-O4 1.931(6), Ir1-Al1-Ir2 126.42(10), O1-Al1-Ir2 107.8(2), O1-Al1-O4 86.1(3), O4-Al1-Ir1 106.5(2). Al1-Ir1-Cp*_{centroid} 136.80, Al1-Ir2-Cp*_{centroid} 136.74.

The reaction co-product, $[(\text{IrCp}^*\text{H}_3)_2\text{Al}(\text{OTf})(\text{THF})]$ **21** (Scheme 65) remains soluble in THF solution, and is isolated as an orange powder by removing volatiles from the reaction filtrate. The ^1H NMR spectrum of **21** displays new hydride and Cp* signals at $\delta = -17.41$ ppm and $\delta = +2.12$ ppm integrating respectively for 6H and 30H, in agreement with the proposed structure. In addition, the ^{19}F NMR spectrum of **21** depicts an upfield resonance at $\delta = -80.7$ ppm, which supports the presence of a triflate moiety.^[280,281] This is corroborated by the DRIFT spectrum of **21** displaying the presence of a S=O vibrator at $\sigma = 1347$ cm^{-1} and a C-F vibration band at $\sigma = 1201$ cm^{-1} , which are typical of a triflate signature.^[280] To unequivocally identify the 3D molecular structure of **21**, we performed a single-crystal X-ray diffraction study on the isolated crystalline material (obtained from a cold recrystallization in Et_2O). The solid-state structure of **21** is represented in Figure 58 (bottom). The Al^{3+} center is surrounded by two $[\text{Cp}^*\text{IrH}_3]$ units and its coordination sphere is completed by the coordination two oxygen atoms: one from a monodentate triflate anion and the other one from a THF molecule. The Ir-Al distances – averaged at 2.451(2) Å – are slightly longer than those in complex **13** (2.43(1) Å) and slightly shorter than those in complex **14** (2.48(1) Å). The noticeable Cp* rings twisting – averaged at 136.8(1)° - is alike that found in **13** and **14** and suggests also the presence of hydrides in terminal position.

Therefore, no redox processes occur in this reaction even though silver salts are well-known oxidizing agents. Some research works highlight the salt metathesis reactivity of AgOTf when treated with chloro-iridium hydrides complexes, which triggers coordination of the triflate anion on the Ir center and elimination of AgCl.^[275,282-287] Also, the interaction of silver(I) with iridium hydride species forming unusual polynuclear silver-iridium derivatives are reported in a few occurrences.^[267,269-272,275] Here, the stoichiometric reaction of silver triflate with cluster **14** leads instead to the transmetallation of a $[\text{Cp}^*\text{IrH}_3]$ moiety from Al to Ag, and the coordination sphere of the aluminum center is substituted by a triflate ligand. Thus, this reactivity provides evidence that the $[\text{Cp}^*\text{IrH}_3]^-$ anion is labile, with a higher affinity for the soft Ag^+ cation rather than the hard Al^{3+} cation. Given the importance of silver species in salt metathesis reactions, compound **20** could potentially serve as a synthetically useful source of the $[\text{Cp}^*\text{IrH}_3]^-$ anion.

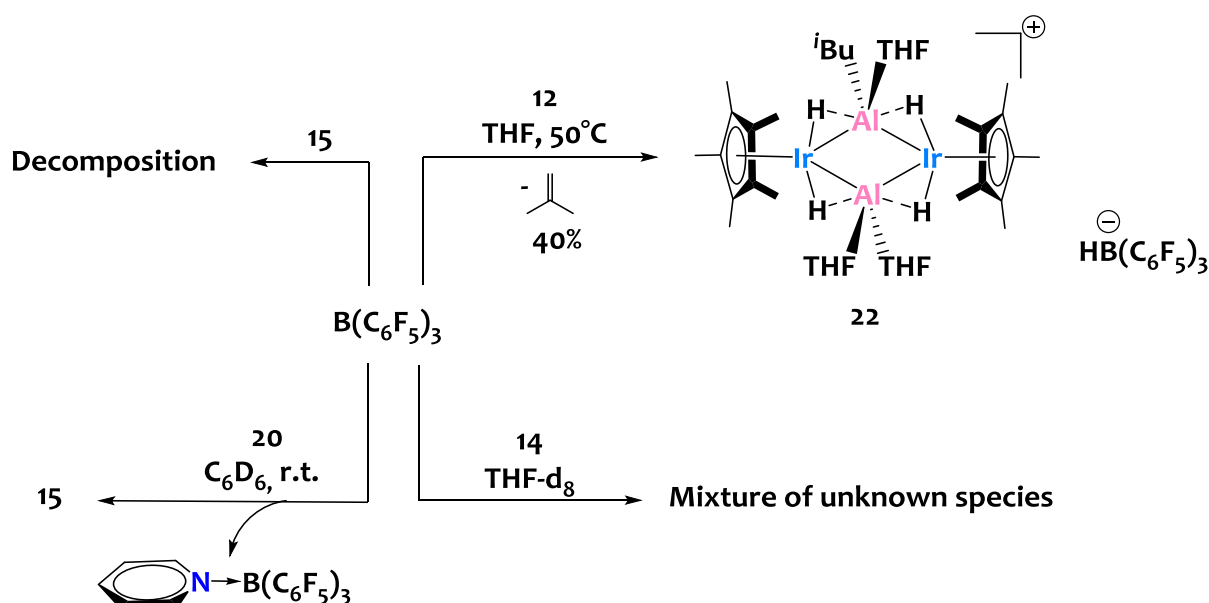
We also explored treatment of **12** with one equivalent of AgOTf, yet this lead to the formation of multiple products that we are unable to isolate (Scheme 65). We do not detect Ag(0) in this reaction, which suggests the absence of redox processes. Rather, transmetallation/ligand redistribution phenomena, similar to that observed with **14**, are most likely at place.

4.3 Reactivity towards Lewis acids

We then explored the reactivity of the Ir-Al species **12**, **14**, **15**, and **17** with Lewis acidic reagents.

Unfortunately, reaction of compounds **14** (Scheme 66, bottom right) and **15** (Scheme 66, top left) with stoichiometric amounts of *tris*(pentafluorophenyl)boron, $B(C_6F_5)_3$, (BCF) leads to complex mixtures of species that we are not able to isolate.

In contrast, the reaction of complexes **12** and **17** with BCF is well-behaved (Scheme 66), as will be discussed in the following sections.



Scheme 66. Reactivity of *tris*(pentafluorophenyl)borane with complexes **12**, **14**, **15**, and **17**.

4.3.1 Pyridine abstraction of adduct **17** leading back to the formation of complex **15**

Since *tris*(pentafluorophenyl)boron is known to abstract Lewis bases to form acid-base adducts, we explored reactivity of adduct **17** towards $B(C_6F_5)_3$.

As expected, the coordinated pyridine molecule can be quantitatively dissociated from Al to restore complex **15** and the $(Py)B(C_6F_5)_3$ adduct (Scheme 66, bottom left). This is confirmed by 1H -NMR and ^{19}F -NMR spectroscopy revealing typical signatures of complex **15** together with that of the $(Py)B(C_6F_5)_3$ adduct (Figure 59).^[288]

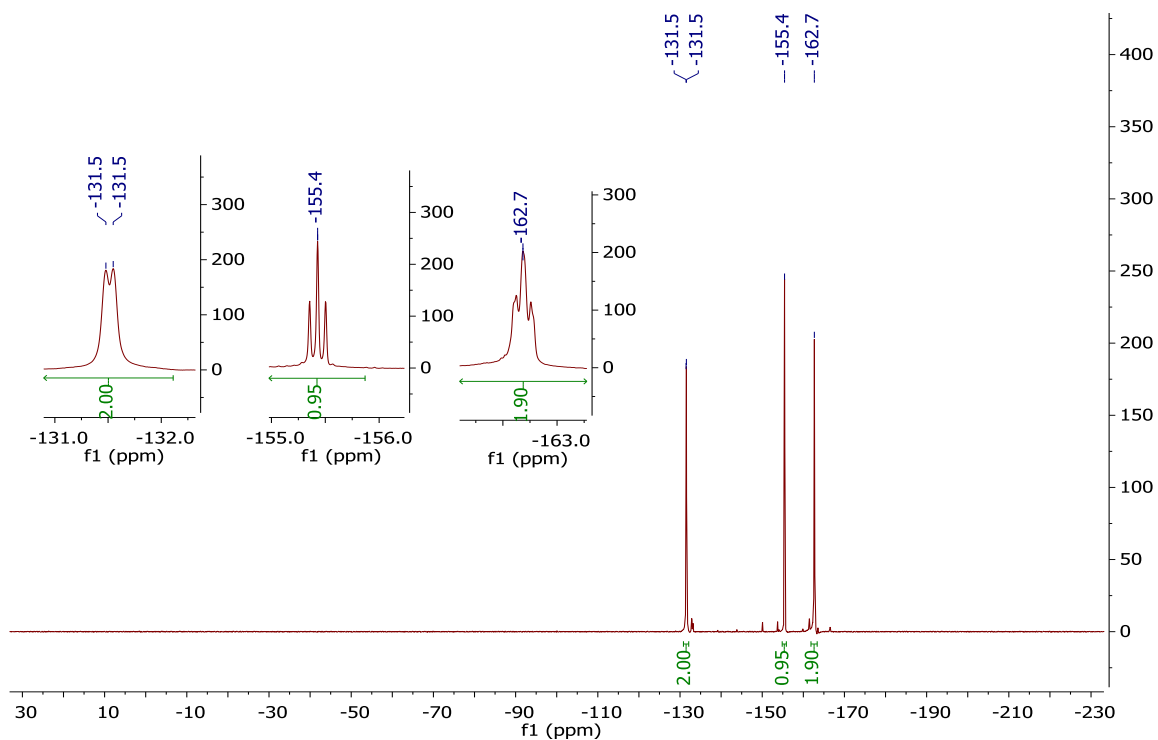
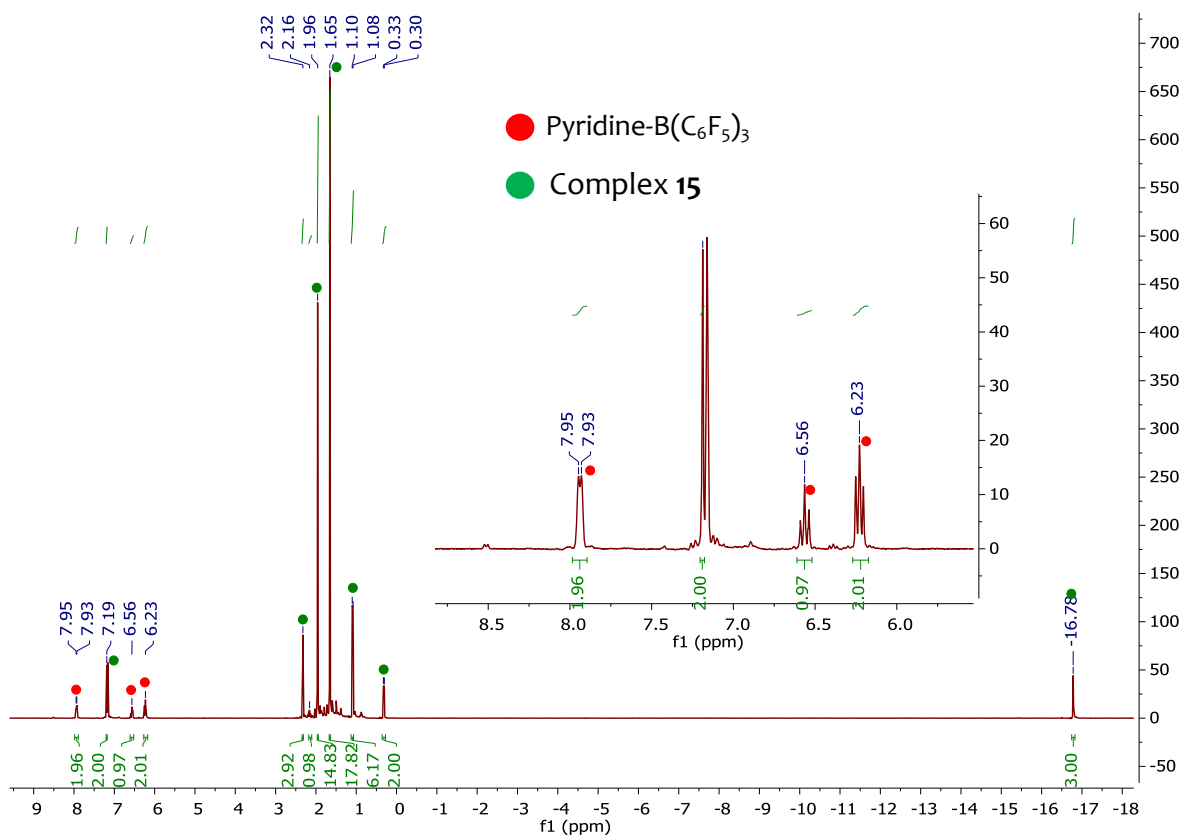


Figure 59. Top: ¹H-NMR spectrum (300.0 MHz, C₆D₆, 293K) of the stoichiometric reaction of complex 17 with B(C₆F₅)₃, showing the quantitative formation of 15 and (Py)B(C₆F₅)₃. Bottom: ¹⁹F-NMR spectrum (282.0 MHz, C₆D₆, 293K) of the stoichiometric reaction of complex 17 with B(C₆F₅)₃. The three displayed signals are assigned to (Py)B(C₆F₅)₃.

4.3.2 Synthesis of a borate salt $[\text{Ir}_2(\text{Cp}^*)_2(\text{H}_2)_2\text{Al}_2(\text{THF})_3(\text{iBu})][\text{HB}(\text{C}_6\text{F}_5)_3]$, **22**

Treatment of **12** with $\text{B}(\text{C}_6\text{F}_5)_3$ in THF at 50°C for 2 days cleanly yields the de-alkylated compound **22** (Scheme 66, top right). 1 equivalent of isobutene is evolved during the reaction (triplet at $\delta = 1.70$ ppm and septuplet at $\delta = 4.62$ ppm in THF-d_8),^[224] as quantified by $^1\text{H-NMR}$ reaction monitoring in THF-d_8 (Figure 60). $\text{B}(\text{C}_6\text{F}_5)_3$ therefore performs the abstraction of one isobutyl fragment from **12** through a beta-H elimination process releasing one equivalent of isobutene. The resulting cationic cluster **22** is associated with a $\text{HB}(\text{C}_6\text{F}_5)_3$ borate counter anion. This reaction confirms the high propensity of $\text{B}(\text{C}_6\text{F}_5)_3$ for performing alkyl abstractions, as already described several times in the literature,^[289,290] including by our group for alkyl aluminum species (see section 2.2.4, page 116).^[21] Note that the reaction is carried out in THF for solubility reasons since compound **22** is an ion pair, but also since THF can stabilize this dealkylated compound through coordination to the Lewis-acidic Al sites.

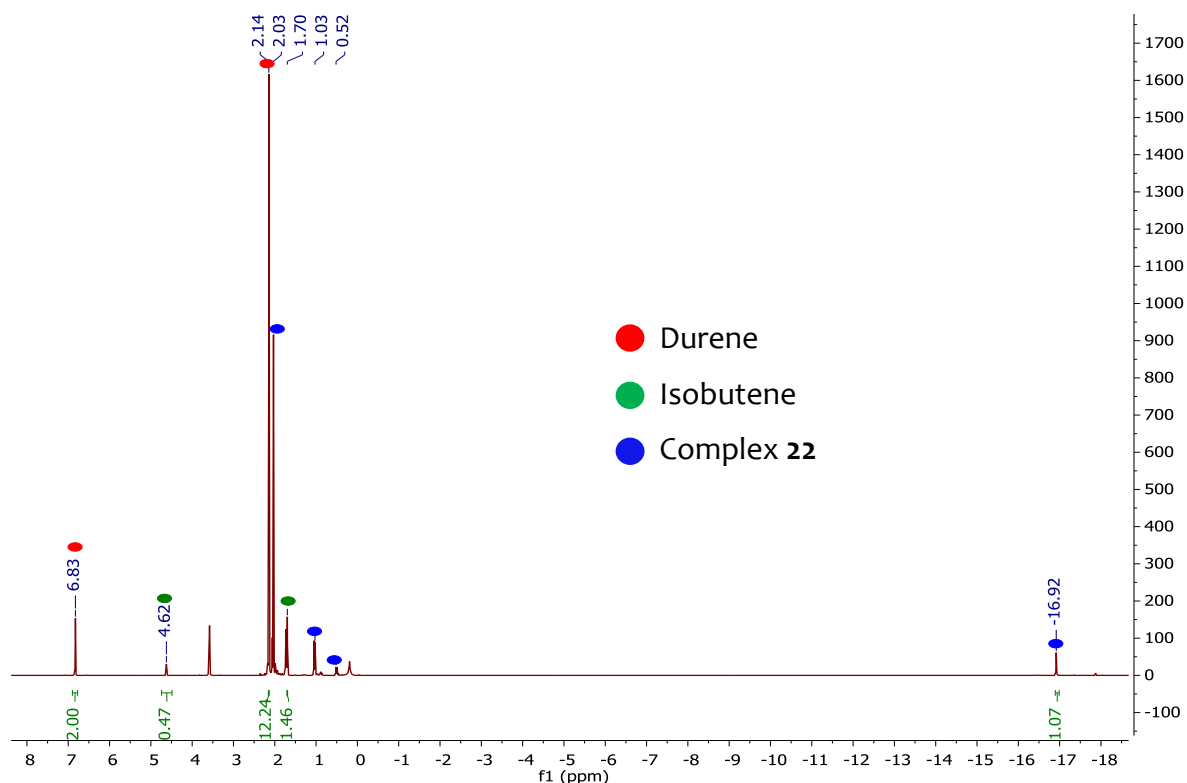


Figure 60 $^1\text{H-NMR}$ spectrum (300 MHz, THF-d_8 , RT) relating to the end of reaction of complex **12** (25.8 μmol) with $\text{B}(\text{C}_6\text{F}_5)_3$ (25.8 μmol) yielding complex **22** (23.8 μmol , 0.9 eq.) and isobutene (21.7 μmol , 0.8 eq.). Durene is used as standard (90.9 μmol).

The identity of **22** is underpinned by multi-nuclei (^1H , ^{11}B , ^{13}C) solution NMR spectroscopy, infrared spectroscopy, elemental analysis and X-ray diffraction investigations. The ^1H -NMR spectrum of **22** in THF- d_8 indicates the retaining of one isobutyl- aluminum fragment in the structure, as expected, since $\text{CH-}^i\text{Bu}$ (1.93 ppm), $\text{CH}_3\text{-}^i\text{Bu}$ (1.03 ppm) and $\text{CH}_2\text{-}^i\text{Bu}$ (0.51 ppm) signals are integrating for 1H, 6H, and 2H respectively. The ^{11}B -NMR spectrum of **22** displays a typical doublet at $\delta = -23.60$ ppm ($J_{\text{B-H}} = 94$ Hz) matching with the $\text{HB}(\text{C}_6\text{F}_5)_3^-$ anion signature.^[21,222,291] The DRIFT spectrum of **22** exhibits a typical H-B stretching vibration at 2364.1 cm^{-1} which further confirms the formation of $\text{HB}(\text{C}_6\text{F}_5)_3^-$.^[291]

Suitable crystals of **22** for XRD analysis are obtained from a cold and saturated mixture of pentane/THF (8/1). The resulting solid-state molecular structure (Figure 61), shows two $\{\text{Cp}^*\text{IrH}_2\}^{2-}$ motifs bridged by $\{\text{Al}(^i\text{Bu})(\text{THF})\}^{2+}$ and $\{\text{Al}(\text{THF})_2\}^{3+}$ fragments. The coordination geometries around the Al centers are pseudo tetrahedral with angles in the range $[88.1\text{-}122.7^\circ]$. The Al_2Ir_2 core is almost planar (mean deviation from plane = $0.037(3)\text{ \AA}$) and the Cp^* ligands almost perpendicular to the metallic core plane ($\alpha=176.28^\circ$, Figure 26), suggesting bridging hydrides. This geometry is comparable to that observed in **11**, in which the Al sites also adopt a pseudo-Td geometry. The Ir-Al₂ distances ($2.522(7)\text{ \AA}$) are much longer than the Ir-Al₁ distances ($2.422(3)\text{ \AA}$), as a result of an increased charge density on the de-alkylated Al₁ site. These Ir-Al distances in **22** are much shorter than those of the fully-alkylated complex **11** ($2.72(1)\text{ \AA}$ on average), which attest to a greater charge density on the Al sites, and stronger electronic donation from the $[\text{Cp}^*\text{IrH}_2]^{2-}$ fragments in **6**, as expected.

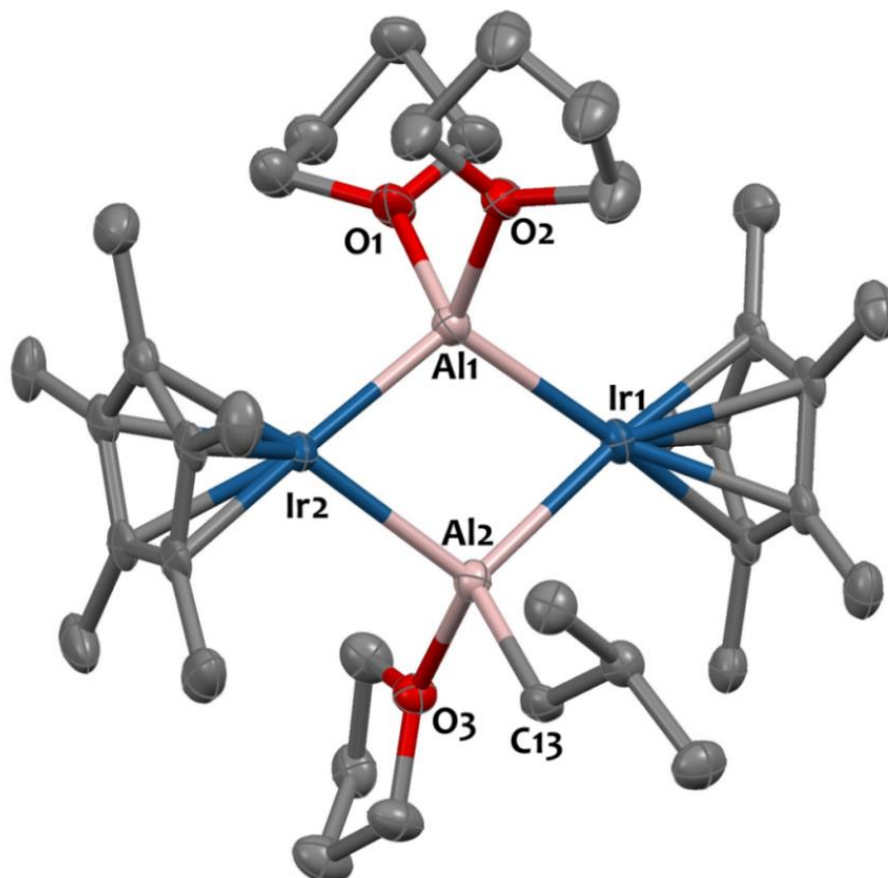


Figure 61. Solid-state molecular structure of **22**. Displacement ellipsoids are plotted at a 30% probability level. Hydrogen atoms have been omitted for clarity. Selected bond distances (Å) and angles (°) Ir1-Al1 2.431(3), Ir1-Al2 2.521(2), Ir2-Al1 2.414(3), Ir2-Al2 2.524(2), Al1-O1 1.914(7), Al1-O2 1.950(7), Al2-O3 1.976(6), Al2-C13 1.983(8), Ir1-Al2-Ir2 105.21(9), Al1-Ir1-Al2 71.37(8), (Ir1-Al1-Ir2-Al2)_{centroid}-Ir1-Cp*_{centroid} 177.30, (Ir1-Al1-Ir2-Al2)_{centroid}-Ir2-Cp*_{centroid} 175.27.

Theoretical investigations of complex **22** by DFT (B3PW91) methods are undertaken. A conformational analysis reveals four possible conformers in an energy range of 6.5 kcal.mol⁻¹ (see appendix section for more information). As for complex **12**, the most stable structure exhibits four hydrides in terminal position on Ir centers (Figure 62). The conformers with two terminal hydrides and two bridging hydrides Ir-H-Al plus those with four bridging hydrides Ir-H-Al are 3.0, 5.9 and 6.5 kcal.mol⁻¹ less stable, respectively. Computed parameters regarding complex **22** are gathered on Table 6. As experimentally observed, the calculated Al₂Ir₂ core is almost planar and the Ir-Al2 distances (2.533 and 2.597 Å) are much longer than the Ir-Al1 distances (2.453 and 2.460 Å). Compared to complex **11**, a larger negative charge is observed on Ir atoms (-1.405 vs. -0.958). The NPA charge on Al2 (+1.821) is also larger than in complex **11** (+1.776) while that on Al1 is similar in both complexes (+1.758).

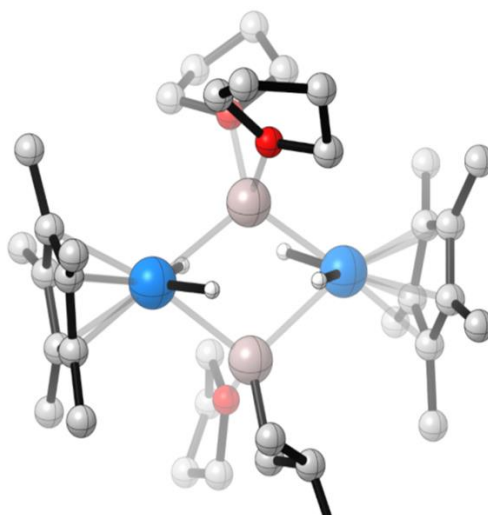


Figure 62. Most stable calculated structure of compound 22.

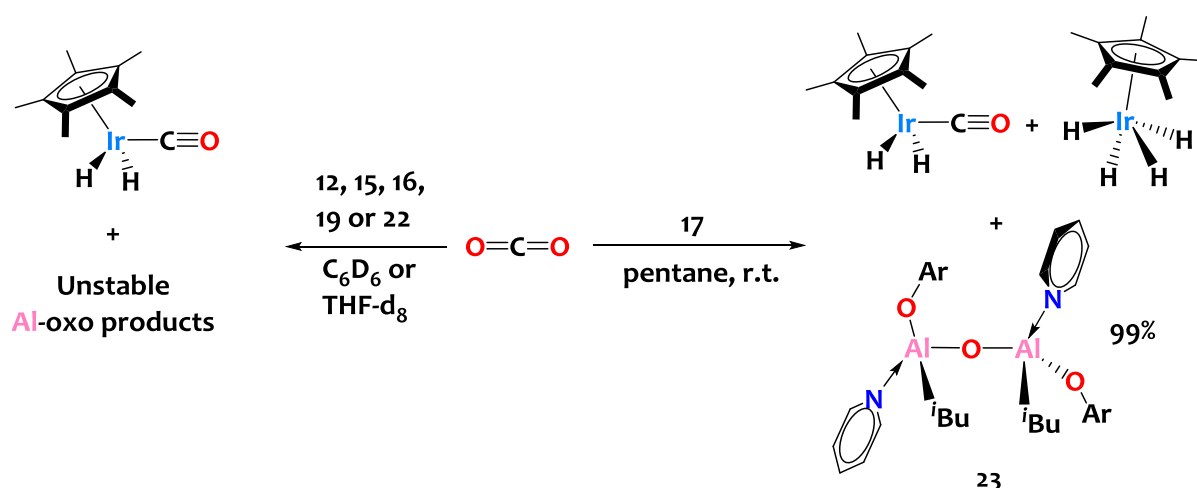
Complex 22	
NPA charges	Al1: 1.76 / Al2: 1.82 / Ir: -1.40
WBIs	Ir-H(η): 0.68 / Ir-Al1: 0.44 / Ir-Al2: 0.37 / Al1-O1 & Al1-O2: 0.17 / Al2-O3: 0.14 / Al2-C13: 0.40
Ir-H bands (cm^{-1})	η : 2248.7 / 2224.8. η : 2197.4 / 2176.4
Ir-H distances (\AA)	1.599x2 / 1.601 / 1.606
Al-H distances (\AA)	2.131 / 2.137 / 2.166 / 2.180 / 2.180 / 2.306 / 2.331 / 2.370 / 2.497
Ir-Al distances (\AA)	2.453 / 2.460 / 2.533 / 2.541
XRD Ir-Al distances (\AA)	2.414 / 2.431 / 2.521 / 2.524
Ir-Al-Ir angle ($^\circ$)	107.9
XRD Ir-Al-Ir angle ($^\circ$)	108.4
Al-Ir-Al angle ($^\circ$)	71.9
XRD Al-Ir-Al angle ($^\circ$)	71.5
α angle ($^\circ$) ^a	174.4
XRD α angle ($^\circ$) ^a	176.3

Table 6. Computed NPA charges, Wiberg bond indexes (WBIs), and structural data for cluster 22. Labels on atoms are the same as those employed on Figure 61. ^aGeometrical description of this angle is explained on Figure 26.

4.4 Reactivity with heteroallenes

4.4.1 Reactivity with carbon dioxide

Next, we probed the reactivity of these $\text{Al}^{\delta+}\text{-Ir}^{\delta-}$ derivatives towards electrophiles, and we first targeted carbon dioxide, given the importance of CO_2 activation by transition metals.^[292,293] NMR-monitoring of the reaction (in C_6D_6 or in THF-d_8) of compounds **12**, **15**, **16**, **19**, and **22** with CO_2 shows that a reaction occurs smoothly at room temperature in all cases, generating complex mixtures of species. Among them, $\text{Cp}^*\text{Ir}(\text{CO})\text{H}_2$ ^[294] is unambiguously identified. However, unstable aluminum-oxo co-products are, likely, formed in the process and might explain why this reaction affords multiple products (Scheme 67, left).



Scheme 67. Reactivity of CO_2 with complexes **12**, **16**, **17**, **19**, and **22**.

Gratifyingly, the mono-pyridine adduct **17** does not quench the reactivity of the Ir-Al motif and help stabilize the resulting Al derivatives, leading to cleaner reactions which are easier to decipher.

4.4.1.1 Synthesis of an atypical alkyl aluminum-oxo, species **23**

Treatment of **17** with CO_2 (0.8 atm, 10 eq., r.t.) in pentane leads to the clean reductive cleavage of CO_2 , affording the iridium carbonyl species, $\text{Cp}^*\text{Ir}(\text{CO})\text{H}_2$,^[294] together with Cp^*IrH_4 ^[181] and two rotamers of an aluminum-oxo co-product, $[(i\text{Bu})(\text{OAr})\text{Al}(\text{Py})]_2(\mu\text{-O})$, **23** (see Figure 63), which is isolated in 99% yield (Scheme 67, right).

Existence of two rotamers in solution is proved by a variable temperature (VT) $^1\text{H-NMR}$ experiment recorded in deuterated toluene (Figure 64). This study shows first an equilibrium

between two rotamers in a ratio 93/7 at 297 K. NMR spectral signatures of these two rotamers is well identified for the *ortho*-pyridine resonances in **23** with a major doublet (93%) at $\delta=8.58$ ppm and a minor one (7%) at $\delta=8.72$ ppm (see first spectrum in red on Figure 64). Then, upon heating, we notice progressive shifting of these doublets into a broad signal averaged at $\delta=8.63$ ppm. Total disappearance of the initial doublets is observed from 84°C meaning these two rotamers interconvert above this coalescence temperature.

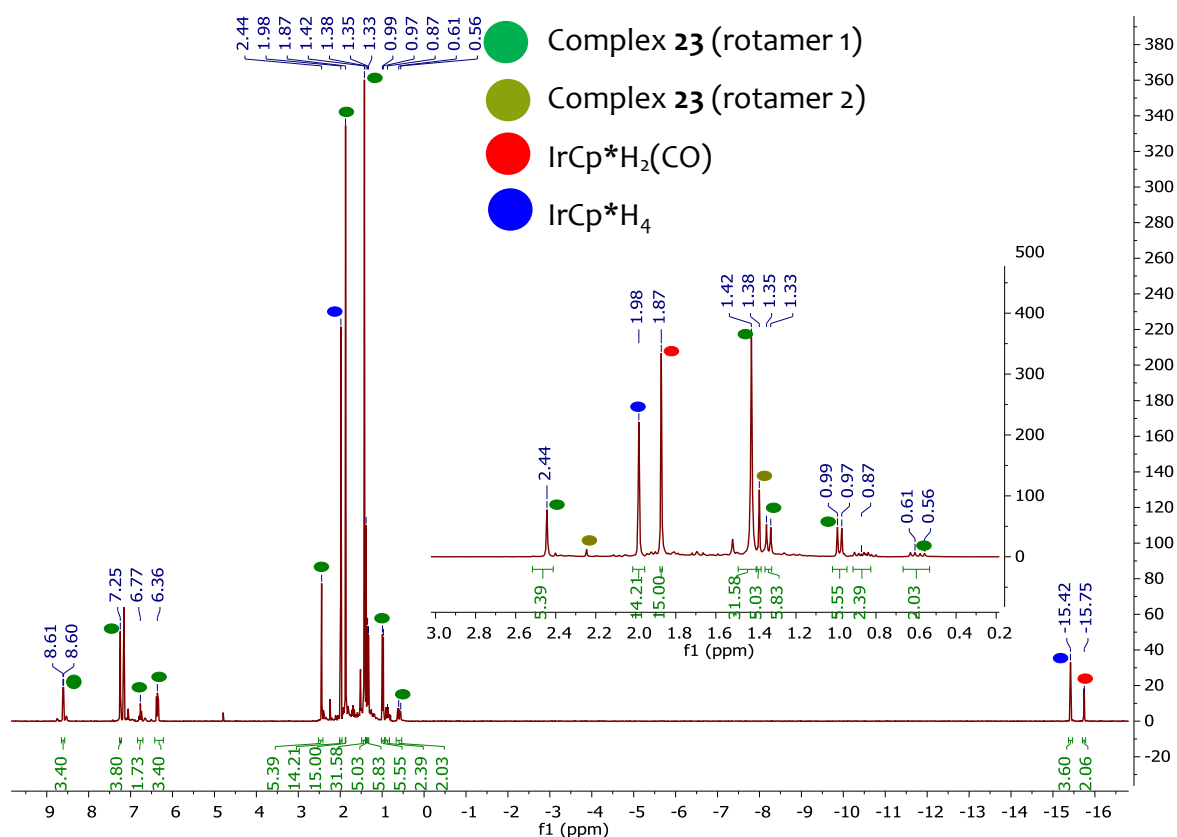


Figure 63. ¹H-NMR spectrum (300 MHz, C₆D₆, 293K) of the crude reactional mixture relating to the treatment of **17** with CO₂ (800 mbars, 10 eq.) in a J-Young NMR tube. The spectrum was recorded after 24 hours of reaction showing a total consumption of **17** and a stoichiometric formation of species **23** along with IrCp*H₂(CO) and IrCp*H₄ products.

Successfully, colorless single block-shaped crystals of compound **23** suitable for XRD studies (while IrCp*H₄ and Cp*Ir(CO)H₂ remain soluble in pentane) grew from the crude reactional mixture. The resulting solid-state structure of **23** is shown on Figure 65. The two tetra-coordinate Al atoms are connected by a bridging oxo group in a nearly linear fashion (Al1-O1-Al2 angle of 174.4(1)°). Here, the substituents at the tetrahedral Al sites adopt an eclipsed conformation with the two isobutyl ligands pointing in the same direction. The Al1-O1 and Al2-O1 bond distances (1.697(2) and 1.701(2) Å respectively) are in the expected range.^[295,296] Note that DRIFT spectroscopy analysis of **23** reveals absence of O-H vibrators, in agreement with the presence of a bridging oxo ligand (versus a bridging hydroxo).

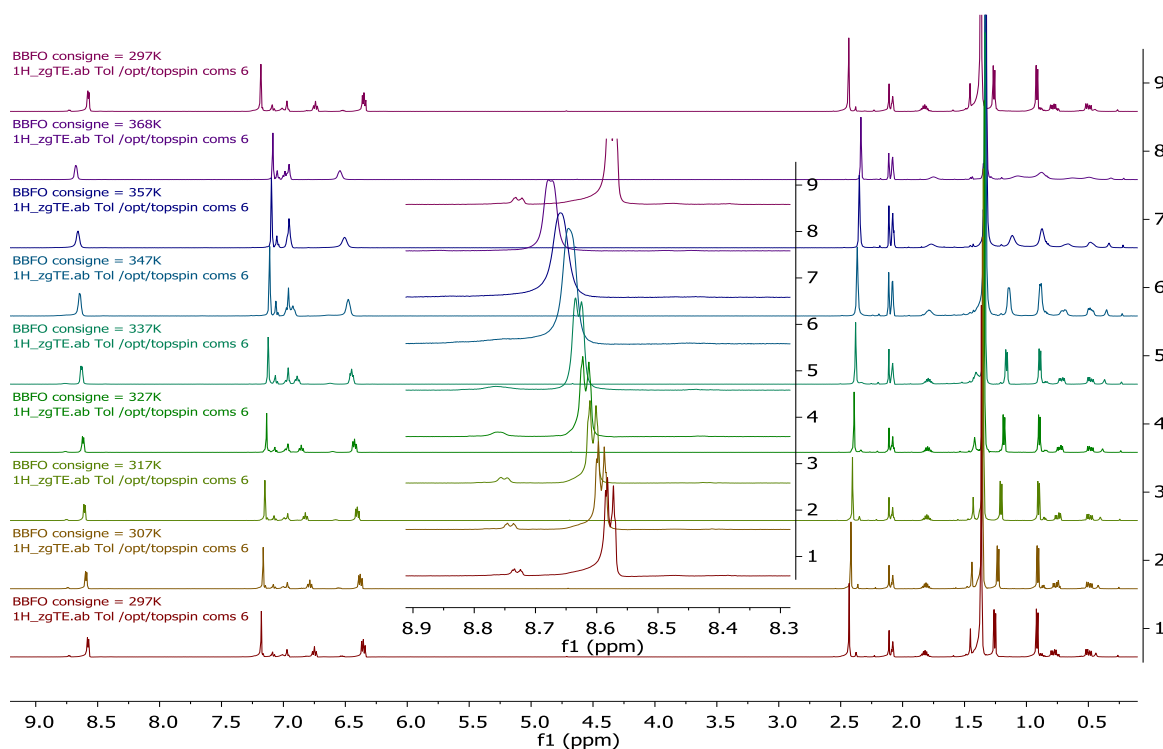


Figure 64. VT $^1\text{H-NMR}$ spectra (500 MHz, toluene- d_8) of compound 23. Central spectral window is an expansion of the *ortho*-pyridine signal. The top spectrum relates to a new acquisition at room temperature after heating. Analysis shows a coalescence temperature associated with the exchange between the two rotamers at $T=357$ K.

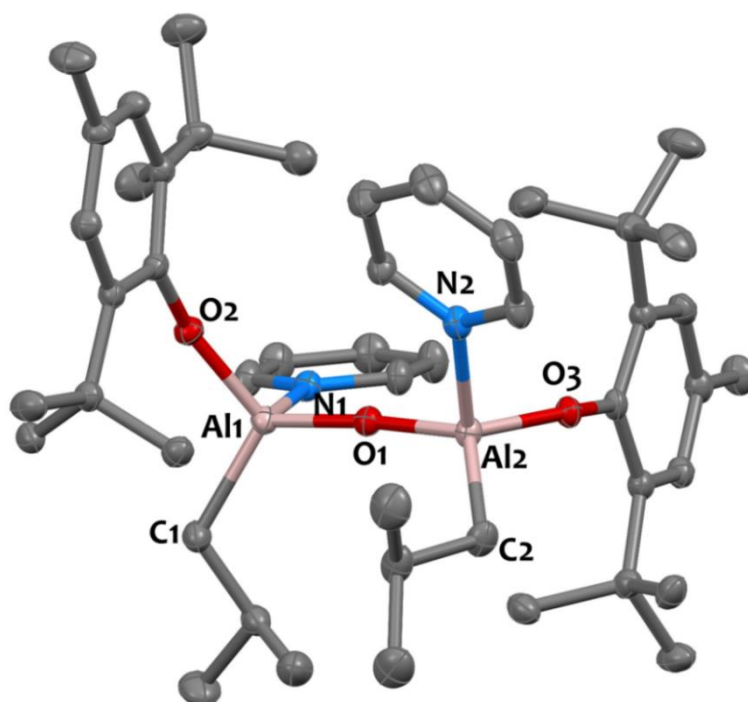


Figure 65. Solid-state molecular structure of 23. Displacement ellipsoids are plotted at a 30% probability level. Hydrogen atoms have been omitted for clarity. Selected bond distances (\AA) and angles ($^\circ$): Al1-O1 1.697(2), Al1-O2 1.744(2), Al1-C1 1.971(3), Al1-N1 2.006(2), Al2-O1 1.701(2), Al2-O3 1.750(2), Al2-C2 1.977(3), Al2-N2 2.005(2), Al1-O1-Al2 174.4(1).

Despite the pivotal role of methylaluminumoxane derivatives in catalysis, very few well-defined molecular alkylaluminumoxanes are known to date. This can be attributed to the hydrolytic conditions classically used to prepare such derivatives, which are extremely difficult to control, together with the propensity of Al-O linkages to oligomerize to form insoluble amorphous materials. Complex **23** thus adds to the handful list of structurally characterized molecular aluminum oxide species.^[295-301] Note that examples of stoichiometric CO₂ reduction by low-valent Al species leading to C-O bond cleavage only emerged recently.^[300-302] A parallel can be drawn between these redox reactions and the reactivity observed here. Indeed, from the perspective of aluminum, complex **23** behaves as a masked Al(II) site and allows the preparation of an unconventional Al-oxo species without having to isolate the low-valent Al derivative, which is remarkable. While insertion of CO₂ into polar metal-metal bonds^[87,303-305] and main group Lewis pairs^[306-308] is reported, to our knowledge the reductive cleavage of CO₂ leading to CO and O²⁻ by heterobimetallic systems is described in only two occurrences. C. M. Thomas described the oxidative addition of CO₂ onto a Zr-Co bond, affording a (OC)Co(μ-O)Zr species and M. Mazzanti described the CO₂ cleavage to CO gas and a U(V) oxo species involving a bimetallic uranium-potassium cooperative mechanism.^[303,309]

4.4.1.2 DFT studies

To better understand the reaction mechanisms operating in this CO₂ activation by Ir-Al metal-metal pairs, DFT calculations (B3PW91) are undertaken. The resulting enthalpy profile of the reaction from reactant **17** to product **23** is represented on Figure 66.

- 1) The first step of the calculated mechanism begins by the replacement of the pyridine, in reagent **17**, by a CO₂ molecule, which binds to Al and Ir centers. This substitution is endothermic by 7.5 kcal.mol⁻¹.
- 2) From this adduct, the CO₂ undergoes a nucleophilic attack by the iridium center forming a first transition state – **TS1** – represented in Table 7. **TS1** features a bent CO₂ molecule with an overlapping of an empty orbital at the carbon of CO₂ with a lone pair of the iridium center (see the associated molecular orbital on Figure 67). The aluminum center ensures an electrophilic assistance by binding to the oxygen. The associated energetic barrier is 18.9 kcal/mol in line with a kinetically accessible reaction.
- 3) Following the intrinsic reaction coordinates, a 4-member metallacyclic species, noted **I1**, is yielded, which formation is slightly endothermic (+3.6 kcal/mol) with respect to the reactants.
- 4) Next, the small size of the CO₂ molecule allows a migratory insertion onto the Ir-Al bond. This is

easily achieved through a low-lying transition state (barrier of 10.5 kcal/mol), noted **TS2**, and leads to the formation of a stable metalla carboxylate intermediate (-11.5 kcal/mol), noted **I2**, where the two oxygens bind to Al while C is bound to Ir. This complex is similar to the few examples where CO₂ is reductively inserted in polar metal-metal bonds.^[87,305]

5) The presence of three hydrides on the Ir center, in close vicinity to the inserted CO₂, allows an easy hydrogen migration from Ir to one of the oxygen atoms. This migration occurs through a kinetically accessible **TS3** (barrier of 25.8 kcal/mol) and leads to the formation of another cyclic intermediate, noted **I3**.

6) Then, a C-O bond breaking occurs through a favorable **TS4** (barrier of 2.7 kcal/mol) yielding ultimately to the formation of an Al hydroxide molecule, noted **I4**, and Cp*Ir(CO)H₂, which formation is exothermic by 7.1 kcal/mol with respect to the reactants (the hydrogen transfer + CO bond breaking step being slightly endothermic by 4.4 kcal/mol from the Ir(CO₂)Al carboxylate intermediate **I2**).

7) The Al hydroxide species **I4** is then subject to protonolysis with a second equivalent of complex **17**. This reaction occurs through a kinetically accessible **TS5** (barrier of 13.4 kcal/mol) and yields, after pyridine recoordination of intermediate **I5**, the experimentally observed product **23** and Cp*IrH₄.

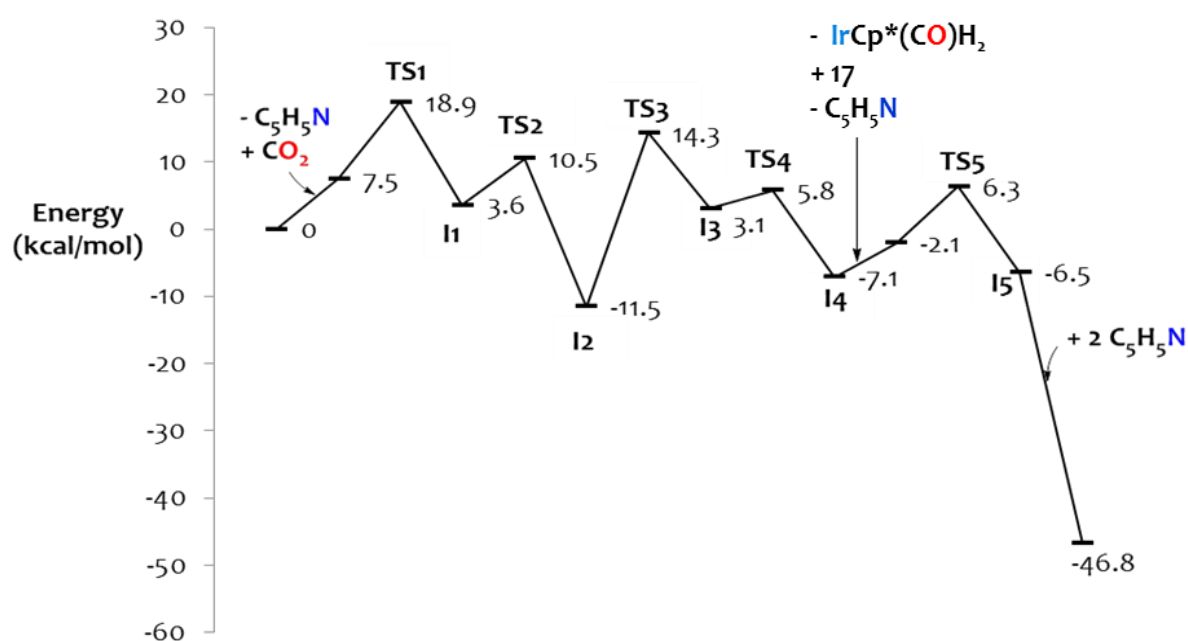


Figure 66. Computed enthalpy profile for the reaction of CO₂ with 17 at room temperature.


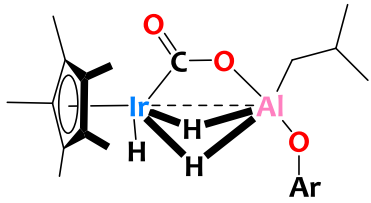
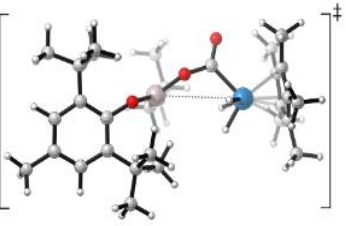
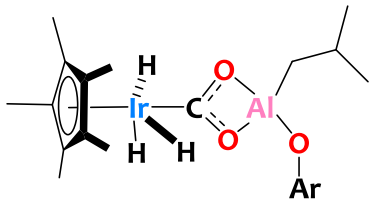
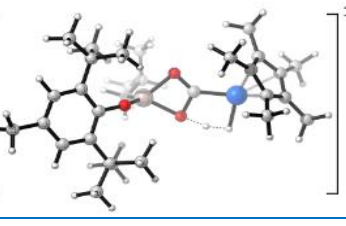
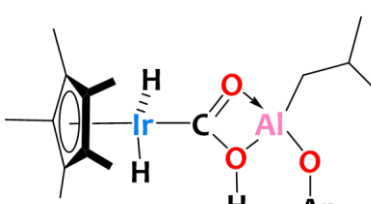
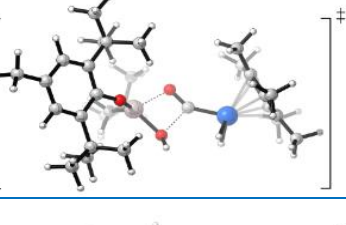
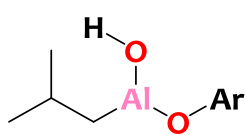

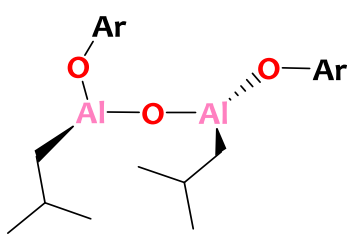
Transition state (TS)	DFT optimized structure	Intermediate (I)	Related structure
TS1		I1	
TS2		I2	
TS3		I3	
TS4		I4	
TS5		I5	

Table 7. Transition states and intermediates corresponding to the labels depicted on Figure 66.

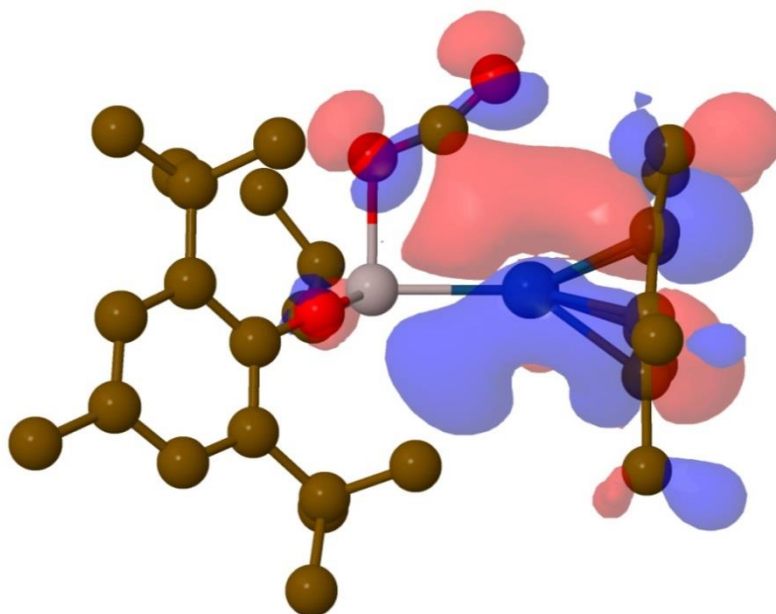


Figure 67. Molecular Orbital (HOMO-2) describing the nucleophilic attack of the CO₂ molecule by the iridium center.

Note that other pathways have been investigated (see appendix for more details) but the one reported here is found to be the most favorable.

This CO₂ reduction mechanism is very different from the one reported by L. J. Murray and coworkers for a diiron-hydride complex^[310] where the first step is an hydrogen transfer to CO₂, or the reaction reported by C.C. Lu and his team^[311] using nickelate-group13 complexes where a CO₂ disproportionation is observed.

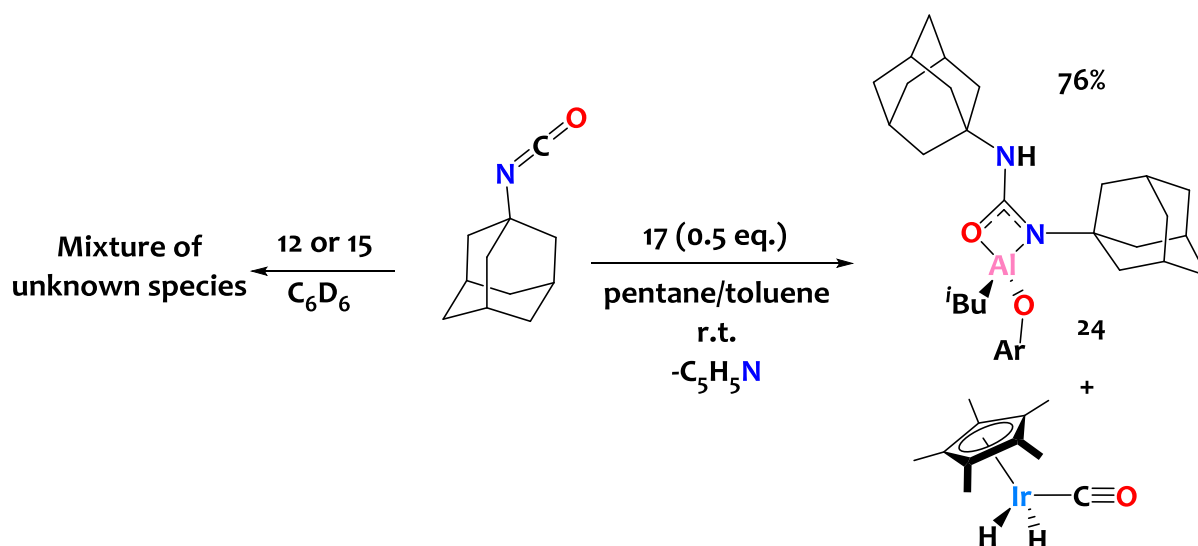
On the other hand, this reactivity is slightly reminiscent of what is observed in *f*-elements chemistry^[309,312-317], in particular with the formation of intermediates **I1** and **I2** (Table 7) where CO₂ is inserted in between Ir and Al atoms.

Eventually, the protonation of CO₂ (intermediate **I3**) and the formation of a terminal hydroxyl unit **I4** is unique, since, to the best of our knowledge, no similar mechanism is found in literature.

4.4.2 Reactivity with adamantyl isocyanate

The discussed bimetallic reductive cleavage of CO₂ pushed us to explore further reactivity of the Ir-Al species towards other heteroallenes. We first contemplated an isocyanate R-N=C=O derivative, namely adamantyl isocyanate (Ad-NCO).

NMR monitoring (in C₆D₆) of the reactions between Ad-NCO and archetypal complexes **12** or **15** lead to a complex mixture of species, which we can not identify (Scheme 68, left).



Scheme 68. Reactivity of adamantly isocyanate with complexes **12**, **15**, and **17**.

However, similarly as for CO₂ reactivity, employing the mono-pyridine adduct **17** fixes the aforementioned problem and leads to a clean reaction.

4.4.2.1 Synthesis of a new Al-ureate species, **24**

Treatment of **17** with 2 equiv. of adamantly isocyanate in a mixture of pentane/toluene at room temperature, results, after one day, in the cleavage of the N=C bond to produce Cp*Ir(CO)H₂ and the aluminum ureate species {Al(OAr)(^{*i*}Bu)[κ²-(N,O)AdNC(O)NHAd]}, **24** (Scheme 68, right). When only 1 equiv. of AdNCO is used, an equimolar mixture of **17** and **24** is obtained. The ¹H-NMR spectrum (recorded in C₆D₆) of the crude mixture (Cp*Ir(CO)H₂ and **24**) displays a distinctive singlet at δ = +4.40 ppm attributed to the NH proton from the ureate ligand in **24** (Figure 68). The ¹³C resonance corresponding to the ureate central carbon appears at a diagnostic chemical shift of +164.0 ppm, which is in agreement with literature data.^[318]

Infrared spectroscopy of **24** confirms the presence of a secondary amine with a typical ν(N-H) stretch at a wavenumber of 3448 cm⁻¹.

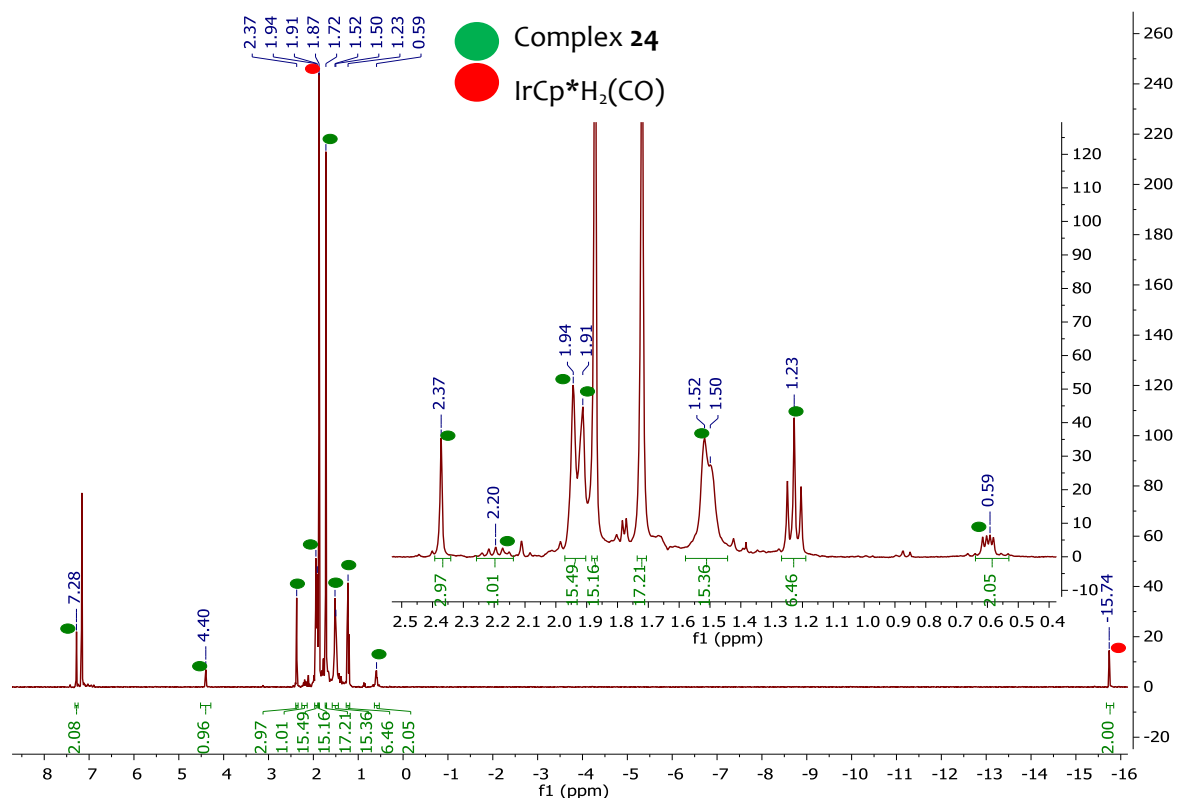


Figure 68. $^1\text{H-NMR}$ spectrum (300 MHz, C_6D_6 , 293K) of the crude powder from the treatment of **17** with 1-adamantylisocyanate (2 equivalents) after 1 day of reaction and removing the volatiles. The spectrum shows and equimolar formation of $\text{IrCp}^*\text{H}_2(\text{CO})$ and product **24**.

Block-shaped crystals of **24**, suitable for single-crystals XRD analysis, are obtained from a cold and saturated pentane solution of the crude powder ($\text{Cp}^*\text{Ir}(\text{CO})\text{H}_2$ and **24**). The solid-state molecular structure of **24** is shown on Figure 69.

The complex is four-coordinate, with a κ^2 -ureate ligand arranged to favor a typical tetrahedral geometry around Al ($\text{O1-Al1-O2} = 109.36(8)^\circ$). The ureate ligand is bound to Al in a non-symmetric fashion, where the Al1-O1 bond length ($1.863(2) \text{ \AA}$) is shorter than the Al1-N1 length ($1.911(2) \text{ \AA}$), as in previously characterized ureate complexes.^[318,319] The planarity of the $[\text{OCN}_2]$ ureate core as well as the short O-C ($1.309(4) \text{ \AA}$) and N-C ($1.331(3)$ and $1.341(3) \text{ \AA}$) distances are consistent with electron delocalization and compare well with reported values for metal-bound ureates.^[318,319]

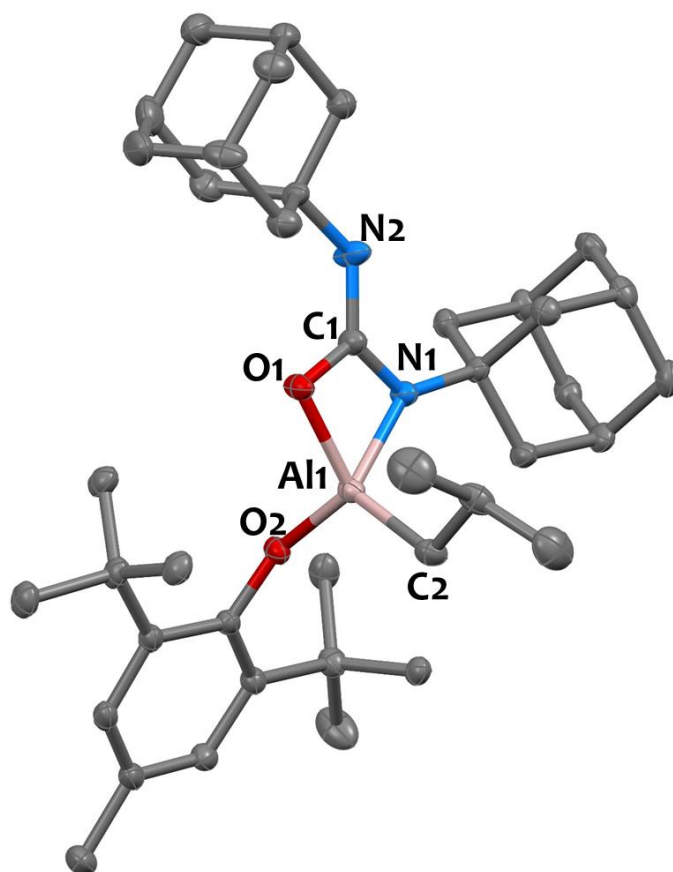


Figure 69. Solid-state molecular structure of **24**. Displacement ellipsoids are plotted at a 30% probability level. Hydrogen atoms have been omitted for clarity. Selected bond distances (Å) and angles (°): Al1-O1 1.863(2), Al1-O2 1.710(2), Al1-C2 1.961(3), Al1-N1 1.911(2), N1-C1 1.331(3), N2-C1 1.341(3), O1-C1 1.309(4), N1-C1-O1 111.7(2), N1-C1-N2 127.8(2), O1-Al1-N1 70.73(7), O1-Al1-O2 109.36(8).

By analogy with the reaction with CO₂ and in agreement with computational data (see below), we postulate that this aluminum ureate complex arises from a transient Al-amido species generated after CO extrusion. Complex **24** might thus arise from isocyanate insertion into such Al-NHAd intermediate. This chemistry is reminiscent of the oxidation of Al(I) reagents with azides, leading to rare terminal aluminum imides which are highly reactive and prone to H-abstraction to lead Al-amidos as well as insertion chemistry with unsaturated substrates (CO, CO₂, isocyanides).^[320–323] Overall, this uncommon reaction adds to the handful of examples of metal-mediated decarbonylation of isocyanates and cyanates.^[324–328]

4.4.2.2 DFT calculations

Similar calculations are conducted for the reaction of **17** with AdNCO (Figure 70). The reaction sequence present similarities and differences compare to that of CO₂ (see section 4.4.1.2, page 195

for comparisons).

1) In particular, like for CO₂, reactant **17** undergoes a substitution of pyridine by an AdNCO moiety, this step is endothermic by 9.7 kcal/mol.

2) From this adduct, AdNCO is subjected to a nucleophilic attack by the Ir center allowing to reach a kinetically accessible (23.2 kcal/mol) transition state, noted **TS1** (see Table 8) , which ultimately yields an unstable 4-members metallacyclic intermediate, **I1** (+7.2 kcal/mol).

3) The next step is different from that reported for CO₂ and is likely due to the steric bulk of the adamantly group. Indeed, AdNCO cannot easily insert in between Ir and Al atoms. The hydrogen transfer from Ir to N occurs instead on the 4-member ring metallacycle through a transition state, noted **TS2**, of 27.7 kcal/mol. This H-migration yields the intermediate **I2**. Note that hydride transfer to the oxygen as well as AdNCO insertion followed by hydrogen transfer were also computed and were found not to be competitive (see appendix for more details).

4) Then, **I2** is subjected to a C-N bond breaking through a kinetically accessible **TS3** (barrier of 4.7 kcal/mol), which allows the formation of an Al amido complex, **I3** and a molecule of Cp*Ir(CO)H₂ (exothermic by 2.3 kcal/mol with respect to the reactants).

5) The resulting Al amide derivative does not react with a molecule of **17** (as observed in the case CO₂) because its high bulkiness. It rather undergoes a [2+2] cycloaddition with another molecule of AdNCO through an accessible barrier of 6.9 kcal/mol - **TS4** - forming a stable cycloaddition product **I4** (-23.1 kcal/mol).

6) Eventually, **I4** is subjected to a rearrangement reaction (likely 1,3 hydrogen shift) through a kinetic barrier of 15.2 kcal.mol⁻¹ (**TS5**), which ultimately yields the stable isomer **24**.

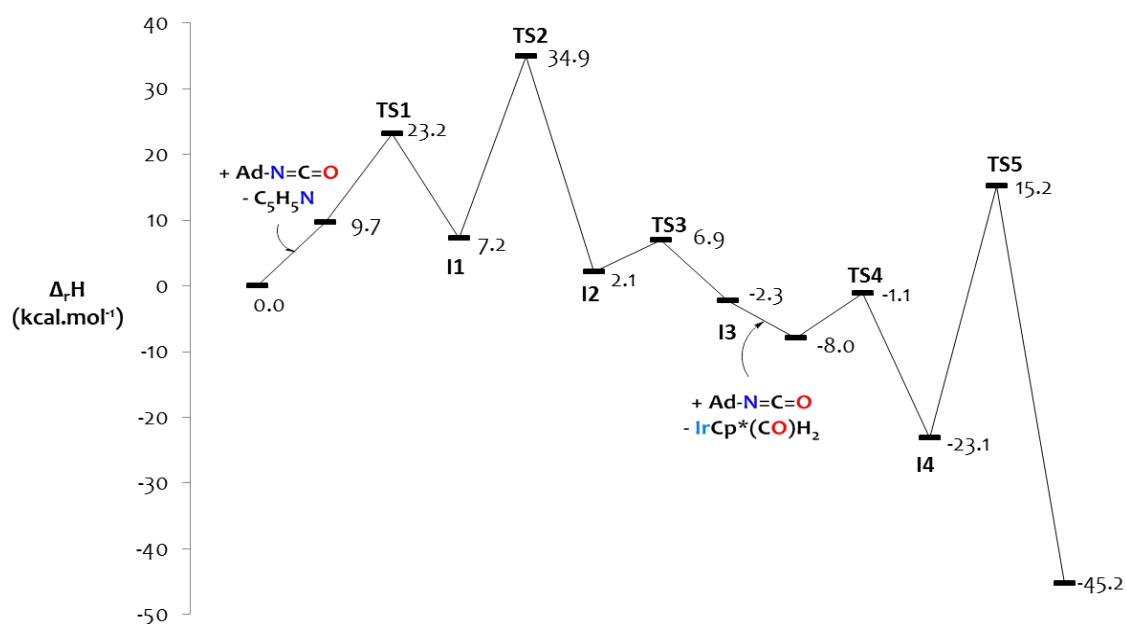


Figure 70. Computed enthalpy profile for the reaction of AdNCO with **17** at room temperature.

Transition state (TS)	DFT optimized structure	Intermediate (I)	Related structure
TS1		I1	
TS2		I2	
TS3		I3	
TS4		I4	
TS5			

Table 8. Transition states and intermediates corresponding to the labels depicted on Figure 70.

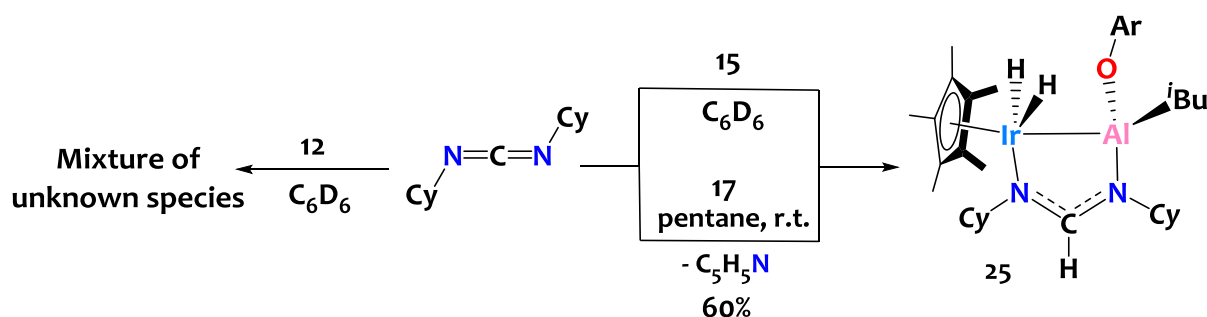
To conclude, these DFT studies support an original bimetallic decarbonylation of Ad-NCO

promoted by complex **17**. Such reactivity is almost unexplored^[329–331]. Indeed, isocyanates are much more known to undergo catalytic polymerization or cyclotrimerization,^[332–336] and, to our knowledge, this original cooperative decarbonylation mechanism of AdNCO is unprecedented.

4.4.3 Reactivity with dicyclohexylcarbodiimine

We also contemplated the reactivity of a typical carbodiimine, dicyclohexylcarbodiimine (Cy-N=C=N-Cy noted DCC), towards the same Ir-Al complexes (**12**, **15**, and **17**).

Unfortunately, treatment of dimer **12** with DCC leads to a complex mixture of species that we are not able to identify (Scheme 69, left).



Scheme 69. Reactivity of dicyclohexylcarbodiimine with complexes **12**, **15**, and **17**.

Nonetheless, heterobimetallic complex **15** and its relative pyridine mono-adduct **17**, cleanly reacts with a stoichiometric amount of DCC forming a new amidinate Ir-Al species, noted **25** (Scheme 69, right).

4.4.3.1 Synthesis of an amidinate Ir-Al complex, **25**

Stoichiometric reaction of **17** with DCC leads to the formation of a bridged amidinate species, Cp*IrH₂(μ-CyNC(H)NCy)Al(^{*i*}Bu)(OAr) **25** with elimination of pyridine (Scheme 69, right). Note that the reaction of complex **15** with 1 eq. of DCC also leads to product **25** revealing the spectator role of the pyridine ligand.

Contrary to CO₂ and AdNCO, DCC is not subjected to a reductive cleavage of a C=N bond but rather stops at the hydride migration step. The protonation of the central carbon of the amidinate bridge is confirmed by NMR spectroscopy: the ¹H-NMR spectrum of **25** shows a characteristic singlet at δ = +6.99 ppm coupling in the ¹H-¹³C HSQC NMR experiment to the diagnostic ¹³C resonance found at δ = +162.9 ppm (Figure 71). Interestingly and contrary to all reported iridium hydride species in this manuscript, the ¹H NMR spectrum of **25** displays two non-equivalent

hydrides singlets at $\delta = -14.52$ ppm and $\delta = -14.99$ ppm (Figure 71). We attribute this phenomenon to the rigidity of this complex, which most likely originates from chelating effect of the amidinate ligand and steric hindrance of the aryloxy group, which prevents rotation of the hydrides in solution.

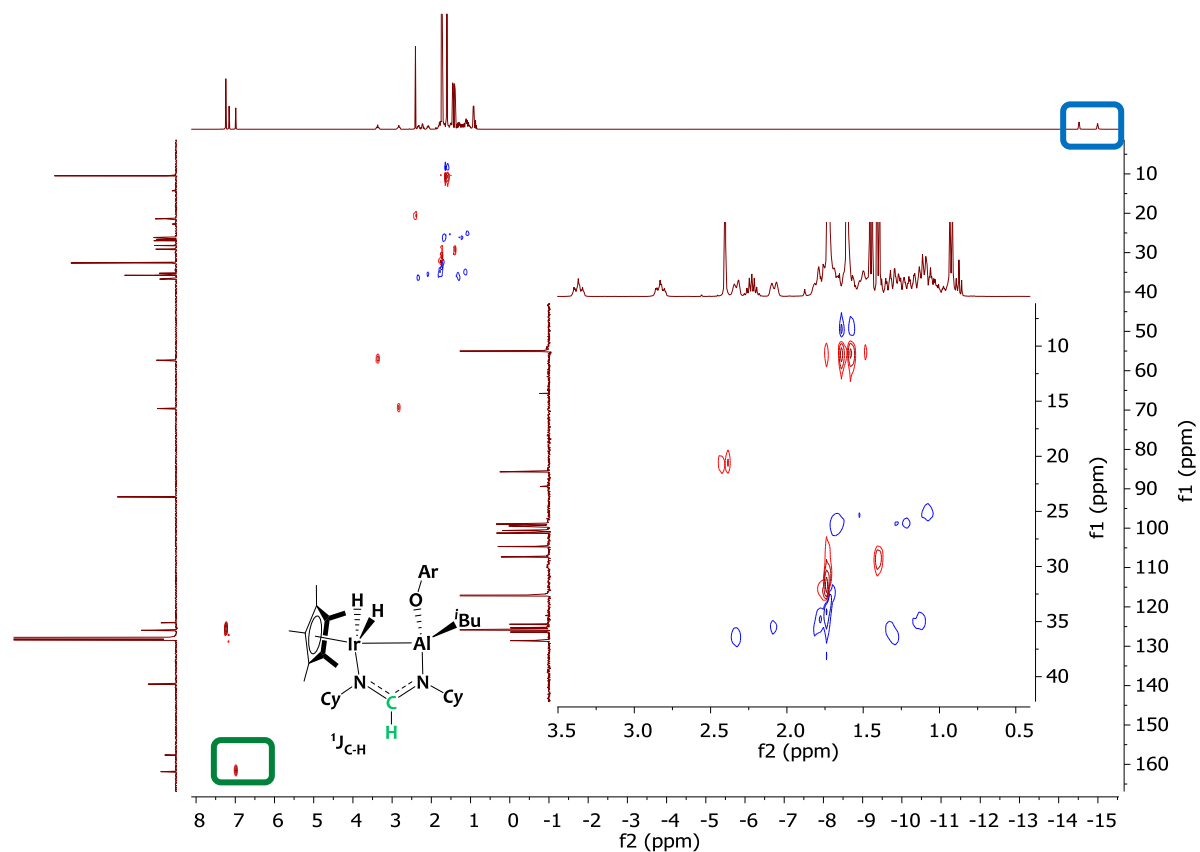


Figure 71. ^1H - ^{13}C -HSQC NMR spectrum (400 MHz, C_6D_6 , 293K) of **25**. The green rectangle shows the heteronuclear ^1H - ^{13}C correlation of the central C-H amidinate bridge. The blue rectangle shows two distinct Ir-H signals in the ^1H dimension (f1).

Compound **25** is isolated as light yellow block-shaped crystals after a cold recrystallization in pentane. Its crystallographic structure (obtained from XRD studies) is shown in Figure 72. The bridging μ - η^1, η^1 amidinate ligand is located parallel to the metal-metal axis, as commonly found in metal-metal bonded dinuclear amidinate species.^[337–339] This results in an elongation of the Ir-Al distance to 2.617(1) Å (versus 2.502(2) Å in **17**). The five-member Ir1-Al1-N2-C2-N1 ring is almost perfectly planar and the N1-C2 and N2-C2 bond distances (1.311(6) and 1.328(6) Å respectively) are in the expected range for an amidinate motif.^[339,340] The N1-C2-N2 angle (124.8(4)°) is much larger than that classically found in η^2 amidinates, but this value compares well with that reported for μ - η^1, η^1 amidinates bridging heavy metal ions.^[339,341] The N1-Ir1 (2.088(4) Å) and N2-Al1 (1.905(4) Å) bond lengths are comparable to that found in Al and Ir amidinate complexes respectively.^[102,342–344]

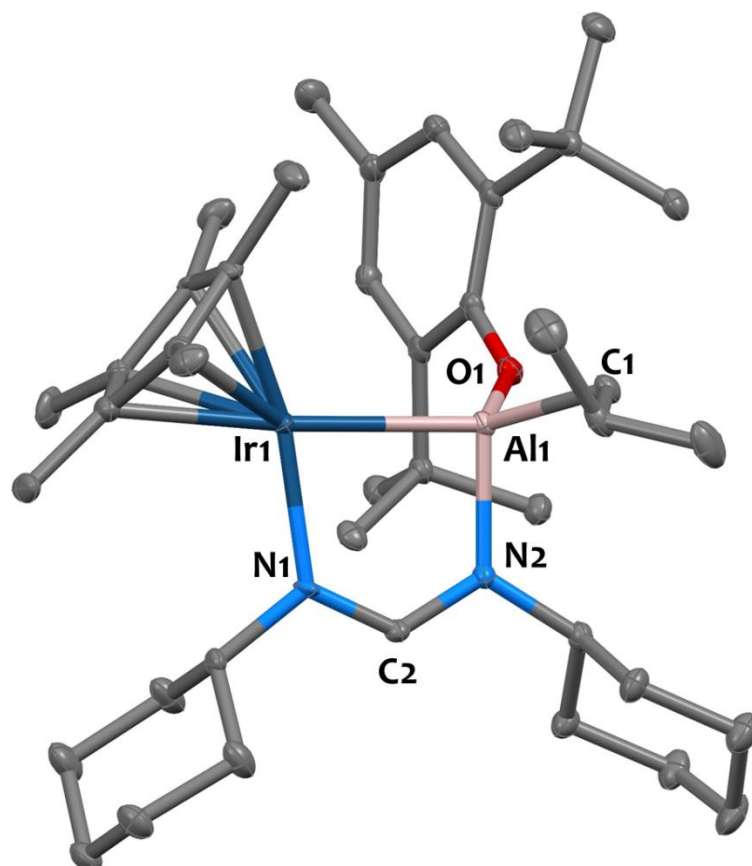


Figure 72. Solid-state molecular structure of **25**. Displacement ellipsoids are plotted at a 30% probability level. Hydrogen atoms have been omitted for clarity. Selected bond distances (Å) and angles (°): Ir1-Al1 2.617(1), Al1-O1 1.766(4), Al1-C1 1.986(5), Al1-N2 1.905(4), Ir1-N1 2.088(4), N1-C2 1.311(6), N2-C2 1.328(6), N1-C2-N2 124.8(4), N2-Al1-Ir1 91.0(1), O1-Al1-C1 107.5(2), N1-Ir1-Al1 81.2(1), Al1-Ir1-Cp*_{centroid} 144.85(1).

4.4.3.2 DFT calculations

Calculations are performed on the reaction of **17** with CyN=C=NCy. The resulting computed enthalpy profile is shown in Figure 73. In that case, the reaction sequence is more straightforward than those observed for CO₂ or AdNCO.

- 1) Notably, like for CO₂ or AdNCO, reagent **17** undergoes a substitution of pyridine by DCC to form a new adduct, intermediate **I1**, where the DCC derivative is N-coordinated to the Al center. The associated transition of state, noted **TS1** (see Table 9), has an associated barrier of +3.3 kcal/mol.
- 2) Then, **I1** is subjected to a hydrogen transfer from Ir to the central carbon of DCC through a kinetically accessible barrier (noted **TS2**) of +7.2 kcal/mol, which yields an amidinate species, noted **I2**.
- 3) Eventually, the second nitrogen is coordinated onto the Ir atom forming the stable bridging amidinate product **25**.

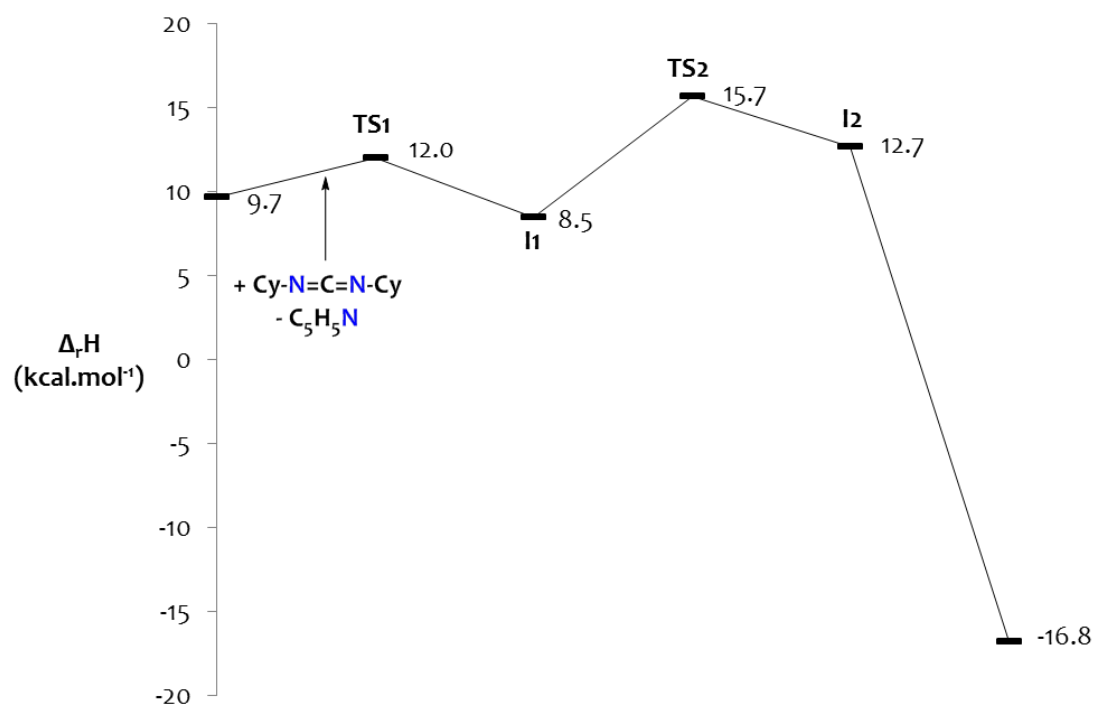


Figure 73. Computed enthalpy profile for the reaction of DCC with 17 at room temperature.

Transition state (TS)	DFT optimized structure	Intermediate (I)	Related structure
TS1		I1	
TS2		I2	

Table 9. Transition states and intermediates corresponding to the labels depicted on Figure 73.

In conclusion, this reaction stops at the H-migration step yielding a bridging amidinate species. No

further reductive C=N bond cleavage is occurring probably because of the increased steric bulk of the complex imparted by the cyclohexyl moieties.

4.5 Conclusions

The conclusion of this chapter will be built on the points listed in the introductory section (part 4.1, page 167).

i) First of all, we have shown that the aluminum sites in compounds **12**, **14**, and **15** are electrophilic and accessible and can accommodate Lewis bases – such as pyridines and DMAP – to form adducts (compounds **16**, **17**, and **18**), without cluster dissociation. The Al centers can also interact with anionic ligands – such as benzyl anion – to form anionic species, as observed for the formation of compound **19**, or eventually leading to ligand exchange through the displacement of $[\text{Cp}^*\text{IrH}_3]$ units.

ii) This study also demonstrated that the H-Ir motifs of species **12** and **14** are no longer acidic upon reaction with a strong Brønsted base such as benzyl potassium since no deprotonation took place. Instead, hydrides are retained at the iridium sites and $[\text{Cp}^*\text{IrH}_3]$ fragments are labile and can be subjected to transmetallation reactions leading to potassium or silver derivatives as seen for the formation of complexes **20** and **21**.

iii) $\text{B}(\text{C}_6\text{F}_5)_3$ is employed to abstract pyridine from complex **17** and restore the Lewis acidic Al site in complex **15**, with release of the $\text{B}(\text{Py})(\text{C}_6\text{F}_5)_3$ adduct. When cluster **12** is treated with $\text{B}(\text{C}_6\text{F}_5)_3$, an alkyl moiety is cleaved from the Al site through a β -H elimination leading to the formation of salt **22**.

iv) We did not notice any redox behavior in these processes. For instance, instead of an oxidation reaction when employing silver triflate and complex **14**, we observed an unexpected transmetallation from Al to Ag (formation of complex **20**) and a nucleophilic addition of the triflate anion onto the Al center (formation of complex **21**). This behavior is indicative to fragile Ir-Al interactions. Note that we also attempted to reduce these clusters with potassium, and this led to the formation of $[\text{KIrCp}^*\text{H}_3]_n$ species among other products, again showing that these Ir-Al assemblies are not robust. All these aspects will be specifically considered during the next chapter concerning SOMC.

v) These Ir-Al species and in particular complex **17** promote the heterobimetallic cooperative reductive activation of heteroallenes, as confirmed by spectroscopic, crystallographic, and computational data. Notably, in the reaction with **17**, dicyclohexylcarbodiimide is reduced into an

amidinate species – complex **25** – where the key step is a H-migration from Ir to C. But more importantly, this reduction mechanism can go further when carbon dioxide and adamantly isocyanate are used, triggering decarbonylation. Indeed, this study revealed uncommon cooperative reductive cleavages of CO₂ and AdNCO fostered by the strongly polarized Ir^{δ-}-Al^{δ+} motif that leads to the formation of uncommon Al-oxo and Al-ureate species (complexes **23** and **24** respectively). From the viewpoint of iridium, these are rare examples where Ir(III) of d⁶ configuration acts as a nucleophile, and such a result opens up attractive prospects for reactivity in catalysis. From the viewpoint of aluminum, these complexes behave as masked low-valent Al species and provide access to unconventional motifs in molecular Al chemistry (e.g. oxos). These aspects are reminiscent to the reductive cleavage of CO₂ by low oxidation state aluminum species,^[300–302] which are very challenging to isolate. This work thus embodies a scientific breakthrough in this area.

Overall, this study provides an overview of the reactivity of the iridium-aluminum complexes **12**, **14**, **15**, and **17**. We will see in the next chapter how this knowledge can be useful and valuable in view of grafting these complexes onto dehydroxylated silica supports.

CHAPTER 5. Development Of Al/Ir Heterobimetallic Sites Supported On A Mesostructured SBA-15₇₀₀ Silica

5.1 Introduction

As discussed in CHAPTER 1-section 1.3.4 (from page 89), surface organometallic chemistry (SOMC) is a powerful approach for reaching well-defined heterobimetallic surface sites immobilized onto a solid support. In particular, we have discussed the major advantage of directly grafting pre-assembled heterobimetallic edifices onto SiO₂ (**D** type materials, see Scheme 43-page 98). We have also shown the interests of SOMC to generate isolated monometallic sites together with highly dispersed nanoparticles (Nps) homogeneously distributed at the surface of solid supports (**B** and **C**-type materials, see Scheme 43-page 98). Importantly, reaching well-defined surface sites is strongly dependent on the nature of the support. In this PhD work we turned our attention to the use of a mesostructured Santa Barbara Amorphous-15 silica – abbreviated SBA-15 thereafter – for many reasons, detailed below.

5.1.1 Description and interests of the SBA-15 support

SBA-15 features a well-defined and structured mesoporous network with large and accessible longitudinal pores of internal diameter of about 8 nm. These pores, in the form of parallel channels, are organized in a 2D hexagonal network and the silica grains form micrometric fibers (Figure 74).^[345,346] As a consequence, SBA-15 has a very high specific surface area of about 1000 m².g⁻¹. These structural and textural properties make SBA-15 a particularly suitable material for the incorporation of relatively large organometallic species into the pores since the size of the pores is relatively big (in comparison with zeolite materials for instance), and internal diffusion process are generally not limiting in catalysis. In addition, unlike other mesoporous silicas, SBA-15 has the added advantage of being relatively robust during thermal treatments, without collapse of the mesoporous network, up to at least 750°C. This is particularly important since a dehydroxylation process of the material at high temperature is required to control the surface chemistry of the solid support, as discussed in section 1.3.1.2 (from page 75). In our case, SBA-15 is dehydroxylated at T=700°C – noted as SBA-15₇₀₀ hereafter – in order to ensure good isolation of the surface silanols and thus result in isolated surface organometallic sites after their grafting (Figure 75). As a result, the density of sites at the surface is quite low, typically below 1 site per nm². Characterizing surface organometallic species at such dilution is quite challenging, yet this is compensated by the large surface area of SBA-15, making possible a significant incorporation of organometallic species, and thus facilitating its characterization *via* spectroscopic techniques by increasing the

signal-to-noise ratio.

In order to anticipate the reactivity of organometallic complexes on the surface of SBA-15₇₀₀ and to provide molecular models of the surface species, the SOMC community is paying particular attention to the construction of molecules that mimic the isolated surface silanols. Description and interests to develop molecular models of SBA-15 surface will be presented hereunder.

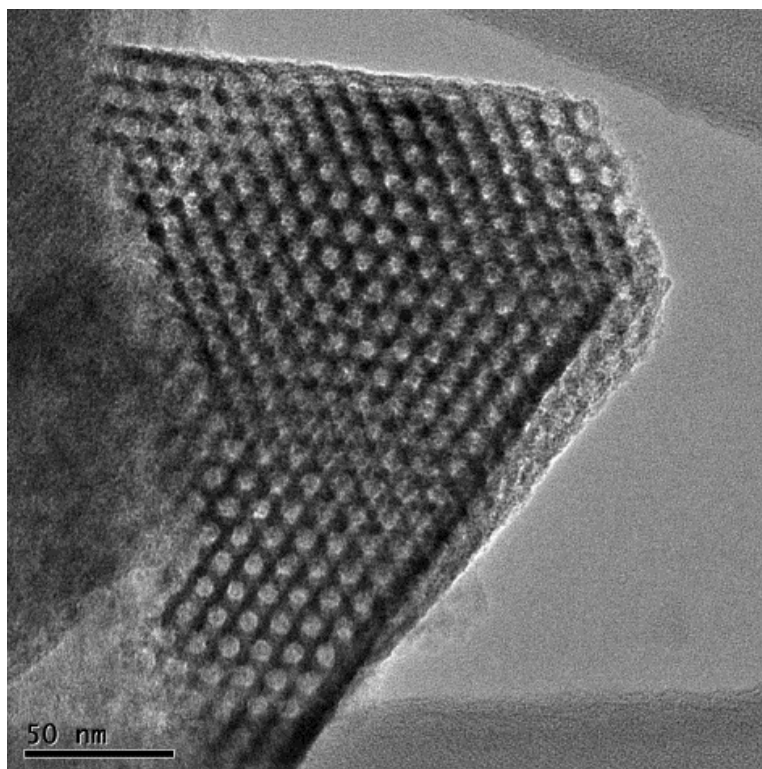


Figure 74. TEM image of SBA-15₇₀₀.

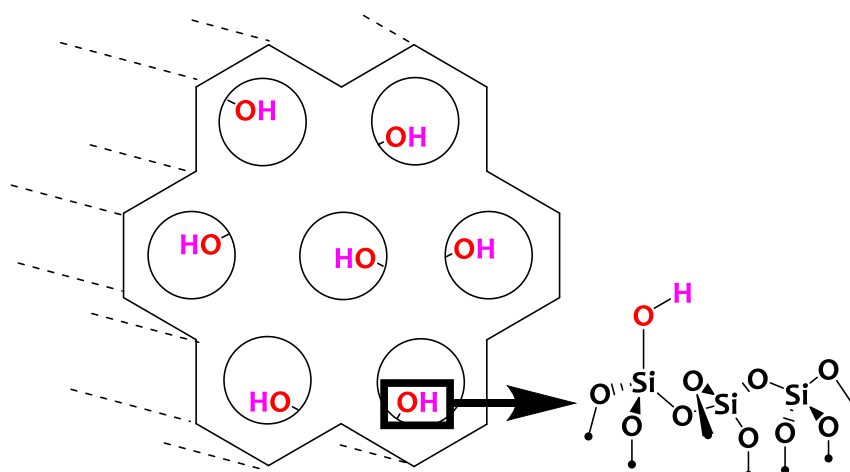


Figure 75. Schematic representations of SBA-15.

5.1.2 Molecular models of silica surface

In order to provide a detailed understanding of the elementary mechanisms involved in heterogeneous catalysis and thus to develop new and more efficient catalysts in a rational way, it is essential to establish structure-activity relationships of the active sites. The fine determination of the molecular structure of organometallic sites present on the surface of these solids is thus key, and requires advanced characterization techniques such as vibrational spectroscopy (IR), advanced solid-state NMR spectroscopy or also Extended X-Ray Absorption Fine Structure (EXAFS) and X-ray Absorption Near Edge Structure (XANES).

However, despite many advances, the precise characterization of these active sites in the solid state remains a challenge, and is much more delicate than the classical characterization of molecular organometallic species (whose solid state structure can, in many cases, be solved by single crystal X-ray diffraction).

Therefore, the search for molecular models, reproducing the interactions with the solid support, by using ligands with steric and electronic properties close to this latter, is particularly interesting to model the surface species while using usual structural characterization techniques employed in molecular organometallic chemistry (single-crystal XRD, liquid NMR etc.). Such work makes also possible to anticipate the reactivity of an organometallic precursor with the solid support, prior to grafting.

The reactivity of silicic surfaces with transition metal derivatives is mainly localized at the surface silanol groups, as described in CHAPTER 1. In order to model these surface species, siloxide and aryloxide ligands appear then to be prime candidates. The pKa of silica surface isolated silanols is about 7.0.^[347] Silanol derivatives (HOSiR₃) with oxygenated substituents are thus preferred because of their more acidic properties (R=Et, pKa=13.7; R=Ph, pKa=10.8; R=OR', pKa=9.0). Another alternative can be aryloxide ligands, which are more acidic than alkoxides (pKas of phenol derivatives are around 10) and whose steric profiles are easily tuned.

Polyhedral oligomeric silsequioxanes (POSS) are analogues of choice to mimic the surface of SBA-15₇₀₀, *i.e.* isolated silanols.^[120] However these ligands are expensive or requires long synthetic procedures, and can be difficult to crystallize. Tris-tert(butoxy)silanol (HOSi(OtBu)₃) is a more straightforward alternative, as reported by some works (Figure 76).

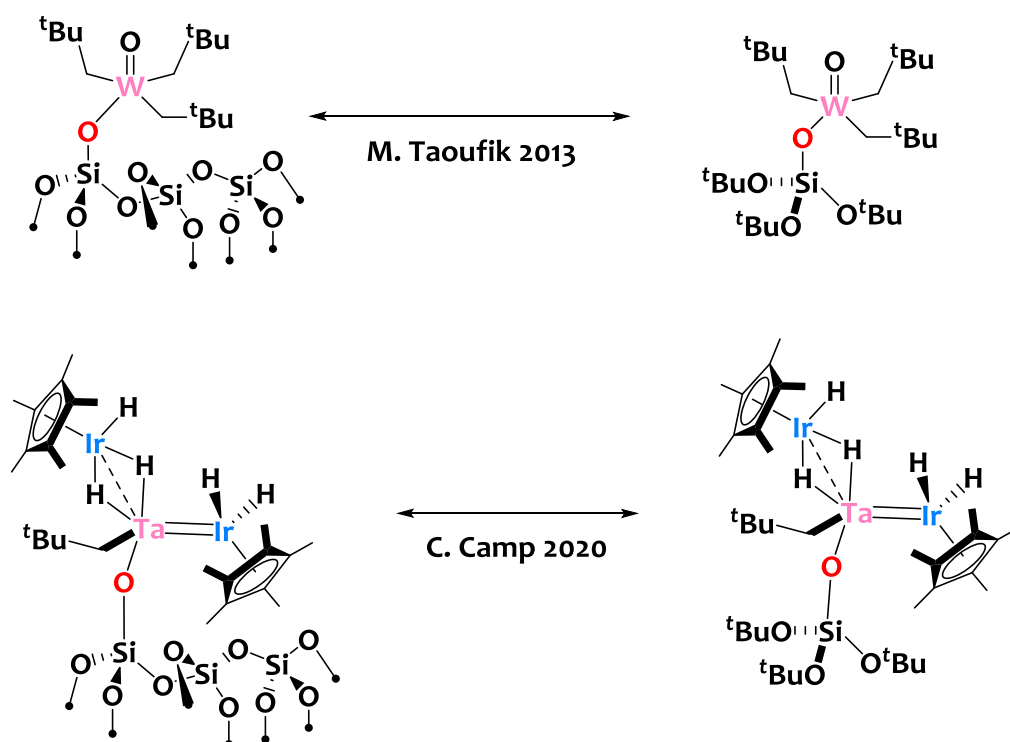


Figure 76. Two reported instances of well-defined organometallic complexes immobilised on SBA-15₇₀₀ (left side) and their related molecular analogues based on tris-tert(butoxy)siloxyl ligand (right side). Figure adapted from references^[28,348].

In these two cases, the bulkiness of O^tBu pendant groups is sufficiently important to get monosubstituted (or monopodal) species. But some works demonstrated that the steric profile of HOSi(O^tBu)₃ is not so high and similar to a cyclopentadienyl ligand^[312,349]. As a result poly-substituted or oligomeric organometallic species can form, and are not anymore suitable analogues of the related monopodal grafted species, as illustrated on Figure 77, top.

The use of phenoxy ligands with a steric profile more important than that of the tris(tert-butoxy)siloxy ligand is therefore an interesting alternative, as demonstrated recently in our laboratory (Figure 77, bottom).^[27]

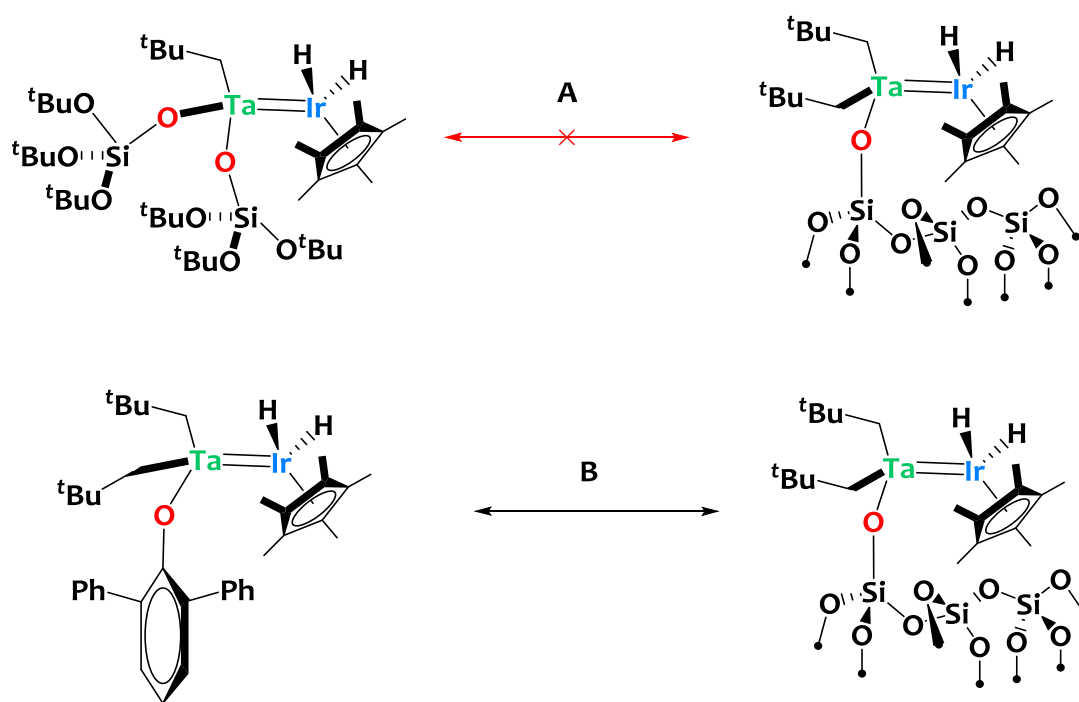


Figure 77. (A) Molecular bipodal bis(tris-tert(butoxy)siloxy organometallic species (top left) not representative to the monopodal grafted species on SBA-15₇₀₀ (top right). (B) Molecular monopodal 2,6-diphenyl-phenoxy organometallic complex (bottom left) representative to the supported species (bottom right). Figure adapted from reference ^[27].

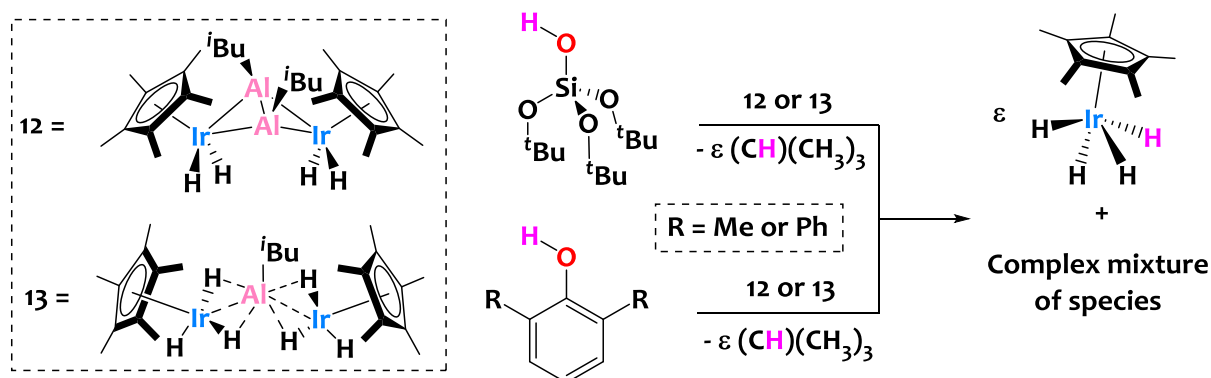
We will see in the next sections that all these aspects have to be considered for the grafting of Al/Ir systems.

In this chapter, we will first describe the reactivity of the Ir-Al complexes with molecular models of silica surfaces. Next, we will present the preparation and characterization of a new iridium-aluminum surface species grafted onto SBA-15₇₀₀. We will also show that this material is a gateway to generate supported Ir-NPs of small sizes with interfacial monometallic Al sites homogeneously distributed on the surface of the silica. In view of undertaking comparative catalytic studies, we will also describe the synthesis of the Ir monometallic analogue of the heterobimetallic material.

5.2 Reactivity with molecular models of the silica surface

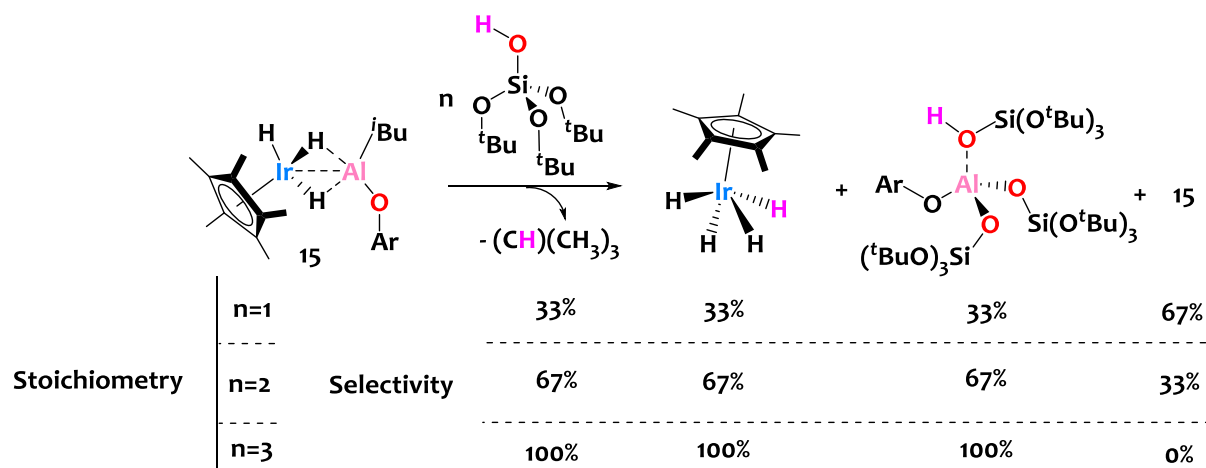
We first turned our attention to the reactivity of complexes **12**, **13**, **14**, and **15** towards molecular models of silica surface. The objective is to investigate the viability of these Ir-Al compounds in view of getting grafted on a SBA-15₇₀₀ support.

The reaction of the alkyl-aluminum/iridium clusters **12** and **13** with tris(tert-butoxy)silanol (HOSi(O^tBu)₃), performed in C₆D₆, is monitored by ¹H NMR (Scheme 70). In both cases, multiple products are observed, which are impossible to clearly identify except traces of isobutane gas and IrCp*H₄ (Scheme 70). Changing the stoichiometry (from 1.0 to 4.0 equivalents of HOSi(O^tBu)₃), the temperature (from room temperature to 80°C) or the solvent (THF-d₈) do not change this assessment. Tuning HOSi(O^tBu)₃ to phenol derivatives (2,6-xylenol and 2,6-diphenyl-phenol) also result in complicated mixture of unidentified species. Note that when using 2,6-Di-tert-butyl-4-methylphenol, no reaction occurs even at high temperature (up to T=80°C), which we attribute to the high steric profile of this derivative.



Scheme 70. Reaction of tris-(tert-butoxy)-silanol and phenol derivatives with complexes **12**, **13**, and **15**.

In the case of the heterobimetallic complex **15**, processes are still complicated but it is possible to understand what happens. Treatment of species **15** with 3 equivalents of tris-(tert-butoxy)silanol (Scheme 71) produces one equivalent of IrCp*H₄ and isobutane gas along with a new Al-product which was assigned to [Al(OAr){HOSi(O^tBu)₃}{OSi(O^tBu)₃]₂] derivative (Figure 78, blue spectrum). Surprisingly, the same products are observed when using 1 or 2 equivalents of HOSi(O^tBu)₃, along with unreacted **15**, in the following ratio: for two equivalents of HOSi(O^tBu)₃ - 67% of IrCp*H₄, 67% of [Al(OAr)(HO^tBu)(O^tBu)₂], 67% of isobutane, and 33% of unreacted **15** - for one equivalent of molecular silanol, 33% of IrCp*H₄, 33% of [Al(OAr)(HO^tBu)(O^tBu)₂], 33% of isobutane and 67% of unreacted **15** (see Scheme 71 and ¹H NMR spectra on Figure 78). This advocates to polysubstitution phenomena, as in the case discussed on Figure 77A, see page 217.



Scheme 71. Reaction of tris-(tert-butoxy)-silanol (1, 2, or 3 equivalents) with complex 15.

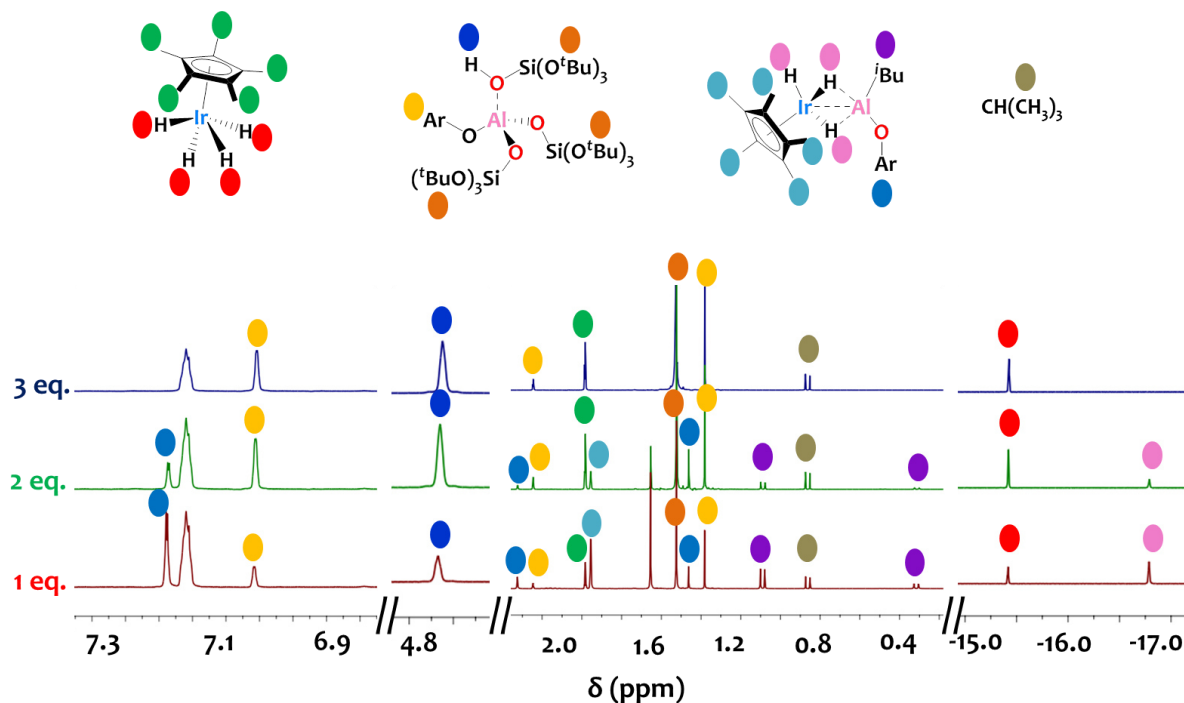
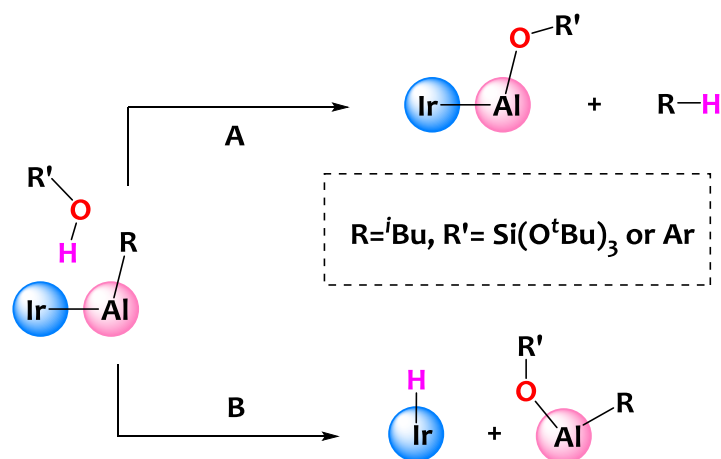


Figure 78. $^1\text{H-NMR}$ (300 MHz, C_6D_6 , 293K) spectra recorded after treatment of 15 with $\text{HOSi}(\text{OtBu})_3$ (1 eq. = red line; 2 eq. = green line; 3 eq. = blue line).

In light of these studies, several conclusions can be drawn. First, there is a competition between two protonolysis reactions, either between the hydroxyl groups and the $\text{Al-C}_{\text{alkyl}}$ bonds (Scheme 72, path A) or across the two metals (Scheme 72, path B), leading to multiple possible products. Thus, even though these systems display non-negligible Ir-Al interactions (see CHAPTER 3), and are further stabilized by bridging hydrides, these are likely not enough to get exclusively a protonolysis phenomenon centred on the Al-alkyl motif. This is in agreement with the reactivity reported in CHAPTER 4 in which we demonstrated that these Ir-Al species are prone to be cleaved by polar substrates (such as nucleophiles, heteroallenes, and in this case protic derivatives).

Quite importantly, these are rare instances where heterobimetallic M₁/M₂ (M₁=B, Ta, Zr; M₂=Ru, Ir, Cu, Au) edifices promote cleavage of H-O bonds across the M₁-M₂ bond to yield alkoxy/siloxy (RO-M₁) moieties and hydride (H-M₂) motifs.^[218,350–356] Second, polysubstitution phenomena cannot be avoided, as reflected by the NMR titration discussed above. Finally, the capability of HOSi(O^tBu)₃ to act as a Lewis acid and coordinate to the Al site further complicates the distribution of species in the final mixtures.

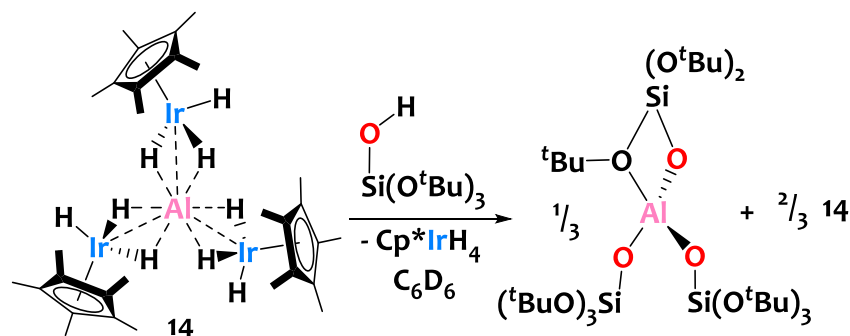


Scheme 72. (Path A) O-H activation of silanol or phenol derivatives (HOR') across the Al-R bond, which yields a Ir-Al(OR') product and a RH co-product. (Path B) O-H activation of silanol or phenol derivatives (HOR') on Ir-Al(R) species across the Al-Ir bond, which yields a Ir-H product and an Al(R)(OR') co-product.

Consequently, species **12**, **13**, and **15** generate multiple products upon reaction with silanol or phenol derivatives. This shows the unsuitability of using these alkyl-aluminum/iridium as preassemblies for grafting upon silica support since multiple surface products would be obtained, removing the benefit of using tailored, well-defined heterobimetallic precursors.

A key to circumvent the deadlock discussed above would be to eliminate the competition between Al-alkyl protonolysis and Al-Ir oxidative addition. Cluster $[\{\text{Ir}(\text{Cp}^*)(\text{H})(\mu\text{-H}_2)\}_3\text{Al}]$ **14** embodies therefore an ideal candidate since only hydrides are linked to the Al atom. We thus investigated the reactivity of **14** with 1 eq. of HOSi(O^tBu)₃. This leads, within minutes, to the partial formation of a tris-substituted siloxide aluminum species, Al(OSi(O^tBu)₃)₃, along with unreacted **14** and IrCp*H₄ coproduct in ratios 0.3/0.7/1.0 respectively (Scheme 73). Indeed, the ¹H-NMR spectrum of the reactional medium (recorded in C₆D₆) displays a tert-butoxide resonance at $\delta = 1.52$ ppm matching that of the reported Al(OSi(O^tBu)₃)₃ derivative,^[147] as well as the signatures of IrCp*H₄ and **14** (see Figure 79). This first experiment highlights the suitability of **14** for protonolysis reactivity, but at the same time the difficulty to prevent polyaddition phenomena on

the aluminum site, even when sub-stoichiometric amounts are used. This most likely arises from the high reactivity of the mono-siloxy Al species in solution.



Scheme 73. Reaction of tris(tert-butoxy)silanol with complex **14**.

Since the surface silanol groups on SBA-15₇₀₀ are isolated from each other's, such polyaddition phenomena are not possible at the surface of silica, and monopodal species are formed. In view of better mimicking the first coordination sphere of the putative Al-grafted species, we thus contemplated other molecular models aiming at preventing these polysubstitution phenomena. To do so, we focused our studies on phenol derivatives with different steric profiles. 2,6-Di-tert-butyl-4-methylphenol (BHT) does not react with **14**, even after prolonged heating at T=80°C. Such inertness is attributed to the high steric bulkiness of the BHT molecule. On the opposite, 2,6-dimethylphenol (xylenol) is highly reactive with **14**, leading to multiple products, which likely relates to a mixture of mono and poly-substituted Al phenoxy species. In this case, the steric profile of xylenol seems too low to avoid polyaddition phenomena. Successfully, when using a phenol derivative with a steric profile between BHT and xylenol, the desired mono-substituted product is obtained. Indeed, stoichiometric treatment of complex **14** with propofol (2,6-diisopropylphenol) in pentane, generates, after 2 hours at room temperature, the mono-substituted $[\{(\text{Ir}(\text{Cp}^*)(\text{H})(\mu\text{-H}_2))_2\text{Al}(\text{OAr}')\}]$ complex, **26**, along with one equivalent of IrCp*H₄ as coproduct of the reaction (Scheme 74). We also investigated the reaction of **14** with 2,6-diphenylphenol, which also exclusively yields a mono-substituted aryloxy species, but only partly (remaining of reactant **14**) even after prolonged heating in refluxing C₆D₆ for a few days.

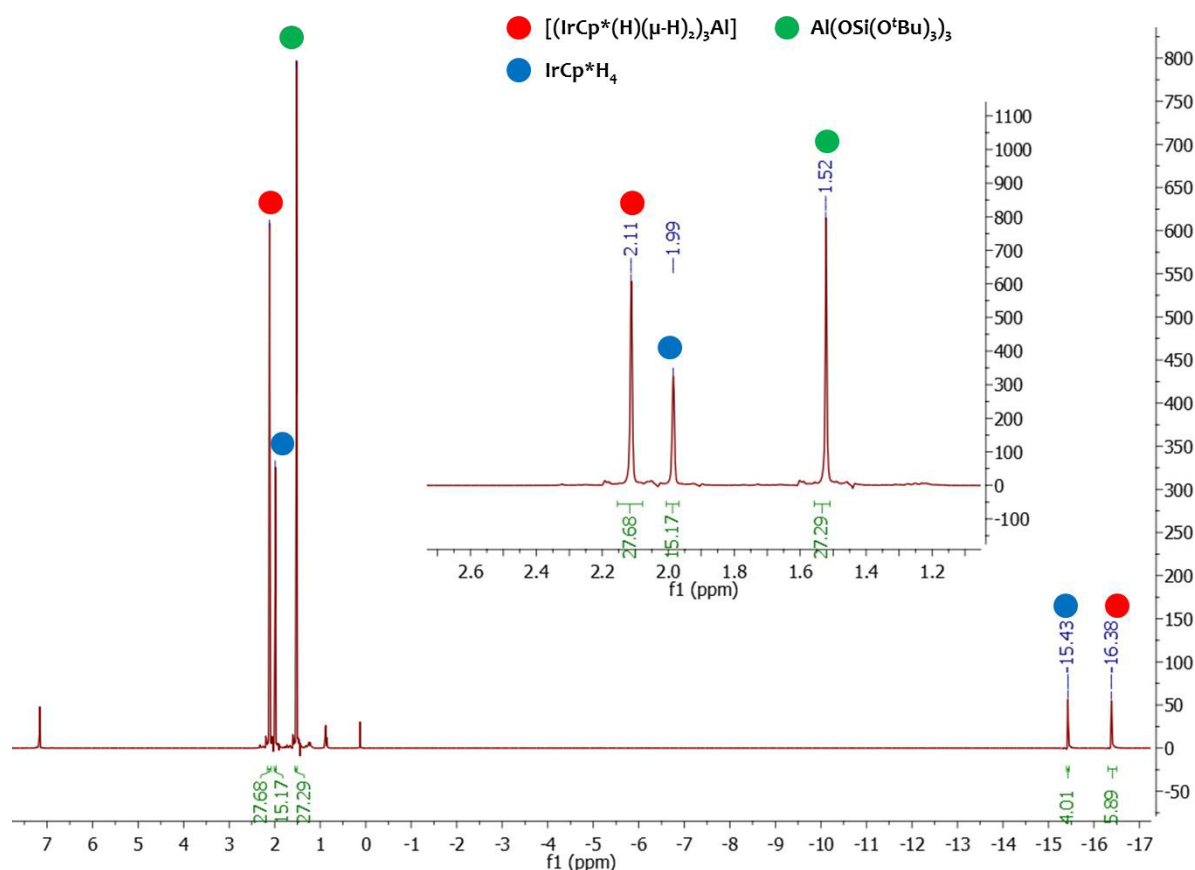
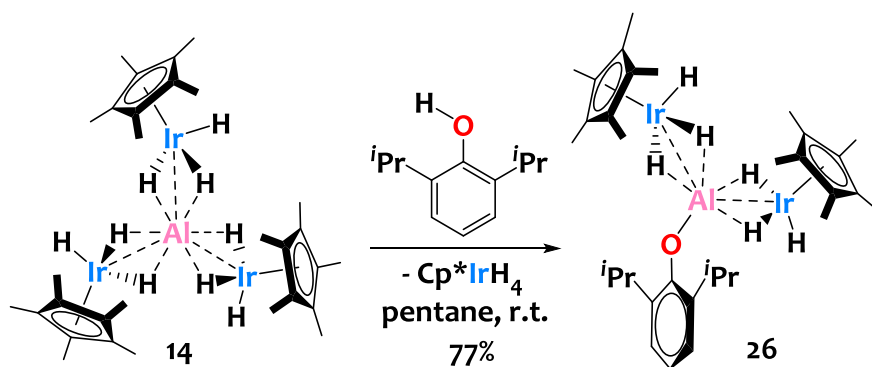


Figure 79. $^1\text{H-NMR}$ spectrum (300 MHz, C_6D_6 , 293K) relating to the stoichiometric reaction of **14** with $\text{HOSi}(\text{O}^t\text{Bu})_3$. This reaction leads to the formation of $\text{Al}(\text{OSi}(\text{O}^t\text{Bu})_3)_3$ (0.34 equiv.) along with IrCp^*H_4 (1 equiv.) and unreacted compound **14** (0.66 equiv.).



Scheme 74. Reaction of propofol with complex **14**.

Compound **26** is isolated in 77% yield as colorless block-shaped crystals by a cold recrystallization in a saturated solution of pentane. The $^1\text{H-NMR}$ spectrum of **26** (Figure 80) displays slightly upfield hydride ($\delta = -16.55$ ppm integrating for 6H) and Cp^* ($\delta = 1.98$ ppm integrating for 30H) signals compared to those in **14** ($\delta_{\text{Ir-H}} = -16.38$ ppm, $\delta_{\text{Cp}^*} = 2.11$ ppm). The presence of one phenol fragment per Al atom is confirmed by the integration of the aromatic ($\delta = 7.21$ and 7.01 ppm, 3H) and isopropyl resonances ($\delta_{\text{CH}} = 3.75$ ppm and $\delta_{\text{CH}_3} = 1.47$ ppm, 14 H). The DRIFT spectrum of **26** is quite

similar to that of **14**, with typical metal hydride stretches at $\sigma = 2139$ and 1998 cm^{-1} , assigned to terminal and bridging hydrides (Figure 81).

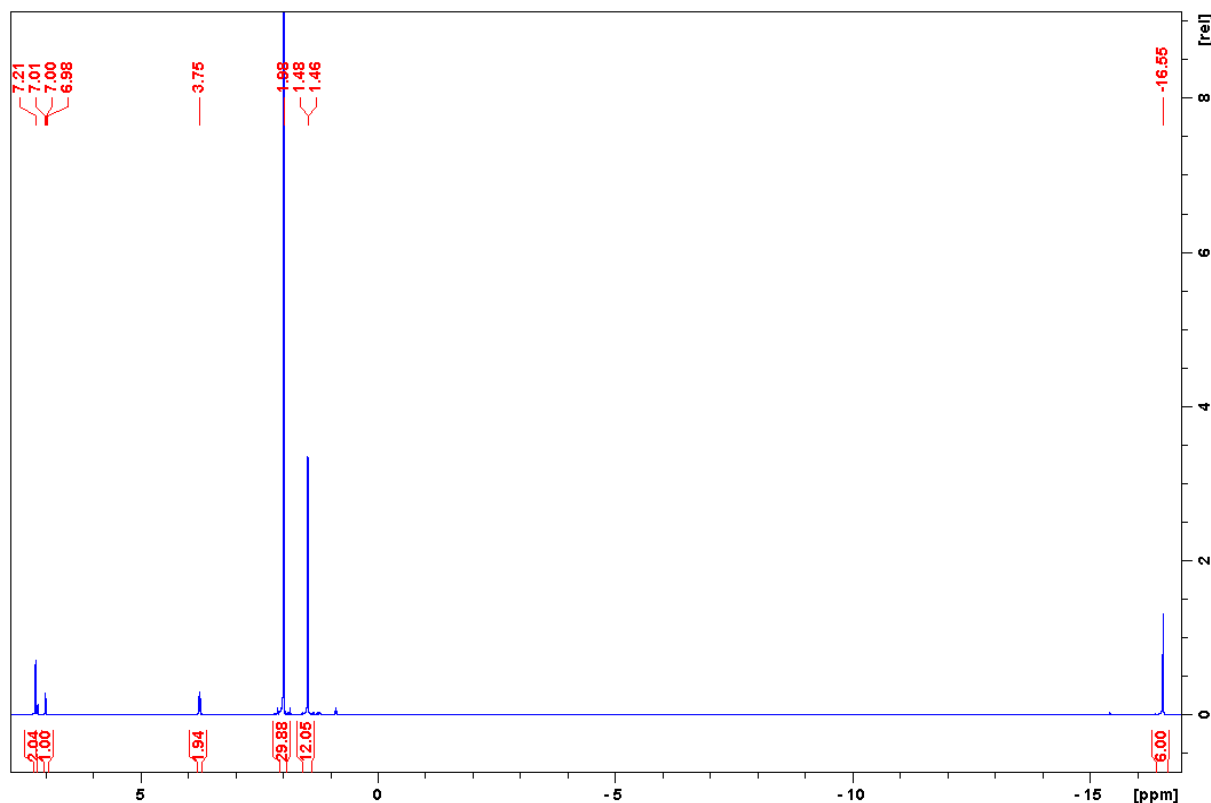


Figure 80. $^1\text{H-NMR}$ spectrum (500 MHz, C_6D_6 , 293K) of compound **26**.

XRD studies of **26** were also carried out. The resulting solid-state structure (see Figure 82) confirms the ligation of one phenoxy fragment and two IrCp^* units onto the Al atom. Apparent geometry of the Al center is nearly trigonal planar with angles ranging from 116.1° to 137.1° . Remarkably, the averaged Ir-Al distance is shortened compared to precursor **14** ($2.40(0)\text{ \AA}$ vs 2.48 \AA in **14**), which translate into a formal shortness ratio of 0.96. The strengthening of the interaction between Ir and Al upon ligand substitution in **26** either suggest that the aryloxy ligand is a weaker donor compared to $[\text{Cp}^*\text{IrH}_3]$, or alternatively that steric constraints in **14** prevent closer contact of Al with the surrounding Ir sites. Note that, to the best of our knowledge, only one reported structure has a shorter Ir-Al distance.^[65] The averaged distortion of the Cp^* rings with respect to the Ir-Al bonds is at 136.5° , which is close to the one for precursor **14** (140.8°) thereby suggesting one terminal and two bridging hydrides *per* iridium atom. The aryloxy angle at the oxygen ($\text{Al1-O1-C1}=135.3(9)^\circ$) is considerably bent with respect to linearity advocating to a weak π -donation of the oxygen lone-pair into the empty *p* orbital of the Al center.^[357]

Consequently, this study supports the relevance of using complex **14** as a precursor for supporting Al-Ir species upon the surface or silica.

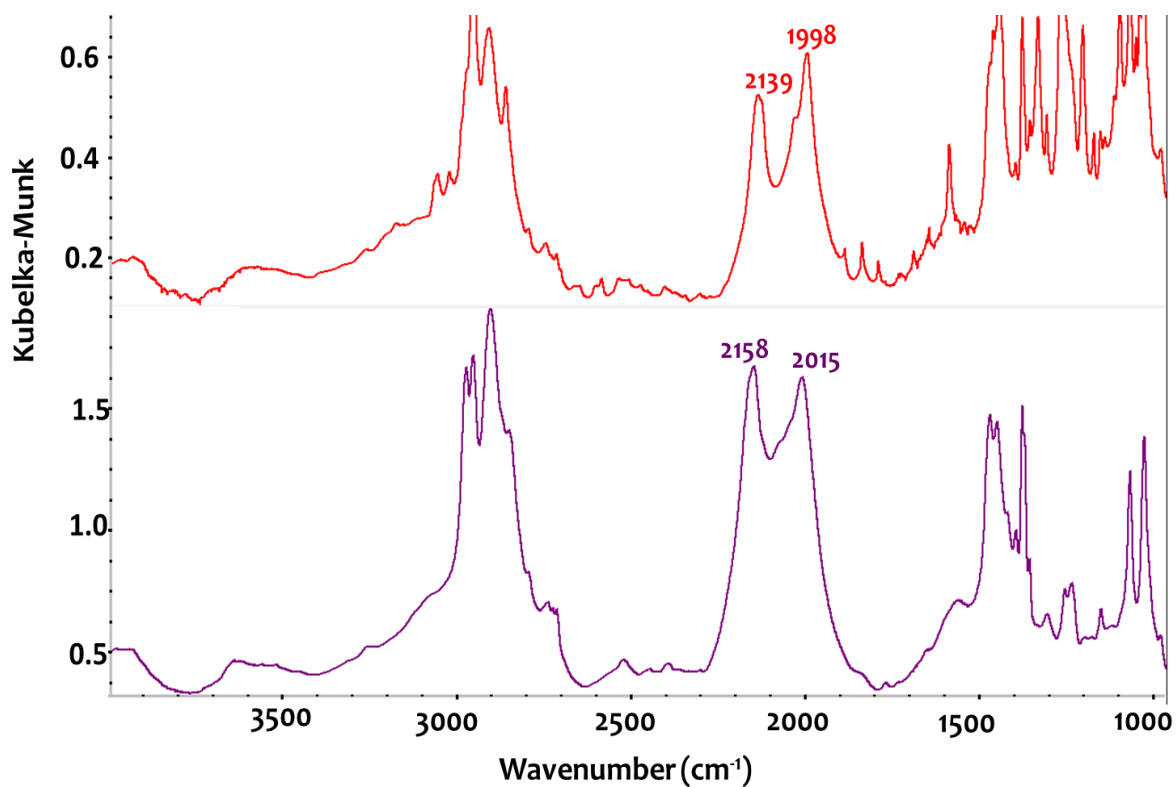


Figure 81. DRIFT spectra (298K, diluted in KBr, under argon) of complex 14 (purple) vs complex 26 (red).

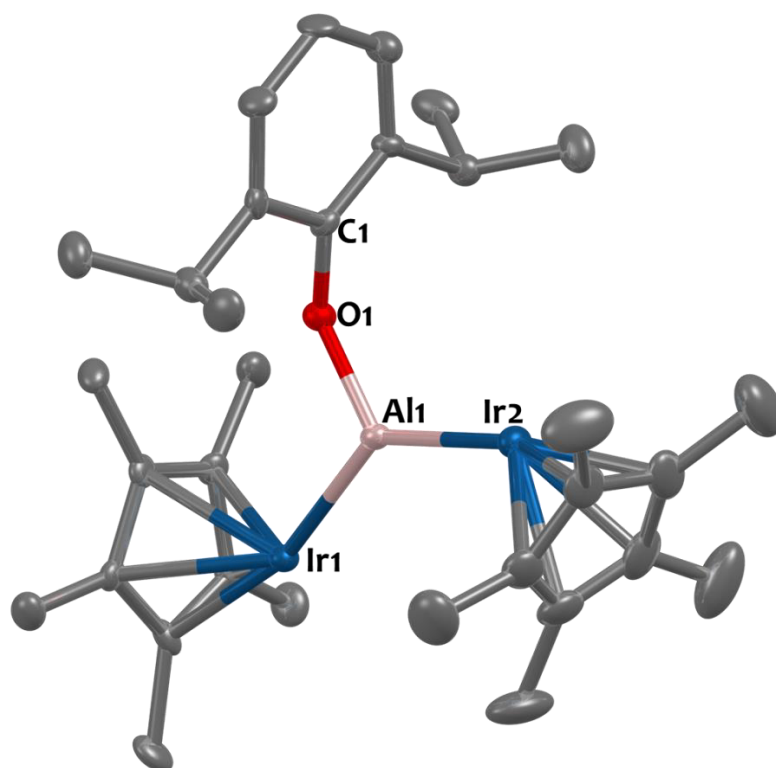
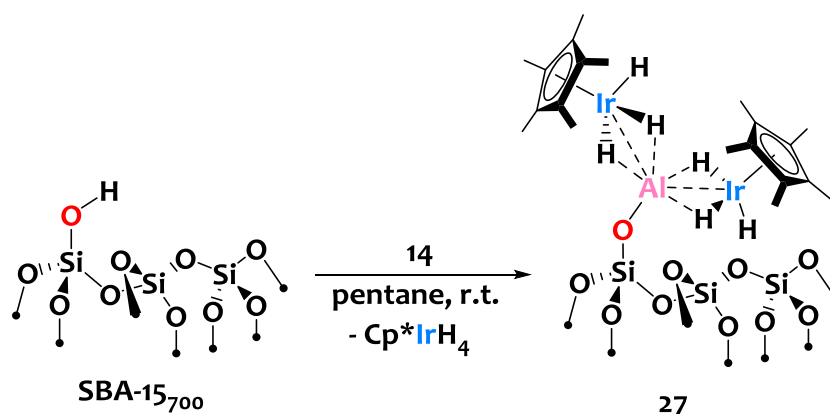


Figure 82. Solid-state molecular structure of 26. Ellipsoids are plotted at a 30% probability level. Hydrogen atoms have been omitted for clarity. Selected bond distances (Å) and angles (°): Ir1-Al1 2.405(4), Ir2-Al1 2.396(4), Al1-O1 1.735(10), O1-C1 1.341(15), Ir2-Al1-Ir1 137.06(17), O1-Al1-Ir1 106.8(4), O1-Al1-Ir2 116.1(4), C1-O1-Al1 135.3(9), Al1-Ir1-Cp*_{centroid} 133.22, Al1-Ir2-Cp*_{centroid} 139.73.

5.3 Preparation of silica-supported iridium-aluminum catalysts

5.3.1 Grafting of complex 14 onto dehydroxylated silica: preparation of the surface species $[\equiv\text{SiOAl}\{(\mu\text{-H})_2\text{Ir}(\text{H})\text{Cp}^*\}_2]$, 27

Treatment of SBA-15₇₀₀ with a pentane solution of 14 at room temperature, leads, after 2 hours, to the monopodal species $[\equiv\text{SiOAl}((\mu\text{-H})_2\text{Ir}(\text{H})\text{Cp}^*)_2]$, 27 (Scheme 75). The typical sharp $\nu(\text{OH})$ IR band at 3748 cm^{-1} in SBA-15₇₀₀ (corresponding to isolated surface silanols) is substituted in 27 by new signals attributed to metal-hydride stretches at 2131 and 2000 cm^{-1} and to $\nu(\text{CH})$ stretches of the Cp* ligands at $2913\text{-}2989\text{ cm}^{-1}$ (Figure 83). Note that DRIFT spectra of 27 and 26 are quite similar especially regarding intensity and positions of the Ir-H stretches, which testify to the relevance of 26 as molecular model for 27. During the reaction, 1 equiv. of IrCp^*H_4 is formed per grafted Al as quantified by $^1\text{H-NMR}$ spectroscopy. These analyses coincide with the chemical grafting of the precursor onto silica *via* protonolysis of one $\text{Al}(\mu\text{-H})_2\text{Ir}(\text{H})\text{Cp}^*$ group by a surface silanol, as seen in the preparation of 26, yielding a monopodal surface species. Furthermore, the elemental analysis data for 27 (expected % weight: %C 10.62, %H 1.60, %Ir 17.00, %Al 1.19; found: %C 10.87, %H 1.69, %Ir 16.40, %Al 1.21; expected ratios, C/Al=20.00, C/Ir=10.00, H/Al=36.00, H/Ir=18.00, H/C=1.80, Ir/Al=2.00; found: C/Al=20.18, C/Ir=10.61, H/Al=37.39, H/Ir=19.65, H/C=1.85, Ir/Al=1.90) are in accordance with the proposed formula for 27 and relates to 0.53 organometallic sites *per nm*² of silica, which is expected for this type of materials.^[27]



Scheme 75. Preparation of materials 27 from SBA-15₇₀₀ support and complex 26.

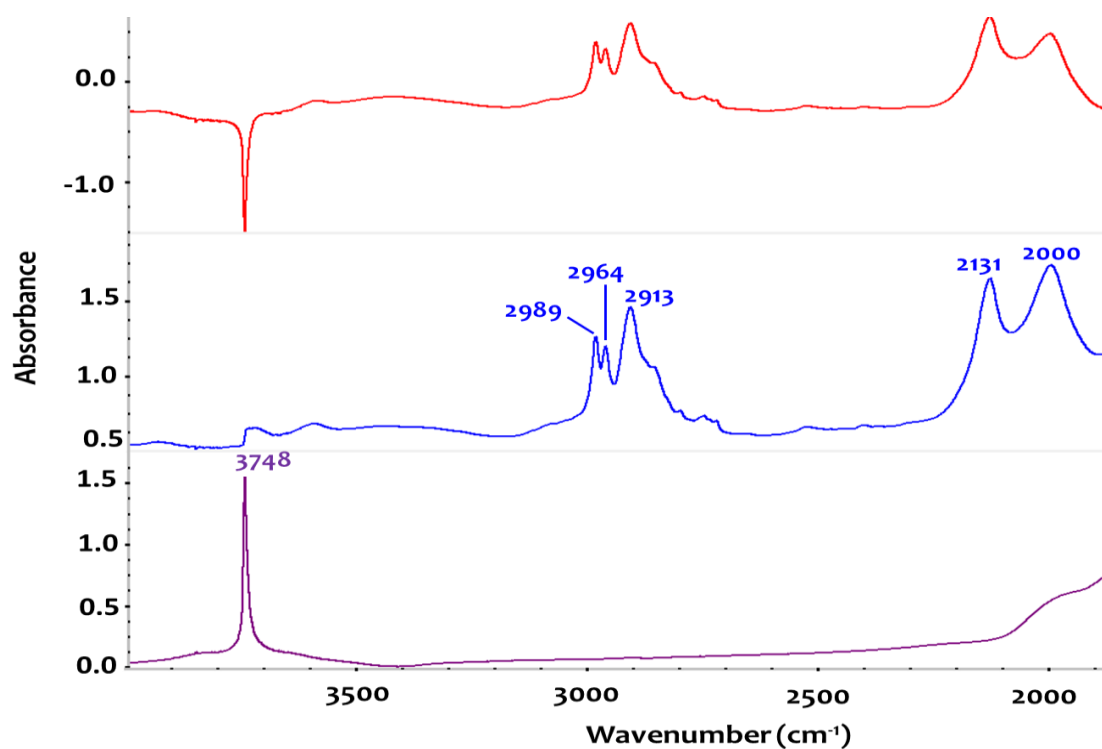


Figure 83. Diffuse reflection infrared Fourier transform spectra (recorded on powder materials under argon) of (1) SBA-15₇₀₀ (purple line), (2) **27** (blue line), and (3) subtraction of spectrum (2) – spectrum (1) (red line).

The ¹H solid-state NMR spectra of **27** (Figure 84, left side) shows an intense Cp* signal at $\delta = 1.95$ ppm and a broad Ir-H resonance averaged at $\delta = -17.14$ ppm. The ¹³C CP-MAS NMR spectrum of **27** (Figure 84, right side) displays two Cp* signals ($\delta = 94.4$ and 9.5 ppm). These data therefore support the proposed structure for **27**.

Thus, we are able to quantitatively immobilize complex **14** on the surface of SBA-15₇₀₀. The resulting material **27** adds to the small handful known supported heterobimetallic species (**D**-type materials in Scheme 37) designed by direct grafting of a heterobimetallic precursor (Figure 85).

Next, we aimed to study the thermal stability of material **27** to gain preliminary insights into its reactivity and robustness.

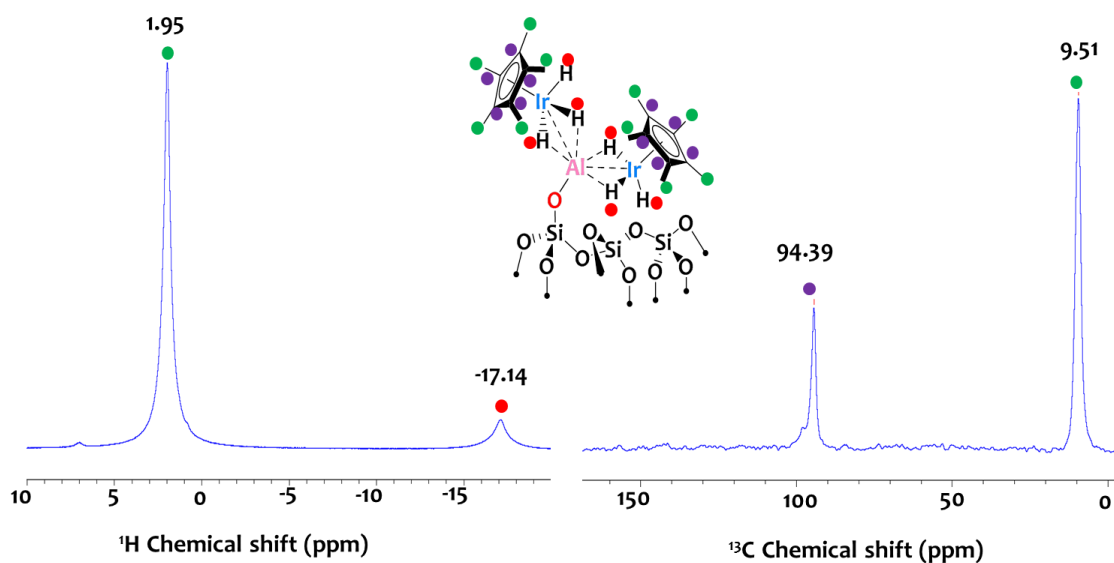


Figure 84. (Left) ^1H solid state MAS NMR spectrum (293K, 300 MHz, 4 mm probe) of **27**. (Right) ^{13}C solid state MAS NMR spectrum (293K, 75 MHz, 4 mm probe) of **27**.

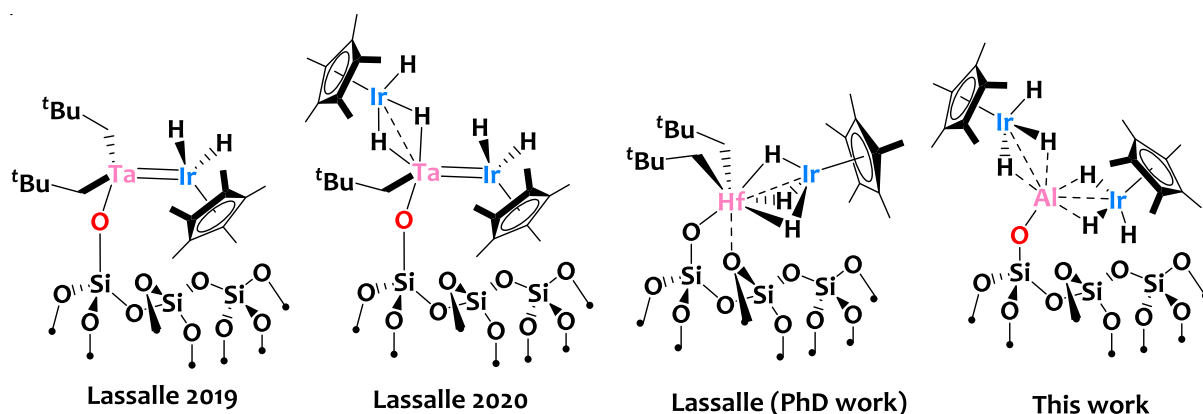


Figure 85. Reported heterobimetallic materials of type D (general structure shown in Scheme 37).^[27–29,346]

5.3.2 Stability studies

In the perspective to assess the viability to form **B** and **C**-type materials (Scheme 37) from species **27**, we studied its stability under a hydrogen atmosphere and under progressive heating. Material **27** is pelleted, transferred in a closed reactor, and then exposed to H_2 gas at atmospheric pressure (1030 mbars), which corresponds to a huge excess of H_2 with respect of Al (1200 equivalents), in a temperature range from $T=25^\circ\text{C}$ to $T=250^\circ\text{C}$. The reaction is monitored by transmission Fourier Transform IR (FT-IR) spectroscopy. Particularly, we set up the monitoring as follow: i) The reactor is left for 40 minutes at RT under an argon atmosphere (ca. 25°C) and the pellet (material **27**) is analyzed by FT-IR. ii) the Ar atmosphere is evacuated, H_2 is added to the system, and then the

reactor is left again at RT for 40 minutes, and finally analyzed by FT-IR. iii) A temperature of 50°C is applied to the system for 40 minutes and a spectrum of the pellet is recorded on the FT-IR facility. iv) The latter procedure is repeated 9 times with increasing temperatures (75, 100, 125...250°C) with a temperature step of 25°C.

The obtained overlaid IR spectra for each temperature are shown in Figure 86. A first noticeable feature is a progressive declining flattening of the two initial Ir-H stretches at $\sigma=2000\text{ cm}^{-1}$ and 2131 cm^{-1} into one stretch at $\sigma\approx 2000\text{ cm}^{-1}$. A similar trend is observed for the $\nu(\text{C-H})$ bands at wavenumbers ranging from 2900 cm^{-1} to 3000 cm^{-1} . Eventually, the isolated Si-OH vibrator at $\sigma=3748\text{ cm}^{-1}$ starts to clearly reappear from $T=125^\circ\text{C}$ and then gradually increases in intensity until $T=250^\circ\text{C}$.

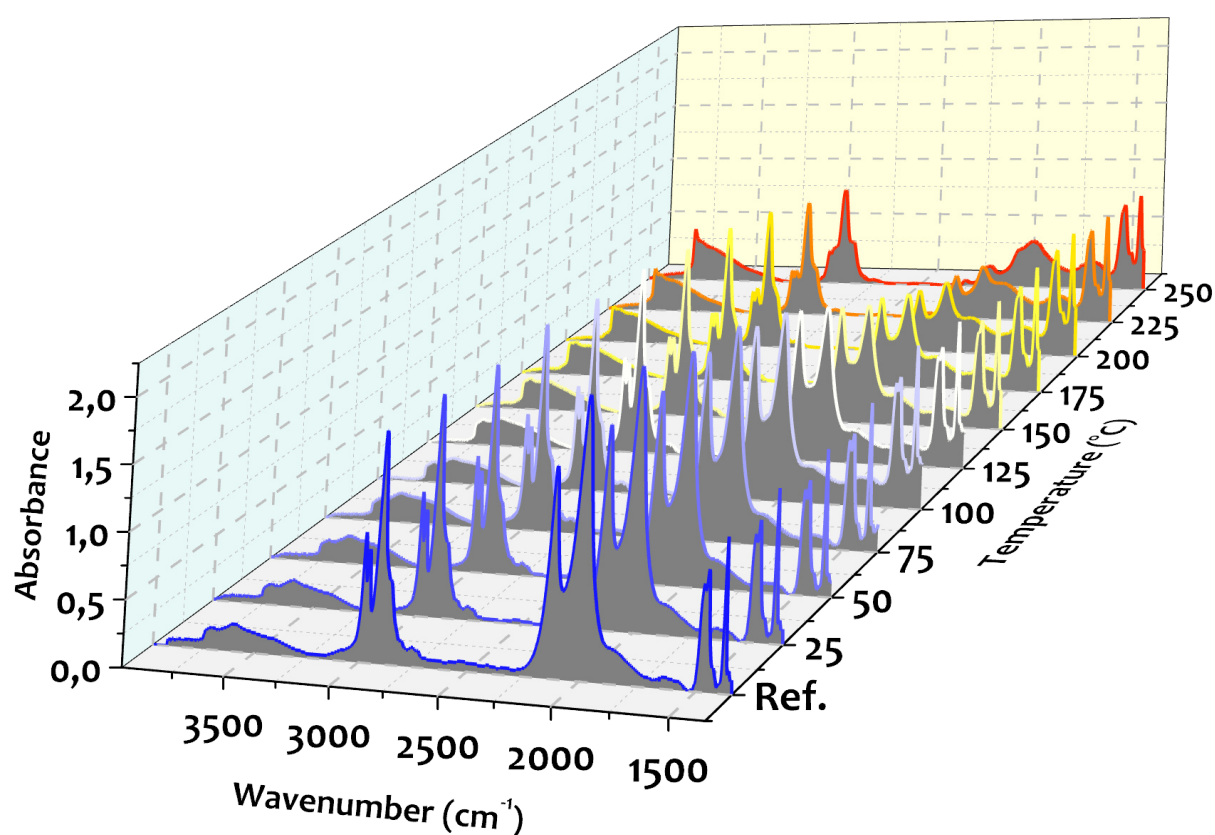


Figure 86. Fourier Transform Infra-Red (FT-IR) spectroscopy monitoring of materials 27 (pellet of 35 mg, 0.0157 mmol) exposed to a H₂ atmosphere (1030 mbars, 19 mmol, 1200 equivalents/Al) from T=25°C to T=250°C. The reference spectrum (labelled Ref.) represents the FT-IR spectrum of materials 27 before adding the hydrogen gas. Each temperature was applied for 40 minutes.

These observations are in favor of a decomposition reaction, *i.e.* a partial removing and rearrangement of the organic ligands in material 27. Furthermore, we noticed a drastic color changing of the pellet, being white and becoming ultimately deep brown. We thus believe that formation of nanoparticles is occurring during the process.

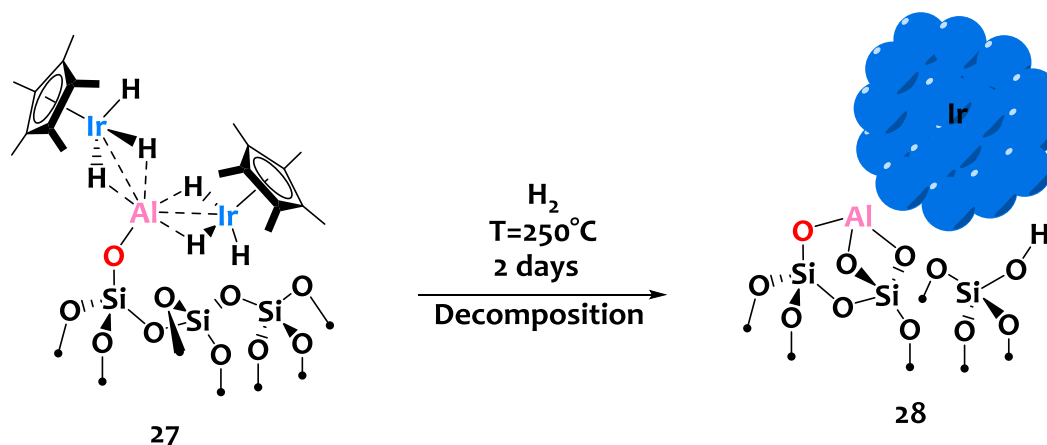
Consequently, this preliminary study confirms the viability of promoting a decomposition

reaction, likely into metallic nanoparticles. We therefore sought to streamline our study by performing a large-scale synthesis of this new material and following experimental conditions inspired by this preliminary work.

5.4 Formation of a new heterobimetallic material – Ir-Al/SiO₂

5.4.1 Synthesis and preliminary characterizations

Material **27** is treated under H₂ (1 bar, excess) and at T=250°C for 2 days. These reaction conditions yields a new material – named Ir-Al/SiO₂ or material **28** - as a deep brown powder (Scheme 76).



Scheme 76. Treatment of materials **27** in H₂ atmosphere at T=250°C leading to the formation of surface Ir NPs supported on an Al functionalized SBA-15₇₀₀, Ir-Al/SiO₂, noted materials **28**.

The IR spectrum of material **28** (Figure 87-c.) shows a significant change in the Ir-H stretch signature compared to that of material **27** (Figure 87-b.). Indeed, the IR spectrum of Ir-Al/SiO₂ no longer display the vibrator at $\sigma=2131\text{cm}^{-1}$ (observed for material **27**). Also, the signal at 2000 cm^{-1} for material **27** is slightly shifted to a wavenumber of 2011 cm^{-1} . Furthermore, the $\nu(\text{C-H})$ bands (in the spectrum of material **28**) have completely disappeared compared to those for material **27**, and some isolated silanols are regenerated ($\nu_{\text{OH}} = 3748\text{ cm}^{-1}$).

These spectral data support the decomposition of the surface species, **27**, with removal of the organic Cp* ligands. The elemental analysis of material **28** confirmed this spectral observation since a low C and H weight percent (%C = 0.69 and %H = 0.24, C/Al ratio = 1.2) is noticed. The Ir/Al atomic ratio (1.9) between materials **27** and **28** is unchanged.

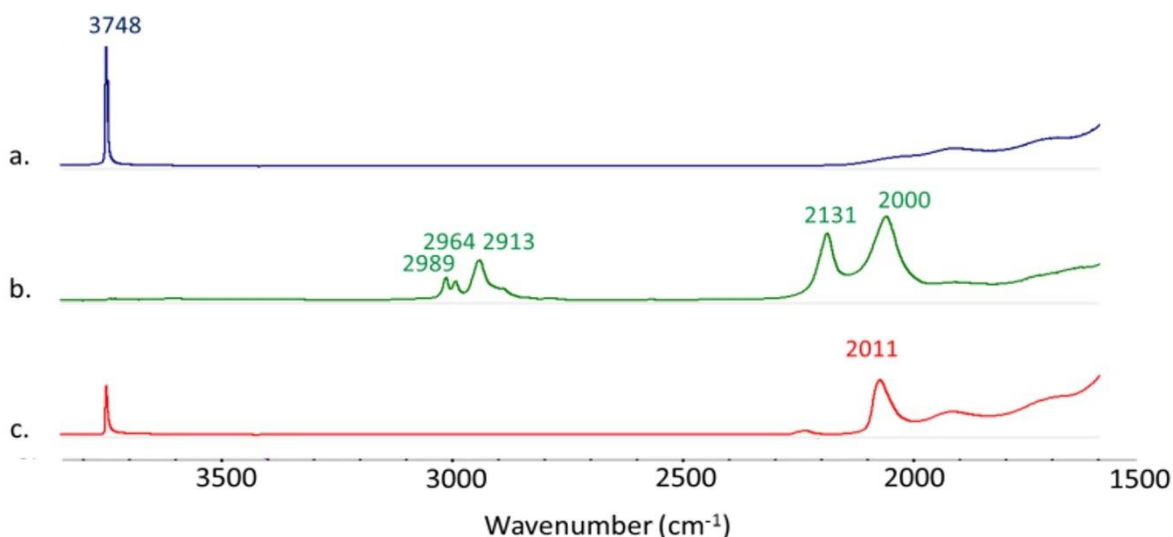


Figure 87. DRIFT spectra of SBA-15₇₀₀ (a), $\equiv\text{SiOAl}(\text{Cp}^*\text{IrH}_3)_2$, material 27 (b), and Ir-Al/SiO₂, material 28 (c), recorded on powder materials under argon.

5.4.2 Advanced characterizations

Analysis of material **28** by high-angle annular dark-field scanning transmission electron microscopy (HAADF-STEM) shows some interesting features. First, it shows the formation of metallic nanoparticles on the surface of the SBA-15 support characterized by a small average size and narrow distribution of 1.6 ± 0.4 nm (see Figure 88). Also, energy-dispersive X-ray (EDX) spectrum of Ir-Al/SiO₂ shows a homogeneous distribution of the Al and Ir components on the silica support (see Figure 89). It is important to mention that the determination of the metal composition of the NPs (monometallic or alloys) by electron microscopy or X-ray diffraction is not possible because the size of the NPs is too small (and therefore at the resolution limit of the apparatus). However, we discussed in CHAPTER 1 that Al(III) sites are known to form robust bonds with the surface of a silica support due to their strong oxophilic properties.^[135] In addition, we have also shown that Al(III) sites are generally not reduced. Conversely, as shown in introduction, interactions of iridium centers with silica surfaces are much more fragile and this is even more so when reduced conditions are applied. For instance, iridium can be readily reduced into Ir(o) Nps as already observed by C. Copéret and colleagues.^[33,34] Furthermore, as demonstrated in section 5.2 (from page 217), the Ir-Al interactions in these species are not robust and therefore reactive. We thus postulate that material **28** features supported monometallic Ir NPs surrounded with a high density of isolated interfacial Al(III) sites as represented on Scheme 76, and belong to **B**-type materials presented in Scheme 37 (page 90).^[166,167]

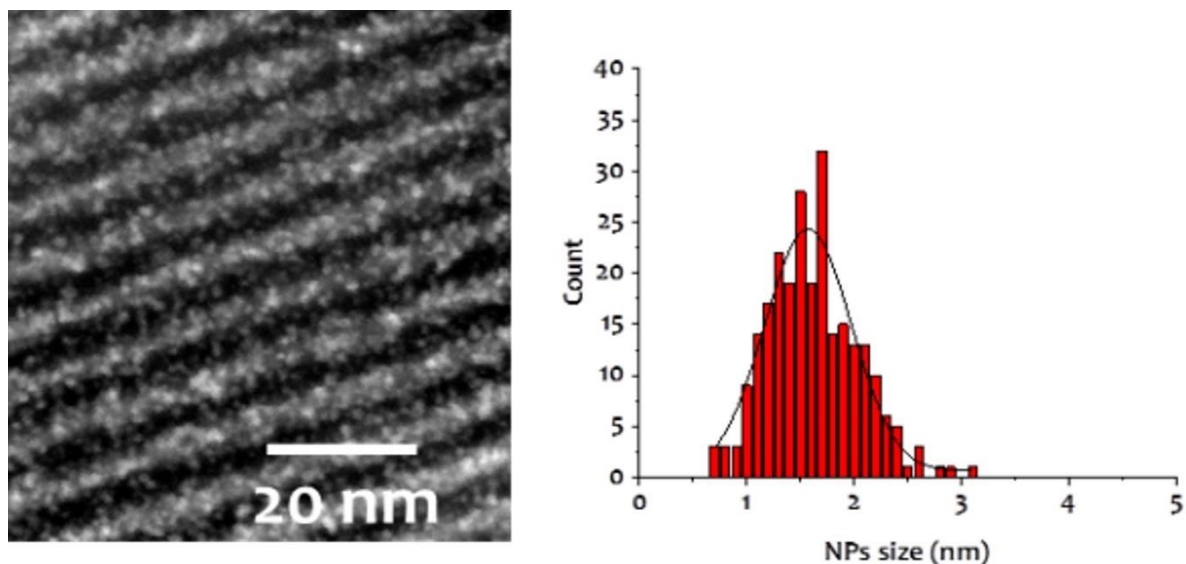


Figure 88. HAADF-STEM micrograph (left) and Nps size distribution (right) of material 28.

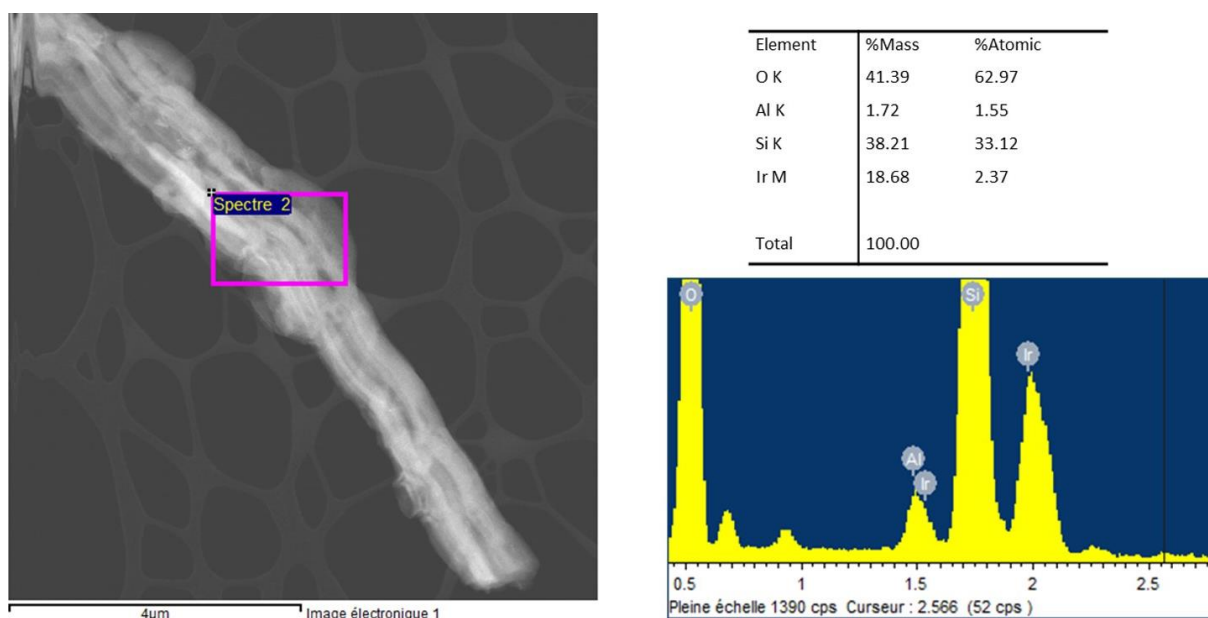


Figure 89. HAADF-STEM micrograph of material 28 (left) and related EDX spectrum (right). Bar scales: 4 μm .

In order to consolidate these experimental results and to better understand the state of the metal surface, we performed H_2 chemisorption studies. This experiment is inspired by the research works published by C. Copéret and his collaborators on the chemisorptions of Ir NPs [33,34] and Os NPs.[358] i) In a first stage, material 28 is subjected to a pretreatment at $T=250^\circ\text{C}$ under high vacuum (10^{-6} mbars) for 3 hours (a temperature ramp of $5^\circ\text{C}/\text{min}$ is used), this allows to desorb all the remaining organic molecules (even in traces amounts) from the surface of the NPs or, in other words, to completely perform a surface stripping of the NPs. ii) In a second stage, the adsorption isotherms are measured at exactly $T=25.0^\circ\text{C}$ in the pressure range [30-265 mbar]. The

isotherms obtained are presented in Figure 90.

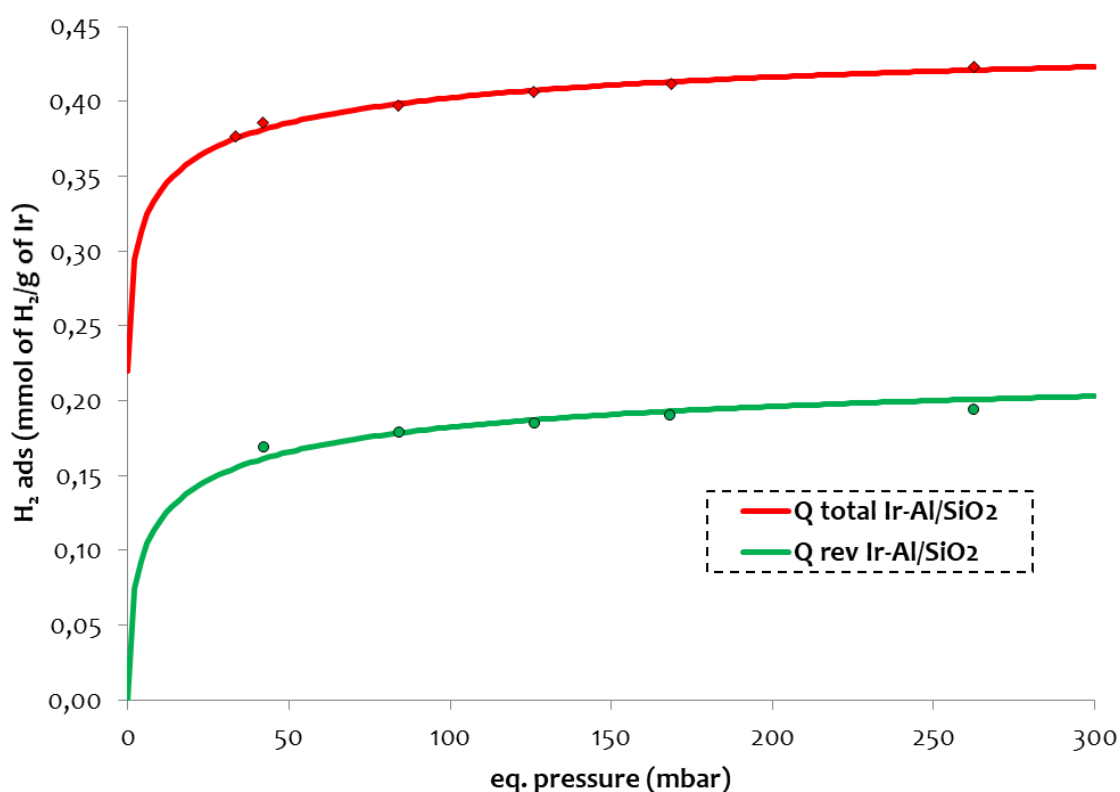


Figure 90. Total H₂ chemisorption isotherm at 298K for Ir NPs from material 28 - experimental points (red diamonds) and double Langmuir fit (red curve). Reversible H₂ chemisorption isotherm at 298K for Ir NPs from material 28 - experimental points (green circles) and double Langmuir fit (green curve)

The total H₂ chemisorption isotherm (top of Figure 90, red diamonds) is for the so called reversible and irreversible adsorbed hydrogen. It indicates rapid adsorption in the 30-50 mbar pressure range, consistent with a relatively strong chemisorption. Above that range, the adsorption is much slower and reaches a plateau at 260 mbar (0.42 mmol of H₂/g of Ir). Note that these data are fitted by a double Langmuir model (red line on Figure 90). iii) In a third step, the H₂ gas is partially desorbed at 298K and under high vacuum. iv) Finally, a second hydrogen isotherm - commonly referred to as reversible hydrogen or retro adsorbed hydrogen - is performed under the same experimental conditions as point ii). The experimental points and the corresponding double Langmuir fit of the reversible hydrogen isotherm are shown by green circles and a green curve, respectively. In this case, the adsorption reaches a maximum of 0.19 mmol H₂/g Ir, which means that about 55% of the H₂ is desorbed during step iii).

Next, the data are processed to extract the parameters of interest. The results obtained are presented in Table 10. The different calculations are carried out as follows: i) From the double Langmuir fit, we extracted the following parameter: H/Ir (column 3 of Table 10), which translates the total adsorbed atomic hydrogen per total iridium (calculated using the metal loading

extracted from elemental analysis). ii) Then, we calculate the metallic dispersion of Ir for material **28** (column 4 of Table 10) by using an equation proposed by F. Drault and colleagues^[359]: $D_{Ir}(\%) = a_{\gamma} (H/Ir)^5 + b_{\gamma} (H/Ir)^4 + c_{\gamma} (H/Ir)^3 + d_{\gamma} (H/Ir)^2 + e_{\gamma} (H/Ir)$ with $a_{\gamma} = -2.116$, $b_{\gamma} = 13.163$, $c_{\gamma} = -20.633$, $d_{\gamma} = -23.073$, and $e_{\gamma} = 100.361$ for iridium. iii) From this dispersion, we calculate the stoichiometric coefficient $H/Ir_{surface}$, (column 5 of Table 10), which translates into the adsorbed atomic hydrogen per surface iridium. Eventually, we determine the Ir NPs size using a truncated cubic octahedral geometry (column 6 of Table 10).

Material	Ir loading (% wt) ^a	H/Ir	Dispersion (%) ^b	H/Ir _{surface}	Average NP size (nm) ^c
Ir-Al/SiO ₂	16.7	0.97	67	1.45	1.4

Table 10. Parameters extracted from the H₂ chemisorption isotherm of material **28**.^aData from elemental analysis. ^bDetermined by an equation proposed by Drault et. al.^[359] ^cDetermined using a truncated octahedron geometry.

Comparing with the STEM results, a similar average size of the NPs is obtained - 1.4 nm vs. 1.6±0.4 nm - which means that the Ir NPs are homogeneous in terms of size and distribution on the silica support.

To get insights into the metal oxidation state of aluminum and iridium, materials **27** and **28** are analyzed by X-ray photoelectron spectroscopy (XPS). This XPS study is performed in collaboration with Pr. Victor Mougel and Dr. Daniel F. Abbott from ETH Zurich. In the present case, the XPS spectra reveal an Al 2p peak position fixed at 74.6 eV both before and after the thermal treatment under H₂ and is in agreement with aluminum(III) sites (see Figure 91).

On the other hand, the reduction of iridium in material **28** is confirmed through the evolution of the Ir 4f_{5/2} and Ir 4f_{7/2} XPS spectra of materials **27** and **28** (see Figure 92). Indeed, material **27** exhibit Ir 4f_{5/2} and Ir 4f_{7/2} binding energies (B.E.) of 64.7 eV and 61.7 eV respectively, which are consistent with an iridium(III) complex containing electron-rich ligands such as Cp*.^[360] After H₂ treatment, a new set of signals with lower B.E. (Ir 4f_{5/2} of 63.5 eV and Ir 4f_{7/2} of 60.6 eV) is noticed in agreement with the generation of Ir(o) NPs. A small contribution of an Ir(III) peak is still present in material **28** with a Ir(o):Ir(III) ratio of ca. 3:1 (Figure 92, bottom right). This remaining Ir(III) signature is either due to the presence of Ir(III) hydride sites at the surface of the Nps or to incomplete reduction of the Ir(III) species in material **27**.

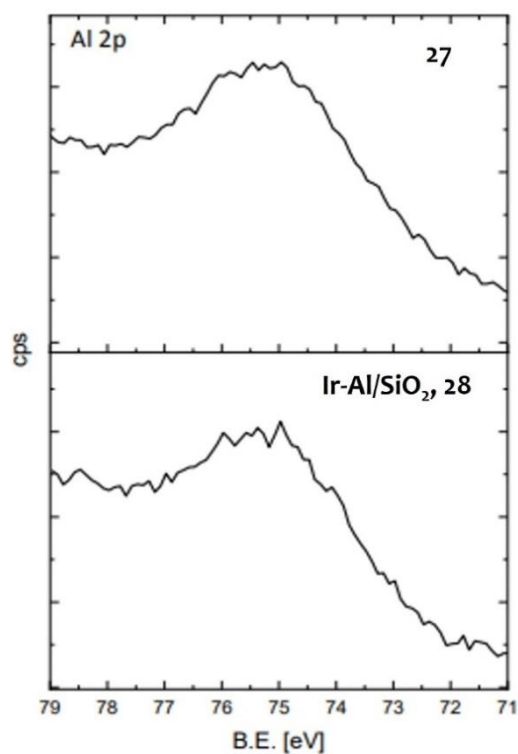


Figure 91. XPS Al 2p spectra of materials 27 (top) and 28 (bottom).

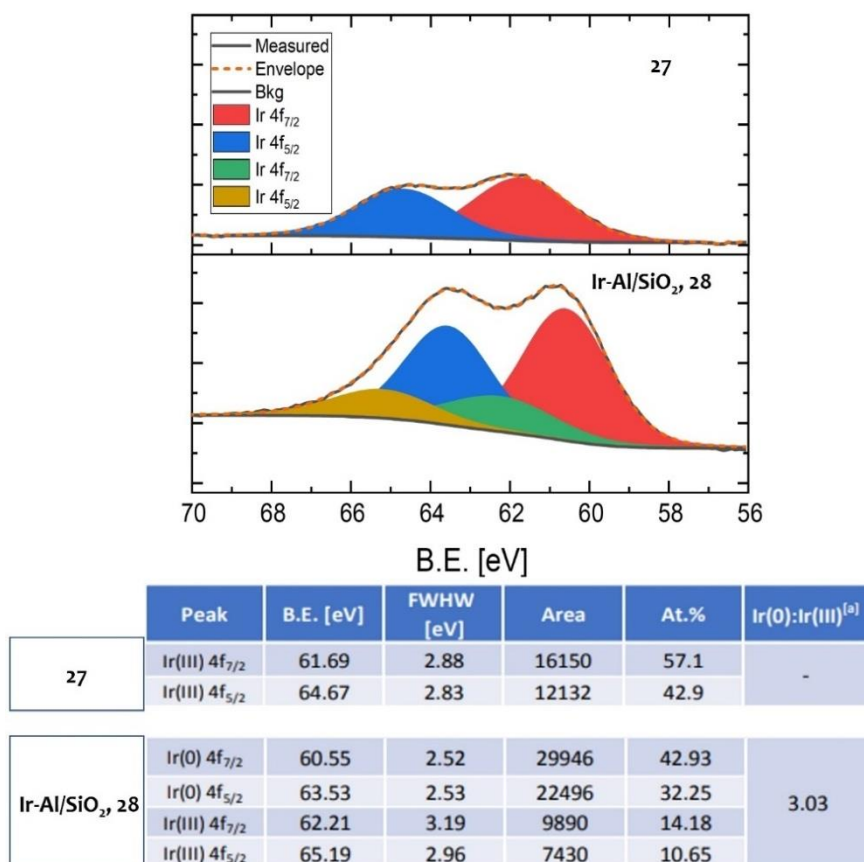


Figure 92. XPS Ir 4f spectra of materials 27 and 28 (top). XPS Ir 4f data analysis of materials 27 and 28 (bottom)^[a] Ir(0):Ir(III) ratio was calculated as the areas of $[\text{Ir}(0) 4f_{7/2} + \text{Ir}(0) 4f_{5/2}] / [\text{Ir}(III) 4f_{7/2} + \text{Ir}(III) 4f_{5/2}]$.

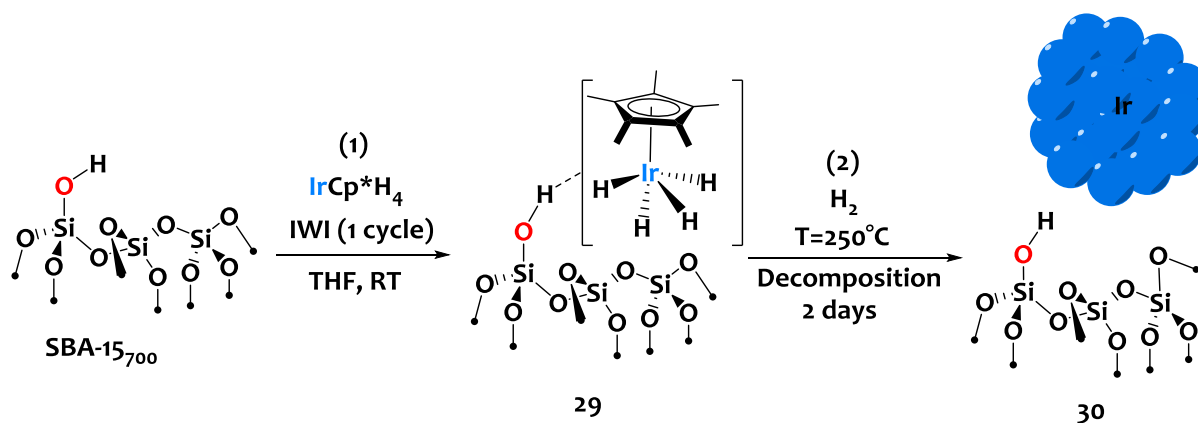
In conclusion, material **28** has been fully characterized by different advanced techniques that allow us to obtain in-depth information on its composition, the nature of the sites, the metallic surface state, etc. This heterobimetallic material presents very interesting features such as the presence of small Ir(o) NPs narrowly distributed and surrounded by interfacial Al(III) sites. Therefore, we considered to evaluate the potential of Ir-Al/SiO₂ for heterobimetallic catalysis processes. In order to establish a comparative study and to show the value of combining aluminum and iridium in material **28**, we turned to the preparation of a monometallic Ir analog to serve as a benchmark for catalysis.

5.5 Synthesis of a monometallic analogue - Ir/SiO₂

5.5.1 Preparation and preliminary characterizations

The synthesis methodology to prepare the monometallic Ir material involves two steps.

i) A 340 μ L solution of IrCp*H₄ in THF (1.24M) is added dropwise onto SBA-15₇₀₀ (295 mg) over a vigorous stirring in order to achieve incipient wetness impregnation (IWI) and to reach a similar iridium loading than in the bimetallic material **28**. The solvent is then evacuated under argon and *in vacuo* at room temperature, which gives material **29** (Scheme 77, first step). Our laboratory reported before that IrCp*H₄ is only physisorbed at the surface of the SBA-15₇₀₀ and does not react with isolated surface silanols.^[28] This feature is underpinned by DRIFT spectroscopy of material **29** (Figure 93-d). Indeed, the $\nu(\text{Ir-H})$ peak at $\sigma=2150\text{ cm}^{-1}$ is identical to that of the IrCp*H₄ precursor.^[181] Note that a very broad band is identified at a wavenumber of about 3500 cm^{-1} assigned to the silanol groups forming weak interactions (such as H-bonding) with the physisorbed complex (see schematic representation of material **29** in Scheme 77). This phenomenon, called “umbrella effect”, was reported previously in other SOMC systems.^[361]



Scheme 77. (1) Incipient wetness impregnation (IWI) of IrCp*H₄ upon SBA-15₇₀₀ yielding material 29 (2) Treatment of 29 in H₂ atmosphere at T=250°C leading to the formation of surface Ir NPs supported on SBA-15₇₀₀, Ir/SiO₂, noted material 30.

ii) Material **29** is then reduced under the same conditions (1 bar H₂, 250°C) employed for the bimetallic material **28**, to give a new material Ir/SiO₂, noted material **30**, as a dark brown powder (Scheme 77, second step). As for Ir-Al/SiO₂, the IR spectrum of material **30** (Figure 93-e) reveals the disappearance of the ν(C-H) signals around 2950 cm⁻¹ (Figure 93-d vs e) suggesting the removal of the organic ligands. This is confirmed by elemental analysis of material **30** showing very low weight % of C and H (1.04 and 0.22 respectively). Also, the IR spectrum of Ir/SiO₂ displays a significant shift of the Ir-H stretch from 2150 to 2024 cm⁻¹ (Figure 93-d vs e). This band is very similar to that of Ir-Al/SiO₂ (Figure 93-c vs e). Therefore, these preliminary characterizations suggest the formation of similar Nps than in the heterobimetallic material **28**.

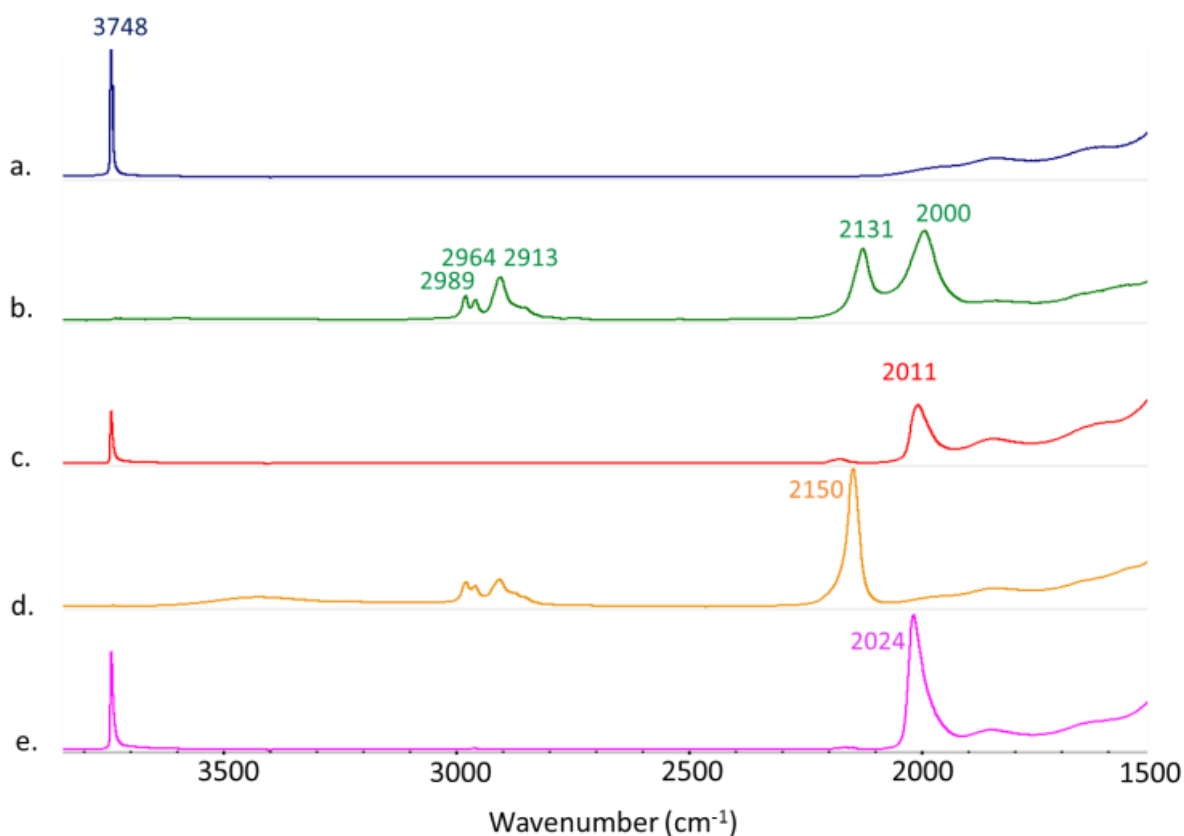


Figure 93. DRIFT spectra of SBA-15₇₀₀ (a), $\equiv\text{SiOAl}(\text{Cp}^*\text{IrH}_3)_2$ material 27 (b), Ir-Al/SiO₂, material 28 (c), Cp*IrH₄ physisorbed on SBA-15₇₀₀, material 29 (d) and Ir/SiO₂, material 30 (e) recorded on powder materials under argon.

5.5.2 Advanced characterizations

To confirm these hypotheses, we carried out STEM analyses of Ir/SiO₂. Micrographs of material **30** show the presence of small Ir NPs (1.6 ± 0.4 nm) and a narrow distribution at the surface of the SBA-15₇₀₀ support (Figure 94, left), alike that in Ir-Al/SiO₂ (Figure 94, right). Most Ir NPs are homogeneously distributed at the surface of the silica support (Figure 95), although a few Ir aggregates (≈ 5 -30 nm) are also noticed in some silica grains by STEM (see Figure 96).

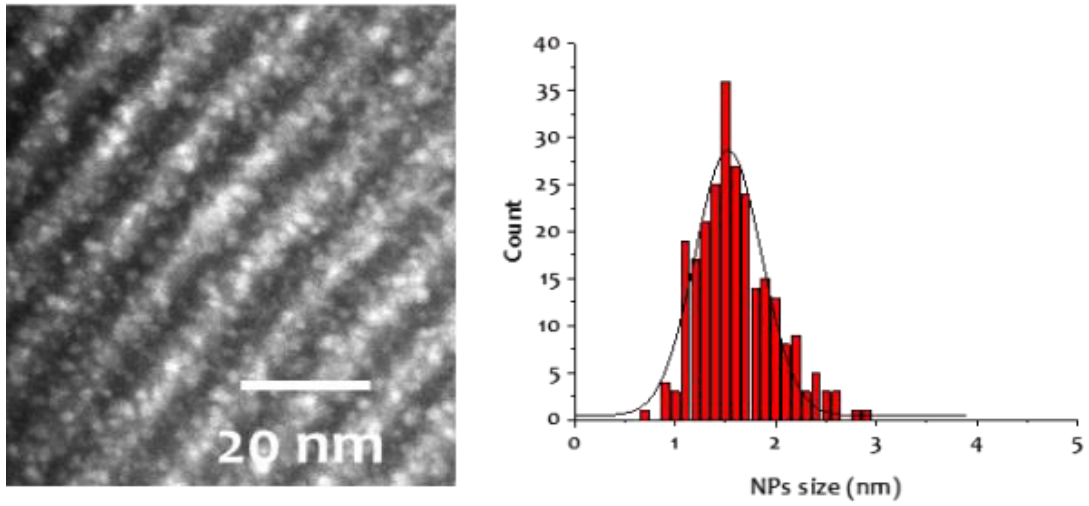


Figure 94. HAADF-STEM micrograph (left) and Nps size distribution (right) of material 30.

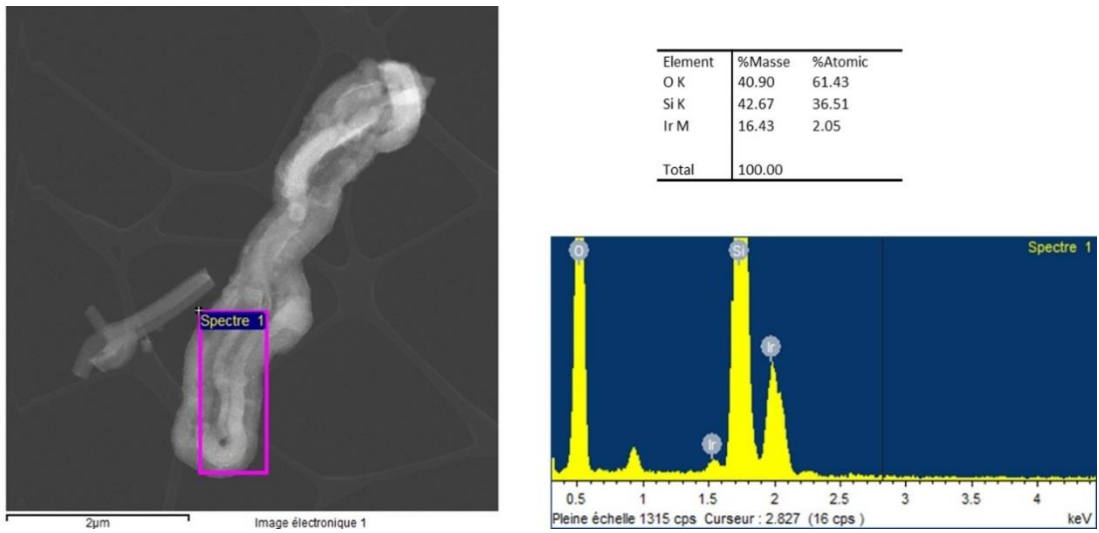


Figure 95. HAADF-STEM micrographs of material 30 (left) and related EDX spectrum (right). Bar scales: 2 μm.

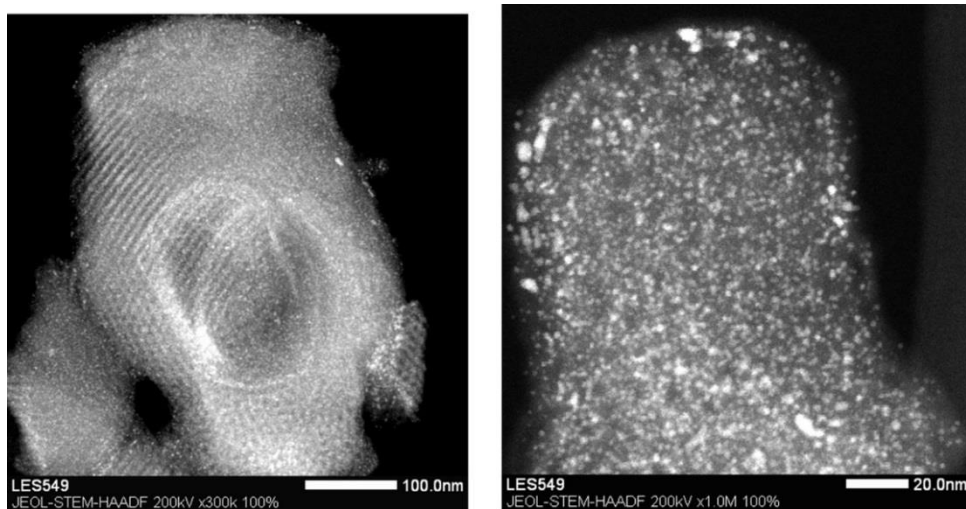


Figure 96. HAADF-STEM micrographs of material 30 (Ir/SiO₂) showing some Ir aggregates in the range of [3-15 nm].

In order to establish exhaustive and comparative data with the bimetallic material **28**, we also conducted H₂ chemisorption studies on material **30**. We used exactly the same experimental conditions as for material **28** (see details on section 5.4.2, from page 230). The comparative isotherms are plotted on Figure 97.

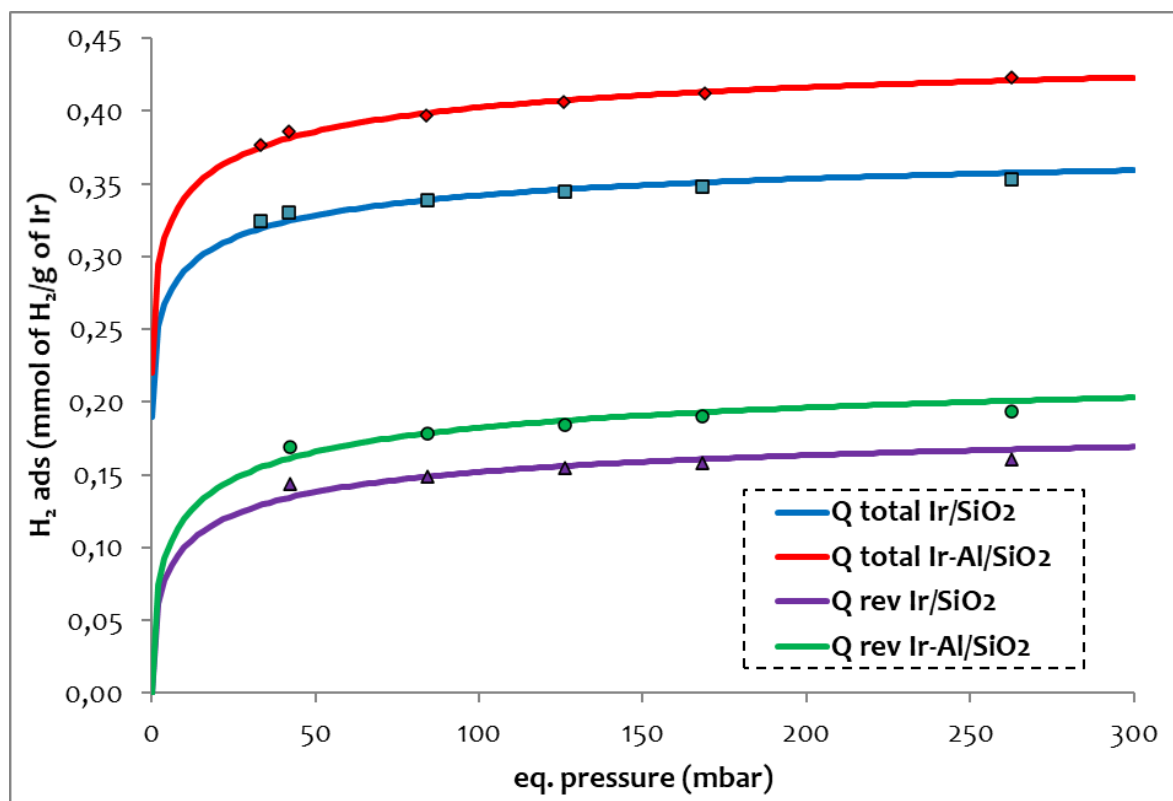


Figure 97. Total H₂ chemisorption isotherm at 298K for Ir NPs from material **28** - experimental points (red diamonds) and double Langmuir fit (red curve) – and material **30** - experimental points (blue squares) and double Langmuir fit (blue curve). Reversible H₂ chemisorption isotherm at 298K for Ir NPs from material **28**- experimental points (green circles) and double Langmuir fit (green curve) – and material **30**- experimental points (purple triangles) and double Langmuir fit (purple curve).

The total and the reversible isotherms of Ir/SiO₂ are relatively close to those of Ir-Al/SiO₂ in terms of trends and order of magnitude. However, the monometallic material **30** adsorbs slightly less hydrogen gas than the bimetallic counterpart. For instance, the total isotherm of Ir/SiO₂ displays an adsorption of 0.35 mmol of H₂/g of Ir for a pressure of 260 mbars, while Ir-Al/SiO₂ displays 0.42 mmol of H₂/g of Ir at this same pressure.

Processed data are gathered on Table 11. Small differences are noticed but in the overall, relatively close parameters between Ir/SiO₂ and Ir-Al/SiO₂ are found. Notably, an Ir dispersion of 56% is found for Ir/SiO₂ compared to 67% for Ir-Al/SiO₂ (Table 11, column 4). This ultimately leads to a Np average diameter of 1.7 nm (vs 1.4 nm for Ir-Al/SiO₂) consistent with the STEM analyses. The conclusions are thus similar than those discussed for the bimetallic material **28**. More importantly, these data testify to a comparable amount of accessible surface metal atoms for both materials.

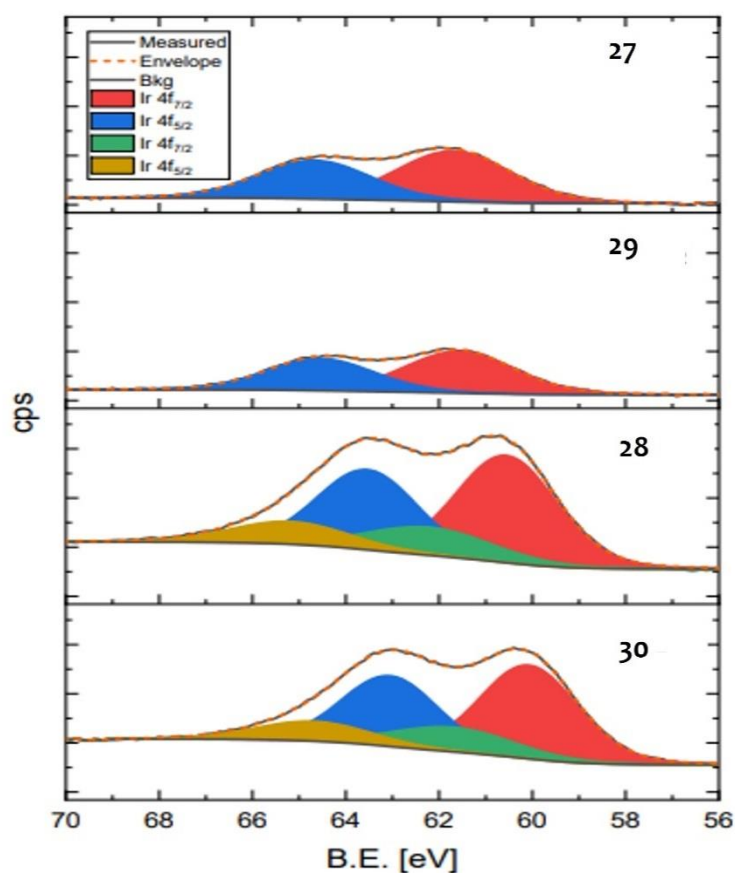
Material	Ir loading (% wt) ^a	H/Ir	Dispersion (%) ^b	H/Ir _{surface}	Average NP size (nm) ^c
Ir/SiO ₂	18.8	0.73	56	1.32	1.7
Ir-Al/SiO ₂	16.7	0.97	67	1.45	1.4

Table 11. Parameters extracted from the H₂ chemisorption isotherm of material 30 (Ir/SiO₂) and comparison with material 28 (Ir-Al/SiO₂).^aData from elemental analysis. ^bDetermined by an equation proposed by Drault *et. al.*^[359] ^cDetermined using a truncated octahedron geometry.

In collaboration with Pr. Victor Mougel and Dr. Daniel F. Abbott from ETH Zurich, we also analyzed materials 29 and 30 by XPS techniques. Comparative spectra and processed data with materials 27 and 28 are represented in Figure 98. Similarly as the evolution between materials 27 and 28, the Ir 4f_{5/2} and Ir 4f_{7/2} XPS spectra of material 30 clearly indicate the decrease of the Ir(III) peaks at 64.5 eV and 61.6 eV and the appearance of the Ir(o) peaks at 63.1 eV and 60.1 eV after the reduction step (material 30 vs 29). This low B.E. for metallic iridium is corroborant with the reduced average coordination number of surface atoms found in Nps.^[362] Also, in the same way as material 28, signatures of Ir(III) peaks are still present after H₂ treatment in material 30 with a Ir(o):Ir(III) ratio of ca. 3:1. Conclusions of this observation are therefore the same as for material 28: there is an incomplete reduction or the presence of Ir(III) hydride sites at the surface of the Ir(o) nanoparticles.

More importantly, these XPS data show very similar trends between materials 28 and 30.

To conclude this section, a monometallic material – Ir/SiO₂ - featuring Ir(o) NPs supported on the surface of a SBA-15₇₀₀ has been successfully prepared. In-depth characterizations of Ir/SiO₂ highlight comparable properties (size and distribution of the Ir NPs, metallic surface states) than the heterobimetallic material – Ir-Al/SiO₂.



	Peak	B.E. [eV]	FWHM [eV]	Area	At. %	Ir(0):Ir(III) ^[a]
27	Ir(III) 4f _{7/2}	61.69	2.88	16150	57.1	-
	Ir(III) 4f _{5/2}	64.67	2.83	12132	42.9	
29	Ir(III) 4f _{7/2}	61.56	2.76	12773	57.1	-
	Ir(III) 4f _{5/2}	64.54	2.7	9596	42.9	
28	Ir(0) 4f _{7/2}	60.55	2.52	29946	42.93	3.03
	Ir(0) 4f _{5/2}	63.53	2.53	22496	32.25	
	Ir(III) 4f _{7/2}	62.21	3.19	9890	14.18	
	Ir(III) 4f _{5/2}	65.19	2.96	7430	10.65	
30	Ir(0) 4f _{7/2}	60.07	2.46	25441	42.96	3.04
	Ir(0) 4f _{5/2}	63.05	2.44	19112	32.27	
	Ir(III) 4f _{7/2}	61.7	3.08	8374	14.14	
	Ir(III) 4f _{5/2}	64.68	2.88	6291	10.62	

Figure 98. (Top) XPS Ir 4f spectra of materials 27, 28, 29, and 30. (Bottom) XPS Ir 4f data analysis of materials 27, 28, 29, and 30^[a] Ir(0):Ir(III) ratio was calculated as the areas of [Ir(0) 4f_{7/2}+ Ir(0) 4f_{5/2}]/[Ir(III) 4f_{7/2}+ Ir(III) 4f_{5/2}].

5.6 Conclusions

In this chapter, we have shown that protonolysis of the aluminum-iridium unit (from most of the compounds described in CHAPTER 3) readily occurs in the presence of hydroxyl groups, resulting in the formation of Al-O bonds and releasing Cp*IrH₄. We took advantage of this reactivity to form a heterobimetallic material of type **D** (Scheme 37, page 90) through the grafting of complex **14** on a SBA-15₇₀₀ support. The resulting material (**27**) features well-defined trinuclear [$\equiv\text{SiOAl}\{(\mu\text{-H})_2\text{Ir}(\text{H})\text{Cp}^*\}_2$] surface sites as supported by IR, solid-state NMR spectroscopy and elemental analyses. Robust structural evidence of the [$\equiv\text{SiOAl}\{(\mu\text{-H})_2\text{Ir}(\text{H})\text{Cp}^*\}_2$] sites has been also demonstrated by the rational construction of its molecular analogue - [$\{(\text{Ir}(\text{Cp}^*)(\text{H})(\mu\text{-H}_2)\}_2\text{Al}(\text{OAr}')\}$] (Ar'=1,3-diisopropylbenzene).

We then showed that applying thermal treatment under reducing conditions (250°C, H₂) onto [$\equiv\text{SiOAl}\{(\mu\text{-H})_2\text{Ir}(\text{H})\text{Cp}^*\}_2$] results in the formation of highly dispersed NPs surrounded with interfacial Al(III) sites – material **28** – reminiscent of **B**-type materials (Scheme 37, page 90). In particular, advanced characterizations of this bimetallic material (STEM, H₂ chemisorption, XPS) reveals the formation of small, narrowly distributed monometallic Ir(o) NPs which are well dispersed on the silica support. In view of future comparative studies, we also prepared an iridium monometallic analogue of Ir-Al/SiO₂ – Ir/SiO₂ (material **30**) – using an IWI/TMP approach. In-depth analyses of the Ir/SiO₂ material demonstrated comparable properties with respect to the Ir-Al/SiO₂ material.

Therefore, this exhaustive work opens perspectives for the establishment of a comparative catalytic study. We particularly choose to assess the potential of these materials for the hydrogen/deuterium exchange (HDE) catalysis of methane.

CHAPTER 6. Towards Bimetallic Cooperative Catalysis: Example On The Hydrogen/Deuterium Exchange Reaction Of Methane

6.1 Introduction

6.1.1 Interests of using methane

The search for efficient ways to valorize methane into relevant chemicals, fuels or value-added products (such as methanol or heavier alkanes) is of great importance in today's context of having to meet the criteria of a sustainable energy and money economy. This is especially true since methane is an abundant and clean source of fossil energy that can be found in natural gas and shale gas.^[363] However, CH₄ is the most inert alkane and one of the most stable molecule characterized by a highly symmetric tetrahedral geometry and a very high C-H BDE of 438.8 kJ.mol⁻¹.^[363,364] As a consequence, industry employs nowadays very harsh conditions (such as high temperature or high pressure) to promote the activation of CH₄, which, in addition to high economic and energy costs, results to undesired products and decreased selectivity. In order to overcome these obstacles, the scientific community in catalysis is interested in the development of catalytic systems operating under mild conditions, *i.e.* where CH₄ is transformed in a non-energy intensive way. In the quest to meet these needs, some research works are focused on the study of HDE catalysis of methane.

6.1.2 HDE catalysis of methane

This part draws on a recent review published in 2018.^[365]

The HDE catalysis of methane consists in replacing the hydrogen atoms by deuterium atoms by contacting a CH₄ molecule with a deuterium source (such as D₂) in the presence of a catalyst. As a result, this reaction produces a mixture of deuteromethanes – noted CH_{4-x}D_x (x being between 0 and 4) – whose ratio and formation rate depend on the experimental conditions (nature of the catalyst, temperature, pressure of reactants, stoichiometry H/D, metal loading etc.). To date, a range of transition metal films can foster HDE of methane, with different efficiencies and selectivities.^[365-367] However these systems are ill-defined and it is difficult to rationalize their catalytic activity. Dehydrated aluminas are also effective in methane deuteration^[368] *via* a mechanism involving heterolytic C-H bond splitting across Al-O moieties.^[369] Combining transition metal with Lewis acidic Al sites thus appears attractive for potentially promoting this transformation, yet this strategy has not been described to the best of our knowledge, and is the purpose of this study. Silica-supported molecular metal hydrides (typically Zr or Ta), are highly

active in methane deuteration, but extremely air sensitive and deactivate easily.^[40,41] Some organometallic complexes are also able to promote this reaction but suffer from the same drawbacks.^[370,371]

The primary reason for studying HDE catalysis of methane is to gain insights into the mechanisms underlying the formation of key intermediates. Furthermore, this conceptual study not only serves the field of fundamental catalysis but also has direct implications in understanding other relevant transformations such as non-oxidative coupling, hydrogenolysis, or pyrolysis of methane.^[372,373]

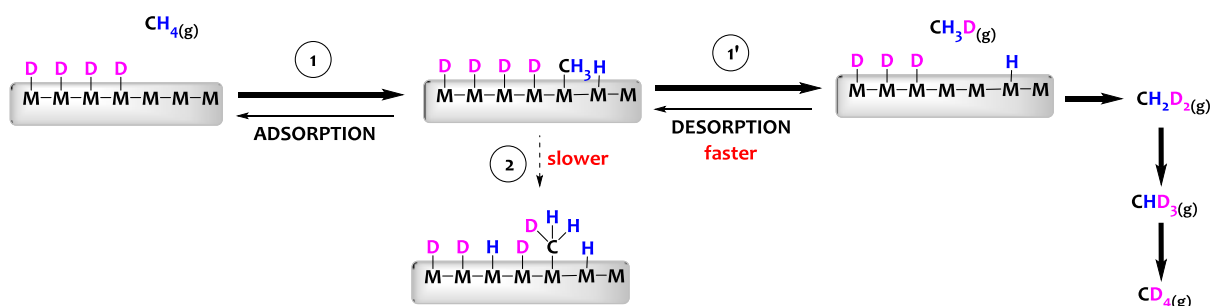
General features regarding HDE of methane are described below:

In the absence of side-reactions and after a certain time, the exchange process reaches a thermodynamic equilibrium position which can be predicted using the number of H and D atoms introduced into the reaction medium. For instance, when an excess of 10 equivalents of D_2 gas is employed with respect to CH_4 gas, an atomic ratio D/H of 5 is obtained. This means that the reaction is in equilibrium when 80% of the hydrogen atoms are exchanged by deuterium atoms.

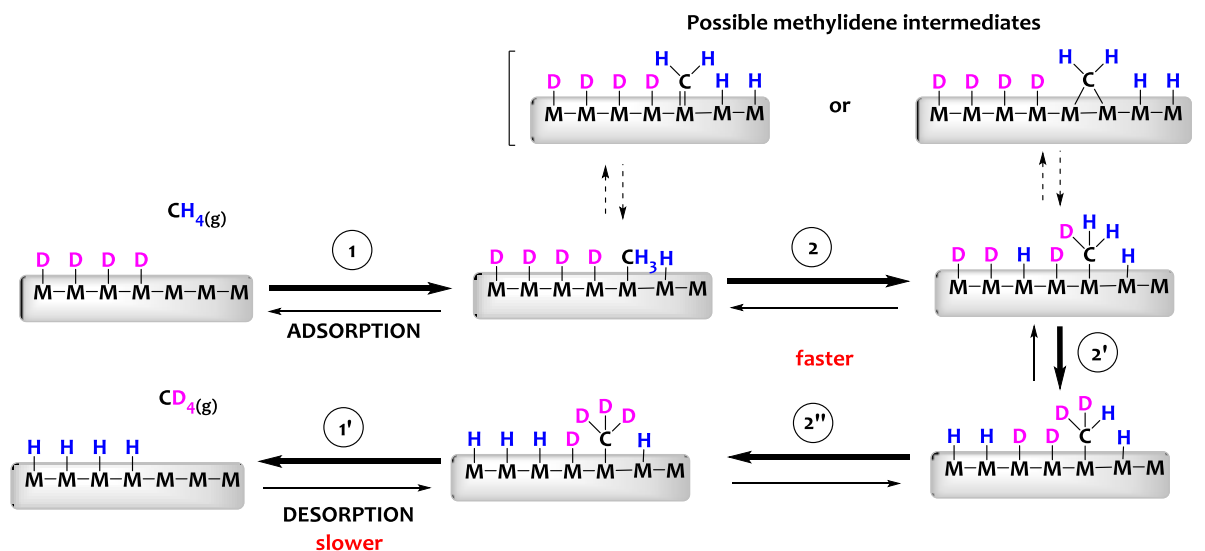
Kinetic behaviors of this reaction are very complex, especially when heterogeneous metal films catalysts are used, which feature distributions of active sites. However, some research groups have rationalized the main mechanisms that are at work for methane HDE:^[374]

First, it is assumed that H/D exchange on metal catalysts are much faster than the activation of the C-H/D bonds,^[365,375] thus the mobile hydrides on the surface are rapidly exchanged with deuterides in presence of excess D_2 .

Two main mechanisms are known for methane H/D exchange on noble metal surfaces: (i) stepwise exchange – noted SE (Scheme 78) and (ii) multiple exchange – noted ME (Scheme 79).^[365–367]



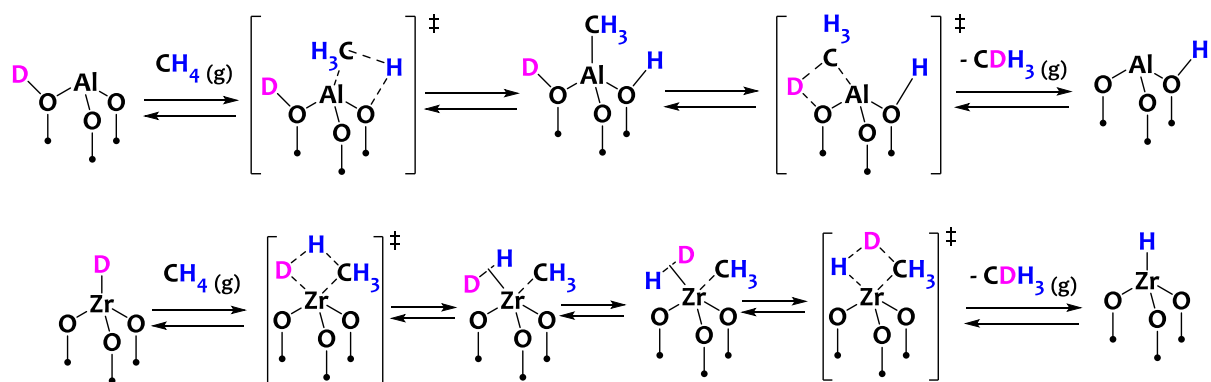
Scheme 78. Mechanism for stepwise exchange between CH_4 and excess D_2 on a noble metal catalyst, which is expected to give CH_3D as major product at low conversion.



Scheme 79. Mechanism for multiple exchange between CH_4 and excess D_2 on a noble metal catalyst, which is expected to give CD_4 as major product at low conversion.

The first step in both mechanisms is the chemisorption of $\text{CH}_4(\text{g})$ which cleaves a C-H bond and gives alkyl and hydride fragments *via* a process analogous to an oxidative addition. In the SE mechanism (Scheme 78), monodeuteromethane (CDH_3) is the major product at low conversion with negligible amount of CD_4 since the C-H activations of the surface methyl fragment subsequent to adsorption are slower than the desorption step. In contrast, a ME mechanism (Scheme 79) gives CD_4 (full deuteration) as major product at low CH_4 conversion as the rate determining step is the adsorption/desorption of CH_4 and the C-H activations subsequent to adsorption are fast. It is possible that these subsequent C-H activations result from the rapid dissociation and recombination of the adsorbed methyl groups to form methylene groups.^[365-367] The distribution of each isotopomers as a function of conversion is therefore an excellent way to obtain mechanistic insights, as reported with various metal catalysts.^[365-367] In most of cases both mechanisms can occur concomitantly to some extent and the distribution of products depends on the relative rates of each steps.

Two other known mechanisms are reported for methane H/D exchange. iii) H/D exchange of CH_4 on dehydrated γ -alumina operating through a mechanism in which CH_4 is dissociatively adsorbed across the Al-O moieties (Scheme 80, top).^[369,376] iv) When using early metal hydrides (eg. Zr), CH_4 H/D exchange can operate *via* a σ -bond metathesis mechanism (Scheme 80-bottom).^[40,377] In these two mechanisms, stepwise exchange producing CH_3D at low conversion is the only reported exchange distribution shown in the literature thus far.^[365]



Scheme 80. Metal-ligand (top) and sigma bond metathesis (bottom) mechanisms for exchange between CH₄ and excess D₂, which both give CH₃D as major product at low conversion.

Consequently, all these aspects will be considered for the next sections. In this chapter, we will present the catalytic performances of our materials, especially Ir-Al/SiO₂ (material **28**) and Ir/SiO₂ (material **30**) for the HDE catalysis of methane.

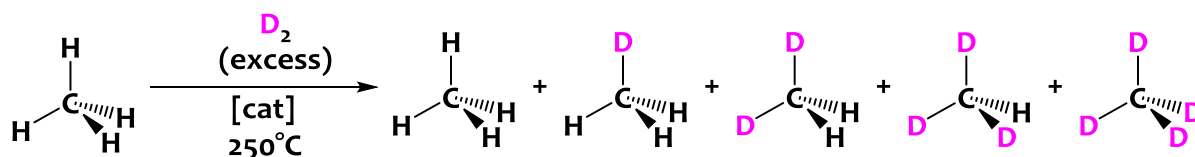
6.2 Description of the catalytic system

6.2.1 Experimental conditions and preliminary studies

HDE of methane is carried out in a 480 mL batch reactor at 250°C. The catalyst powder (ca 10 mg for 1 mol% Ir loadings) is charged in a glass reactor and sealed under argon. For low metal loadings of ca 0.1 mol% Ir, the catalyst powder is first diluted in SBA-15₇₀₀ by a factor 10 and the resulting powder is vigorously shaken in a closed 20 mL vial in the glovebox to ensure good mixing. Next, about 10 mg of the resulting light brownish powder is charged in the same reactor. Note that this approach increases the uncertainties on the final Ir loading since it consists in making two weighings (dilution in silica and transfer in the reactor) and the solid-solid mixing does not necessarily ensure a perfectly homogeneous dispersion (at the local level) of the catalyst in the silica.

The catalysts (1 mol% or 0.1 mol%/Ir with respect to the amounts of methane) are exposed to a mixture of dry CH₄ (at a partial pressure of 42 mbars) and dry D₂ (at a partial pressure of about 980 mbars) such as the D/H atomic ratio in the gas phase is ≈12. In this study, the catalyst loading used for Ir-Al/SiO₂ is slightly lower (1.0 mol%±0.1 mol% or 0.1 mol%±0.01 mol%) than that for Ir/SiO₂ (1.2 mol%±0.1 mol% or 0.12 mol%±0.01 mol%) to reach similar amounts of accessible metal surface for both catalysts (0.67 mol% ±0.03 mol% or 0.067 mol% ±0.003 mol%) since their dispersion are

slightly different (67% vs 56%, see section 5.5.2, page 237). When the reaction is launched under these experimental conditions, deuteromethanes are rapidly formed in the reactional medium (Scheme 81).



Scheme 81. Deuteration of methane (≈ 40 mbars) into $\text{CH}_{4-x}\text{D}_x$ isotopomers at $T=250^\circ\text{C}$ using D_2 gas (≈ 1 atm.) as a deuterium source

The formation of deuteromethanes is confirmed by the FT-IR analysis of the gas phase after catalysis, which shows characteristic vibration signals of CDH_3 (1242 cm^{-1}), CDH_3 (1087 cm^{-1}), CD_2H_2 (1034 cm^{-1}), and CD_4 (992 cm^{-1}) (Figure 99).^[41] The intense signals in the $2100\text{-}2300\text{ cm}^{-1}$ region are assigned to the elongation bands of C-D bonds.

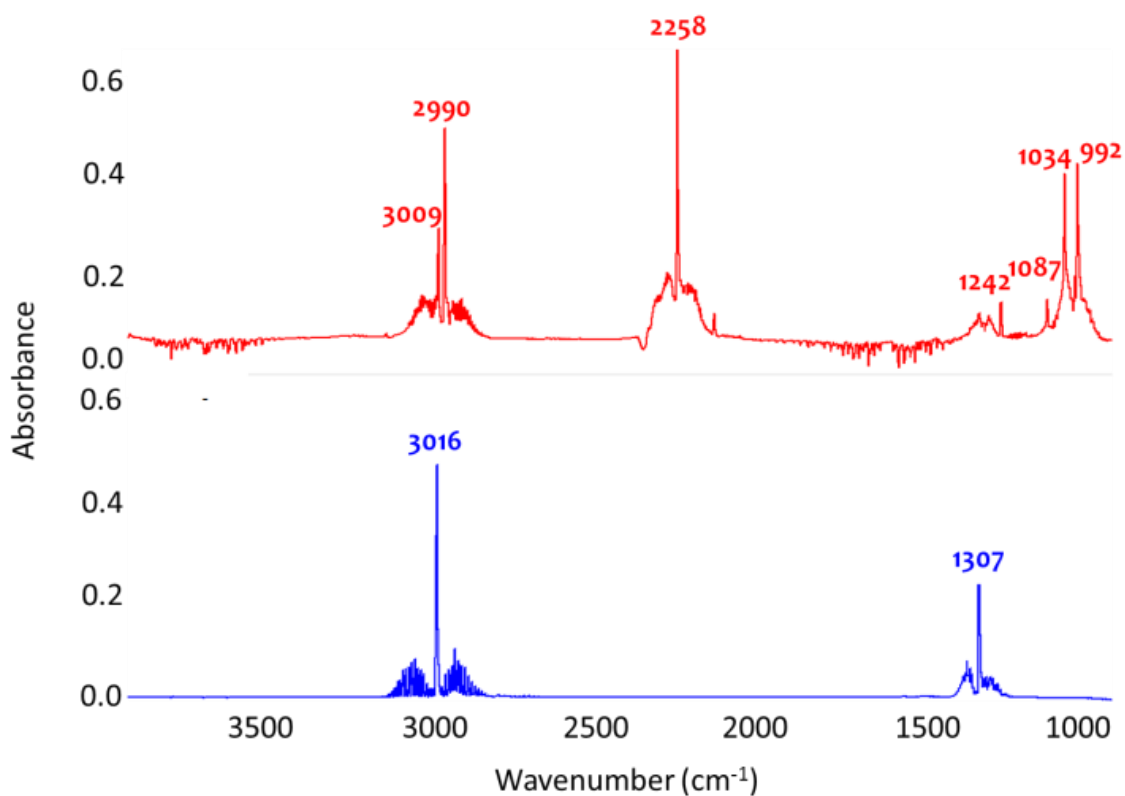


Figure 99. FT-IR spectra of the gas phase before (bottom) and after (top) catalysis.

6.2.2 Data processing

The reaction is also regularly monitored by GC-MS. From the resulting spectrograms, the precise amount of each $\text{CH}_{4-x}\text{D}_x$ isotopomer at a given time is calculated using fragmentation models given by Dibeler and Mohler.^[42] Notably, the following equations are applied:

$$(1) [\text{CD}_4] = [\text{m/z}=20].$$

$$(2) [\text{CD}_3\text{H}] = [\text{m/z}=19].$$

$$(3) [\text{CD}_2\text{H}_2] = [\text{m/z}=18] - 0.435[\text{CD}_3\text{H}] - 0.865[\text{CD}_4]$$

$$(4) [\text{CDH}_3] = [\text{m/z}=17] - 0.657[\text{CD}_2\text{H}_2] - 0.519[\text{CD}_3\text{H}].$$

$$(5) [\text{CH}_4] = [\text{m/z}=16] - 0.798[\text{CDH}_3] - 0.333[\text{CD}_2\text{H}_2] - 0.107[\text{CD}_3\text{H}] - 0.137[\text{CD}_4].$$

To consolidate these results, the isotopic distribution is also determined by a complementary mathematical approach developed by Schoofs and his team.^[43] In this case, the following equations are applied:

(o) $F_1 = [\text{m/z}=15]/[\text{m/z}=16]$; $F_2 = [\text{m/z}=14]/[\text{m/z}=16]$ where F_1 and F_2 relate respectively to the loss of one and two protons in the CH_4 mass spectrum reference.

$$(1) [\text{CD}_4] = [\text{m/z}=20]$$

$$(2) [\text{CD}_3\text{H}] = [\text{m/z}=19]$$

$$(3) [\text{CD}_2\text{H}_2] = [\text{m/z}=18] - 0.25F_1[\text{CD}_3\text{H}] - F_1[\text{CD}_4]$$

$$(4) [\text{CDH}_3] = [\text{m/z}=17] - 0.5F_1[\text{CD}_2\text{H}_2] - 0.75F_1[\text{CD}_3\text{H}].$$

$$(5) [\text{CH}_4] = [\text{m/z}=16] - 0.75F_1[\text{CDH}_3] - 0.5F_1[\text{CD}_2\text{H}_2] - 0.167F_2[\text{CD}_2\text{H}_2] - 0.5F_2[\text{CD}_3\text{H}] - F_2[\text{CD}_4].$$

From these data, some kinetic parameters can be extracted: i) the deuteration rate (or deuteration incorporation) of methane – noted τ thereafter – by using the following equation: $\tau_{(t)} = 0.25\text{CH}_3\text{D}_{(t)} + 0.5\text{CH}_2\text{D}_{2(t)} + 0.75\text{CHD}_{3(t)} + \text{CD}_{4(t)}$. Note that for a ratio $\text{D}/\text{H} \approx 12$, the thermodynamic equilibrium – noted τ_{eq} – of the reaction is reached for a deuteration rate of 92%. ii) The catalyst turnover number – TON – that is calculated as follows: $\text{TON} = \tau \cdot n_{\text{CH}_4} / n_{\text{Ir}}$ where n_{Ir} is the total number of moles of iridium in the catalyst and n_{CH_4} is the initial number of moles of methane in the reactor. iii) The catalyst surface turnover number – surface TON – which translates to the corrected turnover number from the calculated Ir dispersion (67% and 56% for Ir-Al/SiO₂ and Ir/SiO₂ respectively, see section 5.5.2, page 237) and is obtained as follows: surface TON = TON/Dispersion. iv) Distribution of $\text{CH}_{4-x}\text{D}_x$ with respect to the conversion of methane.

From these kinetic parameters, the following graphs can be plotted: percentage of each $\text{CH}_{4-x}\text{D}_x$ isotopomers = $f(t)$, distribution of deuteromethanes = $f(\text{methane conversion})$, $\tau = f(t)$, TON = $f(t)$,

and surface $\text{TON} = f(t)$.

Also, the $\text{TON} = f(t)$ curves are fitted by polynomial equations of degrees 3, 4, 5 or 6 in view of accurately calculating the maximum turnover frequency (TOF). For this catalytic system, an induction time of 5 minutes is noticed that corresponds to the thermic transfer into the reactor, *i.e.* the time to reach the desired temperature in the system. Therefore, in the next parts, time origin of the graphs will correspond to this induction time. The TOF will be also calculated after this period of 5 minutes.

6.3 Catalytic performances

6.3.1 Comparative activities between Ir-Al/SiO₂ and Ir/SiO₂.

Comparative methane deuteration rates for both catalysts are plotted on Figure 100. Here, the graph clearly shows improved catalytic performances of the bimetallic Ir-Al/SiO₂ catalyst compared to its Ir/SiO₂ monometallic analogue. Indeed, 50% deuterium incorporation into methane is noticed after 12 minutes of reaction for Ir-Al/SiO₂ versus 34 minutes for Ir/SiO₂. Furthermore, the end of reaction characterized by the thermodynamic equilibrium τ_{eq} is reached within 65 minutes for Ir-Al/SiO₂ versus 145 minutes for Ir/SiO₂.

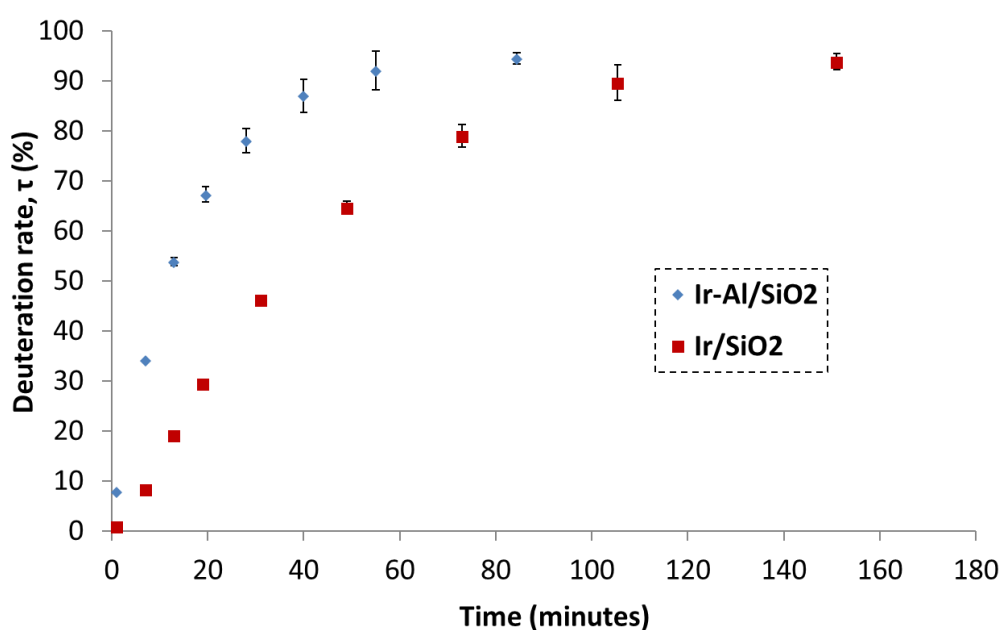


Figure 100. CH₄ deuteration rate as a function of reaction time at $T=250^{\circ}\text{C}$ for catalyst Ir-Al/SiO₂ (red diamond); and Ir/SiO₂ (blue squares) at $\approx 1 \text{ mol\%/Ir}$. All the data were extracted by averaging Dibeler-Mohler and Schoofs calculations. Errors bars account on the standard deviation between Dibeler-Mohler and Schoofs calculations.

In order to extend this study, we plotted the comparative turnover number of the catalysts as a function of reaction time (see Figure 101). It is important to note that the catalyst loading of Ir/SiO₂ is slightly higher than that of Ir-Al/SiO₂ to compensate the small dispersion difference, and achieve a similar Ir surface sites quantity for both catalysts. This is done intentionally to ensure that the difference in activity is not just related to a dispersion effect and prove the promotional effect of Al. The total amount of iridium metal introduced in the reaction for Ir/SiO₂ is therefore higher than that for Ir-Al/SiO₂, which is the reason why higher TONs are achieved for the latter. The Ir-Al/SiO₂ operates the H/D exchange of methane at a maximum turnover frequency (TOF) of 339 h⁻¹ versus 117 h⁻¹ for Ir/SiO₂ (slope of the curves at the origin of Figure 101).

More importantly, similar trends are obtained when turnover numbers are corrected from the Ir dispersion – surface TON – as represented on Figure 102. In this case, a maximum surface TOF of 506 h⁻¹ is obtained for Ir-Al/SiO₂ versus 209 h⁻¹ for Ir/SiO₂. Therefore, the catalyst loading used for Ir/SiO₂ is higher than that of Ir-Al/SiO₂, but still the latter has faster kinetics. These kinetic data thus demonstrate an enhanced catalytic activity of the bimetallic aluminum-iridium catalyst compared to its monometallic iridium counterpart by a factor of about three, which is significant. It is also important to mention that these kinetic behaviors are reproduced on independently synthesized samples.

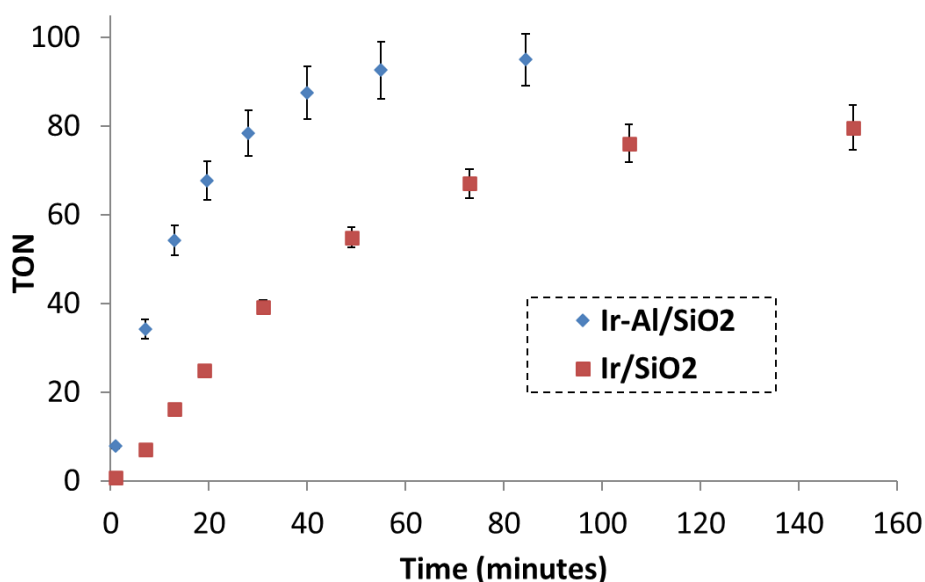


Figure 101. Monitoring catalytic H/D exchange of methane. Turnover number as a function of reaction time for catalysts Ir-Al/SiO₂ (blue diamonds) and Ir/SiO₂ (red squares) at 250°C and 0.67 mol% Ir surface sites. All the data were extracted by averaging Dibeler-Mohler^[42] and Schoofs^[43] calculations. Error bars account for uncertainty on catalyst loading and on the standard deviation between Dibeler-Mohler and Schoofs calculations.

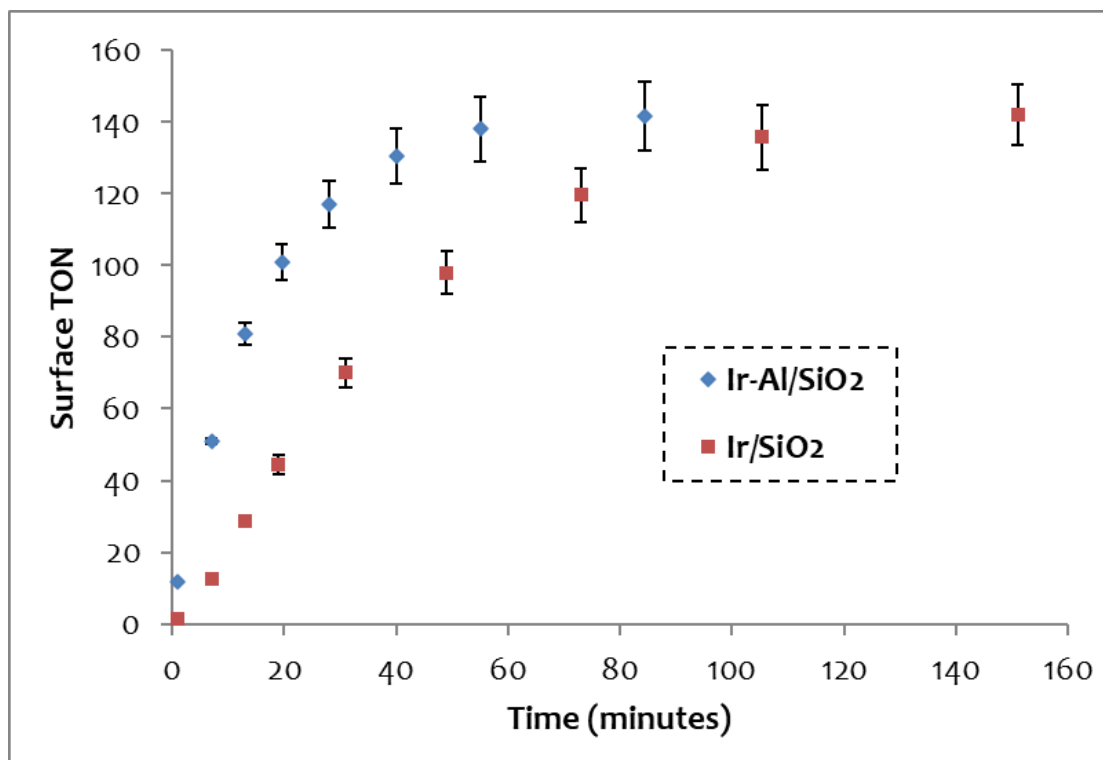


Figure 102. Surface turnover number (TON for surface iridium) as a function of reaction time at $T=250^{\circ}\text{C}$ for catalyst Ir-Al/SiO₂ (blue diamond); and Ir/SiO₂ (red squares) at ≈ 1 mol%/Ir. All the data were extracted by averaging Dibeler-Mohler^[42] and Schoofs^[43] calculations. Error bars account for uncertainty on catalyst loading and on the standard deviation between Dibeler-Mohler and Schoofs calculations.

The robustness of both catalysts is assessed as follows: the catalysts are exposed to air and then re-used in catalysis under the same experimental conditions. The obtained results are plotted on Figure 103 and Figure 104. Here, identical performances are obtained in the second catalytic run highlighting a good stability and robustness of these materials.

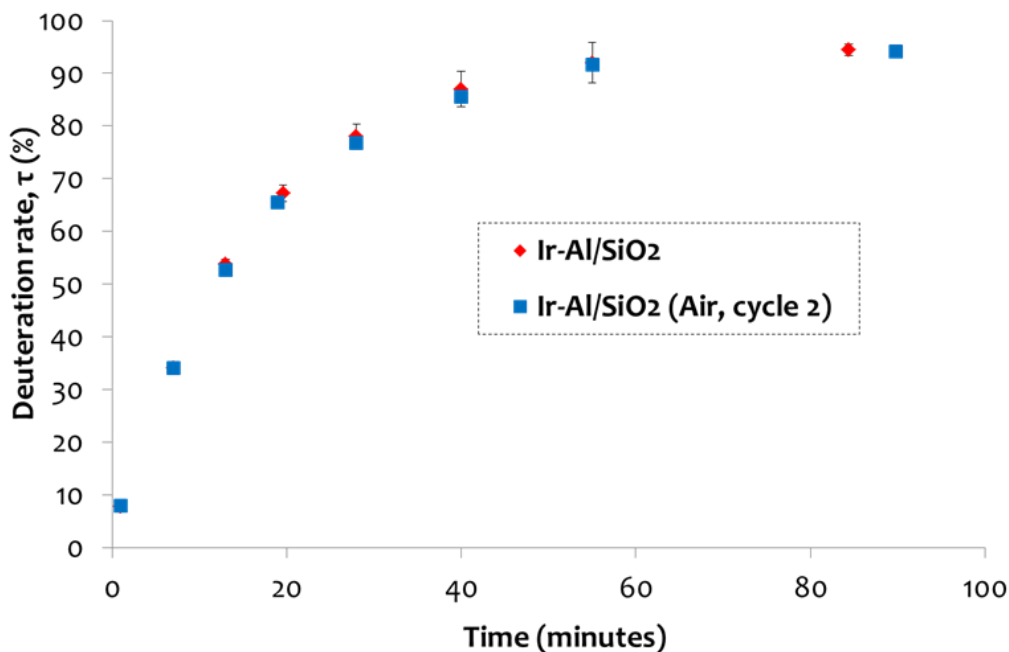


Figure 103. CH₄ deuteration rate as a function of reaction time at T=250°C for catalyst Ir-Al/SiO₂ at 1 mol%/Ir after a first cycle over inert atmosphere (red diamond); after opening the reactor over air for 1 hours and running a second catalytic cycle (blue squares). All the data were extracted by averaging Dibeler-Mohler and Schoofs calculations. Errors bars relate to the standard deviation between Dibeler-Mohler and Schoofs calculations.

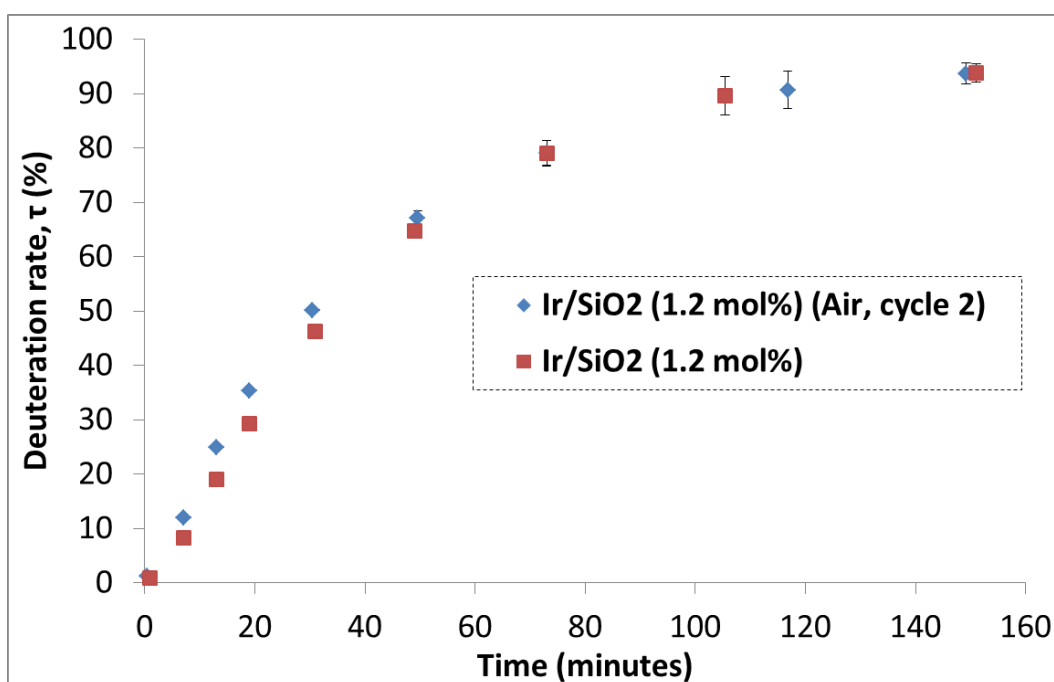


Figure 104. CH₄ deuteration rate as a function of reaction time at T=250°C for catalyst Ir/SiO₂ at 1.2 mol%/Ir (0.67 mol%/surface Ir) after a first cycle over inert atmosphere (red squares); after opening the reactor over air for 1 hours and running a second catalytic cycle (blue diamonds). All the data were extracted by averaging Dibeler-Mohler and Schoofs calculations. Errors bars relate to the standard deviation between Dibeler-Mohler and Schoofs calculations.

Decreasing the catalyst loading to 0.1 mol% resulted in an increased TON up to 900 after 9 hours, without evidence of catalyst deactivation (see Figure 105). Under these experimental conditions, the behaviors of Ir-Al/SiO₂ and Ir/SiO₂ are consistent with those observed for a metal loading of 1 mol%.

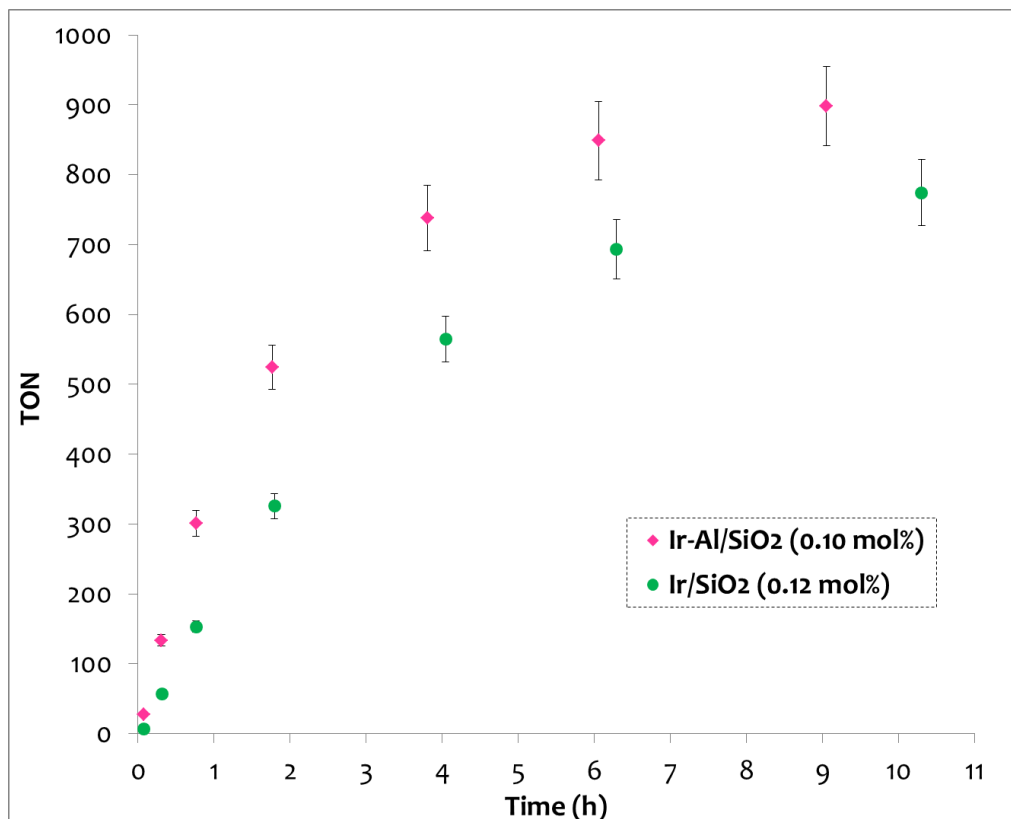


Figure 105. Turnover number (TON) as a function of reaction time at $T=250^{\circ}\text{C}$ for catalyst Ir-Al/SiO₂ (pink diamonds); and Ir/SiO₂ (green circles) at 0.10 mol% and 0.12 mol% respectively, i.e. 0.067 mol% Ir surface sites. All the data were extracted by averaging Dibeler-Mohler and Schoofs calculations. Errors bars account for uncertainties on the catalyst loading and on the standard deviation between Dibeler-Mohler and Schoofs calculations. The catalysts turnover numbers are calculated as follow: $\text{TON} = \tau \cdot n_{\text{CH}_4} / n_{\text{Ir}}$ where n_{Ir} is the total number of moles of iridium in the catalyst.

To get comparisons with materials without nanoparticles, we also tested material **27** under the same experimental conditions. The CH₄ deuteration rate as a function of reaction time is represented in Figure 106. In this case, material **27** shows a maximum activity after a long induction period of several hours, corresponding to the removal of the Cp* ligands and the *in-situ* formation of iridium nanoparticles.

Overall, this first set of catalytic investigation highlight synergistic effects between the interfacial aluminum sites and the supported iridium nanoparticles. To get deeper insights into the nature of these synergistic effects, we turned our attention to the selectivity of the catalysts: Ir-Al/SiO₂ and Ir/SiO₂.

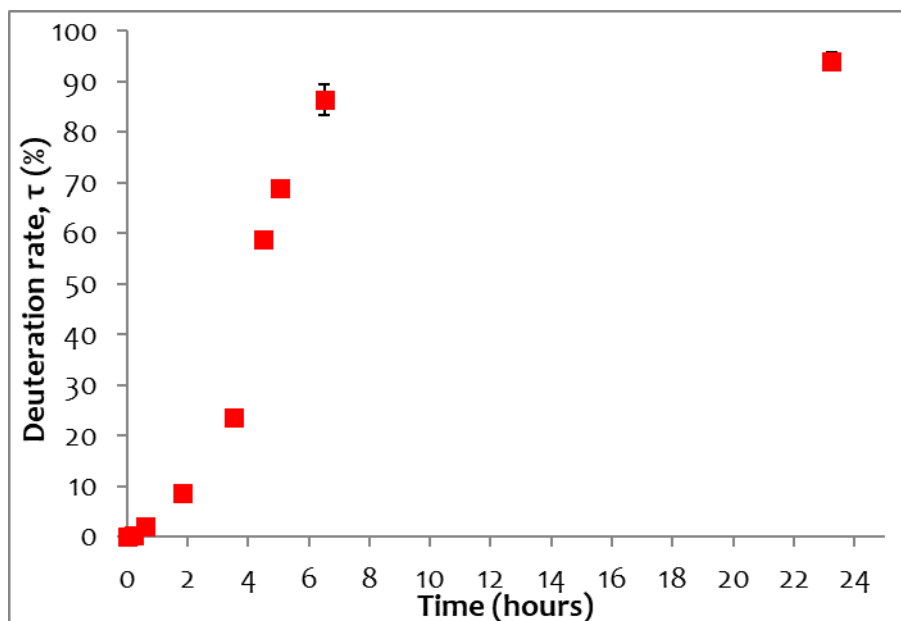


Figure 106. CH_4 deuteration rate as a function of reaction time at $T=250^\circ\text{C}$ for catalyst 27 (red squares) at 1 mol%/Ir. This graph shows a long induction time of about 4 hours. All the data were extracted by averaging Dibeler-Mohler and Schoofs calculations. Errors bars relate to the standard deviation between Dibeler-Mohler and Schoofs calculations.

6.3.2 Selectivity

In order to gain insight into the mechanisms operating between the gas phase ($\text{CH}_{4-x}\text{D}_x$ and D_2) and the catalyst surface, we are interested in the distribution of deuteromethane isotopomers as a function of the methane conversion (see Figure 107). Here, a comparable selectivity is observed for catalysts Ir-Al/SiO₂ and Ir/SiO₂ where CD_4 is predominant at low CH_4 conversion (10 to 20%). Note that a non-negligible amount of CH_3D is also observed. Next, an increase of the CD_4 proportion is noticed while the relative amount of CH_3D drops as CH_4 is consumed. It is important to mention that the proportion of CH_2D_2 is maintained at trace amount (<2%) whatever the CH_4 conversion. Eventually, when the conversion of methane is close to 100%, *i.e.* when the system reaches τ_{eq} , the following distribution is obtained CD_4 ($\approx 75\%$), CD_3H ($\approx 20\%$), and the other deuteromethanes (CH_2D_2 and CH_3D) at negligible quantities (<2%).

As mentioned in the introductory section of this chapter, two main mechanisms are known to describe a chemical event between the gas phase (CH_4 and D_2) and the surface of the catalyst for the methane HDE. In this instance, an important contribution of a multiple exchange mechanism is noticed. As also discussed in section 6.1 (page 247), the rate determining step of the ME mechanism is the CH_4 dissociative adsorption step. We thus propose that this step is facilitated when interfacial Al^{3+} sites are at the direct proximity of the Ir(o) nanoparticles.

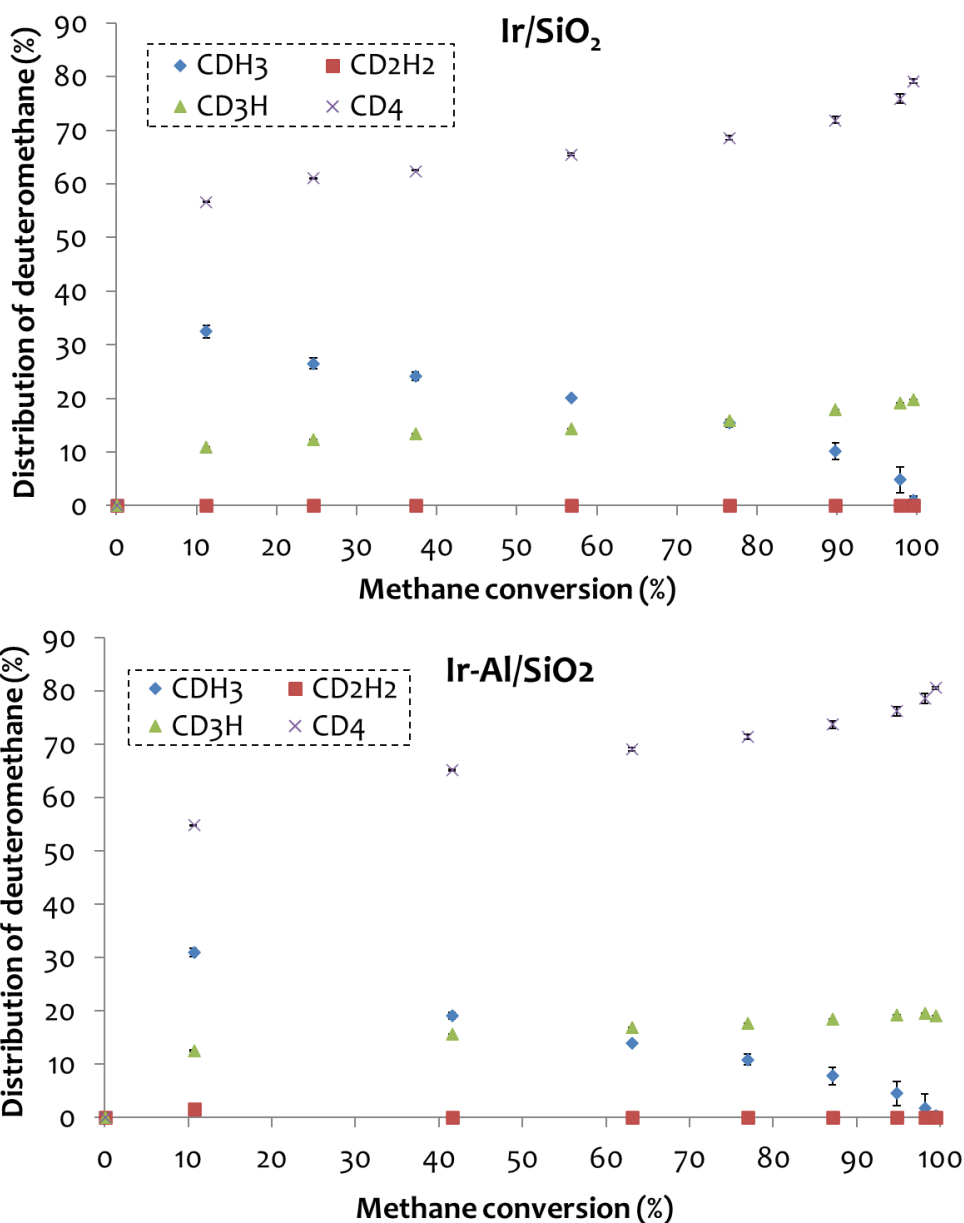


Figure 107. Distribution of deuteromethanes as a function of methane conversion for Ir/SiO₂ (top) and Ir-Al/SiO₂ (bottom). All the data were extracted by averaging Dibeler-Mohler and Schoofs calculations. Errors bars relate to the standard deviation between Dibeler-Mohler and Schoofs calculations.

Consequently, this study shows no impact of the Al sites on the selectivity of the methane HDE process. In this present case, the selectivity seems to be driven by the surface iridium NPs. However, the presence of aluminum sites adjacent to the Ir(o) NPs plays on the kinetics of the reaction where H/D exchange processes with the surface of the catalyst are faster (compared to a catalyst without aluminum - Ir/SiO₂).

6.4 Conclusions

In this chapter, we have described the catalytic performances of Ir-Al/SiO₂ and Ir/SiO₂ materials towards the HDE of methane. This comparative study revealed three main points: i) the bimetallic catalyst outperforms its monometallic counterpart by a factor of about three in terms of catalytic activity (TOF, time to reach equilibrium etc.). ii) A TON up to 900 is achievable after 9 hours, without evidence of catalyst deactivation, and identical performances are achieved after air exposure highlighting the good robustness of both Ir-Al/SiO₂ and Ir/SiO₂ catalysts. iii) The selectivity of the reaction is reminiscent of a ME mechanism and is almost identical between both catalysts.

Therefore, this preliminary catalytic study shows a promoting effect of the interfacial Al sites on the supported Ir(o) NPs. This work is quite unique as no anterior study (to the best of our knowledge) regarding the promoting effect of a second metal on the HDE of methane has been described. Furthermore, the air stability and robustness of these materials is a clear advantage compared to highly air-sensitive silica-supported molecular metal hydrides, which are known to deactivate easily.^[40]

Prospects for this study may involve substitution of Al³⁺ sites with different Lewis acid metal centers (e.g., Ga³⁺ or Y³⁺) to assess the influence of the promoter. On a similar note, it would be interesting to test siliceous supports with Lewis acidic properties, such as silica/alumina materials. It may also be interesting to modify the experimental conditions (e.g. methane partial pressure, temperature, catalyst loading) to see how these factors influence catalyst performances, and extend this study to the deuteration of larger alkanes.

CHAPTER 7. General Conclusions And Prospects

This doctoral research work has embarked on an ambitious project that lies at the interface of many research areas such as organometallic molecular chemistry, SOMC, materials chemistry, and catalysis. Indeed, the general objective of this research project was to develop new methodologies to prepare and study homogeneous and surface-supported heterobimetallic edifices associating so-called "hard" and "soft" metals and more particularly aluminum and iridium. The underlying hypothesis was to take advantage of (1) metal-metal (Al-Ir) and (2) metal-support cooperativity effects by immobilizing the heterobimetallic site on mesostructured silica. One of the ultimate goals of this thesis was to demonstrate the interest of these heterobimetallic architectures through their stoichiometric and catalytic reactivity. This work thus aimed to bring milestones to a building still little established. In the process, this project has provided concrete solutions, laid foundations and opened up new dimensions at each stage of its progress. The latter is reflected by the development of a series of innovative heterobimetallic aluminum/iridium complexes and bimetallic Al/Ir sites supported on silica used for cooperative reactivity and catalysis. This manuscript reported these findings in six chapters.

In a first chapter (chapter 2), we have envisioned to develop heterobimetallic complexes assembled by a bifunctional alcohol-NHC ligand, which was recently reported by our research team for bridging tantalum and rhodium derivatives. Inspired by this preliminary work, we extended the reactivity of this bifunctional alcohol-NHC ligand with alkyl aluminum and late transition metal precursors in order to access new monometallic and heterobimetallic complexes. This strategy successfully led to a series of original monometallic aluminum-NHC species and imidazolium aluminate zwitterions. Next, we studied the reactivity of these complexes with protic species (such as phenol). Out of all these species, we noticed a competitive protonolysis between the Al-C_{NHC} and the O-H units that is regulated by the steric profile of the Al derivative. The non-innocence of this aluminum-carbene bond in these systems is very interesting and provides valuable insights for the scientific community interested in Al-NHC chemistry. However, this diversified reactivity argues for some limitations of accessing to heterobimetallic species where in fact only one heterobimetallic Al/Cu complex was evidenced in this study.

This is why, in chapter 3, we were interested in another approach to access heterobimetallic complexes: the elimination of alkanes. This strategy has been used recently by our team for the design of innovative tantalum-iridium species. Therefore, inspired by these recent findings, we have successfully used the alkane elimination approach for the rational preparation of a new family of multinuclear aluminum-iridium polyhydride species, using isobutyl aluminum derivatives and an iridium tetrahydride precursor (IrCp*H₄). In all the cases, iridium hydrides are sufficiently

acidic to induce isobutyl-aluminum cleavage (Brønsted base) leading to Al-Ir motifs with direct intermetallic interactions and evolution of isobutane gas. The obtained heterobimetallic complexes feature strongly polarized $\text{Ir(III)}^{\delta-}\text{-Al(III)}^{\delta+}$ interactions that are described by two bonding situations (their contributions depend on the species): 3c-2e bonds ($\text{Ir-H}\rightarrow\text{Al}$) as well as direct electronic donation from Ir to Al.

In order to gain insights into the Ir-Al bimetallic interactions, we studied their reactivity towards various reagents in chapter 4. A first set of experiments revealed that the Al center in these systems is highly electrophilic and can accommodate Lewis bases (e.g. pyridine) or nucleophiles (e.g. benzyl anion). Also, the hydrides in these species are no longer acidic (no deprotonation with strong Brønsted bases). Instead, the Ir-Al units are reactive and can be subjected to transmetallation reactions with silver or potassium for instance. Importantly, no redox behaviors was noticed in these complexes upon their reaction with common redox agents (such as silver(I) triflate).

Eventually, original bimetallic cooperative activation of heteroallenes (CO_2 , R-NCO , R-NCN-R) was highlighted. For instance, the $\text{Cp}^*\text{IrH}_3\text{-Al}^i\text{(Bu)(OAr)(Py)}$ complex foster the cooperative reductive cleavage of carbon dioxide into CO (trapped as carbonyl iridium dihydride) and O^{2-} (trapped as a dimeric aluminum oxo species) through unconventional heterobimetallic reactional pathways.

Backed by an in-depth understanding of these Ir-Al species' behaviors, we considered in chapter 5 to transpose this knowledge in the field of SOMC. In particular, we demonstrated by the reactivity of Ir-Al species with molecular models of silica surfaces, that only $[\{\text{Ir}(\text{Cp}^*)(\text{H})(\mu\text{-H}_2)\}_3\text{Al}]$ is a suitable complex to achieve clean grafting onto a SBA-15 support. Accordingly, we designed a new well-defined heterobimetallic supported species - $[\equiv\text{SiOAl}\{(\mu\text{-H})_2\text{Ir}(\text{H})\text{Cp}^*\}_2]$ - which the structure was supported by IR and solid-state NMR spectroscopy, elemental analysis, and by the design of its molecular analogue - $[\{(\text{Ir}(\text{Cp}^*)(\text{H})(\mu\text{-H}_2))_2\text{Al}(\text{OAr}')\}]$. The thermal stability of $[\equiv\text{SiOAl}\{(\mu\text{-H})_2\text{Ir}(\text{H})\text{Cp}^*\}_2]$ site under H_2 was also investigated and revealed the possibility of forming a new material - Ir-Al/SiO₂ - with small NPs of Ir(o) narrowly distributed on the silica surface and surrounded by interfacial sites of Al(III). In order to provide a monometallic Ir counterpart of Ir-Al/SiO₂ for future catalytic studies, we also designed a new material - Ir/SiO₂ - by an IWI/TMP approach. Characterizations of Ir-Al/SiO₂ and Ir/SiO₂ by advanced techniques (STEM, chemisorption, XPS) revealed similar properties of the iridium nanoparticles (size, dispersion, and surface metallic state).

In a final chapter, we conducted comparative catalytic studies between Ir-Al/SiO₂ and Ir/SiO₂

materials for the hydrogen/deuterium exchange of methane at 250°C. This work showed i) enhanced catalytic performances of the bimetallic material compared to its monometallic analogue and ii) the air stability and robustness of both catalysts. These observations highlighted: i) the promoter effect of the Al(III) site and demonstrates the interest of adding a Lewis acid in the vicinity of the reactive metal nanoparticles and ii) the interest of materials Ir-Al/SiO₂ and Ir/SiO₂ compared to silica-supported metal-hydride species, which are highly sensitive to air and deactivate easily.

This thesis project has thus allowed us to lay new cornerstones in the high potential field of molecular and surface heterobimetallic chemistry and in particular the chemistry associating aluminum and iridium. Specifically, this work has highlighted original metal-metal cooperativities, capable of promoting innovative stoichiometric reactivities and which can be used to improve catalytic transformations.

Therefore, we believe that this doctoral research work represents an important contribution for the scientific community concerned with heterobimetallic chemistry. Also, in the continuity of two recent thesis works carried out in our laboratory on this type of chemistry, we also believe this PhD project embodies a springboard towards a new field of investigations. Among the avenues to be explored in a near and distant future to deepen and extend this work, we can cite:

- (i) Extension of **strategy 1** - bifunctional ligand - by using other types of bifunctional bridges (amino-NHC for example) and other metal/metal couples such as the association of other Lewis acids (Ga(III), Sc(III), Y(III)) with other d-block metals (Co, Rh, Ir, Cu etc.).
- (ii) Extension of **strategy 2** - the elimination of alkanes - to other late metal-hydride/hard alkyl-metal pairs (Ir/Ga, Ir/Y, Co/Al etc.).
- (iii) Development of supported-bimetallic sites combining other metal partners and/or supports (e.g. Ir/Y on alumina or Sc/Ir on silica/alumina)
- (iv) Extension of the SOMC/TMP approach to other surface heterobimetallic sites to form silica-supported metal(o) nanoparticles surrounded with monometallic interfacial sites.
- (v) Extending the stoichiometric and catalytic reactivities of these heterobimetallic species to a wider range of substrates and reactions to demonstrate the broader applicability of these constructs and establish robust structure-activity relationships to better understand their synergistic behavior.

CHAPTER 8. Experimental Section

8.1 General considerations

Unless otherwise noted, all reactions were performed either using standard Schlenk line techniques or in an MBraun inert atmosphere glovebox under an atmosphere of purified argon (<1 ppm O₂/H₂O). Glassware and cannulae were stored in an oven at ~100 °C for at least 12 h prior to use. Toluene, *n*-pentane, THF, and diethyl ether were purified by passage through a column of activated alumina, dried over Na/benzophenone, vacuum-transferred to a storage flask and freeze-pump-thaw degassed prior to use. Deuterated solvents (THF-*d*₈, toluene-*d*₈, C₆D₆, and pyridine-*d*₅) were dried over Na/benzophenone (THF-*d*₈, toluene-*d*₈, C₆D₆) or calcium hydride (pyridine-*d*₅), vacuum-transferred to a storage flask and freeze-pump-thaw degassed prior to use. Fluorobenzene was freeze-pump-thaw degassed and stored over molecular sieves (4Å) prior to use. Cp*IrH₄^[181], Al(^{*i*}Bu)(OAr)₂^[191] Al(^{*i*}Bu)₂(OAr)^[191] (Ar = 2,6-(^{*t*}Bu)-3-MeC₆H₂), and NHC-OH ligand^[20] were prepared using literature procedures. All other chemical reagents were purchased from commercial suppliers and used without further purification. The SBA-15 mesoporous silica was synthesized^[378] and dehydroxylated^[13] at 700°C according to the reported procedures (see SI for details). All other reagents were acquired from commercial sources and used as received. D₂, H₂, CH₄, CO₂ gases were dried and deoxygenated over freshly regenerated R311G BASF catalyst/molecular sieves (4Å) prior to use. For the synthesis and treatment of surface species, reactions were carried out using high-vacuum lines (10⁻⁵ mBar) and glovebox techniques.

8.2 Characterizations

IR spectroscopy. Samples were prepared in a glovebox (diluted in KBr for molecular complexes), sealed under argon in a DRIFT cell equipped with KBr windows and analyzed on a Nicolet 670 FT-IR spectrometer. FT-IR (transmission) reactions monitoring under H₂ or D₂ atmosphere were performed on pelleted solids mounted in a cell fitted with CaF₂ windows and designed for in-situ reactions under controlled atmosphere with a Nicolet 6700-FT-IR spectrometer.

Elemental analyses were performed under inert atmosphere either at the School of Human Sciences, Science Center, London Metropolitan University or at Mikroanalytisches Labor Pascher, Germany.

X-ray structural determinations. Crystal structures were determined using an Xcalibur Gemini

kappa-geometry diffractometer equipped with an Atlas CCD and a Molybdenum X-ray source ($\lambda = 0.71073 \text{ \AA}$). Intensities were collected by means of the CrysAlisPro software (Rigaku Oxford Diffraction, (2019), CrysAlisPro Software system, version 1.171.40.67a, Rigaku Corporation, Oxford, UK). Reflection indexing, unit-cell parameters refinement, Lorentz-polarization correction, peak integration and background determination were carried out with the CrysAlisPro software (Rigaku Oxford Diffraction, (2019), CrysAlisPro Software system, version 1.171.40.67a, Rigaku Corporation, Oxford, UK.). An analytical absorption correction was applied using the modelled faces of the crystal.^[379] The resulting set of hkl was used for structure solution and refinement. The structures were solved with the ShelXT^[380] structure solution program using the intrinsic phasing solution method and by using Olex2^[381] as the graphical interface. The model was refined with version 2018/3 of ShelXL^[382] using least-squares minimization.

NMR Spectroscopy. Solution NMR spectra were recorded on Bruker AV-300, AVQ-400 and AV-500 spectrometers. Peaks are reported in ppm (δ) and were referenced to a tetramethyl silane (Me_4Si) internal standard for proton (^1H) and carbon (^{13}C) experiments, to a 85 wt% phosphoric acid solution in water for phosphorous (^{31}P) experiment, and to a hexaaquaaluminum(III) ($\text{Al}(\text{H}_2\text{O})_6^{3+}$) internal standard for aluminum (^{27}Al) experiment. ^{11}B and ^{19}F chemical shifts are reported relative to $\text{BF}_3\cdot\text{OEt}_2$ set at 0.00 ppm. ^1H and ^{13}C NMR assignments were confirmed by bidimensionnal NMR ^1H - ^1H COSY plus ^1H - ^{13}C HSQC and HMBC experiments. Regarding the peaks' multiplicity, the following caption will be considered: s for singlet, d for doublet, t for triplet, q for quadruplet, m for multiplet, b for broad, dd for doublet of doublets, dt for doublet of triplets. The 1D ^1H and ^{13}C solid-state NMR spectra were obtained on a Bruker 300 MHz wide-bore spectrometer using a double resonance 4-mm MAS probe. The samples were introduced under argon in a zirconia rotor, which was then tightly closed. Dry nitrogen gas was used to spin the samples to avoid sample degradation. The ^{13}C spectra were obtained from cross polarization (CP) from protons using a linear ramped CP to optimize the magnetization transfer efficiency.

Computational data. All DFT calculations were carried out with the Gaussian 09 suite of programs.^[383] Geometries were fully optimized in gas phase without symmetry constraints, employing the B3PW91 functional.^[384] The nature of the extrema was verified by analytical frequency calculations. The calculation of electronic energies and enthalpies of the extrema of the potential energy surface (minima and transition states) were performed at the same level of theory as the geometry optimizations. IRC calculations were performed to confirm the connections of the optimized transition states. Iridium atoms were treated with a small-core effective core potential (60 MWB), associated with its adapted basis set^[385] augmented with a

polarization function ($\zeta_f = 0.938$).^[386] Aluminum atoms were treated with a Stuttgart effective core potential^[387] augmented with a polarization function ($\zeta_d = 0.325$). For the other elements (H, C, B, F and O), Pople's double- ζ basis set 6-31G(d,p) was used.^[388-391] The electronic charges (at the DFT level) were computed using the natural population analysis (NPA) technique.^[392]

TEM and STEM-HAADF

Electron microscopy experiments were used to understand the structural and morphological characteristics of the catalysts by using a MET JEOL 2100F (FEG) microscope at the “Centre Technologiques des Micro-structures”, CT μ Villeurbanne, France; equipped with an Oxford Instruments Energy-Dispersive Spectroscopy (EDS) SDD detector. The samples were transferred to the microscope apparatus under inert atmosphere.

Chemisorption of H₂

Chemisorption experiments were performed on a Belsorb-Max apparatus from BEL Japan. In a measuring cell, 32 mg of Ir-Al/SiO₂ and 43 mg of Ir/SiO₂ were treated at 10⁻⁶ mbar at 523 K for 3 h using a ramp of 5K min⁻¹. After this pretreatment, adsorption isotherms were measured at 298 K in the pressure range of [30-265 mbars]. In this study, we quantify the total adsorption, *i.e.* adsorption on fully degassed nanoparticles. For each experimental points, the pressures at equilibrium were recorded after a time of one hour. The quantification of gas adsorbed on surface metal atoms was calculated from the adsorption at saturation deriving from a double Langmuir adsorption equation model, assuming complete reduction of the metal and truncated cubic octahedron geometry.

X-ray photoelectron spectroscopy (XPS) data.

X-ray photoelectron spectroscopy (XPS) measurements were performed on a Sigma II instrument (Thermo Electron) equipped with an Alpha 110 hemispherical analyzer. The instrument was operated in large area XPS mode using an Al K α X-ray source at 200 W. All samples were prepared in a Arglovebox by pressing the sample powder into a piece of indium foil (Alfa Aesar, Puratronic® 99.9975% trace metal basis, 0.25 mm thickness). The supported samples were then mounted in a home-made sample holder that allows for the samples to be transferred into the FEAL chamber under vacuum without being exposed to the ambient atmosphere. The pressure in the XPS analysis chamber was maintained under 5.0 x 10⁻⁸ mbar during all measurements. Survey scan spectra were collected up to a binding energy of 1100 eV using a pass energy of 50 eV, a step size of 1 eV, and a dwell time of 50 ms. Narrow region scans were collected using a pass energy of 25

eV, a step size of 0.1 eV, and dwell time of 50 ms. All spectra were calibrated to the Si 2p peak of SiO₂ at 103.5 eV. A Shirley background was used when fitting the Ir 4f spectra. The Ir 4f_{7/2}- 4f_{5/2} peak doublet separation was fixed at 2.98 eV and the 4f_{5/2}:4f_{7/2} peak area ratio was fixed at 3:4.

General procedure for the catalysis.

The catalyst powder (1.0 mol%/Ir) was charged in a 480 mL glass reactor and sealed under argon. The system was then evacuated on a high-vacuum line (10⁻⁵ mBar) and dry methane (~42 mbars, 0.8 mmol, 1 eq.) and dry deuterium gas (~1020 mbars, 20.1 mmol, 25 equiv.) were transferred in the reactor. The reactional medium was heated at 250°C and the gas phase was regularly monitored by GC-MS.

8.3 Synthesis

8.3.1 CHAPTER 2 Towards Heterobimetallic Aluminum/M Complexes Bridged By Bifunctional NHC Ligands

Synthesis of Al(L)(ⁱBu₂) and ¹³C-labelled Al(L)(ⁱBu₂): compounds **2** and **2-¹³C**

Within a cooled bath of acetone and liquid nitrogen at -40°C, a 20 mL orange-yellow THF solution of the bifunctional ligand NHC **1** (205 mg, 0.79 mmol, 1.00 eq.) was added slowly (in 2 minutes) to a 20 mL THF solution of triisobutylaluminum 1M in hexanes (0.8 mL, 0.80 mmol, 1.01 eq.). The resulting yellowish solution was left over stirring for 20 minutes at -40°C and heated to room temperature (*via* the discarding of the cooled bath) for one hour. Volatiles were removed *in vacuo* for two hours yielding 310 mg (7.78 mmol, 98.5 %) of an orange oil-tar. This crude compound was dissolved in ~1.5 mL of pentane and put in freezer at -40°C for 12 hours yielding yellow crystals that were recovered by filtration and dryness *in vacuo*.

Alternative procedure: A 3 mL THF solution of neat triisobutylaluminum (177 mg, 0.89 mmol, 1 equiv.) was prepared and cooled to -40°C in the freezer inside the glovebox. A cold (-40°C) 15 ml orange THF suspension of the NHC-OH ligand **1** (232 mg, 0.89 mmol, 1 equiv.) was slowly added to the cold triisobutylaluminum THF solution. The resulting yellow-orange solution was stirred for 1h30 at room temperature. Volatiles were removed *in vacuo* for four hours and the resulting residue was dissolved in ~2 mL of pentane and stored in the glovebox freezer at -40°C for 14 hours yielding yellow-orange crystals that were recovered by filtration and dried *in vacuo* (348 mg, 98%).

$^1\text{H-NMR}$ (300 MHz, C_6D_6 , 293 K): δ = 6.68 (s, 2H, $m\text{-CH}_{\text{Mes}}$), 5.99 (s, 1H, CH_{imid}), 5.84 (s, 1H, CH_{imid}), 3.46 (s, 2H, NCH_2), 2.08 (m, 2H, $\beta\text{-CH}_{\text{iBu}}$), 2.04 (s, 3H, $p\text{-CH}_3\text{Mes}$), 1.88 (s, 6H, $o\text{-CH}_3\text{Mes}$), 1.27 (q, 12H, $\gamma\text{-CH}_{2\text{-iBu}}$), 1.24 (s, 6H, $\text{C}(\text{CH}_3)_2$), 0.02 (m, 4H, $\alpha\text{-CH}_{2\text{-iBu}}$). $^1\text{H-NMR}$ (500 MHz, THF-d_8 , 293 K): δ = 7.38 (d, 1H, CH_{imid} , $^3J_{\text{C-H}} = 1.6$ Hz), 7.20 (d, 1H, CH_{imid} , $^3J_{\text{C-H}} = 1.6$ Hz), 7.00 (s, 2H, $m\text{-CH}_{\text{Mes}}$), 4.01 (s, 2H, NCH_2), 2.32 (s, 3H, $p\text{-CH}_3\text{Mes}$), 2.00 (s, 6H, $o\text{-CH}_3\text{Mes}$), 1.58 (m, 2H, $\beta\text{-CH}_{\text{iBu}}$, $^3J_{\text{C-H}} = 6.6$ Hz), 1.12 (s, 6H, $\text{C}(\text{CH}_3)_2$), 0.78 (dd, 12H, $\gamma\text{-CH}_{2\text{-iBu}}$, $^3J_{\text{C-H}} = 6.6$ Hz, $^4J_{\text{C-H}} = 1.4$ Hz), -0.51 (d, 4H, $\alpha\text{-CH}_{2\text{-iBu}}$, $^3J_{\text{C-H}} = 6.9$ Hz). $^{13}\text{C}\{^1\text{H}\}$ -NMR (125 MHz, THF-d_8 , 293 K): δ = 173.51 ($\text{C}_{\text{NHC-Al}}$), 139.79 (C_{Ar}), 135.95 (C_{Ar}), 135.64 (C_{Ar}), 129.60 ($m\text{-CH}_{\text{Ar}}$), 124.02 (C_{imid}), 121.98 (C_{imid}), 69.34 ($\text{OC}(\text{CH}_3)_2$), 62.55 (NCH_2), 29.49 ($\text{OC}(\text{CH}_3)_2$), 28.82 ($\gamma\text{-C}_{\text{iBu}}$), 28.50 ($\gamma\text{-C}_{\text{iBu}}$), 27.49 ($\beta\text{-C}_{\text{iBu}}$), 23.60 (b, $\alpha\text{-C}_{\text{iBu-Al}}$), 23.02 ($\alpha\text{-C}_{\text{iBu-Al}}$), 20.89 ($p\text{-CH}_3\text{Mes}$), 17.61 ($o\text{-CH}_3\text{Mes}$). $^{27}\text{Al-NMR}$ (130 MHz, THF-d_8 , 293 K): δ = 72.0 (b, Al 4-coordinated). Elemental analysis: calculated for $\text{C}_{24}\text{H}_{39}\text{N}_2\text{OAl}$: C, 72.32; H, 9.86; N, 7.03. Found: C, 72.34; H, 9.94; N, 6.89.

Compound 2 ^{13}C $^1\text{H-NMR}$ (300 MHz, C_6D_6 , 293 K): δ = 6.68 (s, 2H, $m\text{-CH}_{\text{Mes}}$), 5.99 (t, 1H, CH_{imid}), 5.84 (t, 1H, CH_{imid}), 3.46 (d, 2H, NCH_2), 2.07 (m, 2H, $\beta\text{-CH}_{\text{iBu}}$), 2.03 (s, 3H, $p\text{-CH}_3\text{Mes}$), 1.89 (s, 6H, $o\text{-CH}_3\text{Mes}$), 1.27 (q, 12H, $\gamma\text{-CH}_{2\text{-iBu}}$), 1.24 (s, 6H, $\text{C}(\text{CH}_3)_2$), 0.03 (m, 4H, $\alpha\text{-CH}_{2\text{-iBu}}$). $^{13}\text{C}\{^1\text{H}\}$ -NMR (75 MHz, C_6D_6 , 293 K): δ = 173.91 ($^{13}\text{C}_{\text{NHC-Al}}$).

Synthesis of $\text{Al}(\text{Me})(\text{OAr})_2$ (inspired from ref.^[191])

A 20 mL pentane solution of 2,6-Di-tert-butyl-methylphenol (5.00 g, 22.69 mmol, 2.00 eq.) was added dropwise to a 10 mL pentane solution of trimethylaluminum(III) (2M in toluene) (5.7 mL, 11.34 mmol, 1.00 eq.). The resulting yellowish solution was left over stirring for 2 hours yielding an off-white suspension that was recovered by filtration (1.150 g, 10.5% of yield). As for the filtrate, it was left again over stirring for 2 hours yielding a white powder (0.450 g, 4.1%). The resulting solid residue was dissolved in 60 mL of pentane and kept at room temperature for 6 days and at -28°C for 16 hours yielding yellow crystals that were recovered by filtration and dryness (1.300 g, 11.9%). In total, compound **6** is generated with a yield of 27%. $^1\text{H-NMR}$ (300 MHz, C_6D_6 , 293 K): δ = 7.14 (s, 4H, H_{Ar}), 2.29 (s, 6H, $\text{CH}_3\text{-Ar}$), 1.57 (s, 36H, $o\text{-}^t\text{Bu}_{\text{Ar}}$), -0.27 (s, 3H, Al-CH_3).

Synthesis of the zwitterion $[\text{HL}][\text{Al}(^t\text{Bu})(\text{OAr})_2]$: compound **3**

In a vial, a 14 mL toluene suspension of ligand **1** (348 mg, 1.35 mmol, 1 eq.) was added onto $\text{Al}(^t\text{Bu})(\text{OAr})_2$ (707 mg, 1.35 mmol, 1 eq.). Rapidly, the orange suspension became an orange solution. The reaction mixture was stirred for 2 hours at room temperature and turned from an orange solution to an off-white suspension. The solids were recovered by filtration, washed with

2x2 mL of toluene, and dried *in vacuo* for 18 hours yielding zwitterion **3** as a white powder (945 mg, 1.21 mmol, 90 %). Single crystals suitable for X-ray diffraction were grown from recrystallization in benzene. Elemental analysis: Calculated for C₅₀H₇₇O₃N₂Al: C, 76.88; H, 9.94; N, 3.59. Found: C, 76.53; H, 10.05, N, 3.73. ¹H NMR (500 MHz, C₆D₆, 293 K) δ = 7.51 (t, 1H, CH_{imid}, ⁴J_{HH} = 1.5 Hz), 7.19 (s, 4H, *m*-CH_{Ar}), 6.53 (s, 2H, *m*-CH_{Mes}), 6.27 (t, 1H, CH_{imid}, ⁴J_{HH} = ³J_{HH} = 1.5 Hz), 5.48 (t, 1H, CH_{imid}, ⁴J_{HH} = ³J_{HH} = 1.5 Hz), 3.53 (s, 2H, NCH₂), 2.33 (m, 1H, β-CH_{iBu}), 2.31 (s, 6H, *p*-CH_{3Ar}), 2.01 (s, 3H, *p*-CH_{3Mes}), 1.79 (s, 36H, *o*-^tBu_{Ar}), 1.45 (s, 6H, *o*-CH_{3Mes}), 1.31 (d, 6H, γ-CH_{3iBu}, ³J_{HH} = 6.0 Hz), 1.22 (s, 6H, O(CH₃)₂), 0.71 (d, 2H, α-CH_{2iBu}, ³J_{HH} = 6.0 Hz). ¹³C{¹H} NMR (125 MHz, C₆D₆, 293 K) δ = 158.2 (C_{Ar}), 141.6 (C_{Ar}), 139.2 (C_{Ar}), 135.6 (CH_{imid}), 134.1 (C_{Ar}), 130.6 (C_{Ar}), 129.8 (*m*-CH_{Mes}), 126.2 (*m*-CH_{Ph}), 124.3 (C_{Ar}), 122.7 (CH_{imid}), 121.7 (CH_{imid}), 69.8 (OC(CH₃)₂), 64.1 (NCH₂), 35.9 ((CH₃)₃CAr), 33.0 ((CH₃)₃CAr), 29.7 (γ-C_{iBu}), 29.4 (OC(CH₃)₂), 27.0 (β-C_{iBu}), 21.5 (*p*-CH_{3Ar}), 20.9 (*p*-CH_{3Mes}), 17.0 (*o*-CH_{3Mes}). ²⁷Al NMR (130 MHz, C₆D₆, 293 K) δ = 78.0.

Formation of the ¹³C-labelled zwitterion [HL][Al(Me)(OAr)₂]: compound **4**-¹³C

A 0.7 mL C₆D₆ colorless solution of Al(Me)(OAr)₂ (30.2 mg, 0.063 mmol, 1.00 eq.) was added onto the ¹³C-labelled bifunctional ligand **1** (16.3 mg, 0.063 mmol, 1.00 eq.). The resulting yellow mixture containing an off-white suspension was sealed in a J-Young NMR tube and transiently heated to increase its solubility. ¹H-NMR (300 MHz, C₆D₆, 293 K): δ = 8.40 (d, 1H, ¹³C-H_{imid}, ¹J_{C-H} = 226 Hz), 7.06 (s, 4H, *m*-CH_{Ar}), 6.48 (s, 2H, *m*-CH_{Mes}), 5.89 (t, 1H, CH_{imid}), 5.32 (t, 1H, CH_{imid}), 3.48 (d, 2H, N-CH₂), 2.32 (s, 6H, *p*-CH_{3Ar}), 2.02 (s, 3H, *p*-CH_{3Mes}), 1.68 (s, 36H, *o*-^tBu_{Ar}), 1.38 (s, 6H, *o*-CH_{3Mes}), 1.26 (s, 6H, O(CH₃)₂), 0.20 (s, 3H, Al-CH₃). ¹H-NMR (300 MHz, tol-d₈, 293 K): δ = 8.28 (d, 1H, ¹³C-H_{imid}, ¹J_{C-H} = 227 Hz), 6.94 (s, 4H, *m*-CH_{Ar}), 6.49 (s, 2H, *m*-CH_{Mes}), 6.11 (t, 1H, CH_{imid}), 5.51 (t, 1H, CH_{imid}), 3.55 (d, 2H, N-CH₂), 2.23 (s, 6H, *p*-CH_{3Ar}), 2.04 (s, 3H, *p*-CH_{3Mes}), 1.55 (s, 36H, *o*-^tBu_{Ar}), 1.37 (s, 6H, *o*-CH_{3Mes}), 1.24 (s, 6H, O(CH₃)₂), 0.00 (s, 3H, Al-CH₃). ¹³C{¹H}-NMR (75 MHz, C₆D₆, 293 K) δ = 136.6 (¹³C-H_{imid}).

Synthesis of [K(THF)₂L][Al(^tBu)(OAr)₂]: compound **5**

KHMDS (94 mg, 0.47 mmol, 1 eq.) was added to a 5 mL toluene suspension of the imidazolium aluminate **3** (365 mg, 0.47 mmol, 1 eq.). The reaction mixture was stirred overnight at room temperature. The volatiles were removed *in vacuo*. A minimum amount of THF (2mL) was added to dissolve the off-white residue and the solution was layered with 10 mL pentane and kept at -40 °C for 3 days, yielding white crystals of [K(THF)₂L][Al(^tBu)(OAr)₂] **5** that were recovered and dried *in vacuo* (324 mg, 0.34 mmol, 73%). Single crystals suitable for X-ray diffraction were grown from

slow diffusion of pentane into a saturated THF solution of **5**. ^1H NMR (500 MHz, THF- d_8 , 293 K) δ = 7.00 (d, 1H, CH_{imid} , $^3J_{\text{HH}} = 1.6$ Hz), 6.94 (s, 2H, $m\text{-CH}_{\text{Mes}}$), 6.79 (s, 4H, $m\text{-CH}_{\text{Ar}}$), 6.77 (d, 1H, CH_{imid} , $^3J_{\text{HH}} = 1.6$ Hz), 4.04 (s, 2H, NCH_2), 3.62 (m, 8H, THF), 2.29 (s, 3H, $p\text{-CH}_3$), 2.11 (s, 6H, $p\text{-CH}_3$), 1.06 (m, 1H, $\beta\text{-CH}_{\text{iBu}}$), 1.96 (s, 6H, $o\text{-CH}_3$), 1.78 (m, 8H, THF); 1.46 (s, 36H, $o\text{-}^t\text{Bu}_{\text{Ar}}$), 1.18 (s, 6H, $\text{O}(\text{CH}_3)_2$), 0.83 (d, 6H, $\gamma\text{-CH}_3$, $^3J_{\text{HH}} = 6.4$ Hz), 0.23 (d, 2H, $\alpha\text{-CH}_2$, $^3J_{\text{HH}} = 6.4$ Hz). $^{13}\text{C}\{^1\text{H}\}$ NMR (125 MHz, THF- d_8 , 293 K) δ = 211.1 (C_{NHC}), 158.1 (C_{Ar}), 139.5 (C_{Ar}), 139.0 (C_{Ar}), 137.8 (C_{Ar}), 135.8 (C_{Ar}), 129.2 ($m\text{-CH}_{\text{Mes}}$), 125.6 ($m\text{-CH}_{\text{Ph}}$), 122.7 (C_{Ar}), 121.4 (CH_{imid}), 119.8 (CH_{imid}), 71.0 ($\text{OC}(\text{CH}_3)_2$), 68.0 (THF), 65.4 (NCH_2), 35.8 ($((\text{CH}_3)_3\text{C}_{\text{Ar}}$), 32.9 ($((\text{CH}_3)_3\text{C}_{\text{Ar}}$), 30.2 ($\gamma\text{-C}_{\text{iBu}}$), 29.6 ($\text{OC}(\text{CH}_3)_2$), 27.0 ($\beta\text{-C}_{\text{iBu}}$), 26.2 (THF), 21.3 ($p\text{-CH}_3$), 20.9 ($p\text{-CH}_3$), 17.7 ($o\text{-CH}_3$). $^{13}\text{C}\{^1\text{H}\}$ NMR (75 MHz, C_6D_6 , 293 K) δ = 211.1 (C_{NHC}), ^{27}Al NMR (130 MHz, THF- d_8 , 293 K) δ = 80.1. Anal. calcd for $\text{C}_{58}\text{H}_{92}\text{N}_2\text{O}_5\text{AlK}$: C, 72.31; H, 9.63; N, 2.91. Found: C, 72.19; H, 9.43; N, 2.79.

Note that upon heating (100°C for 2h in toluene), compound **5** is cleanly transformed into a new compound of unknown structure. Unfortunately, NMR data are ambiguous and thus insufficient to conclude on the precise structure of this thermal decomposition product, and attempts to crystallize it have failed in our hands to date.

Alkyl abstraction from $[\text{HL}][\text{Al}(^t\text{Bu})(\text{OAr})_2]$: formation of $\{[\text{HL}][\text{Al}(\text{OAr})_2]\{\text{HBC}_6\text{F}_5\}$, **6**

A 0.5 mL C_6D_6 suspension of the ^{13}C -labelled imidazolium aluminate **3** (20.0 mg, 0.03 mmol 1eq.) was added onto *tris*(pentafluorophenyl)borane (13.1 mg, 0.03 mmol, 1 eq.) at r.t., yielding a colorless solution. NMR monitoring of the reaction shows the quantitative formation of the imidazolium borate complex $[(\text{HL})\text{Al}(\text{OAr})_2][\text{HB}(\text{C}_6\text{F}_5)_3]$, **6** and release of isobutene. ^1H NMR (300 MHz, C_6D_6 , 293 K) δ = 7.66 (m, 1H, CH_{imid}), 7.08 (s, 4H, $m\text{-CH}_{\text{Ar}}$), 6.58 (s, 2H, $m\text{-CH}_{\text{Mes}}$), 6.20 (m, 1H, CH_{imid}), 5.90 (m, 1H, CH_{imid}), 4.75 (sept., $\text{H}_2\text{C}=\text{C}(\text{CH}_3)_2$), 4.01 (br, 1H, $\text{HB}(\text{C}_6\text{F}_5)_3^-$), 3.66 (s, 2H, NCH_2), 2.22 (s, 6H, $p\text{-CH}_3$), 2.09 (s, 3H, $p\text{-CH}_3$), 1.60 (t, 6H, $\text{H}_2\text{C}=\text{C}(\text{CH}_3)_2$), 1.54 (s, 6H, $o\text{-CH}_3$), 1.53 (s, 36H, $o\text{-}^t\text{Bu}_{\text{Ar}}$), 0.82 (s, 6H, $\text{O}(\text{CH}_3)_2$). $^{13}\text{C}\{^1\text{H}\}$ NMR (75 MHz, C_6D_6 , 293 K) δ = 136.1 (CH_{imid}). ^{11}B NMR (96 MHz, C_6D_6 , 293 K) δ = -24.3 (d, $^1J_{\text{BH}} = 79$ Hz, $\text{HB}(\text{C}_6\text{F}_5)_3$). ^{19}F NMR (282 MHz, C_6D_6 , 293 K) δ = -133.2 (d, 6F, $o\text{-C}_6\text{F}_5$), -162.8 (t, 3F, $m\text{-C}_6\text{F}_5$), -166.1 (t, 6F, $p\text{-C}_6\text{F}_5$).

Synthesis of $\text{Al}(\text{L})(\text{OAr})_2$: compound **7** and compound **7**- ^{13}C

NMR-scale reaction monitoring on the ^{13}C -labelled carbene derivative:

A 0.5 mL C_6D_6 suspension of the ^{13}C -labelled imidazolium aluminate **3**- ^{13}C (20.0 mg, 0.03 mmol 1eq.) was added onto *tris*(pentafluorophenyl)borane (13.1 mg, 0.03 mmol, 1 eq.) at r.t., yielding a colorless solution. This solution was then transferred onto KHMDS (5.1 mg, 0.03 mmol, 1 eq.).

NMR monitoring of the reaction shows the quantitative formation of Al(L)(OAr)_2 .

Isolation procedure:

In a vial of 20 mL, a 8 mL toluene solution of tris(pentafluorophenyl)borane (615 mg, 0.79 mmol, 1.00 eq) was added dropwise onto the imidazolium aluminate zwitterion **3** (402 mg, 0.79 mmol, 1.00 eq). The resulting orange solution was left over stirring for 10 minutes and added onto 157 mg of KHMS (0.79 mmol, 1.00 eq). The resulting mixture was kept over stirring at room temperature for 18 hours yielding an off-white suspension. Volatiles were removed *in vacuo* for 3 hours yielding a white-brown solid. A part of this residue was extracted with 18 mL of diethyl ether (fraction 1, 450 mg) while the other was recovered by filtration and dryness *in vacuo* yielding complex **7** as a white powder (350 mg, 61% of yield). Colorless microcrystals of **7** suitable for XRD studies were grown from a cold ($T = -40^\circ\text{C}$) saturated solution of **7** in THF or diethyl ether. $^1\text{H-NMR}$ (500 MHz, THF-d_8 , 293 K): $\delta = 7.35$ (d, 1H, CH_{imid} , $^3J_{\text{H-H}} = 1.7$ Hz), 7.14 (d, 1H, CH_{imid} , $^3J_{\text{H-H}} = 1.7$ Hz), 6.93 (s, 1H, $m\text{-CH}_{\text{Mes}}$), 6.92 (s, 1H, $m\text{-CH}_{\text{Ar}}$), 6.86 (s, 1H, $m\text{-CH}_{\text{Ar}}$), 6.80 (s, 1H, $m\text{-CH}_{\text{Ar}}$), 6.58 (s, 1H, $m\text{-CH}_{\text{Ar}}$), 6.45 (s, 1H, $m\text{-CH}_{\text{Mes}}$), 3.66 (d, 1H, N-CH-H , $^2J_{\text{H-H}} = 12$ Hz), 3.36 (d, 1H, N-CH-H , $^2J_{\text{H-H}} = 12$ Hz), 2.27 (s, 3H, $p\text{-CH}_3\text{Mes}$), 2.22 (s, 3H, $o\text{-CH}_3\text{Mes}$), 2.18 (s, 3H, $o\text{-CH}_3\text{Mes}$), 2.11 (s, 3H, $p\text{-CH}_3\text{Ar}$), 1.59 (s, 3H, $p\text{-CH}_3\text{Ar}$), 1.42 (s, 9H, $o\text{-}^t\text{Bu}_{\text{Ar}}$), 1.38 (s, 9H, $o\text{-}^t\text{Bu}_{\text{Ar}}$), 1.20 (s, 9H, $o\text{-}^t\text{Bu}_{\text{Ar}}$), 1.07 (s, 9H, $o\text{-}^t\text{Bu}_{\text{Ar}}$), 0.81 (s, 6H, $\text{O}(\text{CH}_3)_2$). $^{13}\text{C}\{^1\text{H}\}\text{-NMR}$ (125 MHz, THF-d_8 , 293 K): $\delta = 157.0$ (C_{Ar}), 155.4 (C_{Ar}), 140.3 (C_{Ar}), 139.4 (C_{Ar}), 139.1 (C_{Ar}), 136.0 (C_{Ar}), 135.8 (CH_{Ar}), 135.1 (C_{Ar}), 130.1 (CH_{Mes}), 129.7 (CH_{Mes}), 127.6 (CH_{Ar}), 125.9 (CH_{Ar}), 125.4 (CH_{Ar}), 124.7 (CH_{imid}), 124.3 (CH_{imid}), 69.8 ($\text{OC}(\text{CH}_3)_2$), 68.0 (THF), 67.7 (THF), 62.3 (NCH_2), 36.2 (C_{tBu}), 35.8 (C_{tBu}), 35.4 (C_{tBu}), 35.2 (C_{tBu}), 34.1 ($\text{CH}_3\text{-C}_{\text{tBu}}$), 32.8 ($\text{CH}_3\text{-C}_{\text{tBu}}$), 32.5 ($\text{CH}_3\text{-C}_{\text{tBu}}$), 30.5 ($\text{CH}_3\text{-C}_{\text{tBu}}$), 29.5 ($\text{OC}(\text{CH}_3)_2$), 28.0 ($\text{OC}(\text{CH}_3)_2$), 26.2 (THF), 25.6 (THF), 21.2 ($o\text{-CH}_3\text{Mes}$), 20.8 ($p\text{-CH}_3\text{Mes}$), 18.7 ($p\text{-CH}_3\text{Ar}$).

Formation of the ^{13}C -labelled $[\text{HL}][\text{Al}(^i\text{Bu})_2(\text{OPh})]$: compound **8- ^{13}C**

A 0.5 mL THF-d_8 solution of phenol (5.3 mg, 0.05 mmol, 1 eq.) was added slowly to a 0.5 mL THF-d_8 solution of the ^{13}C labelled complex **2** (22.7 mg, 0.05 mmol, 1 eq.). The colorless reaction mixture is sealed under argon in a J-Young NMR tube and kept at room temperature for 3 days. $^1\text{H-NMR}$ (300 MHz, THF-d_8 , 293 K) $\delta = 9.65$ (d, 1H, $^1J_{\text{C-H}} = 225.9$ Hz, CH_{imid}), 7.75 (m, 1H, CH_{imid}), 7.51 (m, 1H, CH_{imid}), 7.05 (s, 2H, $m\text{-CH}_{\text{Mes}}$), 6.76 (m, 2H, CH_{Ph}), 6.53 (m, 1H, CH_{Ph}), 6.34 (m, 2H, CH_{Ph}), 4.09 (s, 2H, NCH_2), 2.35 (s, 3H, $p\text{-CH}_3\text{Mes}$), 2.03 (s, 6H, $o\text{-CH}_3\text{Mes}$), 1.80 (m, 2H, $\beta\text{-CH}_{i\text{Bu}}$, $^3J_{\text{H-H}} = 6.6$ Hz), 1.17 (s, 6H, $\text{O}(\text{CH}_3)_2$), 0.84 (d, 12H, $\gamma\text{-CH}_{2-i\text{Bu}}$, $^3J_{\text{H-H}} = 6.6$ Hz), -0.22 (d, 4H, $\alpha\text{-CH}_{2-i\text{Bu}}$, $^3J_{\text{H-H}} = 6.9$ Hz). $^{13}\text{C}\{^1\text{H}\}\text{-NMR}$ (75 MHz, THF-d_8 , 293 K) $\delta = 139.4$ ($^{13}\text{C-H}_{\text{imid}}$).

Reactivity of Al(L)(OAr)_2 with phenol, formation of $[\text{HL}][\text{Al}(\text{OAr})_2(\text{OPh})]$, **9**

A 0.5 mL colorless C₆D₆ solution of the ¹³C-labelled complex **7** (synthesized *in-situ*) was added onto phenol (4.8 mg, 0.05 mmol, 2 eq.). The colorless reaction mixture was sealed under argon in a J-Young NMR tube and heated at 75°C for 1h. ¹³C NMR reaction monitoring (C₆D₆, 75 MHz, 293 K) showed the clean formation of an alkoxy-imidazolium zwitterion species **9** with the diagnostic disappearance of the carbene resonance at δ = 167.7 ppm from **7** and the appearance of a characteristic imidazolium resonance at δ = 135.8 ppm (Fig. S14-d) for the ¹³C-labelled carbon from the C₃N₂ heterocycle in **9**. A characteristic imidazolium resonance for **9** is also observed in the ¹H NMR spectrum δ = 7.31 (d, 1H, ¹J_{C-H} = 222.6 Hz, CH_{imid}). Data for **7**: ¹H NMR (300 MHz, C₆D₆, 293 K) δ = 7.31 (d, 1H, ¹J_{C-H} = 222.6 Hz, CH_{imid}), 7.12 (s, 4H, *m*-CH_{Ar}), 7.11-7.00 (m, 5H, CH_{Ph}), 6.54 (s, 2H, *m*-CH_{Mes}), 6.17 (m, 1H, CH_{imid}), 5.52 (m, 1H, CH_{imid}), 3.49 (s, 2H, NCH₂), 2.21 (s, 6H, *p*-CH_{3Ar}), 2.05 (s, 3H, *p*-CH_{3Mes}), 1.71 (s, 36H, *o*-^tBu_{Ar}), 1.44 (s, 6H, *o*-CH_{3Mes}), 1.04 (s, 6H, O(CH₃)₂). ¹³C{¹H} NMR (75 MHz, C₆D₆, 293 K) δ = 135.8 (CH_{imid}).

Formation of the heterobimetallic [Cu(L)₂Al(O₃N)(^tBu)] complex: compound **10**

To a 10 mL orange toluene solution of Al(L)(^tBu)₂ **2** (268.0 mg, 0.67 mmol, 1.00 eq.), was added a 5 mL toluene suspension of [Cu(PPh₃)₂NO₃] (437.2 mg, 0.67 mmol, 1.00 eq.). The resulting brownish mixture was stirred at room temperature for 2 hours and then heated at 100°C for 36 hours yielding an off-brown suspension in a yellow solution. The reactional medium was filtered over vacuum to remove the brown solid. Volatiles of the yellow filtrate were removed *in vacuo* and dissolved in the minimum of toluene (2-3 mL). Afterwards, 12 mL of pentane was added dropwise onto this yellow-orange toluene solution and kept for 9 days yielding suitable colorless crystals (a few mg) at the bottom of the vial.

8.3.2 CHAPTER 3 Development Of Molecular Aluminum/Iridium Heterobimetallic Species Using An Alkane Elimination Approach

Isolation of intermediate [Cp*IrH₃Al(^tBu)₂]₂, compound **11**

A 8 mL colorless pentane solution of IrCp*H₄ (199.0 mg, 0.60 mmol, 1.0 eq.) was added dropwise to a 6 mL colorless pentane solution of triisobutylaluminum (152 μL, 119.0 mg, 0.60 mmol, 1.0 eq.). Within minutes, the solution turned to a yellowish color. The solution was stirred for 2 hours at

room temperature. Then, the volatiles were removed under vacuum yielding ca. 250 mg of a crude yellow powder containing a mixture of species. This solid was dissolved in the minimum amount of pentane (ca. 2 mL), filtered, and stored at -40°C for 3 days yielding 50 mg of block-shaped yellow crystals. One of these crystals was suitable for analysis and is relating to the species $[\text{Cp}^*\text{IrH}_3\text{Al}(\text{iBu})_2]_2$, **11**. ^1H NMR (300 MHz, C_6D_6 , 293 K) δ 2.21 (m, 4H, CH^iBu), 1.94 (s, 30H, CH_3Cp^*), 1.27 (d, 24H, $\text{CH}_3\text{-}^i\text{Bu}$), 0.55 (d, 8H, $\text{CH}_2\text{-}^i\text{Bu}$), -16.54 (s, 6H, Ir-H). Elemental analysis could not be performed on this unstable compound.

Synthesis of $[\text{Cp}^*\text{IrH}_2\text{Al}(\text{iBu})]_2$, compound **12**

A 20 mL colorless pentane solution of IrCp^*H_4 (979.0 mg, 2.95 mmol, 1.0 eq.) was added dropwise to a 30 mL colorless pentane solution of triisobutylaluminum (585.0 mg, 2.95 mmol, 1.0 eq.). Within minutes, the solution turned to a yellowish color. The solution was stirred at room temperature for 2 days. Then, the volatiles were removed under vacuum yielding a yellow powder. The solid was dissolved in the minimum amount of pentane (ca. 6 mL), filtered, and stored at -40°C for 1 day yielding plate-shaped yellow crystals of **12** that were recovered by filtration and dried under vacuum (1.02 g, 83% yield). ^1H NMR (500 MHz, C_6D_6 , 293 K) δ 2.45 (m, 2H, CH_{iBu}), 2.07 (s, 30H, CH_3Cp^*), 1.35 (d, $^3J_{\text{HH}} = 6.6$ Hz, 12H, $\text{CH}_3\text{-iBu}$), 1.01 (d, $^3J_{\text{HH}} = 7.2$ Hz, 4H, $\text{CH}_2\text{-iBu}$), -16.68 (s, 4H, H-Ir). $^{13}\text{C}\{^1\text{H}\}$ NMR (125 MHz, C_6D_6 , 293 K) δ 93.54 (C_{Cp^*}), 28.17 ($\text{CH}_3\text{-iBu}$), 27.70 ($\text{CH}_2\text{-iBu}$), 27.00 (CH_{iBu}), 11.47 ($\text{CH}_3\text{-Cp}^*$). DRIFTS (293 K, cm^{-1}) σ 2977 (s), 2942 (s, $\nu\text{C-H}$), 2910 (s, $\nu\text{C-H}$), 2855 (s, $\nu\text{C-H}$), 1990 (s, $\nu\text{Ir-H}$), 1455 (s). Elemental analysis calcd (%) for $\text{C}_{28}\text{H}_{52}\text{Al}_2\text{Ir}_2$: C 40.66, H 6.34. Found: C 40.79, H 6.36.

Synthesis of $[(\text{Cp}^*\text{IrH}_3)_2\text{Al}(\text{iBu})]$, compound **13**

From triisobutylaluminum. A 6 mL pentane solution of IrCp^*H_4 (501.2 mg, 1.51 mmol, 2.0 eq.) was added dropwise (within 10 minutes) into a 4 mL colorless pentane solution of triisobutylaluminum (150.3 mg, 0.76 mmol, 1.0 eq.). The resulting light yellowish solution was stirred at room temperature for 17 hours. This procedure triggered precipitation of an off-yellow solid that was recovered by filtration (ca. 130 mg). Pentane volatiles of the filtrate were removed *in vacuo* yielding 390 mg of **3** as a white/yellow powder (69 % yield). Single yellow needle crystals suitable for XRD analysis were grown by slow evaporation of a cold ($T=-40^{\circ}\text{C}$) and saturated pentane solution of **13**.

From compound **12** (NMR-scale synthesis). A 0.4 mL C_6D_6 solution of IrCp^*H_4 (11.8 mg, 35.6 μmol , 2.0 eq.) was added into a 0.3 mL C_6D_6 solution of complex **12** (14.5 mg, 17.5 μmol , 1.0 eq.). The

resulting yellow solution was sealed under argon in a 2.5 mL J-Young NMR tube and kept at room temperature for 24 hours. NMR analysis of the tube shows a complete consumption of **2** with evolution of free isobutane gas along with the formation of product **13**. ^1H NMR (400 MHz, C_6D_6 , 293 K) δ 2.49 (m, 1H, CH_{iBu}), 2.03 (s, 30H, CH_{3Cp^*}), 1.29 (d, $^3J_{\text{HH}} = 6.4$ Hz, 6H, $\text{CH}_{3\text{-iBu}}$), 0.56 (d, $^3J_{\text{HH}} = 7.0$ Hz, 2H, $\text{CH}_{2\text{-iBu}}$), -16.64 (s, 6H, H-Ir). $^{13}\text{C}\{^1\text{H}\}$ NMR (125 MHz, C_6D_6 , 293 K) δ 93.88 (C_{Cp^*}), 42.51 ($\text{CH}_{2\text{-iBu}}$), 28.24 ($\text{CH}_{3\text{-iBu}}$), 27.56 (CH_{iBu}), 11.28 ($\text{CH}_{3\text{-Cp}^*}$). DRIFTS (293 K, cm^{-1}) σ 2977 (s), 2955 (s, $\nu\text{C-H}$), 2910 (s, $\nu\text{C-H}$), 2857 (s, $\nu\text{C-H}$), 2151 (s, $\nu\text{Ir-H}$), 2014 (s, $\nu\text{Ir-H}$), 1456 (s), 1386 (s), 1033 (s). Elemental analysis calcd (%) for $\text{C}_{28}\text{H}_{52}\text{Al}_2\text{Ir}_2$: C 38.69, H 6.09. Found: C 38.63, H 6.12.

Synthesis of $[(\text{Cp}^*\text{IrH}_3)_3\text{Al}]$, compound **14**

From triisobutylaluminum. A 7 mL light yellow toluene solution of IrCp^*H_4 (502.6 mg, 1.52 mmol, 3.0 eq.) was added dropwise into a 4 mL colorless pentane solution of triisobutylaluminum (99.1 mg, 0.50 mmol, 1.0 eq.). The resulting light yellowish solution was sealed in a 80 mL-Schlenk bomb and stirred at $T=50^\circ\text{C}$ for 1 week yielding an intense orange solution. Toluene and pentane volatiles were removed *in vacuo* yielding a brown-white solid. This powder was dissolved in the minimum of pentane (ca. 6 mL), filtered, and stored at $T=-40^\circ\text{C}$ for 1 day yielding single colorless block crystals (269.5 mg, 53% yield). The resulting filtrate was concentrated by a factor 2 and put at $T=-40^\circ\text{C}$ for 2 weeks yielding a new batch of **14** as crystals (80.0 mg, 16% yield).

From compound **13**. A 7 mL pentane/toluene (7/2) solution of IrCp^*H_4 (176 mg, 0.53 mmol, 1.2 eq.) was added dropwise into a 4 mL yellow pentane suspension of complex **13** (346 mg, 0.46 mmol, 1.0 eq.). The resulting solution was stirred at $T=65^\circ\text{C}$ for 2 days producing a deep orange-brown solution. Volatiles were removed over vacuum yielding a white-brown powder, which was dissolved in the minimum of pentane (ca. 5.5 mL), filtered, and put at $T=-40^\circ\text{C}$ for 18 hours yielding **14** as yellow/colorless crystals (320 mg, 68% yield). ^1H NMR (500 MHz, C_6D_6 , 293 K) δ 2.11 (s, 45H, CH_{3Cp^*}), -16.38 (s, 9H, H-Ir). $^{13}\text{C}\{^1\text{H}\}$ NMR (125 MHz, C_6D_6 , 293 K) δ 93.62 (C_{Cp^*}), 11.26 ($\text{CH}_{3\text{-Cp}^*}$). DRIFTS (293 K, cm^{-1}) σ 2980 (s, $\nu\text{C-H}$), 2957 (s, $\nu\text{C-H}$), 2912 (s, $\nu\text{C-H}$), 2158 (s, $\nu\text{Ir-H}$), 2015 (s, $\nu\text{Ir-H}$), 1476 (m), 1456 (m), 1385 (m).). Elemental analysis calcd (%) for $\text{C}_{45}\text{H}_{54}\text{AlIr}_3$: C 35.38, H 5.34. Found: C 35.45, H 5.36.

Synthesis of $[\text{Cp}^*\text{IrH}_3\text{Al}(\text{iBu})(\text{OAr})]$, compound **15**

A 4 mL pentane solution of IrCp^*H_4 (282.5 mg, 0.85 mmol, 1.0 eq.) was added dropwise to a 8 mL colorless pentane solution of (2,6-di-tertbutyl-4-methylphenoxy)diisobutylaluminum, $\text{Al}(\text{iBu})_2(\text{OAr})$ (310.0 mg, 0.86 mmol, 1.0 eq.). The resulting solution was stirred at room

temperature for 20 hours. Then, the volatiles were removed under vacuum yielding a white solid (550 mg of crude solid). This powder was dissolved in the minimum of pentane (*ca.* 7 mL), filtered and stored at -40°C for 16 hours yielding compound **15** as white microcrystals (390.0 mg, 72% yield). ¹H NMR (500 MHz, C₆D₆, 293 K) δ 7.18 (s, 2H, CH_{Ar}), 2.32 (s, 3H, CH₃-Ar), 2.15 (m, 1H, CH_{iBu}), 1.96 (s, 15H, CH₃Cp*), 1.65 (s, 18H, CH₃-tBu), 1.08 (d, ³J_{HH} = 6.4 Hz, 6H, CH₃-iBu), 0.31 (d, ³J_{HH} = 7.1 Hz, 2H, CH₂-iBu), -16.80 (s, 3H, H-Ir). ¹³C{¹H} NMR (125 MHz, C₆D₆, 293 K) δ 155.46 (C_{Ar}), 138.18 (C_{Ar}), 126.41 (C_{Ar}), 126.10 (CH_{Ar}), 94.64, (C_{Cp*}), 35.00 (ArC(CH₃)₃), 32.88 (CH₂-iBu) 32.18 (ArC(CH₃)₃), 28.04 (CH₃-iBu), 25.93 (CH_{iBu}), 21.59 (ArCH₃), 11.04 (CH₃-Cp*). DRIFTS (293 K, cm⁻¹) σ 2946 (s, νC-H), 2916 (s, νC-H), 2877 (s, νC-H), 2857 (s, νC-H), 2144 (s, νIr-H), 1973 (s, νIr-H), 1464 (s), 1425 (s), 1297 (s), 1286 (s), 1262 (s). Elemental analysis calcd (%) for C₂₉H₅₀AlIrO: C 54.95, H 7.95. Found: C 54.96, H 8.00.

8.3.3 CHAPTER 4 Reactivity Studies Of Al/Ir Heterobimetallic Complexes

Synthesis of [IrCp*H₂(Py)Al(ⁱBu)]₂, compound **16**

A 0.5 mL colorless pentane solution of pyridine (12.6 μL, 0.17 mmol, 1.1 eq.) was added dropwise into a yellow pentane solution of **12** (130.0 mg, 0.16 mmol, 1.0 eq.). In the course of the addition, the solution turned to a blood red mixture that was further stirred at room temperature for 20 minutes. The volatiles were removed under vacuum yielding 130 mg of a red solid. This powder was dissolved in the minimum amount of toluene (*ca.* 1.0 mL), filtered, and stored at -40°C for 18 hours yielding **16** as dark orange needle crystals (60 mg, 42% isolated yield). ¹H NMR (500 MHz, C₆D₆, 293 K) δ 8.72 (d, 2H, CH_{ortho-Py}), 6.81 (t, 1H, CH_{para-Py}), 6.55 (t, 2H, CH_{meta-Py}), 2.55 (m, 2H, CH_{iBu}), 1.92 (s, 30H, CH₃Cp*), 1.47 (d, ³J_{HH} = 6.4 Hz, 12H, CH₃-iBu), 0.93 (d, ³J_{HH} = 6.7 Hz, 4H, CH₂-iBu), -16.89 (s, 4H, H-Ir). ¹³C{¹H} NMR (125 MHz, C₆D₆, 293 K) δ 148.27 (CH_{ortho-Py}), 137.69 (CH_{para-Py}), 124.02 (CH_{meta-Py}), 92.16 (C_{Cp*}), 28.68 (CH₃-iBu), 27.91 (CH₂-iBu), 27.15 (CH_{iBu}), 11.12 (CH₃-Cp*). DRIFTS (293 K, cm⁻¹) σ 2942 (s, νC-H), 2910 (s, νC-H), 2856 (s, νC-H), 2110 (m, νIr-H), 2005 (m, νIr-H), 1607 (m), 1484 (m), 1439 (m), 1377 (m), 1158 (m). Elemental analysis calcd (%) for C₃₃H₅₇Al₂Ir₂N: C 43.74, H 6.34, N 1.55. Found: C 43.16, H 6.34, N 1.52.

Synthesis of [Cp*IrH₃Al(ⁱBu)(OAr)(Py)], compound **17**.

A 0.5 mL colorless pentane solution of pyridine (15.6 mg, 0.20 mmol, 1.0 eq.) was added dropwise into a 8.5 mL light yellow pentane solution of **15** (123.5 mg, 0.20 mmol, 1.0 eq.). The resulting pale

yellow solution was stirred at room temperature for 30 minutes. Then, the volatiles were removed under vacuum yielding a crude off-white oily material. This crude material was dissolved in the minimum of pentane (ca. 1.5 mL), filtered, and stored at -40°C for 16 hours yielding **17** as colorless needle crystals (94 mg, 68% yield). Colorless block single crystals of **17** suitable for XRD studies were grown by slow recrystallization of **17** in an octane:toluene (7:1) mixture at -40°C within 48 hours. ¹H NMR (500 MHz, C₆D₆, 293 K) δ 8.89 (d, 2H, CH_{ortho-Py}), 7.24 (s, 2H, CH_{Ar}), 6.73 (t, 1H, CH_{para-Py}), 6.43 (t, 2H, CH_{meta-Py}), 2.37 (s, 3H, CH_{3-Ar}), 2.03 (s, 15H, CH_{3-Cp*}), 1.86 (m, 1H, CH_{iBu}), 1.61 (s, 18H, CH_{3-tBu}), 1.06 (bs, 6H, CH_{3-iBu}), 0.74 (d, 2H, CH_{2-iBu}, ³J_{HH} = 6.9 Hz), -17.26 (s, 3H, H-Ir). ¹³C{¹H} NMR (125 MHz, C₆D₆, 293 K) δ 157.02 (C_{Ar}), 149.63 (CH_{ortho-Py}), 139.15 (CH_{para-Py}), 126.31 (CH_{Ar}), 124.61 (C_{Ar}), 124.04 (CH_{meta-Py}), 93.50 (C_{Cp*}), 35.30 (C_{tBu}), 32.61 (CH_{3-tBu}), 31.61 (CH_{2-iBu}), 28.35 (CH_{3-iBu}), 26.58 (CH_{iBu}), 21.42 (CH_{3-Ar}), 11.29 (CH_{3-Cp*}). DRIFTS (293 K, cm⁻¹) σ 2962 (s, νC-H), 2912 (s, νC-H), 2860 (s, νC-H), 2128 (s, νIr-H), 2109 (s, νIr-H), 1611 (m), 1449 (m), 1265 (s). Elemental analysis calcd (%) for C₃₅H₅₉AlIrNO: C 57.66, H 8.16, N 1.92. Found: C 57.11, H 7.78, N 1.99.

Synthesis of [(IrCp*(H)₃)₃Al(DMAP)], adduct **18**

A 1 mL colorless toluene solution of 4-dimethylaminopyridine (11.9 mg, 0.097 mmol, 1.0 eq.) was added dropwise into a 2 mL colorless pentane solution of cluster **14** (100.3 mg, 0.098 mmol, 1.0 eq.). The resulting solution was stirred at room temperature for 1 hour. Then, volatiles were removed in vacuo yielding a white solid (c.a. 110 mg). This was dissolved in a saturated mixture of pentane/toluene (15/1 mL), filtered, and put at T=-40°C for 1 day yielding a first batch of colorless block-shaped crystals (20 mg). The supernatant from this batch was again put at T=-40°C for 3 days yielding a second batch of [(IrCp*(H)₃)₃Al(DMAP)], product **18**, as colourless block-shaped crystals (80 mg). In total, 100 mg (90 % yield) of pure adduct **18** was obtained. ¹H NMR (500 MHz, C₆D₆, 293 K) δ 8.64 (d, ³J_{H-H}=5.0 Hz, 2H, CH_{ortho-DMAP}), 6.05 (d, ³J_{H-H}=5.0 Hz, 2H, CH_{meta-DMAP}), 2.15 (s, 6H, CH_{3-N}), 2.14 (s, 45H, CH_{3-Cp*}), -16.47 (s, 9H, H-Ir). ¹³C{¹H} NMR (125 MHz, C₆D₆, 293 K) δ 150.52 (CH_{ortho-DMAP}), 106.28 (CH_{meta-DMAP}), 93.25 (C_{Cp*}), 38.28 (CH_{3-N}), 11.20 (CH_{3-Cp*}). DRIFTS (293 K, cm⁻¹) σ 3080 (m, νC-H_{alkene}), 2957 (s, νC-H), 2907 (s, νC-H), 2149 (s, νIr-H), 2111 (s, νIr-H), 1626 (m), 1538 (m), 1232 (s, C-N_{aromatic}).

Synthesis of [Ir₂(Cp*)₂(H₂)₂Al₂(KBn)(ⁱBu)₂], compound **19**

A 4 mL red THF solution of benzyl potassium (27.8 mg, 0.21 mmol, 1.0 eq.) was added dropwise to a 6 mL yellow THF solution of **12** (175.5 mg, 0.21 mmol, 1.0 eq.). The resulting yellow solution was stirred for 18 hours at room temperature. Then, the volatiles were removed under vacuum

yielding a yellow powder. This solid was dissolved in the minimum of diethyl ether (ca. 2 mL), filtered and stored at 40°C for 3 hours yielding **19** as yellow block crystals (120 mg, 52% yield). ¹H NMR (500 MHz, THF-*d*₈, 293 K) δ 7.00 (d, 4H, CH_{Ar}), 6.65 (m, 1H, CH_{Ar}), 3.39 (q, ³J_{HH} = 6.9 Hz, CH_{2-Et2O}), 2.13 (s, 2H, CH_{2-benzyl}), 2.11 (s, 30H, CH_{3Cp*}), 2.04 (m, 2H, CH_{iBu}), 1.12 (t, ³J_{HH} = 7.0 Hz CH_{3-Et2O}), 0.98 (d, ³J_{HH} = 6.4 Hz, 12H, CH_{3-iBu}), 0.57 (d, 4H, CH_{2-iBu}), -18.35 (s, 4H, H-Ir). ¹³C{¹H} NMR (125 MHz, THF-*d*₈, 293 K) δ 156.00 (C_{Ar}), 127.71 (CH_{Ar}), 127.13 (CH_{Ar}), 117.77 (CH_{Ar}), 91.65, (C_{Cp*}), 66.14 (CH_{2-Et2O}), 28.83 (CH_{iBu}), 28.17 (CH_{2-iBu}), 26.67 (CH_{3-iBu}), 25.62 (CH_{2-benzene}), 15.50 (CH_{3-Et2O}), 11.77 (CH_{3-Cp*}). DRIFTS (293 K, cm⁻¹) σ 3062 (w, νC-H), 2971 (s, νC-H), 2941 (s, νC-H), 2913 (s, νC-H), 2848 (s, νC-H), 2140 (m, νIr-H), 2001 (m, νIr-H), 1965 (m, νIr-H), 1593 (m), 1483 (m), 1453 (m), 1379 (m), 1105 (m). Elemental analysis calcd (%) for C₄₃H₇₉Al₂Ir₂KO₂: C 46.71, H 7.20. Found: C 46.27, H 7.08.

Synthesis of [IrCp*H₃Ag], compound **20**; and [((Ir(Cp*)(H)(μ-H₂))₂Al(OTf)(THF))], compound **21**

A 1.5 mL colorless THF solution of silver triflate (50.2 mg, 0.195 mmol, 1.0 eq.) was added dropwise into a 1.5 mL yellow THF solution of compound **14** (200.4 mg, 0.197 mmol, 1.0 eq.). In the course of the addition, the solution turned deep orange and some off-white solids precipitated. The resulting mixture was stirred at room temperature for one hour leading to the precipitation of further whitish materials that were filtered-off using a 4-micro-sintered funnel, washed with 1.5 mL of THF, and dried in *vacuo* for 2 hours. The resulting white powder relates to product **20** (82 mg, 93 %). Volatiles of the orange filtrate were removed over vacuum yielding product **21** as an orange powder (159 mg, 90% yield). Crystals of **20** were obtained by following the same procedure but without any stirring for 16 hours, which afforded growing of colorless microcrystals suitable for XRD studies. Single colorless plate-shaped crystals of **21** (suitable for XRD studies) were grown in a cold (T=-40°C) and saturated solution of diethyl ether For complex **20**. ¹H NMR (400 MHz, pyridine-*d*₅, 293 K) δ 2.31 (s, 60H, CH_{3Cp*}), -14.76 (s, 12H, H-Ir). ¹³C{¹H} NMR (100 MHz, pyridine-*d*₅, 293 K) δ 91.55 (C_{Cp*}), 13.01 (CH_{3-Cp*}). DRIFTS (293 K, cm⁻¹) σ 2980 (s, νC-H), 2945 (s, νC-H), 2895 (s, νC-H), 1917 (s, νIr-H), 1467 (m), 1375 (m), 866 (s).). Elemental analysis calcd (%) for C₁₀H₁₈AgIr: C 27.40, H 4.14, Ir 43.8. Found: C 27.49, H 4.15, Ir 42.7.

For complex **21**. ¹H NMR (400 MHz, THF-*d*₈, 293 K) δ 2.12 (s, 30H, CH_{3Cp*}), -17.41 (s, 6H, H-Ir). ¹⁹F NMR (282 MHz, THF-*d*₈, 293 K) δ -80.65 (s). ¹³C{¹H} NMR (100 MHz, THF-*d*₈, 293 K) δ 94.92 (C_{Cp*}), 11.05 (CH_{3-Cp*}). DRIFTS (293 K, cm⁻¹) σ 2986 (s, νC-H), 2962 (s, νC-H), 2914 (s, νC-H), 2152 (s, νIr-H), 2070 (s, νIr-H), 1347 (s, νS=O), 1238 (m), 1201 (s, νC-F), 1032 (m).). Elemental analysis calcd (%) for C₂₅H₄₄Allr₂F₃O₄S: C 33.03, H 4.88. Found: C 32.92, H 4.81.

Reaction of **17** with B(C₆F₅)₃, yielding complex **15** and (Py)B(C₆F₅)₃

A 0.4 mL colorless C₆D₆ solution of tris(pentafluorophenyl)borane (8.2 mg, 16.0 μmol, 1.0 eq.) was added into a 0.2 mL C₆D₆ solution of complex **17** (11.7 mg, 16.0 μmol, 1.0 eq.). The resulting light yellow solution was sealed under argon in a J-Young NMR tube and was kept at room temperature for 24 hours. Analysis of the resulting reaction mixture by ¹H-NMR and ¹⁹F-NMR spectroscopy showed a quantitative formation of complex **15** together with the (Py)B(C₆F₅)₃ adduct. The NMR data for (Py)B(C₆F₅)₃ is in agreement with the previously reported data:^[288] ¹H NMR (300 MHz, C₆D₆, 293 K) δ 7.94 (d, ³J_{HH} = 5.6 Hz, 2H, CH_{ortho-Py}), 6.57 (m, 1H, CH_{para-Py}), 6.23 (t, ³J_{HH} = 7.2 Hz, 2H, CH_{meta-Py}). ¹⁹F NMR (282 MHz, C₆D₆, 293 K) δ -131.5 (d, ³J_{FF} = 20 Hz, 6F, CF_{ortho}), -155.4 (t, ³J_{FF} = 21 Hz, 3F, CF_{para}), -162.7 (m, 6F, CF_{meta}).

Synthesis of [Ir₂(Cp*)₂(H₂)₂Al₂(THF)₃(^tBu)] [HB(C₆F₅)₃], compound **22**

Quantitative NMR-scale reaction. A 0.5 mL colorless THF-d₈ colorless solution of B(C₆F₅)₃ (13.2 mg, 25.8 μmol, 1.0 eq.) and durene (12.2 mg, 90.9 μmol, 3.5 eq.) – used as standard – were added into a 2.0 mL yellow THF-d₈ solution of species **12** (21.3 mg, 25.8 μmol, 1.0 eq.). The resulting solution was sealed under argon in a 2.5 mL J-Young NMR tube. Then, the tube was left at room temperature for 3 days and heated at T=50°C for 5 hours leading to the disappearance of **12** and the formation of complex **22** and evolution of isobutene gas. Regularly, the tube was analyzed by ¹H-NMR and ¹⁹F-NMR to assess the course of the reaction. The amount of species **22** and released isobutene were determined when the reaction went to completion. Amount of substance calc at the end of reaction: 21.4 μmol (0.83 eq.) for isobutene and 24.6 μmol (0.95 eq.) for product **22**.

Large-scales reaction. A 4 mL colorless THF solution of B(C₆F₅)₃ (93.4 mg, 0.18 mmol, 1.0 eq.) was added dropwise to a 6 mL yellow THF solution of **12** (150.2 mg, 0.18 mmol, 1.0 eq.). The resulting yellow solution was stirred at room temperature for 19 hours. The reaction mixture was then heated at 50°C for 5 hours. Then, the volatiles were removed under vacuum, yielding a light yellow powder. This solid was dissolved in 2 mL of pentane, 250 μL of THF was added to the solution which was filtered and stored at -40°C for 14 hours. This procedure yielded compound **22** as plate-shaped yellow crystals (110 mg, 40% yield). ¹H NMR (500 MHz, THF-d₈, 293 K) δ 3.62 (t, 8H, CH_{2-THF}), 2.03 (s, 30H, CH_{3-Cp*}), 1.93 (m, 1H, CH_{iBu}), 1.77 (m, 8H, CH_{2-THF}), 1.04 (d, ³J_{HH} = 6.6 Hz, 6H, CH_{3-iBu}), 0.51 (d, ³J_{HH} = 6.6 Hz, 2H, CH_{2-iBu}), -16.92 (s, 4H, H-Ir). ¹³C{¹H} NMR (125 MHz, THF-d₈, 293 K) δ 93.00, (C_{Cp*}), 68.03 (C_{THF}), 28.08 (CH_{2-iBu}), 27.13 (CH_{3-iBu}), 26.18 (CH_{iBu}), 25.61 (C_{THF}), 11.33 (CH_{3-Cp*}). ¹¹B-NMR (160 MHz, THF-d₈, RT) δ -23.60 (d, ¹J_{BH} = 94 Hz). DRIFTS (293 K, cm⁻¹) σ 2956 (s, νC-H), 2918 (s, νC-H), 2852 (s, νC-H), 2364 (m, νB-H), 2137 (m, νIr-H), 1640 (m), 1509 (s), 1462 (s). Elemental analysis calcd (%) for C₅₇H₇₃Al₂BF₁₅Ir₂O₃: C 44.45, H 4.78. Found: C 44.31, H 4.89.

Reaction of **17** with CO₂, yielding [(ⁱBu)(OAr)Al(Py)]₂(μ-O), compound **23**.

Complex **17** (174 mg, 0.24 mmol, 1.0 eq.) was dissolved in 20 mL of pentane. The resulting solution was charged in one compartment of a two-sided Schlenk reaction vessel featuring two isolated chambers of 74 cm³. This double-Schlenk vessel was sealed under argon, the pentane solution was frozen in liquid nitrogen and then the whole system was evacuated (10⁻⁴ mbars). The two compartments were isolated from each-other using a J-Young high vacuum PTFE valve. Afterwards, dry CO₂ (800 mbars, 2.43 mmol, 10.2 eq.) was introduced in the first compartment. Then, the J-Young valve was opened for 15 minutes to let CO₂ diffuse at room temperature from the first compartment into the pentane solution of **17** located in the second compartment and the system was left in this configuration for five days without any stirring. This procedure triggered the nucleation of **23** as colorless block-shaped crystals in a yellow solution. The yellow filtrate was removed from the flask and analyzed by NMR spectroscopy which showed the equimolar formation of Cp*IrH₄ and Cp*Ir(CO)H₂. The colorless crystals were extracted with 6.0 mL of toluene. Then, volatiles were removed under vacuum for 3 hours yielding complex **23**·C₇H₈ as a white powder (92 mg, 99% yield). In solution, two rotamers of complex **23** are in equilibrium at 293K in a 7:93 ratio. ¹H NMR (500 MHz, C₆D₆, 293 K) δ rotamer #1 8.76 (m, 4H, CH_{ortho-Py}), 7.24 (s, 4H, CH_{Ar}), 6.81 (m, 2H, CH_{para-Py}), 6.51 (m, 4H, CH_{meta-Py}), 2.40 (s, 6H, CH_{3-Ar}), 1.64 (m, 2H, CH_{iBu}), 1.51 (s, 36H, CH_{3-tBu}), 0.97 (d, 6H, CH_{3-iBu}), 0.82 (d, 6H, CH_{3-iBu}), 0.69 (d, ³J_{HH} = 5.8 Hz, 1H, CH_{2-iBu}), 0.66 (d, ³J_{HH} = 5.6 Hz, 1H, CH_{2-iBu}), 0.60 (d, 1H, CH_{2-iBu}), 0.58 (d, 1H, CH_{2-iBu}); rotamer #2 8.61 (m, 4H, CH_{ortho-Py}), 7.24 (s, 4H, CH_{Ar}), 6.77 (m, 2H, CH_{para-Py}), 6.36 (m, 4H, CH_{meta-Py}), 2.44 (s, 6H, CH_{3-Ar}), 1.88 (m, 2H, CH_{iBu}), 1.42 (s, 36H, CH_{3-tBu}), 1.34 (d, ³J_{HH} = 6.4 Hz, 6H, CH_{3-iBu}), 0.99 (d, ³J_{HH} = 6.4 Hz, 6H, CH_{3-iBu}), 0.89 (d, ³J_{HH} = 6.6 Hz, 1H, CH_{2-iBu}), 0.86 (d, ³J_{HH} = 6.4 Hz, 1H, CH_{2-iBu}), 0.61 (d, ³J_{HH} = 6.7 Hz, 1H, CH_{2-iBu}), 0.59 (d, ³J_{HH} = 6.6 Hz, 1H, CH_{2-iBu}). ¹³C{¹H} NMR (125 MHz, C₆D₆, 293 K) δ rotamer #1 156.40 (C_{Ar}), 149.38 (CH_{ortho-Py}), 140.48 (CH_{para-Py}), 139.12 (C_{Ar}), 126.01 (CH_{Ar}), 124.57 (C_{Ar}), 124.46 (CH_{meta-Py}), 34.96 (C_{tBu}), 31.61 (CH_{3-tBu}), 29.61 (CH_{3-iBu}), 28.68 (CH_{3-iBu}), 26.26 (CH_{iBu}), 24.40 (CH_{2-iBu}), 21.48 (CH_{3-Ar}). DRIFTS (293 K, cm⁻¹) σ 3101 (m, νC-H), 3022 (m, νC-H), 2948 (s, νC-H), 2913 (s, νC-H), 2855 (s, νC-H), 1616 (m), 1451 (s), 1423 (s), 1271 (s). Elemental analysis calcd (%) for C₄₈H₇₄Al₂N₂O₃·C₇H₈: C 75.65, H 9.47, N 3.21. Found: C 75.42, H 9.24, N 3.24.

Synthesis of {Al(OAr)(ⁱBu)[κ²-(N,O)AdNC(O)NHAd]}, compound **24**

A 3 mL colorless toluene solution of 1-adamantylisocyanate (82.5 mg, 0.47 mmol, 2.0 eq.) was added dropwise into a 8 mL colorless pentane solution of **17** (167 mg, 0.23 mmol, 1.0 eq.). The

reaction mixture was stirred at room temperature for 24 hours yielding a brownish solution. Volatiles were removed *in vacuo* yielding a brownish solid containing an equimolar mixture of Cp*IrH₂(CO) and complex **24** (ca. 240 mg). This solid was dissolved in the minimum of pentane (ca. 8 mL), filtered, and stored at -40°C for 3 weeks yielding **24** as colorless block crystals suitable for XRD analysis (110 mg, 76% yield). ¹H NMR (500 MHz, C₆D₆, 293 K) δ 7.27 (s, 2H, CH_{Ar}), 4.40 (s, 1H, NH), 2.37 (s, 3H, CH₃-Ar), 2.19 (m, 1H, CH_{iBu}), 1.88-1.98 (m, 18H, CH_{Ad} & CH_{2-Ad}), 1.72 (s, 18H, CH_{3-tBu}), 1.45-1.55 (m, 12H, CH_{2-Ad}), 1.22 (dd, 6H, CH_{3-iBu}), 0.59 (m, 2H, CH_{2-iBu}). ¹³C{¹H} NMR (125 MHz, C₆D₆, 293 K) δ 163.96 (C_{ureate}) 154.47 (C_{Ar}), 138.59 (C_{Ar}), 126.13 (CH_{Ar}), 126.08 (C_{Ar}), 53.11 (C_{Ad}), 50.27 (C_{Ad}), 43.54 (CH_{2-Ad}), 42.82 (CH_{2-Ad}), 36.62 (CH_{2-Ad}), 36.37 (CH_{2-Ad}), 35.28 (C_{tBu}), 31.71 (CH_{3-tBu}), 29.94 (CH_{Ad}), 29.89 (CH_{Ad}), 28.45 (CH_{3-iBu}), 28.02 (CH_{3-iBu}), 26.66 (CH_{iBu}), 21.81 (CH_{2-iBu}), 21.58 (CH_{3-Ar}). DRIFTS (293 K, cm⁻¹) σ 3448 (m, νN-H), 2944 (s, νC-H), 2911 (s, νC-H), 2847 (s, νC-H), 1575 (s), 1451 (s), 1490 (m), 1429 (m), 1278 (m). Elemental analysis calcd (%) for C₄₀H₆₃AlN₂O₂: C 76.15, H 10.07, N 4.44. Found: C 76.02, H 10.12, N 4.39.

Synthesis of [Ir(Cp)*H₂(μ-CyNC(H)NCy)Al(ⁱBu)(OAr)], compound **25**

NMR-scale reaction from complex **15**. A 0.3 mL colorless C₆D₆ solution of dicyclohexylcarbodiimide (6.2 mg, 30.0 μmol, 1.0 eq.) was added into a 0.3 mL C₆D₆ solution of complex **15** (18.7 mg, 29.5 μmol, 1.0 eq.). The resulting light yellowish solution was sealed in a J-Young NMR tube and left at room temperature for 3 hours. Analysis of the solution revealed the quantitative formation of complex **25**.

From complex **17**. A 3 mL colorless pentane/toluene (1/1) solution of N,N'-dicyclohexylcarbodiimide (44.5 mg, 0.22 mmol, 1.1 eq.) was added dropwise into a 6.5 mL colorless pentane solution of **2** (144.5 mg, 0.20 mmol, 1.0 eq.). The resulting solution was stirred and heated at T=50°C for 3 hours triggering a color change from colorless to yellow. The crude reaction mixture was then cooled to room temperature and stirred for 24 hours. Volatiles were then removed *in vacuo* yielding a yellow crude powder (ca. 150 mg). This solid was dissolved in the minimum of pentane (ca. 6 mL), filtered, and stored at -40°C yielding **5** as light yellow block crystals suitable for XRD analysis (100 mg, 60% yield). ¹H NMR (500 MHz, C₆D₆, 293 K) δ 7.24 (s, 2H, CH_{Ar}), 6.99 (s, 1H, CH_{Amidinate}), 3.37 (m, 1H, CH_{Cy}), 2.83 (m, 1H, CH_{Cy}), 2.41 (s, 3H, CH₃-Ar), 2.35 (d, 1H, CH_{2-Cy}), 2.32 (m, 1H, CH_{iBu}), 2.23 (d, 1H, CH_{2-Cy}), 1.80 (m, 2H, CH_{2-Cy}), 1.73 (s, 18H, CH_{3-tBu}), 1.66 (m, 2H, CH_{2-Cy}), 1.61 (s, 15H, CH_{3Cp*}), 1.54 (m, 2H, CH_{2-Cy}), 1.45 (d, ³J_{HH} = 6.7 Hz, 3H, CH_{3-iBu}), 1.41 (d, ³J_{HH} = 6.6 Hz, 3H, CH_{3-iBu}), 0.95-1.39 (10H, m, CH_{2-Cy}), 0.93 (d, ³J_{HH} = 6.6 Hz, 2H, CH_{2-iBu}), -14.52 (s, 1H, H-Ir), -14.99 (s, 1H, H-Ir). ¹³C{¹H} NMR (125 MHz, C₆D₆, 293 K) δ 161.86 (CH_{Amidinate}), 157.63 (C_{Ar}), 139.62 (C_{Ar}), 125.96 (CH_{Ar}), 124.03 (C_{Ar}), 92.05 (C_{Cp*}), 69.61 (CH_{Cy}), 57.33 (CH_{Cy}), 36.72 (CH_{2-Cy}), 35.95 (CH_{2-Cy}), 35.76 (C_{tBu}), 35.57 (CH_{2-Cy}), 35.24 (CH₂₋

C_y), 34.46 ($\text{CH}_{2\text{-iBu}}$), 32.63 ($\text{CH}_{3\text{-tBu}}$), 29.13 ($\text{CH}_{3\text{-iBu}}$), 28.18 ($\text{CH}_{2\text{-Cy}}$), 26.97 ($\text{CH}_{2\text{-Cy}}$), 26.75 ($\text{CH}_{2\text{-Cy}}$) 26.73 ($\text{CH}_{2\text{-Cy}}$), 26.36 (CH_{iBu}), 26.32 ($\text{CH}_{2\text{-Cy}}$), 26.16 ($\text{CH}_{2\text{-Cy}}$), 21.41 ($\text{CH}_{3\text{-Ar}}$), 10.48 ($\text{CH}_{3\text{-Cp}^*}$). DRIFTS (293 K, cm^{-1}) σ 2949 (s, $\nu\text{C-H}$), 2915 (s, $\nu\text{C-H}$), 2851 (s, $\nu\text{C-H}$), 2145 (w, $\nu\text{Ir-H}$), 2071 (w, $\nu\text{Ir-H}$), 1614 (s, $\nu\text{C=N}$), 1447 (m), 1421 (s), 1264 (s). Elemental analysis calcd (%) for $\text{C}_{43}\text{H}_{76}\text{AlIrN}_2\text{O}$: C 60.32, H 8.95, N 3.27. Found: C 60.13, H 8.84, N 3.28.

8.3.4 CHAPTER 5 Development Of Al/Ir Heterobimetallic Sites Supported On A Mesoporous SBA-15₇₀₀ Silica

Synthesis of $[\{\{\text{Ir}(\text{Cp}^*)(\text{H})(\mu\text{-H}_2)\}_2\text{Al}(\text{OAr}')\}]$, compound **26**

A 1 mL colorless pentane solution of propofol (26.4 mg, 0.15 mmol, 1.0 eq.) was added dropwise into a 3.5 mL colorless pentane solution of **14** (151.0 mg, 0.15 mmol, 1.0 eq.). The resulting solution was stirred at RT for 90 minutes. Then, volatiles were removed in *vacuo* yielding white solids (c.a. 170 mg). This latter was dissolved in the minimum of pentane (c.a. 8 mL), filtered, and cooled at $T = -40^\circ\text{C}$ for 24 hours yielding compound **26** as single colorless needle-shaped crystals (100 mg, 77% yield). ^1H NMR (400 MHz, 293K, C_6D_6) δ 7.21 (d, $^3J_{\text{HH}} = 7.5$ Hz, 2H, $\text{CH}_{\text{Ar-meta}}$), 7.00 (t, $^3J_{\text{HH}} = 7.6$ Hz, 1H, $\text{CH}_{\text{Ar-para}}$), 3.75 (m, 2H, CH_{iPr}), 1.98 (s, 30H, Cp^*), 1.47 (d, $^3J_{\text{HH}} = 6.8$ Hz, 12H, $\text{CH}_{3\text{-iPr}}$), -16.55 (s, 6H, Ir-H). $^{13}\text{C}\{^1\text{H}\}$ NMR (75 MHz, 293K, C_6D_6) δ 154.83 ($\text{C}_{\text{Ar-O}}$), 137.10 ($\text{C}_{\text{Ar-iPr}}$), 123.38 ($\text{CH}_{\text{Ar-meta}}$), 119.24 ($\text{CH}_{\text{Ar-para}}$), 94.64 (C_{Cp^*}), 27.65 (CH_{iPr}), 24.49 ($\text{CH}_{3\text{-iPr}}$), 11.10 ($\text{CH}_{3\text{-Cp}^*}$). DRIFT (293K, cm^{-1}) σ 2962 (s, $\nu\text{C-H}$), 2915 (s, $\nu\text{C-H}$), 2866 (s, $\nu\text{C-H}$), 2139 (s, $\nu\text{M-H}$), 1998 (s, $\nu\text{M-H}$), 1456 (m), 1381 (m), 1333 (m), 1277 (m). Elemental analysis calcd (%) for $\text{C}_{32}\text{H}_{53}\text{OAlIr}_2$: C 44.42, H 6.17; found: C 44.69, H 6.21.

Synthesis of $[\equiv\text{SiOAl}\{(\mu\text{-H})_2\text{Ir}(\text{H})\text{Cp}^*\}_2]$, materials **27**

SBA-15₇₀₀ (340 mg dehydroxylated at 700°C under 10^{-5} mBar vacuum for 18 hours, 0.22 mmol of OH, 1.0 eq.) is charged in one compartment of a two-sided Schlenk reaction vessel equipped with a sintered glass filter. On the other side, a 20 mL dried pentane solution of complex $[\text{Al}\{(\text{H})(\mu\text{-H})_2\text{IrCp}^*\}_3]$, **14** (280 mg, 0.27 mmol, 1.2 eq.) is transferred in the other compartment. In the glovebox, the double-Schlenk vessel is smoothly and rapidly evacuated (10^{-2} mBar for a few seconds, pentane solution of **14** over stirring). The colorless solution of complex **14** is then transferred through the frit to the SBA-15₇₀₀ powder and stirred at room temperature for 2 h. After the reaction, the colorless supernatant is filtered away from the solid. The solid is washed

with fresh pentane and the supernatant is removed again. This procedure is repeated four times to ensure removal of any unreacted **14** as well as IrCp*H₄, which is formed as coproduct. Afterwards, pentane volatiles were gently removed *in vacuo* (10⁻² mBar for about 15 minutes, pentane solution of IrCp*H₄ over stirring) since IrCp*H₄ can be subjected to sublimation. This procedure leads to a mixture of IrCp*H₄ (70 mg, 0.21 mmol, 1 eq./OH) and unreacted **14** (50 mg, 0.05 mmol, 0.2 eq.) as a white powder in the first chamber (content analyzed by ¹H-NMR spectroscopy in C₆D₆) and 460 mg of materials **27** as white solids in the second chamber after drying over high vacuum (10⁻⁵ mBar) for 2 hours at room temperature. ¹H MAS SSNMR (300 MHz, 293 K) δ 1.95 (Cp*), -17.14 (Ir-H). ¹³C CP-MAS SSNMR (126 MHz, 293 K) δ 94.39 (C_{Cp*}), 9.51 (CH_{3-Cp*}). DRIFT (293K, cm⁻¹) σ 2989 (m, ν_{C-H}), 2964 (s, ν_{C-H}), 2913 (s, ν_{C-H}), 2131 (s, ν_{M-H}), 2000 (s, ν_{M-H}), 1468 (m), 1388 (w). Elemental analysis calcd (%) for **27**: C 10.62, H 1.60, Ir 17.00, Al 1.19; found: C 10.87, H 1.69, Ir 16.40, Al 1.21.

Synthesis of Ir-Al/SiO₂, material **28**

Material **27** (230 mg, 0.2 mmol/Ir) was charged under argon in a 300 mL glass reactor that was evacuated under high vacuum (10⁻⁵ mbar). Then, excess of dry hydrogen gas (1036 mbar, 12.8 mmol) was introduced in the reactor. The system was heated at 250°C for about 48 hours before hydrogen was removed under high vacuum. The resulting material was dried for 30 minutes under high vacuum at 250°C. The system was then transferred in the glovebox and 195 mg of Ir-Al/SiO₂ was recovered as a brown powder. DRIFT (293K, cm⁻¹) σ 3748 (m, ν_{SiO-H}), 2011 (s, ν_{M-H}). Elemental analysis found for Ir-Al/SiO₂ (% wt): C 0.69, H 0.24, Ir 16.70, Al 1.22.

IWI of IrCp*H₄ on SBA-15₇₀₀, material **29**

A 0.34 mL THF colorless solution of Cp*IrH₄ (140 mg, 0.42 mmol, concentration was adjusted to achieve the desired metal loading of material **27**) was added dropwise onto SBA-15₇₀₀ (295 mg) to achieve incipient wetness impregnation under argon atmosphere and with vigorous stirring (using a glass spatula) to ensure homogeneous repartition of the precursor upon the support. The resulting white powder was dried *in vacuo* while stirring for 10 minutes yielding Cp*IrH₄@SiO₂ as a fine white powder. DRIFT (293K, cm⁻¹) σ 3450 (br and w, ν_{SiO-H}, umbrella effect), 2150 (s, ν_{M-H}). Elemental analysis found for material **29** (% wt): C 11.80, H 1.92, Ir 16.30.

Synthesis of Ir/SiO₂, material **30**

Material **29** (350 mg, 0.3 mmol/Ir) was charged in a 300 mL glass reactor. Then, argon was evacuated on a high vacuum line (until reaching a pressure of about $2 \cdot 10^{-3}$ mbar from which point Cp*IrH₄ can start to sublime). Then dry hydrogen gas (1044 mbars, 12.9 mmol) was added in the system. The reactor was heated at 250°C for 48 hours before hydrogen was removed under high vacuum. The resulting material was dried for 30 minutes under high vacuum at 250°C. Then the system was transferred in the glovebox and 300 mg of Ir/SiO₂ was recovered as a dark brown powder. DRIFT (293K, cm⁻¹) σ 3748 (s, $\nu_{\text{SiO-H}}$), 2024 (s, $\nu_{\text{M-H}}$). Elemental analysis found for material **30** (% wt): C 1.04, H 0.22, Ir 18.80.

CHAPTER 9. References

- [1] P. Buchwalter, J. Rosé, P. Braunstein, *Chem. Rev.* **2014**, *115*, 28–126.
- [2] N. P. Mankad, *Chem. Commun.* **2018**, *54*, 1291–1302.
- [3] I. G. Powers, C. Uyeda, *ACS Catal.* **2016**, *7*, 936–958.
- [4] B. G. Cooper, J. W. Napoline, C. M. Thomas, *Catal. Rev.* **2012**, *54*, 1–40.
- [5] E. Bodio, M. Picquet, P. Le Gendre, *Top. Organomet. Chem.* **2015**, *59*, 139–186.
- [6] L. H. Gade, *Angew. Chem. Int. Ed* **2000**, *39*, 2658–2678.
- [7] F. Rekhroukh, W. Chen, R. K. Brown, A. J. P. White, M. R. Crimmin, *Chem. Sci.* **2020**, *11*, 7842–7849.
- [8] M. J. Butler, M. R. Crimmin, *Chem. Commun.* **2017**, *53*, 1348–1365.
- [9] P. G. Andersson, in *Top. Organomet. Chem.*, **2011**, p. 234.
- [10] C. Copéret, D. P. Estes, K. Larmier, K. Searles, *Chem. Rev.* **2016**, *116*, 8463–8505.
- [11] V. Vidal, A. Théolier, J. Thivolle-Cazat, J. M. Basset, *Science (80-)*. **1997**, *276*, 99–102.
- [12] P. Avenier, M. Taoufik, A. Lesage, X. Solans-Monfort, A. Baudouin, A. De Mallmann, L. Veyre, J. M. Basset, O. Eisenstein, L. Emsley, E. A. Quadrelli, *Science (80-)*. **2007**, *317*, 1056–1060.
- [13] C. Copéret, A. Comas-Vives, M. P. Conley, D. P. Estes, A. Fedorov, V. Mougél, H. Nagae, F. Núñez-Zarur, P. A. Zhizhko, *Chem. Rev.* **2016**, *116*, 323–421.
- [14] L. M. Slaughter, P. T. Wolczanski, *Chem. Commun.* **1997**, 2109–2110.
- [15] B. P. Greenwood, G. T. Rowe, C. H. Chen, B. M. Foxman, C. M. Thomas, *J. Am. Chem. Soc.* **2010**, *132*, 44–45.
- [16] T. Miyazaki, Y. Tanabe, M. Yuki, Y. Miyake, Y. Nishibayashi, *Organometallics* **2011**, *30*, 2394–2404.
- [17] L. J. Clouston, R. B. Siedschlag, P. A. Rudd, N. Planas, S. Hu, A. D. Miller, L. Gagliardi, C. C. Lu, *J. Am. Chem. Soc.* **2013**, *135*, 13142–13148.
- [18] R. Srivastava, M. Jakoobi, C. Thieuleux, E. A. Quadrelli, C. Camp, *Dalt. Trans.* **2021**, *50*, 869–879.
- [19] R. Srivastava, E. A. Quadrelli, C. Camp, *Dalt. Trans.* **2020**, *49*, 3120–3128.
- [20] R. Srivastava, R. Moneuse, J. Petit, P. A. Pavard, V. Dardun, M. Rivat, P. Schiltz, M. Solari, E. Jeanneau, L. Veyre, C. Thieuleux, E. A. Quadrelli, C. Camp, *Chem. - A Eur. J.* **2018**, *24*, 4361–4370.
- [21] V. Dardun, L. Escomel, E. Jeanneau, C. Camp, *Dalt. Trans.* **2018**, *47*, 10429–10433.
- [22] M. V. Butovskii, C. Döring, V. Bezugly, F. R. Wagner, Y. Grin, R. Kempe, *Nat. Chem.* **2010**, *2*, 741–744.
- [23] J. A. Marsella, J. C. Huffman, K. G. Caulton, B. Longato, J. R. Norton, *J. Am. Chem. Soc.* **1982**, *104*, 6360–6368.

- [24] M. Oishi, M. Oshima, H. Suzuki, *Inorg. Chem.* **2014**, *53*, 6634–6654.
- [25] J. T. Golden, T. H. Peterson, P. L. Holland, R. G. Bergman, R. A. Andersen, *J. Am. Chem. Soc.* **1998**, *120*, 223–224.
- [26] M. Ohashi, K. Matsubara, T. Iizuka, H. Suzuki, *Angew. Chemie - Int. Ed.* **2003**, *42*, 937–940.
- [27] S. Lassalle, R. Jabbour, P. Schiltz, P. Berruyer, T. K. Todorova, L. Veyre, D. Gajan, A. Lesage, C. Thieuleux, C. Camp, *J. Am. Chem. Soc.* **2019**, *141*, 19321–19335.
- [28] S. Lassalle, R. Jabbour, I. Del Rosal, L. Maron, E. Fonda, L. Veyre, D. Gajan, A. Lesage, C. Thieuleux, C. Camp, *J. Catal.* **2020**, *392*, 287–301.
- [29] I. Del Rosal, S. Lassalle, C. Dinoi, C. Thieuleux, L. Maron, C. Camp, *Dalt. Trans.* **2021**, *50*, 504–510.
- [30] L. Escomel, I. Del Rosal, L. Maron, E. Jeanneau, L. Veyre, C. Thieuleux, C. Camp, *J. Am. Chem. Soc.* **2021**, *143*, 4844–4856.
- [31] L. Escomel, N. Soulé, E. Robin, I. Del Rosal, L. Maron, E. Jeanneau, C. Thieuleux, C. Camp, *Inorg. Chem.* **2022**, *61*, 5715–5730.
- [32] J. Llop Castelbou, K. C. Szeto, W. Barakat, N. Merle, C. Godard, M. Taoufik, C. Claver, *Chem. Commun.* **2017**, *53*, 3261–3264.
- [33] F. Héroguel, G. Siddiqi, M. D. Detwiler, D. Y. Zemlyanov, O. V. Safonova, C. Copéret, *J. Catal.* **2015**, *321*, 81–89.
- [34] F. Héroguel, D. Gebert, M. D. Detwiler, D. Y. Zemlyanov, D. Baudouin, C. Copéret, *J. Catal.* **2014**, *316*, 260–269.
- [35] L. Rochlitz, K. Searles, J. Alfke, D. Zemlyanov, O. V. Safonova, C. Copéret, *Chem. Sci.* **2020**, *11*, 1549–1555.
- [36] E. Lam, G. Noh, K. W. Chan, K. Larmier, D. Lebedev, K. Searles, P. Wolf, O. V. Safonova, C. Copéret, *Chem. Sci.* **2020**, *11*, 7593–7598.
- [37] S. R. Docherty, N. Phongprueksathat, E. Lam, G. Noh, O. V. Safonova, A. Urakawa, C. Copéret, *JACS Au* **2021**, *1*, 450–458.
- [38] K. Searles, K. W. Chan, J. A. Mendes Burak, D. Zemlyanov, O. Safonova, C. Copéret, *J. Am. Chem. Soc.* **2018**, *140*, 11674–11679.
- [39] L. Escomel, D. F. Abbott, V. Mougel, L. Veyre, C. Thieuleux, C. Camp, *Chem. Commun.* **2022**, 8214–8217.
- [40] G. L. Casty, M. G. Matturro, G. R. Myers, R. P. Reynolds, R. B. Hall, *Organometallics* **2001**, *20*, 2246–2249.
- [41] L. Lefort, C. Copéret, M. Taoufik, J. Thivolle-Cazat, J. M. Basset, *Chem. Commun.* **2000**, *12*, 663–664.
- [42] F. L. Mohler, V. H. Dibeler, E. Quinn, *J. Res. Natl. Bur. Stand. (1934)*. **1958**, *61*, 171.

- [43] B. Schoofs, J. A. Martens, P. A. Jacobs, R. A. Schoonheydt, *J. Catal.* **1999**, *183*, 355–367.
- [44] R. H. Crabtree, *Organomet. Chem. Transit. Met. Sixth Ed.* **2014**, 9781118138076, 1–504.
- [45] R. H. Crabtree, *Organomet. Chem. Transit. Met.* **2005**, 1–546.
- [46] J. A. Gladysz, Z. T. Ball, G. Bertrand, S. A. Blum, V. M. Dong, R. Dorta, F. E. Hahn, M. G. Humphrey, W. D. Jones, J. Klosin, I. Manners, T. J. Marks, J. M. Mayer, B. Rieger, J. C. Ritter, A. P. Sattelberger, J. M. Schomaker, V. W. W. Yam, *Organometallics* **2012**, *31*, 1–18.
- [47] R. M. Charles, H. Tupkar, S. D. Helland, A. A. Mercado, W. T. Eckenhoff, N. D. Schley, N. J. DeYonker, T. P. Brewster, *Eur. J. Inorg. Chem.* **2020**, 2020, 1192–1198.
- [48] R. M. Charles, T. W. Yokley, N. D. Schley, N. J. Deyonker, T. P. Brewster, *Inorg. Chem.* **2019**, *58*, 12635–12645.
- [49] T. P. Brewster, T. H. Nguyen, Z. Li, W. T. Eckenhoff, N. D. Schley, N. J. Deyonker, *Inorg. Chem.* **2018**, *57*, 1148–1157.
- [50] R. M. Charles, N. S. Taylor, A. A. Mercado, C. E. Frost, T. W. Yokley, W. T. Eckenhoff, N. D. Schley, N. J. Deyonker, T. P. Brewster, *Dalt. Trans.* **2020**, 49, 13029–13043.
- [51] J. F. Lefebvre, M. Lo, J. P. Gisselbrecht, O. Coulembier, S. Clément, S. Richeter, *Chem. - A Eur. J.* **2013**, *19*, 15652–15660.
- [52] T. Asada, Y. Hoshimoto, S. Ogoshi, *J. Am. Chem. Soc.* **2020**, *142*, 9772–9784.
- [53] M. Devillard, E. Nicolas, A. W. Ehlers, J. Backs, S. Mallet-Ladeira, G. Bouhadir, J. C. Slootweg, W. Uhl, D. Bourissou, *Chem. - A Eur. J.* **2015**, *21*, 74–79.
- [54] M. Devillard, E. Nicolas, C. Appelt, J. Backs, S. Mallet-Ladeira, G. Bouhadir, J. C. Slootweg, W. Uhl, D. Bourissou, *Chem. Commun.* **2014**, 50, 14805–14808.
- [55] M. Devillard, R. Declercq, E. Nicolas, A. W. Ehlers, J. Backs, N. Saffon-Merceron, G. Bouhadir, J. C. Slootweg, W. Uhl, D. Bourissou, *J. Am. Chem. Soc.* **2016**, *138*, 4917–4926.
- [56] C. Appelt, H. Westenberg, F. Bertini, A. W. Ehlers, J. C. Slootweg, K. Lammertsma, W. Uhl, *Angew. Chemie - Int. Ed.* **2011**, *50*, 3925–3928.
- [57] T. Saito, N. Hara, Y. Nakao, *Chem. Lett.* **2017**, *46*, 1247–1249.
- [58] Q. Lai, M. N. Cosio, O. V. Ozerov, *Chem. Commun.* **2020**, 56, 14845–14848.
- [59] P. A. Rudd, S. Liu, L. Gagliardi, V. G. Young, C. C. Lu, *J. Am. Chem. Soc.* **2011**, *133*, 20724–20727.
- [60] N. Hara, K. Semba, Y. Nakao, *ACS Catal.* **2022**, 1626–1638.
- [61] B. J. Graziano, M. V. Vollmer, C. C. Lu, *Angew. Chemie Int. Ed.* **2021**, *60*, 15087–15094.
- [62] Q. Lai, N. Bhuvanesh, O. V. Ozerov, *J. Am. Chem. Soc.* **2020**, *142*, 20920–20923.
- [63] K. Semba, I. Fujii, Y. Nakao, *Inorganics* **2019**, *7*, 140.
- [64] J. Takaya, N. Iwasawa, *J. Am. Chem. Soc.* **2017**, *139*, 6074–6077.
- [65] S. Morisako, S. Watanabe, S. Ikemoto, S. Muratsugu, M. Tada, M. Yamashita, *Angew.*

- Chemie - Int. Ed.* **2019**, *58*, 15031–15035.
- [66] N. Hara, T. Saito, K. Semba, N. Kuriakose, H. Zheng, S. Sakaki, Y. Nakao, *J. Am. Chem. Soc.* **2018**, *140*, 7070–7073.
- [67] N. Kuriakose, J. J. Zheng, T. Saito, N. Hara, Y. Nakao, S. Sakaki, *Inorg. Chem.* **2019**, *58*, 4894–4906.
- [68] W. Zhao, S. M. McCarthy, T. Y. Lai, H. P. Yennawar, A. T. Radosevich, *J. Am. Chem. Soc.* **2014**, *136*, 17634–17644.
- [69] S. Bajo, M. G. Alférez, M. M. Alcaide, J. López-Serrano, J. Campos, *Chem. - A Eur. J.* **2020**, *26*, 16833–16845.
- [70] J. Bauer, H. Braunschweig, R. D. Dewhurst, *Chem. Rev.* **2012**, *112*, 4329–4346.
- [71] J. M. Burlitch, M. E. Leonowicz, R. B. Petersen, R. E. Hughes, *Inorg. Chem.* **1979**, *18*, 1097–1105.
- [72] J. Bauer, H. Braunschweig, P. Brenner, K. Kraft, K. Radacki, K. Schwab, *Chem. - A Eur. J.* **2010**, *16*, 11985–11992.
- [73] H. Braunschweig, K. Gruss, K. Radacki, *Angew. Chemie - Int. Ed.* **2007**, *46*, 7782–7784.
- [74] J. Bauer, R. Bertermann, H. Braunschweig, K. Gruss, F. Hupp, T. Kramer, *Inorg. Chem.* **2012**, *51*, 10, 5617–5626.
- [75] J. W. Bruno, J. C. Huffman, K. G. Caulton, *J. Am. Chem. Soc.* **1984**, *106*, 444–445.
- [76] M. Amati, F. Lelj, *Can. J. Chem.* **2009**, *87*, 1406–1414.
- [77] A. Storr, B. S. Thomas, *Can. J. Chem.* **1971**, *49*, 2504–2507.
- [78] L. Pauling, *J. Am. Chem. Soc.* **1947**, *69*, 542–553.
- [79] J. A. Chipman, J. F. Berry, *Chem. Rev.* **2020**, *120*, 2409–2447.
- [80] X. Zhang, L. L. Liu, *Angew. Chemie Int. Ed.* **2021**, *60*, 27062–27069.
- [81] C. Cui, H. W. Roesky, H. G. Schmidt, M. Noltemeyer, H. Hao, F. Cimpoesu, *Angew. Chemie - Int. Ed.* **2000**, *39*, 4274–4276.
- [82] C. Dohmeier, C. Robl, M. Tacke, H. Schnöckel, *Angew. Chem., Int. Ed.* **1991**, *30*, 564–565.
- [83] T. Agou, K. Nagata, N. Tokitoh, *Angew. Chemie Int. Ed.* **2013**, *52*, 10818–10821.
- [84] J. Hicks, P. Vasko, J. M. Goicoechea, S. Aldridge, *Nat.* 2018 5577703 **2018**, *557*, 92–95.
- [85] R. J. Schwamm, M. P. Coles, M. S. Hill, M. F. Mahon, C. L. McMullin, N. A. Rajabi, A. S. S. Wilson, *Angew. Chemie - Int. Ed.* **2020**, *59*, 3928–3932.
- [86] M. J. Evans, M. D. Anker, M. P. Coles, *Inorg. Chem.* **2021**, *60*, 4772–4778.
- [87] J. Hicks, A. Mansikkamäki, P. Vasko, J. M. Goicoechea, S. Aldridge, *Nat. Chem.* **2019**, *11*, 237–241.
- [88] J. Hicks, P. Vasko, J. M. Goicoechea, S. Aldridge, *Angew. Chemie - Int. Ed.* **2021**, *60*, 1702–1713.
- [89] H. Y. Liu, R. J. Schwamm, M. S. Hill, M. F. Mahon, C. L. McMullin, N. A. Rajabi, *Angew.*

- Chemie - Int. Ed.* **2021**, *60*, 14390–14393.
- [90] C. Dohmeier, C. Robl, M. Tacke, H. Schnöckel, *Angew. Chemie - Int. Ed.* **1991**, *30*, 564–565.
- [91] D. Weiss, T. Steinke, M. Winter, R. A. Fischer, N. Fröhlich, J. Uddin, G. Frenking, *Organometallics* **2000**, *19*, 4583–4588.
- [92] T. Steinke, C. Gemel, M. Winter, R. A. Fischer, *Chem. – A Eur. J.* **2005**, *11*, 1636–1646.
- [93] T. Cadenbach, T. Bollermann, C. Gemel, R. A. Fischer, *J. Chem. Soc. Dalt. Trans.* **2008**, 322–329.
- [94] T. Steinke, M. Cokoja, C. Gemel, A. Kempter, A. Krapp, G. Frenking, U. Zenneck, R. A. Fischer, *Angew. Chemie - Int. Ed.* **2005**, *44*, 2943–2946.
- [95] T. Steinke, C. Gemel, M. Cokoja, M. Winter, R. A. Fischer, *Angew. Chemie - Int. Ed.* **2004**, *43*, 2299–2302.
- [96] A. Kempter, C. Gemel, R. A. Fischer, *Chem. - A Eur. J.* **2007**, *13*, 2990–3000.
- [97] A. Kempter, C. Gemel, R. A. Fischer, *Chem. Commun.* **2006**, *3*, 1551–1553.
- [98] T. N. Hooper, M. Garçon, A. J. P. White, M. R. Crimmin, *Chem. Sci.* **2018**, *9*, 5435–5440.
- [99] K. L. Mears, C. R. Stennett, E. K. Taskinen, C. E. Knapp, C. J. Carmalt, H. M. Tuononen, P. P. Power, *J. Am. Chem. Soc.* **2020**, *142*, 19874–19878.
- [100] R. Y. Kong, M. R. Crimmin, *Dalt. Trans.* **2021**, *50*, 7810–7817.
- [101] K. Nagata, T. Agou, N. Tokitoh, *Angew. Chemie Int. Ed.* **2014**, *53*, 3881–3884.
- [102] I. M. Riddlestone, J. Urbano, N. Phillips, M. J. Kelly, D. Vidovic, J. I. Bates, R. Taylor, S. Aldridge, *Dalt. Trans.* **2013**, *42*, 249–258.
- [103] S. Sinhababu, M. R. Radzhabov, J. Telser, N. P. Mankad, *J. Am. Chem. Soc.* **2022**, DOI 10.1021/jacs.1c13108.
- [104] J. Weiss, D. Stetzkamp, B. Nuber, R. A. Fischer, C. Boehme, G. Frenking, *Angew. Chemie Int. Ed. English* **1997**, *36*, 70–72.
- [105] H. Fölsing, O. Segnitz, U. Bossek, K. Merz, M. Winter, R. A. Fischer, *J. Organomet. Chem.* **2000**, *606*, 132–140.
- [106] H. Braunschweig, J. Müller, B. Ganter, *Inorg. Chem.* **1996**, *35*, 7443–7444.
- [107] B. N. Anand, I. Krossing, H. Nöth, *Inorg. Chem.* **1997**, *36*, 1979–1981.
- [108] T. Agou, T. Yanagisawa, T. Sasamori, N. Tokitoh, *Bull. Chem. Soc. Jpn.* **2016**, *89*, 1184–1186.
- [109] R. A. Fischer, M. M. Schulte, J. Weiss, L. Zsolnai, A. Jacobi, G. Huttner, G. Frenking, C. Boehme, S. F. Vyboishchikov, *J. Am. Chem. Soc.* **1998**, *120*, 1237–1248.
- [110] A. S. Borovik, S. G. Bott, A. R. Barron, *Organometallics* **1999**, *18*, 2668–2676.
- [111] R. A. Fischer, D. Weiß, M. Winter, I. Müller, H. D. Kaesz, N. Fröhlich, G. Frenking, *J. Organomet. Chem.* **2004**, *689*, 4611–4623.
- [112] J. Li, M. Hermann, G. Frenking, C. Jones, *Angew. Chemie Int. Ed.* **2012**, *51*, 8611–8614.

- [113] D. Sorbelli, L. Belpassi, P. Belanzoni, *J. Am. Chem. Soc.* **2021**, *143*, 14433–14437.
- [114] T. Nakamura, K. Suzuki, M. Yamashita, *J. Am. Chem. Soc.* **2017**, *139*, 17763–17766.
- [115] T. Zhang, Y. X. Luan, N. Y. S. Lam, J. F. Li, Y. Li, M. Ye, J. Q. Yu, *Nat. Chem.* **2021**, *13*, 1207–1213.
- [116] N. Hara, K. Aso, Q. Z. Li, S. Sakaki, Y. Nakao, *Tetrahedron* **2021**, *95*, DOI 10.1016/j.tet.2021.132339.
- [117] N. Hara, N. Uemura, Y. Nakao, *Chem. Commun.* **2021**, *57*, 5957–5960.
- [118] I. Fujii, K. Semba, Q. Z. Li, S. Sakaki, Y. Nakao, *J. Am. Chem. Soc.* **2020**, *142*, 11647–11652.
- [119] C. Marcilly, *J. Catal.* **2003**, *216*, 47–62.
- [120] C. Copéret, M. Chabanas, R. Petroff Saint-Arroman, J. M. Basset, *Angew. Chemie - Int. Ed.* **2003**, *42*, 156–181.
- [121] C. Copéret, A. Fedorov, P. A. Zhizhko, *Catal. Letters* **2017**, *147*, 2247–2259.
- [122] M. K. Samantaray, S. K. Mishra, A. Saidi, J. M. Basset, *J. Organomet. Chem.* **2021**, *945*, 121864.
- [123] L. T. Zhuravlev, *Colloids Surfaces A Physicochem. Eng. Asp.* **2000**, *173*, 1–38.
- [124] M. P. Conley, C. Copéret, C. Thieuleux, *ACS Catal.* **2014**, *4*, 1458–1469.
- [125] F. Pourpoint, Y. Morin, R. M. Gauvin, J. Trébosc, F. Capet, O. Lafon, J. P. Amoureux, *J. Phys. Chem. C* **2013**, *117*, 18091–18099.
- [126] J. Li, J. A. DiVerdi, G. E. Maciel, *J. Am. Chem. Soc.* **2006**, *128*, 17093–17101.
- [127] R. N. Kerber, A. Kermagoret, E. Callens, P. Florian, D. Massiot, A. Lesage, C. Copéret, F. Delbecq, X. Rozanska, P. Sautet, *J. Am. Chem. Soc.* **2012**, *134*, 6767–6775.
- [128] J. R. Severn, J. C. Chadwick, R. Duchateau, N. Friederichs, *Chem. Rev.* **2005**, *105*, 4073–4147.
- [129] L. K. Van Looveren, D. F. Geysen, K. A. Vercruysse, B. H. Wouters, P. J. Grobet, P. A. Jacobs, *Angew. Chem. Int. Ed. Engl* **1998**, *37*, 3802–3804.
- [130] M. R. Mason, *Encycl. Inorg. Bioinorg. Chem.* **2016**, 1–26.
- [131] A. Kermagoret, R. N. Kerber, M. P. Conley, E. Callens, P. Florian, D. Massiot, C. Copéret, F. Delbecq, X. Rozanska, P. Sautet, *Dalt. Trans.* **2013**, *42*, 12681–12687.
- [132] B. Werghi, A. Bendjeriou-Sedjerari, J. Sofack-Kreutzer, A. Jedidi, E. Abou-Hamad, L. Cavallo, J. M. Basset, *Chem. Sci.* **2015**, *6*, 5456–5465.
- [133] J. Pelletier, J. Espinas, N. Vu, S. Norsic, A. Baudouin, L. Delevoye, J. Trébosc, E. Le Roux, C. Santini, J. M. Basset, R. M. Gauvin, M. Taoufik, *Chem. Commun.* **2011**, *47*, 2979–2981.
- [134] B. Werghi, A. Bendjeriou-Sedjerari, A. Jedidi, E. Abou-Hamad, L. Cavallo, J. M. Basset, *Organometallics* **2016**, *35*, 3288–3294.
- [135] I. B. Moroz, P. Florian, J. Viger-Gravel, C. P. Gordon, A. Lesage, C. Copéret, *Angew. Chemie - Int. Ed.* **2020**, *59*, 16167–16172.
- [136] C. Copéret, *Acc. Chem. Res.* **2019**, *52*, 1697–1708.
- [137] M. F. Delley, F. Núñez-Zarur, M. P. Conley, A. Comas-Vives, G. Siddiqi, S. Norsic, V. Monteil,

- O. V. Safonova, C. Copéret, *Proc. Natl. Acad. Sci. U. S. A.* **2014**, *111*, 11624–11629.
- [138] M. P. Conley, M. F. Delley, G. Siddiqi, G. Lapadula, S. Norsic, V. Monteil, O. V. Safonova, C. Copéret, *Angew. Chemie Int. Ed.* **2014**, *53*, 1872–1876.
- [139] D. A. Ruddy, T. D. Tilley, *Chem. Commun.* **2007**, 3350–3352.
- [140] R. L. Brutchey, C. G. Lugmair, L. O. Schebaum, T. D. Tilley, *J. Catal.* **2005**, *229*, 72–81.
- [141] R. L. Brutchey, D. A. Ruddy, L. K. Andersen, T. Don Tilley, *Langmuir* **2005**, *21*, 9576–9583.
- [142] P. J. Cordeiro, T. D. Tilley, *ACS Catal.* **2011**, *1*, 455–467.
- [143] K. Yamamoto, K. W. Chan, V. Mougél, H. Nagae, H. Tsurugi, O. V. Safonova, K. Mashima, C. Copéret, *Chem. Commun.* **2018**, *54*, 3989–3992.
- [144] J. Jarupatrakorn, M. P. Coles, T. D. Tilley, *Chem. Mater.* **2005**, *17*, 1818–1828.
- [145] V. Mougél, K. W. Chan, G. Siddiqi, K. Kawakita, H. Nagae, H. Tsurugi, K. Mashima, O. Safonova, C. Copéret, *ACS Cent. Sci.* **2016**, *2*, 569–576.
- [146] C. G. Lugmair, K. L. Furdala, T. D. Tilley, *Chem. Mater.* **2002**, *14*, 888–898.
- [147] M. Valla, D. Stadler, V. Mougél, C. Copéret, *Angew. Chemie Int. Ed.* **2016**, *55*, 1124–1127.
- [148] E. Mazoyer, J. Trébosc, A. Baudouin, O. Boyron, J. Pelletier, J.-M. Basset, M. J. Vitorino, C. P. Nicholas, R. M. Gauvin, M. Taoufik, L. Delevoye, *Angew. Chemie Int. Ed.* **2010**, *49*, 9854–9858.
- [149] K. C. Szeto, W. Sahyoun, N. Merle, J. L. Castelbou, N. Popoff, F. Lefebvre, J. Raynaud, C. Godard, C. Claver, L. Delevoye, R. M. Gauvin, M. Taoufik, *Catal. Sci. Technol.* **2016**, *6*, 882–889.
- [150] D. W. Sauter, N. Popoff, M. A. Bashir, K. C. Szeto, R. M. Gauvin, L. Delevoye, M. Taoufik, C. Boisson, *Chem. Commun.* **2016**, *52*, 4776–4779.
- [151] Y.-R. Luo, **2010**.
- [152] D. J. Lucas, L. A. Curtiss, J. A. Pople, *J. Chem. Phys.* **1998**, *99*, 6697.
- [153] S. Nassreddine, G. Bergeret, B. Jouguet, C. Geantet, L. Piccolo, *Phys. Chem. Chem. Phys.* **2010**, *12*, 7812–7820.
- [154] F. Locatelli, B. Didillon, D. Uzio, G. Niccolai, J. P. Candy, J. M. Basset, *J. Catal.* **2000**, *193*, 154–160.
- [155] F. Locatelli, J. P. Candy, B. Didillon, G. P. Niccolai, D. Uzio, J. M. Basset, *J. Am. Chem. Soc.* **2001**, *123*, 1658–1663.
- [156] I. Göttker-Schnetmann, P. White, M. Brookhart, *J. Am. Chem. Soc.* **2004**, *126*, 1804–1811.
- [157] M. Rimoldi, D. Fodor, J. A. Van Bokhoven, A. Mezzetti, *Chem. Commun.* **2013**, *49*, 11314–11316.
- [158] D. M. Kaphan, R. C. Klet, F. A. Perras, M. Pruski, C. Yang, A. J. Kropf, M. Delferro, *ACS Catal.* **2018**, *8*, 5363–5373.

- [159] M. Renom-Carrasco, P. Mania, R. Sayah, L. Veyre, G. Occhipinti, D. Gajan, A. Lesage, V. R. Jensen, C. Thieuleux, *Dalt. Trans.* **2019**, *48*, 2886–2890.
- [160] T. K. Maishal, J. Alauzun, J. M. Basset, C. Copéret, R. J. P. Corriu, E. Jeanneau, A. Mehdi, C. Reyé, L. Veyre, C. Thieuleux, *Angew. Chemie Int. Ed.* **2008**, *47*, 8654–8656.
- [161] I. Romanenko, D. Gajan, R. Sayah, D. Crozet, E. Jeanneau, C. Lucas, L. Leroux, L. Veyre, A. Lesage, L. Emsley, E. Lacôte, C. Thieuleux, *Angew. Chemie - Int. Ed.* **2015**, *54*, 12937–12941.
- [162] M. K. Samantaray, J. Alauzun, D. Gajan, S. Kavitate, A. Mehdi, L. Veyre, M. Lelli, A. Lesage, L. Emsley, C. Copéret, C. Thieuleux, *J. Am. Chem. Soc.* **2013**, *135*, 3193–3199.
- [163] B. T. Flatt, R. H. Grubbs, T. Arnold, M. Beckman, R. L. Blanski, J. C. Calabrese, J. Feldman, *Organometallics* **1994**, *13*, 2728–2732.
- [164] M. K. Samantaray, R. Dey, S. Kavitate, E. Abou-Hamad, A. Bendjeriou-Sedjerari, A. Hamieh, J. M. Basset, *J. Am. Chem. Soc.* **2016**, *138*, 8595–8602.
- [165] M. K. Samantaray, S. Kavitate, N. Morlanés, E. Abou-Hamad, A. Hamieh, R. Dey, J. M. Basset, *J. Am. Chem. Soc.* **2017**, *139*, 3522–3527.
- [166] E. Lam, K. Larmier, P. Wolf, S. Tada, O. V. Safonova, C. Copéret, *J. Am. Chem. Soc.* **2018**, *140*, 10530–10535.
- [167] G. Noh, E. Lam, J. L. Alfke, K. Larmier, K. Searles, P. Wolf, C. Copéret, *ChemSusChem* **2019**, *12*, 968–972.
- [168] E. Lam, G. Noh, K. Larmier, O. V. Safonova, C. Copéret, *J. Catal.* **2021**, *394*, 266–272.
- [169] G. Takahiro, K. Takayuki, A. Yoshimoto, *J. Sol-Gel Sci. Technol.* **1998**, *13*, 975–979.
- [170] J. P. Dombrowski, G. R. Johnson, A. T. Bell, T. D. Tilley, *Dalt. Trans.* **2016**, *45*, 11025–11034.
- [171] K. Searles, G. Siddiqi, O. V. Safonova, C. Copéret, *Chem. Sci.* **2017**, *8*, 2661–2666.
- [172] K. Larmier, W. C. Liao, S. Tada, E. Lam, R. Verel, A. Bansode, A. Urakawa, A. Comas-Vives, C. Copéret, *Angew. Chemie Int. Ed.* **2017**, *56*, 2318–2323.
- [173] K. Weiss, W. Guthmann, S. Maisuls, *Angew. Chemie Int. Ed. English* **1988**, *27*, 275–277.
- [174] G. L. Rice, S. L. Scott, *Chem. Mater.* **1998**, *10*, 620–625.
- [175] K. Weiss, M. Denzner, *J. Organomet. Chem.* **1988**, *355*, 273–280.
- [176] K. Weiss, W. Guthmann, M. Denzner, *J. Mol. Catal.* **1988**, *46*, 341–349.
- [177] F. Rataboul, C. Copéret, L. Lefort, A. De Mallmann, J. Thivolle-Cazat, J. M. Basset, *J. Chem. Soc. Dalt. Trans.* **2007**, 923–927.
- [178] F. Rataboul, A. Baudouin, C. Thieuleux, L. Veyre, C. Copéret, J. Thivolle-Cazat, J.-M. Basset, A. Lesage, L. Emsley, *J. Am. Chem. Soc.* **2004**, *126*, 12541–12550.
- [179] R. R. Schrock, J. D. Fellmann, *J. Am. Chem. Soc.* **1978**, *100*, 3359–3370.
- [180] E. Le Roux, M. Chabanas, A. Baudouin, A. De Mallmann, C. Copéret, E. A. Quadrelli, J. Thivolle-Cazat, J. M. Basset, W. Lukens, A. Lesage, L. Emsley, G. J. Sunley, *J. Am. Chem. Soc.*

- 2004, 126, 13391–13399.
- [181] T. M. Gilbert, F. J. Hollander, R. G. Bergman, *J. Am. Chem. Soc.* **1985**, 107, 3508–3516.
- [182] P. de Frémont, N. Marion, S. P. Nolan, *Coord. Chem. Rev.* **2009**, 253, 862–892.
- [183] M. N. Hopkinson, C. Richter, M. Schedler, F. Glorius, *Nature* **2014**, 510, 485–496.
- [184] A. C. Hillier, W. J. Sommer, B. S. Yong, J. L. Petersen, L. Cavallo, S. P. Nolan, *Organometallics* **2003**, 22, 4322–4326.
- [185] M. Hans, J. Lorkowski, A. Demonceau, L. Delaude, *Beilstein J. Org. Chem* **2015**, 11, 2318–2325.
- [186] S. Bauri, S. N. R. Donthireddy, P. M. Illam, A. Rit, *Inorg. Chem.* **2018**, 57, 14582–14593.
- [187] K. J. Evans, S. M. Mansell, *Chem. - A Eur. J.* **2020**, 26, 5927–5941.
- [188] P. K. Majhi, S. C. Serin, G. Schnakenburg, D. P. Gates, R. Streubel, *Eur. J. Inorg. Chem.* **2014**, 2014, 4975–4983.
- [189] A. L. Liberman-Martin, M. S. Ziegler, A. G. DiPasquale, R. G. Bergman, T. D. Tilley, *Polyhedron* **2016**, 116, 111–115.
- [190] E. Y.-X. Chen, T. J. Marks, *Chem. Rev.* **2000**, 100, 1391–1434.
- [191] A. P. Shreve, R. Mulhauot, W. Fultz, J. Calabrese, W. Robbins, S. D. Ittel, *Organometallics* **1988**, 7, 409–416.
- [192] C. Fliedel, G. Schnee, T. Avilés, S. Dagorne, *Coord. Chem. Rev.* **2014**, 275, 63–86.
- [193] C. Romain, C. Fliedel, S. Bellemin-Laponnaz, S. Dagorne, *Organometallics* **2014**, 33, 5730–5739.
- [194] A. J. Arduengo, H. V. R. Dias, J. C. Calabrese, F. Davidson, *J. Am. Chem. Soc.* **1992**, 114, 9724–9725.
- [195] M. Uzelac, A. R. Kennedy, E. Hevia, *Inorg. Chem.* **2017**, 56, 8615–8626.
- [196] D. W. Stephan, *Science (80-.)*. **2016**, 354, aaf7229.
- [197] D. W. Stephan, *J. Am. Chem. Soc.* **2015**, 137, 10018–10032.
- [198] A. L. Schmitt, G. Schnee, R. Welter, S. Dagorne, *Chem. Commun.* **2010**, 46, 2480–2482.
- [199] M. Wu, M. A. M. Gill, L. Yunpeng, L. Falivene, L. Yongxin, R. Ganguly, L. Cavallo, F. García, *Dalt. Trans.* **2015**, 44, 15166–15174.
- [200] G. Schnee, A. Bolley, F. Hild, D. Specklin, S. Dagorne, *Catal. Today* **2017**, 289, 204–210.
- [201] G. Schnee, D. Specklin, J. P. Djukic, S. Dagorne, *Organometallics* **2016**, 35, 1726–1734.
- [202] G. Schnee, O. NietoFaza, D. Specklin, B. Jacques, L. Karmazin, R. Welter, C. Silvalópez, S. Dagorne, *Chem. - A Eur. J.* **2015**, 21, 17959–17972.
- [203] C.-C. Tai, Y.-T. Chang, J.-H. Tsai, T. Jurca, G. P. A. Yap, T.-G. Ong, *Organometallics* **2012**, 31, 637–643.
- [204] W. C. Shih, C. H. Wang, Y. T. Chang, G. P. A. Yap, T. G. Ong, *Organometallics* **2009**, 28, 1060–1067.

- [205] V. A. Pollard, M. A. Fuentes, S. D. Robertson, C. Weetman, A. R. Kennedy, J. Brownlie, F. J. Angus, C. Smylie, R. E. Mulvey, *Polyhedron* **2021**, 209, 115469.
- [206] V. A. Pollard, M. A. Fuentes, S. D. Robertson, C. Weetman, A. R. Kennedy, J. Brownlie, F. J. Angus, C. Smylie, R. E. Mulvey, *Polyhedron* **2021**, 209, 115469.
- [207] S. Bellemin-Laponnaz, S. Dagorne, *Chem. Rev.* **2014**, 114, 8747–8774.
- [208] A. J. I. Arduengo, S. F. Gamper, M. Tamm, J. C. Calabrese, F. Davidson, H. A. Craig, *J. Am. Chem. Soc.* **1995**, 117, 572–573.
- [209] A. J. Arduengo, H. V. R. Dias, R. L. Harlow, M. Kline, *J. Am. Chem. Soc.* **1992**, 114, 5530–5534.
- [210] L. L. Anderson, J. A. R. Schmidt, J. Arnold, R. G. Bergman, *Organometallics* **2006**, 25, 3394–3406.
- [211] A. P. Duncan, S. M. Mullins, J. Arnold, R. G. Bergman, *Organometallics* **2001**, 20, 1808–1819.
- [212] C. Janiak, P.-G. Lassahn, *Macromol. Symp.* **2006**, 236, 54–62.
- [213] D. A. Walker, T. J. Woodman, M. Schormann, D. L. Hughes, M. Bochmann, *Organometallics* **2003**, 22, 797–803.
- [214] J. Klosin, G. R. Roof, E. Y. X. Chen, K. A. Abboud, *Organometallics* **2000**, 19, 4684–4686.
- [215] A. D. Horton, J. De With, *Organometallics* **1997**, 16, 5424–5436.
- [216] P. A. Cameron, V. C. Gibson, C. Redshaw, J. A. Segal, A. J. P. White, D. J. Williams, *J. Chem. Soc., Dalt. Trans.* **2002**, 31, 415–422.
- [217] S. Dagorne, I. Janowska, R. Welter, J. Zakrzewski, G. Jaouen, *Organometallics* **2004**, 23, 4706–4710.
- [218] S. Dagorne, F. Le Bideau, R. Welter, S. Bellemin-Laponnaz, A. Maise-François, *Chem. - A Eur. J.* **2007**, 13, 3202–3217.
- [219] N. Bavarian, M. C. Baird, *Organometallics* **2005**, 24, 2889–2897.
- [220] N. Millot, C. C. Santini, B. Fenet, J. M. Basset, *Eur. J. Inorg. Chem.* **2002**, 2002, 3328–3335.
- [221] X. Chen, F. C. Liu, C. E. Plečnik, S. Liu, B. Du, E. A. Meyers, S. G. Shore, *Organometallics* **2004**, 23, 2100–2106.
- [222] M. Ullrich, A. J. Lough, D. W. Stephan, *J. Am. Chem. Soc.* **2009**, 131, 52–53.
- [223] C. Camp, L. N. Grant, R. G. Bergman, J. Arnold, *Chem. Commun.* **2016**, 52, 5538–5541.
- [224] C. Camp, C. E. Kefalidis, J. Pécaut, L. Maron, M. Mazzanti, *Angew. Chemie Int. Ed.* **2013**, 52, 12646–12650.
- [225] J. Zhu, D. Mukherjee, A. D. Sadow, *Chem. Commun.* **2012**, 48, 464–466.
- [226] A. Pindwal, A. Ellern, A. D. Sadow, *Organometallics* **2016**, 35, 1674–1683.
- [227] T. Steinke, B. K. Shaw, H. Jong, B. O. Patrick, M. D. Fryzuk, J. C. Green, *J. Am. Chem. Soc.* **2009**, 131, 10461–10466.
- [228] Z. R. Turner, R. Bellabarba, R. P. Tooze, P. L. Arnold, *J. Am. Chem. Soc.* **2010**, 132, 4050–4051.

- [229] T. Hatanaka, Y. Ohki, K. Tatsumi, *Angew. Chemie Int. Ed.* **2014**, *53*, 2727–2729.
- [230] D. Prema, Y. L. N. Mathota Arachchige, R. E. Murray, L. M. Slaughter, *Chem. Commun.* **2015**, *51*, 6753–6756.
- [231] D. Tapu, D. A. Dixon, C. Roe, *Chem. Rev.* **2009**, *109*, 3385–3407.
- [232] S. Díez-González, E. D. Stevens, N. M. Scott, J. L. Petersen, S. P. Nolan, *Chem. - A Eur. J.* **2008**, *14*, 158–168.
- [233] S. Guo, M. H. Lim, H. V. Huynh, *Organometallics* **2013**, *32*, 7225–7233.
- [234] F. Lazreg, F. Nahra, C. S. J. Cazin, *Coord. Chem. Rev.* **2015**, *293–294*, 48–79.
- [235] T. M. Gilbert, R. G. Bergman, *Organometallics* **1983**, *2*, 1458–1460.
- [236] T. M. Gilbert, R. G. Bergman, J. S. Merola, A. P. Ginsberg, *Inorg. Synth.* **1990**, *27*, 19–22.
- [237] X. Gao, N. Li, R. B. King, *Inorganica Chim. Acta* **2015**, *436*, 94–102.
- [238] M. Findlater, K. M. Schultz, W. H. Bernskoetter, A. Cartwright-Sykes, D. M. Heinekey, M. Brookhart, *Inorg. Chem.* **2012**, *51*, 4672–4678.
- [239] S. S. Rozenel, R. Padilla, C. Camp, J. Arnold, *Chem. Commun.* **2014**, *50*, 2612–2614.
- [240] F. A. Cotton, C. A. Murillo, R. A. Walton, *Multiple Bonds between Metal Atoms*, Springer Science And Business Media, New York, USA, **2005**.
- [241] P. Bag, C. Weetman, S. Inoue, *Angew. Chemie Int. Ed.* **2018**, *57*, 14394–14413.
- [242] P. Bag, A. Porzelt, P. J. Altmann, S. Inoue, *J. Am. Chem. Soc.* **2017**, *139*, 14384–14387.
- [243] C. Pluta, K.-R. Pörschke, C. Krüger, K. Hildenbrand, *Angew. Chemie Int. Ed. English* **1993**, *32*, 388–390.
- [244] R. J. Wright, A. D. Phillips, P. P. Power, *J. Am. Chem. Soc.* **2003**, *125*, 10784–10785.
- [245] B. Li, S. Kundu, H. Zhu, H. Keil, R. Herbst-Irmer, D. Stalke, G. Frenking, D. M. Andrada, H. W. Roesky, *Chem. Commun.* **2017**, *53*, 2543–2546.
- [246] C. Weetman, A. Porzelt, P. Bag, F. Hanusch, S. Inoue, *Chem. Sci.* **2020**, *11*, 4817–4827.
- [247] N. Etkin, D. W. Stephan, *Organometallics* **1998**, *17*, 763–765.
- [248] T. Shima, Z. Hou, *Organometallics* **2009**, *28*, 2244–2252.
- [249] M. Nagaoka, H. Tsuruda, M. A. Amako, H. Suzuki, T. Takao, *Angew. Chemie - Int. Ed.* **2015**, *54*, 14871–14874.
- [250] T. Shima, Y. Sugimura, H. Suzuki, *Organometallics* **2009**, *28*, 871–881.
- [251] M. Saito, S. Kojima, A. Inagaki, K. Seki, T. Takao, *J. Organomet. Chem.* **2019**, *885*, 7–20.
- [252] A. I. Sizov, T. M. Zvukova, V. K. Belsky, B. M. Bulychev, *J. Organomet. Chem.* **2001**, *619*, 36–42.
- [253] H. Nöth, A. Schlegel, J. Knizek, I. Krossing, W. Ponikvar, T. Seifert, *Chem. - A Eur. J.* **1998**, *4*, 2191–2203.
- [254] P. Vajeeston, P. Ravindran, A. Kjekshus, H. Fjellvåg, *Phys. Rev. B - Condens. Matter Mater.*

- Phys.* **2004**, 69, 1–4.
- [255] H. W. Brinks, B. C. Hauback, *J. Alloys Compd.* **2003**, 354, 143–147.
- [256] A. R. Barron, G. Wilkinson, *Polyhedron* **1986**, 5, 1897–1915.
- [257] T. M. Gilbert, R. G. Bergman, *J. Am. Chem. Soc.* **1985**, 107, 3502–3507.
- [258] J. J. Am ; Wasserman, H. J. Kubas, G. J. Ryan, R. R. Upmakis, R. R. Gadd, G. E. Poliakoff, M. Simpson, . B Turner, J. J. Wyman, R. Simpson, A. F. Church, S. P. Grevels, F.-W. Herman, H. Schaffner, K. Sweany, R. L. Crabtree, R. H. Lavin, M. Morris, *J. Am. Chem. Soc* **1986**, 108, 6994–7001.
- [259] K. Abdur-Rashid, D. G. Gusev, S. E. Landau, A. J. Lough, R. H. Morris, *J. Am. Chem. Soc.* **1998**, 120, 11826–11827.
- [260] K. Hobson, C. J. Carmalt, C. Bakewell, *Chem. Sci.* **2020**, 11, 6942–6956.
- [261] O. Ekkert, A. J. P. White, H. Toms, M. R. Crimmin, *Chem. Sci.* **2015**, 6, 5617–5622.
- [262] T. H. Peterson, *Organometallics* **1999**, 18, 2005–2020.
- [263] R. P. Hughes, A. Williamson, R. D. Sommer, A. L. Rheingold, *J. Am. Chem. Soc.* **2001**, 123, 7443–7444.
- [264] V. Miranda-Soto, D. B. Grotjahn, A. G. DiPasquale, A. L. Rheingold, *J. Am. Chem. Soc.* **2008**, 130, 13200–13201.
- [265] T. M. Gilbert, R. G. Bergman, *J. Am. Chem. Soc.* **1985**, 107, 6391–6393.
- [266] S. Kurumada, S. Takamori, M. Yamashita, *Nat. Chem.* **2020**, 12, 36–39.
- [267] M. Gorol, N. C. Mösch-Zanetti, H. W. Roesky, M. Noltemeyer, H. G. Schmidt, *Chem. Commun.* **2003**, 46–47.
- [268] H. Schmidbaur, A. Schier, *Angew. Chemie Int. Ed.* **2015**, 54, 746–784.
- [269] P. Braunstein, T. M. G. Carneiro, D. Matt, A. Tiripicchio, M. T. Camellini, *Angew. Chemie Int. Ed. English* **1986**, 25, 748–749.
- [270] F. Bachechi, *J. Organomet. Chem.* **1994**, 474, 191–197.
- [271] A. Albinati, C. Anklin, P. Janser, H. Lehner, D. Matt, P. S. Pregosin, L. M. Venanzi, *Inorg. Chem.* **1989**, 28, 1105–1111.
- [272] M. Maekawa, Y. Kubo, K. Sugimoto, T. Okubo, T. Kuroda-Sowa, M. Munakata, *Eur. J. Inorg. Chem.* **2016**, 2016, 78–91.
- [273] T. Kimura, K. Ishiwata, S. Kuwata, T. Ikariya, *Organometallics* **2012**, 31, 1204–1207.
- [274] A. Sykes, K. R. Mann, *J. Am. Chem. Soc.* **1988**, 110, 8252–8253.
- [275] C. R. Turlington, D. P. Harrison, P. S. White, M. Brookhart, J. L. Templeton, *Inorg. Chem.* **2013**, 52, 11351–11360.
- [276] A. G. Sykes, K. R. Mann, *Inorg. Chem.* **1990**, 29, 4449–4453.
- [277] F. W. B. Einstein, R. H. Jones, X. Zhang, ' And, D. Sutton', X. Zhang, D. Sutton, *Synthesis and*

X-Ray Structure Determination of the Ir-Ag-Ir Donor-Acceptor Metal-Metal Bonded Complex
[{(Q5~5~e5)(~),~r}~g][~4], n.d.

- [278] D. J. Liston, C. A. Reed, C. W. Eigenbrot, W. R. Scheidt, *Inorg. Chem.* **1987**, *26*, 2739–2740.
- [279] Z. Xie, T. Jelinek, R. Bau, C. A. Reed, *J. Am. Chem. Soc.* **2002**, *116*, 1907–1913.
- [280] B. Qian, D. L. Ward, M. R. Smith, *Organometallics* **1998**, *17*, 3070–3076.
- [281] E. Rivard, P. J. Ragogna, A. R. McWilliams, A. J. Lough, I. Manners, *Inorg. Chem.* **2005**, *44*, 6789–6798.
- [282] F. Acha, M. A. Garralda, R. Hernández, L. Ibarlucea, E. Pinilla, M. R. Torres, M. Zarandona, *Eur. J. Inorg. Chem.* **2006**, *2006*, 3893–3900.
- [283] K.-I. Fujita, H. Nakaguma, F. Hanasaka, R. Yamaguchi, **2002**, DOI 10.1021/om020266.
- [284] E. Suárez, P. Plou, D. G. Gusev, M. Martín, E. Sola, *Inorg. Chem.* **2017**, *56*, 7190–7199.
- [285] P. Sangtrirutnugul, T. D. Tilley, *Organometallics* **2007**, *26*, 5557–5568.
- [286] R. Lalrempuia, M. Iglesias, V. Polo, P. J. Sanz Miguel, F. J. Fernández-Alvarez, J. J. Pérez-Torrente, L. A. Oro, *Angew. Chemie - Int. Ed.* **2012**, *51*, 12824–12827.
- [287] T. Kimura, N. Koiso, K. Ishiwata, S. Kuwata, T. Ikariya, *J. Am. Chem. Soc.* **2011**, *133*, 8880–8883.
- [288] T. J. J. Sciarone, C. A. Nijhuis, A. Meetsma, B. Hessen, *Dalt. Trans.* **2006**, 4896–4904.
- [289] G. Erker, *Dalt. Trans.* **2005**, 1883–1890.
- [290] S. Dagorne, F. Le Bideau, R. Welter, S. Bellemin-Laponnaz, A. Maise-François, *Chem. - A Eur. J.* **2007**, *13*, 3202–3217.
- [291] S. Litters, E. Kaifer, M. Enders, H. J. Himmel, *Nat. Chem.* **2013**, *5*, 1029–1034.
- [292] A. M. Appel, J. E. Bercaw, A. B. Bocarsly, H. Dobbek, D. L. Dubois, M. Dupuis, J. G. Ferry, E. Fujita, R. Hille, P. J. A. Kenis, C. A. Kerfeld, R. H. Morris, C. H. F. Peden, A. R. Portis, S. W. Ragsdale, T. B. Rauchfuss, J. N. H. Reek, L. C. Seefeldt, R. K. Thauer, G. L. Waldrop, *Chem. Rev.* **2013**, *113*, 6621–6658.
- [293] D. H. Gibson, *Chem. Rev.* **1996**, *96*, 2063–2095.
- [294] D. M. Heinekey, D. A. Fine, T. G. P. Harper, S. T. Michel, *Can. J. Chem.* **1995**, *73*, 1116–1125.
- [295] M. R. Mason, A. R. Barron, J. M. Smith, S. G. Bott, *J. Am. Chem. Soc.* **1993**, *115*, 4971–4984.
- [296] G. Bai, H. W. Roesky, J. Li, M. Noltemeyer, H. G. Schmidt, *Angew. Chemie - Int. Ed.* **2003**, *42*, 5502–5506.
- [297] D. Neculai, H. W. Roesky, A. M. Neculai, J. Magull, B. Walfort, D. Stalke, *Angew. Chemie - Int. Ed.* **2002**, *41*, 4294–4296.
- [298] R. J. Wehmschulte, P. P. Power, *J. Am. Chem. Soc.* **1997**, *119*, 8387–8388.
- [299] C. J. Harlan, M. R. Mason, A. R. Barron, *Organometallics* **1994**, *13*, 2957–2969.
- [300] J. Hicks, A. Heilmann, P. Vasko, J. M. Goicoechea, S. Aldridge, *Angew. Chemie - Int. Ed.* **2019**,

58, 17265–17268.

- [301] C. Weetman, P. Bag, T. Szilvási, C. Jandl, S. Inoue, *Angew. Chemie - Int. Ed.* **2019**, *58*, 10961–10965.
- [302] M. D. Anker, M. P. Coles, *Angew. Chemie Int. Ed.* **2019**, *58*, 18261–18265.
- [303] J. P. Krogman, B. M. Foxman, C. M. Thomas, *J. Am. Chem. Soc.* **2011**, *133*, 14582–14585.
- [304] H. Memmler, U. Kauper, L. H. Gade, I. J. Scowen, M. McPartlin, *Chem. Commun.* **1996**, 1751–1752.
- [305] J. R. Pinkes, B. D. Steffey, J. C. Vites, A. R. Cutler, *Organometallics* **1994**, *13*, 21–23.
- [306] C. M. Mömning, E. Otten, G. Kehr, R. Fröhlich, S. Grimme, D. W. Stephan, G. Erker, *Angew. Chemie - Int. Ed.* **2009**, *48*, 6643–6646.
- [307] G. Ménard, D. W. Stephan, *Angew. Chemie - Int. Ed.* **2011**, *50*, 8396–8399.
- [308] G. Ménard, D. W. Stephan, *J. Am. Chem. Soc.* **2010**, *132*, 1796–1797.
- [309] O. Cooper, C. Camp, J. Pécaut, C. E. Kefalidis, L. Maron, S. Gambarelli, M. Mazzanti, *J. Am. Chem. Soc.* **2014**, *136*, 6716–6723.
- [310] D. H. Hong, L. J. Murray, *Eur. J. Inorg. Chem.* **2019**, 2019, 2146–2153.
- [311] M. V. Vollmer, R. C. Cammarota, C. C. Lu, *Eur. J. Inorg. Chem.* **2019**, 2019, 2140–2145.
- [312] V. Mougél, C. Camp, J. Pécaut, C. Copéret, L. Maron, C. E. Kefalidis, M. Mazzanti, *Angew. Chemie - Int. Ed.* **2012**, *51*, 12280–12284.
- [313] A. Schmidt, F. W. Heinemann, C. E. Kefalidis, L. Maron, P. W. Roesky, K. Meyer, *Chem. – A Eur. J.* **2014**, *20*, 13501–13506.
- [314] A. Formanuk, F. Ortu, C. J. Inman, A. Kerridge, L. Castro, L. Maron, D. P. Mills, *Chem. – A Eur. J.* **2016**, *22*, 17976–17979.
- [315] L. Castro, O. P. Lam, S. C. Bart, K. Meyer, L. Maron, *Organometallics* **2010**, *29*, 5504–5510.
- [316] N. Tsoureas, L. Castro, A. F. R. Kilpatrick, F. G. N. Cloke, L. Maron, *Chem. Sci.* **2014**, *5*, 3777–3788.
- [317] C. Camp, L. Chatelain, C. E. Kefalidis, J. Pécaut, L. Maron, M. Mazzanti, *Chem. Commun.* **2015**, *51*, 15454–15457.
- [318] D. C. Leitch, L. L. Schafer, *Organometallics* **2010**, *29*, 5162–5172.
- [319] D. C. Leitch, R. H. Platel, L. L. Schafer, *J. Am. Chem. Soc.* **2011**, *133*, 15453–15463.
- [320] J. Li, X. Li, W. Huang, H. Hu, J. Zhang, C. Cui, *Chem. – A Eur. J.* **2012**, *18*, 15263–15266.
- [321] A. Heilmann, J. Hicks, P. Vasko, J. M. Goicoechea, S. Aldridge, *Angew. Chemie - Int. Ed.* **2020**, *59*, 4897–4901.
- [322] H. Zhu, J. Chai, V. Chandrasekhar, H. W. Roesky, J. Magull, D. Vidovic, H. G. Schmidt, M. Noltemeyer, P. P. Power, W. A. Merrill, *J. Am. Chem. Soc.* **2004**, *126*, 9472–9473.
- [323] M. D. Anker, R. J. Schwamm, M. P. Coles, *Chem. Commun.* **2020**, *56*, 2288–2291.

- [324] H. Bock, O. Breuer, *Angew. Chemie Int. Ed. English* **1987**, *26*, 461–462.
- [325] M. Joost, W. J. Transue, C. C. Cummins, *Chem. Commun.* **2017**, *53*, 10731–10733.
- [326] K. Eller, H. Schwarz, *Inorg. Chem.* **1990**, *29*, 3250–3252.
- [327] M. G. Fickes, A. L. Odom, C. C. Cummins, *Chem. Commun.* **1997**, 1993.
- [328] É. Bonfada, U. Abram, J. Strähle, *Zeitschrift für Anorg. und Allg. Chemie* **1998**, *624*, 757–762.
- [329] H. M. Wang, H. X. Li, X. Y. Yu, Z. G. Ren, J. P. Lang, *Tetrahedron* **2011**, *67*, 1530–1535.
- [330] X. Zhu, J. Fan, Y. Wu, S. Wang, L. Zhang, G. Yang, Y. Wei, C. Yin, H. Zhu, S. Wu, H. Zhang, *Organometallics* **2009**, *28*, 3882–3888.
- [331] H. X. Li, M. L. Cheng, H. M. Wang, X. J. Yang, Z. G. Ren, J. P. Lang, *Organometallics* **2011**, *30*, 208–214.
- [332] A. Hernán-Gómez, T. D. Bradley, A. R. Kennedy, Z. Livingstone, S. D. Robertson, E. Hevia, *Chem. Commun.* **2013**, *49*, 8659–8661.
- [333] F. Paul, S. Moulin, O. Piechaczyk, P. Le Floch, J. A. Osborn, *J. Am. Chem. Soc.* **2007**, *129*, 7294–7304.
- [334] Y. S. Han, K. Y. Jung, Y. J. Kim, K. K. Baeck, G. M. Lee, S. W. Lee, *New J. Chem.* **2019**, *43*, 15614–15625.
- [335] M. A. Bahili, E. C. Stokes, R. C. Amesbury, D. M. C. Ould, B. Christo, R. J. Horne, B. M. Kariuki, J. A. Stewart, R. L. Taylor, P. A. Williams, M. D. Jones, K. D. M. Harris, B. D. Ward, *Chem. Commun.* **2019**, *55*, 7679–7682.
- [336] M. Siebert, R. Sure, P. Deglmann, A. C. Closs, F. Lucas, O. Trapp, *J. Org. Chem.* **2020**, *85*, 8553–8562.
- [337] A. R. Sadique, M. J. Heeg, C. H. Winter, *J. Am. Chem. Soc.* **2003**, *125*, 7774–7775.
- [338] F. A. Cotton, L. M. Daniels, C. A. Murillo, *Angew. Chemie Int. Ed.* **1992**, *31*, 737–738.
- [339] H. Leopold, M. Tenne, A. Tronnier, S. Metz, I. Münster, G. Wagenblast, T. Strassner, *Angew. Chemie - Int. Ed.* **2016**, *55*, 15779–15782.
- [340] C. Camp, N. Settineri, J. Lefèvre, A. R. Jupp, J. M. Goicoechea, L. Maron, J. Arnold, *Chem. Sci.* **2015**, *6*, 6379–6384.
- [341] Y. Zhou, D. S. Richeson, *Inorg. Chem.* **1996**, *35*, 1423–1424.
- [342] S. Dagorne, I. A. Guzei, M. P. Coles, R. F. Jordan, *J. Am. Chem. Soc.* **2000**, *122*, 274–289.
- [343] A. L. Brazeau, Z. Wang, C. N. Rowley, S. T. Barry, *Inorg. Chem.* **2006**, *45*, 2276–2281.
- [344] R. D. Simpson, W. J. Marshall, *Organometallics* **1997**, *16*, 3719–3722.
- [345] D. Zhao, J. Feng, Q. Huo, N. Melosh, G. H. Fredrickson, B. F. Chmelka, G. D. Stucky, *Science (80-.)*. **1998**, *279*, 548–552.
- [346] S. Lassalle, Vers Une Catalyse Coopérative : Conception de Nouveaux Édifices Hétérobimétalliques Supportés Sur Silice, Université Claude Bernard - Lyon 1, **2021**.

- [347] E. A. Quadrelli, J.-M. Basset, *Coord. Chem. Rev.* **2010**, *254*, 707–728.
- [348] N. Merle, G. Girard, N. Popoff, A. De Mallmann, Y. Bouhoute, J. T. Trébosc, E. Berrier, J.-F. O. Paul, C. P. Nicholas, I. Del Rosal, L. Maron, J. Régis, R. M. Gauvin, L. Delevoye, M. Taoufik, *Inorg. Chem* **2013**, *52*, 25.
- [349] C. C. Camp, J. P. Pécaut, M. Mazzanti, **2013**, DOI 10.1021/ja405815b.
- [350] A. M. Baranger, R. G. Bergman, *J. Am. Chem. Soc.* **1994**, *116*, 3822–3835.
- [351] B. Chattopadhyay, J. E. Dannatt, I. L. Andujar-De Sanctis, K. A. Gore, R. E. Maleczka, D. A. Singleton, M. R. Smith, *J. Am. Chem. Soc.* **2017**, *139*, 7864–7871.
- [352] Y. Cao, W. C. Shih, O. V. Ozerov, *Organometallics* **2019**, *38*, 4076–4081.
- [353] M. Oishi, M. Kino, M. Saso, M. Oshima, H. Suzuki, *Organometallics* **2012**, *31*, 4658–4661.
- [354] C. M. Zinser, F. Nahra, L. Falivene, M. Brill, D. B. Cordes, A. M. Z. Slawin, L. Cavallo, C. S. J. Cazin, S. P. Nolan, *Chem. Commun.* **2019**, *55*, 6799–6802.
- [355] B. Marciniak, J. Walkowiak, *Chem. Commun.* **2008**, 2695–2697.
- [356] C. M. Wyss, J. Bitting, J. Bacsá, T. G. Gray, J. P. Sadighi, *Organometallics* **2016**, *35*, 71–74.
- [357] B. Marciniak, H. Maciejewski, *Coord. Chem. Rev.* **2001**, *223*, 301–335.
- [358] J. E. Low, A. Foelske-Schmitz, F. Krumeich, M. Würle, D. Baudouin, F. Rascón, C. Copéret, *Dalt. Trans.* **2013**, *42*, 12620–12625.
- [359] F. Drault, C. Comminges, F. Can, L. Pirault-Roy, F. Epron, A. Le Valant, *Materials (Basel)*. **2018**, *11*, DOI 10.3390/ma11050819.
- [360] B. Van Dijk, G. M. Rodriguez, L. Wu, J. P. Hofmann, A. MacChioni, D. G. H. Hetterscheid, *ACS Catal.* **2020**, *10*, 4398–4410.
- [361] S. Barman, N. Maity, K. Bhatte, S. Ould-Chikh, O. Dachwald, C. Haeßner, Y. Saih, E. Abou-Hamad, I. Llorens, J.-L. Hazemann, K. Köhler, V. D' Elia, J.-M. Basset, *ACS Catal.* **2016**, *6*, 5908–5921.
- [362] J. Radnik, C. Mohr, P. Claus, *Phys. Chem. Chem. Phys.* **2003**, *5*, 172–177.
- [363] L. Sun, Y. Wang, N. Guan, L. Li, *Energy Technol.* **2020**, *8*, 1900826.
- [364] C. Hammond, R. L. Jenkins, N. Dimitratos, J. A. Lopez-Sanchez, M. H. Ab Rahim, M. M. Forde, A. Thetford, D. M. Murphy, H. Hagen, E. E. Stangland, J. M. Moulijn, S. H. Taylor, D. J. Willock, G. J. Hutchings, *Chem. – A Eur. J.* **2012**, *18*, 15735–15745.
- [365] A. Sattler, *ACS Catal.* **2018**, *8*, 2296–2312.
- [366] C. Kemball, *Proc. R. Soc. London. Ser. A. Math. Phys. Sci.* **1953**, *217*, 376–389.
- [367] A. Frennet, *Catal. Rev.* **1974**, *10*, 37–68.
- [368] P. J. Robertson, M. S. Scurrall, C. Kemball, *J. Chem. Soc. Faraday Trans. 1 Phys. Chem. Condens. Phases* **1975**, *71*, 903–912.
- [369] J. Joubert, A. Salameh, V. Krakoviack, F. Delbecq, P. Sautet, C. Copéret, J. M. Basset, *J.*

- Phys. Chem. B* **2006**, *110*, 23944–23950.
- [370] D. L. Strout, S. Zarić, S. Niu, M. B. Hall, *J. Am. Chem. Soc.* **1996**, *118*, 6068–6069.
- [371] M. E. Thompson, S. M. Baxter, A. R. Bulls, B. J. Burger, M. C. Nolan, B. D. Santarsiero, W. P. Schaefer, J. E. Bercaw, *J. Am. Chem. Soc.* **1987**, *109*, 203–219.
- [372] A. Mirich, T. H. Miller, E. Klotz, B. Mattson, *J. Chem. Educ.* **2015**, *92*, 2087–2093.
- [373] J. Zeng, M. Tarazkar, C. Palmer, M. J. Gordon, H. Metiu, E. W. McFarland, *J. Phys. Chem. C* **2021**, *125*, 18665–18672.
- [374] G. C. Bond, in *Met. React. Hydrocarb.* (Ed.: G.C. Bond), Springer US, Boston, MA, **2005**, pp. 257–289.
- [375] R. L. Burwell, *Acc. Chem. Res.* **1969**, *2*, 289–296.
- [376] R. Wischert, C. Copéret, F. Delbecq, P. Sautet, *Angew. Chemie - Int. Ed.* **2011**, *50*, 3202–3205.
- [377] C. Thieuleux, E. A. Quadrelli, J.-M. Basset, J. Döbler, J. Sauer, *Chem. Commun.* **2004**, 1729–1731.
- [378] R. J. P. Corriu, Y. Guari, A. Mehdi, C. Reyé, C. Thieuleux, L. Datas, *Chem. Commun.* **2001**, *37*, 763–764.
- [379] R. C. Clark, J. S. Reid, *Acta Crystallogr. Sect. A Found. Crystallogr.* **1995**, *51*, 887–897.
- [380] G. M. Sheldrick, *Acta Crystallogr. Sect. A Found. Crystallogr.* **2015**, *71*, 3–8.
- [381] O. V. Dolomanov, L. J. Bourhis, R. J. Gildea, J. A. K. Howard, H. Puschmann, *J. Appl. Crystallogr.* **2009**, *42*, 339–341.
- [382] G. M. Sheldrick, *Acta Crystallogr. Sect. C Struct. Chem.* **2015**, *71*, 3–8.
- [383] M. J. Frisch, G. W. Trucks, H. B. Schlegel, G. E. Scuseria, M. a. Robb, J. R. Cheeseman, G. Scalmani, V. Barone, G. a. Petersson, H. Nakatsuji, X. Li, M. Caricato, a. V. Marenich, J. Bloino, B. G. Janesko, R. Gomperts, B. Mennucci, H. P. Hratchian, J. V. Ortiz, a. F. Izmaylov, J. L. Sonnenberg, Williams, F. Ding, F. Lipparini, F. Egidi, J. Goings, B. Peng, A. Petrone, T. Henderson, D. Ranasinghe, V. G. Zakrzewski, J. Gao, N. Rega, G. Zheng, W. Liang, M. Hada, M. Ehara, K. Toyota, R. Fukuda, J. Hasegawa, M. Ishida, T. Nakajima, Y. Honda, O. Kitao, H. Nakai, T. Vreven, K. Throssell, J. a. Montgomery Jr., J. E. Peralta, F. Ogliaro, M. J. Bearpark, J. J. Heyd, E. N. Brothers, K. N. Kudin, V. N. Staroverov, T. a. Keith, R. Kobayashi, J. Normand, K. Raghavachari, a. P. Rendell, J. C. Burant, S. S. Iyengar, J. Tomasi, M. Cossi, J. M. Millam, M. Klene, C. Adamo, R. Cammi, J. W. Ochterski, R. L. Martin, K. Morokuma, O. Farkas, J. B. Foresman, D. J. Fox, **2016**, Gaussian 16, Revision C.01, Gaussian, Inc., Wallin.
- [384] J. P. Perdew, J. A. Chevary, S. H. Vosko, K. A. Jackson, M. R. Pederson, D. J. Singh, C. Fiolhais, *Phys. Rev. B* **1992**, *46*, 6671–6687.
- [385] D. Andrae, U. Häußermann, M. Dolg, H. Stoll, H. Preuß, *Theor. Chim. Acta* **1990**, *77*, 123–141.
- [386] A. W. Ehlers, M. Böhme, S. Dapprich, A. Gobbi, A. Höllwarth, V. Jonas, K. F. Köhler, R.

- Stegmann, A. Veldkamp, G. Frenking, *Chem. Phys. Lett.* **1993**, 208, 111–114.
- [387] A. Bergner, M. Dolg, W. Küchle, H. Stoll, H. Preuß, *Mol. Phys.* **1993**, 80, 1431–1441.
- [388] R. Ditchfield, W. J. Hehre, J. A. Pople, *J. Chem. Phys.* **1971**, 54, 724–728.
- [389] W. J. Hehre, R. Ditchfield, J. A. Pople, *J. Chem. Phys.* **1972**, 56, 2257–2261.
- [390] P. C. Hariharan, J. A. Pople, *Theor. Chim. Acta* **1973**, 28, 213–222.
- [391] M. M. Francl, W. J. Pietro, W. J. Hehre, J. S. Binkley, M. S. Gordon, D. J. DeFrees, J. A. Pople, *J. Chem. Phys.* **1982**, 77, 3654–3665.
- [392] A. E. Reed, L. A. Curtiss, F. Weinhold, *Chem. Rev.* **1988**, 88, 899–926.

Appendix

S1. XRD DATA

Table S1. Crystallographic parameters for compounds 2,3,5,7

Compound	2	3	5	7
CCDC #	1836207	1836205	1836206	1850906
Formula	$2(\text{C}_{24}\text{H}_{39}\text{Al}_1\text{N}_2\text{O}_1)$	$2(\text{C}_{50}\text{H}_{77}\text{Al}_1\text{N}_2\text{O}_3) \cdot 3(\text{C}_6\text{H}_6)$	$\text{C}_{66}\text{H}_{108}\text{Al}_1\text{K}_1\text{N}_2\text{O}_7$	$\text{C}_{46}\text{H}_{67}\text{Al}_1\text{N}_2\text{O}_3$
cryst syst	Orthorhombic	Monoclinic	Monoclinic	Monoclinic
space group	$Pc a 2_1$	$P2_1/c$	Cc	$P2_1/c$
volume (\AA^3)	4878.2(7)	10950(3)	7558.6(20)	4329.6(9)
a (\AA)	16.3437(11)	25.392(5)	23.374(3)	11.5882(11)
b (\AA)	9.6410(8)	21.778(2)	14.3114(9)	9.9069(14)
c (\AA)	30.959(3)	21.355(4)	26.926(3)	38.069(4)
α (deg)	90	90	90	90
β (deg)	90	111.99(2)	122.947(17)	97.839(9)
γ (deg)	90	90	90	90
Z	8	4	4	4
formula weight (g/mol)	797.14	1796.65	2213.33	723.03
density (g cm^{-3})	1.085	1.090	0.972	1.109
absorption coefficient (mm^{-1})	0.099	0.080	0.125	0.087
F(000)	1744	3928	2420	1576
$2\theta_{\text{max}}$ ($^\circ$)	29.573	29.706	29.651	29.749
temp (K)	150.0(1)	150.0(1)	150.0(1)	150.0(1)
total no. reflections	46949	111871	67904	43850
unique reflections [R(int)]	11928 [0.084]	27442[0.068]	18429 [0.047]	10796 [0.15]
no. refined parameters	506	1171	694	470
Final R indices [$I > 2\sigma(I)$]	R1 = 0.102, wR2 = 0.192	R1 = 0.065, wR2 = 0.120	R1 = 0.053, wR2 = 0.109	R1 = 0.080, wR2 = 0.115
Largest diff. peak and hole ($\text{e}\cdot\text{\AA}^{-3}$)	1.97 and -1.06	0.69 and -0.80	0.33 and -0.41	1.24 and -1.22
GoF	1.00	0.98	0.94	1.07

Table S2. Crystallographic parameters for compounds 10-14

Compound	10	11	12	13	14
CCDC #	/	2108876	2108877	2108878	2108879
Formula	C ₃₆ H ₅₁ AlCuN ₅ O ₅	C ₃₆ H ₆₆ Al ₂ Ir ₂	C ₂₈ H ₄₈ Al ₂ Ir ₂	C ₂₄ H ₃₉ Allr ₂	AlC _{32.5} H ₅₁ Ir ₃
cryst syst	Monoclinic	Triclinic	Monoclinic	Orthorhombic	Triclinic
space group	P2 ₁ /c	P-1	P2 ₁ /c	Pnma	P-1
volume (Å ³)	3853.8(4)	987.69(10)	3129.8(4)	2711.5(3)	3544.8(2)
a (Å)	16.9574(9)	9.1811(4)	14.8959(12)	17.4319(9)	11.7250(4)
b (Å)	12.9296(9)	11.5725(6)	16.6191(13)	12.8825(7)	15.4698(5)
c (Å)	17.5944(12)	11.6674(6)	12.6572(8)	12.0745(10)	20.2149(7)
α (deg)	90	61.824(5)	90	90	82.468(3)
β (deg)	92.545(5)	69.364(5)	92.728(6)	90	80.662(3)
γ (deg)	90	67.652(4)	90	90	80.183(3)
Z	4	1	4	4 (Z'=0.5)	4 (Z'=2)
formula weight (g/mol)	724.36	937.24	823.02	738.93	1045.31
density (g cm ⁻³)	1.248	1.576	1.747	1.810	1.959
absorption coefficient (mm ⁻¹)	0.635	6.795	8.564	9.844	11.277
F(000)	1536.0	462.0	1584.0	1400.0	1876.0
θ _{max} (°)	28.9250	29.586	29.639	29.777	29.699
temp (K)	150.01(10)	150.01(10)	150.01(10)	150.00(10)	150.01(10)
total no. reflections	9926	51034	41635	52459	93104
independent reflections [R(int)]	9904 [0.0682]	5151 [0.0652]	7944 [0.0844]	3823	18179
no. refined parameters	434	191	304	159	644
Final R indices [I > 2σ(I)]	R1 = 0.0461, wR2 = 0.1020	R1 = 0.0451, wR2 = 0.0872	R1 = 0.0921, wR2 = 0.2381	0.064(0)	0.052(0)
GoF	/	1.149	1.094	1.109	1.107

Table S3. Crystallographic parameters for compounds 15,17,23-25.

Compound	15	17	23	24	25
CCDC #	2059453	2059454	2059455	2059456	2059457
Formula	C ₂₉ H ₄₇ AlIrO	C ₃₄ H ₅₂ AlIrNO	C ₄₈ H ₇₄ Al ₂ N ₂ O ₃ · C ₅ H ₁₁	C ₄₀ H ₆₃ AlN ₂ O ₂	C ₄₂ H ₇₀ AlIrN ₂ O
Formula Weight (g.mol ⁻¹)	630.84	709.94	852.18	630.90	838.18
Crystal System	Triclinic	Monoclinic	Monoclinic	Monoclinic	Triclinic
Space Group	<i>P</i> -1	<i>P</i> ₂ / <i>c</i>	<i>P</i> ₂ / <i>n</i>	<i>C</i> ₂ / <i>c</i>	<i>P</i> -1
Temperature (K)	150	150	150	150	150
<i>a</i> (Å)	9.4210(5)	10.8251(7)	14.3130(12)	22.6528(13)	10.7834(5)
<i>b</i> (Å)	12.5263(6)	17.0529(9)	19.0982(14)	16.2776(9)	12.5228(6)
<i>c</i> (Å)	12.7346(6)	18.9985(12)	20.1954(17)	20.2247(16)	16.2730(5)
α (°)	92.871(4)	90	90	90	92.513(3)
β (°)	94.762(4)	104.875(7)	101.947(8)	92.438(6)	95.552(3)
γ (°)	98.459(4)	90	90	90	107.863(4)
Volume (Å ³)	1478.37(13)	3389.6(4)	5400.9(8)	7450.8(8)	2075.45(16)
Density (g.cm ⁻³)	1.417	1.391	1.048	1.125	1.341
<i>Z</i>	2	4	4	8	2
Radiation type	Mo <i>K</i> α	Mo <i>K</i> α	Mo <i>K</i> α	Mo <i>K</i> α	Mo <i>K</i> α
μ (mm ⁻¹)	4.56	3.99	0.09	0.09	3.27
<i>T</i> _{min} , <i>T</i> _{max}	0.335, 0.865	0.596, 1.000	0.969, 0.979	0.966, 0.979	0.303, 0.577
No. Measured Reflections	38883	46204	30866	46421	52189
No. Independent Reflections	7503	8728	12879	9499	10603
No. Observed Reflections	6398	6960	8851	7146	9621
<i>R</i> _{int}	0.071	0.063	0.042	0.049	0.070
(<i>sin</i> θ / λ) _{max} (Å ⁻¹)	0.700	0.699	0.697	0.698	0.700

Table S4. Crystallographic parameters for compounds 16,18-20.

Compound	16	18	19	20
CCDC #	2108881	2124619	2108882	2108883
Formula	C ₃₃ H ₅₃ Al ₂ Ir ₂ N	C ₃₇ H ₅₅ Allr ₃ N ₂	C ₄₃ H ₇₄ Al ₂ Ir ₂ KO ₂	C ₄₀ H ₆₀ Ag ₄ Ir ₄
cryst syst	Triclinic	Monoclinic	Monoclinic	Tetragonal
space group	P-1	P2 ₁ /n	P2 ₁ /c	P4 ₂ /mbc
volume (Å ³)	3542.0(3)	9178.2(8)	4810.8(4)	2671.7(2)
a (Å)	11.4132(5)	22.3311(11)	18.9602(10)	17.7609(5)
b (Å)	16.4538(6)	19.0090(7)	12.6664(7)	17.7609(5)
c (Å)	20.5471(8)	22.7354(13)	20.2862(10)	8.4696(4)
α (deg)	78.218(3)	90	90	90
β (deg)	82.322(3)	108.008(6)	99.085(5)	90
γ (deg)	70.048(4)	90	90	90
Z	4 (Z' ^t =2)	8	4	2
formula weight (g/mol)	902.12	1131.41	1100.48	1741.16
density (g cm ⁻³)	1.692	1.638	1.519	2.164
absorption coefficient (mm ⁻¹)	7.577	8.719	5.680	11.374
F(000)	1752.00	4280.0	2188.0	1592.0
θ _{max} (°)	29.796	29.779	29.666	29.623
temp (K)	150.00(10)	150.00(10)	150.01(10)	150.00(10)
total no. reflections	93090	125567	64166	44550
independent reflections [R(int)]	18263 [0.0639]	23279 [0.0708]	12367 [0.0818]	1965
no. refined parameters	810	1002	470	108
Final R indices [I > 2σ(I)]	R1 = 0.0570 wR2 = 0.1324	R1 = 0.0538 wR2 = 0.1231	R1 = 0.0628, wR2 = 0.1502	R1 = 0.0583 wR2 = 0.1533
GoF	1.097	1.100	1.074	1.166

Table S5. Crystallographic parameters for compounds 21, 22, and 26.

Compound	21	22	26
CCDC #	2108884	2108880	2149676
Formula	C ₂₅ H ₃₈ AlF ₃ Ir ₂ O ₄ S	C ₅₄ H ₆₃ Al ₂ BF ₁₅ Ir ₂ O ₃	C ₃₂ H ₄₇ Allr ₂ O
cryst syst	Monoclinic	Monoclinic	Monoclinic
space group	P ₂ ₁ /n	P ₂ ₁ /n	P21/c
volume (Å ³)	3047.1(4)	6139.2(5)	3333.7(3)
a (Å)	12.1489(8)	11.8477(5)	8.8760(5)
b (Å)	12.2054(7)	17.9699(8)	20.4157(9)
c (Å)	20.7875(18)	29.1945(15)	18.4320(9)
α (deg)	90	90	90
β (deg)	98.676(7)	98.989(4)	93.526(4)
γ (deg)	90	90	90
Z	4	4	4
formula weight (g/mol)	902.99	1494.21	859.07
density (g cm ⁻³)	1.968	1.617	1.712
absorption coefficient (mm ⁻¹)	8.868	4.443	8.022
F(000)	1720.0	2924.0	1656.0
θ _{max} (°)	29.676	29.718	29.817
temp (K)	150.00(10)	150.01(10)	150.00(10)
total no. reflections	41557	82842	44351
independent reflections [R(int)]	7867	15537 [0.0582]	8532
no. refined parameters	335	976	340
Final R indices [I > 2σ(I)]	0.052(1)	R1 = 0.0630, wR2 = 0.1450	R1=0.0767, wR2=0.1824
GoF	1.079	1.071	/

S2. COMPUTATIONAL DATA

Figure S1. Computed data of complex 12

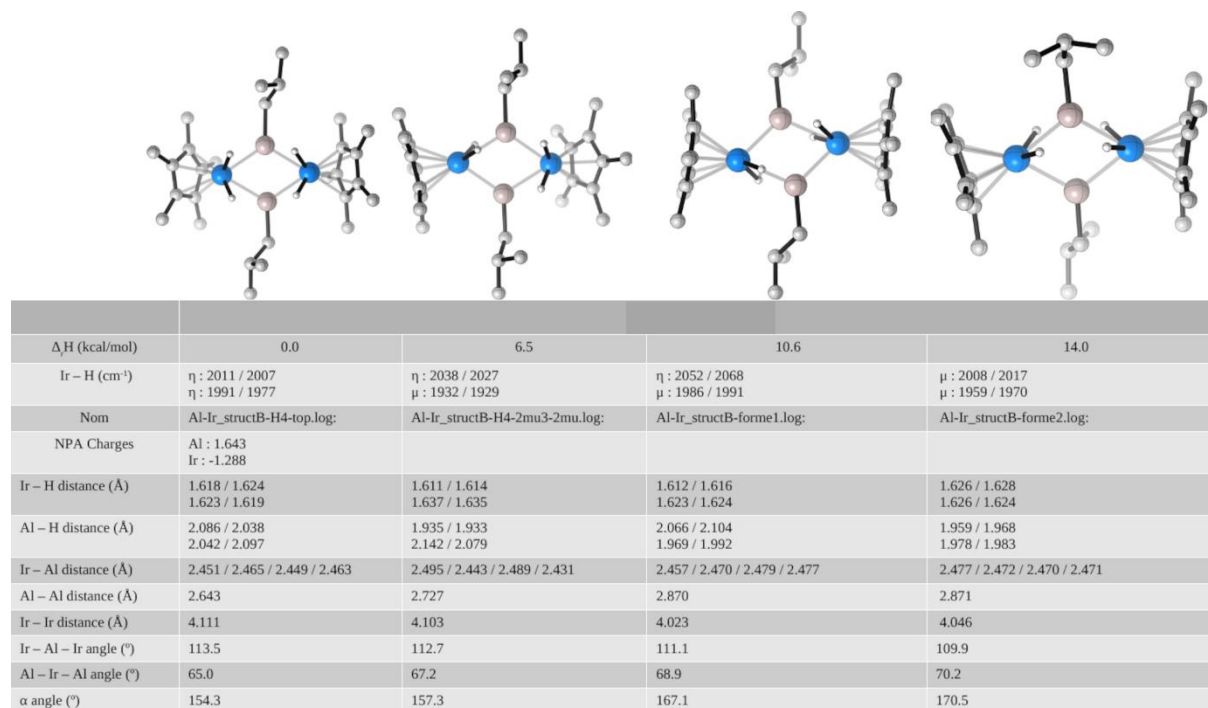


Figure S2. Computed data of complex 22

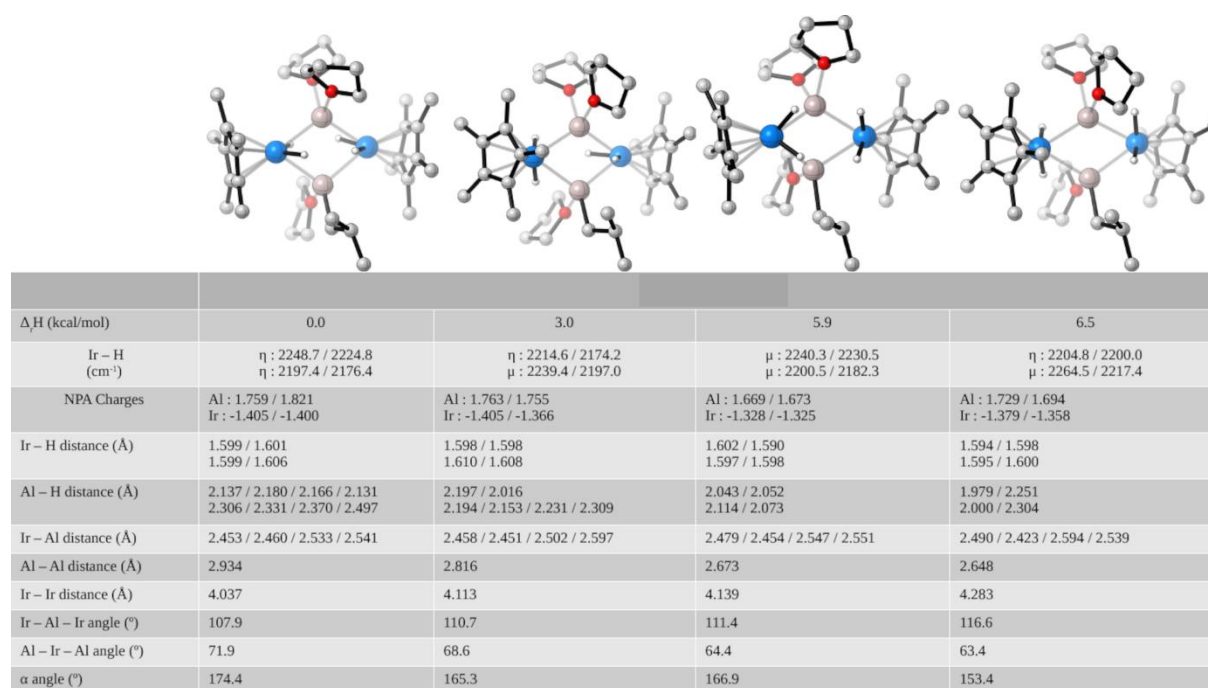


Figure S3. Computed enthalpy alternative pathways for the reaction of CO₂ with 15 (black line) and 17 (red line).

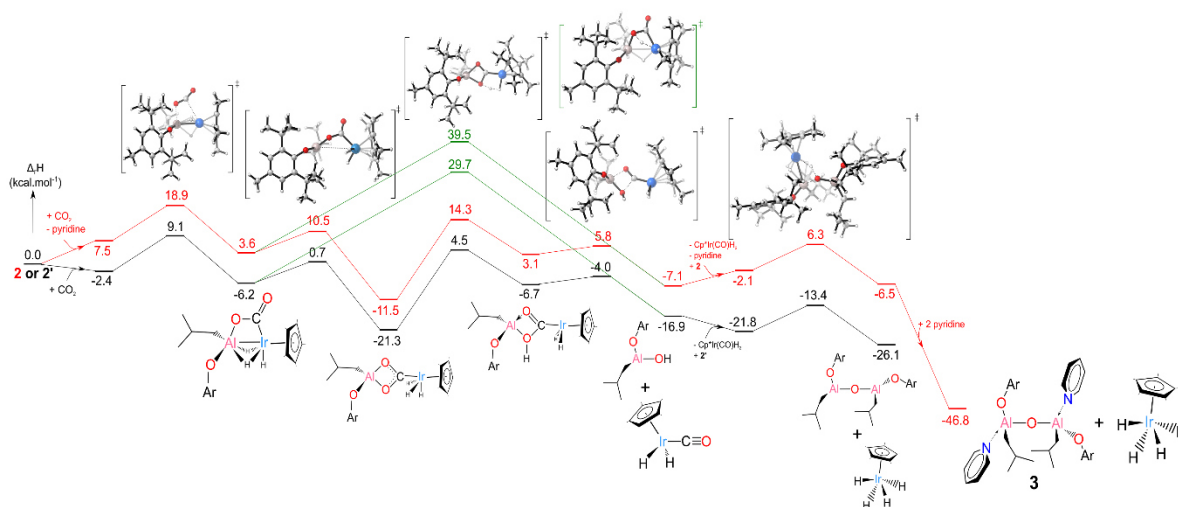


Figure S4. Computed enthalpy alternative pathways for the reaction of AdNCO with 17. The N-coordination is depicted in black whereas the O-coordination is the red line.

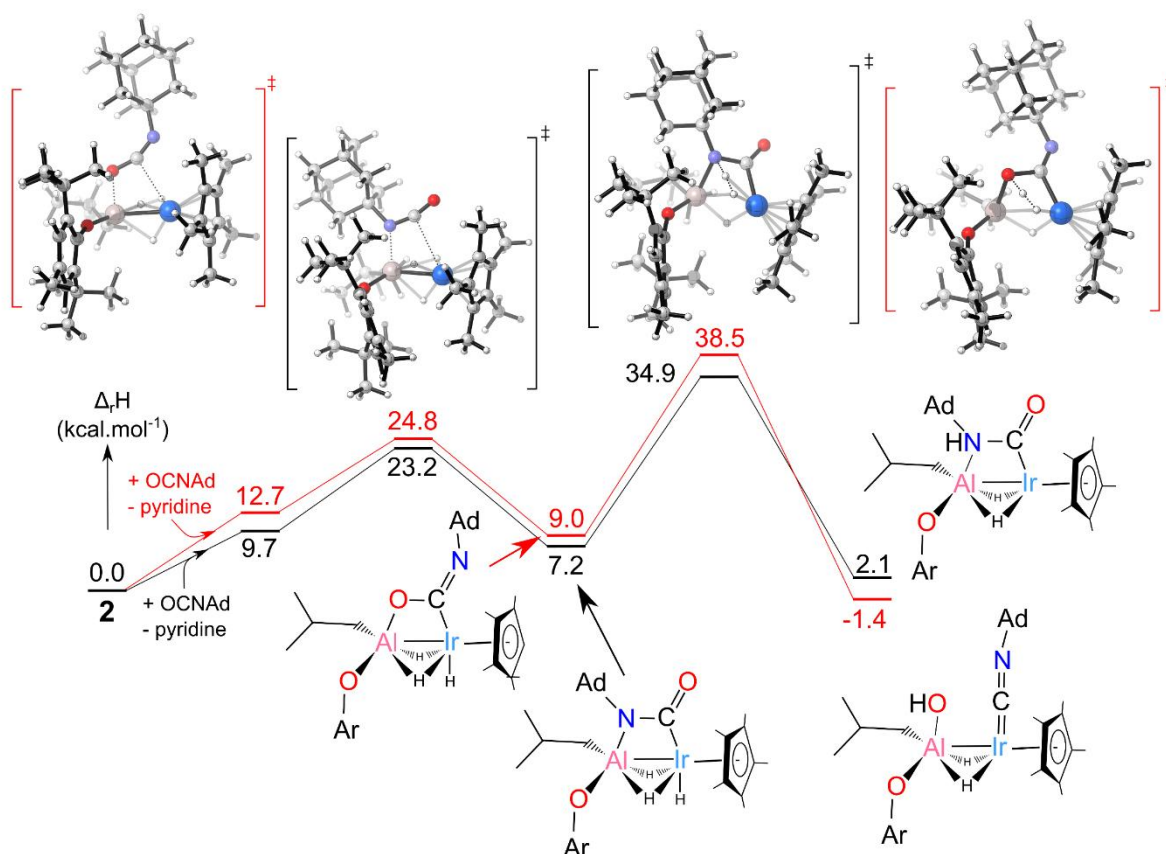


Figure S5. Other computed enthalpy alternative pathways for the reaction of AdNCO with 17.

